AN OVERVIEW OF RESID CHARACTERIZATION BY MASS SPECTROMETRY AND SMALL ANGLE SCATTERING TECHNIQUES

R. E. Winans and J. E. Hunt
Chemistry Division
Argonne National Laboratory
Argonne, IL 60439

Keywords: petroleum asphaltene, mass spectrometry, small angle X-ray and neutron scattering

ABSTRACT

The purpose of this presentation is to discuss what is known about the molecular structures found in petroleum resid from mass spectrometry and small angle neutron and X-ray scattering methods. The question about molecular size distributions and the occurrence of aggregation in the asphaltene fraction will be examined. Our understanding of this problem has evolved with the application of new analytical methods. Also, correlations with results from other approaches will be discussed. In addition, the issue of the nature of the heteroatom-containing molecules will be examined and the challenges that remain in this area.

INTRODUCTION

As light crudes disappear, there is a need to process heavier crudes with increasing amounts of resid. Petroleum resids can be fractionated by solubility with asphaltenes, the heptane insoluble fraction being the greatest problem in upgrading processing. This fraction is more aromatic than any of the other fractions and contains much of the heteroatoms and metals. Speciation of asphaltenes is extremely difficult and even measuring an accurate molecular weight distribution is problematic. As more is learned about the nature of petroleum asphaltenes, their apparent molecular weights are being lowered. Much of this information is the result of mass spectrometric and small angle X-ray and neutron scattering measurements. These studies suggest that asphaltenes are comprised of molecules with molecular weights less than 1500 and typically are aggregated even in high temperature processing.

Mass Spectrometry

Because of the low volatility of the various components of resid, direct thermal or laser desorption in the MS source has been the most successful MS method to characterize these complex mixtures. Various MS methods have been used including: field ionization mass spectrometry (FIMS), low-voltage (LVMS) and chemical ionization (CIMS), laser desorption mass spectrometry (LDMS), and high resolution mass spectrometry (HRMS).

Some of the first work using this method was reported by Boduszynski, who described a multistep separation followed by characterization of a series of atmospheric resids. The volatile fractions were separated by vacuum distillation and the non-distillable fraction was separated by a sequential elution fractionation (SEF).[1] FIMS data was shown for one of the suite of separation fractions. The mass ranges broaden with succession fractions and the average molecular mass increased until they reached the first SEF fraction, then there was a decrease in subsequent fraction. It was stated that the mass distribution varied with the petroleum source. No significant amount of ions were observed at over a mass of 1900. Although no data was shown, it was stated that field desorption MS gave similar results to FIMS. A more recent FIMS study looked at high molecular weight hydrocarbons from a crude oil and solid bitumen.[2] Several series of hydrocarbons up to C_{110} were observed, which corresponds to an upper mass of ~1500, consistent with what has been seen in other studies.

A Middle East vacuum resid was separated by solubility into four fractions: pentane soluble oil, heptane soluble pentane insoluble resins, cyclohexane soluble/heptane insoluble asphaltenes [1], and cyclohexane insoluble asphaltenes [2].[3] These fractions were analyzed by thermal volatilization (50-300 °C), low voltage low resolution, mass spectrometry (triple quadrupole MS). The measured average mass decreased within the series: oil (615), resin (485), asphaltene 1 (440) and asphaltene 2 (410). Also, the yields from the thermolysis decreased with an increase in the series and they speculated that upper bounds molecular mass may be higher. However, since the FIMS data showed the same trends, the relative ratios of molecular weights between the fractions may not change even if the entire sample was ionized. CIMS gave similar results to the low voltage experiment.

Although HRMS has been one of the methods of choice for characterizing volatile petroleum fractions, it has only more recently been applied to the complex polar resid fractions.[4,5] In the HRMS studies, the samples were desorbed from a high temperature probe that was heated from 200-700 °C. Quantitative experiments showed that >95% of the samples, even the asphaltenes, were desorbed. In both HRMS and LDMS, the oil samples gave a larger average molecular weight[5] distribution compared to the asphaltene samples. This was also the case in the comparison of a non-colloidal (soxhlet extractable) asphaltene. However, the size of the aromatic rings were larger for the asphaltene compared to the oil, as seen in Figure 1. From HRMS data, formulae can be calculated that can yield the type of data shown in Figure 1. The oil, aromatic cores, contained on an average, longer aliphatic side chains that increased the average molecular weight and decreased the tendency for forming colloids. Also, the yield of heteroatom containing molecules was much greater for the asphaltene, as is shown for sulfur in Figure 1.

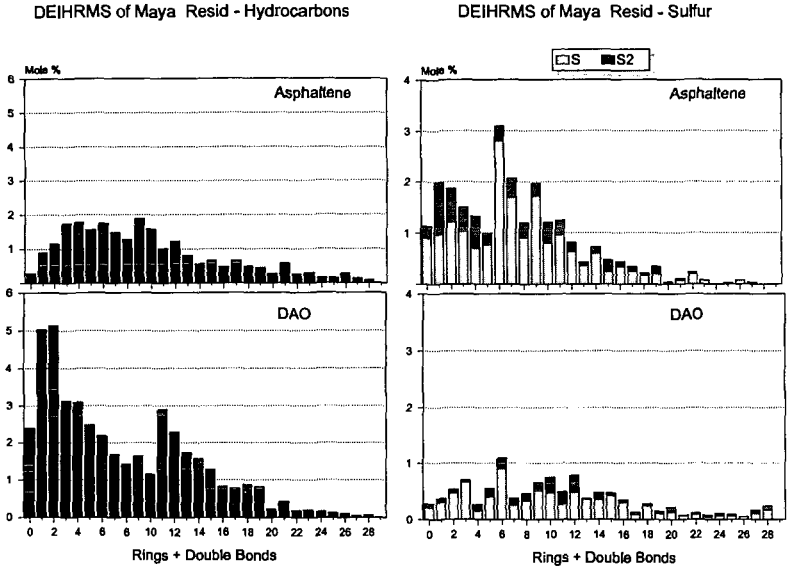

Figure 1. Double bond equivalent distributions for hydrocarbons and sulfur compounds from DEIHRMS analysis.

Small Angle Scattering

Using small angle X-ray and neutron scattering methods, the nature of disordered materials over length scales of 6-6000 Å can be observed. Depending on the system, the methods can provide information on molecular or particle size, shape, and surface properties. X-rays scatter off electrons, which are z number dependent phenomena, while neutrons scatter off the nucleus and are dependent on the scattering length density, which can even vary between isotopes such as hydrogen and deuterium.

Initial studies using SAXS suggest that vacuum resid asphaltene particles dispersed in resid oil are spherical aggregates that range in radii from 30-60 Å with a polydispersity of 15-20%, depending on the petroleum source.[6] Using SANS, it has been shown that the size of the asphaltene aggregates do not change with variation of solvent composition for toluene/pyridine mixtures and concentrations of asphaltene in solution. However, from SANS analyses of coal pyridine extracts, it has been shown that pyridine is not a good solvent for complex polar mixtures and does not yield true solutions.[7]

Maya-derived asphaltenes were studied by SANS in d_{10}-1-methylnaphthalene from 20-400 °C. Using a modified Guinier analysis, it was shown that the colloidal materials were rod-shaped at the lower temperatures.[8] These rod-shaped particles had a fairly uniform radius but were polydispersed in length. At high temperature, spherical particles formed resulting in uniform 12 Å spheres at 400 °C. Scheme 1 depicts changes in particle shape and size with temperature. The changes at high

temperature were irreversible and secondary density with covalent bond formation probably occurred. The oils were non-aggregated and showed no scattering.

SCHEME 1

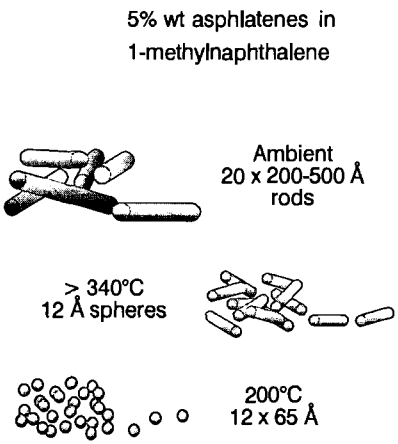

Also using SANS, it was found that the size of the colloidal asphaltene particles decreasing with heating as with increasing with dilution with resin material, and increase with the addition of n-hexane.[9] Apparently resin makes a better solvent than pyridine. Recently, the age hardening of resin was followed by both SAXS and SANS.[10] The asphaltene macrostructure appears not to change with aging and the major effect is the changes in the maltenes.

CONCLUSIONS

From MS and small angle scattering studies, it is apparent that petroleum asphaltenes are colloidal in nature even in "good" solvents and at high temperatures. They are not large polycyclic aromatics, but instead have a maximum ring number of typically 10-11, with the average being 5-6. Asphaltenes are rich in heteroaromatic compounds.

ACKNOWLEDGMENTS

This work was performed under the auspices of the Office of Basic Energy Sciences, Division of Chemical Sciences, U.S. Department of Energy, under contract number W-31-109-ENG-38.

REFERENCES

1. Boduszynski, M. M. *Energy Fuels* **1987**, *1*, 2-11.
2. del Rio, J. C.; Philp, R. P. *Org. Geochem.* **1999**, *30*, 279-286.
3. DeCanio, S. J.; Nero, V. P.; DeTar, M. M.; Storm, D. A. *Fuel* **1990**, *69*, 1233-1236.
4. Miller, J. T.; Fisher, R. B.; Thiyagarajan, P.; Winans, R. E.; Hunt, J. E. *Energy Fuels* **1998**, *12*,1290 -1298.
5. Hunt, J. E.; Winans, R. E.; Miller, J. T. *Prepr. Pap. - Am. Chem. Soc., Div. Fuel Chem.* **1997**, *42*, 427-430.
6. Storm, D. A.; Sheu, E.Y.; DeTar, M. M. *Fuel* **1993**, *72*, 977-981.
7. Storm, D. A.; Sheu, E. Y. *Fuel* **1995**, *74*, 1140-1145.
8. Thiyagarajan, P.; Hunt, J. E.; Winans, R. E.; Anderson, K. B.; Miller, J. T. *Energy Fuels* **1995**, *9*, 829-33.
9. Espinat, D.; Ravey, J. C.; Guille, V.; Lambard, J.; Zemb, T.; Cotton, J. P. *J. Phys. IV* **1993**, *3*, 181-184.
10. Scarsella, M.; Mastrofini, D.; Barre, L.; Espinat, D.; Fenistein, D. *Energy Fuels* **1999**, *13*, 739-747.

PETROLEUM ASPHALTENE MOLECULAR SIZE AND STRUCTURE

Henning Groenzin and Oliver C. Mullins
Schlumberger-Doll Research
Ridgefield, CT 06877

Key words: Asphaltene molecular size, Asphaltene molecular structure, Fluorescence depolarization

Abstract

The rotational correlation times of individual petroleum asphaltene molecules have been determined using fluorescence depolarization techniques, addressing an active, long standing controversy. Using simple theoretical models and using model independent comparisons with known chromophores, a range of asphaltene molecular diameters is obtained of 12 Å to 24 Å and indicates a molecular mass for asphaltene molecules of 500 to 1000 amu. An alkyl-substituted aromatic hydrocarbon with 7 fused rings is shown to correspond to the average molecular size of asphaltenes. Furthermore, the very strong correlation between molecular size and individual chromophore size establishes that the bulk of asphaltene molecules possess 1 or 2 aromatic chromophores per molecule.

I. INTRODUCTION

Petroleum asphaltenes are the heaviest, most aromatic component of crude oil. Asphaltenes are a complex molecular mixture which are colloidally dispersed in crude oil with a mass fraction of 0 to 10% or more.[1-6] Asphaltenes generally impede producing, transporting and refining of crude oil resources for a variety of reasons; mitigation of deleterious effects requires a thorough knowledge of the chemical and physical properties of asphaltenes. In addition, the heavy ends of crude oils have many familiar applications related to protective coatings and road paving which can be enhanced by judicious application of asphaltene science. Many bulk properties of asphaltenes have been extensively studied by traditional methods such as NMR, IR, EPR, XANES and optical spectroscopy revealing a great deal about their molecular structure and aggregation propensities.[1-6]

In spite of the wealth of information about asphaltenes, several fundamental properties are not known. The molecular weight of asphaltene molecules has been a matter of controversy for more than a decade. Colligative methods such as vapor pressure osmometry (VPO) generally yield high values[1-6] quite possibly due to aggregation. Mass spectral techniques yield much lower values (in spite of significant effort to rule out fragmentation).[7-9] In addition, there has been considerable uncertainty about the (dominant) number of fused aromatic rings in the asphaltene moieties; estimates have ranged from 4 to >20.[1-6] Scanning tunneling microscopy (STM) has been used to image directly the aromatic (conductive) components of asphaltene molecules.[10] Size estimates of the fused aromatic ring moieties from these images are approximately 10 Å. NMR[11] and optical techniques[12] indicate 7 fused rings on average. Furthermore, there has been uncertainty in the number of fused ring systems per asphaltene molecule with estimates varying widely.

Here, we analyze the fluorescence depolarization rates of very dilute solutions of asphaltenes. These rates give the molecular size with a robust, widely used model. In addition, we analyze known chromophores to provide a model independent analysis of these results. Furthermore, the known dependence of chromophore size to spectral properties has allowed us to correlate the rotation rate of chromophores imbedded in asphaltene molecules with the rotation rate of the molecule as a whole. The excellent correlation of chromophore size to total molecular size over a very broad range strongly implies that asphaltene molecules have one or two fused ring systems per molecule.

II. EXPERIMENTAL SECTION

For all solutions used for fluorescence work, we checked optical densities using a CARY 5 UV-visible-NIR spectrometer. For collection of fluorescence spectra, we employed the PTI C-72 + A-720 fluorescence spectrometer using a 75 watt Xe compact arc lamp source.

The PTI C-72 system was used for collection of fluorescence time-dependent depolarization spectra. This system employs a PTI GL-3300 nitrogen laser source along with a PTI GL-302 high-resolution dye laser with a fiber optic coupling to the measurement cell to excite the

fluorescence. The excitation and emission light from the cell are oriented 90° from each other with vertical polarization defined to be perpendicular to this plane. The wavelength of the PTI model 101 M emission monochromator is fixed while two Glan-Thompson polarizers are used to select the polarizations. One polarizer is placed at the output of the fiber optic, immediately before the measurement cell, and the other polarizer is placed at the entrance to the emission monochrometer. Fluorescence time decay curves are collected for four polarizations; vertical on the source side, vertical on the emission side (v-v), vertical-horizontal (v-h), horizontal-vertical (h-v), and horizontal-horizontal (h-h).

The following procedure is used to acquire the time decay spectra; the laser firing triggers a box car delay gate which then triggers a high voltage pulse at known delay to the PMT. The short duration of the high voltage pulse "turns on" the PMT for a short time interval. The integrated current over this time interval from the PMT is detected. The delay time is sequentially scanned over the desired time rauge providing the fluorescence decay curve. The time resolution of the system is about 80 picoseconds.

A complete data set for one excitation and emission wavelength pair corresponds to acquisition of the four polarization combinations mentioned above. Typically, the total acquisition time for the four curves is 2 hours. Reproducibility of signal levels were checked periodically during the acquisition time to validate the data. Duplicate (or more) runs were performed for all wavelength pairs to assure precision. Typically, chi-square values of 1.2 or less were obtained for a good run. Changes in laser power during the run was associated with large values of chi-square.

The v-h curve has a higher intensity than the v-v curve. This is due to the fact that horizontal and vertical polarized light have different transmission efficiencies through the emission channel of the instrument. This effect can be compensated by introducing a calibration factor, which is usually denoted with a capital G and is defined as $G = I_{hv} / I_{hh}$. Where I_{ij} refers to excitation with i polarization and emission with j polarization. All experimental data sets are corrected by multiplication of G with I_{vh}. I_{vv} then refers to $I_{\parallel}$, and $I_{vh} \cdot G$ to $I_{\perp}$.

The crude oil sample we used was obtained from Kuwait (UG8). We prepared the n-heptane insoluble asphaltenes from this oil. Optical densities of all solutions were kept below 0.2 OD to avoid complications from self absorption. We maintained asphaltene concentrations at or below 0.025 g/liter for analysis. All rotational correlation times were determined at room temperature 19°C, and in toluene with a viscosity of 0.59 cP. Two dyes, obtained from Aldrich Chemicals, were also used in this study, octaethyl porphyin (OEP) and a solar dye, N,N'-Ditridecyl-3,4,9,10-perylenetetracarboxylic diimide.

In order to determine the rotational correlation time of the anisotropy decay, a difference curve $D(t)$ and a sum curve $S(t)$ according to Eq. 1 and 2 were created and fitted by a least squares method. The sum curve corresponds to the fluorescence decay alone. For the fluorescence intensity decay (sum curve) a double exponential decay was assumed. Since the anisotropy decay is much faster than the fluorescence decay for our cases, then the difference curve is governed by the anisotropy decay. Consequently, the difference curve was fitted in accordance to the theory to a single exponential decay. A mean lifetime of the fluorescence intensity decay was calculated and the rotational correlation time was obtained by combining the mean fluorescence intensity lifetime of the sum curve with the fluorescence intensity lifetime of the difference curve according to Eq. 3.

III. THEORY

We use the anisotropy decay treatment[13] which approximates molecules as spheres. This model is widely used to analyze experimental data in part because inclusion of moderate molecular asymmetries does not affect calculated parameters too much.

The following definitions are used:

$$D(t) = I_{\parallel}(t) - I_{\perp}(t) \tag{1}$$

$$S(t) = I_{\parallel}(t) + 2I_{\perp}(t) \tag{2}$$

and

$$r(t) = \frac{D(t)}{S(t)} \tag{3}$$

where $I_{\parallel}(t)$ and $I_{\perp}(t)$ denote a detection of light linear polarized parallel and perpendicular to the linear polarized excitation and $r(t)$ represents the anisotropy of the fluorescence emission. The anisotropy is given by[13]

$$r(t) = \frac{2}{5} e^{-6Dt}. \tag{4}$$

where D is given by

$$6D = \frac{kT}{V\eta}, \tag{5}$$

where η is the viscosity of the solvent, which makes it easy to relate the fluorescence anisotropy to the volume of the sphere. The decay time of the anisotropy $\tau_{r,sph}$, the parameter of our experiment, can now be written as

$$\tau_{r,sph}^{-1} = \frac{kT}{V\eta}. \tag{6}$$

IV. REULTS AND DISCUSSION

Figure 1b shows the fluorescence emission spectrum of a dilute solution of UG8 asphaltene obtained with 365 nm excitation. This spectrum represents the overlapping spectra of the many chromophores contained within the asphaltene and indicates the range of aromatic moieties in asphaltenes. The asphaltene fluorescence emission is significant in the range of from 400 nm to 650 nm indicating the number of fused rings in the asphaltene chromophores is on the order to 4 to 10.[12] By selection of excitation and emission wavelength, one can select a subset of chromophores. Long wavelength excitation precludes excitation of small chromophores. Correspondingly, with short wavelength excitation, detection of fluorescence from large chromophores can be precluded by detecting short wavelength emission; large chromophores emit long wavelength fluorescence. The full range of chromophores is probed by tuning the excitation wavelength over the relevant spectral range, while keeping a fixed wavelength difference between excitation and emission.

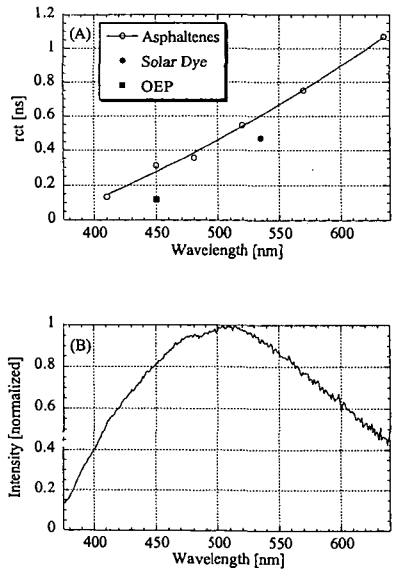

Figure caption 1. a) The rotational correlations of asphaltenes (and two dyes) vs emission wavelength. For each wavelength, the excitation wavelength is about 40 nm to shorter wavelength. b) the emission spectrum of the asphaltenes, showing the relevant spectral range.

Figure 1a shows the rotational correlation time of asphaltenes as a function of the emission wavelength. These emission wavelengths correspond to the largest populations of asphaltene chromophores as seen in Fig. 1b. For each point in Fig. 1a, the excitation wavelengths are ~40 nm to shorter wavelength. In addition, two known chromophores are also plotted in figure 1a to provide a model independent estimate of molecular size and molecular weight. Figure 1a is rich in results. The variation of a factor of 10 for the rotational correlation times for the most prominent asphaltene molecules. Using Eq. 6, one finds that the radius varies by about a factor of two. In table 1, we list molecular rotational correlation times along with the calculated diameters.

Table 1. Fluorescence absorption and emission wavelengths, rotational correlation times and the molecular diameter for asphaltenes and two dyes.

Sample	λex (nm)	λem (nm)	rtc (ns)	Diameter(Å)
Asphaltenes	365	410	0.1340	12.0
	406	450	0.3115	15.9
	440	480	0.3561	16.6
	480	520	0.5464	19.2
	530	570	0.7518	21.3
	595	635	1.0688	24.0
Solar Dye	480	535	0.4704	18.2
OEP	406	450	0.1194	11.6

Table 1 shows the diameters for the asphaltenes to be in the range of 12 Å to 24 Å. The STM results quoted a mean value of the aromatic component of asphaltenes to be 10 Å in diameter. The fluorescence depolarization technique is sensitive to the size of the entire molecule, while the STM method is sensitive to the size of the aromatic portion only which is roughly 40% of the molecule. Both techniques yield comparable and small sizes for the asphaltene molecules.

Table 1 also lists the diameters for two dyes. Previously, the size of a metallo-OEP was determined by measuring the rotational correlation time using the very different technique, perturbed angular correlation of gamma rays (PAC).[14] (The central metal in the porphyrin has no impact on the diameter of the porphyrin.) In that work, a spherical model was used and a diameter of 11.6 Å was found in excellent agreement with results reported here.

The two disk shaped dyes provide a good estimation of the molecular weight for asphaltenes. The rotational correlation time of the porphyrin OEP is at the lower limit for the asphaltenes. The molecular weight of the porphyrin is 535 amu giving the lower value estimation for the asphaltene molecular weights of 500 amu. The rotational correlation time of the solar dye is located roughly at the mean correlation time of the asphaltenes. The molecular weight of the solar dye is 755 amu giving an estimate of 750 amu for the mean asphaltene molecular weight. Extrapolating the size, molecular weight relation, we estimate the maximum molecular weight of the asphaltenes to be about 1000 amu.

Fig. 1 also shows that there is a monotonic, order-of-magnitude increase in the rotational correlation time across the asphaltene spectral range. That is, there is a strong correlation between the size of the asphaltene chromophore given by the emission wavelength and the size of the molecule, given by the rotational correlation time. This correlation requires that asphaltene molecules have only one or two chromophores per molecule. If an asphaltene molecule possessed say 10 chromophores per molecule, then there would be no correlation between chromophore size and molecular size. A small chromophore attached to a large molecule would exhibit the slow rotational correlation time of the entire, large molecule. The fact that we measure fast rotation for small chromophores and a factor of 10 slower rotation for large chromophores means that these chromophores are an appreciable fraction of the asphaltene molecule. Thus, asphaltene molecules possess one or two chromophores per molecule on average.

V. CONCLUSIONS

The asphaltene rotational correlation times have been measured and corresponding asphaltene molecular diameters are in the range of 12 Å to 24 Å. Using known chromophores, asphaltene molecular weights are estimated to be in the range of 500 to 1000 amu. Furthermore, a strong correlation between chromophore size and asphaltene molecular size indicates that asphaltenes possess 1 or 2 chromophores per molecules, confirming the small molecular weights. Our results

are consistent with previously reported STM results and mass spectroscopy results for petroleum asphaltenes. The confluence of evidence from three very different techniques should end the controversy over the values of asphaltene molecular weights.

VI. REFERENCES

1) G. V. Chilingarian, T. F. Yen, Eds., "Bitumens, Asphalts, and Tar Sands," Elsevier Scientific Publishing Co., New York, (1978)
2) J.G. Speight, "The Chemistry and Technology of Petroleum," Marcel Dekker, New York, (1980)
3) B.P. Tissot, D.H. Welte, "Petroleum Formation and Occurrence," Springer-Verlag, Berlin, (1984)
4) J.W. Bunger, N.C. Li, Eds., "Chemistry of Asphaltenes," American Chemical Society, Washington D.C., (1984)
5) E.Y. Sheu, O.C. Mullins, Eds., "Asphaltenes, Fundamentals and Applications," Plenum Press, New York, (1995)
6) O.C. Mullins, E.Y Sheu, Eds. "Structures and Dynamics of Asphaltenes," Plenum Press, New York, (1998)
7) M.M. Boduszynski, in ref. 4.
8) M.M. Boduszynski, Energy & Fuels, 2, 597, (1988)
9) J.T. Miller, R.B. Fisher, P. Thiyagarajan, R.E. Winans, J.E. Hunt, Energy & Fuels, 12, 1290, (1998)
10) G.W. Zajac, N.K. Sethi, J.T. Joseph, Scan. Micros. 8, 463 (1994)
11) R. Scotti, L. Montanari, Ch 3 in ref. 6.
12) O.C. Mullins, Ch 2 in ref. 6.
13) T. Tao, Biopolymers, 8, 607, (1962)
14) O.C. Mullins, M. Kaplan, J. Chem. Phys. 79, 4475, (1983)

USE OF LASER TECHNIQUES FOR THE STUDY OF ASPHALTENE AGGREGATION AND ADSORPTION.

Sócrates Acevedo*,[1], María A. Ranaudo[1], Jimmy Castillo[2], Manuel Caetano[2] and Alberto Fernández[2]. Labs of Físico Química de Hidrocarburos[1] and Espectroscopía Laser[2], Escuela de Química, Facultad de Ciencias, 47102, Caracas, 1041 Venezuela.

Keywords: Asphaltenes, Adsorption, Laser

Introduction.

The adsorption of asphaltenes on mineral surfaces is an important phenomena related to many process in crude oil processing such as changes in humectability of oil well, asphaltene precipitation during production, transportation and storage, pore well clogging, catalysis fouling, etc. This has promoted some studies of asphaltene adsorption in the past[1,2]. Most of these studies, performed with very diluted solutions, afforded L-type isotherms, suggesting the saturation of the interface without further adsorption of sample. However, as shown below, using several laser techniques, we found that adsorption of asphaltenes on silica and glass surfaces could lead to step-wise adsorption and to the formation of thick multilayers which in some cases amount to grams of sample per gram of adsorbent. In this communication we review our previous work in this area and some new results are presented.

Methods.

Furrial crudc oil (20° API, and 10% asphaltene) was used. This crude is from Monagas State in the east part of Venezuela and was selected due to the severe asphaltene precipitation problems it presents. Asphaltenes were obtained by precipitation, by the addition of 40 volumes of n-heptane to the crude oil as described elsewhere[3]. Commercial samples of silica gel for chromatography were used as the adsorbent. Using the dye method (methylen blue-water), an area of about 35 m^2/g was obtained for this solid when an area of 120 A^2 per molecule was used for the dye[4]. For kinetic runs, small silica plates (2.5x1 cm^2, 24 mg of silica) were introduced in small glass vials containing 8 mL of asphaltene-toluene solution. These vials were well sttopered to avoid solvent evaporation. Changes in absorbance with time was continuously monitored by passing a He-Ne laser beam (632.8 nm) throught the vials and the intensity registered by using a photodiodc. In one experiment (asphaltene concentration equal to 200 mgL^{-1}) the solution was stirred by using a small magnetic stirrer. Since no difference in rate was observed with and without stirring all experiment were carried out without stirring. A desorption experiment was performed as follows: Asphaltenes were adsorbed on a silica plate from a 200 mgL^{-1} solution as described above. After 72 h, the quantity of sample adsorbed was equivalent to 133 mgL^{-1}. The plate was withdrawn, dried and embedded in pure toluene. The absorbance increase was monitored as usual and after 50 h no further change was observed. The amount desorbed was equivalent to 4 mgL^{-1}.

Isotherms were measured using the photothermal surface deformation (PSD) method described earlier[3]. Briefly, in this method the amount of solute adsorbed on the surface is determined directly. That is, by using a procedure similar to the one described for the kinetic runs (see above) the sample was adsorbed on the silica plate. After the required time, the plate was withdrawn, dried and set for analysis. This was performed by using two lasers, one for pumping and the other as the probe. The pumping beam heat the sample and produces a dilatation that is proportional to the sample mass. This is measured by the probe beam. Signal calibration was performed by comparing with the adsorption measured by tramitance measured as described in the kinetic runs.

In another experiment a silica plate was contacted with a toluene solution of asphaltene (5000 mgL^{-1}) during 24 h in the same way as described above for the kinetic studies. After this time, the plate was withdrawn from this solution, allowed to dry and the sample adsorbed was determined by weight difference. After this, the same plate was contacted with a fresh solution of the same concentration and the procedure was repeated for one day periods during 21 days.

Number average molecular weight (M_n) and molecular weight distribution (MWD) were measured by GPC in THF as described earlier[5]. The samples were analyzed as follows: Toluene solution of asphaltenes were contacted with silica for periods of 1, 4, 8 and 24 hours. After these times, an aliquot was withdrawn, the toluene was evaporated, the residue dissolved in THF and the above M_n and MWD of Furrial asphaltenes were determined in

each case.

When required the area per asphaltene molecule A_a was estimated from equation 1:

$$A_a = 0.166(MA_s/v) \qquad 1$$

Here A_s is the area of the silica in m^2/g, v the sample adsorbed is in mg/g, A_a is in A^2 per molecule and M is the molecular weight.

Results.

On Table 1 the values for the apparent first order constants *k*, obtained for the studied solutions are shown. These were obtained by fitting the results to a first order kinetics. The fittings were quite good for the 5-50 mgL^{-1} runs. However, for the 200 and 400 mgL^{-1} runs the results suggested that the readings at long times should correspond to a slower rate (see Figure 1). Results from the desorption experiment (see above) showed that desorption from the surface could be neglected in the concentration range examined. The adsorption isotherms obtained are shown in the Figure 2. Note that for 18 and 48 h, the isotherms are L-type whereas the one measured at 96 h shows a tendency towards H-type. In other words, the isotherm slope increases with time and moves to smaller c_s values in the more diluted region. Using the procedure described above, no significative changes in M_n or MWD were detected as a function of the contact time between the asphaltene solution and the silica. M_n values remained constant around 1000 and the MWD measured was in the range from 12000 to 200 in all cases.

In order to have an approximated idea of the amount of asphaltenes that could be adsorbed when the surface is in permanent contact with a liquid with a constant asphaltene concentration, such as the the surfaces in the crude oil well, the experiment above, where the surface is contacted with fresh toluene solutions after 24 h periods was carried out. After 21 days we found that the equivalent of 10g of asphaltene adsorbed on one gram of silica.

Discussion.

Since adsorption rates were not changed significantly by stirring (see above), diffusion to the outer surface of the solid is not rate determining. Also neither average molecular weight nor molecular weight distribution were affected by adsorption (see Methods), suggesting that diffusion into solid pores is not kinetically important. Thus it appears that diffusion along the surface to find a site for adsorption is rate determining, since desorption in this concentration range is unimportant. Using a Langmiur treatment for the dye we found that only 14.4 mg/g of this compound were needed to saturate the silica surface. By using any reasonable value of A_a for asphaltene lying on the surface, one should expect saturation values much smaller than this. However, according to Figure 2, these "saturation" values are higher than 20 mg/g and show a slow increase with time. These results and the first order found, suggest that when asphaltenes are adsorbed they create new adsorption sites were other asphaltene molecules could be adsorbed. In this way the sample could pile up at different places in the surface and by the time the silica surface is completely covered an asphaltene multilayer is already present. This would explain the somewhat slower adsorption rate found at long times with the more concentrated solutions (see above and Figure 1). Also, adsorption of small aggregates, such as dimmers, trimmers, etc is likely in this concentration range. Using a thermal lens technique it was suggested that aggregation of asphaltenes in toluene could begin at very low concentrations, probably around 50 mgL^{-1} [6].

When the adsorption of toluene solutions of asphaltene on glass plates was studied by the above PSD technique in a wider concentration range (0- 6000 mgL^{-1}) step-wise adsorption isotherms were found for several asphaltene samples (Furrial, Hamaca, Jobo)[3]. The occurrence of such steps as a result of the adsorption of large aggregates is an interesting possibility. In any case, thick multilayers were apparent from these adsorption measurements.

According to the results above, under appropriated conditions, very large quantities of asphaltenes could be adsorbed on silica (up to 10 g/g or more). This suggest that adsorption alone could easily leads to plugging of pore wells and other problems related to solid formation during oil production.

Conclusions.

Use of lasers, either in the usual tramitance mode or in the PSD mode allows the quantitative study of asphaltene adsorption. Also, reasonable inferences about aggregate formation in solution could be made from these studies. The first order adsorption rates measured in this work were found consistent with multilayer formation and aggregate

adsorption. The L-type isotherm found after 18 h is probably due to saturation of the surface by a multilayer of asphaltene formed either as usual, or by the adsorption of aggregates. Change of these isotherms with time after long periods are due to the adsorption of asphaltene or asphaltene aggregates on the multilayer. Since adsorption alone could lead to plugging of pores and the formation of organic solid deposits, treatment with surfactants and solvents should consider, as a very important consideration, the displacement of asphaltenes from the surface.

Acknowledgments.

Finantial support from CONICIT (Grant N° G97000722) and CDCH (Grants 03.12.4897/98, 03.12.3872/98, 03.12.4031/97, 03.12.4087/98) is gratefully acknowledged.

References.

1. S. H. Collins and J. C. Melrose, Soc. pet. Eng. SPE11800, 249 (1983).
2. González, G., and Middea, A. Colloids and Surfaces, 33, (1988), 217.
3. Acevedo, S., Castillo, J., Fernández, A., Goncalves, S., and Ranaudo, M. A., Energy and Fuels, 12, (1997), 386.
4. Giles, H. Ch. In: "Anionic Surfactant. Physical Chemistry of Surfactant Action". (E. H. Lucassen – Reynders, Ed). Surfactant Science Series. V 11. Marcel Dekker, Inc. 1981, Chap. 4.
5. Acevedo, S., Escobar, G., Gutiérrez, L. B., and D'Aquino, J., Fuel, 71, (1992), 1077.
6. Acevedo, S., Ranaudo, M. A,. Pereira, J. C., Castillo, J., Fernández, A., Pérez, P., and Caetano, M., Fuel, 1999, to be published.

Table I. Apparent first order rate constant *k*, for the adsorption of Toluene Solution of Furrial Asphaltenes on Silica[a].

Initial concentration ($mg\ L^{-1}$)	$k \times 10^3$ (min^{-1})[a]	$R^{2,b}$
5	1.09 ± 0.8	0.991
20	1.24 ± 0.3	0.993
50	1.12 ± 0.3	0.996
200[c]	1.62 ± 0.3	0.992
400[c]	0.79 ± 0.3	0.994

a: At Room temperature. b: Correlation coefficient for first order fitting. C: see text.

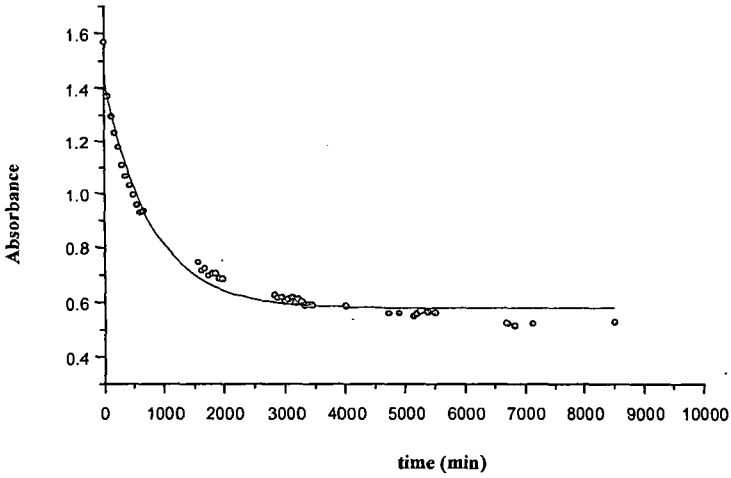

Figure 1. Adsorption kinetics for a toluene solution of Furrial asphaltenes (200 mg L^{-1}) obtained on silica at room temperature. Points are experimental and the curve is the fitting to a first order.

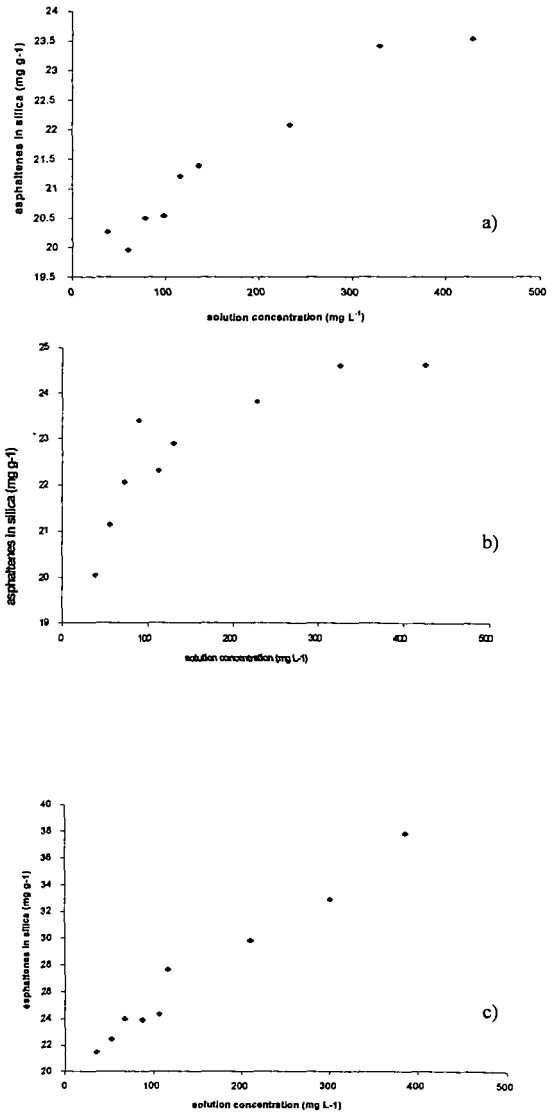

Figure 2. Adsorption isotherm of toluene solutions of Furrial asphaltenes on silica measured by PSD at room temperature. a) after 18 hours, b) after 48 hours, c) after 96 hours.

STUDY ON THE MICELLE SIZE OF ASPHALTENES IN VACUUM RESIDUE BY DIELECTRIC LOSS

M. Fujii , T. Yoneda, and Y. Sanada*
Advanced Catalysts Research Laboratory
Petroleum Energy Center, Japan
KSP D-1237, 3-2-1, Sakato, Takatsu-ku,
Kawasaki, Kanagawa 213-0012, Japan

* Honor Professor of Hokkaido University
16-1-1, Hiraghishi-ichijyo, Toyohira-ku
Sapporo, Hokkaido 062, Japan

KEYWORDS: asphaltene, micelle size, dielectric loss

INTRODUCTION

Asphaltene contained in heavy oils, such as crude oil or vacuum residue is obtained usually as the precipitates when adding alkane to heavy oil. It is defined as n-heptane insoluble-toluene soluble, for example. As asphaltenes are mainly composed of poly-condensed aromatics, they intend to form micelles in the oils by interacting each other, and their stacking governs physical and chemical properties of asphaltene rich heavy oils. A number of analyses have been made by using various kinds of measurements and micellar structural models have been proposed [1,2]. The size of micelle has been studied by using many techniques, such as X-ray diffraction (XRD), dielectric relaxation, rheological measurements, small angle neutron scattering (SANS) technique, X-ray absorption near edge structure (XANES) [3,4]. XRD was done for asphaltene powder, and the others were in various solvents. Therefore, it would not be clear the substantial size of micelles in the real heavy oil. During the course of characterization of asphaltene derived from Arabian heavy vacuum residue (AH-VR), we have found that the mass distribution was in the range from m/z=200 to 6000, having a broad peak near 1500 with a shoulder peak near 400, by means of laser desorption mass spectroscopy (LDMS) [5]. In this study, we have attempted to measure the dielectric response for AH-VR by an impedance analyzer, and found the loss peak due to asphaltene component. From the results about the effect on the concentration of asphaltene and resin in VR, the mechanism of micelle formation and the size of micelles are discussed.

EXPERIMENTAL

Samples used were AH-VR and VR fractions (b.p. of 793$^+$K) of the hydrotreated oil from AH atmospheric residue (616$^+$K). Asphaltene was prepared from VR with addition of n-heptane (solvent and VR ratio was 1g / 30ml). Maltene (n-heptane soluble) was separated to three fractions (i.e. saturate, aromatic and resin) by column chromatography. Hydrotreatment was performed in a fixed bed continuos flow reactor system, in which hydrodemetallization (HDM) and hydrodesulfurization (HDS) catalysts were installed respectively. The reactor system and reaction conditions were the same described previously except catalyst and LHSV of 0.75 hr^{-1} [5].

Dielectric loss was measured with a Hewlett-Packard Impedance Analyzer (HP4194A), connecting with Liquid Test Fixture (HP16452A) at 403K. Electrodes with diameter of 38 mm each have been kept space of 1 mm. The working frequency range was from 100 Hz to 15 MHz. Viscosity measurement was made using a TOKIMEC B type viscometer.

RESULTS AND DISCUSSION

In a condenser of parallel plates, the dielectric loss (ε'') is represented as follows:

$$\varepsilon'' = 1/2\pi f C_V R_p \quad (1)$$

where f is the frequency, C_V the capacity in vacuum ($= \varepsilon_0 A/d$), R_p the impedance, d the distance between electrode plates, ε_0 the dielectric constant of vacuum, and A the area of electrode [6]. As the conductivity (ρ) is equal to $d/R_p A$, eq.(1) becomes:

$$\varepsilon'' = \rho/2\pi f \varepsilon_0 \quad (2)$$

In our results, the values of ρ at range from 10^2 to 10^3 Hz were rather small than those of higher frequency. So, we evaluated the difference dielectric loss ($\Delta \varepsilon''$) calculated the following equation:

$$\Delta \varepsilon'' = (\rho - \rho_{100})/2\pi f \varepsilon_0 \quad (3)$$

where ρ_{100} is the ρ at 100 Hz.

The dielectric loss spectra for AH-VR and fractions derived from it are shown in Figure 1. For AH-VR two peaks were observed at the low frequency side (7.94×10^2 Hz) and the high side (3.98×10^6 Hz), which were appeared due to the existence of the dipole. As the high frequency peak was also observed for maltene, the low frequency peak was contributed from asphaltene. The loss spectra for saturate and aromatic were also shown in Figure 1 (The spectrum for resin was not obtained because of its poor fusibility). Dielectric loss curve for the saturate was almost flat, while the one for aromatic showed a clear peak at about 3.98×10^6 Hz . The dielectric loss curve for resin would not behave any particular peaks. This is due to that the resin fraction is defined as the difference of maltene and the sum of saturate + aromatic. Dielectric loss spectrum for the resin, which has more or less polarity, was broad without any particular peaks. The relation between a dielectric relaxation frequency and a rotation radius is known as Stokes-Einstein equation:

$$f = k_B T/4\pi \eta R_d^3 \quad (4)$$

where k_B is the Boltzmann constant, T the temperature, η the effective viscosity, and R_d the dipole moment weighted particle radius [7]. According to eq.(4), the dipole radius of asphaltene was calculated, that is 10.4 nm.

In order to built up the molecular structure of the asphaltene; we have provided the following characterization parameters: Mw (by LDMS)=2040, carbon aromaticity, fa (by ^{1}H-NMR)=0.52. Structural parameters of the asphaltene molecules were calculated by a computer aided structure analysis method [8], and average structure model was drawn, where we were taking consideration the fact that the LDMS result suggested cata type of aromatic condensed ring in shape [5]. The longitudinal size of the asphaltene molecule was about 6 nm, which was about a half of the micelle radius obtained above. This is reasonable value from the mechanism of stacking of asphaltene molecules, because they interact each other by their polarity of aromatic sheets and/or metallic ions.

Figure 2 shows the dielectric loss curves for the mixtures of asphaltene with maltene. When the asphaltene content increased from 15.3 wt% (corresponding to the composition of VR) to 20 wt%, the loss peak became larger and shifted to the lower frequency side. On the other hand, the peak became smaller and shifted to the higher side for the mixture with 5 wt% of asphaltene. It was noticeable that the peak shape was rather flat in the case of 10 wt%, which might show the uncontinuous change in size. These evidences imply that the shape of dielectric loss spectra depend upon the content of asphaltene. It has been investigated the surface and interfacial tensions system for asphaltenes in aromatic solvents and indicated possible asphaltene aggregation as well as the probable existence of critical micelle concentration [2,9]. From the frequency at the maximum intensity of dielectric loss, we can calculate the micelle size in medium. The micelle radius for 5 wt% of asphaltene content is 8.4 nm, 9.7 nm for 10 wt%, 10.4 nm for 15.3 wt% (as shown above) and 10.4 nm for 20 wt%, respectively. It is suggested a critical micelle formation point at the given asphaltene concentration, which is below 5 wt% in our case.

The spectra changes of resin content in VR matrix are shown in Figure 3. The

frequency at the maximum loss were almost unchanged at the range from 23 wt% (corresponding to VR) to 0 wt% of resin content in matrix as well as the viscosity of the same specimens. The facts suggest the size of micelles might be independent on resin content. The intensity changes would be caused by the change of relative content.

Further, we have obtained dielectric property for VR fractions derived from hydrotreated oils with HDM and HDS catalysts. Characterization data were illustrated in Table 1, where asphaltene content decreased from 15.3 wt% in the original VR to 7.6 and 5.7 wt%, respectively. Although molecular weight distribution by LDMS for HDM and HDS shifted slightly to lower side, averages molecular weight was almost unchanged. Chemical structure expressed with fa altered some extent with the hydrotreatment. In fact, structural parameters, such as the number of aromatic carbon, Ca, and the number of aromatic ring, Ra, were decreased by the hydrotreatment; Ca: 109 to 79 for HDM and 85 for HDS, Ra: 28 to 22 for HDM and 25 for HDS, respectively. Figure 4 shows the dielectric loss spectra for those VRs. The intensities for both samples decreased to the same extent and the shape was almost the same too. It is not clear why the shape of dielectric loss spectra did not change nevertheless decreasing the asphaltene content. From the results that metal content decreased from 121 ppm in the original VR to 66 and 31 ppm by HDM and HDS, respectively, it seems that the aromatic structure would be more effective on the intensity than metal. The loss spectra for these VRs became flat and the peaks were resultantly collapsing with the hydrotreatment, which was almost similar to that of 10 wt% of asphaltene as already illustrated in Figure 2. The micelle radii were calculated from the shoulder peak frequencies for reference, 9.3 nm of HDM and 10 nm of HDS, respectively. It would be suggested that the critical micelle formation point is deeply dependent upon the structural changes.

CONCLUSIONS

The micelle size of the asphaltene in Arabian heavy vacuum residue was investigated from the dielectric loss measurements at 403K. It was observed that the loss spectrum of asphaltene in AH-VR was in the wide range from 1×10^2 to 1.5×10^7 Hz having two peaks, and that the former was at low frequency and the latter was at high frequency. We found that the low frequency peak was contributed from asphaltene by comparing with that of maltene. The micelle size in VR was determined from the frequency at the maximum intensity of the loss spectra and the viscosity, using Einstein-Stokes equation, 10.4 nm in radius. This value was about two times of the length of the average molecular structure drawn from its characterization.

From the results of loss spectra changes with asphaltene and resin contents in maltene, and those for VR derived from the hydrotreated oils, it was found that the intensity of loss spectra was affected by not only asphaltene but also metal contents. And, it was also suggested that the aromatic structure would be more effective than metal.

Then, we discussed about the size of micelles determined from the loss spectra to make sure the mechanism of micelle formation. It was suggested that the micelle size might be depend upon the asphaltene content and the size of condensed aromatic rings of asphaltene, not upon the resin content, which implied the critical micelle formation point.

ACKNOWLEDGMENTS

This work has been carried out as a research project of the Petroleum Energy Center with the subsidy of the Ministry of International Trade and Industry.

LITERRATURE CITED
(1) Speight, J. G., *The Chemistry and Technology of Petroleum*, Marcel Dekker Inc.
(2) Yen, T. F. and Chilingarian, G. V., *asphaltenes and asphalts, 1*, Elsevier Science
(3) Fujii, M., Sanada, Y., Yoneda, T., and Sato, M., Prep. Div. Fuel Chem., ACS, 43, (3), 735(1998)
(4) Sheu, E. Y. and Mullins, O. C., *Asphaltenes Fundamentals and Applications*, Plenum Publishing
(5) Yen, T. F., Erdman, J. G. and Pollack, S. S., Anal. Chem., 33, 1587(1961)
(6) Nihonkagakukai edition, *Jikkenkagakukouza*, 9, Maruzen co.
(7) Sheu, E. Y., Storm, D. A. and Shields, M. B., Energy & Fuels, 8, 552(1994)
(8) Katayama, Y., Hosoi, T., Takeya, G., Nihonkagakukaishi, (1), 127(1975)
(9) Mohamed, R. S. and Ramos, A. C. S., Energy & Fuels, 13, 323(1999)

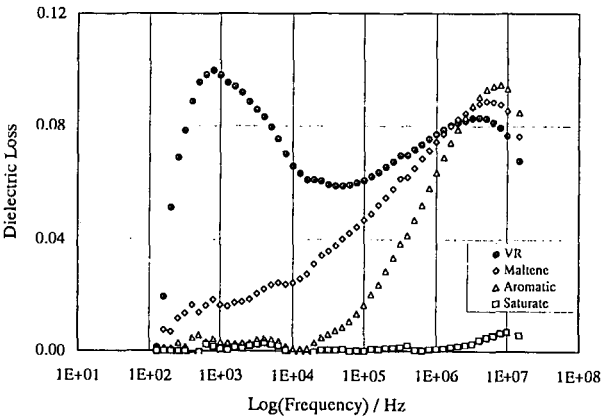

Figure 1. Dielectric loss spectra for AH-VR and fractions derived from it

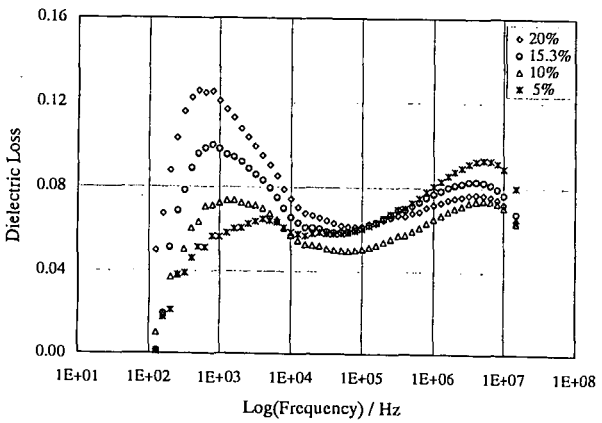

Figure 2. Dielectric loss spectra for mixture of asphaltene and maltene

Table 1. Properties of asphaltenes

Sample	Asph. Content	Density	H/C	Mw	fa	Ca	Ra
	wt%	g/cm3	-	LDMS	1H-NMR		
AH-VR	15.3	1.165	1.05	2040	0.52	109	28
HDM	7.6	1.180	1.07	2140	0.48	79	22
HDS	5.7	1.141	1.04	2130	0.54	85	25

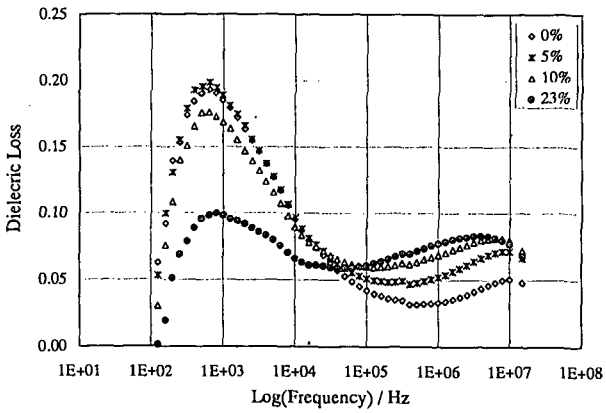

Figure 3. Dielectric loss spectra for mixture of resin and matrix

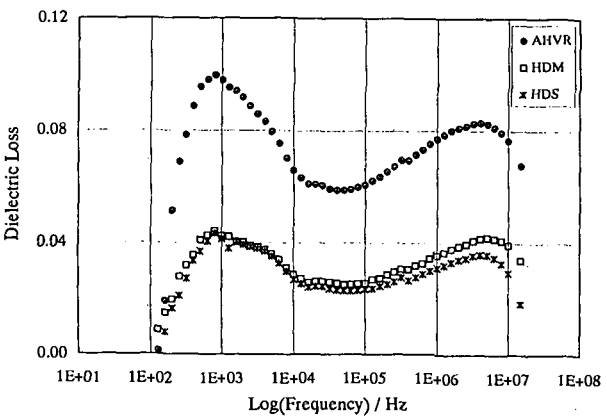

Figure 4. Dielectric loss spectra for VR obtained with hydrotreatment

COVALENT STRUCTURE AND MOLECULAR ARCHITECTURE OF ATHABASCA ASPHALTENE

O.P. Strausz, Department of Chemistry, University of Alberta, Edmonton, AB T6G 2G2, Canada; P. Peng, Guangzhou Institute of Geochemistry, Guangzhou 510640, People's Republic of China; J. Murgich, Centro di Quimica, Instituto Venezolano de Investigaciones Cientificas, Apartado 21827, Caracas 1020-A, Venezuela.

INTRODUCTION

Extensive research in the recent past has led to new insights into the composition,[1] covalent structure[2] and molecular architecture[3,4] of Athabasca asphaltene (AA). Employing thermolytic and chemolytic degradations such as the nickel boride (Ni/B) cleavage of the C–S bonds in sulfides, the ruthenium ions-catalyzed oxidation (RICO) of the C_{arom}–$C_{arom/aliph}$ bonds, the basic hydrolytic cleavage of the ≡CO–C(O)–C ester bonds and the BBr_3 cleavage of the ≡C–O–C≡ ether bonds yielded an array of products representing structural elements in the asphaltene molecules. Thus, the principal products from the mild thermolysis were homologous series of thiolanes, thianes, thiophenes, benzothiophenes, dibenzothiophenes, methylbenzenes and fluorenes. All these structures were *n*-alkyl substituted—in the C_{12}–C_{28} total carbon range—in such a fashion that upon ring cleavages at approriate places the entire carbon skeleton of the molecules could be stretched out into an *n*-alkane chain, pointing to the *n*-alkanoic origin of these cyclic structures. Significantly, cyclic terpenoid sulfides, abundant in the maltene fraction of the parent bitumen, appear to be lacking in the asphaltene. Additional products identified were: series of partially hydrogenated di-, tri- and tetrabenzothiophenes, two- and three-ring aromatics and hydroaromatics, and one-through three-ring naphthenes, all alkyl substituted with a total carbon number up to ~28, *n*-alkanes, iso- and anteisoalkanes and isoprenoids. Among the polar products the dominant ones were *n*-alkanoic acids, *n*-alcohols and *n*-alkanoic amides (originally hydrogen-bonded acid–amine complexes?), all exhibiting a marked even-to-odd carbon preference. The latter feature is the fingerprint of a relatively recent origin related to secondary microbial degradation of the precursor oil of the present-day bitumen. Small quantities of alkylpyridines and alkylquinolines were also detected.

The Ni/B cleavage of the sulfide bonds in acetone-extracted AA afforded about 2.5% aromatics, 2.5% polars and 0.1% saturates. The saturates comprised entirely biomarkers, *n*-alkanes, di-, tri- and pentacyclic terpenoids including γ-cerane and regular steranes, all corresponding to distribution representing a significantly lower level of thermal maturity than that of the maltene of the parent bitumen. These compounds were originally present in the asphaltene molecule as sulfur-bound appendages and possibly bridges. And, what is from a structural point of view an even more noteworthy phenomenon, is the drastic fourfold drop in the MW of the residual asphaltene after Ni/B reduction, proving a molecular architecture in which four asphaltene core segments are bound together by three (or more) sulfur atoms, e.g.

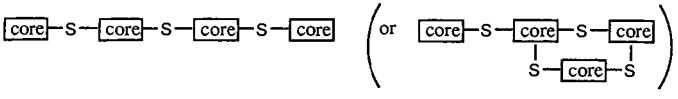

The RICO produced, among other products, series of *n*-alkanoic and α,ω-di-*n*-alkanoic acids, signifying the presence of *n*-alkyl side chains and bridges attached to aromatic carbons.

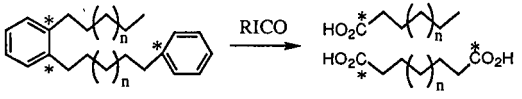

Lastly, cleavage of ester and ether bonds resulted in the formation of *n*-alkanoic acids and *n*-alcohols, again dominated by the even carbon members.

In the present context the important structural elements in the asphaltene molecules are the alkyl (polymethylene) bridges connecting aromatic or naphthenic rings, the alkyl, ether and ester appendages as well as other types of appendages. Long bridges (up to C_{28}) can connect distant carbon sites and create loops and internal cavities. From RICO studies the evidence for the existence of long polymethylene bridges connecting two aromatic carbons and an aromatic carbon with a naphthenic carbon is unambiguous. The Ni/B cleavage of the C–S bonds in sulfides shows that there are small amounts of long alkyl sulfide bridges as well. In the cleavage of C–O bonds it is only the external moiety in the bond that is liberated, e.g.

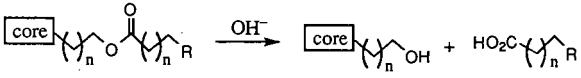

If the ether or ester represents a bridge anchored at both ends to the core then no GC-detectable products would result from the cleavage reaction, e.g.

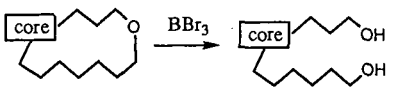

The total amounts of acids and alcohols liberated in the C–O cleavage reaction are quite substantial, alcohols ~3.0% and acids ~ 0.5%, and therefore it would be reasonable to assume that there are some ethers and esters present in bridge positions as well as in side-chain appendages. Indirect experimental evidence appears to support this conclusion. The total number of bridges can be estimated to be about eight per asphaltene molecule or about two per core segment. Consequently, internal cavities of varying sizes have to be an integral feature of the molecular structure of asphaltene. This has been discussed previously in connection with a model for asphaltene structure and has been confirmed by molecular mechanics computations on the isolated model.

The present communication deals with some aspects of the adsorption properties of AA and the question related to its pore structure.

RESULTS AND DISCUSSION

Several series of studies have been carried out on the adsorption properties of AA. Here, only some, yielding information on the pore structure and adsorption capacity, will be discussed.

When, in a series of experiments,[5] the adsorption of C_9–C_{32} alkanes, squalane and squalene was investigated in CH_2Cl_2 solutions, it was observed that the *n*-alkanes were not adsorbed, squalane was adsorbed moderately and squalene, substantially. Thus, AA in a 10% solution adsorbed 0, 20 and 46% of 10,000-ppm dissolved *n*-alkanes, squalane and squalene. If the adsorption mechanism were purely physical adsorption by van der Waals forces, then *n*-alkanes should adsorb more readily than squalane because the presence of the branched methyl groups in squalane hinders a close contact between the methylene groups of the alkane chain and the adsorbent. Since the experimental finding was the reverse of this intuitive expectation, other factors must be involved. The simplest explanation at hand would be the operation of an adduct mechanism, implicating an appropriate-size pore structure. *n*-Alkanes have a molecular diameter of about 3.0 Å and can be adducted to molecular sieves 5 Å which have an internal pore diameter of 3.0 Å. Molecular sieves 5 Å would not adduct squalane because the effective molecular diameter of squalane exceeds 3 Å. Squalane (along with other isoprenoids) with a molecular diameter of about 7 Å could, however, be clathrated with substrates of appropriate size pore structure, such as thiourea. On the other hand, *n*-alkanes cannot be clathrated with thiourea because the narrow *n*-alkane molecules would not be held firmly enough in the wide pores.

Thus, from the experimental observation that squalane can be adsorbed on AA whereas *n*-alkanes cannot, we conclude that the adsorption is, in effect, an adduction of the squalane molecule into an appropriate-size cavity in the asphaltene structure. The cavity may be present in the covalent molecular structure, in the micelle-loke aggregates or in the form of a combination of the two. The simplest assumption one can make is that the cavity is located in the covalent molecular structure because in the micelle-like aggregate the dynamic equilibrium continuously rearranges the structure, rendering the adduction (clathration) process ineffective.

The high value of the adsorbed squalene can be viewed as the result of the combined effects of adduction and adsorption, the latter being due to the higher dispersion force in the interaction of the olefinic π bond with the aromatic ring systems of the asphaltene.

Another important question in this regard is the capacity, that is, the maximum amount of squalane a unit weight of the asphaltene is capable of adducting. This would provide a measure of the number of cavities (in the appropriate size range) present in the asphaltene. The same question is also relevant to the amount of resins the asphaltene can hold, and whether a precipitated asphaltene (say *n*-C_5-AA with 21.1% adsorbed maltene, resins and low-MW asphaltene fragments) represents a (unimolecularly) saturated state of the asphaltene–adsorbate system or rather a steady-stae equipartition distribution of the adsorbate between the oil and the adsorbed phase.

In order to answer this question, an experiment was carried out[6] in which *n*-C_5-AA was sequentially re-precipitated seven times and the desorbed material combined. A portion of this desorbed material was then dissolved in *n*-pentane and freshly *n*-C_5-precipitated solid asphaltene was added to the *n*-C_5/CH_2Cl_2 (40:1) solution. After standing overnight the asphaltene adsorbed 44% of the desorbed material (corresponding to 8.8% of the asphaltene), clearly manifesting that the precipitated solid asphaltene is capable of adsorbing significantly more resinous material than it contained.

ACKNOWLEDGEMENT

We thank the Natural Sciences and Engineering Research Council of Canada and the Alberta Oil Sands Technology and Research Authority for financial support.

REFERENCES

1. Payzant, J.D.; Montgomery, D.S.; Strausz, O.P. *AOSTRA J. Res.* **1988**, *4*, 117–131; Payzant, J.D.; Lown, E.M.; Strausz, O.P. *Energy & Fuels* **1991**, *5*, 445–453.
2. Mojelsky, T.M.; Montgomery, D.S.; Strausz, O.P. *AOSTRA J. Res.* **1985**, *2*, 131–137.
3. Peng, P.; Morales-Izquierdo, A.; Hogg, A.; Strausz, O.P. *Energy & Fuels* **1997**, *11*, 1171–1187.
4. Strausz, O.P.; Mojelsky, T.W.; Faraji, F.; Lown, E.M. *Energy & Fuels* **1999**, *13*, 207–227.
5. Strausz, O.P.; Ignasiak, T.M.; Kotlyar, L.; Montgomery, D.S. to be published.
6. Strausz, O.P.; Torres, M. to be published.

THE STABILITY OF THE ASPHALTENE AND RESIN AGGREGATES AND THEIR CHEMICAL REACTIVITY

J. Murgich, R. Isea, J. Abanero, and O. P. Strausz*

Centro de Química, IVIC, Apartado 21827,

Caracas 1020A, Venezuela;

*Department of Chemistry, University of Alberta,

Edmonton, Canada T6G 2G2

KEYWORDS asphaltenes, micelles, chemical reactivity

INTRODUCTION

The structure of the known asphaltenes can be divided into two main types: one formed by molecules with a large aromatic "continent" with many rings plus alkyl branches (see Fig. 1) (1) and another composed by smaller aromatic islands connected by alkyl bridges ("archipelago" type) (2) (Fig. 2). These different 3D shapes play an important role in the reactivity of the different atoms of these molecules and in the formation and stability of the molecular aggregates or micelles that are responsible for its solubility in crude oil and residue. An analysis of the three dimensional shape of the available asphaltene molecules and of the factors involved in the stability of aggregates formed with resins will help in the understanding of their reactivity in crude oils or residues.

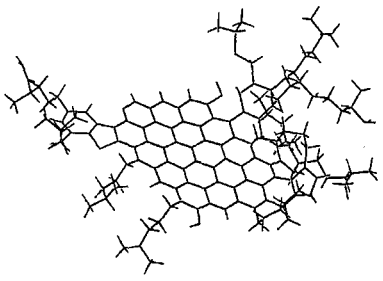

Figure 1. Molecular structure of an asphaltene extracted from a 510°C residue of a Venezuelan crude. No heteroatoms are shown in any of the figures for simplicity.

THEORY

Crude oil is a complex molecular fluid that has been classified as a colloidal dispersion of asphaltenes in a nonaqueous solvent (3). The micelles in oil are formed by asphaltenes peptized mainly by resin molecules. Similar micelles were found in many residues of different crude oils (3b). As in all complex molecular liquids, the noncovalent interactions (van der Walls, Coulomb, and repulsive ones) (4) are responsible for the molecular recognition process that exists between the heavy

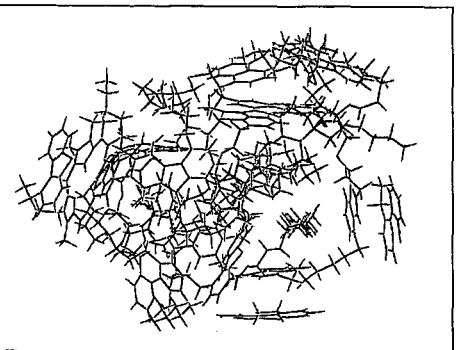

Figure 2. Average 3D molecular structure of an asphaltene from the Athabasca bitumen.

components of crude oils and residues. The resulting recognition between these molecules are very important in determining the structure and the lifetime of their aggregates (5).

MOLECULAR SHAPES AND CHEMICAL REACTIVITY

Figure 3. Space filling structure of the Athabasca asphaltene.

The acetone fraction of the asphaltenes of the Athabasca sands has been studied (6) and a 3D structure was proposed recently using molecular dynamics calculations (1) (Fig. 2). The resulting average structure showed a noticeable similarity with that proposed for an asphaltene obtained from a Boscan crude (7). On the other hand, molecules with a central condensed aromatic core with alkyl branches were found in an asphaltene isolated from a 510 °C residue of a Venezuelan crude (Fig. 1) (1), and for several others extracted from different oils (3a).

From Figs. 2 and 3, one can see that the asphaltene from Athabasca has a very complex three dimensional form that includes cavities and tunnels of different shapes and sizes. The alkyl bridges act as elastic links between the more rigid aromatic regions that form the molecule. The final structure reflects this difference and shows a compromise between the bond and angle requirements of these two main regions. The Athabasca (also Boscan) asphaltene molecule contains a significant number of atoms that are inside these cavities or are located in places where the steric interference is high. Consequently, these sites are not always available for reactions with other molecules. This means that the number of different types of atoms obtained from elemental analysis for this kind of asphaltenes is always larger than the number that is actually available for chemical reactions. This is important in the study of the removal of atoms such as S or N because not all of them will be available for the required reactions. Clearly, not only is important to know the heteroatom content but it is also convenient to have information about its distribution for its efficient removal.

In macrocycles and other concave structures, the reactivity of atomic groups residing in the interior of molecular cavities differs from that of the same groups located on external sites (8). Significant changes were found in the acidity and other proprieties of internal and external groups in a variety of macrocycles and enzymes (8). The existence of internal cavities in asphaltenes of the archipelago type suggests that the reactivity of its atoms will depend on their relative position within these molecules and the size and shape of the internal cavities.

In the structure of lowest energy shown in Fig.2, the asphaltene molecule showed some alkyl bridges with strained bonds, C atoms with perturbed tetrahedral angles and also departures from planarity in some of its aromatic regions. The departures from the normal bond values influences the reactivity of these macromolecules. Strained bonds are weaker than normal ones and, consequently, chemically more reactive (9). Then, they are more easily broken in these asphaltenes than the unstrained ones, thus adding another factor to the complex reactivity of these molecules. In the case of asphaltenes of the continental type (Fig. 1), only the steric interference in crowded atoms will affect their reactivity as no internal cavities are present in these molecules. Consequently, the reactivity of these asphaltenes is reflected in its elemental analysis better than in the case of the archipelago type.

The formation of micelles that are peptized by resins further complicates the chemistry of the asphaltenes in residues and crude oils. Micelles are dynamic units, constantly forming and dissociating (5). For typical surfactants in water, the micelles are generated on a time-scale in the microsecond to millisecond range (5). The chemical complexity of crude oils and its residues implies the existence of many heavy molecules with different 3D shapes. These shapes influence the type, number and lifetime of the micelles of asphaltenes and resins formed in these fluids. It is expected that a polydisperse system composed by a large variety of micelles will be formed with the asphaltene and resin molecules (3b). It is difficult to estimate their lifetimes but one may reasonably assume that they are at least similar to that of the surfactants in water. The existence of these molecular aggregates adds a new dimension to the chemistry of the asphaltenes. These large molecules will not longer be available for reactions as readily as in the case of being a monomer in solution of a simple liquid. If the asphaltene solubility is low, the concentration of free molecules will be also quite small so most of them will be part of some micelle. This will have an impact in the catalytic conversion of this part of the crudes and residues because the diffusion of such micelles are much slower than for the free molecules. The resins that are located in the periphery of the micelles introduces also an additional obstacle to the direct contact of the asphaltenes with the catalysts. The strength of the asphaltene-resin interactions will determine the importance of this contribution to the availability of the asphaltenes for re-action.

The asphaltene of the continental type interacts strongly with other molecules containing planar aromatic regions (2) (Fig. 4). The large contact area produces a favorable contribution to the enthalpy of complexation of this type of asphaltenes and resins (1). The contact in the archipelago type is much smaller as seen at the bottom right of Fig. 2, where a resin is noncovalently attached to this type of asphaltene. The smaller contact area indicates the formation of weaker aggregates if all the other enthalpic and entropic factors are equal (1). This difference shows the importance of the aromatic regions in the stability of the micelles of asphaltenes and resins.

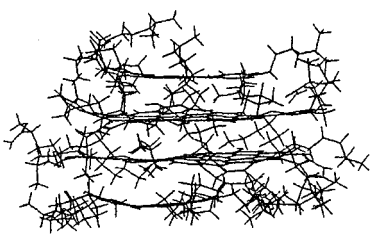

Figure 4. Lateral view of the micelle formed with two internal asphaltene molecules of Fig. 1 and two external resins molecules found in the same residue.

The chemical changes occurring during the cracking process modify the structure of asphaltenes and resins. As in other colloidal systems, these changes produce variations in the micelles present in the residue (5). It is important to monitor these changes and control them with conveniently design additives. They can be designed taking into account the studies of the interaction between different asphaltene and resins present in micelles of typical residues. These additives can be such that they will be able to change the properties of the resulting residue through association with the micelles and the free asphaltenes. In this way, the conversion of asphaltenes to lighter fractions can be noticeably improved.

ACKNOWLEDGMENT

This work was partially supported by the Natural Sciences and Engineering Research Council of Canada.

REFERENCES

1) Murgich, J.; Abanero, J.A.; and Strausz, O.P. Energy Fuels, 13, 278-286 (1999)

2) Murgich, J., Rodríguez, J., and Aray, Y., Energy Fuels, 10, 68-76 (1996)
3a) Speight, J. G. The Chemistry and Technology of Petroleum, 2nd. ed., Marcel Dekker, New York, (1991) and b) Syuniaev, Z.I.; Safieva, R.Z. and Syuniaev, R.Z., Neftyanie Dispersnye Sistemy, Kisilorda, Moscow, 1997
4) Israelachvili, J., Intermolecular and Surface Forces, 2nd. ed., Academic, New York, 1991.
5) Evans, F.D., and Wennerström, The Colloidal Domain, VCH Publishers, New York, 1994.
6) Strausz, O. P., Mojelsky, T. W. and Lown, E. M. Fuel, 71, 1355-1362, (1992),
7) Kowalewski, I., Vandenbroucke M., Huc, A.Y., Taylor, M.J., and Faulon, J.L., Energy Fuels, 10, 97-107 (1996)
8)Lüning, U.; Adv. Phys. Org. Chem., 30, 63-116 (1995)
9)Isaacs, N.S.; Physical Organic Chemistry, Longman, Harlow, Essex, 1987

STOCHASTIC MODELING OF PETROLEUM RESID - THE USE OF REACTIVITY INFORMATION IN STRUCTURE DETERMINATION

Achin Vasudeva, Ankush Kumar
Department of Chemical Engineering
University of Delaware, Newark, DE 19716

Michael T. Klein
College of Engineering
Rutgers, The State University of New Jersey
Piscataway, New Jersey 08854-8058

KEYWORDS : resid, stochastic, reaction

INTRODUCTION

Structural characterization of petroleum resid has gained importance in the petroleum industry in recent years owing to the increasing abundance of such material in the petroleum produced worldwide. It is estimated that at least 85% of the world proven reserves of petroleum contain large amounts of "heavy" material boiling above 650°F. On the other hand, according to recent reports, about 50% of the petroleum products consumed in the United States at the present time are gasoline and an additional 40% are other distillate fuels boiling below about 650°F [1]. These trends have focused attention on the efficient upgrading of petroleum resids to light distillates. In order to meet the challenge of optimal upgrading of heavy petroleum fractions, a detailed understanding of the resid structure is required.

The traditional approach for modeling such complex systems has been to use lumped models where molecular species are grouped according to some physical property, such as boiling point or solubility [2]. However, lumped models are clearly incapable of providing molecular information about the feedstock since, by lumping molecules according to some physical characteristic, the molecular detail is lost. With recent government regulations having established concentration limits for specific molecules in a feedstock, an example being benzene, a known carcinogen, molecularly explicit models are required that can predict the concentrations of individual species. Lumping strategies can also lead to difficulties in developing an accurate model. For instance, a C_{10} paraffin and a C_{10} aromatic (alkyl benzene) would be lumped together in the same boiling point range and the lumped model would represent them by the same pseudo component. Clearly, however, an alkyl benzene would react quite differently from a paraffin.

The limitations of lumped models motivate the development of molecule-based models. The development of such molecularly explicit models has been made possible by the explosion in available computational resources. To develop molecule-based models, the initial conditions need to incorporate molecular level details. For models dealing with a feedstock as complex as a petroleum resid, which has tens of thousands of molecules, tracking each species is impractical considering the prohibitively large solution times associated with solving such a reaction model. A stochastic description of the complex feedstock provides a path forward. Such a model retains the molecular detail of the feedstock and at the same time can be reduced to generate a small set of representative molecules (of the order of ~ 50-100) to be used in the reaction model.

STOCHASTIC DESCRIPTION OF PETROLEUM RESID

The construction algorithm for petroleum resid is presented in Figure 1. For each molecule, the molecular type (e.g., paraffin, naphthenic, aromatic/resin, or asphaltene) is determined first. The stochastic description of a feedstock involves viewing each molecule as a collection of molecular attributes. Once the molecular type has been identified, the value of each attribute needed to specify the molecule is determined. For instance, an aromatic molecule would be specified by the number of aromatic rings, the number of naphthenic and thiophenic rings attached to it, the number of side chains, the length of side chains and the number of side chain sulfur atoms.

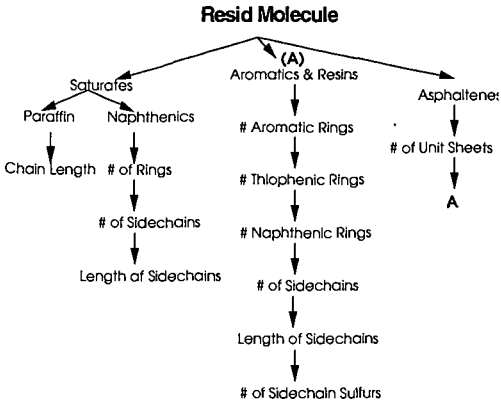

Fig. 1 Construction algorithm for petroleum resid

Each molecular attribute is characterized by a probability distribution function (pdf) which provides the quantitative probability of finding the value or less of a given attribute. The applicability of probability distribution functions to describe complex mixtures in general and petroleum fractions in particular has been well documented in the literature [7,9,11,14,17]. Monte Carlo sampling of the set of pdf's (one set for each feed) provides a large ensemble of molecules (of the order of 10^5). The properties of this set of molecules generated are compared to experimentally obtained analytical data to obtain an optimal set of pdf parameters, which define the feedstock. The pdf parameters are optimized using the following objective function:

$$\chi^2 = \left(\frac{MW_{exp} - MW_{pred}}{0.05 * MW_{exp}}\right)^2 + \left(\frac{HtoC_{exp} - HtoC_{pred}}{0.02 * HtoC_{pred}}\right)^2 + \left(\frac{Halpha_{exp} - Halpha_{pred}}{0.02}\right)^2 + \left(\frac{Harom_{exp} - Harom_{pred}}{0.01}\right)^2 + \left(\frac{1}{\#Comps}\right)\sum_{i=1}^{\#Comps}\left(\frac{SARAWt_{i,exp} + SARAWt_{i,pred}}{0.03}\right)^2 + \left(\frac{1}{\#Fracs}\right)\sum_{i=1}^{\#Fracs}\left(\frac{SIMDIS_{i,exp} - SIMDIS_{i,pred}}{0.01}\right)^2 \quad (1)$$

The numerator in each term of the above equation is the difference between the experimentally determined property and the predicted property, and the denominator is a weighting factor equal to one experimental standard deviation. A simulated annealing global optimization technique is employed to minimize the objective function and generate an optimal set of pdf parameters.

In general, the only information available about petroleum resids are some average properties like molecular weight (Vapor Pressure Osmometry), elemental analysis, boiling point distribution (SIMDIS) and NMR (^1H and ^{13}C) data. Analytical techniques like GC/MS which yield molecular level details also provide only broad lumps due to the extreme complexity of the feedstock. This limited amount of structural information often renders the optimal set of pdf parameters non-unique, thus preventing the development of an accurate stochastic description of the resid. To tackle the issue of non-uniqueness, further structural information is required. One possible source of such information is a detailed product distribution from the controlled reaction of the resid.

The approach adopted in this study has been to crack the resid in the presence of hydrogen under conditions where the reaction pathways and associated rate constants can be estimated with reasonable accuracy. The light fractions obtained as a result of the controlled reaction are subject to detailed compositional analyses (GC/MS, High Detail Hydrocarbon Analysis) to obtain a molecularly explicit description of the product. This information is incorporated into the objective function as a term representing the difference between experimental and predicted weight fractions of all the species in the product. The objective function is thus modified as follows:

$$\chi^2 = \left(\frac{MW_{exp} - MW_{pred}}{0.05 * MW_{exp}}\right)^2 + \left(\frac{HtoC_{exp} - HtoC_{pred}}{0.02 * HtoC_{pred}}\right)^2 + \left(\frac{Halpha_{exp} - Halpha_{pred}}{0.02}\right)^2 + \left(\frac{Harom_{exp} - Harom_{pred}}{0.01}\right)^2 + \left(\frac{1}{\#Comps}\right)\sum_{i=1}^{\#Comps}\left(\frac{SARAWt_{i,exp} + SARAWt_{i,pred}}{0.03}\right)^2 + \left(\frac{1}{\#Fracs}\right)\sum_{i=1}^{\#Fracs}\left(\frac{SIMDIS_{i,exp} - SIMDIS_{i,pred}}{0.01}\right)^2 + \left(\frac{1}{\#Species}\right)\sum_{i=0}^{T}\sum_{i=1}^{\#Species}\left(\frac{Wtfrac_{i,exp} - Wtfrac_{i,pred}}{0.01}\right)^2 \quad (2)$$

Minimization of the modified objective function thus yields an improved stochastic description of the feedstock.

In cases where such complex feedstocks are to be part of a molecularly explicit reaction model, a much more compact molecular description of the feedstock is desirable. This is because handling the thousands of molecules generated by Monte Carlo sampling and their associated reactions and rate constants can result in enormous solution times using present day computers. This molecular lumping is achieved by means of a quadrature technique, wherein ordered sampling of attribute values based on equiprobable regions (to allow sampling over the entire range of attribute values) results in the finite set of representative molecules (of the order of ~10-100 molecules) to be used in the reaction model. The entire modeling approach is thus outlined in Fig.2.

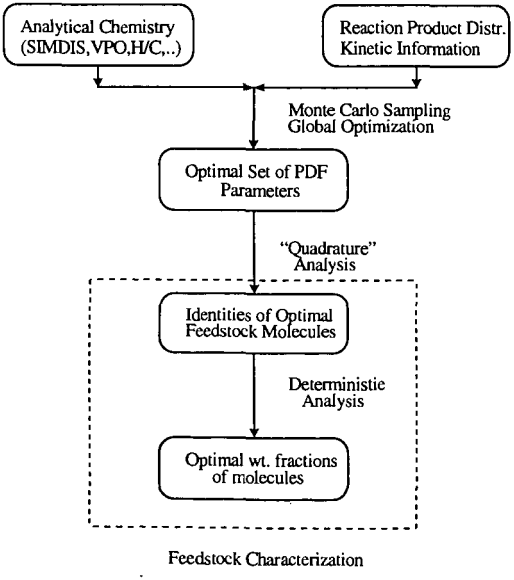

Fig. 2. Modeling approach for stochastic description of petroleum resid

EXPERIMENTAL

The resid was cracked in the presence of excess hydrogen in a flow reactor setup. The catalyst precursor employed was molybdenum naphthenate containing 6% by wt. Mo (obtained from The Shephard Oil Company). Molybdenum naphthenate was sulfided in situ by sulfur present in the petroleum resid to generate the active catalytic species, MoS_2. The particular choice of dispersed catalyst ensured sufficient conversion of resid to light products while at the same time inhibiting coke production [6,8,15]. A catalyst concentration of 3000 ppm (by weight of Mo in resid) was used. The resid was dissolved in toluene in the ratio of 1:3.5 by weight (resid : toluene). Toluene was the choice of solvent because of its excellent solvation properties (for the resid under investigation) and its inertness under reaction conditions. The hydrogen pressure in the reactor was maintained at 1100 psig and the reaction was carried out at 470°C. The liquid flow rate was about 0.28 ml/min while the hydrogen flow rate was controlled at 150 std ml/min. The residence time of the liquid in the reactor was about 15 minutes.

The gas product was analyzed online in an HP 5890 GC equipped with a 100 m HP-1 capillary column (ID : 0.25 mm, film thickness : 0.5 μm) coupled with an FID for identification of hydrocarbons and a 1 m HayeSep C packed column coupled with a TCD for detection of polar gases such as ammonia and hydrogen sulfide. The liquid product was collected and subjected to HDHA (High Detail Hydrocarbon Analysis) and GC/MS analysis to yield the product distribution.

REACTION MODEL

The driving force for cracking of petroleum resid in the presence of excess hydrogen employing molybdenum naphthenate as the catalyst precursor is thermal activation. At a mechanistic level, the catalyst has no effect on C-C bond cracking so that the initial population of free radicals is determined by the severity of conditions. The next step in the reaction sequence is the saturation of the reactive fragments, which is promoted by the catalyst. The efficient uptake of hydrogen facilitated by the catalyst ensures that the reactive fragments do not undergo fast undesirable reactions, such as condensation reactions, which give rise to the appearance of mesophase and then to coke deposition. Instead, the catalyst controls the rate of free radical propagation that, via β-scission reaction, favors the process of resid conversion to lighter products [4,5].

A pathways level model describing the resid cracking reaction has been employed in this study. At the pathways level, the main reactions are considered to be breaking of intersheet linkages for asphaltene molecules and side chain cracking reactions including dealkylation for aromatic and naphthenic molecules. Hydrogenation of ring molecules and subsequent ring opening, although not significant, are also considered. The above reactions are used to generate a reaction network consisting of about 250 molecular species. The rate constants for all the species and their associated reactions have been estimated from previous studies conducted with model compounds under similar reaction conditions [12,13]. For example, rate constants for alkyl aromatics undergoing side chain cracking are calculated from the reaction of pentadecyl benzene (PDB) using first order approximations as :

$$k_i = k_{PDB}\,(i/15)^{0.5} \qquad (3)$$

where i is the number of carbon atoms in the side chain of the alkyl aromatic molecule. The breaking of intersheet linkages in asphaltene molecules has also been modeled as side chain cracking of alkyl aromatic species. Similarly, the rate constants for reactions of alkyl hydroaromatic and alkyl naphthenic species have been estimated from available data on ethyl tetralin and tridecyl cyclohexane respectively.

Monte Carlo sampling of the pdf parameters describing the structural attributes of resid molecules generates a large ensemble of molecules which provide the initial condition for the reaction model. Solution of the reaction model results in predicted product concentrations which are compared to experimentally obtained data and the difference forms part of the objective function, which is minimized. Reactivity information is thus utilized to develop an improved stochastic description of the petroleum resid.

REFERENCES

1. Altgelt, K. H., and Boduszynski, M. M., *Composition and Analysis of Heavy Petroleum Fractions*, Marcel Dekker Inc., New York, pp 1-7 (1994).
2. Beaton, W. I., and Bertolacini, R. J., *Catalysis Reviews - Science and Engineering*, 33, 281-317 (1991).
3. Campbell, D. M., *Stochastic Modeling of Structure and Reaction in Hydrocarbon Conversion*, Ph.D. Dissertation, University of Delaware (1998).
4. Cebolla, V. L., Membrado, L., Vela, J., Bacaud, R., and Rouleau, L., *Energy & Fuels*, 9, 901-905 (1995).
5. Del Bianco, A., Panarati, N., Di Carlo, S., Beltrame, P. L., and Carniti, P., *Energy & Fuels*, 8, 593-597 (1994).
6. Fixari, B., Peureux, S., Elmouchnino, J., Le Perchec, P., Vrinat, M., and Morel, F., *Energy & Fuels*, 8, 588-592 (1994).
7. Flory, P. J., *J. Am. Chem. Soc.*, 58, 1877 (1936).
8. Kim, H., and Curtis, C. W., *Energy & Fuels*, 4, 206-214 (1990).
9. Libanati, C., Monte Carlo Simulation of Complex Reactive Macromolecular Systems, Ph.D. Dissertation, University of Delaware (1992).
10. Logwinuk, A. K., and Caldwell, D. L., *Chem. Econ. Eng. Rev.*, 15, 31 (1983).
11. Pederson, K. S., Blilie, A. L., and Meisingset, K. K., *Ind. Eng. Chem. Res.*, 31, 1378-1384 (1992).
12. Savage, P. E., *Chemical and Mathematical Modeling of Asphaltene Reaction Pathways*, Ph.D. Dissertation, University of Delaware (1986).
13. Savage, P. E., and Klein, M.T., *Ind. Eng. Chem. Res.*, 26, 488-494 (1987).
14. Shibata, S. K., Sandler, S. I., and Behrens, R. A., *Chem. Eng. Sci.*, 42, 1977-1988 (1987).
15. Ting, P., Curtis, C. W., and Cronauer, D. C., *Energy & Fuels*, 6, 511-518 (1992).
16. Trauth, D. M., *Structure of Complex Mixtures through Characterization, Reaction, and Modeling*, Ph.D. Dissertation, University of Delaware (1990).
17. Whitson, C. H., *Soc. Pet. Eng. J.*, 683 (1990).

STRUCTURE AND REACTIVITY OF THE ASPHALTENE FRACTION OF AN ARABIAN LIGHT/MEDIUM CRUDE MIXTURE

Masakatsu Nomura[a], Koh Kidena[a], Satoru Murata[a], Yan Su[a], Levent Artok[b], and Yasuhiro Miyatani[a]

[a] Department of Molecular Chemistry, Graduate School of Engineering, Osaka University, 2-1 Yamada-oka, Suita, Osaka, 565-0871, JAPAN
[b] Department of Chemistry, Çukurova University, Adana 01330, TURKEY

Keywords: Asphaltene, Structure, Cracking reaction

INTRODUCTION

In the petroleum industry, further utilization of distillation end points (i.e. residua) is of high interest because petroleum refineries will have to deal with much heavier crude in the future decades. Petroleum asphaltenes, which are operationally defined as pentane- or heptane-insoluble and toluene-soluble organic materials of crude oil or the bottoms from a vacuum still, are the heaviest fraction of the crude oil, and their amounts and structures are known to be source dependent. In upgrading processes of residua, asphaltenes are responsible in sludge formation due to their flocculation, which reduces the flow and plugs down stream separators, exchangers, and towers. They show bad behavior in poisoning and reducing the activity of hydrocracking catalysts with its high heteroatom content, trace metals, and high tendency in coke formation. In order to overcome their problematic issues, the role of asphaltenic materials in the upgrading processes should also be interpreted at the level of molecule. Under these circumstances, the better comprehension of asphaltene structure is essential. Although enormous amount of effort has been paid to the structural elucidation of asphaltenes for several decades, their precise molecular description does not exist yet. On the basis of detailed NMR work along with complementary information from various analytical techniques employed, many researchers have concluded that asphaltenes are the mixture of polydispersed-condensed polyaromatic units, with heteroatoms contents, bearing alicyclic sites, and substituted and connected with each other via aliphatic chains. In their researches, asphaltenes were precipitated either from the crude sample or residue. The latter type asphaltene structurally may be different from the former type because at distillation temperatures, in general 300-500°C, some extent of cracking and condensation reactions may take place simultaneously. There are a number of studies which have postulated chemical models for asphaltenes, the most recent ones being based on the $^{1}H/^{13}C$ NMR data and elemental composition. The models, in general, consist of one or two units of polyaromatic units in varying condensation degree combined with alicyclic sites and connected by aliphatic chains, most of the aliphatic chains being attached to the aromatic carbons[1-7]. Some researchers have used degradative methods such as pyrolysis and oxidation methods to gain more precise insight into the molecular characteristics of asphaltenes. The former method involves formation of smaller fragments and accompanies their identification, the identified components being considered as covalently bonded moieties of asphaltene molecules[8]. Strausz *et al.* were the first group applied the ruthenium-ions catalyzed oxidation (RICO) reaction to asphaltenes to recognize aliphatic types[9]. They processed the invaluable information from the RICO reaction along with those from NMR and pyrolysis studies to comprehend the structure of Alberta oil sand asphaltenes and consequently proposed a very different model structure: instead of a single condensed aromatic system with a large number of rings, a set of smaller aromatic units, heteroaromatics and naphthenic units with aliphatic substituents linked by aliphatic bridges comprised the structure. Particularly, the presence of relatively polymeric naphthenic and aliphatic sites in this molecule is a striking feature. The structure of heavy fraction of crude oil and their conversion to value products have also been of our interest.

In this paper, we have processed the information from the NMR work of the asphaltene sample together with data from the RICO reaction of the asphaltene to elucidate the distribution of the aliphatic carbons more precisely. The detailed analytical information over this sample is summarized within a model structure. As to the reactivity of the asphaptene, its hydrocracking reaction using metal loaded Y-type zeolite catalyst was elucidated, the results being compared with the case of the other lighter fractions.

EXPERIMENTAL SECTION

Samples.

The propane insoluble fraction of the vacuum residue of Arabian crude mixture (80% light and 20% medium) was provided from Nippon Oil Ltd. Co. The asphaltene sample used in this study was the insoluble fraction (21wt% yield, based on propane insoluble) from the pentane Soxhlet extraction of the provided sample. The elemental composition of the asphaltene sample is 83.7% C, 7.5% H, 0.84% N, 6.8% S, 0.012% Ni, 0.038% V, on dry basis and has an H/C atomic ratio of about 1.08.

Analysis of the asphaltene sample.

The RICO reaction was performed by stirring the mixture of the asphaltene sample (1 g), H_2O (30 ml), CCl_4 (20 ml), CH_3CN (20 ml), $NaIO_4$ (15 g), and $RuCl_3 \cdot nH_2O$ (40 mg) at 40°C for 24 h. During the reaction, N_2 gas was flowed and the resulting CO_2 was purged through $CaCl_2$ and ascarite containing tubes. The amount of CO_2 formed was determined from the weight increase of ascarite. The details of the workup procedure have been given elsewhere[10]. NMR analyses were conducted by a JEOL JNM-GSX-400 spectrometer operating at 400 MHz for ^{1}H NMR and 100 MHz for ^{13}C NMR measurements. The NMR samples were prepared by mixing approximately 100 mg of the sample with 1 ml of $CDCl_3$; tetramethylsilane (TMS) was used as an internal standard. The quantitative ^{13}C NMR measurements were acquired by adding a relaxation agent, chromium

trisacetylacetonate ($Cr(acac)_3$, 0.2 *M*) in inverse gated decoupling system with a pulse delay of 5 s, acquisition time of 1.088 s and pulse width of 3.3 μs. The distortionless enhancement by polarization transfer (DEPT) spectra were collected for flip angles of 45°, 90°, and 135°. The acquisition time was the same as those for the quantitative carbon runs. A pulse delay of 2 s and a carbon-proton coupling constant of 125 Hz were used. The carbon 90° pulse was 10 μs, while proton 90° pulse was 26.3 μs. The GPC tests of the THF or $CHCl_3$ solutions of the asphaltene (0.5 mg/ml and 1.4 mg/ml, respectively) were performed by a Shimadzu system with 1 ml/min flow rate of THF or $CHCl_3$ carrier solvents, respectively, at a UV wavelength of 270 nm. The columns used in these tests were Shodex KF-802 and Shodex AC-802 for THF and $CHCl_3$ carrier solvents, respectively. Standard polystyrene samples were used for the calibration of relationships between molecular weight and retention time. MALDI-TOF/MS (Matrix assisted lader desorption ionization-time of flight/mass spectroscepy) spectra were obtained by a Voyager RP mass spectrometer of Perspective Biosystems Co. The linear TOF mode was used with an accelerating voltage of 30 kV *in* positive ion. One μl of THF solution of the sample with 2.5 μg/ml concentration was applied to target and let it evaporate at atmospheric condition.

Hydrocracking reaction of the asphaltene sample.

A mixture of heavy oil (1.0 g) and metal-loaded zeolite (0.5 g) was placed in a 70 ml SUS316 autoclave, which was pressurized up to 6.9 MPa with cold hydrogen, and heated up to a desired temperature range (400°C) at a heating rate of 8K/min. Before collection of the gaseous products, these were passed through aqueous iodine solution (1 mol/l, 20 ml) to recover hydrogen sulfide produced. Gaseous hydrocarbon products were analyzed quantitatively by a gas chromatograph. The iodine solution was diluted to 200 ml by deionized water, 20 ml of which was submitted to titration with sodium thiosulfate solution (0.1 mol/l), using aqueous starch solution as an indicator. After the collection of gaseous products, the autoclave was opened, the inside of which was then washed with tetrahydrofuran (THF) to recover liquid and solid products. After the filtration of the resulting mixture to remove coke and catalyst, the products were separated into three fractions, gasoline + THF (the fraction distilled off by a rotary evaporator at 65°C, atm. 5 mmHg), gas oil (the fraction distilled off by a glass tube oven at 150°C, atm. 5 mmHg, corresponds to the fraction with bp < 310°C), and residue (THF soluble and undistilled fraction). Due to the severe difficulty in weighing of THF plus gasoline fraction in an accurate way the yield of gasoline fraction was calculated based on subtraction of the yield of the other fractions (gas, light oil, residue, hydrogen sulfide, and coke) from total of 100%. Amounts of coke were estimated based on the weight and elemental analysis of THF insoluble portion.

RESULTS AND DISCUSSION

Structural analysis of the asphaltene

RICO reaction afforded the acid products from the aliphatic portion of the sample. The amount of lower carboxylic acids (C_2-C_5) was 3.9 mol/100molC in asphaltene, corresponding to ~5.5 aliphatic carbon/ 100C. Figure 1 shows the distribution of aliphatic monoacids up to C_{28} including C_2-C_5 acids. The amount of longer *n*-alkanoic acids showed a smooth decrease as the carbon number increased. Therefore, the most of the alkyl groups attached to the aryl carbon or the monomethylene bridge carbon are in the range of C_1-C_3. We recovered the diacids ranging from C_4 to C_{20} from aqueous and dichloromethane (DCM) soluble phases of the product. Their distribution was shown in Figure 2. These acids represent alkyl bridge structures connecting two aryl units and α,α,ω-triaryl substituted bridges, however, short chain acids (C_4-C_6) may also arise from oxidation of various hydroaromatic structures. Several amounts of ethanedioic acids were detected, this acid representing biaryl linkages in the sample. Although this acid implies the significance of biaryl linkages, its amount can not represent the amount of such type of bond due to its relative instability. Propanedioic acid could not be observed, because it can not survive the RICO reaction. Therefore, no direct evidence could be obtained from the reaction products. We also recovered the aliphatic polycarboxylic acids which were formed from three or more aryl-substituted alkyl bridges or alicyclic parts of partially saturated condensed structures. Other polymeric aliphatic fraction could not be analyzed by GC, but was analyzed by NMR in detail. The weight of this fraction was >90% of the DCM extract. The weight and elemental composition of DCM soluble fraction indicates that the amount of carbon atom in this fraction corresponds to 24.6 C per 100 C atoms in asphaltene. GPC analysis of this fraction after methylation (methyl esterification of acids) shows a number-averaged MW of 821 Da. Figure 3 shows the ^{13}C NMR spectrum of DCM soluble fraction before methylation. This fraction had <4% aromatic, 87.9% aliphatic, 6% carboxylic and 3.1% carbonyl carbon. The results indicated that the dominant part of this fraction is comprised of polymeric aliphatic structures. The fact that this fraction had an aliphatic hydrogen to aliphatic carbon ratio of 1.72, calculated on the basis of $^1H/^{13}C$ NMR and elemental analysis data, confirms the presence of alicyclic sites. The aliphatic region of the ^{13}C NMR spectrum (Figure 3) consists of sharp bands on a broad hump between 10 and 50 ppm, much of this broad hump being ascribed to naphthenic carbon. DEPT analysis of this fraction was also very helpful to assume the structure of this fraction. Aromatic acids were recovered from the aqueous phase of the products workup. Such acids correspond to the presence of condensed aromatic moieties.

The GPC test for the whole asphaltene sample show a range starting well below 200 Da extending over 100 000 Da, while MALDI-TOF/MS indicates the ions higher than 200 Da. This discrepancy confirmed the existence of adsorption phenomenon in the case of GPC procedure. On the other hand, MALDI-TOF/MS test led ionization above 200 m/z extending over 3000 m/z, giving maximum abundance about 450 m/z. Nevertheless, inefficient ionization for polydispersed materials are known to be an impediment of this method to lead underestimation of the higher mass components[11]. Thus, caution must be exercised when interpreting average molecular weight distribution values from MALDI, especially for highly polydispersed complex molecules. We understand that no conclusive-absolute molecular weight could be estimated based on the techniques presented above, however, it seems that GPC method with THF eluent provides more

applicable information compared to others employed in our study: the number averaged molecular weight was estimated as 801 Da.

The structural information was drawn from the combination use of ^{1}H and ^{13}C NMR data and elemental data. Figure 4 shows the ^{13}C NMR spectrum of the asphaltene sample, having the general features in accordance with previous work. The aromatic region consists of a broad featureless absorption, whereas the aliphatic region contains discrete sharp peak overlapping a broad hump. These sharp peaks are commonly attributed to the chain carbon and methyl substituents on aromatics, alkyl chains, and naphthenic units. Also here, DEPT analysis provides helpful information to differentiation of CH_3, CH_2, and CH carbons.

We applied a methodology in construction of a model structure for the asphaltene tentatively in a manner similar to that of bituminous coal[12]. The types of aromatic main units were deduced from the results obtained by the pyrolysis(py)/GC and RICO reaction. The XPS study revealed the sulfur structures as sulfide, thiophenic and sulfoxide. The type and distribution of aliphatic chain structure, functionality, and naphthenic structure were postulated based on the RICO, py/GC, and NMR data. We should emphasis that the asphaltene is consisted of mixture of hundreds of organic molecules rather than a single macromolecule structure. We tried to draw several molecules in the proposed chemical structural model for asphaltene, and four molecules of different structures were contained in the proposed model (Figure 5).

Hydrocracking reactions of the asphaltene

Figure 6 compares the hydrocracking results of the propane-insoluble heavy oil and its deasphalted (pentane-soluble) fractions at the temperature range of 350-400°C with the presence of Pd-Ni loaded Y type zeolite catalyst. As it can clearly be seen deasphalted heavy oil sample showed higher reactivity toward hydrocracking reaction. The removal of asphaltene increased the total liquid and gaseous products (bp. <310°C) roughly by the factor of 2 at 350°C, from 30% to 53% at 375°C, and 42% to 65% at 400°C. Even if we consider the conversion values of the propane-insoluble sample on asphaltene frec basis, i.e. it is assumed that asphaltene do not convert to low boiling yields, but contributes to the residue fraction, the resulting values, except for the highest temperature, are far less than those of the deasphalted sample. Asphaltene free calculations of total hydrocracked products were 24, 44 and 64 % with respective increase of the reaction temperature. The comparison of these values with those from deasphalted sample suggests that the effect of the removal of asphaltene on the hydrocracking of the heavy oil became less with increasing the reaction temperature. The effect of asphaltene removal was more remarkable on HC gaseous product formation at all temperatures, their increase varying by the factor of 2-3 even at higher temperature, this indicating the effect of asphaltene removal on hydrocracking activity even at 400°C. These results reveal that asphaltene greatly retards hydrockracking reactions upon probably reducing the activity of the catalyst, especially at the lower temperatures.

The polymerized fraction or coke formations seem to be not likely reason for the detrimental effect of the asphaltene since both the whole and deasphalted residue approximately yielded similar amount of these fractions. Our laboratory recently showed that Pd-Ni-Y catalyst is very active in hydrocracking and hydrodesulfurization reactions[13]. We have also showed that the molecule should diffuse into the cage so that sufficient reactions take place[14,15]. The asphaltene molecules with large molecular segments probably reduce the effective diffusion of molecules which are capable to enter through the pores, by plugging the entrance points. At higher temperatures, probably, the adsorption phenomenon becomes less favorable, due to the reduced adsorption strength and the more effective solubility of the asphaltene molecules within the reaction medium, thus resulting in overall increased effective diffusibility of the units with appropriate sizes.

SUMMARY

This work summarized the structural characterization of the vacuum residue asphaltene based on the mainly spectroscopic and pyrolytic methods, and discussed the results with combination use of those from the RICO reaction. Then, a structural model for the asphaltene was presented. The reactivity of the asphaltene was also discussed from the catalytic hydrocracking reaction of it in a batch reactor using metal-loaded Y-type zeolite catalyst.

ACKNOWLEDGMENT

This work was carried out as a research project of The Japan Petroleum Institute commissioned by The Petroleum Energy Center with the subsidy of The Ministry of International Trade and Industry.

REFERENCES

1. Hirsch, E.; Altgelt, K. H. *Anal. Chem.* **1970**, *42*, 1330.
2. Takegami, Y.; Watanabe, Y.; Suzuki, T.; Mitsudo, T.-aki; Itoh, M. *Fuel* **1980**, *59*, 253.
3. Suzuki, T.; Itoh, M.; Takegami, Y.; Watanabe, Y. *Fuel* **1982**, *61*, 402.
4. Cristopher, J.; Sarpal, A. S.; Kapur, G. S.; Krishna, A.; Tyagi, B. R.; Jain, M. C.; Jain, S. K.; Bhatnagar, A. K. *Fuel* **1996**, *75*, 999.
5. Storm, D. A.; Edwards, J. C.; DeCanio, S. J.; Sheu, E. Y. *Energy Fuels* **1994**, *8*, 561.
6. Ali, L. H.; Al-Ghanman, K. A.; Al-Rawi, J. M. *Fuel* **1990**, *69*, 519.
7. Rafenomanantsoa, A.; Nicole, D.; Rubini, P.; Lauer, J.-C. *Energy Fuels* **1994**, *8*, 618.
8. Ritchie, R. G. S.; Roche, R. S.; Steedman, W. *Fuel* **1979**, *58*, 523.
9. Strausz, O. P.; Mojelsky, T. W.; Lown, E. M. *Fuel* **1992**, *71*, 1355, and references therein.
10. Artok, L., Murata, S., Nomura, M. Satoh, T. *Energy Fuels*, **1998**, *12*, 391.
11. Burlingame, A. L.; Boyd, R. K.; Gaskell, S. J. *Anal. Chem.* **1998**, *70*, 647R, and references therein.
12. Nomura, M., Artok, L., Murata, S., Yamamoto, A., Hama, H., Gao, H., Kidena K., *Energy Fuels*, **1998**, *12*, 512.

13. Wada, T.; Kaneda, K.; Murata, S.; Nomura, S. *Catalysis Today* **1996**, *31*, 113.
14. Matsui, H.; Akagi, K.; Murata, S.; Nomura, M. *Energy Fuels* **1995**, *9*, 435.
15. Nomura, M.; Akagi, K.; Murata, S.; Matsui, H. *Catalysis Today* **1996**, *29*, 235.

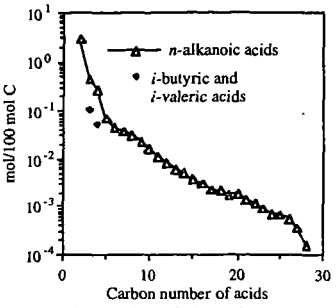

Figure 1. Distribution of aliphatic monoacids from RICO reaction.

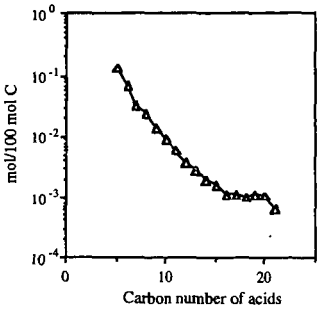

Figure 2. Distribution of aliphatic diacids from RICO reaction.

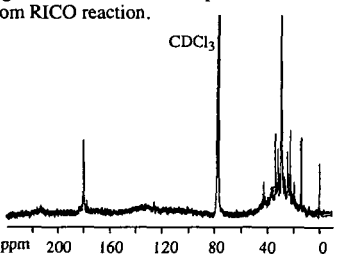

Figure 3. ^{13}C NMR spectrum of the dichloromethane soluble fraction of RICO product.

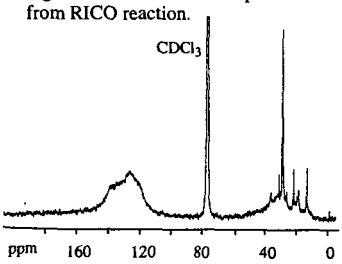

Figure 4. ^{13}C NMR spectrum of the asphaltene.

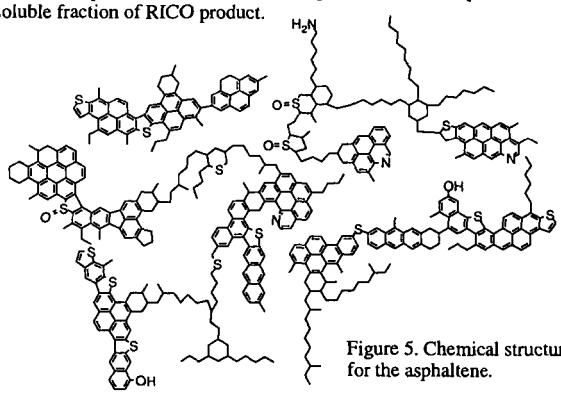

Figure 5. Chemical structural model for the asphaltene.

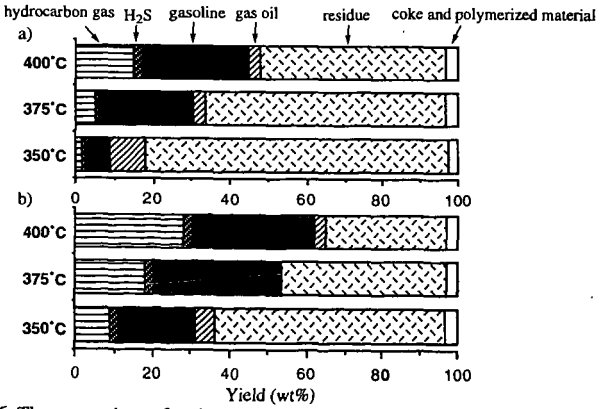

Figure 6. The comparison of hydrocracking conversion results on (a) C_3-heavy oil sample and (b) C_5-soluble portion of the C_3-heavy oil sample.

CHARACTERIZATION AND ADSORPTION TREATMENT OF VACUUM RESIDUE FRACTIONS WITH CARBONS

Kinya Sakanishi, Toru Manabe, Izumi Watanabe, and Isao Mochida

Institute of Advanced Material Study, Kyushu University
Kasuga, Fukuoka 816-8580, Japan

Keywords: Vacuum residue fractions, step scan liquid mode XRD, adsorption treatments

ABSTRACT

The adsorption treatment of VR by using variable amounts of carbon particles was performed with stirring at 60 °C for 1 h. After the treatment, the adsorbent was first washed with n-hexane and then thoroughly washed with THF(tetrahydrofuran) under the ultrasonic irradiation to recover the soluble fractions of hexane soluble(HS) and hexane insoluble but THF soluble(HI-THFS) from the adsorbent. The THF insoluble(THFI) yield increased with the added amount of Ketjen Black(KB). The HI but THF soluble fraction decreased with the increased amount of THFI fraction. About 3 wt% of KB addition based on VR appeared enough for the selective removal of the heavier fraction without increasing the HI-THFS fractions. The slow step scan XRD revealed that the untreated KB showed a very slight peak around 26°. The adsorbed THFI exhibited a broad peak around 26°, while the relatively sharp peak of the original asphaltene around 26° decreased with the addition of KB, indicating selective adsorption of the heavier fraction in the asphaltene. Based on the above results, it is suggested that a certain amount of KB addition may selectively separate the heavier fraction, where the more polar and metal-containing compounds are concentrated, from the VR. Such an adsorption treatment using carbon nanoparticles is expected to remove the catalyst poisons such as the heavier asphaltene and metallic compounds prior to the catalytic upgrading hydrotreatments.

INTRODUCTION

It is desirable to remove metallic compounds in petroleum residues before catalytic hydrocracking and hydrodesulfurization reactions in refineries, because they cause severe catalyst deactivation.[1-3] They are usually concentrated in the asphaltene fraction which is known to be comprised of micellular aggregates.[4] The micellular structure is believed to be formed through intermolecular aromatic plane stacking, hydrogen bonds, and charge transfer interactions. Such a micelle structure of the asphaltene interferes with its conversion into smaller molecules as it promotes the production of sludge and coke precursors over the catalyst through retrogressive reactions of dealkylation and dehydrogenative condensations, especially under the severe conditions used to achieve high conversions via hydrocracking.[5-8]

The metallic compounds in the asphaltene and/or polar fractions are deposited onto the catalyst along with a considerable amount of carbon precursors, and deactivate the hydrogenation activity. These deposits also enhance dehydrogenation reactions and coke formation in the hydrotreating processes. Hence, the decoagulation of the asphaltene fraction is very important for its depolymerization so as to allow the demetallation to proceed with minimal carbon deposition. There have been many reports on attempted ways to handle the asphaltene, such as extractive removal, solvation, and hydrogenation.[9]

In the present study, the aggregate sutucture of a vacuum residue and its fractions is investigated by step scan XRD at variable temeperatures with or without solvent, in order to clarify the changes in

their micellular structure during the heating or the solvation. In addition, adsorptive concentration of the heavy asphaltene fraction from the vacuum residue by using carbon particles is also applied for the removal of catalyst poisons in the following catalytic upgrading processes.

EXPERIMENTAL

An Arabian mix crude vacuum residue (VR) was used in the present experiments. VR was fractionated by hexane extraction. In the present study, the hexane insoluble(HI) and soluble (HS) fractions were defined as asphaltene and maltene, respectively. The HS was further fractionated into three components of saturates(Sa), aromatics(Ar), and polars(Po) by a conventinal alumina column chromatography. The elemental analyses of the fractions before and after the hexane fractionation are summarized in Table 1. Some properties of carbon supports used in the present study are summarized in Table 2.

The adsorption treatment of VR(20 g) by using variable amounts of carbon adsorbent(0 - 4.0 g) was performed with stirring at 60 °C for 1 h. After the treatment, the adsorbent was first washed with n-hexane and then thoroughly washed with THF(tetrahydrofuran) under the ultrasonic irradiation to recover the soluble fractions of hexane soluble(HS) and hexane insoluble but THF soluble(HI-THFS) from the adsorbent. The yield of the THF insoluble residue was calculated based on the weight of the dried adsorbent.

The step scan XRD(a high resolution liquid mode by Rigaku-2000) of VR fractions was measured by the scan speed of 0.4 sec/0.01 ° at variable temperatures of 30 to 300 °C with or without solvent of toluene of variable amounts.

RESULTS AND DISCUSSION

Composition and Structure of VR Fractions

The VR was consisted of 7.4 % HI and 92.6 % of HS, the latter of which was further fractionated into 16.3 % of Sa, 50.2 % of Ar, and 26.1 % of Po. The heteroatom-containing compounds including metallic compounds were concentrated in the HI as summarized in Table 1.

The XRD patterns of VR fractions are shown in Figure 1. The original VR showed a broad peak around 20 ° with a rather sharp shoulder peaks around 22 ° and 24 °. The HI showed a relatively sharp peak around 26 ° with a slight peak of 20 °, reflecting their larger aromatic rings and their stacking aggregate structure. Ar and Sa showed a rather sharp peak around 20 °, indicating entanglement of their longer alkyl chains of variety and polymethylene entangement. The Po fraction showed a similar peak around 26 ° to that of the HI with a higher peak around 20 °, suggesting the similar structure to the asphaltene but with a smaller aromatic ring and molecular weight, and longer alkyl chains as reported in a previous paper.[9]

The Effect of the Heating and Solvent on the Aggregate Structure of the Asphaltene

Figure 2 shows the XRD patterns of VR during the heating from 30 to 300 °C. The sharp peaks around 22 and 24 ° disappeared by the heating to 100 °C, and the broad peak around 20 ° was shifted to the smaller angle direction during the heating up to 300 °C, suggesting that the aliphatic chain entanglement may be liberated by the heating. The shoulder peak around 26 ° derived from the asphaltene fraction also disappeared by the heating up to 200 °C. Figure 3 shows the XRD pattern of HI during the heating to 300 °C. The peak around 26 ° was not changed by the heating to 200 °C, while the further heating to 300 °C weakened the peak very much, but it was still survived at a high temperature 300 °C in the case of the asphaltene fraction alone.

10 to 30 % addition of toluene to VR decreased the peaks around 22 ° and 24 ° with the broadening of the peak around 20 °. These peaks were almost completely removed by the addition of 50 % toluene. On the other hand, the addition of toluene to the HI broadened the whole peak with decreasing markedly the peak of 26 °. The larger amount of toluene addition over 75 % appeared necessary for the complete removal of the peak around 26 ° derived from aromatic plane stacking.

Adsorption Treatment of VR by Carbon Supports

Figure 4 shows the yields in the adsorption treatment of VR by KB at 60 °C. The THF insoluble(THFI) yield increased with the added amount of KB, and 2.0 g of KB addition removed almost completely the HI fraction from VR as THFI. The HI but THF soluble fraction decreased with the increased amount of THFI fraction. 0.6 to 1.0 g of KB addition appeared enough for the selective removal of the heavier fraction without increasing the HI-THFS fractions. Figure 5 illustrates the XRD profiles of the THFI before and after the adsorption treatment by KB. The untreated KB showed a very slight peak around 26°. The adsorbed THFI exhibited a broad peak around 26 °, while the relatively sharp peak of the original asphaltene around 26 ° decreased with the addition of KB, indicating selective adsorption of the heavier fraction in the asphaltene.

Figure 6 illustrates the comparison of the adsorption treatments of VR with variable carbon adsorbents. The heavier fraction in VR was selectively adsorbed on carbon blacks and mesoporous carbons, but never adsorbed onto the microporous activated carbon fibers such as OG-7A and 15A.

Table 2 also summarizes the adsorbed amount of THF insoluble(THFI) with the metal concentrations analyzed by XRF measurements. MA 600 adsorbed the very small amount of THFI (0.37 wt%) with the higher concentrations of V(489 ppm) and Ni(187 ppm), although its surface are was as low as 150 m^2/g. Carbon blacks of KB-600JD and BP2000 were also effective for the removal of the concentrated heavy fraction from VR, although the adsorbed amount of THFI was relatively higher than the other carbon adsorbents. A efficient recovery procedure of the heavier fraction from carbon black particles of high surface area should be designed for the application of such adsorbent to the upgrading of VR.

Based on the present study, mesoporous carbon particles can be a candidate for the selective removal of metal-containing heavy asphaltene fraction from VR and the regenerative recovery without too strong adsorption of the polar and heavier fraction.

ACKNOWLEDGMENT

This work has been carried out as a research project of The Japan Petroleum Institute commissioned by the Petroleum Energy Center with the subsidy of the Ministry of International Trade and Industry.

REFERENCES

1. Speight, J.G. "*The Desulfurization of Heavy Oils and Residua*", Dekker, New York, **1981**.
2. Nelson, W.L. *Oil & Gas J.* **1976**, 74, 72.
3. H.R.Siewert, H.R.; Koenig, A.H.; Ring, T.A. *Hydrocarbon Process.* **1985**, 64, 61.
4. Yen, T.F.; Erdman, J.G.; Pollack, S.S. *Anal.Chem.* **1961**, 33, 1587.
5. Howell, R.L.; Hung, C.W.; Gibson, K.R.; Chen, H.C. *Oil & Gas J.* **1985**, 83, 121.
6. Mochida, I.; Zhao, X.Z.; Sakanishi, K.; Yamamoto, S.; Takashima, H.; Uemura, S. *Ind. Eng. Chem. Res.*, **1989**, 28, 418.
7. Mochida, I.; Zhao, X.Z.; Sakanishi, K. *Ind.Eng.Che.Res.*, **1990**, 29 334.
8. Sakanishi, K.; Zhao, X.Z.; Mochida, I. *J. Petrol. Inst. Jpn.* **1992**, 35, 203.
9. Sakanishi, K.; Yamashita, N.; Whitehurst, D.D.; Mochida, I. *Catal. Today*, **1998**, 43, 241.

Table 1 Elemental Analysis of Arabian mixed crude vacuum residue

Sample	Content [wt%]	wt% C	H	N	Others	H/C	N/C	Vanadium [ppm]
Original VR	100.0	84.4	10.4	0.29	4.9	1.48	0.003	87
HS	92.6	84.5	10.8	0.24	4.4	1.53	0.002	90
Sa	16.3	85.6	13.3	0.04	0.74	1.85	0.000	-
Ar	50.2	84.3	10.2	0.20	5.4	1.45	0.002	-
Po	26.1	82.6	8.6	0.82	8.1	1.24	0.009	-
HI	7.4	84.1	7.4	0.82	7.6	1.06	0.008	998

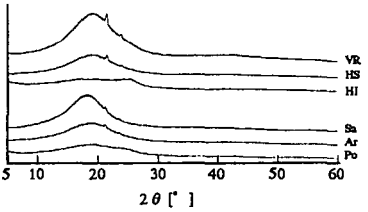

Figure 1 XRD of each Fraction in VR (Step Scan 4sec/0.01°)

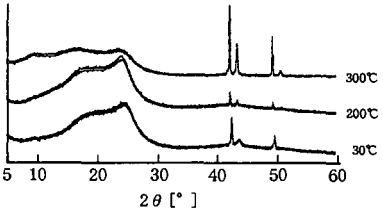

Figure 3 XRD of Heated HI (Measuring Temp. 30 to 300°C, Step Scan 4sec/0.01°)

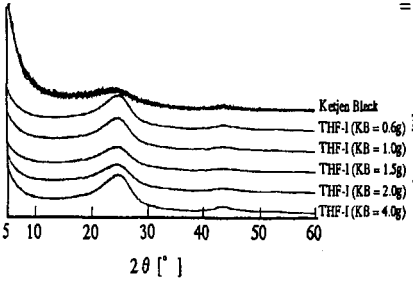

Figure 5 XRD of THFI adsorbedon KB (VR/KB = 20.0g/Xg, Mixing Time = 1h, Temp = 60°C, Step Scan 4sec/0.01°)

Table 2 Some properties of carbon adorbents and their adsorption performance of VR

	S.A. [m2/g]	ave. radius [A]	adsorbed as THF-I [wt %]	V of adsorbed fraction [ppm]	Ni of adsorbed fraction [ppm]
KB 600JD	1270	-	1.42	301	128
MA600	150	-	0.37	489	187
BP2000	1475	-	2.00	256	132
OG-7A	957	8.36	0.00	-	-
OG-15A	1776	9.76	0.00	-	-
OG-20A	1930	9.83	0.10	61	192
MP-60	1276	16.50	0.78	188	70
MP-90	1371	21.10	1.62	200	69

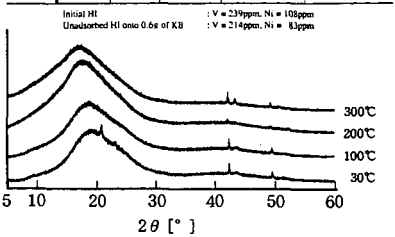

Figure 2 XRD of Heated VR (Measuring Temp. 30 to 300°C, Step Scan 4sec/0.01°)

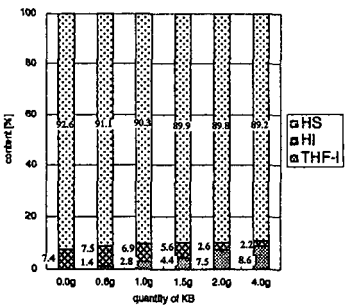

Figure 4 Adsorption of VR into KB (VR/KB = 20.0g/Xg, Mixing Time = 1h, Temp = 60°C)

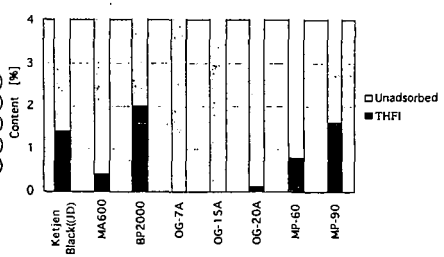

(VR= 20.0g, Carbon = 0.6g, Mixing Time 1h, Temp 60℃)

Figure 6 Adsorption treatment of VR with variable carbons

SULFUR CHARACTERIZATION IN ASPHALTENE, RESIN, AND OIL FRACTIONS OF TWO CRUDE OILS

Sudipa Mitra-Kirtley, Oliver C. Mullins, Corie Y. Ralston, and Courtney Pareis

Rose-Hulman Institute of Technology, IN 47803 (SMK, CP)
Schlumberger Doll Research, Old Quarry Road, Ridgefield, CT 06877 (OCM)
Albert Einstein University, New York, NY 10461 (CYR)

Sulfur chemical species have been determined for asphaltene, resin, and oil fractions of two crude oils by using X-ray absorption near-edge structure (XANES) spectroscopy. The prevalent sulfur species are thiophene, sulfide, and sulfoxide. The asphaltene fraction of one of the oils, CAL, is known to have a very high sulfoxide content. The asphaltene fractions of both the crude oils were analyzed several years ago, and had generated similar sulfur fractions as the present study. This shows that the oxidation of the sulfides in CAL occurred within the earth formation, and not by air oxidation after the production of the crude oil. This also confirms the robustness of the analysis method. Results from this study also show that large sulfoxide fractions are obtained for *all* components of CAL, even in the (typically) non-polar oil fractions. The second crude oil is lower in oxygen, and shows similar composition in *all* three fractions.

Key Words: Sulfur, XANES, Asphaltenes

INTRODUCTION

Crude oils are described as consisting of three fractions—asphaltenes, resins, and oils; these fractions are determined by solubility classification.[1-3] One definition is that the oil fractions are the pentane-soluble portion of crude oils, resins are pentane-insoluble and heptane-soluble portions and asphaltenes are heptane-insoluble portions of crude oil. The solubility classification of these crude oil components correlates strongly with chemical properties of the derived components. For instance, asphaltenes from different crude oils are remarkably similar in their chemical properties. Asphaltenes interfere with producing, transporting, and refining of crude oils, and the resins stabilize the suspension of asphaltenes in crude oils; they are, therefore, both prominent in crude oil utilization. Asphaltenes and resins contain higher fractions of heteroatoms, compared to the oil fraction. Consequently, heteroatoms, particularly their polar moieties, partly determine the chemical properties of these crude oil fractions, and, to the extent that solubility is influenced, partly define these fractions. For example, chromatographic studies have shown that certain alkyl sulfides are present in the resin fraction, while the corresponding sulfoxides are present in the asphaltene fraction. The much greater polarity of the sulfoxide group moves the oxidized component from the resin to the asphaltene fraction. The object of this paper is to investigate the relative abundances of the different sulfur chemical forms, especially the polar groups, in the different fractions. The asphaltenes had been studied by the same method about a decade ago, and the present study verified the reproducibility of the results.

XANES spectroscopy has been successfully employed to probe the chemical nature of sulfur in different fossil-fuel components[3-10] such as asphaltenes[3,5,6], crude oils[3,7], and coals[3,8,9]. Generally, each different chemical form of sulfur gives rise to its own characteristic single, large peak (1s-3p electronic transition). The resonance peaks of sulfide and thiophene are resolvable but are close, introducing some errors in their fractions. The sulfoxide peak, however, is well resolved from all others, and has less associated errors. In asphaltenes, sulfur occurs as mostly thiophenic (aromatic) and sulfidic (saturated) forms. Sulfoxide is the oxidized form of sulfur found in asphaltenes, and usually appears to have resulted from oxidation of sulfide present in crude oils. In some asphaltenes, thiophenic sulfur dominates, while in others, thiophenic and sulfidic forms are comparable. More thermally matured crude oils have prominent thiophenic fractions in the asphaltene fractions. In coal sulfur exists in both organic and inorganic forms. Many coals contain pyrite, and the lowest rank coals may contain sulfate. The organic forms of sulfur in coals are in thiophenic and sulfidic forms, similar to asphaltenes except that coals lack sulfoxides. Nitrogen has also been explored in XANES studies on asphaltenes and other carbonaceous materials.[3] These studies have shown that in asphaltenes nitrogen occurs almost entirely in aromatic forms,

in pyrrolic and pyridinic structures.

In this study, we present results of sulfur XANES spectroscopy on asphaltenes, resins, and oil fractions obtained from two crude oils. One of the two asphaltenes is known to be high in sulfoxide, the other low, thus the two crude oils constitute a good test case for the deposition of polar sulfur chemical groups in different crude oil fractions. The asphaltene fractions from both the crude oils had been analyzed by XANES method several years ago, and one of the issues this paper addresses is to verify the robustness of the analysis method, as well as to investigate if there is any considerable air oxidation. In both the studies, XANES sulfur spectra were analyzed with the use of reference spectra of model compounds in the usual fashion.[3] The principal finding here is that the three components of the crude oils have similar fractions of sulfoxide. The very polar sulfoxide group does not alter solubility sufficiently to transfer all sulfoxide-containing molecules to the heavy ends.

EXPERIMENTAL

Sulfur K-edge XAFS spectra were collected at beam-line X-19A at the National Synchrotron Light Source (NSLS) at Brookhaven National Laboratory. A double-crystal monochromator of Si (111) crystals was used for dispersion. In order to minimize effects from higher order harmonics, about 80% detuning were used. The X-ray beam exited the UHV through a beryllium window immediately adjacent to the sample chamber, which was filled with helium in order to ensure minimum X-ray absorption by the atmosphere. The data were collected in the fluorescence mode with the use of a Stern-Heald detector and Mylar films were used in the sample chambers to hold the sample.

The sulfur model compound samples were first diluted in boric acid, finely ground, and then smeared on sulfur-free Mylar film, which was placed in the beam path. The fossil fuel samples were either ground and mounted on the film, or diluted in CCl_4 and evaporated to dryness on a film that was then placed in the beam path.

All the sulfur models were obtained from Aldrich Chemical Company; they were dibenzyl sulfide, dibenzothiophene, thianaphthene, dibenzyl sulfoxide, iron (II) sulfide, potassium sulfate, and sodium thiosulfate. The fossil-fuel samples were the asphaltene, resin, and on fractions obtained from CAL and KUW2 (UG8) crude oils.

Virgin stock-tank crude oils CAL and KUW2 were used for analysis. Samples were prepared as follows: a solution was prepared with 40 cc of pentane per gram of crude oil. The solution was stirred for 24 h and filtered. The filtered soil was washed with pentane until the pentane wash was colorless. Pentane was removed from the filtrate by evaporation to yield the on fraction. The separated solid was dissolved in a small volume of toluene; heptane was then added in the volume ratio of 40: 1. After being stirred for 24 h, the asphaltenes were filtered, and the heptane solution was taken to dryness to obtain the resins. We note that in the non-unique definitions of crude oil components, one could label all pentane-insoluble as asphaltenes. According to this classification, our three fractions would be the heavier asphaltene fraction (heptane-insoluble), the lighter asphaltene fraction (pentane-insoluble and heptane-soluble) and the maltenes. This classification was noted to help comparisons with other work.

A least-squares fitting program was used to quantitatively analyze the sulfur spectra. The spectra were analyzed by methods previously described[8]. The spectra of models and the fossil fuels were first normalized with respect to the step heights and then fitted to a sum of several Lorentzian peaks and an arctangent step. The Lorentzian peaks correspond to resonant electronic transitions,

Figure 1

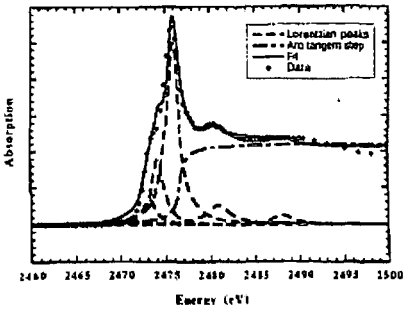

whereas the step accounts for electronic transition to the continuum. The curves from the model compounds were used as basis vectors to fit the curves of the crude oil components. Concentration corrections were applied to the model spectra. Figure 1 illustrates the fitting procedure of a typical sulfur XANES

spectrum, here a spectrum for CAL resin. The fitting procedure was performed on a Macintosh computer using the curve-fit routine of KaleidaGraph software. Using this procedure, all the XANES spectra of the models and the crude oil fractions were fitted. The spectra of the crude oil fractions were then represented as a linear sum of the spectra of model compounds in order to generate sulfur fractions. The error for the sulfide and thiophene fractions is about 10% due to the close proximity of their peaks and the error is smaller for the sulfoxide and higher oxide fractions, which all have isolated peaks.

RESULTS AND DISCUSSION

Figure 2 is a plot of the sulfur XANES of the asphaltene, as well as resin and oil fractions

Figure 2

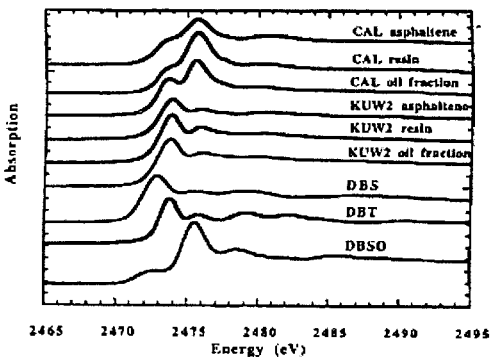

obtained from CAL and KUW2 crude oils. All these spectra have been normalized to the same step height. In addition, Fig. 2 shows the spectra of dibenzyl sulfide, dibenzothiophene, and dibenzyl sulfoxide, the three relevant model compounds. The model compounds show the dramatic effect that oxygen has on the energy of the ls-3p resonance; higher oxidation states of sulfur yield higher transition energies. The thiophene and sulfide both have a formal oxidation state of zero, but the thiophene is at a slightly higher energy. This is probably due to effects of aromatic electron delocalization.[3] Some electron density in the sulfur lone-pair p_z orbital is delocalized in the ring, thereby reducing electron density on the sulfur site. This effect is very large on nitrogen in the more aromatic pyrrole rings.[3]

The most striking difference between the two suites of oil component data is seen in the relative intensities of the oxidized (sulfoxide) and reduced sulfur resonance's. For *all* components of the CAL crude oil, the sulfoxide peak dominates. In *all* KUW2 fractions, the sulfoxide is a minor component and reduced sulfur species dominate. The spectra immediately show that sulfoxide is present in approximately the same amounts in all the three components for each crude oil and is not limited to the more polar resin and the asphaltene fractions.

Table 1. Relative abundances of sulfur forms in the asphaltene, resin, and oil fractions of CAL, and KUW2 (UG8).

	Sulfide	Thiophene	Sulfoxide	Sulfone	Sulfate
CAL Asph	15	29	50	5	1
CAL Resin	11	27	59	1	1
CAL Oil	24	27	46	1	1
KUW2 Asph	40	55	2	1	1
KUW2 Resin	40	52	5	1	1
KUW2 Oil	45	47	5	1	1

The relative abundance's of the different sulfur forms of the asphaltenes, resins and oil fractions obtained from CAL and KUW2 crude oils is tabulated in Table I. These samples are not expected to have any sulfone or sulfate, and, within error, which is estimated to be within 10%, none was found. All the fractions of CAL and KUW2 show considerable fractions of organic

sulfide and thiophene. In addition, all fractions of CAL contain high and comparable quantities of sulfoxide. Asphaltenes and resins are known to be more polar than the oil fraction; moreover, sulfoxide is very polar. In spite of this observation, the oil fraction of CAL contains a high fraction of oxidized sulfur. Of course, sulfur represents a smaller mass fraction of the oil phase than of the heavier ends. The resin fraction of CAL has a greater sulfoxide fraction than the asphaltene fraction does, perhaps making the resins the most polar fraction for this crude oil. The sulfur compositions of the KUW2 fractions are all low in sulfoxide and are also comparable in their sulfide and thiophene fractions. For both CAL and KUW2, the oil fractions have slightly higher sulfide fractions. Similarly, the carbon in the oil fraction is also less aromatic in the oil fraction than in the heavy ends.[1-3]

Table II. Results from XANES analysis by Waldo et al [7]

Asphaltene	Sulfide	Thiophene	Sulfoxide	Sulfone	Sulfate
CAL	16	36	44	3	<1
KUW2	43	52	4	2	<1

Previously, asphaltene fractions from CAL and KUW2 were studied by Waldo et al, by XANES spectroscopy, and yielded similar results, as shown in Table II[7], in spite of the seven-year difference in the isolation and analysis of the different CAL and KUW2 asphaltene samples. Error analysis performed on the analysis procedure confirms that the above analysis method is robust, and the numbers are within a 10% error margin. The present study also confirms that the most likely source of sulfoxide is oxidation of the sulfide *within* the crude oil,[6] which is consistent with the well-known lability of some sulfides towards oxidation. A stock tank oil sample was used for the experiments, and not a sealed-bottom-hole sample. Therefore, it is unlikely that the sulfoxide in CAL was generated after production of the crude on by air oxidation. We have treated all our asphaltene and crude oil samples in a similar manner, yet CAL asphaltene has a sulfoxide fraction four times greater than any other we examined,[6] while the KUW2 asphaltene has little sulfoxide. Furthermore, the CAL resin and the CAL oil phase contain large sulfoxide fractions, while the corresponding KUW2 fractions show little sulfoxide in spite of identical treatment of these crude oil samples. Thus, we believe that the extreme oxidation of the sulfides in CAL occurred within the earth formation, perhaps due to contact with meteoric water. The small thiophene fraction in CAL is consistent with low maturity, the shallow depth of burial allowing for exposure to meteoric water.

CONCLUSIONS

Sulfur XANES analysis shows that the sulfoxide-to-sulfur ratios are comparable in all fractions of a given crude oil. Sensitivity analysis confirms the robustness of the XANES analysis method, previous results were similar, in spite of the seven-year difference in the isolation and analysis of the different CAL and KUW2 asphaltene samples. This study also supports the contention that the oxidation process took place in situ; thus, the sulfur speciation of different virgin asphaltenes and crude oils can be very different in nature, with sulfoxide fractions varying from 0 to 50%. Such large variations in the chemistry of different petroleum asphaltenes are unusual. These results should be considered when comparing asphaltene results from different studies and samples, because sulfoxides are very polar and thereby partly determine the asphaltene fraction.

ACKNOWLEDGMENT

The XANES experiments were carried out at me National Synchrotron Light Source at Brookhaven National Laboratory, which is supported by the US. Department of Energy.

REFERENCES

1. *Bitumens, Asphalts, and Tar Sands,* G.V. Chilingarian and T.E. Yen, Eds. (Elsevier, New York, 1978.
2. J. G. Speight, *The Chemistry and Technology of Petroleum* (Marcel Dekker, New York, 1980).
3. O. C. Mullins, in *Asphaltenes: Fundamentals and Applications*, E. Y. Sheu and O. C. Mullins, Eds. (Plenum Press, New York, 1995).

4. O. P. Strausz, The Fine Particle Soc. Meeting, Chicago, Illinois (1995); Also see J. D. Payzant, T. W. Mojelsky, and O. P. Strausz, Energy & Fuels, **3**, 449 (1989).
5. G. N. George and M. L. Gorbaty, J. Am. Chem Soc. **111**, 3182 (1989). 6. G. S. Waldo, O. C. Mullins, J. E. Penner-Hahn, and S. P. Cramer, Fuel **71**, 53 (1992).
7. G. S. Waldo, R. M. K. Carlson, J. M. Moldowan, K. E. Peters, J. E. Penner-Hahn, Geochim, Cosmochim. Acta **55**, 802 (1991).
8. G. P. Huffman, S. Mitra, F. E. Huggins, N. Shah, S. Vaidya, and F. Lu, Energy & Fuels **5**, 574 (1991).
9. M. L. Gorbaty, G. N. George, and S. R. Kelemen, Fuel **69**, 945 (1990).
10. S. Mitra-Kirtley, O. C. Mullins, J. van Elp, S. J. George, J. Chen, and S. P. Cramer, J. Am. Chem. Soc. **115**, 1, 252 (1993).

FRACTIONATION AND MOLECULAR ANALYSIS OF A VACUUM RESIDUE ASPHALTENES

Ming-Gang Yang[1] and Semih Eser[1, 2]

1.Lab.for Hydrocarbon Proc.Chem, The Energy Institute, Penn State Univ., 209 Acad. Proj. Bldg.
2. Dept. of Energy and Geo-Environmental Eng., Penn State Univ., 154 Hosler Building, University Park, PA 16802

KEYWORDS: Petroleum asphaltenes, Pyrolysis-GC/MS, NMR, LDIMS

INTRODUCTION

Petroleum asphaltenes are defined as the n-pentane or n-heptane insoluble but toluene soluble fraction of crude oils or petroleum residua. This operational definition is a consequence of the extremely complex structure of asphaltenes which consist of thousands of compounds containing highly aromatic cores, long chain aliphatic groups, heteroatoms (sulfur, nitrogen, and oxygen) as well as trace quantities of heavy metals (vanadium and nickel). Therefore, it is extremely difficult to elucidate the molecular structure of petroleum asphaltenes.

A number of studies have been carried out including asphaltene pyrolysis[1, 2], chemical reduction[3] and oxidation (RICO)[4] with catalysts using many analytical techniques[5-9] such as GC-MS, MALDI, LDIMS, HRMS, $^{1}H/^{13}C$ NMR, FT-IR, UV-vis spectra, EXAFS, SEC, ESR, XRD, SANS, etc., to investigate the asphaltene structure at the molecular level. The results from these studies have brought to light a wealth of valuable information on asphaltenes. Recent structural models suggest that asphaltene molecules be composed of an aromatic core with six condensed aromatic rings on average that is substituted by n-alkyl groups averaging C_8 in length[10]. In addition, bridging polymethylene groups may be present which connect the aromatic core to smaller aromatic and thiophenic rings. In general, about 25% of the sulfur is thermally labile alkyl and cyclic sulfides, while the remaining sulfur is present in the aromatic core along with the majority of the N and O heteroatoms [11, 12]. The distribution and structure of the heteroatoms in the aromatic core is largely unknown. The molecular weight of individual asphaltene molecules averages less than 1000 amu, but the asphaltene molecules interact strongly in solution, forming colloidal aggregates with very high apparent molecular weights[13].

In this study, a petroleum residue asphaltenes were separated into six subfractions based on their solubility in binary solutions of n-pentane and toluene at different proportions. The separated subfractions were analyzed by laser desorption ionization mass spectrometry (LDIMS), $^{1}H/^{13}C$ NMR, and pyrolysis gas chromatography/mass spectrometry (Py-GC/MS).

EXPERIMENTAL

The n-pentane (HPLC grade, 99.8 %) and toluene (HPLC grade, 100 %) were supplied by Fisher Chemicals, and J.T. Baker Inc. respectively. Chloroform-d (99.8 atom% D) and Chrom(III)-acetylacetonate (97 % UV) used in $^{1}H/^{13}C$ NMR analysis were supplied by Aldrich Chemical Company, Inc., and Fluxa Chemika. A commercial petroleum vacuum residue sample was used as a source of asphaltenes.

The vacuum residue sample was separated into maltenes (n-pentane soluble) and asphaltenes (n-pentane insolubale) by adding n-pentane in a volume/weight ratio of n-pentane to residue of 60:1 (mL/g) followed by filtration. A sample of 1 g asphaltenes was dissolved in 27 mL toluene, and 33 mL n-pentane was added into the solution by stirring with a magnetic bar at ambient temperature. After adding n-pentane, the ratio of the total volume of the two solvents to asphaltenes was 60:1 mL/g with an n-pentane to toluene ratio of 55/45 in volume. The solution was covered and stirred overnight for precipitation of insolubles. After filtration, the insoluble fraction was collected and dried in an oven at 75 °C and 0.1MPa vacuum overnight to obtain the first subfraction (Sample AS6). The n-pentane and toluene in the filtrate were evaporated in a rotary evaporator to collect the remaining asphaltenes that were dried in an oven at 75 °C and 0.1MPa vacuum overnight. The dried sample was dissolved in toluene again, and following the procedure described above, sample AS5 was precipitated in a solution with an n-pentane to toluene ratio of 65/35 in volume. Similarly, samples AS4 (n-pentane to toluene = 75/25), AS3 (85/15) and AS2 (95/5) were precipitated in binary solutions with the increasing proportion of n-pentane. The last fraction, AS1, (dissolved in the solution of n-pentane to toluene = 95/5) was obtained by evaporating the solvents. The asphaltene fractionation scheme is shown in Figure 1.

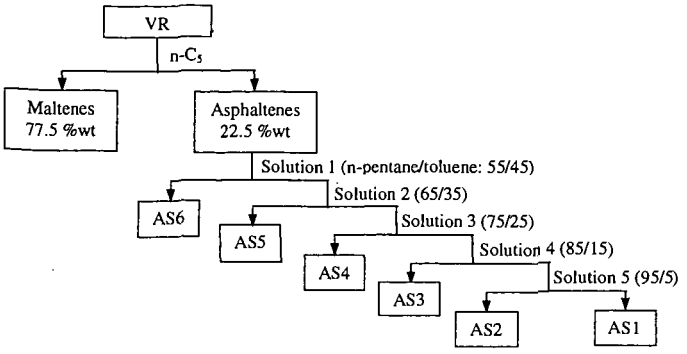

Figure 1. Flow chart for fractionation of petroleum vacuum residue asphaltenes.

The LDIMS spectra were acquired on a PerSeptive Biosystems Voyager-DE STR mass spectrometer using 337 nm light from a pulsed nitrogen laser for ionization. High-resolution spectra (M/ΔM ~ 10000 at m/z 500) were obtained using the reflector mode. Samples were prepared by dissolving approximately 50 micrograms of material in 200 microliters of tetrahydrofuran. The sample solution of 0.5 microliters was deposited on the gold-plated target, and the solvent allowed to evaporate under ambient laboratory conditions. Samples were introduced into the mass spectrometer and analyzed as soon as possible to minimize evaporation of more volatile components. Ionization was conducted using laser fluency slightly above the threshold for ionization (laser power ~ 106 W/cm^2), and a total of 256 laser shots acquired over numerous sites within each sample were averaged.

The NMR spectra were obtained using a BRUKER AMX360 NMR instrument operating at 360 MHz for ^{1}H NMR, and 89 MHz for ^{13}C NMR measurements. The NMR samples were prepared by dissolving about 100 mg asphaltenes into 1 mL chloroform-d solvent. Tetramethylsilane (TMS) was used as an internal standard mixed with chloroform-d solvent as received. A relaxation agent, chrom(III)-acetylacetonate, was added into the sample solution (0.03M) to get quantitative ^{13}C NMR measurements

For Pyrolysis-GC/MS experiments, samples (about 6 mg) were first loaded in an unsealed quartz tube. Then, the tube was inserted into a filament coil that is placed in the probe gun. The gun tube was inserted into an interface where the sample was pyrolyzed. Pyrolysis temperature, time, and the interface temperature were controlled by Pyroprobe 1000. Pyrolysis conditions were 800 °C, 10 seconds, and a heating rate of 5 °C/ms. The interface temperature was set 290 °C. Pyrolysis products were collected in a capillary column at liquid nitrogen temperature and then separated in a temperature programmed DB-17 capillary column by HEWLETT 5890 II GC, and characterized by HEWLETT 5971A MS.

RESULTS AND DISCUSSION

The petroleum vacuum residue contained 77.5 wt% maltenes and 22.5 wt% asphaltenes (n-pentane insoluble). Table 1 shows the yields of asphaltene subfractions separated following the scheme shown in Figure 1.

Table 1. Yields of solvent subfractions of asphaltenes.

Subfraction	AS1	AS2	AS3	AS4	AS5	AS6	Loss
Distribution / wt%	25.5	5.3	18.0	22.9	21.0	4.2	3.1

The results in Table 1 show that the vacuum residue asphaltenes could be further fractionated using the binary mixtures of n-pentane and toluene with different composition. The yields of subfractions AS2 and AS6 were much lower than those of the other subfractions.

Laser desorption ionization mass spectrometry (LDIMS) results in little fragmentation of the constituent molecules. Therefore, it is a useful technique to determine the molecular weight distribution in complex mixtures. The mass distributions of samples AS2, AS4 and AS6 are shown in Figure 2. Each asphaltene subfraction displayed a different molecular weight distribution. The distribution became wide and the number average molecular weight increased in mass/charge ratio from AS2 (250-600) to AS4 (300-800), and to AS6 (350-1100). The maximum abundance of

molecular constituents for the three samples, AS2, AS4, and AS6 is at 300, 350 and 500 m/z, respectively.

The ^1H NMR spectra have been divided into four regions consisting of γ-methyl hydrogens (H_γ) between 0 and 1 ppm; hydrogens from β-methyls, methines, and methylenes β or further to the aromatics (H_β) between 1 and 2 ppm; hydrogens from all aliphatic sites attached to aryl carbon (H_α) between 2 and 5 ppm; and aromatic hydrogens (H_{ar}) between 6 and 9 ppm. The ^{13}C NMR spectra have been divided into two integration domains which are aliphatic carbons (C_{al}) between 10 and 65 ppm, and aromatic carbons (C_{ar}) between 100 and 170 ppm. The hydrogen and carbon molar distributions derived from $^1H/^{13}C$ NMR spectra are listed in Table 2.

Table 2. Relative molar distribution of hydrogen and carbon in asphaltene subfractions

	AS2	AS3	AS4	AS5	AS6
H_α	0.17	0.33	0.12	0.21	0.37
H_β	0.63	0.43	0.62	0.57	0.49
H_γ	0.08	0.05	0.04	0.04	0.03
H_{ar}	0.12	0.19	0.22	0.18	0.11
C_{al}	0.60	0.54	0.53	0.52	0.51
C_{ar}	0.40	0.46	0.47	0.48	0.49

The carbon aromaticities of all the subfractions are similar to one another with a slightly lower aromaticity of AS2 compared to the other samples. There are, however, significant differences in the distribution of hydrogen between the subfractions. The relatively low hydrogen aromaticities of AS2 and AS6 can be attributed to more extensive alkyl substitution, and more condensed struetures of aromatic ring systems, respectively. Differences in aliphatic hydrogen distribution between AS2 and AS6 also indicate variations in the nature of the alkyl groups. From the distribution of aliphatic hydrogen groups, similarities are noted between AS2 and AS4, and between AS3 and AS6. The fraction AS5 falls into an intermediate position between the two groups, particularly in H_α and H_β contents.

The average structural parameters do not give much information regarding the type and distribution of molecular constituents and their organization within the molecules. Pyrolysis GC/MS may provide some useful data on thermally labile molecular units and how they are connected. Asphaltenes during Py-GC/MS experiment were converted into three fractions: volatiles, nonvolatile heavy oils or tar, and remainder coke (tetrahydrofuran insoluble). The yield of each fraction was dependent on the pyrolysis conditions and the sample used. The sample AS2, for example, gave volatile fraction yield of 11.8 wt% at 600 °C, while at 800 °C, the yield increased to 45.2 wt%. The yields of volatile fractions from samples AS1 to 6 at 800 °C are listed in Table 3. The samples AS1 and AS6 showed higher yields of volatile fraction than samples AS3 and AS5.

Table 3. Yields of volatile fraction in asphaltene pyrolysis at 800 °C.

Sample	AS1	AS2	AS3	AS4	AS5	AS6
Yield / wt%	54.7	45.2	33.1	41.5	37.1	48.8

A Py-GC/MS total ion chromatogram for AS1 is shown in Figure 3. The volatile products consist mainly of alkanes (C_8 to C_{35}), 1-alkene (C_5 to C_{35}), alkylbenzenes (alkyl: C_1 to C_5), alkylnaphthalenes (alkyl: C_1 to C_3) and sulfur compounds (alkyl substituted thiophene, benzothiophene, dibenzothiophene and naphthothiophene). A small amount of isoalkanes and cycloalkanes (alkyl C_5 and C_6 ring) was also identified in the volatile products. Although the asphaltene subfractions AS1 to 6 gave different yields of volatile products, their composition appeared to be similar.

CONCLUSIONS

Asphaltenes derived from petroleum vacuum residua can be further separated into several subfractions based on their solubility in binary mixtures of n-pentane and toluene with different composition. Each subfraction still contains a large number of individual compounds. Distinct differences were observed between subfractions in average molecular weights, molecular weight distribution, aromaticity, and distribution of aliphatic hydrogen.

ACKNOWLEDGMENTS

We thank Dr. A. Daniel Jones (Director, Penn State Intercollegiate Center for Mass Spectrometry) for providing the data on Laser Desorption Mass Spectrometry analysis of the asphaltene subfractions.

REFERENCES

1. Ritchie, R.G.S.; Roche, R.S.; Steedman, W. *Fuel* **1979**, 58, 523.
2. Calemma, V.; Rausa, R.; D'Antona, P.; Montanari, L. *Energy & Fuels* **1998**, 12, 422.
3. Peng, P.; Morales-I, A.; Lown, E. M.; Strausz, O. P. *Energy & Fuels* **1999**, 13, 248.
4. Su, Y.; Artok, L.; Murata, S.; Nomura, M. *Energy & Fuels* **1998**, 12, 1265.
5. Montanari, L; Scotti, R. In *Structures and Dynamics of Asphaltenes*, Edited by Oliver C. Mullins and Eric Y. Sheu, Plenum Press, New York. **1998**, p 79-113.
6. Miller, J. T.; Fisher, R. B.; Thiyagarajan, P.; Winans, R. E.; Hunt, J. E. *Energy & Fuels* **1998**, 12, 1290.
7. Wilt, B. K.; Welch, W. T.; Rankin, J. G. *Energy & Fuels* **1998**, 12, 1008.
8. Ralston, C. Y.; Mitra-K., S.; Mullins, O. C. *Energy & Fuels* **1996**, 10, 623.
9. Shirokoff, J. W.; Siddiqui, M. N.; Ali, M. F. *Energy & Fuels* **1997**, 11, 561.
10. Strausz, O. P.; Lown, E. M. *Fuel Sci. Technol. Int.* **1991**, 9, 269.
11. Savage, P. E.; Klein, M. T. *Ind. Eng. Chem. Proc. Des. Dev.* **1985**, 24, 1169.
12. Mullins, O. P. In *ASPHALTENES-Fundamentals and Applications,* Edited by Eric Y. Sheu and Oliver C. Mullins, Plenum Press, New York. **1995**, p 53-96.
13. Boduszynski, M. M. *Energy & Fuels* **1988**, 2, 597.

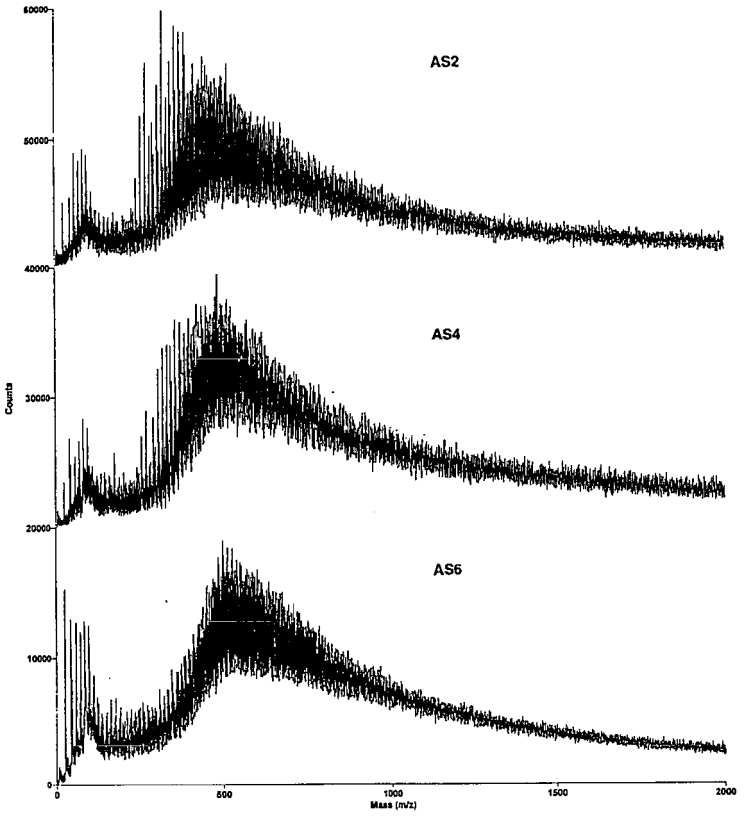

Figure 2. LDIMS spectra of three asphaltene subfractions.

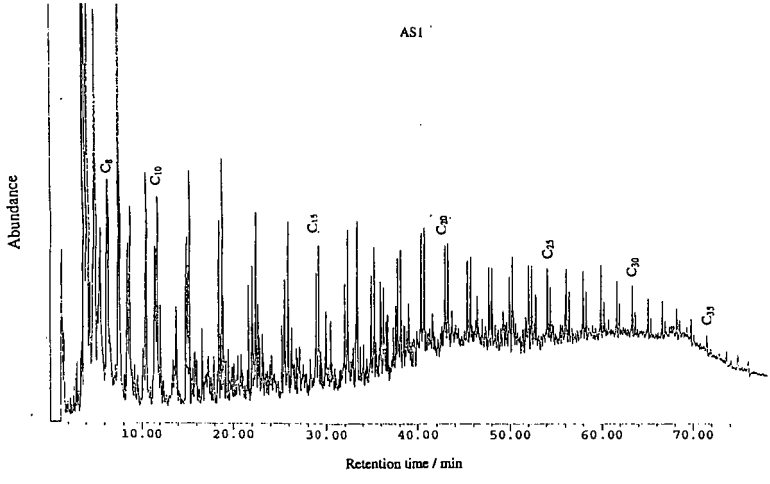

Figure 3. Py-GC/MS total ion chromatogram for asphaltene subfraction AS1.

COLLOIDAL NATURES OF TWO TYPICAL CHINESES VACUUM RESIDUA I: COLLOIDAL STRUCTURES IN TERMS OF SFEF FRACTIONS

Li Shenghua[1] Fu Honglan[2] Liu Chenguang[3] Liang Wenjie[3]

[1]Department of Precision Instrument, Tsinghua University, Beijing 100084
[2]Department of Biology, Peking University, Beijing 100871
[3]Department of Petroleum Refining, University of Petroleum, Shandong 257062

ABSTRACT: The physical structures of vacuum residua are of industrial potentiality in applications such as prevention of heavy organics deposition in petroleum production and phase separation of coke precursors in petroleum refining. Disclosure of the physical structures of two representative Chinese vacuum residua, Daqing and Shengli vacuum residuum, and their SFEF (supercritical fluid extraction and fractionation) fractions on the colloidal scale by FFRTEM (Freezing Fracture Replication Transmission Electronic Microscopy) indicate that all of them assume colloidal structures with different structural details dependent heavily upon their compositions or origins.

KEYWORDS: colloidal structures, vacuum residua, SFEF fractions

INTRODUCTION

Although more and more information has been accumulated about the natures of the physical structures of VR(VR), very limited images of the physical structures of the original VR are now available with the exception of some apriori knowledge about the colloidal aspects of VR with the support of indirect experiments and field experiences[1,2]. It is currently recognized that the physical structures of VR assume locally ordered structures on the molecular scale and heterogeneous micell structures on the colloidal scale[1]. Presently, it seems that the core of all the left issues concerning the colloidal characters of VR is not only to ascertain, with direct evidences, their apparent colloidal features but also to uncover their building units (components or fractions) as well as formation mechanisms.

The authors have attempted with Freezing Fracture Replication Transmission Electronic Microscopy (FFRTEM) to disclose the physical structures of Daqing, Shengli and Gudao VR on the colloidal scale and to evaluate the contributions of the SARA pseudo-pure-components to the colloidal configurations[5]. Conclusions drawn state that VR are of sol structures; asphaltenes and heavy resins construct the dispersed phases and the other fractions form the dispersing media. Useful as the deductions from FFRTEM are, they need further confirmation as there leaves some room for improvement in sample separation and structure identification employed by the authors.

Firstly, the conventional separation procedure of SARA compositions of VR may incur breakdown or distortion of the real physical structures of original VR. With the supercritical fluid extraction and fractionation (SFEF) technique, however, the possible influences on the real physical structures of original VR could be controlled to the minimum for the solubility classes from the SFEF technique can best keep the continuity of both the compositional and the structural distributions of VR; and secondly, though the FFRTEM technique is able to display in a qualitative manner the colloidal nature of VR and the shape and size of the dispersed phases, it presents no information on the chemical compositions of both the dispersed and the dispersing phases without assistance from the sample separation technique. In fact, when solubility class compositions are employed to characterize the colloidal structures of VR, the validity and conciseness of the FFRTEM technique itself to determine the solubility class compositions of both the dispersed and the dispersing phases depend heavily on the fineness of the VR fractionation.

Still, the established FFRTEM technique was adopted in this study to unfold the colloidal structures of two typical Chinese VR and their SFEF fractions. In such a way, more valid and more direct evidences, instead of the apriori and indirect knowledge, could be accumulated to lend some support to the construction details of the colloidal VR.

MATERIALS AND METHODS

Separation of vacuum residua into SFEF fractions

A Supercritical Fluid Extraction and Fractionation (SFEF) technique[4], which was developed by the State Key Laboratory of Heavy Oil Processing, University of Petroleum, China, was

utilized to separate nondestructively Daqing and Shengli VR into the proper number of subfractions. In the operation, n-pentane was used as the extractant with flow rate of 100mL /min; the initial pressure of 4.0MPa was set and the final pressure was controlled to be 12.0MPa with a linear pressure increase being kept at 1.0MPa/hr; the temperatures at the bottom of the extraction batch and at the top of the fractionation column were respectively 240℃ and 250℃.

With the technique, either narrow or wide fractions could be obtained by extracting varied quantity of lighter constituents out of VR. All the fractions left after extraction are the de-oil asphaltenes (DOA). The more the lighter constituents are extracted, the heavier the DOAs are. For example, in view of wider SFEF fractions adopted in this research, they become heavier and heavier from 30%DOA to 40%DOA to 50%DOA to 60%DOA. The original VR are the lightest as compared with their DOAs.

Elemental and SARA compositions of the studied vacuum residua and their SFEF fractions

Daqing vacuum residue (DVR) and Shengli vacuum residue (SVR), derived from two representative Chinese crude oils, were employed. Their main elements and SARA compositions were analyzed as listed in Table 1 and Table 2.

Table 1 Element and SARA compositions of Daqing vacuum residue and its SFEF fractions

	DVR	30%DOA	40%DOA	50%DOA	60%DOA
C, %	86.23	86.71	86.65	86.74	86.68
H, %	12.86	12.52	12.37	12.16	11.94
S, %	0.145	0.17	0.20	0.21	0.22
N, %	0.44	0.43	0.52	0.60	0.66
Saturates, %	41.9	22.3	19.2	14.1	9.15
Aromatics, %	32.7	38.0	38.5	39.3	39.3
Resins, %	25.4	39.6	42.5	46.6	51.2
Asphaltenes, %	0	0.15	0.19	0.20	0.28

Table 2 Element and SARA compositions of Shengli vacuum residue and its SFEF fractions

	SVR	30%DOA	40%DOA	50%DOA	60%DOA
C, %wt	85.88	85.29	85.42	85.30	84.82
H, %wt	11.34	10.99	10.62	10.39	10.04
S, %wt	3.01	3.88	4.05	4.44	4.32
N, %wt	0.95	1.18	1.26	1.37	1.44
Saturates, %wt	16.1	3.58	1.30	0.31	0.53
Aromatics, %wt	30.6	27.9	23.3	15.6	11.4
Resins, %wt	51.1	66.0	72.5	79.7	81.3
Asphaltenes, %wt	2.2	2.46	2.86	4.38	6.77

Microscopic technique for finer structure identification

There are many direct or indirect approaches available to characterize colloidal dispersions and Transmission Electronic Microscopy (TEM) is among those direct viewing techniques most widely employed. Considering that TEM has peculiar requirements on the physical states (e.g. thickness) and properties (e.g. volatility) of the observed samples, the sample freezing and one-time replication technique was adopted in this study to prepare the TEM observed samples of VR and their SFEF fractions. Operational procedure of the freezing fracture replication TEM, abbreviated as FFRTEM, was detailed in Ref.[3].

RESULTS AND DISCUSSION

FFRTEM icons of vacuum residua and their SFEF fractions

In *Figures* 1 through 2 are displayed the FFRTEM photos of the two VR studied and their

SFEF fractions. The fundamental colloidal attributes presented by these photos are clearly seen in terms of the size and size distribution and morphology of the dispersed phases, as well as the colloidal types of which they are.

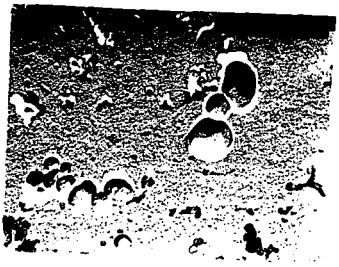

(a) original vacuum residue (61,000 times)

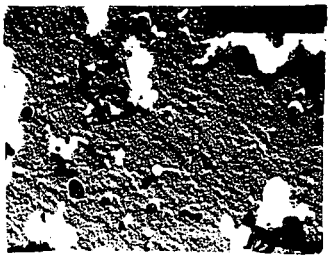

(b) 30% DOA (61,000 times)

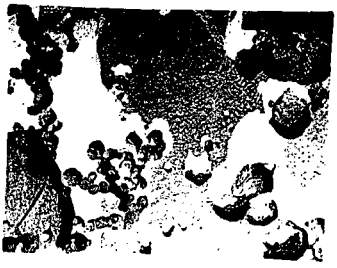

(c) 40% DOA (61,000 times)

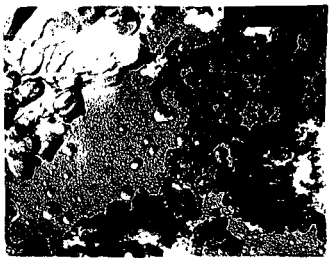

(d) 50% DOA (61,000 times)

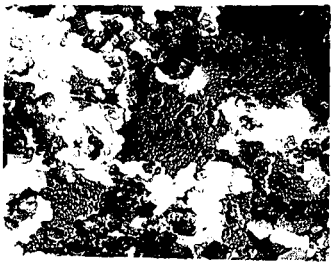

(e) 60% DOA (33,000 times)

Figure 1 FFRTEM icons of Daqing vacuum residue and its SFEF fractions

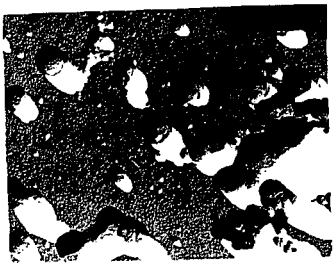

(a) original vacuum residue (61,000 times)

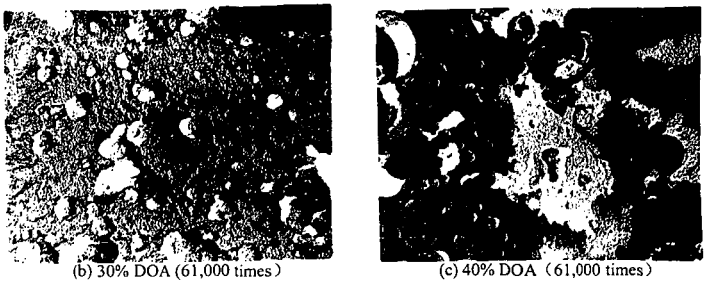

(b) 30% DOA (61,000 times)　　(c) 40% DOA (61,000 times)

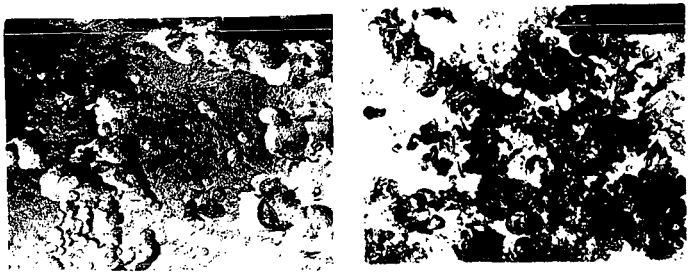

(d) 50% DOA (61,000 times)　　(e) 60% DOA (24,000 times)

Figure 2　FFRTEM icons of Shengli vacuum residue and its SFEF fractions

Colloidal attributes of vacuum residua and their SFEF fractions

Conventionally, the so-called colloidal particles refer to the molecular aggregates with at least one dimension ranging between 1nm and 1 μ m, and considerable interfacial layers exist among the dispersed phases of the colloidal particles and the surrounding dispersing medium[5]. In the two VR and their SFEF fractions, though there occurs a wide size distribution of the dispersed particles, their dimensions are evidently in the spectrum of colloidal particles, and what is more, rather distinct interfaces can be viewed between the dispersed phases and their surrounding phase. It is therefore concluded that both Daqing and Shengli vacuum residue as well as their SFEF fractions are all colloidal dispersion systems.

Morphology of dispersed phases in vacuum residua and their SFEF fractions

The geometrical shapes of the colloidally dispersed phases are among the most distinguished parameters characterizing colloidal dispersing systems. It is evident from the FFRTEM photos in *Figures* 1 through 2 that the colloidal particles in the two VR and their SFEF fractions assume spherical and non-spherical shapes with the spherical or sphere-agglomerated dispersed particles in an overwhelming majority. On the other hand, the abundance of the spherical particles relative to the non-spherical particles exhibits rather differently in the original VR and their SFEF fractions. Concretely, almost all the dispersed particles in the two VR and their 30%DOA, 40%DOA and 50%DOA assume spheres or spherical stacking configurations; while in the 60%DOA of the two VR, there exist not only spherical dispersed particles but some tabulate dispersed phases of larger sizes as well. Such observations were further confirmed by the TEM photos displayed in *Figure* 3.

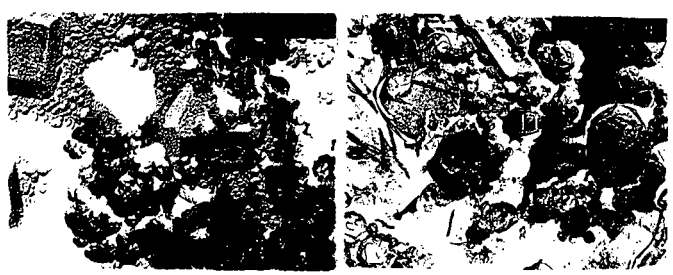

(a) (49,000 times)　　(b) (12,000 times)

Figure 3　FFRTEM icons of 60%DOA of Daqing(a) and Shengli(b) vacuum residue

It is generally considered that, in the aggregated colloidal systems, the dispersed micell assume spherical shapes when the concentration of the surfactant remains low, e.g. not higher than CMC; when the surfactant is in such a high concentration that its content exceeds as ten times CMC as high or reaches more than 10%, the dispersed phases might as well adopt unsymmetrical configurations or layered stackings[5]. Since the asphaltenes and the resins in the VR and their SFEF are of the general characteristics of conventional surfactants both in structures and in behaviors, it is not so difficult to qualitatively clarify, in accordance with colloidal solution theories of surfactants, the variations of the geometrical shapes of the dispersed phases in the VR and their SFEF fractions as they become heavier and heavier.

Multidispersity of colloidal vacuum residua and their SFEF fractions

The multidispersion characteristics of the colloidal systems of the VR and their SFEF fractions are embodied in many aspects such as the morphology, average sizes and size distributions of the dispersed phases. Because of the non-homogeneity of the dispersed phases in size and geometrical shapes in the VR and their SFEF fractions, they are all multi-dispersing systems. On the other hand, as the SFEF fractions of the VR become heavier and heavier, the average size and quantity of the dispersed phases will undergo noticeable variations. Generally, more and more dispersed phases will come into being as the SFEF fractions of the VR go heavier.

Both the morphology and the multidispersity of the dispersed phases in the VR and their SFEF fractions imply that these dispersed phases are made from innumerable non-identical constituents or molecules of VR. Such a fact provides one more proof of the multidispersity of the colloidal VR and their SFEF fractions.

Colloidal types of vacuum residua and their solubility classes

Generally, the colloidal structures of the VR and their SFEF fractions become more advanced in the heavier fractions than in the lighter ones. In average, there appear more cross-linked dispersed phases in Shengli vacuum residue and its SFEF fractions than in those of its Daqing counterparts. In terms of the colloidal types, the original vacuum residua and their 30%DOA are more sol structures, while their 50%DOA and 60%DOA appear more gel structures. The structure of the 40%DOA goes in-between, that is, 40%DOA assumes sol-gel structures.

CONCLUSIONS

(1) The combinatorial SFEF-FFRTEM technique is among the most useful approaches to reveal the colloidal structures and attributes of VR and their SFEF fractions in a qualitative way.

(2) Both Daqing and Shengli vacuum residue as well as their SFEF are of colloidal structures with the basic colloidal attributes dependent upon their fractional compositions.

(3) The fact that the original VR and their SFEF fractions exhibit different colloidal structures and attributes implies that they may find different applications due to their unique physical structures and chemical compositions; or different thermodynamic or dynamic behaviors displayed by the original VR and their SFEF fractions may originate from the subtle differences of their physical and/or chemical structures.

ACKNOWLEDGMENTS

The authors are greatly indebted to the financial support of the project by China Postdoctoral Science Fund.

REFERENCES

[1] S. H. Li, *Physical structures and thermodynamics of petroleum vacuum residua and their applications*. The Postdoctoral Research Report. June 1998.

[2] J. G.Speight, J. Petrol. Sci. Eng., 1999, 22(1-3):3-15

[3] S. H. Li, C. G. Liu, G. H. Que et al. Fuel. 1996, 75(8):1025-1029

[4] *New Evaluation Methods for Vacuum Residua and Evaluations of Some Chinese Vacuum Residua*. A Research Report. The State Key Laboratory of Heavy Oil Processing, University of Petroleum, China. March 1997.

[5] Z. K. Zhou. *Fundamentals of Colloid Chemistry*. Peking University Press. 1987

COLLOIDAL NATURES OF TWO TYPICAL CHINESES VACUUM RESIDUA II: REVISIT AND CHARACTERIZATION OF COLLOIDAL STRUCTURES

Li Shenghua[1] Fu Honglan[2] Liu Chenguang[3] Liang Wenjie[3] Zhang Zhong[4]

[1]Department of Precision Instrument, Tsinghua University, Beijing 100084
[2]Department of Biology, Peking University, Beijing 100871
[3]Department of Petroleum Refining, University of Petroleum, Shandong 257062
[4]Research Institute of Criminalistics, Chongqing 400016

ABSTRACT: Evidences both from TEM observation of Daqing and Shengli vacuum residue and their DOAs prepared by ultra-microtomy and from environmental SEM observation of the untreated Daqing and Shengli vacuum residue and their de-oil asphaltenes confirmed that all of them are of colloidal configurations. It has been generally concluded that, of the microscopic observation tools and the sample treatment techniques employed in the current study of the physical structures of VR, the freezing fracture replication TEM is the best approach in terms of its efficaciousness of displaying the fundamental features of colloidal VR. The independent and combinatorial distribution characteristics of the resins and the asphaltenes are the pivotal parameters in determining the general colloidal features of VR and their de-oil asphaltenes.
KEYWORDS: colloidal structures, vacuum residua, SFEF fractions, SARA fractions

INTRODUCTION

Identification of the colloidal structures of vacuum residua (VR) and their solubility classes is just one aspect concerned by the *Petroleum Physics* studies[1]. As well documented in previous reports and in the first part of this article[2,3], the combined SFEF-FFRTEM technique is a sound way in the revelation and characterization of the physical structures of VR on the colloidal scale. For better recognition of the technique, further proofs are strongly required from cross validation experiments in which factors affecting the colloidal structure identification could be manipulated. Among those contributing much to the physical structures of VR, the influence of temperature of the bulk VR on their physical structures accounts for the most besides chemical compositions.

In the procedure of the FFRTEM technique, one issue at point is that the observed samples are to be prepared by freezing replication: the sample is firstly frozen in the liquid nitrogen of -196℃ and then replication of the fractured cross-sections of the samples by carbon-coating is conducted in the environment of ca.-120℃. The doubt is that such a process might bring some unrecoverable changes to the physical structures of the bulk VR, which finally results in false deductions about the features and properties of the physical structures of VR. TEM observation of very thin VR samples prepared by ultra-microtomy minimizes the thermal effects on the physical structures of VR. However, it is not clear enough whether the solidification of VR by the solidifying agents in the technique will exert any influences upon their physical structures.

All in all, the VR have to go through a long procedure of physical and/or chemical treatments before they could finally be observed under TEM whether they are prepared by the freezing fracture replication or the ultra-microtomy. In order to take the real images of the untreated VR, Environmental Scanning Electronic Microscopy (ESEM) was attempted to unfold in different manners the physical structures of VR and their formation in terms of solubility classes.

In this part of the paper, not only TEM observations of samples prepared by ultra-microtomy but also their ESEM observations without any physical or chemical treatments were conducted so as to derive more direct evidences, and to lend support to the construction details of the colloidal VR. For deeper understanding of the colloidal VR structures, an attempt will be made to correlate their colloidal features, such as colloidal types and attributes, multidispersity and morphology of dispersed phases, to the SARA pseudo-pure-components.

EXPERIMENTAL

Employment of sample imbedding and ultra-microtomy for TEM observation were made in the present endeavor which serves two purposes: one is to ascertain the comparability of freezing fracture replication in the validity of revelation of the physical structures of VR, and the other is to compare the reliability of different techniques in the reflection of the true physical structures of VR. The introduction of ESEM for the demonstration of the physical structures of VR and their DOAs is another attempt to supply additional proofs to the colloidal identity of VR.

RESULTS AND DISCUSSION

Ultra-microtomy TEM icons of vacuum residua and their SFEF fractions

In *Figure* 1 is exhibited the TEM photos of Shengli vacuum residue and its DOAs, with the observed samples prepared by ultra-microtomy. As both the solidifying agent and the procedure, such as sample solidifying and the ultra-microtomy, do not interfere with the structural properties of the samples, so the TEM microphotos present images of the vacuum residue and its DOAs without noticeable distortions to the true physical structures.

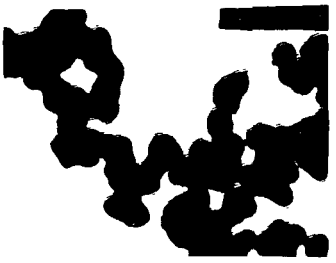

(a) original vacuum residue (81,000 times)

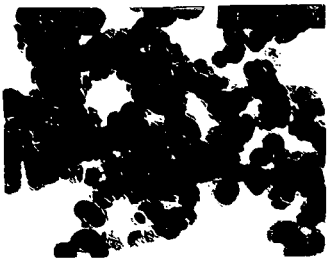

(b) 30% DOA (61,000 times)

(c) 40% DOA (49,000 times)

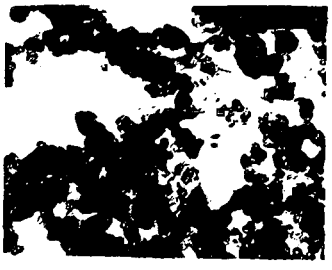

(d) 50% DOA (61,000 times)

(e) 60% DOA (49,000 times)

Figure 1 TEM icons of Shengli vacuum residue and its SFEF fractions by ultra-microtomy

It is understandable that, since it is difficult to keep complete consistency of the samples and their viewing areas under microscopes, only the general colloidal features of VR and their DOAs could be compared, such as the morphology of the dispersed phases and the colloidal types. As seen, both the FFRTEM photos and the photos in Figure 1 could reflect, in almost the same patterns and similar textures, the colloidal features of the studied vacuum residue and its DOAs.

ESEM icons of vacuum residua and their SFEF fractions

The most useful advantage of ESEM is that not any pretreatment is required for the samples. Thus, it presents true physical structures of samples in a nondestructive manner. However, the ESEM images are not demonstrating the structure details of the bulk phase of samples.

Figure 2 exhibits the ESEM icons of Shengli vacuum residue and its solubility classes. It is obvious that both TEM and SEM can, in combination with appropriate sample preparation procedures, be employed to ascertain and identify the colloidal characteristics of VR and their solubility classes. Therefore it is advisable to select suitable sample preparation techniques and

finer observation tools to compare and contrast the general colloidal features of various VR or their solubility classes. However, it should be reminded that each combination has its own preferable application circumstances. Generally, the FFRTEM technique is the best candidate for studying the physical structures of VR and their solubility classes on the colloidal level while the ESEM technique is preferred when major concerns are about the elemental compositions of the dispersed and dispersing phases. The ultra-microtomy, while useful in exhibiting the colloidal features of VR in combination with common TEM technique, is more appropriate to disclose the pseudo-orderliness of the bulk VR in combination with high resolution TEM technique. Details of the latter two techniques and their usefulness in providing more detailed physical and/or chemical information of the physical structures of VR will be reported later.

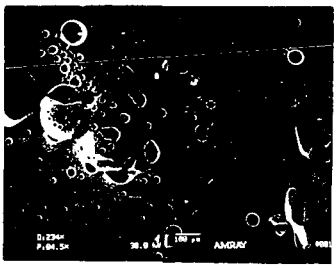

(a) original vacuum residue

(b) 30% DOA

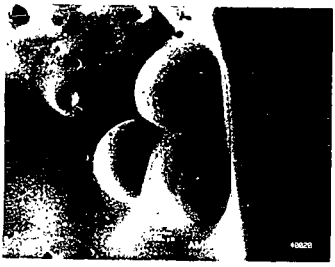

(c) 40% DOA

(d) 50% DOA

(e) 60% DOA

Figure 2 ESEM icons of Shengli vacuum residue and its solubility classes

Characterization of colloidal structures of vacuum residua in terms of SARA compositions

Of all the compositional and structural parameters of VR, their SARA compositions, i.e., saturates, aromatics, resins and asphaltenes, are among the most potential ones capable of characterizing the identity of VR. So it is natural to employ these four pseudo-pure-components of VR to correlate the possible relations which might occur between the general colloidal features of VR and their compositions.

It was confirmed that it was the n-pentane insoluble asphaltenes, which is tantamount to the n-heptane insoluble asphaltenes plus the heavy resins, which construct the micell in the colloidal systems of VR[5]. Considering the difficulty with which to determine the content of the heavy resins of VR, the content of the total resins is taken, in combination with the content of the asphaltenes (the n-heptane insolubles and toluene solubles), to have an approximate appraisal of the colloidal features of VR and their DOAs, i.e., it is both the asphaltenes and the total resins,

the two kinds of surfactant-like constituents, which are supposed to participate the formation of the micell in the VR. As a matter of fact, since the determination of the SARA compositions of VR has come into the widest use in common petroleum chemistry laboratories, so it is of great significance to employ the SARA compositions of VR to characterize their colloidal structures and general properties. With these in mind, some rough understandings of the relations between the colloidal features of the VR and the quantities of the asphaltenes and/or the resins could be derived by three parameters as defined and specified below.

(1) $W_{Asp} + W_{Re}$: The total amount of asphaltenes and resins is an index which could be used to approximately estimate the quantity of the dispersed phases and their geometrical shapes, as well as their colloidal types. Generally, with the increase of $W_{Asp} + W_{Re}$, more dispersed phases will be formed with their morphologies changing, in the main, from spherical to tabulate, and the bulk structures of the VR and their DOAs transform from sol to sol-gel or gel.

(2) W_{Asp}, W_{Re}: These two independent parameters, in addition to their significance of $W_{Asp} + W_{Re}$, concern the sizes and size distributions of the dispersed phases in VR and their DOAs. Due to the variations in molecular sizes and elemental compositions, the average size of the micell formed by the resins is smaller than that of the micell of the asphaltenes.

(3) W_{Re}/W_{Asp}: The quantity ratio of the resins and the asphaltenes is an indicator for rough evaluation of the aggregation states of the dispersed phases. As the micell of the resins are looser and the micell of the asphaltenes are tighter in terms of the compactness of their molecularly aggregated configurations, so the lower the W_{Re}/W_{Asp}, the tighter the mixed resin-asphaltene micell, which leads to the worse compatibility of these micell with the surrounding dispersing media and less stable colloidal VR and their DOAs.

With the three parameters outlined above, the independent and combinatorial distribution characteristics of the resins and the asphlatenes in the VR and their DOAs are plotted, as shown in *Figures* 3 through 4. It is obvious that, as the VR and their DOAs become heavier and heavier, both the independent parameter (W_{Re}, W_{Asp}) and the combinatorial parameters ($W_{Re}+W_{Asp}$, W_{Re}/W_{Asp}) vary in rather systematic ways: W_{Re}, W_{Asp} and $W_{Re}+W_{Asp}$ increase and W_{Re}/W_{Asp} decreases as the VR and their DOAs go from lighter to heavier. As the colloidal types and stability of VR and their DOAs are of potential significance in industrial practices, it is instructive to have knowledge of the colloidal types and stability of VR and their DOAs in terms of the independent and combinatorial parameters based on the SARA compositions.

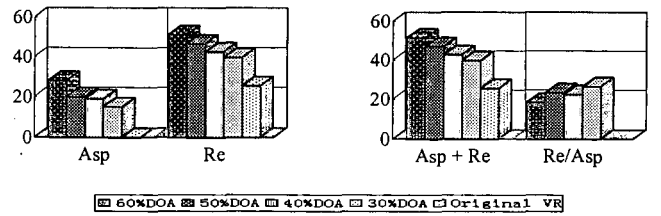

Figure 3 Independent and combinatorial distributions of resins and asphaltenes of Daqing vacuum residue (Data of the asphaltenes in the first graph are plotted in 100 times of their true values, while data of the Re/Asp in the seeond graph at a tenth of their true values)

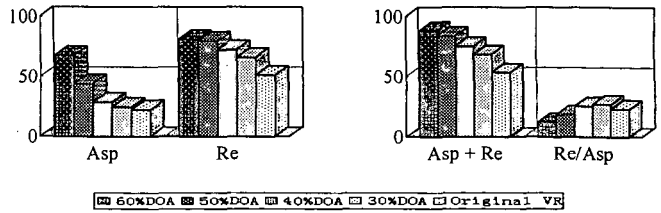

Figure 4 Independent and combinatorial distributions of resins and asphaltenes of Shengli vacuum residue (Data of the asphaltenes in the first graph are plotted in 10 times of their true values)

(1) With the VR and their DOAs becoming heavier, their W_{Re}, W_{Asp} and $W_{Re}+W_{Asp}$ all keep increasing. As both the resins and the asphaltenes are of the characters of surface active molecules, so the average size of the dispersed phases in the VR and their DOAs becomes larger and their quantity becomes more as the VR and their DOAs goes from lighter to heavier. Roughly, for Daqing vacuum residue and its DOAs, the colloidal systems with $W_{Re}+W_{Asp} < 40\%$

are in sol states and the colloidal systems with $W_{Re}+W_{Asp}$ >50% are in gel states, while for the colloidal systems with $W_{Re}+W_{Asp}$ going in-between, they are of the sol-gel states. For Shengli vacuum residue and its DOAs, the approximate values of $W_{Re}+W_{Asp}$ corresponding respectively to the sol, sol-gel and gel state are less than 60%, in the range of 60~70% and higher than 70%. The reason why Daqing vacuum residue and its DOAs become the gel states at lower Asp + Re than its Shengli counterparts could be contributed to the fact that, in Daqing vacuum residue and its DOAs, the micell are mainly composed of the resins and the micell of the resins are of loosely aggregated molecular assembles. These simple analyses not only corroborate again that the dispersed phases in the VR consist of both the resins and the asphaltenes species but also suggest that the relevance of the colloidal types of VR to their critical values of $W_{Re}+W_{Asp}$ may be attributed the molecular properties of the resins and the asphaltenes of the specific vacuum residua. It is evident, therefore, that more precise relationship between the colloidal types of VR and such parameters as W_{Re}, W_{Asp} and $W_{Re}+W_{Asp}$ could be well defined if the narrower fractions of VR are employed to conduct their colloidal studies and the heavier resins are quantitated.

It is of industrial implication for the colloidal types of VR to be related to W_{Re}, W_{Asp} and/or $W_{Re}+W_{Asp}$. In the thermal or catalytic conversion of vacuum residua, both W_{Asp} and $W_{Re}+W_{Asp}$ keep increasing; once they reach some critical values, the reaction system comes into the sol-gel state, signifying that the reaction system arrives at the critical state in which the second liquid phase of condensed asphaltenes is about to occur[4]. As in the thermal conversion of vacuum residua, the appearance of the second liquid phases is immediately followed by the commencement of coke formation, it is therefore of great industrial significance to predict the induction period of coke formation by the real-time monitoring of the variations of W_{Asp} and $W_{Re}+W_{Asp}$ or by the establishment of their dynamic equations.

(2) With the VR and their DOAs becoming heavier, their $W_{Re}+W_{Asp}$ continues to decrease and accordingly, their colloidal stability keeps decreasing. Since the sol-gel system corresponds to the critical state between stable and unstable colloidal VR, it is estimated from Figures 3 through 4 that the critical W_{Re}/W_{Asp} ratio for keeping stability of colloidal VR is ca. 20~25. Such a fact implies that, for Daqing and Shengli vacuum residue and their DOAs, when the value of W_{Re}/W_{Asp} is lower than 20~25, their colloidal systems are thermodynamically unstable while when the value of W_{Re}/W_{Asp} is greater than 20~25, they remain stable in the sense of thermodynamics.

CONCLUSIONS

(1) With evidences from the FFRTEM, ultra-microtomy TEM and ESEM techniques, it can be well assumed that both Daqing and Shengli vacuum residue as well as their de-oil asphaltenes are all colloidal systems.

(2) Of the three combination techniques for sample preparation and observation, both the FFRTEM and the ultra-microtomy TEM are suitable to study the colloidal structures of VR and their solubility classes in the qualitative way. And just from the viewpoint of the qualitative study of the colloidal structures of VR and their solubility classes, influences from either the freezing in FFRTEM or the solidification in ultra-microtomy TEM could be neglected to some extent.

(3) The colloidal features of VR and their solubility classes could be well characterized by their compositions of the saturates, the aromatics, the resins and the asphaltenes. Particularly, the contents of the resins and the asphaltenes are the two key parameters in the finer characterization of the important colloidal properties of VR, such as the colloidal types of the bulk VR, the morphology and the size and size distribution of the dispersed phases.

ACKNOWLEDGMENTS

The authors are greatly indebted to the financial support of the project by China Postdoctoral Science Fund.

REFERENCES

[1] S. H. Li, *Physical structures and thermodynamics of petroleum vacuum residua and their applications*. The Postdoctoral Research Report. June 1998.

[2] S. H. Li, C. G. Liu, G. H. Que et al. Fuel. 1996, 75(8):1025-1029

[3] S. H. Li, W. J. Liang, Y. J. Zhu. Oil and Gas Processing. 1994, 4(1):1-9

[4] S. H. Li, C. G. Liu, G. H. Que et al. Preprints, Div. Petro. Chem., ACS, 1995, 40(3):736

PRELIMINARY RESULTS ON THE MOLECULAR STRUCTURES OF THE ATHABASCA AND COLD LAKE ASPHALTENES

Jonathan P. Mathews#, Semih Eser#, and Parviz-Rahimi*
The Energy Institute, College of Earth and Mineral Sciences, The Pennsylvania State University, University Park, PA 16802
* National Center for Upgrading Technology, Suite A202, 1 Oil Patch Drive, Devon, Alberta, Canada, T9G 1A8

Keywords: Asphaltene structure, high-resolution mass spectroscopy

INTRODUCTION

Asphaltene research has recently undergone a significant revitalization to facilitate utilization of heavier crude oils and to develop the massive oil sand reserves in Canada. The average chemical properties of natural asphaltenes tend to fall in a narrow range despite wide variations in their chemical behavior. In other words, the average bulk parameters of asphaltenes do not necessarily provide useful information for upgrading and behavioral studies. The final objective of this study is to generate molecular models for asphaltenes from two different sources, Cold Lake and Athabasca, to understand the differences in their molecular composition. These two asphaltenes give similar average structural parameters, yet behave quite differently (carbonization yields). Analysis by high-resolution laser pyrolysis indicated a distribution of molecular masses (100 to 1,500 AMU). Elemental compositions of these peaks will provide the input for molecular models without the need for extensive "averaging" of bulk parameters, thus, better indicating some of the structural diversity within the asphaltenes.

EXPERIMENTAL

Pentane asphaltenes from Athabasca and Cold Lake bitumens were prepared using 40:1 solvent to sample ratios. Briefly, 10 g bitumen was placed in a flask and 400 mL of n-pentanc was added. The flask was placed in an ultrasonic bath for 45 min and left to settle overnight at room temperature. The mixture was then placed in an ultrasonic bath again for 30 min and the asphaltenes were filtered using a medium porosity (10-15 μm) fritted glass disk. The solid asphaltenes were rinsed with excess pentane until the washing was clear. To ensure that asphaltenes were free from residual maltenes, the collected asphaltenes were mixed with 50 mL of n-pentane, sonicated and filtered as before. Asphaltenes were then dried under vacuum at 45°C for 3 h.

Elemental analysis including C, H, S and N contents were determined using Perkin Elmer 2400 and O was determined using Carlo Erba 1104. Molecular weights of asphaltenes were determined in o-dichlorobenzene at 120°C using VPO.

Coking potential was obtaining using a modified Conradson carbon residue test(1) utilizing a TGA instead of the prescribed glass sample vial. The results are not directly comparable to the Conradson method, as secondary cracking and mass transfer will significantly differ and hence underestimate the coke yield potential. Briefly 5 ± 0.5 mg of sample was heated from 30 °C to 400 °C at 15 °C/min under nitrogen. The temperature has held constant for 90 minutes. The weight remaining was attributed to coke and ash. Ash was determined by heating the sample to 600 °C and changing the atmosphere to air, the remaining mass after 10 minutes was attributed to ash.

Mass spectra were acquired on a PerSeptive Biosystems Voyager-DE STR mass spectrometer using 337 nm light from a pulsed nitrogen laser for ionization. High-resolution results were obtained using reflector mode. Samples were prepared by dissolving approximately 50 micrograms of material in 500 ml of THF. Aliquots of 0.5 ml were deposited on the gold-plated target, and the solvent allowed to evaporate under ambient laboratory conditions. Samples were introduced into the mass spectrometer and analyzed as soon as possible to minimize evaporation of more volatile components. Ionization was conducted using laser setting slightly above the threshold for ionization. A total of 256 laser shots acquired over numerous sites within each sample were averaged. Calculated elemental analysis for mass spectral fragments where calculated using the non-weighted averages of 10 major peaks spanning 100 AMU's.

RESULTS AND DISCUSSION

Unfortunately, asphaltene structural research is hampered by the use of the term "asphaltene" to describe such diverse structural entities as naturally occurring asphaltenes (from coal, crude and oil sands), C_5,C_6 and C_7 'cuts" and products from the refining process where the processing conditions are likely to produce larger aromatic "raft" structures. Utilizing high-resolution mass spectroscopy it is possible to determine the elemental composition of the pyrogram peaks. Utilizing this methodology to generate possible fragments allows us to have more realistic components from which construction of models than from "average structures" which do not demonstrate the structural diversity within the asphaltene. This may be important if only certain structures or certain sizes of structures are responsible for the negative (or positive) aspects of the asphaltene.

Based on the elemental analysis and vapor pressure osmometry the average molecular structure should contain $C_{72}H_{86}N_1S_{2.6}O_1$ (VPO mw = 1,020 AMU) and $C_{176}H_{215}N_2S_{6.5}O_{6.5}$ (VPO mw = 2,468 AMU) for Cold Lake and Athabasca C_5-asphaltenes, respectively. This is comparable with previous work for the Athabasca asphaltene (mw 2,618(2), and 2,750(3)), and for the Cold Lake asphaltene (mw 2,030(3)). However, there is poor agreement between average molecular weights determined by different techniques: laser desoption mass spectroscopy and by VPO(4). The

indication being that either VPO measurements yield molecular weights of strongly bound associations of smaller asphaltene structures or that laser desoption mass spectroscopy fragments larger structures, or does not analyze large structures. The average molecular weights reported here are consistent with the range found by electron impact high-resolution mass spectroscopy of a Mayan (vacuum resid) asphaltene(4). However, the mass spectra technique is known to underestimate the molecular weight, the issue of contention is, by how much? Identification of small multi ring systems is consistent with the general average structural interpretation away from very large aromatic "rafts" structures to smaller sized entities(5). A range of molecular weights and their relative abundance are shown in Table 1. Both asphaltenes are similar in their maximum abundance's in the 300-600 AMU range (74 and 77% or the relative abundance for Cold Lake and Athabasca, respectively). Cold lake has a contribution in the larger mass range (>1,000 AMU) in comparison to the Athabasca asphaltene. The Cold Lake asphaltene has slightly more low-molecular weight material also in comparison to the Athabasca sample.

Previously, identification of electron ionized fragments of an asphaltene was reported to be in good agreement with the traditional elemental analysis, with the aromaticity being slightly underestimated(4) which significantly aids the validity of this type of approach. However, in that study over 90 % of the material was volatilized, while laser desorption in this study volatilized only a small fraction of the asphaltene. Here, only 100 or so of the major peaks have been examined. Furthermore, some calculated elemental assignments were equally valid so there was certain operator bias. The calculated atomic H/C ratios for the Cold Lake sample are shown in Table 1. The weighted atomic H/C ratio of 1.2 is in agreement with the bulk elemental for Cold Lake asphaltene. However, the calculated elemental composition over reports the heteroatom content for sulfur, nitrogen and oxygen (normalized to 100 carbon atoms bulk analysis is $C_{100}H_{120}N_1S_4O_2$ while the calculated weighted elemental composition is $C_{100}H_{116}N_8S_8O_7$). Additional calibration standards in the laser high-resolution mass spectroscopy might aid in closing this discrepancy.

Size-exclusion chromatography of Athabasca bitumen produced size fractions with essentially the same atomic H/C ratios of 1.4 over a molecular weight range of 900 to 3,000 AMU, (as measured by VPO(6)). A similar trend is seen over the much smaller mass range examined here for the Cold Lake asphaltene. This implies that the higher molecular weight structures are not undergoing circular ring condensation, as it would result in a significant reduction in the H/C ratios. Rather, it seems likely that higher molecular weight structures comprise of lower molecular weight structures linked together via sulfur, oxygen, and aliphatic chains(7) or directly via aryl-aryl bonds. Hence the approach of Murgich et al(8) of stinging small structures together without ring growth to produce an interconnected "island structure" seems reasonable. However, selection of these "binding structures" will have a significant influence on the structural model and their "behavior" and "coke formation" potential. It is the ultimate aim of structural modeling not only to present the structural features that are present in the asphaltene, essential the representation of chemical structure, but also the physical structure and provide a rational explanation of processing behavior occurring during cracking or hydrocracking. For example the Athabasca asphaltene sulfur linkages might be more important "binding structures" than in Cold Lake asphaltene which has a higher coke yield (55.4 in comparison to 47% (daf) for Athabasca). However, many other structural features such as differences in molecular weight distributions or differences in the fine chemical structure are also likely contributors. The current state of knowledge regarding Athabasca structural features is eloquently presented in the literature(7). Aromaticity results have been reported in the literature and are the same for both samples (0.49) for the C_7-extracted asphaltene(3). The for the same sample the aliphatic hydrogen to carbon ratios where also in close agreement 2.16 and 2.10 for the Athabasca and Cold Lake asphaltenes, respectively(3). Hence, average parameters although useful in comparing materials do not necessarily provide insight into the behavior of the material. Molecular models produced should bare this in mind and should aim to produce chemically, physically accurate models with appropriate "reactivity" to processing.

CONCLUSIONS

Laser desorption high-resolution mass spectroscopy yielded information regarding the distribution of molecular mass in the range 100 to 1,500 AMU's for Cold Lake and Athabasca asphaltenes. Despite being close in bulk chemical composition (elemental analysis, carbon aromaticity) the asphaltenes differ in coking potential (as determined by thermogravametric analysis). There are slight differences in the molecular weight distribution between the asphaltene samples. Cold lake has higher molecular weight material in the region of 1,000 to 1,500 amu in comparison to the Athabasca asphaltene, which has no significant contribution for molecular weights greater than 1,000 amu (in the analytical window of this technique). Weighted average molecular weights are 523 and 463 for the Cold Lake and Athabasca asphaltenes, respectively. This shows the opposite trend from vapor pressure osmometry, which yielded average molecular weights of 1,020 and 2,468 for the Cold Lake and Athabasca asphaltenes, respectively. Elemental analysis of carbon and hydrogen for Cold Lake was in reasonable agreement with calculated elemental analysis from high-resolution mass spectroscopy, however, other heteroatoms (S, O and N) where overestimated.

ACKNOWLEDGEMENTS

Thanks to A. Daniel Jones (Director, Penn State Intercollegiate Center for Mass Spectrometry) for running the laser desorption mass spectroscopy system and assistance in its interpretation.

REFERENCES
1. ASTM, Designation: D 4530-93, Standard test methods for determination of carbon residue (micro method), in Annual book of ASTM standards, Section 5, Petroleum products, lubricants and fossil fuels, 1998, 919.
2. Kotlyar, L. S., Ripmeester, J. A., Sparks, B. D. and Woods, J., *Fuel*, 1988, **67**, (11), 1529.
3. Suzuki, T., Itoh, M., Takegami, Y. and Watanabe, Y., *Fuel*, 1982, **61**, (5), 402.
4. Hunt, J. E. and Winans, R. E., *Am. Chem. Soc., Div. Fuel Chem. Prepr.*, 1997, **42**, (2), 427.
5. Artok, L., Su, Y., Hirose, Y., Hosokawa, M., Murata, S. and Nomura, M., *Energy & Fuels*, 1999, **13**, (2), 287.
6. Domin, M., Herod, A., Kandiyoti, R., Larsen, J. W., Lazaro, M. -J., Li, S. and Rahimi, P., *Energy & Fuels*, 1999, As soon as publishable web release, ef980065b, http://pubs.acs.org/subscribe/journals/enfuem/browse_asap.html.
7. Strausz, O. P., Mojelsky, T. W., Faraji, F., Lown, E. M. and Peng, P., *Energy & Fuels*, 1999, **13**, (2), 207.
8. Murgich, J., Abanero, J. A. and Strausz, O. P., *Energy & Fuels*, 1999, **13**, (2), 278.

Table 1. Molecular Ion Distribution and Average H/C ratio as Determined from High-Resolution Laser Desorption

M/z Range	Cold Lake %	Cold Lake H/C ratio*	Athabasca %
100-199	2		0
200-299	4	0.9	1
300-399	27	1.0	27
400-499	29	1.3	31
500-599	18	1.3	19
600-699	8	1.3	11
700-799	4	1.3	6
800-899	3		3
900-999	2		2
1,000-1,099	1		0
1,100-1,199	1		0
1,200-1,299	1		0
1,300-1,399	1		0
1,400-1,499	1		0
1,500-1,599	0		0
Average mw	523	Weighted H/C= 1.2	463

*Analysis of at least 10 major fragments in each average H/C calculation

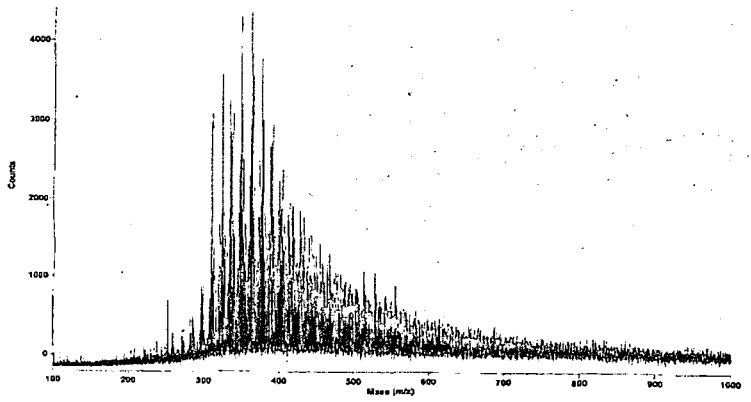

Figure 1. Laser Pyrolysis, High Resolution Mass Spectra Pyrogram of Athabasca Asphaltene

STRUCTURAL ANALYSES OF PETROLEUM ASPHALTENES AND RESINS AFTER HDM AND SUBSEQUENT HDS TREATMENTS

H. Seki and F. Kumata

Advanced Catalysts Research Laboratory, Petroleum Energy Center,
KSP D12F-1237, 3-2-1 Sakado, Takatsu-ku, Kawasaki, Kanagawa, 213-0012 Japan

Introduction

In our laboratory, we are developing a new two-stage process for upgrading petroleum residues, which consists of a slurry phase in the first stage and a fixed bed in the second stage. In this new process, the catalyst life in the second stage is one of the keys and its elongation is an important subject. Thus far we have been investigating the effects of operation conditions in the first stage on the fouling at the middle of run for the catalysts in the second stage, using a quasi two-stage process, *i.e.*, hydrodemetallization (HDM) and hydrodesulfurization (HDS) [1]. Consequently, we found followings: (i) a minimum fouling rate of the HDS catalysts existed around 400 °C of HDM temperature, (ii) the HDS catalysts were deactivated predominantly by coke rather than metals under the present conditions and (iii) effect of substances soluble in light gas oil (soft coke) on HDS catalyst deactivation could not be negligible under certain HDM reaction conditions.

In order to further understand the coke deactivation and to obtain a certain index which reflects coke deactivation, characterization of asphaltenes was performed since asphaltenes are likely to form coke and cause catalyst deactivation in resid hydrotreatings [2-4].

In this study, structural changes of asphaltenes after HDM and HDS treatments were examined, especially paying an attention to the change of polycondensed aromatic skeletons. In addition, resins were also characterized because some parts of resins might act as the soft-coke. We report the results of above characterization.

Experimental

Both HDM (Mo/Al_2O_3) and HDS ($NiCoMo/Al_2O_3$) catalysts were commercially available and supplied from a Japanese catalyst company. HDM treatments were carried out with a fixed-bed reactor using Kuwait atmospheric residue (KW-AR; S = 4.45 wt%, Ni/V = 20/61 ppm) as a feed under the following conditions; temperature 370 - 430 °C, pressure 14 MPa, LHSV 0.5 h^{-1}, H_2/Oil 2000 scfb. HDS treatments were subsequently conducted using the HDM product oils as feeds; temperature 390 °C, pressure 8 MPa, LHSV 0.5 h^{-1}, H_2/Oil 5000 scfb.

Asphaltenes were isolated from the HDM and HDS product oils as *n*-heptane-insoluble and toluene-soluble substances. Resins were separated from maltene by column chromatography.

LD-MS measurements were performed with Thermoquest Co., Ltd. Vision 2000 Spectrometer using angiotensin as a calibration standard. The details on the measurement were described elsewhere [5]. From the LD-MS measurement, we can obtain a molecular weight distribution as well as an average molecular weight (*Mn*). ^1H and ^{13}C-NMR spectra (TMS base) were recorded on a JEOL JNM-

LA400 in a gated proton decoupled mode. Chromium acetonylacetonate was added to obtain quantitative ^{13}C-NMR spectra. The assignments of chemical shift range for ^{1}H and ^{13}C-NMR spectra were made according to the literature [6-9].

The structural parameters listed in Table 1 for asphaltenes and resins were obtained with the data from ^{1}H and ^{13}C-NMR, LD-MS and elemental analyses, referring to the method by other workers [7-9]; *In* brief, *Cs*, *CCH3*, *Cn-ar* and *Cother* were directly obtained from ^{13}C-NMR, and *Cus* from ^{1}H-NMR with the combination of elemental analyses data. Then, *Cint*, *Cout*, *Csub Ra* and *n* were calculated using above parameters.

Results and Discussion

1. Structural change of asphaltenes and resins after HDM treatment

Figure 1 shows the LD-MS spectra of asphaltenes after the HDM treatment with different temperature. A significant difference was observed in the molecular weight distribution; the shape of the broad band tailing to 5800 m/z was almost the same below 400 °C, while it became polydispersed above 400 °C. Especially, two peaks at 600 and 1100 m/z are clearly seen when HDM temperature is 430 °C. On the other hand, the molecular weight distribution of resins became narrow as the HDM temperature increased. The *Mn* for asphaltenes and resins monotonously decreased with HDM temperature.

Variation of structural parameters for asphaltenes and resins with HDM temperature was described in Figure 2. The aromaticity (*fa*) of asphaltenes and resins changed with HDM temperature in a similar manner; the *fa* was almost unchanged up to 400 °C and steeply increased above 400 °C. For asphaltenes, the *Csub* began to decrease around 400 °C while the *Ra* and *n* remained. For resins, on the other hand, the *n* decreased with HDM temperature without remarkable changes in *Ra* and *Csub*. These observations lead to the conclusion that the steep increase of *fa* for asphaltenes and resins is due to the decrease of the number of alkyl side chains and to the shortening of them, respectively. Variations of internal quarternary aromatic carbon (*Cint*) and outernal one (*Cout*) give us useful information on the aromatic skeleton For asphaltenes, an increase of *Cint* from 10 to 17 and a decrease of *Cout* from 21 to 17 were observed with an increase of HDM temperature up to 410 °C, indicating the structural change of the aromatic skeleton from cata- to peri-type. It might be because of the difference in the reactivities of cata- and peri-type polycondensed aromatics that this structural change appeared.

2. Structural change of asphaltenes and resins after HDS treatment

In our previous study, an increase in the fouling rate of HDS catalysts was observed when HDM temperature was raised from 390 to 400 °C. It is, therefore, of interest to examined the structural changes of asphaltenes and resins by the HDS treatment. Variations of *fa* and *Ra* before (B) and after (A) the HDS treatment were shown in Figure 3. In this figure, the symbols, As and Re, indicate asphaltenes and resins, respectively, and the number is an HDM temperature. By the HDS treatment, the aromatic ring number (*Ra*) for asphaltenes increased while that for resins slightly decreased. This indicates that condensation reactions are more likely to occur for asphaltenes than resins during HDS treatments. Although significant difference by the HDM temperature was unfortunately not detected in the structural parameters, the LD-MS measurements for asphaltenes showed the clear difference: when the HDM temperature was 390 °C, the *Mn* and molecular weight distribution were almost unchanged while 410 °C, the *Mn* increased by HDS treatment and heavy fractions which were not detected before

the HDS treatment were observed, indicating that condensation reactions took place. Such condensation reactions of asphaltenes could cause the coke deactivation of HDS catalysts.

Conclusions

Heavy fractions (asphaltenes and resins) after HDM and HDS treatments were characterized to understand the deactivation of HDS catalysts. It was found that the increase of aromaticity (*fa*) for both asphaltenes and resins by HDM treatment was attributed to the loss of alkyl chains and that polycondensed aromatic skeleton of asphaltenes changed toward peri-type. We confirmed that the asphaltenes tended to polycondense during the HDS treatments if the HDM temperature was over 400 °C.

Acknowledgements

This work has been carried out as a research project of Petroleum Energy Center with subsidy of the Ministry of International Trade and Industry. The authors are grateful to Drs. H. Iki and K. Hayasaka of Nippon Mitsubishi Oil Co. Ltd. for their kind help in NMR measurements.

References

1. H. Seki and F. Kumata, submitted to *Studies in surface science and catalysis* (The 8th International Symposium Catalyst Deactivation at Brugge)
2. D. S. Thakur and M. G. Thomas, *Apply. Catalysis*, **15**, 197 (1985)
3. P. E. Savage, M. T. Klein and S. G. Kukes, *Energy Fuels*, **2**, 619 (1988)
4. V. Calemma, P. Iwanski, M. Nali, R. Scotti and L. Montanari, *Energy Fuels*, **9**, 225 (1995)
5. M. Fujii, Y. Sanada, T. Yoneda and M. Sato, *Prepr. ACS Div. Fuel Chem.* **43**, 735 (1998)
6. A. Fonseca, P. Zeuthen and J. B. Nagy, *Fuel*, **75**, 1413 (1996)
7. S. Gillet, P. Rubini, J-J. Delpuech, J-C. Escalier and P. Valentin, *Fuel*, **60**, 221 (1981)
8. E. M. Dickinson, *Fuel*, **59**, 290 (1980)
9. M. F. Ali and M. Saleem, *Arab. J. Sci. Eng.*, **19**, 319 (1994)

Table 1. Structural parameters of average molecules for asphaltenes and resins.

Symbol	Definitions	Symbol	Definition
Car	aromatic carbons	Cother	carbons attached to oxygen
Cal	aliphatic carbons	Cint	internal quarternary aromatic carbons
Cus	unsubstituted aromatic carbons	Cout	outernal quarternary aromatic carbons
Cs	alkyl-substituted (methyl group excluded) aromatic carbons	Csub	alkyl-substituted aromatic carbons
		fa	aromaticity
CCH3	methyl-substituted aromatic carbons	Ra	aromatic ring number
Cn-ar	carbons at the junction of aromatic and naphthenic ring	n	average length of alkyl side chain

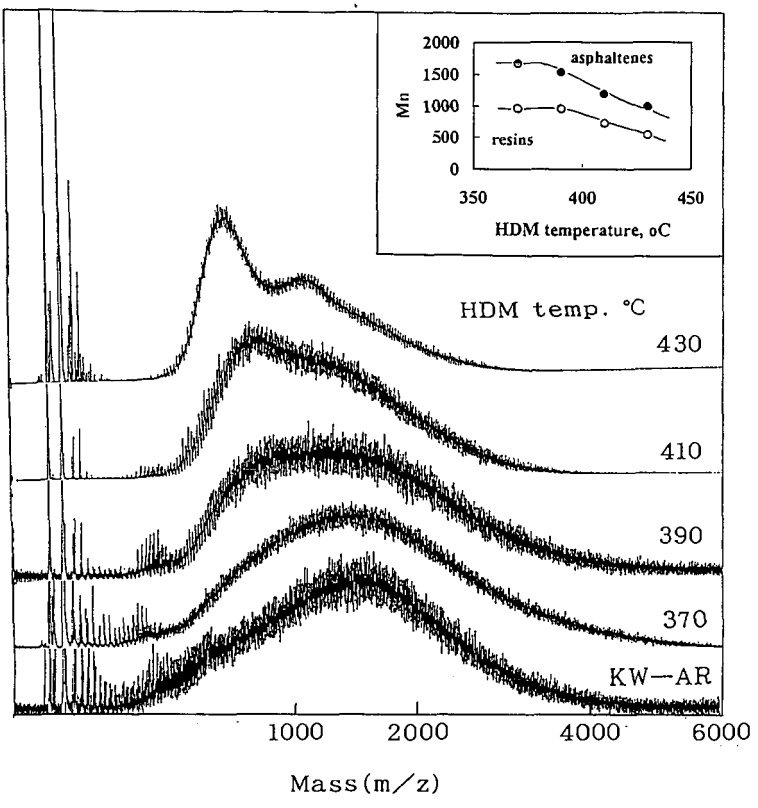

Figure 1. LD-MS spectra of asphaltenes after HDM treatments and average molecular weights of asphaltenes and resins.

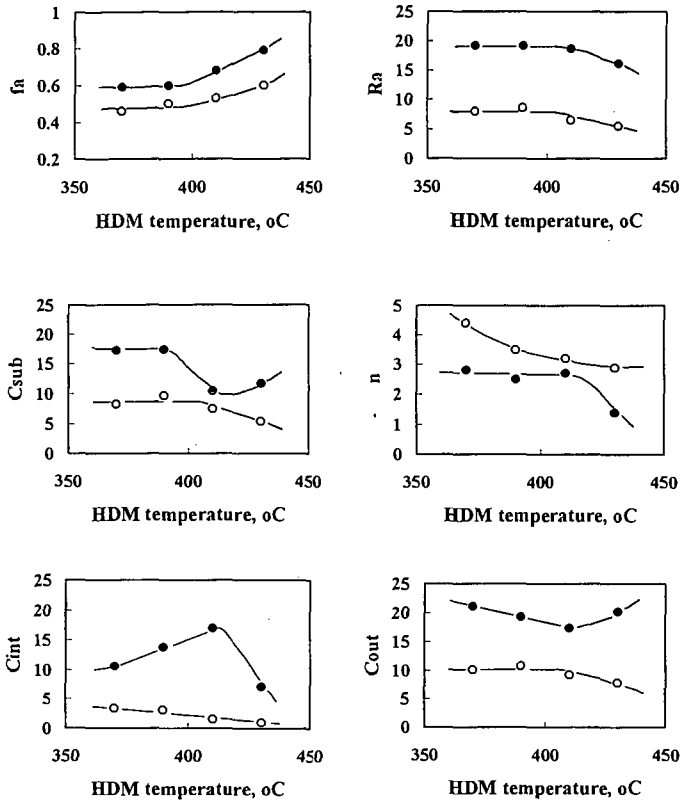

Figure 2. Structural parameters of asphaltenes and resins after HDM treatments; ● asphaltenes, ○ resins.

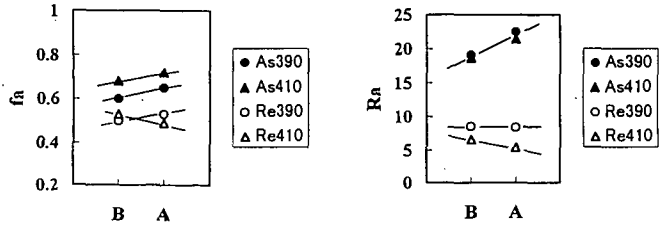

Figure 3. Structural parameters of asphaltenes and resins before(B) and after(A) HDS treatments

STRUCTURAL INSIGHTS TO HEAVY RESID AND COAL FOR DESIGNING UP-GRADING

Isao Mochida

Institute of Advanced Material Study, Kyushu University
Kasuga, Fukuoka 816-8580, Japan

Keywords: Molecular assemble, XRD, hydrotreatment

Objectives and Approaching of Resid Up-grading

Increasing demand for transportation fuel of higher performance and less environmental load and increasing dependence on heavy crude, resid, and coal require the development of more efficient up-grading technology in coming future. Several processes have been practiced for up-grading, which consists of depolymerization, aromatic hydrogenation and ring opening, metal and heteroatoms removals. The degrees of reaction severity varied the yield and quality of the product, charging the responsible cost. Such reactions are derived thermally and catalytically according to the severity of design and cost/performance balances.

Thermal up-grading is usually cheap in facility and running cost, but suffers the limited conversion, and selectivity to wanted products, insufficient quality of product and unwanted coke. Some coke can be designed to be the product of high quality such as those for blast furnace and electrode. Handling of solid coke is often energy-loss, dirty and tedious.

Catalytic process can drive the reactions as wanted, although the deactivation contaminants, and poisoning of the catalyst limit the advantage of the process, increasing the catalyst cost. Sometime cheap catalyst is obliged to use because of limited turn-over number and use of repetition. Combination of thermal and catalytic processes has been designed to optimize their advantages.

The design of up-grading is to define the reactions needed to convert the resid to transportation fuel, the best catalysts for the respective reactions, their optimum use and recovery for their repeated use. Hence the chemistry on the structural changes of organic substrates, catalyst surface, and active species should be described in details as much as possible.

Structural Images of Resid, especially Significance and Liberation of Molecular Assembles

Resid has been described as polyaromatic, polynuclear polymers. The aromatic rings are connected directly (aryl-aryl linkage) or through methylene bridges to form polynuclear chains, carrying heteroatoms within the ring and alkyl substituent on the rings as imaged from the structure of depolymerized units. The alkyl chains in the substituents are basically normal and very long up to 30-40 carbons. The hetero-cyclics such as pyrrole, pyridine, and thiophenes carry heavy metals such as vanadium and nickel as observed in porphyrins.

The primary polyaromatic polynuclear chains form three dimensional network through the non-covalent as well as covalent linkages. The non-covalent bonds link the chains through alkyl chain entanglement, π-π stacking of aromatic rings, acid-base or hydrogen bonding, coordinative bridge of the metal cations, and charge transfers among the heterocyclic rings. Such intermolecular assemble sometime forms micelle, influencing strongly the solubility in the matrix of smaller partners and reaction solvent and reactivity through governing the contact of the

reactive sites with the reagent as well as active site on the catalyst, and favoring the intermolecular condensation.

The asphaltene in the resid which is defined by the solubility in hexane and benzene is a target of up-grading.Its coking/fouling reactivity, inertness for depolymerization and tendency for phase separation and precipitation are ascribed to the structure of its chains and their intermolecular assembles. Liberation of molecular assemble by breaking intermolecular linkage through solvation, ring hydrogenation, removal of bridging cations and heterogroups. Such liberation enhances solubility and the reactivity for depolymerization, reducing the coking reactivity and irreversible adsorption.

Detection of Molecular Assemble

Molecular assemble in resids and coals has been accessed by XRD, NMR and ESR through diffraction of aromatic stacking, different relaxation and rotational narrowing of metal prrphyrins, respectively. XRD of slow step scan provides two broad diffraction peaks at 20°(γ-band) and 26°(π-band), receptively, which are believed to reflect alkyl entanglement and π-stacking. Figure 1 illustrates XRD profiles of a vacuum residue and its fractions. The intensity of π-band increases in the order of saturate, aromatic, polar, and asphaltene fractions, indicating increasing significance of π-π stacking. In addition to two broad bands, very sharp peaks are observable at 22° and 24° , which are attributable to n-paraffin's crystals.

Liberation of Molecular Assemble

High temperature and solvents moderate both stacking. Higher temperature reduced the π-stacking and shifted γ-band to the lower angle. Figures 2 and 3 show XRD of VR in toluene and swollen Beulah-Zap coal by DMF and THF. Both bands of VR were weakened according to the amount of solvent although the γ-band reduced its intensity more rapidly. In contrast, solvent swelling of coal appears to moderate the π-stacking more selectivity.

Removal of cationic bridges in coal liberates the aliphatic entanglement in the coal producing weaker hydrogen bond.

Extraction and Adsorption of Asphaltene

Asphaltene in the VR is the target of conversion while it is a troublemaker in the catalytic conversion. Hence its removal prior to the up-grading of heavy resid is an approach to avoid the trouble. Asphaltene can be selectivity extracted by liquid propane under supercritical conditions.

Some carbon materials adsorb asphaltene rather selectively. Their pore must be larger than 10A. Carbon blacks of nanoparticulate adsorb selectively the asphaltene at a high capacity.Selective and deep removal of metals in VR is most wanted since the demetalation is the first step in a series of hydrotreatment stages, where the capacity of demetalation agent and its completeness govern efficiency of the process.

Inflnence of Hydrotreatment on Molecular Assemble

Hydrotreatment produces distillate and more saturate, converting the polar and asphaltene fractions. Aromatic rings are hydrogreated and polymer chains are broken down by such treatment. Hydrogenation reduces intensities of both γ and π bands.

Configuration and Catalyst for Hydrotreatment of Resid and Coal

Hydrotreatment consists of metal removal, hydrogenation, hydrocracking, hydrodesulfurization and hydrodenitrogenation. Hydrogenation is believed to moderate the coking and sludge formation and enhances the reactivity for cracking. Since the hydrogenation favors thermodynamically the lower temperature, while the cracking does higher temperature. The active catalyst is preferably used at a separate step of lower temperature for the pretreating hydrogenation.

Aromatic and hydrogen donor solvents often help the hydrotreatment by dissolving heavier components and suppressing on retrogressive reactions. Dry sludge produced in the hydrocracking is successfully suppressed by the two stage hydrocracking and added solvent to achieve a high distillation yield.

Catalysts of fine particles are appreciated in the moving bed hydrotreating. Recovering and repeated use as well as penetration into micelle or coal grain are concerned. Carbon black of nano-particles is a candidate support to solve the problems. NiNo/carbon black has been reported to give the very high activity for coal liquefaction NiFe/carbon black shows comparable activity, although its activity for ring hydrogenation is limited, requiring donor solvent in the liquefaction.

Unfortunately such catalysts adsorbs strongly the asphaltene to be insoluble during the hydrotreatment. Some modification of the support is necessary to reduce its surface polarity for limited adsorption, maintaining the dispersion form against sulfide active species.

Molecular Identification of Gas Oil and Vacuum Gas Oil for Desulfurization and Denitrogenation

Gas chromatograph equipped with atomic emission detector can separately identify hydrocarbons, sulfur, nitrogen, oxygen and even metal containing species. Molecular separation by a suitable column and every identification are now in progress. Nevertheless the reactivity of the respective species inhibiting and deactivation factors of partner species are measured very easily. Figure 4 illustrates typical chromatographs of hydrocarbons, sulfur, nitrogen and oxygen species in the coal derived gas oil. Analyses before and after the hydrotreatment tell us their reactivity. Some intermediate products are also identified to establish the reaction scheme in the presence of competitors and inhibitors in the same oil.

The desulfurization schemes of its most refractory 4,6-dimethyldibenzothiophene have been proposed as shown in Figure 5. Based on the scheme, natures of the active site and inhibitors are identified and better catalyst and reaction configuration can be designed. Denitrogenation of nitrogen species in the gas oil is studied by the same approach.

Another significance of the molecular identification is that the products in the hydrotreated resid suggest us the unit molecular structure of the building blocks of the polymeric substances.

Aromatic Ring Opening

Heavy feed and coal tend to yield highly aromatic products. Aromatic rings are hopefully opened into alkylnaphthenes for clean and efficient combustion. Selective hydrogenation of aromatic ring by noble metal catalyst and selective C-C bond fission by adequate zeolite catalyst appear most promising. Pore, crystal sizes, and crystallinity of the wall and zeolite content in the synthesis are necessary to be improved.

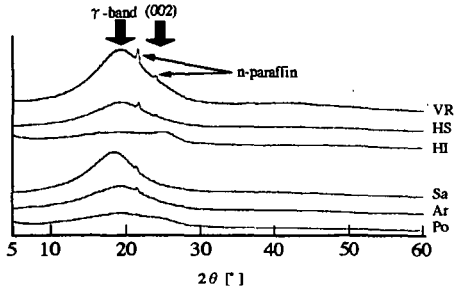

Figure 1 XRD of AM-VR fractions (Step Scan 4 sec. / 0.01°)

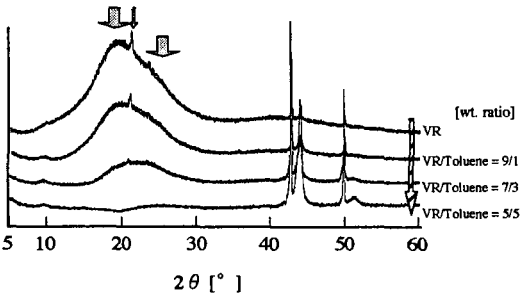

Figure 2 XRD of VR in toluene (Step Scan 4 sec. / 0.01°)

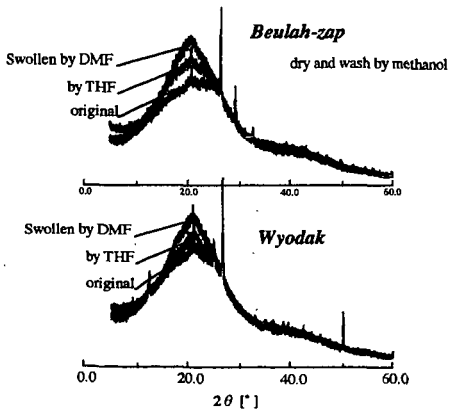

Figure 3 XRD of Swollen coals with DMF and THF
(Step Scan 3 sec. / 0.01°)

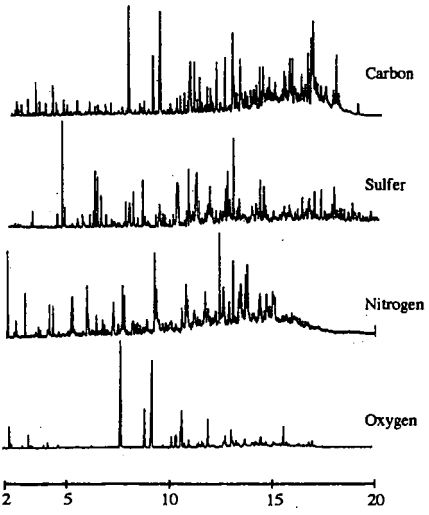

Figure 4 GC-AED chromatograms of C, S , N, O species in South Banko Coal Liquids

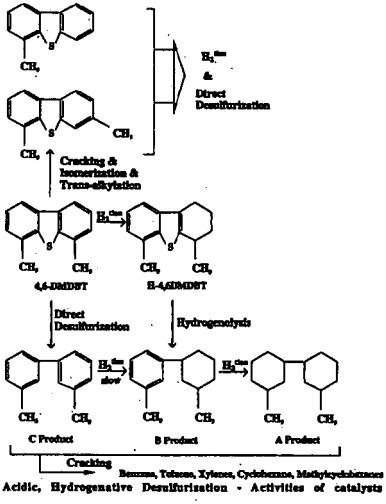

Figure 5 Hydrodesulfurization Reaction Schemes for 4,6-DiMethylDiBenzoTiophene

SEPARABILITY OF COLD LAKE BITUMEN AND ARABIAN HEAVY VACUUM RESID

Irwin A. Wiehe*
Soluble Solutions
3 Louise Lane
Gladstone, NJ 07934

KEYWORDS: heavy oil, separability, molecular limits

INTRODUCTION

While refinery separation of heavy oil is usually restricted to distillation, fluid catalytic cracking (FCC) feed is not required to be volatile, only containing acceptable levels of catalyst poisons: Conradson carbon residue, vanadium, nickel, and basic nitrogen. One method for achieving this objective is to physically separate the higher quality fraction. Therefore, the laboratory separation of Cold Lake bitumen and Arabian Heavy vacuum resid was done to determine the potential for a more molecularly selective separation. The combination of distillation, deasphalting, and adsorption was used to determine the ultimate separation that is possible in order to approximate the molecular limits, or the molecular separability.

The feed specifications for fluid catalytic cracking of resid containing oils depend greatly on the design and practice of the FCC unit, on the catalyst, and on other feeds available for blending. Nevertheless, the typical guidelines of Barnes (1), shown in Table I will be used. Of these, Conradson carbon residue, vanadium content, and nickel content are often the most critical and will be emphasized.

Table I
Feed Specifications for Resid FCC (1)

Feed Property	Limit
Conradson Carbon Residue	3 - 8 wt%
Vanadium Content	10 - 15 ppm
Nickel Content	20 - 25 ppm
Sodium Content	5 - 10 ppm
Basic Nitrogen	800 ppm
Sulfur Content	3 wt%
Maximum Density	0.940 g/cc
Minimum Hydrogen	11.5 wt%

EXPERIMENTAL

The general procedure used for separating heavy oils as shown in Figure 1 is a variation of that published previously (2). The first possible step was batch distillation at 1.4 mm Hg that was done directly out of tubing bombs immersed in a sand bath at 315° C. The second and third steps were repeated using several solvents but the same solvent for each step for a given trial. The second step removed the solvent insolubles by mixing 25 parts solvent to one part oil, waiting eight hours, and filtering. In the third step Attapulgus clay was mixed with the oil dissolved in the solvent and let sit for eight hours. This mixture was filtered with a fine glass frit and washed with additional solvent until the solvent passed through clear of any color. The heavy oil dissolved in the solvent was recovered by rotary evaporation and vacuum drying. The fraction remaining on the clay was recovered by washing on the glass frit with a mixture containing 50% acetone and 50% toluene followed with 10% methanol and 90% toluene. Finally, the adsorbed fraction of heavy oil was recovered from the solvents by rotary evaporation and vacuum drying. The solvents used in the separation trials included n-pentane, n-heptane, cyclohexane, toluene, and carbon disulfide. Once collected, analytical data were measured on each of these fractions.

RESULTS AND DISCUSSION

Separation of Heavy Oils

For the separation of each heavy oil, each quality measurement: Conradson carbon, vanadium, nickel, etc., in the higher quality fraction was plotted versus the yield of the higher quality fraction. Since the highest quality fraction was the distillable liquids, it was the point at the lowest yield for Cold Lake bitumen. The soluble, but unadsorbed, fraction was the next highest quality fraction for each trial solvent. Thus, the quality measurement and yield were calculated as if this fraction and the distillable liquids were mixed to form the second point for each trial

* Research was done at Exxon Corporate Research, Annandale, NJ 08801-0998

solvent. Likewise, the soluble adsorbed fraction and the insolubles were added. This type of data for Conradson carbon residue is shown in Figure 2 for Cold Lake bitumen and in Figure 3 for Arabian Heavy Vacuum resid. In each case a curve is drawn through those of highest yield at a given quality measurement as this determines the best way the heavy oil could be split into two fractions, the separability.

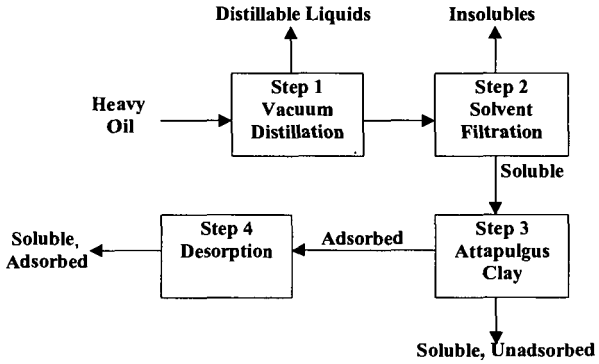

Figure 1. General Procedure for Laboratory Selective Separation

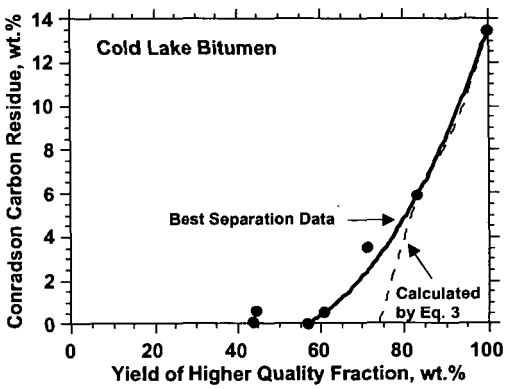

Figure 2. Selective Separation of Conradson Carbon for Cold Lake Bitumen

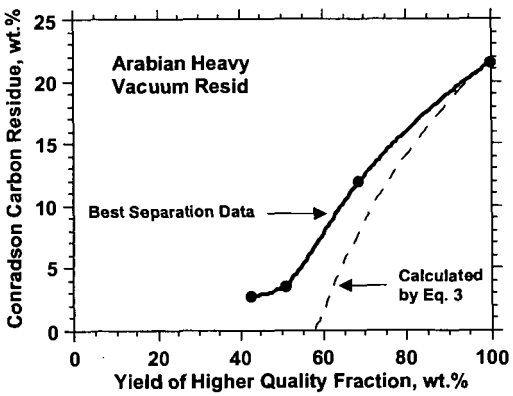

Figure 3. Selective Separation of Conradson Carbon for Arabian Heavy Vacuum Resid

Of the solvents tried, cyclohexane is the best because it gives a high yield of a high quality fraction without insolubles. The yields and analytical data for the cyclohexane separations are shown in Table II and compared with the starting feed data. Thus, for Arabian Heavy vacuum resid that does not require distillation, the separation is achieved in two steps, adsorption and desorption, and about half of the resid would meet the specifications for resid FCC feed in Table I except for sulfur. On the other hand, combining vacuum distillation with cyclohexane adsorption separates 71% of Cold Lake bitumen into a fraction that only slightly misses the example specifications for sulfur and hydrogen.

Table II
Cyclohexane Separations: Yields and Analytical Data

Fraction	Yield wt.%	C wt.%	H wt.%	N wt.%	O wt.%	S wt.%	V ppm	Ni ppm	Conradson Carbon wt.%
Cold Lake Bitumen									
Distillable Liquids	44.5	85.14	11.67	0.09	0.00	2.63	0.6	0.0	0.57
Soluble, Unadsorbed	26.7	84.08	10.96	0.17	0.60	4.11	29	10	8.4
Dist. Liq. + Sol. Unadsorb.	*71.2*	*84.74*	*11.40*	*0.12*	*0.22*	*3.18*	*11*	*4*	*3.5*
Soluble, Adsorbed	30.2	81.07	8.73	0.99	2.39	6.55	359	138	43.8
TOTAL	101.4	83.57	10.60	0.38	0.87	4.19	115	41	15.5
Full Feed	100	83.82	10.46	0.38	0.68	4.57	152	62	13.5
Arabian Heavy Vacuum Resid									
Soluble, Unadsorbed	50.9	85.07	11.47	0.030	0.50	3.57	0.0	0.0	3.4
Soluble, Adsorbed	50.1	82.63	8.53	0.80	1.63	6.78	451	112	36.9
TOTAL	101.0	83.86	10.01	0.41	1.06	5.16	224	56	20.2
Full Feed	100	83.51	9.93	0.45	0.57	5.80	165	40	21.5

Conradson Carbon Separability Limit

Here we will focus on the problem of maximizing the yield of a low Conradson Carbon fraction. 100 parts of heavy oil of C_F Conradson carbon is separated into β parts of a higher quality fraction containing a Conradson carbon of C_H and 100-β parts of a lower quality fraction containing a Conradson carbon of C_L. Since Conradson carbon is conserved for separations (3):

$$100\ C_F = \beta\ C_H + (100 - \beta)\ C_L \qquad [1]$$

Solving for β:

$$\beta = 100\ [\ 1 - (C_F - C_H)/\ (C_L - C_H)] \qquad [2]$$

This shows that to maximize the yield of a high quality fraction meeting a Conradson carbon specification from a given heavy oil feed, one needs to concentrate the Conradson carbon in the low quality fraction. Therefore, for Cold Lake bitumen (Conradson carbon = 13.5 wt.%) to separate 85 wt.% of a fraction meeting a specifications of 5 wt.% Conradson carbon, one would need to isolate 15 wt.% containing 61.7 wt.% Conradson carbon. However, the highest Conradson carbon fraction that was isolated from Cold Lake bitumen is the 14.1 wt.% yield of n-heptane insoluble asphaltenes with a Conradson carbon of 52.5%. Thus, it is unlikely that 85 wt.% of a fraction of Cold Lake bitumen with a Conradson carbon of 5 wt.% or less exists because significant fractions of Conradson carbon much greater than 50 wt.% Conradson carbon are not present in heavy oils. This is because the coke precursors are chemically linked to distillable liquid precursors in the same molecule. In terms of the pendant - core building block model (3), all molecules that contain cores also contain significant fractions of pendants. For instance, Arabian heavy vacuum resid with a Conradson carbon of 21.5 wt.% and an asphaltene Conradson carbon of 51.6 wt.% at a specification of 5 wt.% Conradson carbon:

$$\beta = 100\ [1 - (21.5 - 5)/\ (51.6 - 5)]$$
$$\beta = 64\ \text{wt.\%}$$

Thus, the separation of 64 wt.% of Arabian Heavy vacuum resid with a Conradson carbon of 5 wt.% or less is not possible because there are only 20 wt.% asphaltenes and not the 36 wt.% required. As a result, Eq. 2 with the asphaltene Conradson carbon substituted for C_L is an upper limit on the yield of a fraction of a given Conradson carbon value. Eq. 1 can be rearranged and the asphaltene Conradson carbon, C_A, substituted for C_L to give:

$$C_H = \{C_F - (1 - \beta/100)\, C_A\} / \{\beta/100\} \quad [3]$$

This upper limit, Eq. 3, is plotted on Figures 2 and 3 as a dashed curve. The curve through the best separation data approaches the upper limit at high yields of the higher quality fraction for Cold Lake bitumen. On the other hand, a gap remains between the two curves for Arabian Heavy vacuum resid, indicating further improvements in separability of this heavy oil may be possible.

Separation of Vanadium and Nickel from Heavy Oils

Unlike for Conradson carbon, the separability of vanadium and nickel is not limited much by the heavy oil macromolecules. Vanadium with an atomic weight of 50.9, even as part of the largest macromolecules, the asphaltenes of average molecular weight of 3000, would be 1/60 the weight of the molecule bonded to it. Thus, in Cold Lake bitumen that contains 152 ppm vanadium and Arabian Heavy vacuum resid that contains 165 ppm vanadium, all of the vanadium is in less than 1 wt.% of each heavy oil. Likewise, nickel at 62 ppm in Cold Lake bitumen and 56 ppm in Arabian Heavy vacuum resid must be contained in less than 0.5 wt.% of each heavy oil. Nevertheless, the vanadium and nickel containing molecules physically associate with the Conradson carbon precursors, the polynuclear aromatics. As a result, they tend to separate together. Figure 4 and 6 demonstrates for Cold Lake bitumen and Figures 5 and 7 for Arabian Heavy vacuum resid that only a little more low vanadium and nickel fractions can be separated than low Conradson carbon fractions (Figures 2 and 3). Thus, precipitation and/or Attapulgus clay adsorption do note provide the desired selective separation for vanadium and nickel.

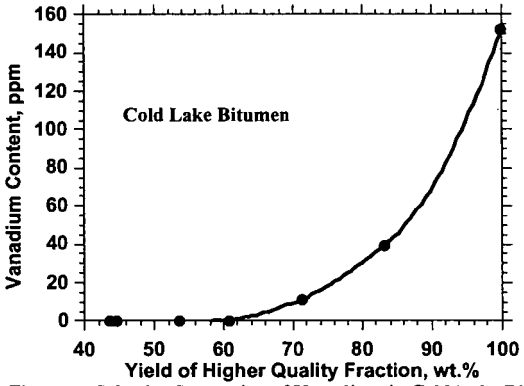

Figure 4. Selective Separation of Vanadium in Cold Lake Bitumen

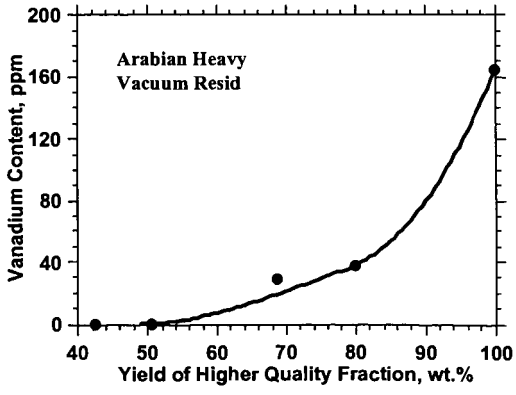

Figure 5. Selective Separation of Vanadium in Arabian Heavy Vacuum Resid

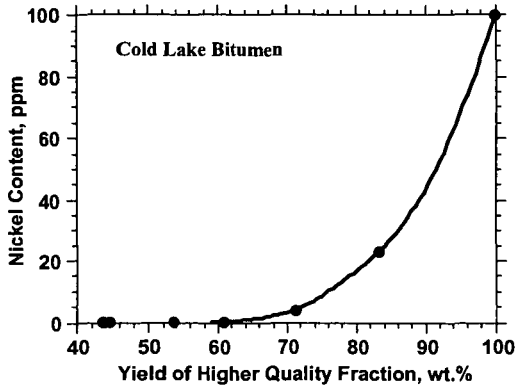

Figure 6. Selective Separation of Nickel in Cold Lake Bitumen

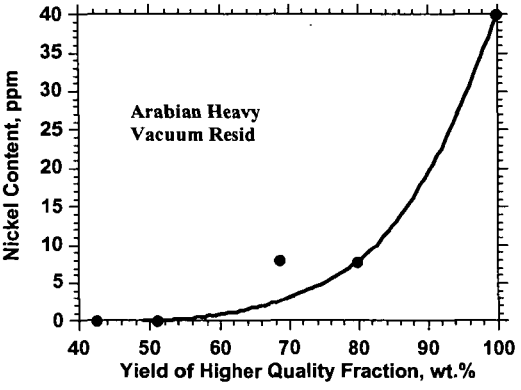

Figure 7. Selective Separation of Nickel in Arabian Heavy Vacuum Resid

CONCLUSIONS

Selective separation has the potential to provide substantial fluid catalytic cracking feed from heavy oils that could compete with resid conversion processes. Further separation of Conradson carbon is limited by heavy oil molecules in which Conradson carbon precursors are chemically bonded to significant fractions of distillable liquid precursors. On the other hand, there are no molecular limitations to the much greater separation of vanadium and nickel. Vanadium is in less than 1 wt.% of heavy oils and nickel is in less than 0.5 wt.%. Although sufficient for resid FCC specifications, physical association with Conradson carbon precursors tends to cause vanadium and nickel to separate with the Conradson carbon precursors in precipitation and adsorption separations. Thus, devising a molecularly selective separation method for attaining the full potential of metals removal from heavy oils remains to be a significant challenge.

REFERENCES

1. Barnes, P.H., AIChE, International Conference on Refinery Processes, Preprints, **1998**, 227.
2. Wiehe, I. A., *Ind. Eng. Chem. Res.* **1992**, 31, 530.
3. Wiehe, I. A., *Energy Fuels* **1994**, 8, 536.

The Promotional Effect of Initiators in Hydro-thermal Cracking of Resids

Jie Chang, Li Fan* and Kaoru Fujimoto

Department of Applied Chemistry, School of Engineering, The University of Tokyo,

Hongo 7-3-1, Bunkyo-ku, Tokyo, 113-8656, Japan Email: tfan@hongo.ecc.u-tokyo.ac.jp

1 Introduction

Based on cracking mechanism, there are three main industrial processes to produce middle distillate from resid. They are thermal cracking, catalytic cracking and hydrocracking. Hydro-thermal cracking, the combination of thermal cracking and catalytic hydrogenation, is a novel method developed by the present authors to upgrade resids aiming at maximum middle distillate (Fujimoto et al., 1988; Yang et al., 1998). The following elementary steps are important during hydro-thermal cracking reactions: (1) Initiation free radical (homolytic cleavage of a hydrocarbon molecule into two free radicals). (2) Free radical dissociation (β scission). (3) Hydrogen transfer (between H_2, radical and hydrocarbon). H transfer from H_2 to radical can suppress the secondary cracking of hydrocarbon, therefore, suppress the yields of coke and gas. It is considered that some effective initiators may enhance the conversion of resids by increasing the concentration of free radicals. Much research has been carried out on catalyst development, reaction mechanism, process design and optimization in the above refinery processes until now. But the issue of adding initiators in the cracking of resids was very rarely addressed. The present work shows the promotional effect of initiators in hydro-thermal cracking of resids as well as its model compound.

2 Experimental

Experiments were carried out in a 75 cm^3 batch reactor. The reaction conditions were as follows: temperature, 673-703K; initial pressure, 5.0 MPa; reaction time, 0-60 min; catalyst/oil ratio, 0.05-0.2. Canadian bitumen (B) and Arabian heavy vacuum resid (AVR) were used in experiments. Their properties are shown in Table 1.

Sulfur and $(CH_3)_3COOC(CH_3)_3$ (DTBP) were used here as initiators to promote heavy oil conversion.

Gas products were analyzed by gas chromatography (Shimadzu GC-8A). Liquid products were separated by a distillation gas chromatography (Shimadzu GC-14A) into 5 components: naphtha (initial boiling point –343K), kerosene (343-503K), gas oil (503-616K), vacuum gas oil (616-798K) and residue (>798K). The conversion of resid was calculated by the following formula:

$$\text{Conversion (wt\%)} = (1-\frac{\text{residue in product}}{\text{residue in feed}})\times 100\% .$$

When alkylbenzene was pyrolyzed or cracked on solid acid catalyst, the selectivities of benzene and toluene were so different that it could be used as a model compound to distinguish a reaction proceeding via carbonium mechanism or free radical mechanism (Szware 1950; Mochida and Yoneda 1967; Nakamura et al, 1997). Study on liquid-phase thermolysis of 1-phenyldodecane (PhDD) demonstrated that PhDD pyrolysis entirely proceeded through free radical mechanism (Savage and Klein, 1987). The reaction of PhDD was used as a probe reaction to study the mechanism of initiator promotional effect. In these experiments, the liquid products were determined by GC-MS (Shimadzu GCMS 1600) and analyzed by gas chromatography (Shimadzu GC-14A).

3 Results and Discussion

3.1 Effect of initiators addition in resids

1 wt% of DTBP was added into bitumen to study the effect of initiator. The properties of products are listed in Table 2. It was obvious that this peroxide was very effective to increase the conversion of bitumen from 59.1% to 91.9% (runs 1 and 2 without catalyst) and from 68.4% to 78.5% (runs 3 and 4 with catalyst) respectively. Coke yield was greatly suppressed by catalyst (runs 3 and 4).

It also was seen from Table 2 that in the cases of adding DTBP, the selectivity of iso-butane was higher than that without DTBP. It is well known that thermal cracking of hydrocarbon molecule proceeded via the chain reaction of free radicals generated from C-C cleavage or hydrogen atom abstraction from C-H bond. In bitumen hydro-thermal cracking, free radicals were generated from C-C cleavage at initial stage. But when DTBP was added into bitumen, it decomposed at high temperature and produced tertiary butoxy radical. This free radical could abstract hydrogen from bitumen and initialized chain reactions at initial stage besides the conventional initiation path, therefore the concentration of radical was higher and the conversion of bitumen was increased.

3 wt% of sulfur was added into AVR to test the effect of initiator addition. The results were compared in Table 3. When catalysts were used, the addition of sulfur increased the conversion from 63.6% to 81.1% (runs 5 and 6). In absence of catalyst, the addition of sulfur raised the conversion from 15.7% to 32.5% (runs 7 and 8). Similarly, sulfur was an effective initiator to the hydro-thermal cracking of AVR.

3.2 Study on model compound

The conversions in different case at different reaction time are depicted in Fig.1. It is clear from Fig.1 that the conversion was obviously enhanced by adding initiator with or without catalyst. Without catalyst and with initiator, when the reaction time was one hour, the conversion increased from 40.1% to 51.9%. In absence of initiator, catalyst greatly decreased the conversion from 40.1% to 16.8% in one-hour reaction. It seemed that free radicals were hydro-quenched over catalyst. After adding initiator to catalyzed reaction, the conversion restored to 40.2% even if the reaction time was just half of an hour. If the reaction time was extended to one hour, the conversion of the catalyzed reaction with addition of peroxide was further enhanced to 47.5%. The selectivities of part products are shown in Table 4. It was found from Table 4 that the ratios of toluene to benzene were about 18.0-22.2 in all of these cases. This indicated that hydro-thermal cracking of PhDD proceeded via free radical mechanism and hydrogenation quench. In the cases of adding peroxide, iso-butene, acetone and tertiary butyl alcohol were detected in products and selectivity of C_1 species was also increased. In run 11, the feed was heated from room temperature to 683K in 10 min and cooled down immediately, to 573K in 5 min and to room temperature in another 15 min (reaction time = 0). The yield of acetone was high. It should be derived from decomposition of tertiary butoxy radical, with the corresponding formation of C_1 species (Fan et al., 1998). This provided the evidence that the decomposition of DTBP was the initial stage of the chain reactions.

The above results suggested that the hydro-thermal cracking of PhDD related with free radical chain reactions. It was considered that in the chain reactions, the initiation step of PhDD molecule dissociation, forming free radicals, was the slowest one, the overall reaction rate was readily controlled by this step. If the concentration of free radicals in reactants was increased, the reaction rate could be elevated. When DTBP was added into PhDD, it easily produced free radicals during hydro-thermal cracking conditions, therefore increased the overall concentration of free radicals, enhanced the conversion of PhDD. If effective free radical initiators are available, the conversion of resid in hydro-thermal cracking, thermal cracking or hydrocracking will be raised and the reaction temperature may be lowered. The experiments showed that DTBT and sulfur are effective promoters to resid conversion.

4 Conclusions

DTBP remarkably enhanced the conversion of resid and its model compound during hydro-thermal cracking. This resulted from tertiary butoxy free radical produced by the decomposition of peroxide at reaction condition. Similarly, sulfur was an effective promoter to the hydro-thermal cracking of AVR.

5 References

Fan, L.; Watanabe, T.; Fujimoto, K. *Stud. Surf. Sci. Catal.* 1998, 119, 581.

Fujimoto, K.; Nakamura, I.; Tominaga, H. *Chem. Lett.* 1988, 167.

Mochida, I.; Yoneda, Y. *J. Catal.* 1967, 7, 386.

Nakamura, I.; Yang, M.; Fujimoto, K. *Preprints Div. Petrol. Chem., ACS* 1997, 42(2), 401.

Savage, P. E.; Klein M. T. *Ind. Eng. Chem. Res.* 1987, 26, 374.

Szware, M. *Chem. Rev.* 1950, 47, 171.

Yang, M.G.; Nakamura, I.; Fujimoto, K. *Catal. Today* 1998, 43, 272.

Table 1 Properties of feedstock

	B	AVR
API Gravity	6.0	5.9
CCR, wt%	14.8	22.4
C, wt%	82.89	84.80
H, wt%	10.14	10.20
S, wt%	4.90	4.02
Ni, wtppm	75	53
V, wtppm	192	180
Naphtha, wt%	0	0
Kerosene, wt%	0	0
Gas oil, wt%	6.8	0
VGO, wt%	28.0	0
Residue, wt%	65.2	100.0

Table 2 Effect of DTBP addition on hydro-thermal cracking of bitumen

Run number	1	2	3	4
Catalyst	no	no	Ni/Al_2O_3	Ni/Al_2O_3
DTBP	no	adding	no	adding
Conversion, %	59.1	91.9	68.4	78.5
yield, wt%				
C_1-C_4	4.3	5.4	4.2	5.0
iC_4H_{10}/nC_4H_{10}	0.50	0.84	0.50	1.46
Naphtha	9.1	12.4	7.4	9.6
Kerosene	9.4	11.9	8.0	9.1
Gas oil	22.6	28.4	22.7	25.0
Vacuum gas oil	21.8	29.9	31.8	32.3
Residue	26.7	5.3	20.6	14.0
Coke	4.6	5.1	3.0	2.8

Temperature 703K, pressure 5.0MPa, Bitumen 10.00g, catalyst 2.00g , DTBP 0.10g

Table 3 Effect of sulfur addition on hydro-thermal cracking of AVR

Run number	5	6	7	8
Catalyst	$NiMo/Al_2O_3$	$NiMo/Al_2O_3$	no	no
Initiator	no	0.3g S	no	0.3g S
Time, min.	60	60	0	0
Conversion, %	63.6	81.1	15.7	32.5
yield, wt%				
C_1-C_4	3.3	4.9	0.1	0.1
Naphtha	4.8	9.2	0.2	1.1
Kerosene	6.1	9.7	0.5	1.4
Gas oil	16.5	21.6	2.3	6.3
Vacuum gas oil	28.6	27.8	12.7	23.6
Residue	34.5	18.8	84.3	67.6
Coke	3.2	6.4	-	-

Temperature 703K, pressure 5.0MPa, AVR 10.00g, catalyst 2.00g

Table 4 Effect of DTBP addition on model compound

Run number	9	10	11	12
Conversion, %	40.1	51.9	19.5	47.5
Selectivity, %				
acetone	0.0	2.86	9.83	0.0
t-butyl alcohol	0.0	0.0	1.56	0.0
n-olefin C_5-C_8	3.03	3.22	0.63	0.0
n-paraffin C_5-C_8	5.76	6.69	0.75	7.03
n-olefin C_9-C_{13}	18.8	7.62	13.8	4.36
n-paraffin C_9-C_{13}	22.2	24.4	15.8	33.9
toluene / benzene	21.3	22.2	18.0	19.2

Temperature 683K, pressure: 5.0MPa

Run 9: reaction time 60 min. no catalyst and no peroxide

Run 10: reaction time 60 min. adding 0.40g peroxide only

Run 11: reaction time 0 min. adding 0.40g peroxide only

Run 12: reaction time 60 min. adding 0.40g peroxide and 0.50g catalyst

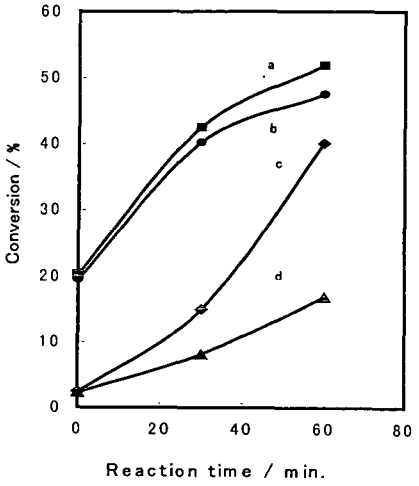

Fig.1 Effect of DTBP on conversion of PhDD

Feed: PhDD 10.00g, temperature 683K

pressure 5.0MPa

a: adding 0.40g DTBP only

b: adding 0.40g DTBP and 0.50g catalyst

c: no DTBP and catalyst

d: adding 0.50g catalyst only

EFFECT OF STEAM ON COKING CHEMISTRY OF ATHABASCA BITUMEN

Richard Dutta, William McCaffrey and Murray Gray

Dept. of Chemical and Materials Eng., University of Alberta,
Edmonton, Alberta, Canada

Key Words: fluid-coking, bitumen, free-radical stabilization

INTRODUCTION

Fluid-coking is an important technology used in upgrading of bitumen and petroleum residues. The process uses a fluidized bed of hot coke particles to crack the feedstock. The bed is fluidized by steam, which also acts as a stripping medium to remove the distillate from the surface of the coke particles. Steam has long been thought of as chemically 'inert' in this process, in that it does not effect the product quality or yields. The use of other fluidizing media has been considered as an alternative to steam, including methane or nitrogen. Therefore, the question as to the chemical influence of steam is an important one and this study was undertaken to determine this on a micro-lab scale and on a larger pilot scale.

Much of the previous research into the effect of steam on hydrocarbons has been limited to the lower temperature regime associated with thermal maturation of kerogen in aqueous environments (<400°C). Research has focussed on hydrous pyrolysis experiments using kerogens and stable isotope analysis[1,2]. The chemical transformation of kerogen to bitumen, oil and gas has been studied to assess the role of water in these reactions. Studies at low temperatures (<150°C) conclude that water-hydrogen may exchange with certain labile organic hydrogen sites, e.g., those bound to nitrogen, sulfur and oxygen[3]. There is some evidence of hydrogen exchange with aromatic hydrogen and alkyl-hydrogen via carbonium ion mechanisms[4,5]. However, the higher temperatures of fluid-coking (530°C) and other upgrading processes, lead to free-radical reactions. Studies by Hoering[6], Lewan[2], and Stalker et al.[7], have shown that at higher temperatures, exchange between water-hydrogen and organic-hydrogen is due to quenching of free organic radical sites. Thermodynamically, the reactions of steam and free-radicals have been shown to be favorable under certain reaction conditions[8].

Song et al.[9] have studied the effect of water on the process of coal liquefaction. Water was seen to have three effects on liquefaction; chemical, physical and surface interactions. The increase in coal conversion was attributed to increased removal of oxygen functionalities in the presence of water, and therefore a reduction in retrogressive reactions. Tse et al.[10] suggested that water can reduce retrogressive reactions such as crosslinking of hydroxy groups. Siskin et al.[11,12] have observed that water may increase depolymerization by cleavage of ether linkages. Clark and Kirk studied the upgrading of bitumen with water at temperatures up to 415°C[13]. Their results show that water has an effect in decreasing insoluble material produced and also decreasing the sulfur content of the liquids produced. This enhancement of product quantity and quality was improved even further in the presence of an iron-based catalyst.

The objective of this research project was to determine the extent to which steam exchanges/donates hydrogen to the reacting bitumen molecules under coking conditions. Experiments were carried out with water doped with D_2O to trace any exchanged deuterium atoms. Comparisons of experiments carried out with and without water were made to ascertain the effect that steam may have on coking chemistry.

EXPERIMENTAL

The feedstock used in this study was Athabasca Bitumen obtained from Syncrude Canada. A 5.6 wt% solution of deuterium oxide (D_2O) in water was used for all reactions. The coking reactions were carried out in 15 ml microautoclave reactors heated in a fluidized sand bath to temperatures in the range of 350-480°C. 3g of bitumen was accurately weighed into the reactor along with 0.6g D_2O solution. The reactor was closed and purged with nitrogen to atmospheric pressure. For the reactions without D_2O solution (dry), the nitrogen pressure in the reactor was increased to account for the pressure generated by steam in the reactions with water. The reactor was lowered into the sand bath for a pre-determined reaction time and then quickly quenched in cold water. Gases were vented from the reactor and analyzed for hydrocarbon composition by Gas Chromatography. The products in the reactor were extracted in toluene to give coke (toluene insolubles) and liquids (toluene solubles). The coke was dried and weighed to give coke yield. The liquids were analyzed by elemental analysis for C, H, N and S content. ^1H and ^2H liquid NMR were used to quantify the % deuterium in the liquid samples.

In order to determine the deuteration of bitumen under conditions more applicable to fluid coking conditions (530°C, fluidized bed, short residence time), the 3" coking pilot plant at Syncrude Research Center was utilized for two reactions. A 5% solution of D_2O in water was used as the fluidizing medium. Liquid products were analyzed by NMR to give %D.

RESULTS

In order to determine the extent to which steam changes the chemistry of the coking process, several analytical procedures were utilized. This section will show the major findings from each of these, followed by a discussion of the possible mechanism that can explain these changes.

Coke Yield: The yield of toluene insoluble material (coke) at various reaction times at 450°C is shown in Figure 1. The MCR of Athabasca bitumen is 14%. The figure shows that coke yield with and without water exceeds 20% after 60 minutes. This is because a closed reactor is used for this study. At 450°C, volatiles produced in the cracking of bitumen can further crack to produce gas or recombine to produce coke. In the presence of steam, coke yield is reduced from 24% to 21%.

Gas Composition: Figure 2 shows the hydrocarbon gas composition after bitumen coking at 450°C and 60 minutes reaction time. The most striking result is the reduction in methane produced when steam is used in the reaction. The presence of steam appears to reduce the cracking of alkyl-aromatics leading to a reduction in methane formation.

Sulfur Analysis: Figure 3 shows the wt% sulfur in the liquid products from bitumen coking at 450°C. Desulfurization of bitumen proceeds by thermal cleavage of C-S bonds (aliphatic sulfides). These bonds are relatively weak (compared to C-C bonds) and are therefore the first to crack, which is observed in that most of the desulfurization takes place in the first 10 minutes of the reaction. In the presence of steam, removal of sulfur is reduced.

^{1}H and ^{2}H Liquid NMR: This technique was used to quantify the percentage of deuterium atoms per total hydrogen atoms (%D) in various liquid products from bitumen coking. The technique also shows the preferred position that exchanged deuterium will attach to bitumen and its products. Figure 4 shows an example of the ^{2}H spectra of bitumen liquid products detailing the areas used to quantify the data. The spectra has been split into 3 sections, namely aromatic protons, α-CH_2 (benzylic) and α-CH_3 protons (i.e., located on carbon atoms adjacent to aromatic rings), and β- and γ- protons (i.e., located on carbon atoms one and two positions removed from an aromatic ring). Figure 5 shows %D at various reaction conditions. The data shown at 530°C is from liquids taken from the Syncrude coking pilot unit discussed in the experimental section of this paper. It should be noted that in the control experiment (530°C, no D_2O), the %D was 0.014% (natural abundance of deuterium is 0.015%). Exchange of deuterium atoms from D_2O with organic protons from the bitumen occurs mostly at the α-position. Aromatic and γ-carbon deuterations occur but to a lesser extent than α-carbon deuteration

DISCUSSION

The results show that steam is reducing coke yield, methane formation and sulfur removal. The most likely explanation of these observations is by considering radical-stabilization by water-hydrogen exchange. This will cause a reduction in radical-recombination reactions that will lead to coke, stabilization of alkyl-aromatic radicals leading to reduction in methane, and stabilization of C-S radicals leading to reduction in sulfur removal. A second stage of sulfur removal has also been postulated by Kakimura et al.[14]. Hydrothermal cracking of C-S bonds in aromatic structures led to increased removal of sulfur and reduction in viscosity. Based on the limited sulfur analysis taken in this study, it is impossible to back-up the ideas put forward by Kakimura. However, the data does agree with conclusions made previously when considering the coke yield and gas composition.

The data obtained by NMR of the liquid samples shows preferential exchange of deuterium at the α-position (benzylic). This would be expected if conclusions from our previous results are correct, in that, water-hydrogen is stabilizing free-radicals in the coking process. Benzylic radicals are resonance-stabilized and are therefore more likely to exist as reactive intermediates in the coking reaction. Stabilization of these radicals can occur more readily and this is shown with the preferential deuteration of benzylic carbons. This hypothesis can be backed up when considering the coking reaction at 350°C. This reaction temperature does not give rise to many free-radicals (compared to >425°C) and the preferential deuteration of the benzylic position does not occur. The %D data obtained for the pilot plant data taken at 530°C does show a decrease in overall deuterium incorporation into the liquids due to the much decreased residence time of the bitumen cracking products in the reactor. The pilot unit also operates at a much lower pressure than the closed reactors used in the other experiments, which could also explain the decrease in deuteration. The results still show evidence for the radical stabilization behavior that is inferred from the results obtained at lower temperatures and in closed microautoclave reactors.

Figure 6 shows a comparison of the coke yield (divided by 100) and %D in the liquids produced under increasing reaction severity. The data shows that increasing reaction severity give increasing coke yield and an overall trend of increasing deuteration. The decrease at the highest severity conditions is probably due to excess hydrocarbon gas formation that will remove some of the deuterium from the liquid fraction. The relationship between coke yield and %D implies that a similar mechanism can account for the effect of steam on these two parameters.

Proposed Mechanism: Steam is changing the chemistry of the coking process by 'stabilizing' free-radicals that are produced by thermal cleavage of C-C and C-S bonds. This process of free-radical 'stabilization' has to be carefully defined. Free-radical 'capping' is a term that has been used to explain termination reactions by gas-phase hydrogen or hydrogen transferred from donor solvents[15,16]. This mechanism does not particularly apply to this system because the hydroxyl radical will tend to abstract a hydrogen from the bitumen This concept of 'stabilization' is more applicable because it is possible that the radical produced in the stabilization of the hydroxyl radical will not recombine to produce coke.

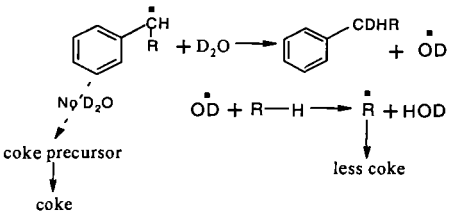

Scheme 1. Mechanism of 'stabilization' of free-radicals produced by cracking of bitumen

CONCLUSIONS

The purpose of this study was to find evidence for the chemical interaction of steam and bitumen under coking conditions. Through various analytical techniques, namely, coke yield, elemental analysis, gas analysis, and liquid NMR, the concept of free-radical stabilization by water-hydrogen has been explored. This free-radical stabilization process can also be inferred by comparing the gas composition and the liquids sulfur content for reactions with and without steam. Water is exchanging/donating hydrogen to the radicals to reduce methane formation and sulfur removal. NMR data has shown preferential deuteration of the benzylic carbons, which would suggest that free-radical stabilization is occurring (benzylic radicals are very stable). Coking reactions carried out in a pilot-unit under conditions similar to real fluid-coking conditions, show this preferential deuteration of the benzylic carbons and suggest that even with the short residence time and low pressures of fluid-coking, water-hydrogen may be exchanged/donated to the reacting bitumen.

ACKNOWLEDGEMENTS

The authors would like to thank the staff of the NMR facility, Dept. of Chemistry, University of Alberta, for NMR analysis of the products. Dr. Karlis Muehlenbachs, Dept. of Earth and Atmospheric Sciences, University of Alberta, has provided the authors with valuable insight into stable isotopes. Thanks to Scott Gillis, Iftikhar Huq and Murray Noble for running the reactions on the pilot plant unit at Syncrude Research Center, Edmonton. Thanks to Dr. Ed. Chan (Syncrude Research Center) for many useful discussions. The work was supported by Syncrude Canada.

REFERENCES

1. Siskin, M. and Katritzky, A. R. *ACS., Div. Fuel. Chem. Prep.* 44(2), 324, 1999
2. Lewan, M. D., *Geochim. Cosmochim. Acta.* 61, 3691-3723, 1997
3. Koepp, M. in *Short papers of the Fourth International Conference, Geochronolgy, Cosmochronology, Isotope Geology*, 1978
4. Alexander, R., Kagi, R. I., and Larcher, A. V., *Geochim. Cosmochim. Acta.*,46, 219-222, 1982
5. Werstiuk, N. H., and Ju, C., *Can. J. Chem.* 67, 812-815, 1989
6. Hoering, T. C., *Org. Geochem.* 5, 267-278, 1984
7. Stalker, L., Larter, S. R., and Farrimond, P. *Org. Geochem.* 28, 238-253, 1998
8. Lewan , M. D., *ACS., Div. Fuel. Chem. Prep.* 44(2), 420, 1999
9. Song, C., Saini, A. K., and Schobert, H. H., *Energy Fuels* 8, 301-312, 1994
10. Tse, D. S., Hirschon, A. S., Malhotra, R., McMillen, D. F., and Ross, D. S., *ACS., Div. Fuel. Chem. Prep.* 36(1), 23, 1991
11. Siskin, M., Katritzky, A. R., Balasubramanian, M., *Energy Fuels* 5, 770, 1991
12. Siskin, M., Bron. G., Vaughn, S. N., Katritzky, A. R., Balasubramanian, M., *Energy Fuels* 4, 488, 1991
13. Clark, P. D. and Kirk, M. J. *Energy Fuels* 8, 380-387, 1994
14. Kakimura, H., Takahashi, S., Kishita, A., Moriya, T., Hong, C. X., and Enomoto, H., *ACS. Div. Fuel. Chem. Prep.* 43(3), 741, 1998
15. Curran, G. P., Struck, R.T., Gorin, E. *Ind. Eng. Chem. Proc. Des. Dev.* 6, 167, 1967.
16. Wiser, W.H. *Fuel.* 47, 475, 1968

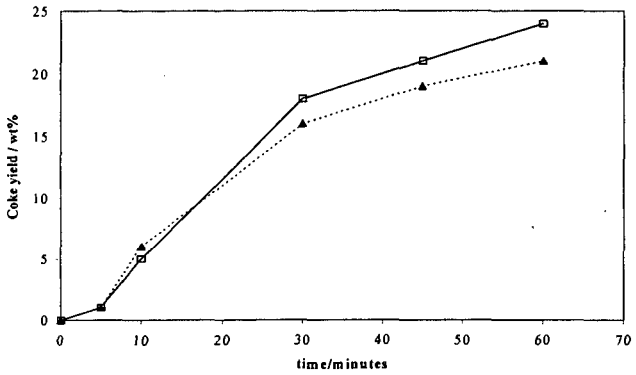

Figure 1. Effect of steam on toluene insoluble (coke) yield from bitumen coking at 450C (▲-steam; □-Dry)

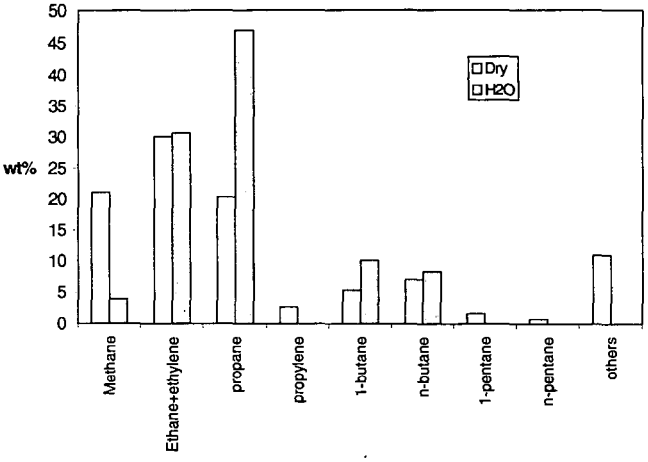

Figure 2. Hydrocarbon gas composition from bitumen coking at 450C and 60 minutes

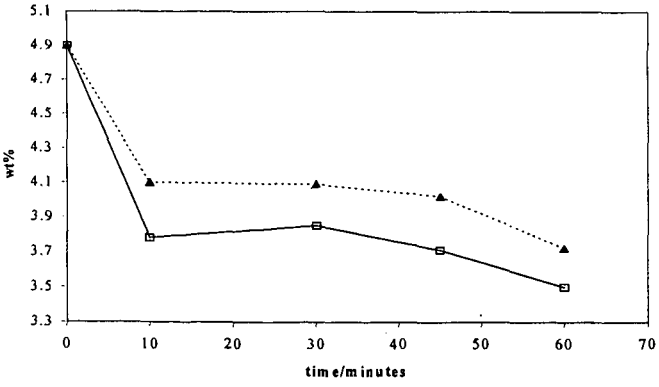

Figure 3. Sulfur content of liquid products from bitumen coking at 450C(▲-steam; □-Dry)

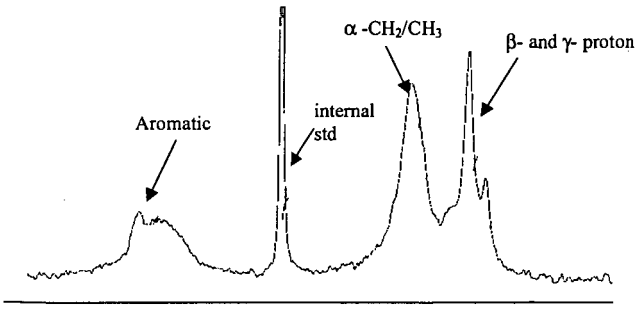

Figure 4. ^{2}H NMR spectra of liquid products from bitumen coking – 450C 60min 5% D_2O in H_2O

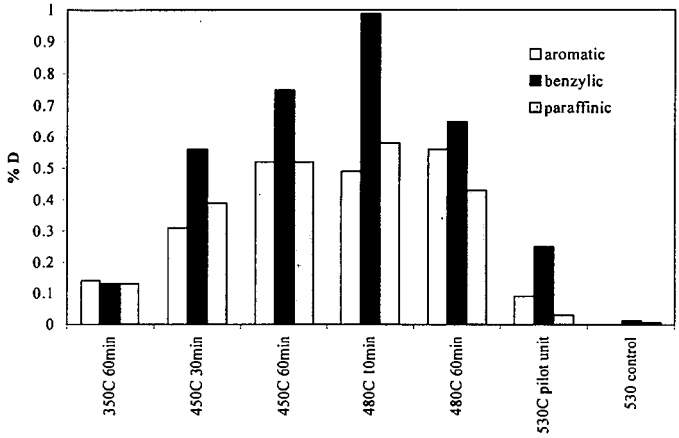

Figure 5. %D in liquid products from bitumen coking (5% D_2O in H_2O)

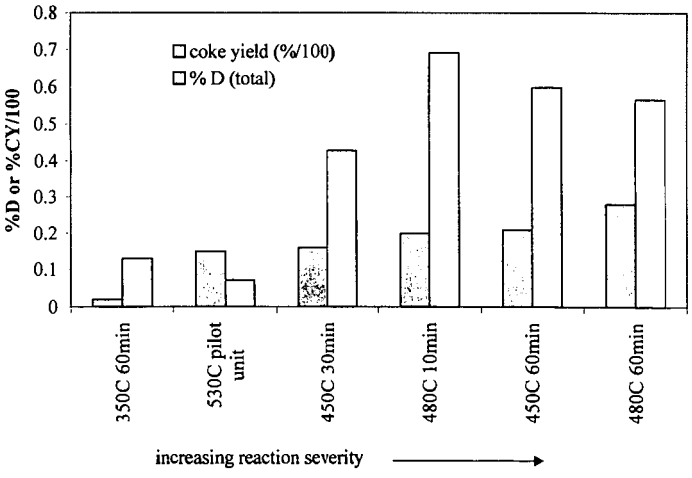

Figure 6. Comparison of %D in liquids and coke yield for bitumen coking at increasing severity

PROCESSABILITY AND THERMAL BEHAVIOUR OF ATHABASCA BITUMEN WITH VARYING ASPHALTENES CONCENTRATION

Thomas Gentzis and Parviz Rahimi. National Centre for Upgrading Technology (NCUT), 1 Oil Patch Drive, Suite A202, Devon, Alberta, Canada T9G 1A8

ABSTRACT

The coking propensity and thermal hydrocracking of extra heavy Athabasca bitumen vacuum bottoms fractions obtained by a short path distillation were investigated using hot-stage microscopy and microautoclave. The microscopy results indicated that the initial boiling point of the feedstocks (ranging from +525°C to +675°C) and asphaltene content (varying from 32 to 56wt%) did not significantly affect the mesophase induction period. However, the coke yield obtained at different severities using a microautoclave correlated with the asphaltene content and the molecular weight of the feedstocks.

INTRODUCTION

The production of synthetic crude oil from Athabasca bitumen in Alberta is increasing from the current 450 K bbl/day to approximately 1.2 MM bbl/day by the year 2005. The main upgrading technologies presently used to convert the vast reserves of oil sands bitumen to SCO are delayed coking at Suncor Energy Inc. and fluid coking at Syncrude Canada Ltd. Both plants process atmospheric bottoms. Recently, Suncor Energy Inc. has installed a vacuum tower and Syncrude Canada Ltd. will soon install a vacuum tower to process vacuum bottoms.

Upgrading by a coking process results in the production of volatile liquids, gases and coke. Heavier and larger molecules present in the vacuum bottoms would have a greater tendency to form macroscopic particles of solid coke by free radical polymerization reactions in the absence of hydrogen and catalyst. Even in a hydrogen addition process semisolid sediment, sometimes referred to as "incompletely polymerized coke," is formed.[1] According to Wiehe[2] heptane insoluble asphaltenes are the main culprit in coke formation. These asphaltenes, under coking temperatures, are first converted to pseudocomponents called "asphaltenes cores" the concentration of which may exceed the solubility limit in the reaction medium. Once these asphaltene cores are produced, phase separation takes place which leads to irreversible polymerization forming solid coke.

Changing the cut point of the feedstocks from atmospheric to vacuum bottoms will affect their chemical composition which in turn will alter the chemistry of the process. It is well known that the ratio of resins to asphaltenes is an important factor in keeping asphaltenes in solution and thus preventing phase separation.[3]

The present work addresses how the changes in the feedstocks as a result of removing lighter boiling point materials by distillation would affect the upgrading of Athabasca bitumen during thermal processing.

EXPERIMENTAL

Athabasca bitumen atmospheric bottoms (+343°C) was distillated using the automated ASTM D1160 procedure to produce vacuum residue (+525°C) to be used as feed to a short path distillation unit (Leybold-Heraeus model KDL4-P). The system pressure and the temperature of the evaporator were adjusted to produce the desired distillate cuts. The yields and some properties of the residue fractions (+525°C, +575°C, +625°C, and +675°C) are shown in Table 1. Thermal hydrocracking experiments were performed in duplicate in a semi-batch 18-mL microautoclave for 30 min with 13.9 MPa hydrogen pressure and 3.0 L/min (STP) hydrogen flow rate. The reaction temperature and residence time were kept constant at 440°C and 32 min respectively. The product distribution is shown in Fig. 1. In this work, coke is defined as methylene chloride insolublcs, asphaltenes as pentane insolubles, and maltenes as pentane soluble fractions.

The coking propensities of these fractions were determined using hot-stage microscopy. The detailed experimental proccdures can be found elsewhere.[4] Briefly, the experiments were conducted at a pressure of 750 psi at 440°C in the presence of nitrogen and hydrogen gases in order to determine the differences in mesophase induction period, mesophase size and growth rate as a function of gas used. The heating rate used was 11°C/min and the flow rate of the gas was kept at 35 mL/min. Photomicrographs were taken at regular intervals to illustrate the mesophase growth rate and optical texture. The long axis of each photo is 300μm.

RESULTS AND DISCUSSIONS

The bitumcn upgrading chemistry is significantly influenced by the composition of the feedstocks. The understanding of the chemical transformation is difficult because of the complex nature of the resid. One way to simplify this complexity is by fractionating the resid into narrow distillate cuts and solubility classes. Some of the properties of the distillation residues from Athabasca bitumen are shown in Table 1. The data in this table show that as the distillate cuts increased, the molecular weight, MCR, asphaltenes, sulphur, nitrogen and the metals also increased. On other hand, there is only a small change in the aromaticity of the fractions as a function of boiling point.

The product distribution from the autoclave experiments is shown in Fig. 1. In this figure the coke yield is based on the weight percent of the feed processed. In general the coke, asphaltenes, and gas yield increased with increasing boiling point of the feedstocks. Since the asphaltenes are the major component of the residues, their conversion was

plotted as a function of boiling point. The asphaltenes conversion {defined as [wt% asphaltenes (in)-wt% asphaltenes (out)] /wt% asphaltenes (in)} is shown in Fig. 2. This figure shows that asphaltenes conversion increases as boiling point increases. Obviously, some of the asphaltenes is converted to coke (Fig. 3) but some liquid products can also be obtained from asphaltenes decomposition. Production of liquid from asphaltenes is in agreement with the findings of Speight,[5] which showed that the thermal decomposition of asphaltenes from Athabasca bitumen produced not only 40wt% coke but also produced a high yield of volatile products.

The coking propensity of the residues was also studied using hot-stage microscopy.[6] The induction period, which is the period of time before the coke precursors (mesophase) are observed, is known to depend on the composition of the feedstock and most importantly on the concentration of asphaltenes.[2] As shown in Table 1, the C_5 asphaltenes content of the residues increased from approximately 32wt% to 56wt% (although not shown there is a corresponding decrease in the maltenes fraction). Mesophase induction period as a function of boiling point is shown in Fig. 4. The results indicate that within the experimental error, the induction period for the boiling point fractions remained relatively constant under either hydrogen or nitrogen atmospheres. Although the asphaltenes content of the fractions increased, no shortening of the mesophase induction period was observed. The maltenes, although present at a relatively low concentration in the highest boiling point fraction, still have the ability to peptize asphaltenes thus keeping them in the solution and prolonging the induction period.

Another important observation worth noting is the size and the optical texture of mesophase. Under hydrogen atmosphere, large mesophase were formed in all fractions. The ultimate result was the development of bulk mesophase having large domains and vacuoles (Fig. 5). Under nitrogen atmosphere, the size of mesophase remained small and the optical texture was fine-grained.[7]

REFERENCES

1- Storm, D.A., Barresi, R.J., Sheu, E.Y., Bhattacharya, A.K. and DeRosa, T.F. "Microphase behavior of asphaltic micelles during catalytic and thermal upgrading", Energy & Fuels, 1998, 12, 120-128.

2- Wiehe, I. A. "A phase separation kinetic model for coke formation", Industrial Engineering Chemical Research, 1993, 32, 2447-2454.

3- Clarke, P.F. and Pruden, B.B. "Asphaltene precipitation from Cold Lake and Athabasca bitumens", Petroleum Science and Technology, 1998, 16, 287-305.

4- Rahimi, P., Gentzis, T., Dawson, W.H., Fairbridge, C., Khulbe, C., Chung, K., Nowlan, V. and DelBianco, A. "Investigation of coking propensity of narrow cut fractions from Athabasca bitumen using hot-stage microscopy", Energy & Fuels, 1998, 12, 1020-1030.

5- Speight, J.G., "Thermal cracking of Athabasca bitumen, Athabasca asphaltenes, and Athabasca deasphalted heavy oil", Fuel, 1970, 49, 134-145

6- Rahimi, P., Gentzis, T., Khulbe, C., Fairbridge, C., Nowlan, V. and Cotté, E. "Effect of boiling point on the mesophase induction period during thermal treatment of Athabasca bitumen", 2nd International Conference on Refinery Processes, AIChE 1999 Spring National Meeting, Houston, TX, March 14-18, 515-519.

7- Rahimi, P., Gentzis, T. and Fairbridge, C. "Interaction of clay additives with mesophase formed during thermal treatment of solid-free Athabasca bitumen fraction", Energy & Fuels, 1999, in press.

Table 1. Properties of Athabasca bitumen distillate residues

	ASTM (D1160)	Distact Distillation*		
Cut point	+525 °C	+575 °C	+625 °C	+675 °C
Yield, wt%	50.8	75.6	67.6	62.2
Mw, Dalton (VPO)	862	1890	2010	2565
MCR, wt%	26.7	31.8	34.0	36.0
Asphaltene, C_5, wt%	32.7	41.5	48.7	56.2
Aromaticity, fa	0.41	0.38	0.40	0.40
Sulphur, wt%	6.53	6.83	6.91	7.20
Fe, ppm	994	989	1088	1217
V, ppm	364	462	471	509
Ni, ppm	148	183	186	209

* The yield of distillate residues are based on +525°C feed

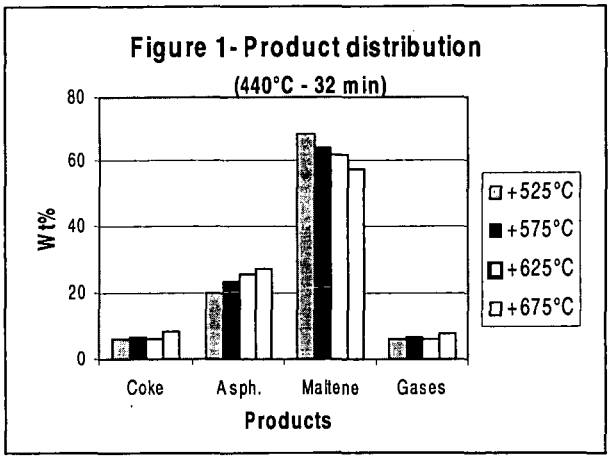
Figure 1- Product distribution
(440°C - 32 min)
80
60
40
20
0
Wt%
Coke
Asph.
Maltene
Gases
Products
+525°C
+575°C
+625°C
+675°C

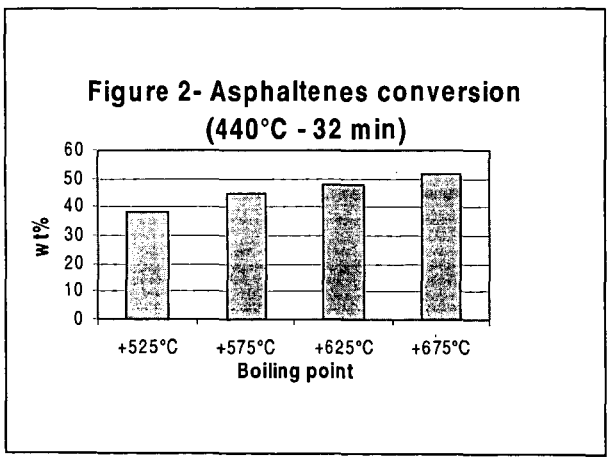
Figure 2- Asphaltenes conversion
(440°C - 32 min)
60
50
40
30
20
10
0
wt%
+525°C
+575°C
+625°C
+675°C
Boiling point

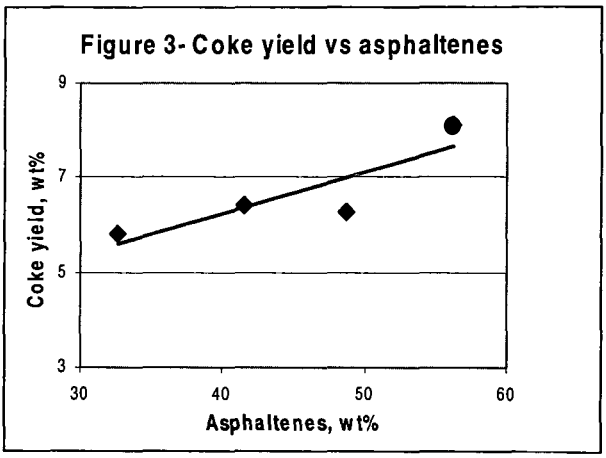
Figure 3- Coke yield vs asphaltenes
Coke yield, wt%
9
7
5
3
30
40
50
60
Asphaltenes, wt%

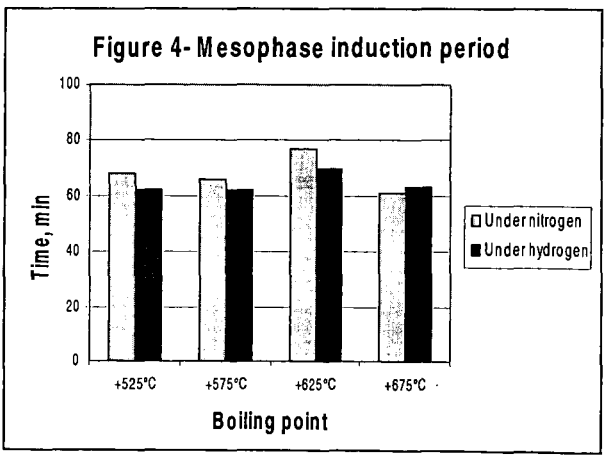
Figure 4- Mesophase induction period
Time, min
100
80
60
40
20
0
+525°C
+575°C
+625°C
+675°C
Boiling point
Under nitrogen
Under hydrogen

Figure 5 - Mesophase formation under hydrogen

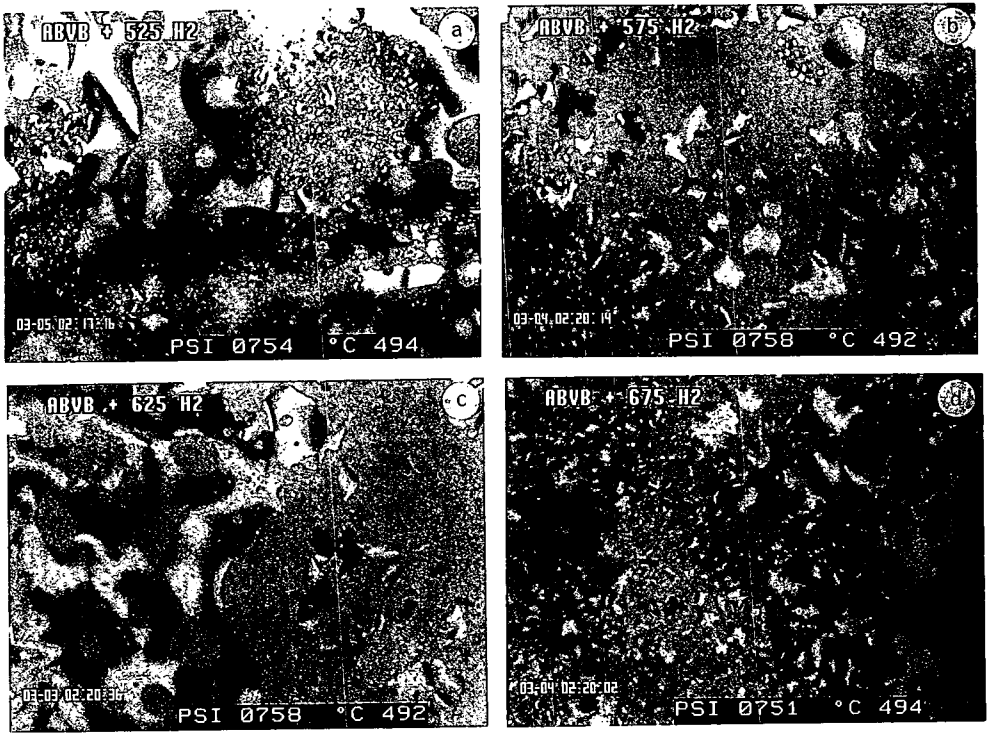

THE INFLUENCE OF CARBONACEOUS ADDITIVES ON MESOPHASE FORMATION FROM ATHABASCA BITUMEN

Thomas Gentzis and Parviz Rahimi, National Centre for Upgrading Technology, 1 Oil Patch Drive, Suite A202, Devon, Alberta T9G 1A8 CANADA; and Ripudaman Malhotra and Al Hirschon, SRI International, 333 Ravenswood Ave, Menlo Park, CA 94025

ABSTRACT

The effect of carbonaceous additives (soot and coke) on the mesophase induction period, growth and coalescence of Athabasca bitumen vacuum bottoms fraction was investigated using hot-stage microscopy. Two types of soot materials and coke from a delayed coking operation at Fort McMurray, Alberta were used in this study. The soot #1 additive did not have a pronounced effect on the mesophase induction period and growth whereas soot #2 additive prolonged the induction period and resulted in very small mesophase (2-4μm) after 120 min. The results were rationalized in terms of the physical interaction between the soot particles and the mesophase spheres. Addition of coke resulted in the shortening of the mesophase induction period and the formation of relatively larger domains.

INTRODUCTION

During bitumen upgrading by thermal treatment for the production of synthetic crude oil, an undesirable by-product known as coke which is insoluble in most organic solvents is formed. Coke formation is believed to be the result of physical and chemical processes. In the process leading to coke formation, phase separation (Cartlidge et al. 1996) and asphaltenes flocculation (Storm and Sheu 1996) are known to occur initially. These occurrences are followed by chemical reactions such as radical polymerization and/or cyclization/dehydrogenation reactions (McMillen et al. 1994). Prior to coke formation, an intermediate phase known as mesophase is formed. The initial time of mesophase formation is referred to as *induction period* which is strongly dependent on the chemical composition of feedstocks (Rahimi et al 1998). Petroleum residua rich in asphaltenes are expected to have a very short induction period (Wiehe 1993) whereas materials containing no asphaltenes generally show a longer but variable induction period for mesophase appearance (Rahimi et al. 1998). Prolonging the induction period during bitumen upgrading has important implications for the upgraders as shown below:

1- Provides longer operation between scheduled shutdowns
2- Results in higher liquid yields (less coke)
3- Leads to a more efficient plant operation
4- Results in less GHG emissions

During thermal conversion of petroleum residua containing asphaltenes to distillable liquid products, an induction period prior to coke formation has been observed by numerous investigators. Prolonging the induction period has been attempted in a number of ways, such as the addition of a hydrogen donor (H-donor) to the feed, the addition of an aromatic gas oil, or the introduction of a donor–refined bitumen in

a pretreatment step (Speight 1999). Using hot-stage microscopy, the effect of a clay additive (kaolinite) on the mesophase induction period during the thermal treatment of Athabasca bitumen was studied at the National Centre for Upgrading Technology (Rahimi et al. 1999). The results showed that there was a small or no effect on the induction period. In the presence of kaolinite the size of mesophase was significantly smaller compared with the experiments where no additive was used. Furthermore, the work by Tanabe and Gray (1997) on the thermal hydrocracking of Athabasca bitumen vacuum bottoms at a relatively short reaction times (20-30 min) using an autoclave showed that the presence of solid additives also resulted in a 7-9wt% reduction in coke yield.

The objective of this study was to investigate the effect of solid carbonaceous additives such as soot and coke on the mesophase induction period during the thermal treatment of Athabasca bitumen vacuum bottoms.

EXPERIMENTAL

The Athabasca bitumen vacuum bottoms fraction (ABVB) used in this study was obtained by super critical extraction using pentane (Rahimi et al. 1998). Soot #1 was obtained from Material and Electrochemical Research Corporation and used as received. Soot #2 was an experimental soot received from TDA Research and was extracted with toluene to remove the soluble portion prior to use. The coke sample used in these experiments was obtained from a delayed coking operation in Alberta.

The mixtures of additives and bitumen fraction were prepared first by dissolving bitumen in methylene chloride, then adding the appropriate concentration of soot #1 at 1wt%, soot #2 at 5wt% and coke at 5wt%, and then sonicating each mixture for 60 min. The mixtures were then allowed to dry under nitrogen stream and left in a vacuum oven at 60°C for 3h.

For hot-stage microscopy tests, small quantities of each mixture (5-10 mg) were placed in aluminum cups at the centre of the heated cell. The experiments were conducted in the presence of hydrogen atmosphere, at a flow rate of 35 mL/min. The gas pressure was 750 psi and the final temperature (dwelling temperature) was 440°C and 450°C. The rate of heating was kept constant at 11°C/min from room temperature to the desired temperature. For a detailed description of the experimental procedure, the reader is referred to Rahimi et al. (1998).

RESULTS AND DISCUSSION

The descriptions of photomicrographs obtained from hot-stage microscopy experiments on ABVB without and with additives are given below and shown in Fig. 1a-d.

ABVB fraction with no additive

The mesophase induction period ranged from 61 min at 450°C to 67 min at 440°C. Mesophase spheres formed, grew, and coalesced to produce large domains (Figure 1a). As was shown previously (Rahimi et al. 1998), in the presence of hydrogen gas, mesophase grew without restrictions. The formation of

mesophase from this solids-free residue may indicate that the presence of dispersed solids is not a prerequisite for the formation of anisotropic mesophase via the nucleation process as proposed by Tillmanns et al. (1978).

Mixture of ABVB with Coke

The mixture was characterized by a very short mesophase induction period: 45 min at 450°C and 53 min at 440°C. The sample appeared to be very reactive and fluid throughout the experiment. The results showed that, in contrast to the presence of clay additives (Rahimi et al. 1999), the presence of coke did not increase the viscosity of the isotropic matrix and did not restrict the movement of mesophase spheres. Mesophase was high viscoelastic and formed large optical domains (Figure 1b). The observed fluidity requires further investigation since it may be related to the role of the chemical composition of the coke (radical scavenging via hydrogen transfer).

It was further observed that in the early stages of the experiment, some mesophase disappeared in the isotropic matrix and reappeared shortly after which may indicate sinking and floating of the particle as its density changed relative to that of the isotropic matrix.

Mixture of ABVB with Soot #1

The mixture of the ABVB fraction and soot #1 at 1wt% resulted in the following mesophase induction period: 62 min at 450°C and 70 min at 440°C. These data indicate that the presence of soot at the above concentration did not have a significant effect on prolonging or shortening the induction period prior to mesophase formation. Mesophase spheres grew almost uninhibited and coalesced to form larger domains (Figure 1c). The observed mesophase texture shown in Fig. 1c is consistent with that reported by Matsumoto et al. (1977): the concentration of soot particles was too small to cover the surface of mesophase spheres completely. As a result the mesophase grew to form larger spheres.

Mixture of ABVB with Soot #2

The addition of soot #2 to the ABVB fraction resulted in a slight prolongation of the mesophase induction period. In this case, mesophase spheres first became visible at about 67 min at 450°C and 75 min at 440°C. The addition of this soot had a significant effect on the size, growth, and coalescence of mesophase and resulted in very small mesophase even after 120 min (Figure 1d). The apparent viscosity of this mixture was higher than the viscosity of bitumen-soot #1 mixture. This observation can simply be the result of the higher concentration of soot #2 used in the current experiment. As the concentration of soot increased from 1wt% to 5wt%, the size of mesophase became smaller and the size distribution more uniform because of the limited coalescence of the spheres (compare Figure 1c with Figure 1d).

Based on the above observations, it was concluded that the use of carbonaceous materials may have beneficial effects in terms of mesophase induction period (soot #2 additive) and in terms of possible chemical reactions that may reduce radical-radical combination (coke additive).

REFERENCES

1. Cartlidge, C.R., Dukhedin-Lalla, L., Rahimi, P.M., and Shaw, J.M. 1996. Preliminary phase diagram for heavy oil and bitumen mixtures, Fuel Science and Technology International, vol. 14, 1-2, p. 163-178.
2. Matsumoto, S., Oi, S., Imamura, T., Nakamizo, N., Yamada, Y., and Honda, H. 1977. Influence of a magnetic field on the molecular arrangement of mesophase spherules, 13th Biennial Conference on Carbon, July 12-18, Irvine, CA, U.S.A., p. 201-202.
3. McMillen, D.F., Manion, J.A., Tse, D.S., and Malhotra, R. 1994. Hydrogen transfer promoted ring growth during catalytic resid hydroprocessing, Preprints, ACS Division of Petroleum Chemistry, vol. 39, no. 3, p. 422-425.
4. Rahimi, P., Gentzis, T., and Fairbridge, C. 1999. Interaction of clay additives with mesophase formed during thermal treatment of solid-free Athabasca bitumen fraction, Energy & Fuels, *In Press*.
5. Rahimi, P., Gentzis, T., Dawson, W.H., Fairbridge, C., Khulbe, C., Chung, K., Nowlan, V., and Del Bianco, A. 1998. Investigation of coking propensity of narrow cut fractions from Athabasca bitumen using hot-stage microscopy, Energy & Fuels, vol. 20, no. 10, p. 1020-1030.
6. Speight, J.G. 1999. *Properties and Upgrading of Oil Sand Bitumen*, Course Material, February 1999.
7. Storm, D.A., and Sheu, E.Y. 1996. Flocculation of asphaltenes in heavy oil at elevated temperatures, Symposium on Thermodynamic of Heavy Oils and Asphaltenes, Fuel Science Technology International, vol. 14, p. 243-260.
8. Tanabe, K. and Gray, M. R. 1997. Role of fine solids in the coking of vacuum residues, Energy & Fuels, vol. 11, p. 1040-1043.
9. Tillmanns, H., Pietzka, G., and Pauls, H. 1978. Influence of the quinoline-insoluble matter in pitch on carbonization behaviour and structure of pitch coke, Fuel, vol. 57, p. 171-173.
10. Wiehe, I.A.1993. A phase–separation kinetic model for coke formation, Industrial & Engineering Chemistry Research, vol. 32, no. 11, p. 2447-2454.

DESCRIPTION OF PHOTOMICROGRAPHS

All photos were taken in reflected light. The long axis of each photo is 300μm.

Figure 1a: Formation of anisotropic mesophase spheres from the ABVB fraction in the absence of additives.

Figure 1b: The presence of coke in the ABVB fraction resulted in the development of larger domain bulk mesophase in a highly fluid matrix.

Figure 1c: Soot #1 did not influence the formation or the size of mesophase from the ABVB fraction.

Figure 1d: The addition of Soot #2 to the ABVB fraction resulted in the formation of much smaller mesophase spheres than with either Soot #1 or coke.

Figure 1 – Mesophase formation in the absence and presence of coke and soot additive

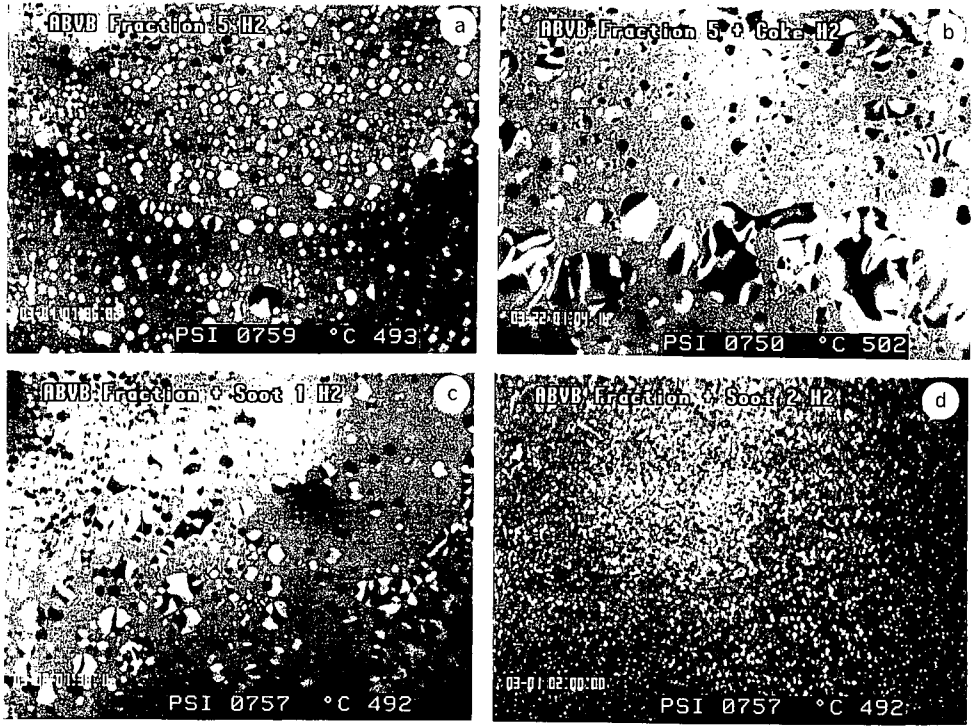

MAXIMIZING CYCLE LENGTH OF VACUUM RESIDUE HYDRODESULFURIZATION UNIT

S. Kressmann [1], V. Harlé [2], S. Kasztelan [2], I. Guibard [1], P. Tromeur [3], F. Morel [1]

IFP,
[1] Centre d'Études et de Développement Industriel "René Navarre",
B.P. 3, 69390 Vernaison, France.
[2] Division Cinétique et Catalyse, 92852 Rueil-Malmaison Cedex, France.
[3] Division Industrielle, 92852 Rueil-Malmaison Cedex, France.

ABSTRACT

Achievement of long cycle length is an important objective for the refiner operating a vacuum residue hydrodesulfurization unit. The fixed bed technology generally used for this purpose requires a specific design such as swing/permutable reactors as well as the use of sophisticated associations of catalysts to reach a long cycle length and constant low sulfur content in the products. In particular, it is shown that the stability of the refining catalyst is a key parameter to improve the run length while keeping a high level of hydrodesulfurization. An efficient HDS catalyst has been designed to respond to this demand and also recommendations to conduct the operation of the VRDS unit have been mentioned.

INTRODUCTION

Atmospheric residue (AR) and vacuum residue (VR) are the most difficult feed to be treated catalytically under hydrogen pressure because they contain all the impurities present in the crude oil and among them, asphaltens and metals (1-3).

The hydrodesulfurization of vacuum residue is nowadays carried out with well-cstablished upgrading process using usually fixed bed technology (4-6). The objectives of the refiner are mainly to desulfurize and to convert the vacuum residue in order to produce a stable low sulfur fuel oil (LSFO) according to the specifications of the market. This objective is driven by an increasing demand for LSFO, residue FCC feed and an increasing needs for clean transportation fuels (gasoline and diesel).

One main aim of the refiner is to maintain cycle length of the Vacuum Residue DeSulfurization (VRDS) unit as long as possible. This is a major challenge for fixed bed technology because, as it is well known, the asphaltens and metals are concentrated in the still bottom and therefore the deactivation of conventional hydrotreating catalysts is strongly enhanced during the treatment of vacuum residue.

Several process technologies have been introduced to improve cycle length of VRDS units such as the moving bed technology (7-8), ebullated bed technology (11) and Swing/Permutable fixed bed reactors (4-6, 9). To increase the cycle length on vacuum residue and improve the protection of downstream HDS catalyst, a concept of fixed bed VRDS process including a permutable-swing guard reactors system has been developed by IFP (HYVAHL process, Figure 1, see also reference 9) and is industrially proven. The process scheme includes permutable fixed bed guard reactors that can be switched in operation allowing the possibility to isolate temporally one reactor for change out of the guard HDM catalyst.

However, in order to maximize the HDM and HDS performances of the unit and to maintain the stability, it is now well recognized that associations of several catalysts with different functions are also mandatory (9). One typical association comprises three types of catalysts :

- a HDM catalyst for the metal removals in front of the unit,
- a HDM/HDS catalyst with balanced HDS and HDM activities,
- a very active and stable HDS catalyst in the last section.

The HDM catalyst has the objective to remove the metals contained in the feed and as a consequence to protect the downstream catalysts from metal deposits. A special porous structure designed for this purpose is the so-called "chestnut-burr" structure (10) in which the porosity has been adjusted to allow access of the heavy molecules to the active phase and to get a high porous volume to accommodate metals deposits accumulated during a minimum of one year of operation. In addition, the coke deposit due to the conversion of asphaltens and resins is minimized by using a low acidity alumina base (10) The stability of this system has been already

reported (5, 6, 10) and can maintain during a long period a good HDM activity on vacuum residue (4-5).

The aim of the second HDM/HDS catalyst is to continue with the demetallization and to begin the desulfurization step. It is in general a large mesoporous monomodal catalyst. The HDS catalyst located in the third and last section is the catalyst for deep refining which remove the sulfur content in the effluent.

In this paper we shall discuss the need for a specifically designed HDS and also the optimum way to carry out this catalyst for improving the cycle length of VRDS unit.

EXPERIMENTAL

HDS Catalyst has been tested in a pilot unit using a demetallized feedstock obtained after the demetallization section and the equilibrium HDM/HDS catalyst section. The pilot unit is a one-liter reactor working in isothermal configuration. The average temperature is calculated from the temperature measurements made in the catalyst bed.

The Arabian vacuum residue (Table 1) previously demetallized contain 3.6 wt% of sulfur and 100 wt ppm of Ni+V. Different severities have been applied to this primary feed in order to obtain three level of demetallization. The analyses of these three demetallized feeds are shown in Table 1 (references : charges 1, 2 and 3). The metals content are ranging from 9.3 to 16.5 wppm and the sulfur content varies from 0.98 to 1.8 wt % depending of the severity of the HDM and equilibrium HDM/HDS section.

The demetallized feeds (charges 2 and 3) with high sulfur and metals content was used to age quickly the HDS catalyst. Dimethyl disulfide was added to the demetallized feeds to generate H_2S in order to be representative of the gas phase composition at the outlet of the previous reactors.

The sulfur compounds of the demetallized feeds are mainly present in asphaltens and aromatics and are therefore very difficult to be desulfurized. Thus, the residence time of the HDS section is around twice more important than in HDM and HDM/HDS section (Figure 2). This residence time of the HDS section must be optimized depending of the HDS done in the two first sections. Thus, for HDS section, we have carried out some variations of LHSV for kinetic studies. The catalyst deactivation for HDS has been evaluated by a correction of LHSV using a kinetic order of reaction. Moreover, for each change of demetallized feeds, we have checked the catalyst activity by using the same Arabian light straight run atmospheric residue feed. The temperature was adjusted in order to maintain on A.L. A.R. a minimum of 90 % of HDS. This proccdure was done all along the test and also has the aim to evaluate the reactivity of each demetallized vacuum residue.

RESULTS AND DISCUSSION

HDS catalysts are often based on high specific surface area carriers with monomodal pore size distribution. It has been found that monomodal catalysts have different selectivities for the HDM and HDS functions depending on the size of the mesopores (HDM=60 %, HDS=90 % on A.L. A.R. for HDS catalyst). An increase of the mean average mesopore diameter leads to a decrease of the HDS and an increase of the HDM performance (HDM=77, HDS=85 %, on A.L. A.R.). This change HDS vs. HDM activity results from the variation of BET surface area and also the change in the level of diffusional limitations. In addition, as the mean average mesopores increases, the penetration of resins, which contain metals, is more important leading to an increase of HDM and therefore a higher rate of deactivation of HDS function. A compromise in term of mean mesopore diameter has to be found between high activity and high diffusional limitations. This has be done to develop a specific HDS catalyst. Performances on demetallized vacuum residue that can be reached with this catalyst are developed in the following.

In Figure 3, the sulfur content of the product from the HDS reactor is plotted versus hours on stream (HOS). The reactor temperature increase is also plotted in Figure 3 showing the deactivation of the HDS catalyst. We have tried during the run to maintain the severity of the HDS section to reach a sulfur content at the reactor outlet around 0.4 to 0.5 wt %. For the first 2000 hours and also during 75% (in hours) of the test, the LHSV is the same than the base. By consequent, 25 % of the points had to be corrected for the LHSV variation.

In Figure 3, we have indicated when we have switched on A.L. A.R. in order to check the catalyst activity for the temperature adjustment if necessary. The total HOS using demetallized feeds from vacuum residue can be evaluated to around 5600 hr, so 75 % of the overall H.O.S.

The overall deactivation of the HDS catalyst on demetallized feed can be estimated if we compare the activity on the same charge (charge 1) from the end of run to the start of run. We begin at 360°C and finish at 390°C for 5600 hours of run on demetallized vacuum residue. The behavior of this HDS catalyst is in line with the expected cycle length of an industrial unit. The end of run temperature of an industrial unit is usually around 415°C. So, the HDS catalyst could reach at least one year of cycle length on pure A.L. V.R.
The use of charges 2 and 3 (metals content around 16 wppm) shows that the slope of deactivation for HDS catalyst doesn't increase even during 4000 HOS on these charges. The HDS catalyst achieves this task because of its monomodal structure protecting the catalyst sites for HDS. This system demonstrates its flexibility in case of problem in HDM section.

Figure 4 shows the calculated temperature to obtain a constant sulfur content (0.45 wt %) of the reactor outlet effluent from HDS section. This temperature was calculated by assuming a constant activation energy along the test.

After 2000 hours, the HDS catalyst is more stabilized and the deactivation becomes lower. An interpretation could be that the A.L. A.R. washes the catalyst by removing one part of the coke. In Figure 4, we have observed that we recovered the slope of HDS deactivation on demetallized vacuum residue after only 200 hour. This effect has been observed at 3000 HOS and 4000 HOS. Thus, we expect to extent the cycle length of the HDS catalyst by suggesting to work in block operation (switch between A.R. and V.R.). We also observed that the slope of desactivation for HDS is lower after this washing period than during S.O.R. This observation confirms also that overall deactivation of HDS catalyst must be calculated only on demetallized vacuum feeds (75 % HOS of the run).

CONCLUSION

The upgrading of vacuum residue to obtain a constant fuel oil quality can be improved by using a complex association of catalysts with particle size, pore size distribution and activity grading. The improvements come from a better optimization of each catalyst and the association of different selectivity in term of HDM/HDS. The synergy effect has been demonstrated and two commercial units are running under this concept. The use of adapted design HDM catalysts and monomodal catalysts for HDS objective insure the stability of the system. Monomodal catalysts for HDS section permit to achieve the goal of a constant sulfur in fuel oil with a run length cycle of at least one-year on Arabian vacuum residue feedstock. The possibility for the refiner to work by block operation (switch between A.R. and V.R.). has certainly a good impact for increase the cycle length.

REFERENCES

1. T. Ohtsuka, Catal. Rev. Sci. Eng., 16, 291, (1977).
2. W.I. Beaton; R.J. Bertolacini, Catal. Rev. Sci. Eng., 33, 281, (1991).
3. H. Koyama, E. Nagai, H. Torii, H. Kumagai, Stud. Surf. Sci. Catal., 100, 147, (1996).
4. F. Morel, S. Kressmann, V. Harlé, S. Kasztelan, Stud Surf. Sci. Catal., 106, 1, (1997).
5. A. Billon, J.P. Peries, M. Espeillac, T. des Courrieres, NPRA 89th Annual Meeting, San Antonio, March 17-19, 1991.
6. A. Billon, G. Henrich, A. Hennico, Pétrole et Techniques, n°388, mai-juin 1994.
7. B.E. Reynolds, J.L. Rogers, R.A. Broussard, NPRA Annual Meeting, San Antonio, March 16-18, 1997.
8. B. Scheffer, K.W. Robschlager, F.C. de Boks, Preprints of ACS San Francisco CA, April 13-17, 1997, 347-350
9. S. Kressmann, F. Morel, V. Harlé, S. Kasztelan, Catalysis Today, 43, 1998, 203-215
10. H. Toulhoat, R. Szymansky, J.C. Plumail, Catal. Today, 7, 1990, 531.
11. S. Kressmann, J. Colyar, E. Peer, A. Billon, F. Morel, 7th Unitar Conference, Beijing, China, October 27-30, 1998, 857-866

Table 1

FEEDS :	S.R. Arabian A.R.	SR Arabian V.R.	Charge 1	Charge 2	Charge 3
Specific gravity	0.959	1.017	0.967	0.980	0.982
Sulfur (wt %)	3.34	3.68	0.98	1.23	1.80
Nitrogen (wppm)	2075	3610	3305	3200	3000.0
Hydrogen (wt %)	11.20	10.48	11.32	11.36	11.23
Nickel (wppm)	9.3	20.0	5.5	7.8	7.7
Vanadium (wppm)	35.0	80.0	3.8	8.7	8.1
Total of metals (wppm)	44.3	100.0	9.3	16.5	15.8
Viscosity @ 100°C	25.6	1028	90.6	182	138
Conradson carbon (wt %)	9.5	19.8	11.3	13.2	13.0
Asphaltens C5 (wt %)	5.6	12.9	4.3	5.4	5.6
Asphaltens C7 (wt %)	3.1	6.2	1.6	1.5	1.8
Saturates (wt %)	30.7	10.2	22.4	18.1	18.2
Aromatics (wt %)	47.5	45.8	47.8	51.2	50.4
Resins (wt %)	17.6	34.6	22.9	26.0	25.4
ASTM D2887					
IBP (°C)	300	385	182	223	234
T(°C) for 5 wt %	325	533	330	433	403
T(°C) for 10 wt %	358	554	426	498	468
T(°C) for 20 wt %	404	580	514	546	518
T(°C) for 30 wt %	436		553	572	547
T(°C) for 40 wt %	468		577	594	572
T(°C) for 50 wt %	503		602		596
EBP (°C)	720	600	620	613	614
wt % EBP	92	25	58	49	57

Figure 1

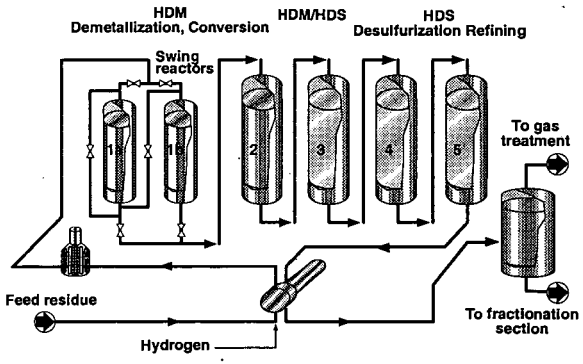

Figure 2

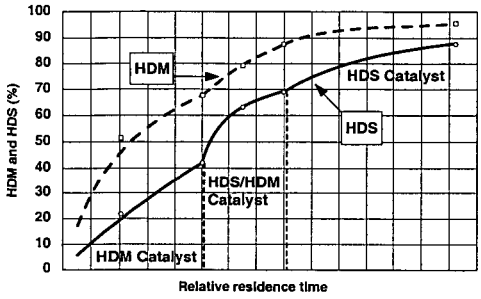

Figure 3

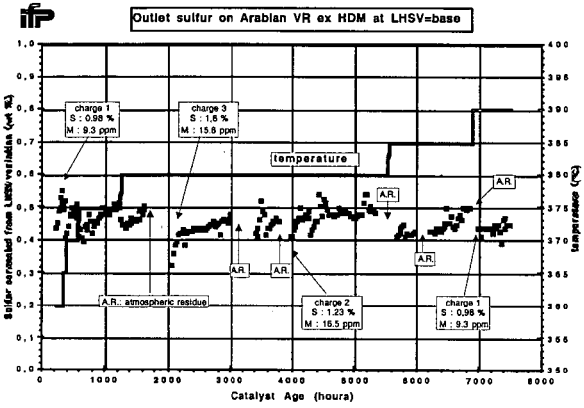

Figure 4

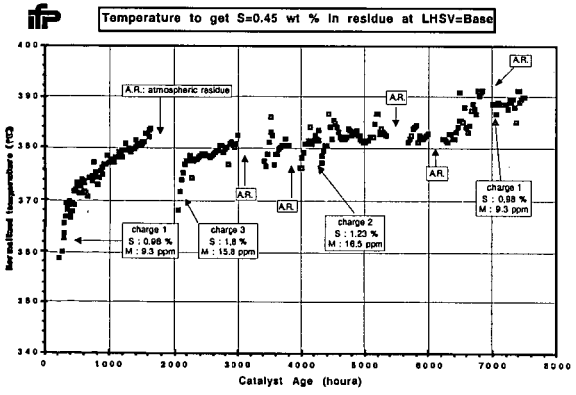

PILOT PLANT STUDY OF THE PERFORMANCE OF AN INDUSTRIAL MoO_3/Al_2O_3 CATALYST IN HYDROTREATMENT OF KUWAIT ATMOSPHERIC RESIDUE

A. Stanislaus[1], S.Fukase[2], R. Koide[2], A. Al-Barood[1], A. Marafi[1], F. Al-Jasem[1], and M. Absi-Halabi[1].

(1) Petroleum Technology Department, Kuwait Institute for Scientific Research, P.O.Box 24885, Safat, 13109, Kuwait

(2) Kuwait Branch Laboratory, Petroleum Energy Center Japan, C/O Kuwait Institute for Scientific Research, P.O.Box 24885, Safat, 13109, Kuwait

INTRODUCTION

Graded catalyst systems with two or more types of catalysts are used in recent years in multiple reactor fixed-bed residue hydrotreators to achieve demetallation (HDM), desulfurization (HDS) and denitrogenation (HDN) together with conversion of residues to distillates at desired levels(1,2). Rapid catalyst deactivation is reduced and the on-stream efficiency is increased with such multiple catalyst systems. Since the overall performance of the process with regard to various conversions and catalyst life is strongly tied up with the performance of the catalysts in different reactors, information on the activity, selectivity and deactivation rate of individual catalysts is highly desirable for optimizing reactor loading with such multiple catalyst systems. In the present work, we have examined the performance of an industrial HDM catalyst containing MoO_3 alone on alumina in hydrotreating Kuwait atmospherie residue in a fixed-bed pilot plant. Systematic studies were conducted to assess the activity and selectivity of the catalyst for various reactions such as HDM, HDS, HDN, asphaltenes conversion and hydroconversion of the residual oil feed to distillates. The reaction kinetics in residual oil hydrotreating was also investigated as part of the study.

EXPERIMENTAL

The hydrotreating experiments were conducted in a fixed-bed reactor unit (manufactured by Vinci Technologies) using Kuwait atmospheric residue as feed. The feedstock contained 4.3 wt% sulfur, 69 wtppm vanadium, 22 wtppm nickel, 0.31 wt% nitrogen, 3.6 wt% asphaltenes and 12.2 wt% CCR. A commercial HDM catalyst containing 4.3 wt% MoO_3 on alumina (surface area = 200 m^2/g; pore volume = 0.67 ml/g) was used in all experiments. 50 ml catalyst charge diluted with an equal amount of carborundum was used for each run. The catalyst was presulfided using straight run gas oil containing 3 wt% dimethyl disulfide (DMDS) by a standard procedure before injecting the feed. The run conditions used for different studies are summarized in Table 1. During the course of each run, product samples were collected every 12 hours and analyzed for sulfur, metals (V and Ni), nitrogen, asphaltenes, CCR, viscosity, density and distillates yield.

Table 1. Run Conditions for Temperature and LHSV Effect Studies

	Range	
Process Parameter	**Temperature Effect Study**	**LHSV Effect Study**
Temperature (°C)	360 – 420	380
Pressure (bar)	120	120
LHSV (h^{-1})	1	0.5 – 4.0
H_2/Oil Ratio (ml/ml)	570	570
Time-on-stream(h)	120	120

RESULTS AND DISCUSSION

In the first set of experiments reactor temperatures were varied in the range 380 – 420 °C to investigate the performance of the HDM catalyst in promoting various reactions such as HDM, HDS, HDN, asphaltenes conversion, CCR reduction and hydrocracking of residues to distillates as well as to examine the deactivation behavior of the catalyst at different temperatures.

In Fig. 1 the desulfurization data for different temperatures are plotted as a function of time-on-stream. It is seen that the extent of desulfurization is very low (around 20%) at 360 °C and increases substantially with increasing temperature reaching about 65% at 420 °C. An interesting observation that can be made in the results presented in Fig. 1 is a gradual increase in the degree of HDS with increasing time-on-stream. The HDS activity is usually expected to decrease with time during the early period of operation due to rapid initial deactivation of the catalyst. But in the present study the HDS activity shows an increase with increasing run time, probably because of the accelerating effect of nickel deposited on the catalyst surface.

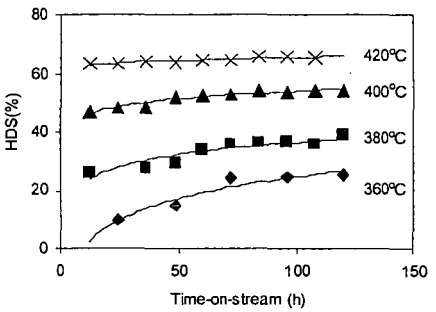

Fig. 1 Sulfur removal vs time-on-stream at different reactor temperatures

The data presented in Fig. 2, which compares the catalysts activity for various reactions such as HDS, HDV, HDNi, HDN and asphaltenes conversion that occur during residual oil hydrotreating shows the following order:

$$HDV > HDNi \approx HDAsph > HDS > HDN$$

The low activity catalyst containing unsupported MoS_2 on alumina with large pores used in the present study appears to favor HDM and asphaltenes cracking reactions which are more diffusion limited than other reactions. The higher activity of the catalyst for HDM and asphaltenes conversion reactions can, thus, be attributed to the large pores in the catalyst which facilitates the diffusion of large metal containing molecules and asphaltenes into the catalyst pellet. The enhanced reactivity of vanadium relative to nickel may be attributed to a combination of factors resulting from the chemistry of oxygen ligand in vanadyl (VO^{2+}) group(3).

In the second set of experiments, the liquid hourly space velocity (LHSV) of the feed was varied in order to investigate the kinetics of various reactions in residual oil hydrotreating. The kinetics of petroleum residue hydrotreating is highly complicated due to the complex composition of the residues which includes high concentrations of asphaltenes, sulfur, nitrogen and metals (V and Ni). The low diffusivities and reactivities for these large molecular species make the kinetics of the process further complicated.

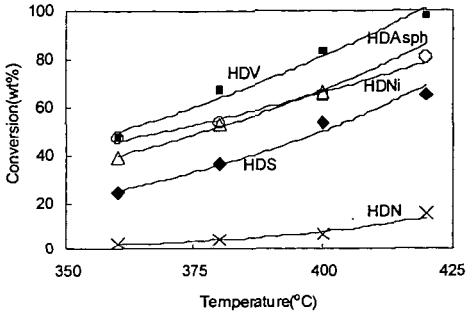

Fig. 2 Comparison of catalyst's activity for various reactions in hydrotreating of Kuwait atmospheric residue

In the present studies, the conversion data generated for various reactions at different space velocities were used to determine the reaction order for different reactions such as HDS, HDV, HDNi and asphaltenes cracking that occur during residual oil hydrotreating. The results presented in Fig. 3 show that HDS and asphaltenes cracking reactions obey second order kinetics. The activation energies calculated from the Arrhenius plots in Fig. 4 are 26.1 kcal/mole for HDS and 23.6 kcal/mole for asphaltenes eracking reactions.

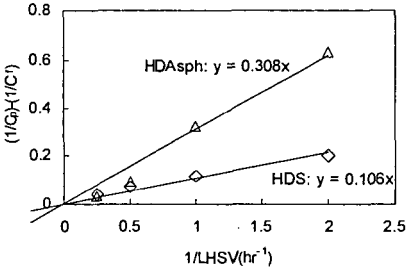

Fig. 3 Second-order plot of kinetic data for HDS and HDAsph of Kuwait atmospheric residue

The plots of kinetic data for vanadium and nickel removal shown in Figs. 5 indicate that a reaction order of 1.5 gives the best fit in correlating kinetic data for HDM reactions. Demetallation kinetic orders varying from 1.0 to 2.0 have been reported by different workers(3). In the case of model compound demetallation studies with pure metalloporphyrins, first order kinetics have been reported for both vanadium and nickel removal. In the present work a reaction order of 1.5 is observed for vanadium removal from Kuwait atmospheric residue. Just as in hydrodesulfurization, several first order reactions with different rates can occur due to the presence of more than one class of metal compounds in the residual oil. This can lead to an apparent order greater than unity.

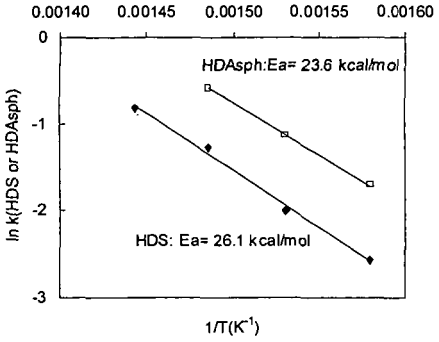

Fig. 4 Arrhenius plot for HDS and HDAsph

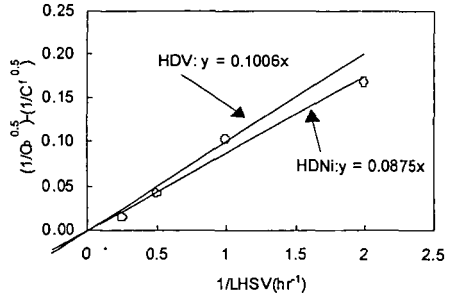

Fig. 5 1.5-order plot of kinetic data HDV and HDNi of Kuwait atmospheric residue

The Arrhenius plots of lnk vs 1/T for both vanadium and nickel removal reactions (Fig. 6) show a sharp increase in the reaction rate at temperatures above 400 °C with two different activation energy values, namely 27.7 and 62.2 kcal/mole for vanadium and 12.5 and 28.9 kcal/mole for nickel.

Apparent activation energy values reported in literature for vanadium removal from residues by HDM reaction range from 10 to 38 kcal/mole depending on the reaction order(3). The discrepancies observed in the activation energy values may reflect differences in crude source resulting in different reactivities of metal containing species and different rate limiting steps. The sharp increase in activation energy for HDM reactions at temperatures above 400 °C is considered to be due to a combination of factors such as improved diffusion and change in reaction mechanism.

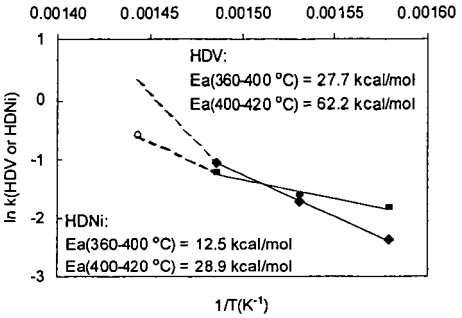

Fig. 6 Arrhenius plots for HDV and HDNi

CONCLUSIONS

Pilot plant studies were conducted to investigate the activity and selectivity of an industrial HDM catalyst for various reactions such as HDS, HDM, HDN, asphaltenes conversion and hydroconversion of residual oil feed to distillates as well as to examine the reaction kinetics in residual oil hydrotreating. The catalyst showed a remarkably high activity for HDM and asphaltenes cracking reactions and a moderate activity for HDS. Its activity for HDN, hydrogenation and hydroconversion reactions was very low. HDS activity increased with time on stream probably because of the promotional effect of nickel deposited on the catalyst surface. Kinetic data analysis showed 2nd order for HDS and asphaltenes cracking and 1.5 order for HDV and HDNi reactions. The apparent activation energies for HDS and asphaltenes cracking reactions were, respectively 26.1 and 23.6 k cal/mole. Arrhenius plots for HDV and HDNi reactions showed a sharp increase of the reaction rate constants at temperatures above 400 °C with two different activation energy values, namely, 27.7 and 62.2 kcal/mole for nickel. The increase in the activation energy of the HDM reactions above 400 °C is considered to be due to a combination of factors such as improved diffusion and change in reaction mechanism.

ACKNOWLEDGEMENT

This work is a joint research project between Petroleum Energy Center (funded by the Ministry of International Trade and Industry), Japan, and Kuwait Institute for Scientific Research, Kuwait. It bears the KISR Project No. PF010C.

REFERENCES

(1) Bartholdy, J. and Cooper, B. H., Stud. Surf. Sci. Catal., 100, p.117(1996)
(2) Yamamoto, U., Mizutami, Y., Shibata, Y., Kitou, Y., Yamazaki, H., Stud. Surf. Sci. Catal., 100, p.181(1996)
(3) Quan, R. J., Ware, R. A., Hung, C. W., Wei, J., Adv. Chem. Eng., 14, p.95(1988)

CHARACTERISATION OF COKE ON DEACTIVATED HYDRODESULFURISATION CATALYSTS AND A NOVEL APPROACH TO CATALYST REGENERATION

Colin E. Snape, Youva R. Tyagi, Miguel Castro Diaz, Peter J. Hall, Ian P. Murray and Shona C. Martin.

University of Strathclyde, Department of Pure and Applied Chemistry,
Thomas Graham Building, 295 Cathedral Street,
Glasgow G1 1XL, Scotland, UK

Keywords: Hydrodesulfurisation catalysts, coke, hydropyrolysis

ABSTRACT

The soft (chloroform-extractable) and hard coke fractions from a suite of deactivated Co/Mo hydrodesulfurisation (HDS) catalysts with carbon contents ranging from 5 to 18% have been characterised. The hard coke accounted for between 50 and 70% of the total carbon, but was responsible for much less of a reduction in BET surface area as the carbon content increased. Indeed, significant variations in structure were revealed by solid state ^{13}C NMR with the aromaticity ranging from 0.6 to over 0.9 with increasing carbon content and time on stream. The relatively high aliphatic contents and atomic H/C ratios for the hard cokes obtained at low levels of carbon deposition (5-7%) suggested that much of the carbon should be removed under reductive conditions. Indeed, hydropyrolysis, in which the deactivated catalysts were heated from ambient to 500°C under a hydrogen pressure of 15 MPa, removed over 90% of the carbon and recovered 70% of the BET surface that had been lost.

INTRODUCTION

Deactivation via coke deposition affects all the catalysts used in hydrocarbon conversion processes with the timescale varying from just a few seconds for fluid catalytic cracking (FCC) of heavy petroleum feeds to several months for naphtha reforming and gas oil hydrotreating. For the latter, controlled oxidation is the established means of regeneration to remove coke (see, for example, refs. 1-3 for hydroprocessing catalysts). However, despite the use of slow heating rates and low oxygen environments, some loss of surface area is inevitably encountered for Ni/Mo and Co/Mo γ-alumina-supported hydroprocessing catalysts and other deleterious effects have been observed, including the loss of Ni promoter due to spinel $NiAlO_4$ formation [4].

Thus far, non-oxidative treatments in the form of reductive heating [4] and solvent extraction [4-6] have received very little attention because they only remove the adsorbed oil that comprises the soft or soluble portion of the coke. For example, Teixeira daSilva *et al.* [4] using a nitrogen/hydrogen mixture for reductive heating after acetone extraction reduced the carbon content of a spent catalyst from hydroprocessing shale oil by approximately 35%. Traditionally, the insoluble or hard coke is considered to be highly intractable aromatic in character even for hydrotreating catalysts operating at relatively low temperatures. To investigate whether or not this is the case, the soft (chloroform-extractable) and hard coke fractions have been characterised for a suite of deactivated Co/Mo HDS catalysts with carbon contents ranging from 5 to 18%. The fact that solid state ^{13}C NMR indicated that the hard coke is normally quite aliphatic and contains small aromatic clusters prompted us to use fixed-bed hydropyrolysis for the reductive regeneration of the catalysts where they were heated from ambient to 500°C under a hydrogen pressure of 15 MPa. This technique typically gives rise to conversions of over 90% for sedimentary organic matter, including low-rank coals and petroleum source rocks (type I and II kerogens) [7]. It has been adapted as an analytical procedure for determining the distribution of organic sulfur forms from H_2S evolution profiles [7,8] and for covalently-bound biomarkers [7,9,10]. Since the temperatures used in hydropyrolysis are potentially lower than in oxidative combustion regeneration, there is the potential that the irreversible loss of surface area can be reduced which offers the possibility of extending catalyst lifetimes and helping to solve the ever-growing disposal problem for spent catalysts.

EXPERIMENTAL

Ten deactivated Co/Mo HDS catalysts, differing in terms of the run time and catalyst bed position, were supplied by BP/Amoco. The carbon contents of the catalysts investigated are listed in Table 1. Samples 1-7 are at different bed heights in the same operation. The final sample (no. 10) with a carbon content of 18% was obtained from a unit that had been left running for 8 years. All the catalysts were extracted in chloroform under reflux to recover the soft coke for

characterisation (designated soft coke 1). To isolate the hard coke, one of the low (no. 8) and the high carbon (no.10) chloroform-extracted catalysts were demineralised using HF/HCl as used previously on FCC catalysts [11,12]. A final wash with dilute nitric acid (2M at 70°C) was required to dissolve the metal sulphides. The hard coke concentrates (carbon contents > 50%) were then extracted in chloroform with the extracts being designated soft coke II.

Carbon, hydrogen and nitrogen contents of the initial deactivated catalysts, the soft coke fractions and the hard coke concentrates were determined using a Perkin-Elmer 2400 analyser and sulphur contents were measured using the Sulphazo III method. BET measurements were carried out using a Micromeritics ASAP 2000 apparatus on the deactivated catalysts before and after chloroform extraction and on two of the hard coke concentrates. A Bruker 250 MHz instrument was used to obtain the ^{1}H NMR spectra of the soft cokes in chloroform-d. HPLC analysis was carried out using Shandon Scientific Hypersil CTA column in conjunction with a Waters 486 UV detector. The soft cokes were separated into aliphatic, aromatic and polar fractions by open column adsorption chromatography using activated silica gel. Size exclusion chromatography (SEC) was carried out to estimate the number and weight average molecular masses (M_n and M_w) of the soft cokes based on polystyrene standards, a mixed bed PL gel column being employed with RI detection and chloroform as the eluting solvent.

The solid state ^{13}C NMR measurements on the hard coke concentrates were carried out at 25 MHz on a Bruker MSL 100 spectrometer with MAS at 4.5-5.0 kHz to give spectra in which the sideband intensities are only *ca.* 6-7% of the central aromatic bands. A contact time of 1 ms was used for the cross polarisation (CP) measurements and the ^{1}H decoupling and spin-lock field was *ca.* 60 kHz. The FIDs were processed using a Lorentzian line broadening factor of 50 Hz. To determine the fraction of protonated and non-protonated carbon, four delay periods between 1 and 100 μs were employed in dipolar dephasing experiments.

Fixed-bed hydropyrolysis tests at 15 MPa were conducted using either *ca.* 0.5 or 1 g of sample for the low and high carbon deactivated catalysts selected for detailed investigation. For some tests, the deactivated catalysts (extrudates) were ground and diluted in sand. The procedure used has been described elsewhere [7,9,10], a slow heating rate of 5°C min^{-1} being used to maximise conversion.

RESULTS AND DISCUSSION

Characteristics of the soft coke

The soft coke obtained from the as-received catalysts accounts for between 25 and 50% of the total carbon with the mean being close to 35% (Table 1). Thus, the high carbon in the case of sample no. 10 does not markedly affect the distribution of soft to hard coke. After demineralisation, further extract was obtained (soft coke II) but the yield was typically no more than *ca.* 3% of the total carbon. Table 2 summarises the analytical data obtained for the chloroform extracts obtained from both the as-received catalysts (soft coke 1) and after the demineralisation treatment (soft coke). Overall, the H/C ratios, heteroatom contents, molecular masses and compound class distributions indicate that the easily extractable soft coke can be described as "heavy and generally polar gas oil" (Table 2). The gas chromatographic profiles comprised broad unresolved shoulders containing small peaks from *n*-alkanes. ^{1}H NMR indicated that the soft cokes have low aromaticities (6-8 mole % aromatic hydrogen) consistent with their relatively high aromic H/C ratios (Table 2). Both HPLC and ^{1}H NMR indicated that the average ring size is quite small (1-2 rings as for initial gas oil).

The relatively small quantities of soft coke physically entrapped within the pore structure that were amenable to extraction after demineralisation (soft coke II) have considerably higher molecular masses, lower atomic H/C ratios and higher heteroatom contents than their easily extractable counterparts (Table 2). If the adsorbed soft coke is the major precursor of hard coke, then it is a case of concentrating the polars as opposed to the large polycyclic aromatic hydrocarbon moieties from the initial gas oil. Further, the aliphatic nature of the soft coke indicates that considerable condensation is required to form large aromatic structures.

Characteristics of the hard coke

The CP/MAS ^{13}C NMR spectra of the hard coke concentrates from the low and high carbon catalysts (nos. 8 and 10, respectively) are shown in Figure 3. The aromaticities and the average ring sizes derived from the normal and dipolar dephasing ^{13}C NMR spectra are listed in Table 3. There is a remarkable difference between the two samples. The concentrate from the low carbon catalyst is quite aliphatic in character (aromaticity of *ca.* 0.6) and contains relatively small aromatic clusters. In contrast, the hard coke from the high carbon catalyst has a high aromaticity and contains large clusters (Table 3). In fact, it is quite comparable in bulk structural terms to catalytic coke obtained in FCC [11,12]. These results indicate that aromatisation to large cluster sizes proceeds extremely slowly under hydrotreating conditions (relatively low temperature, high hydrogen pressure). Further, the aliphatic nature and small aromatic ring

cluster size for the hard coke obtained under typical operating conditions suggests that it should readily be converted into oil by hydropyrolysis under the conditions where high conversions are achieved for type I and II kerogens and low-rank coals [7].

Reductive regeneration using hydropyrolysis

Figure 2 compares the carbon contents of the received, the chloroform-extracted and the hydropyrolysed samples for the low and high carbon samples. Carbon conversions of over 90% were achieved for the low carbon catalyst consistent with the bulk structural characterists of the hard coke concentrate (Table 3). In contrast for the high carbon sample, hydropyrolysis removed only *ca.* 60% of the carbon which correponds to *ca.*40% of the hard coke (Figure 2). Neither sample size nor grinding and diluting the samples in sand had a significant affect on the levels of carbon removal, the differences being below 5% of the total carbon.

Figure 3 indicates that the surface area recovery for the low carbon sample (*ca.* 70%) is comparable to that achieved by controlled combustion. In contrast, for the high carbon sample, the surface area recovery is considerably less than that by combustion (by *ca.* 30 $m^2 g^{-1}$) due to the low carbon conversion. For this catalyst, extraction of the soft coke alone gives rise to approximately 70% of the surface area recovery compared to controlled combustion (Figure 3). Thus, the soft coke is proportionally responsible for a much greater loss of surface area than in the case of the low carbon catalyst.

It is probable that a combination of a lower temperatures (450°C) and higher pressures to those employed in this initial study should probably represent the optimum conditions for maintaining catalyst surface area. It was observed that hydropyrolysis gave rise to sulfur reductions of up to 2% w/w. In order to prevent reduction of the promoter to the corresponding metal (Ni/Co), hydropyrolysis should be carried out in the presence of a small amount of hydrogen sulphide to help maintain the catalyst to remain in a reasonably fully sulfided form. Hydropyrolysis for virtual complete carbon removal will need to be carried out off-line since the combination of temperature, pressure and flow rate required cannot be achieved in hydrotreating units. In terms of potential applications, carbon-supported catalysts may represent the major area since these cannot be regenerated oxidatively.

CONCLUSIONS

Soft coke accounts for typically about one-third of the carbon on deactivated catalysts from gas oil hydrotreating units. The soft coke is highly polar in nature, but possesses significant aliphatic character. The hard coke obtained in normal operating situations (5-7 % carbon) has a carbon aromaticity of not much more than 50% and comprises small clusters. However, prolonged usage (carbon content > 15%) leads to a vast increase in aromaticity (>0.90) and ring cluster size. The majority of the hard coke obtained under normal operating conditions (> 80%) can be effectively removed by carrying out fixed-bed hydropyrolysis at 15 MPa and 500°C. This gives rise to a recovery in surface area comparable to that achieved oxidatively. Further improvements in hydropyrolysis in terms of surface area recovery are likely by operating at lower temperatures and higher pressures.

ACKNOWLEDGEMENTS

The authors thank EPSRC for financial support and Dr. K. Holder and colleagues at BP/Amoco for supplying the suite of deactivated HDS catalysts.

REFERENCES

1. Arteaga, A.; Fierro, J.L.G.; Dellanay, F.; Delmon, B. *Appl. Catal.* **1986**, *26*, 227.
2. George, Z.M.; Mohamed, P.E.; Tower, R. Proc. *Int. Congr. Catal., 9th* **1988**, 230.
3. Teixiera da Silva, V.L.S.; Frety, R.; Schmal., M. *Ind. Chem. Eng. Res.* **1994**, *33*, 1692.
4. Teixiera da Silva, V.L.S.; Lima, F.P.; Dieguez, L.C.; Schmal, M. *Ind. Eng. Chem. Res.* **1998**, *37*, 882.
5. Maraf, M.; Stanislaus, A. *Appl. Catal.* **1989**, *47*, 85.
6. Babcock, K.E.; Hiltzik, L.; Ernst, W.R.; Garruthers, J.D. *Appl. Catal.*, **1989**, *61*, 295.
7. Rocha, J.D.; Brown, S.D.; Love, G.D.; Snape, C.E. *Journal of Anal. and Appl.Pyrolysis* **1997**,*40-41*, 91.
8. Brown, S.D.; Sirkecioglu, O.; Snape, C.E.; Eglinton, T.I. *Energy & Fuels* **1997**, *11*, 532.
9. Snape, C.E.; Love, G.D.; Murray, I.P.; Bailey, N.J.L. *Organic Geochem.* **1998**, *29*, 1487.
10. Love, G.D.; McAulay, A.D.; Snape, C.E.; Bishop, A.N. *Energy & Fuels* **1997**, *11*, 522.

Applied Catalysis A: General **1995**, *129*, 125.
11. Snape, C.E.; McGhee, B.J.; Andrésen, J.M.; Hughes, R.; Koon, C.L.; Hutchings, G.
12. Snape, C.E.; McGhee, B.J.; Martin, S.C.; Andrésen, J.M. *Catalysis Today* **1997**, *37(3)*, 285.

Table 1 Coke contents for the suite of deactivated HDS catalysts

Sample no.	%C	%Soft coke 1 (carbon basis)
1	5.6	30
2	6.1	25
3	5.3	33
4	6.5	36
5	6.4	28
6	6.5	39
7	7.4	32
8* (3 months)	8.2	49
9	6.8	43
10* (8 years)	17.8	31

Samples 1-7 from the same unit, 1 at top and 7 nearest bottom of bed.
* selected for detailed characterisation.

Table 2 Summary of the soft coke composition for the suite of deactivated HDS catalysts

	Soft Coke I	Soft Coke II
Atomic H/C	1.60 – 1.85	1.5
% N	0.5-0.8	1.3
% S	< 0.2	< 0.2
%O (by difference)	3-6	>10
% Aliphatics	<10	n.d.
% Aromatics:	<20	n.d.
% Polars:	>70	n.d.
M_n:	200-300	240-340
M_w:	270-380	420-460

n.d. = not determined.

Table 3 Summary of structural parameters for the hard coke concentrates

Parameter	Low carbon (no. 8)	High carbon (no.10)
Carbon aromaticity	0.58	0.42
Fraction of aromatic C that is non-protonated	0.56	0.53
Fraction of aromatic C that is bridgehead	0.1-0.2	0.44
Inferred ring size	1-2	8

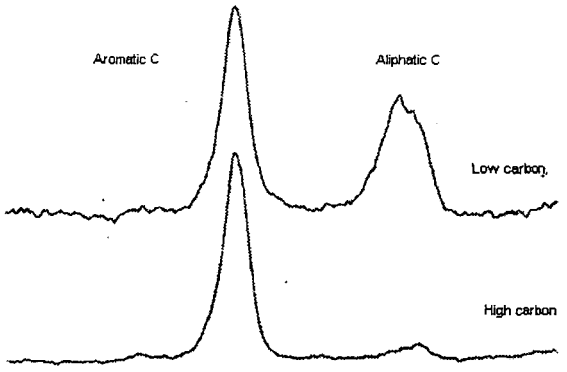

Figure 1. Solid state CP/MAS ^{13}C NMR spectra of hard coke concentrates from low carbon (top) and high carbon (bottom) deactivated HDS catalysts.

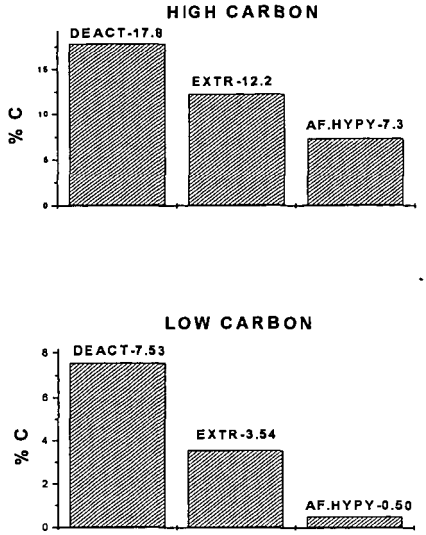

Figure 2. Carbon contents for the low and high carbon deactivated HDS catalysts – as received, after chloroform extraction and after hydropyrolysis.

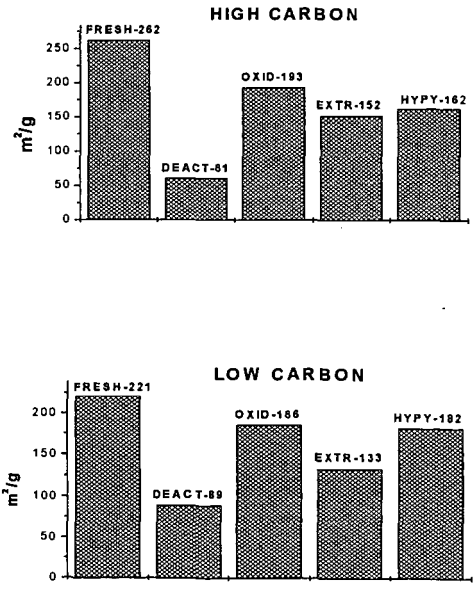

Figure 3. BET surface areas for the low and high carbon deactivated HDS catalysts – as received, after chloroform extraction and after hydropyrolysis.

HYDROGENATION OF PETROLEUM RESIDUA IN DIFFERENT FLUID MEDIA

Ming-Gang Yang[1], Qing-Feng Zha[2] and Semih Eser[1,3]

1.Lab.for Hydrocarbon Proc.Chem., The Energy Institute, Penn State Univ., 209 Acad. Proj. Bldg.
2. The Institute of Coal Chem., Chinese Academy of Sciences, P.O. Box 165, Taiyuan, China
3. Dept. of Energy and Geo-Environmental Eng., Penn State Univ., 154 Hosler Building, University Park, PA 16802

KEYWORDS: Hydrogenation, Residua, Supercritical fluid

INTRODUCTION

In recent decades, hydroprocessing has played a very important role in upgrading petroleum heavy oils. Compared to thermal processes, hydroprocessing gave distillates not only in higher yield but also in higher quality[1, 2] to meet the environmental constraints on petroleum products. In hydroprocessing, the chemical reactions, such as hydrodesulfurization, hydrogenation, and hydrocracking, occur among the three phases that are gaseous hydrogen, liquid heavy oils and solid catalysts. In order to promote diffusion of hydrogen from gas phase into the surface of catalysts and prolong the catalyst life, high operating pressure is necessary in hydroprocessing. Upgrading petroleum heavy oils in supercritical fluids has been studied in recent years to improve diffusion of reactants and products in reaction systems and to prolong catalyst life. A recent study showed that coke deposits on catalysts were decreased and heteroatom removal was increased when hydrotreating shale oils in supercritical fluids such as toluene and n-heptane[3]. In such supercritical reaction processes, however, a large amount of supercritical fluid medium (4 times larger than the amount of reactants) has to be used to see the benefits.

Some researchers[4, 5] studied the effects of adding some solvents, for example, on reducing coke formation and increasing heteroatom removal. The solvents used are usually polynuclear aromatics with partial hydrogen saturation. These solvents are considered to facilitate hydrogen transfer by donating or shuttling hydrogen. The conclusions derived from these studies are still controversial. It appears that the effects of the solvents depend strongly on the feedstocks.

In this study, we investigated the effects of adding small concentration of different fluids, e.g., toluene, hexane and pyridine, on catalytic hydrogenation of pyrene and two petroleum distillation residua. Ammonium tetrathiomolydate was used as a catalyst precursor in the hydrogenation experiments.

EXPERIMENTAL

Pyrene (99% purity) was supplied by Aldrich Chemical Company Inc. The properties of the petroleum residua used in the present work, an atmospheric residue (AR) and a vacuum residue (VR), are listed in Table 1. Hydrogen gas used in the experiments was ultra high purity hydrogen supplied by MG Industries. Ammonium tetrathiomolybdate (ATTM) supplied by Aldrich Chemical Company Inc. was used as a catalyst precursor. Its purity is 99.97%. ATTM decomposes to amorphous MoS_2, H_2S and NH_3 when heated in hydrogen. MoS_2 has catalytic activity for pyrene and petroleum residua hydrogenation.

Table 1. Properties of petroleum residua

	Asphaltene content wt %	H/C atomic ratio	Sulfur content wt %	Residue fraction (525 °C+) / wt %
AR	9.2	1.58	3.9	55.7
VR	14.0	1.33	4.8	88.2

The n-hexane, toluene, pyridine and water were used in the present work to investigate the effect of the fluid media on the pyrene and petroleum residua hydrogenation. The n-hexane and toluene were supplied by J. T. Baker Inc. The purity was more than 95 and 99.9 % for n-hexane and toluene, respectively. Deionized water with high purity was used in the experiments.

Reactions were carried out in 316 stainless steel batch reactors (20 mL) heated in a fluidized-sand bath. Except for investigating the effect of the amount of the fluid media, the quantity of the media used in the experiments was kept a constant at 2 mol % with respect to the quantity of hydrogen initially present. For instance, approximately 0.16 g of toluene was added per 0.083 mol hydrogen. ATTM of 3.8 wt% based on reactant (pyrene or petroleum residue) was added into the reactor in each run, which corresponds to a metal loading of 1.5 wt %. After adding the reactant (pyrene, AR

or VR), ATTM catalyst precursor and liquid fluid medium, the headspace gas in the reactor was replaced three times with hydrogen before the reactor was charged with hydrogen to the desired cold pressure. Then, the reactor was plunged into a preheated sand bath. The reactor contents reached the desired reaction temperature within 3 minutes. At the end of the reaction, the reactor was quenched in cold water. Products and catalyst mixtures were washed with toluene. Then the catalyst was separated from the toluene solution by filtration. After evaporation in Rotavapor, the toluene solvent and the fluid medium were separated and the product mixture was recovered.

Products resulted from pyrene hydrogenation were characterized by GC-MS using standard compounds, and measured quantitatively by GC-FID with a DB-17 capillary column. Products from residue hydrogenation were analyzed by CHN-600 elemental analyzer and LECO sulfur analyzer to determinate H/C atomic ratio and sulfur content of the product mixture. Asphaltene (here defined as materials insoluble in n-hexane) contents of the products were measured by treating the sample (0.2 ± 0.02 g) with n-hexane (20 mL) in an ultrasonic water bath for 5 minutes, followed by setting for another 10 minutes before vacuum filtration through a previously weighed GF/A filter paper. The filtration residue was washed with excess n-hexane (about 30 mL). The solid residue and the sample vial (as some residue remains adhered to the vial wall) were dried in a vacuum oven and then weighed to determine the asphaltene content of the sample.

RESULTS AND DISCUSSION

Pyrene hydrogenation. Products of pyrene hydrogenation were mainly composed of dihydropyrene, tetrahydropyrene and hexahydropyrene. At high pyrene conversion, some amount of decahydropyrene was also found in the product mixture. Pyrene conversion was defined as the difference of pyrene content in reactant and product mixture in percent. Figure 1 compares pyrene conversion obtained in four binary mixtures of hydrogen with n-hexane, toluene, pyridine, and water (containing 2 mol % of each compound in the starting mixtures with respect to the hydrogen) to that obtained in pure hydrogen at 375 °C and 90 min. The cold hydrogen pressure in the reactor determines the hydrogen mole content in the reactant mixture, and changes the initial total pressure at the reaction temperature, as shown in Table 2. A pyrene conversion 23 % was obtained at 0.083 mol hydrogen in pure H_2 gas, reaching the thermodynamic equilibrium. It is notable that a much higher conversion was obtained with the addition of the second compound at the same hydrogen mole content, except in the case of adding pyridine at a relatively high pressure. The highest conversion (64%) was obtained with the addition of toluene, followed by the addition of water (61%) and n-hexane (56%). Although it is not clear why conversion decreases from 42% to 24% there were signs of pyridine hydrogenation at 1750 psi when the total pressure was increased from 1400 to 1750 psi in pyridine + hydrogen mixtures. It is clearly shown in Figure 1 that the addition of toluene, n-hexane or water strongly promoted the pyrene hydrogenation at the some partial pressure of H_2 initially.

Table 2. Changes of cold hydrogen pressure and corresponding hydrogen molar content and initial total reactor pressure at 375 °C

H_2 mole	H_2 cold Pressure /psi	Initial reactor pressure / psi			
		H_2	H_2+n-hexane	H_2+toluene	H_2+pyridine
0.017	200	400	350	430	350
0.034	400	800	700	810	780
0.052	600	1200	1100	1060	1150
0.069	800	1700	1460	1520	1400
0.083	1000	2000	1919	1850	1750

The effect of increasing the toluene concentration in the binary mixture on pyrene conversion is shown in Figure 2. A significant increase in the conversion was observed upon adding a small amount of toluene and the conversion quickly leveled off with further addition of toluene. Toluene, as a mono-ring aromatic compound, does not act as a hydrogen shuttle, like some polynuclear aromatics that transfer radical hydrogen to hydrogen acceptors[6]. The trend in Figure 2 clearly shows that a step increase was obtained in pyrene conversion upon incremental addition of toluene, related most likely to large changes in critical properties of the H_2 and toluene mixture compared to those of H_2 alone. Further increase in toluene concentration may not cause much change in the critical properties of the mixture.

Residua hydrogenation. The change in the n-hexane insoluble components (HI, asphaltenes) content of the residua samples was used as a preliminary measure for the extent of hydrogenation. Figure 3-4 shows the change in HI of AR and VR residua as a function of hydrogen mole content in pure hydrogen and three binary mixtures. The reaction conditions were the same as those of pyrene hydrogenation. For the mixture of hydrogen with toluene, water, and pyridine, the concentration of the second fluid was kept constant at 2 mole % of the initial hydrogen. The trends

are remarkably similar to those obtained with pyrene hydrogenation in the same fluid mixtures. The H_2 + toluene mixtures produced the highest conversion and all binary mixtures gave higher conversions than that achieved with hydrogen alone. The trends of asphaltene reduction in the mixtures of H_2 + water were similar to those with H_2 + toluene mixtures and also gave higher reductions in asphaltenes than those obtained by pure hydrogen. Comparing Figure 3 with 4, under the present reaction conditions, it is clearly shown that the asphaltene reduction by hydrogenation depends strongly on the addition of the second compound for both residua, AR and VR.

Table 3 shows for both residua the H/C atomic ratio and sulfur content of the products obtained by hydrogenation of AR and VR in pure hydrogen, and in mixtures of H_2 + toluene. There was not much change in the elemental composition under the present reaction conditions, and only slight increases were observed in the H/C ratios of the hydrogenated products in the case of H_2 + toluene. The reductions in sulfur contents were small, and showed, in general, that ATTM has little desulfurization activity under the reaction conditions.

Table 3. Comparison of H/C ratio and sulfur content in hydrogenated products

Feedstock	Fluid media	H/C atomic ratio	Sulfur content wt %
AR	H_2	1.58	3.61
	H_2 + Toluene	1.60	3.62
VR	H_2	1.33	4.73
	H_2 + Toluene	1.37	4.60

CONCLUSIONS

The addition of a small amount of fluids (toluene, water or n-hexane) strongly promotes the hydrogenation of pyrene with ATTM. In hydrogenation of petroleum residua, the addition of the fluids reduced the asphaltene content of the products and increased the H/C ratio of hydrogenated products. These promotional effects could result from the changes in the supercritical properties of the fluid media (mixture of hydrogen and the added second compound).

ACKNOWLEDGMENTS

This study was supported by funding from Marathon Oil Company. Many helpful discussions with Dr. Mark A. Plummer and Mr. Rolf R. Schroeder of Marathon Oil are gratefully acknowledged.

REFERENCES

1. Sonnemans, J. W. M. In *Catalysts in Petroleum Refining and Petrochemical Industries* 1995; Stud. Surf. Sci. Catal., Elsevier Sci. B. V. **1996**, Vol. 100, p99-115.
2. Yang, M.-G.; Nakamura, I.; Fujimoto, K. *Catal. Today* **1998**, 43, 273.
3. Low, J. Y. In *Supercritical Fluids*, ACS Symposium Series 329, Sep.8-13, **1985**, p.281.
4. Aaarts, J. J. B., Ternan, M., Parsons, B. I., *Fuel*, **1978**, 57, 473.
5. Kubo, J., *Energy & Fuels*, **1996**, 10, 474.
6. Arends, I. W. C. E., Mulder, P. *Energy & Fuels*, **1996**, 10, 235.

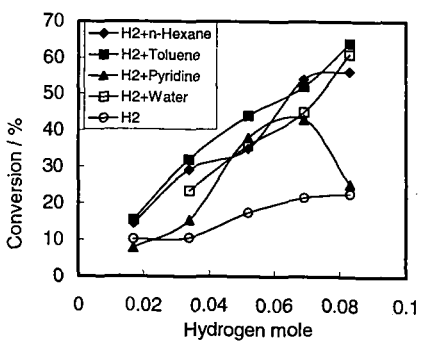

Figure 1. Pyrene hydrogenation in different fluid media. 375 °C, 90 min.

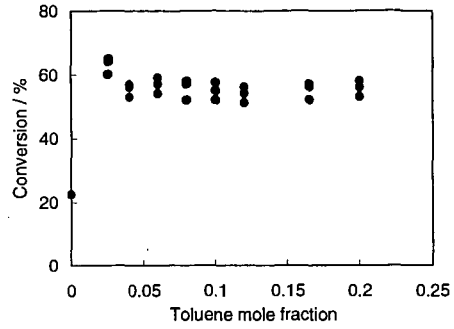

Figure 2. Pyrene conversion as a function of toluene mole fraction in mixtures of H_2-toluene (H_2 = 0.083 mole). 375 °C, 1000 psi H_2 (cold), 90 min.

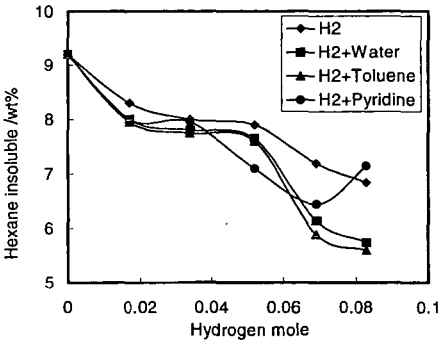

Figure 3. Asphaltene content in products from hydrogenation of AR in different fluid media. 375 °C, 1000 psi H_2 (cold), 90 min.

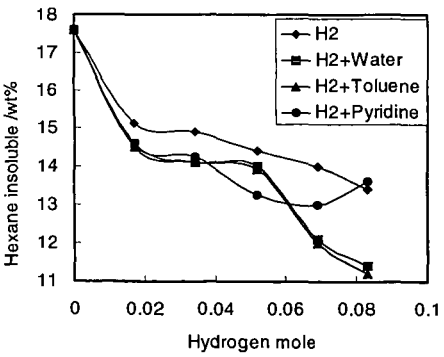

Figure 4. Asphaltene content in products from hydrogenation of VR in different fluid media. 375 °C, 1000 psi H_2 (cold), 90 min.

Hydrogen Research and Development Program

Neil P. Rossmeissl
U.S. Department of Energy
Office of Power Technologies
Washington, D.C. 20585

KEYWORDS: hydrogen, renewable energy, greenhouse gas emissions

INTRODUCTION

Over the last two decades, federal, state, and local institutions have been actively involved in developing technologies to reduce or eliminate air pollution. One technology that offers tremendous potential is hydrogen. Hydrogen can be a cost-effective energy carrier and fuel in reducing greenhouse gas emissions and other toxic emissions from end-use technologies. However, hydrogen is not found in the free state in nature but must be produced from primary energy sources. Producing hydrogen from renewable energy offers the potential for cooperative pre-proprietary research and development projects due to their long-term nature and high risk associated with these technologies.

Hydrogen can be produced directly from sunlight and water by biological organisms and using semiconductor-based systems similar to photovoltaics (PV), or indirectly, via thermal processing of biomass. These production technologies have the potential to produce essentially unlimited quantities of hydrogen in a sustainable manner. Hydrogen production using biological processes or advanced semiconductors is new, innovative and potentially more efficient in the direct conversion of solar energy and biomass to hydrogen. Such processes use, adapt or genetically engineer the biochemical mechanisms present in microalgae or bacteria for the production of hydrogen and use multijunction semiconductors engineered with specific bandgaps to split water, respectively. In order to achieve the goals of practical renewable hydrogen processes, advanced low cost bioreactors, systems with oxygen tolerant hydrogenase and lower cost semiconductor materials with high efficiencies (greater than 10% total solar conversion), need to be developed and engineered.

Storage of hydrogen is also a critical technology area when consideration of energy density is compared to conventional alternatives for the transportation market. Although compressed gas and liquid storage systems have been used in demonstrations worldwide, the issues of safety, capacity and reliablity have not been fully addressed.

The U.S. Department of Energy (DOE) is funding an innovative research and development program focused on exploration of longer-term, higher-risk concepts to address hydrogen as an alternative energy form. The work is challenging, but provides an excellent opportunity for the community to work across political and ideology barriers to develop collaborations.

The DOE has considered the potential use of hydrogen as an energy carrier since the early 1970's following the OPEC oil embargo. At that time, the limitations included the ability to produce low-cost hydrogen and store it for transportation use. Concepts included using base loaded nuclear power to produce "clean" hydrogen with low cost electrical power and store and transport it as a liquid. Over the last 29 years, the Department is still faced with the challenge of producing low-cost hydrogen, storing the hydrogen with an acceptable energy density and converting the hydrogen to useful work with a device that has a high efficiency. In 1990 and 1996, legislation was passed by the Congress to authorize the DOE to conduct a comprehensive hydrogen research and development program to address the limitations that has prevented the introduction of hydrogen as an alternative energy form. This paper presents the Hydrogen Program that was developed and some of the results of the projects funded.

DIRECT HYDROGEN PRODUCTION TECHNOLOGIES

The use of solar energy to split water into oxygen and hydrogen is an attractive means to directly convert solar energy to chemical energy. Biological, chemical, and electrochemical systems are being investigated within DOE as long-term (>10 years), high-risk, high-payoff technologies for the sustainable production of hydrogen.

Biological Systems

In nature, algae absorb light and utilize water and CO_2 to produce cell mass and oxygen. A complex model referred to as the "Z-scheme" has been identified to describe the charge separation and electron transfer steps associated with this process that ultimately drives photosynthesis. A number of enzymatic side pathways that can also accept electrons have been identified. Of interest is a class

of enzymes known as hydrogenases that can combine protons and electrons obtained from the water oxidation process to release molecular hydrogen. These algal hydrogenases are quickly deactivated by oxygen. Researchers have identified mutant algal strains that evolve hydrogen at a rate that is 4 times that of the wild type, and are 3-4 times more oxygen tolerant [1,2].

Photosynthetic organisms also contain light harvesting, chlorophyll-protein complexes that effectively concentrate light and funnel energy for photosynthesis. These antenna complexes also dissipate excess incident sunlight as a protective mechanism. The amount of chlorophyll antennae in each cell is directly related to the amount of "shading" experienced by subsequent layers of microorganisms in a mass culture. In a recent set of experiments, researchers have observed that green alga grown under high light intensities exhibit lower pigment content and a highly truncated chlorophyll antennae size. These cells showed photosynthetic productivity (on a per chlorophyll basis) that was 6-7 times greater than the normally pigmented cells [3], a phenomenon that could lead to significant improvements in the efficiency of hydrogen production on a surface-area basis.

These technical challenges are being addressed by a team of scientists from Oak Ridge National Laboratory (ORNL), the University of California Berkeley, and the National Renewable Energy Laboratory (NREL). Various reactor designs are under development for photobiological hydrogen production processes (single-stage vs two-stage, single organism vs dual organism). At the University of Hawaii's Natural Energy Institute (HNEI), a new, potentially low cost, outdoor tubular photobioreactor is under development to test a sustainable system for the production of hydrogen [4].

In addition to the photosynthetic production of hydrogen from water, the Program supports the development of systems to convert CO (found in synthesis gas) to hydrogen via the so-called water-gas shift reaction ($CO + H_2O = CO_2 + H_2$). This reaction is essential to the widely-used commercial steam methane reforming process for the production of hydrogen. In the industrial process in use today, high-temperature (450°C) and low-temperature (230°C) shift reactors are required to increase the overall hydrogen production efficiency and to reduce the CO content to acceptable levels. In this project, microorganisms isolated from nature are used to reduce the level of CO to below detectable levels (0.1 ppm) at temperatures of around 25-50°C in a single reactor [5]. This process, under develop-ment at NREL, has significant potential to improve the economics of hydrogen production when combined with the thermal processing of biomass or other carbon-containing feeds.

Photochemical Systems

Among the technologies that have been investigated, photocatalytic water splitting systems using relatively inexpensive, durable, and nontoxic semiconductor photocatalysts show promise. Supported catalysts such as Pt-RuO_2/TiO_2 have sufficient band gaps for water splitting, although the current rate of hydrogen production from these systems is too low for commercial processes. Modifications to the system are required to address issues such as the narrow range of solar wavelengths absorbed by TiO_2, the efficiency of subsequent catalytic steps for formation of hydrogen and oxygen, and the need for high surface areas. Binding of catalyst complexes that absorb light in the visible range to the TiO_2 should improve the absorption characteristics. Aerogels of TiO_2 as a semiconductor support for the photocatalysts have potential for addressing reaction efficiency and surface area issues. The University of Oklahoma is investigating these systems.

The Florida Solar Energy Center (FSEC), in conjunction with the University of Geneva, is investigating tandem/dual bed photosystems using sol/gel-deposited WO_3 films as the oxygen-evolving photocatalyst, rather than TiO_2. In this configuration, the dispersion containing the wider band gap photocatalyst must have minimal light scattering losses so that the lower band gap photocatalyst behind it can also be illuminated.

Photoelectrochemical Systems

Multijunction cell technology developed by the PV industry is being used to develop photo-electrochemical (PEC) light harvesting systems that generate sufficient voltage to split water and are stable in a water/electrolyte environment. The cascade structure of these devices results in greater utilization of the solar spectrum, resulting in the highest theoretical efficiency for any photoconversion device. In order to develop cost effective systems, a number of technical challenges must be overcome. These include identification and characterization of semiconductors with appropriate band gaps; development of techniques for preparation and application of transparent catalytic coatings; evaluation of effects of pH, ionic strength, and solution composition on semiconductor energetics and stability, and on catalyst properties; and development of novel PV/PEC system designs. NREL's approach to solving these challenges is to use the most efficient semiconductor materials available, consistent with the energy requirements for a water splitting system that is stable in an aqueous environment. To date, a PV/PEC water splitting system with a

solar-to-hydrogen efficiency of 12.4% (lower heating value, LHV) using concentrated light, has operated for over 20 hours [6]. HNEI is pursuing a low-cost amorphous silicon-based tandem cell design with appropriate stability and performance, and is developing protective coatings and effective catalysts. An outdoor test of the a-Si cells resulted in a solar-to-hydrogen efficiency of 7.8% LHV under natural sunlight [7].

INDIRECT HYDROGEN PRODUCTION TECHNOLOGIES

These systems offer the opportunity to produce hydrogen from renewable resources in the mid-term (5-10 years). Using agricultural residues and wastes, or biomass specifically grown for energy uses, hydrogen can be produced using a variety of processes.

Biomass pyrolysis produces a bio-oil that, like petroleum, contains a wide spectrum of components. Unlike petroleum, bio-oil contains a significant number of highly reactive oxygenated components derived mainly from constitutive carbohydrates and lignin. These components can be transformed into hydrogen via catalytic steam reforming using Ni-based catalysts. By using high heat transfer rates and appropriate reactor configurations that facilitate contact with the catalyst, the formation of carbonaceous deposits (char) can be minimized. The resulting products from the thermal cracking of the bio-oils are steam reformed at temperatures ranging from 750-850°C. At these conditions, any char formed will also be gasified. At NREL and the Jet Propulsion Laboratory, research and modeling are underway to develop processing technologies that take advantage of the wide spectrum of components in the bio-oil, and address reactivity and reactor design issues [8,9]. Evaluation of co-product strategies indicates that high value chemicals, such as phenolic resins, can be economically produced in conjunction with hydrogen [10].

Biomass is typically 50 weight % (wt%) moisture (as received); biomass gasification and pyrolysis processes require drying of the feed to about 15 wt% moisture for efficient and sustained operation, in addition to requiring size reduction (particle size of ~1 cm). In supercritical gasification processes, feed drying is not required, although particle size reduction requirements are more severe. A slurry containing approximately 15 wt% biomass (required size reduction ~1 mm) is pumped at high pressure (>22 MPa, the critical pressure of water) into a reactor, where hydrothermolysis occurs, leading to extensive solubilization of the lignocellulosics at just above the supercritical conditions. If heat transfer rates to the slurry are sufficiently high, little char is formed, and the constituents of biomass are hydrolyzed and solubilized in the supercritical medium. Increasing the temperature to ~700°C in the presence of catalysts results in the reforming of the hydrolysis products. Catalysts have been identified that are suitable for the steam reforming operation [11]. HNEI and Combustion Systems Inc. are investigating appropriate slurry compositions, reactor configurations, and operating parameters for supercritical water gasification of wet biomass.

HYDROGEN STORAGE, TRANSPORT, AND DELIVERY

The storage, transport, and delivery of hydrogen are important elements in a hydrogen energy system. With keen interest in mobile applications of hydrogen systems, and as intermittent renewables penetration of the electric grid increases, storage becomes essential to a sustainable energy economy. Light weight and high energy density storage will enable the use of hydrogen as a transportation fuel. Efficient and cost effective stationary hydrogen storage will permit PV and wind to serve as base load power systems.

Compressed Gas Storage Tanks

Currently, compressed gas is the only commercially available method for ambient-temperature hydrogen storage on a vehicle. Compressed hydrogen stored at 24.8 MPa in a conventional fiberglass-wrapped aluminum cylinder results in a volumetric storage density of 12 kg of hydrogen per m^3 of storage volume and a gravimetric density of 2 wt% (grams of hydrogen per gram of system weight). Carbon fiber-wrapped polymer cylinders achieve higher densities (15 kg/m^3 and 5 wt%), but are significantly below target values required for hydrogen to make major inroads in the transportation sector (62 kg/m^3 and 6.5 wt%). Advanced lightweight pressure vessels have been designed and fabricated by Lawrence Livermore National Laboratory [12]. These vessels use lightweight bladder liners that act as inflatable mandrels for composite overwrap and as permeation barriers for gas storage. These tank systems are expected to exceed 12 wt% hydrogen storage (at 33.8 MPa) when fully developed.

Carbon-based Storage Systems

Carbon-based hydrogen storage materials that can store significant amounts of hydrogen at room temperature are under investigation. Carbon nanostructures could provide the needed technological

breakthrough that makes hydrogen powered vehicles practical. Two carbon nanostructures are of interest: single-walled nanotubes and graphite nanofibers. Single-walled carbon nanotubes, elongated pores with diameters of molecular dimensions (12 Å), adsorb hydrogen by capillary action at non-cryogenic temperatures. Single-walled nanotubes have recently been produced and tested at NREL in high yields using a number of production techniques, and have demonstrated hydrogen uptake at 5-10 wt% at room temperature [13]. Graphite nanofibers are a set of materials that are generated from the metal catalyzed decomposition of hydrocarbon-containing mixtures. The structure of the nanofibers is controlled by the selection of catalytic species, reactant composition, and temperature. The solid consists of an ordered stack of nanocrystals that are evenly spaced at 0.34-0.37 nanometers (depending on preparation conditions). These are bonded together by van der Waals forces to form a "flexible wall" nanopore structure. Northeastern University estimates that excellent hydrogen storage capacities are possible in these structures.

Metal Hydride Storage and Delivery Systems

Conventional high capacity metal hydrides require high temperatures (300-350°C) to liberate hydrogen, but sufficient heat is not generally available in fuel cell transportation applications. Low temperature hydrides, however, suffer from low gravimetric energy densities and require too much space on board or add significant weight to the vehicle. Sandia National Laboratories (SNL) and Energy Conversion Devices (ECD) are developing low-temperature metal hydride systems that can store 3-5 wt% hydrogen. Alloying techniques have been developed by ECD that result in high-capacity, multi-component alloys with excellent kinetics, albeit at high temperatures. Additional research is required to identify alloys with appropriate kinetics at low temperatures.

A new approach for the production, transmission, and storage of hydrogen using a chemical hydride slurry as the hydrogen carrier and storage medium is under investigation by Thermo Power Corporation. The slurry protects the hydride from unanticipated contact with moisture and makes the hydride pumpable. At the point of storage and use, a chemical hydride/water reaction is used to produce high purity hydrogen. An essential feature of the process is recovery and reuse of spent hydride at a centralized processing plant. Research issues include the identification of safe, stable and pumpable slurries and the design of an appropriate high temperature reactor for regeneration of spent slurry.

END USE TECHNOLOGIES

Proton exchange membrane (PEM) fuel cells could provide low-cost, high-efficiency electric power, and be operated "in reverse" as electrolyzers to generate hydrogen. There has been a significant increase in industry activity for the development of PEM fuel cells for vehicular applications, with a number of active demonstration projects. Improvements in catalyst loading requirements, water management, and temperature control have helped move these power units from mere curiosities to legitimate market successes. In order to increase the market penetration in both the transportation and utility sectors, additional improvements are required. Los Alamos National Laboratory is developing non-machined stainless steel hardware and membrane electrode assemblies with low catalyst loadings to achieve cost reductions and efficiency improvements [14]. The most important barriers to implementation of low-cost PEM fuel cells are susceptibility of the metal or alloy to corrosion, water management using metal screens as flow fields, and effective stack sealing. Operating the PEM fuel cell "in reverse" as an electrolyzer is possible, but optimum operating conditions for the power production mode and for the hydrogen production mode are significantly different. Design issues for the reversible fuel cell system include thermal management, humidification, and catalyst type and loading.

In an effort to promote near-term use of hydrogen as a transportation fuel, the Program is investigating the development of cost effective, highly efficient, and ultra-low emission internal combustion engines (ICE) operating on pure hydrogen and hydrogen-blended fuels. Research at SNL is focused on the development of a hydrogen fueled ICE/generator set with an overall efficiency of >40% while maintaining near zero NO_x emissions [15].

SAFETY

Hydrogen leak detection is an essential element of safe systems. The development of low-cost fiber optic and thick film sensors by NREL and ORNL, respectively, will provide affordable and reliable options for hydrogen safety systems. NREL is using optical fibers with a thin film coating on the end that changes optic properties upon reversible reaction with hydrogen. Change in the reflected light signal is an indication of the presence of hydrogen. Sensitivity and selectivity are important research issues. ORNL is focused on the development of monolithic, resistive thick film sensors that

are inherently robust, selective to hydrogen, and easy to manufacture. Research issues include developing appropriate techniques for active (versus traditional passive) thick film applications.

Recognizing the importance of safe use of hydrogen, the DOE, in conjunction with Natural Resources Canada, has compiled a comprehensive document of prevailing practices and applicable codes, standards, guidelines, and regulations for the safe use of hydrogen. The *Sourcebook for Hydrogen Applications* is intended to be a "living document" that can be updated to reflect the current state of knowledge about, and experience with, safely using hydrogen in emerging applications. DOE also supports the development of codes and standards under the auspices of the International Standards Organization.

CONCLUSIONS

The DOE Hydrogen Program conducts R&D in the areas of production, storage, and utilization, for the purpose of making hydrogen a cost-effective energy carrier for utility, buildings, and transportation applications. Research is focused on the introduction of renewable-based options to produce hydrogen; development of hydrogen-based electricity storage and generation systems that enhance the use of distributed renewable-based utility systems; development of low-cost technologies that produce hydrogen directly from sunlight and water; and support of the introduction of safe and dependable hydrogen systems including the development of codes and standards for hydrogen technologies.

REFERENCES

[1] Ghirardi, M.L., R.K. Togasaki, and M. Seibert, 1997, "Oxygen Sensitivity of Algal Hydrogen Production," *Appl. Biochem. Biotechnol.*, 63-65, 141-151.

[2] Seibert, M., T. Flynn, D. Benson, E. Tracy, and M. Ghirardi, 1998, "Development of Selection/Screening Procedures for Rapid Identification of Hydrogen-Producing Algal Mutants with Increased Oxygen Tolerance," International Conference on Biological Hydrogen Production, Plenum, NY, 227-234.

[3] Melis, A., J. Neidhardt, I. Baroli, and J.R. Benemann, 1998, "Maximizing Photosynthetic Productivity and Light Utilization in Microalgal by Minimizing the Light-Harvesting Chlorophyll Antenna Size of the Photosystems," International Conference on Biological Hydrogen Production, Plenum, NY, 41-52.

[4] Szyper, J.P., B.A. Yoza, J.R. Benemann, M.R. Tredici, and O.R. Zaborsky, 1998, "Internal Gas Exchange Photobioreactor: Development and Testing in Hawaii," International Conference on Biological Hydrogen Production, Plenum, NY, 441-446.

[5] Maness, P.-C. and P.F. Weaver, 1997, "Variant O_2-Resistant Hydrogenase from Photosynthetic Bacteria Oxidizing CO," Proceedings of the Fifth International Conference on the Molecular Biology of Hydrogenase, Albertville, France.

[6] Khaselev, O. and J.A. Turner, 1998, "A Monolithic Photovoltaic-Photoelectrochemical Device for Hydrogen Production via Water Splitting," *Science*, 280, 425.

[7] Rocheleau, R., 1998, "High Efficiency Photoelectrochemical H_2 Production using Multijunction Amorphous Silicon Photoelectrodes," *Energy & Fuels*, 12 (1), 3-10.

[8] Wang, D., S. Czernik, and E. Chornet, 1998, "Production of Hydrogen from Biomass by Catalytic Steam Reforming of Fast Pyrolysis Oil," *Energy & Fuels*, 12 (1), 19-24.

[9] Miller, R.S. and J. Bellan, 1997, "A Generalized Biomass Pyrolysis Model Based on Superimposed Cellulose, Hemicellulose and Lignin Kinetics," *Comb. Sci. and Techn.*, 126, 97-137.

[10] Wang, D., S. Czernik, D. Montane, M.K. Mann, and E. Chornet, 1997, "Hydrogen Production via Catalytic Steam Reforming of Fast Pyrolysis Oil Fractions," Proceedings of the Third Biomass Conference of the Americas, Montreal, 845-854.

[11] Matsunaga, Y., X. Xu, and M.J. Antal, 1997, "Gasification Characteristics of an Activated Carbon in Supercritical Water," *Carbon*, 35, 819-824.

[12] Mitlitsky, F., and B. Myers, and A.H. Weisberg, 1998, "Regenerative Fuel Cell Systems," *Energy & Fuels*, 12 (1), 56-71.

[13] Dillon, A.C., K.M. Jones, T.A. Bekkedahl, C.H. Kiang, D.S. Bethune, and M.J. Heben, 1997, "Storage of Hydrogen in Single-Walled Carbon Nanotubes," *Nature*, 386, 377-279.

[14] Cleghorn, S., X. Ren, T. Springer, M. Wilson, C. Zawodzinski, T. Zawodzinski, and S. Gottesfeld, 1997, "PEM Fuel Cells for Transportation and Stationary Power Generation Applications," *Int. J. Hydrogen Energy*, 23, 1137-1144.

[15] Cleghorn, S., X. Ren, T. Springer, M. Wilson, C. Zawodzinski, T. Zawodzinski, and S. Gottesfeld, 1997, "PEM Fuel Cells for Transportation and Stationary Power Generation Applications," *Int. J. Hydrogen Energy*, 23, 1137-1144.

ISOLATION OF *CHLAMYDOMONAS* MUTANTS WITH IMPROVED OXYGEN-TOLERANCE

Timothy Flynn, Maria L. Ghirardi, and Michael Seibert
National Renewable Energy Laboratory, Golden, CO 80401

ABSTRACT

The photoproduction of H_2 from water by anaerobically-induced algae is catalyzed by a bidirectional hydrogenase, an enzyme that is rapidly deactivated by exposure to low levels of O_2. We have developed two selective pressures, with which a mutant's survival depends on hydrogenase activity in the presence of O_2, and a chemochromic screening method to quickly identify and isolate desirable O_2-tolerant hydrogenase mutants. The clones that still produced H_2 after exposure to O_2 were further characterized by gas chromatography for maximal H_2-production rate and tolerance to O_2. The best mutant obtained by a single round of mutagenesis/selection/screening maintained up to 35% of its maximal H_2-production rate (measured with no exposure to O_2) following deactivation of the enzyme by 2% O_2 for 2 minutes, a condition that almost totally inactivates wild-type (WT) H_2 production. A mutant that underwent a second round of mutagenesis and selection exhibited 49% of its maximal activity following the deactivation treatment. This represents a 10-fold improvement over the WT strain and suggests that even better mutants will be forthcoming.

INTRODUCTION

Photobiological H_2-production by green algae is catalyzed by the reversible hydrogenase (1,2), a chloroplast stromal enzyme (3) that catalyzes both H_2 production and H_2 uptake in the organism. This nuclear-encoded protein (4) is induced by anaerobic incubation of algal cells in the dark but is inhibited by the presence of very low concentrations of O_2 (5). This problem has precluded the application of algae up to this point in applied H_2-producing systems.

Future development of a cost-effective, commercial H_2-production system using green algae will depend on the availability of strains that produce H_2 directly from water under aerobic conditions (6). One of our approaches to generate O_2-tolerant, H_2-producing algal mutants was based on a selection pressure involving the H_2-uptake activity of the reversible hydrogenase (7). Hydrogen uptake (or photoreductive) selection is applied to a population of mutagenized *Chlamydomonas reinhardtii* cells in an atmosphere of H_2, CO_2, and controlled concentrations of O_2, as well as in the presence of the herbicides 3-(3,4-dichlorophenyl)-1,1-dimethyl urea (DCMU) and atrazine. These herbicides blocks photosynthetic O_2 evolution and electron flow at the reducing side of photosystem II and prevent electrons from water from reaching the hydrogenase enzyme. The surviving organisms grow by fixing CO_2 with electrons obtained from the oxidation of H_2 catalyzed by the O_2-tolerant hydrogenase, and ATP generated by cyclic electron transport around photosystem I (5).

Since photoreductive selection only exploits the H_2 oxidation activity of the hydrogenase, we have also developed a new selective pressure designed to exploit the H_2-evolving function of the enzyme (8). This selection depends on the fact that, in the absence of CO_2, metronidazole (MNZ) will compete with the hydrogenase at the level of ferredoxin for electrons derived from the photosynthetic electron transport chain (9). Reduced MNZ generates a radical that is reoxidized by O_2 with the concomitant formation of superoxide radicals and H_2O_2, both of which are toxic to the algae. If the hydrogenase is still active following exposure to O_2, then some of the electrons from reduced ferredoxin can be used for H_2 production instead of MNZ reduction, and decreased toxicity can be observed (8).

The traditional assays (Clark electrode or gas chromatograph analysis) used to determine a clone's O_2-tolerance require many time-consuming steps and are a severely limiting factor for rapidly identifying useful mutants (10). This problem was solved by the development of a screening assay using a thin-film, multilayer chemochromic sensor (11) that permits the evaluation of hundreds of mutant clones in a single day. This sensor, when held in close contact to anaerobically induced algal colonies that can evolve H_2 after exposure to O_2, produces an easily visualized blue spot. These spots correspond to colonies that were able to withstand O_2 deactivation treatment, and allow for the rapid identification of desirable mutants clones (10). The combination of random mutagenesis, selection, and screening has yielded H_2-producing *Chlamydomonas* mutants with significantly improved O_2-tolerance.

MATERIALS AND METHODS

Cell Growth: Wild-type (WT) *C. reinhardtii* (137c$^+$) was a gift from Prof. S. Dutcher, University of Colorado, Boulder. Algal cells were grown photoautotrophically in basal salts (BS), a modification of Sueoka's high salt medium (12) that includes citrate to prevent salt precipitation. This formulation contains the following salts: 10 mM NH_4Cl, 1 mM $MgSO_4$, 7.5 mM KH_2PO_4, 7.5 mM K_2HPO_4, 1.5 mM Na_3-citrate, 0.5 mM $CaCl_2$, 20 μM $FeCl_3$, and 1/2 x Hutner's trace elements (12). This medium can be solidified with 1.5% w/v agar and amended with 0.5 g/l yeast extract (Difco) for plates, and may be supplemented with 10 mM sodium acetate depending on the

experiment. Liquid cultures were grown under continuous cool white fluorescent lamp illumination (70 $\mu E \cdot m^{-2} \cdot s^{-1}$ PAR) at 25 °C and agitated on a shaker. Cells were harvested by centrifugation at 2000 x g for 10 min and resuspended in liquid BS medium.

Mutagenesis: Mid-log phase cultures were harvested and resuspended in liquid BS to yield a 10 ml suspension of $7x10^6$ cells/ml. Ethylmethane sulfonate (EMS) was added to a final concentration of 5 µl/ml (46 mM), and the cells were incubated with gentle agitation for various periods of time. At the end of the incubation period the cells were washed and resuspended in 50 ml of the same medium lacking EMS. Liquid cultures were grown in the light as above for at least 7 days before being submitted to the selective pressures.

Photoreductive Selection (PR) Procedure: Liquid cultures of mutagenized algal cells (250 ml, 2.8 x 10^5 cells/ml) in BS were treated with 15 μM each of DCMU and atrazine, and the flasks were placed in anaerobic jars. The gas phase contained 16.5% H_2, 2% CO_2, 5% O_2, balanced with Ar. The cultures were grown for a couple of weeks with stirring and illuminated with fluorescent light (70 $\mu E \cdot m^{-2} \cdot s^{-1}$ PAR). At the end of the selection period, the cells were washed with BS medium and revived in liquid BS medium plus 10 mM sodium acetate.

H_2-Production Selection (MZ) Procedure: A suspension of anaerobically-induced algal cells was mixed with an anaerobic MNZ-Na azide solution to final concentrations of 40 mM MNZ and 1 mM sodium azide and 2.8 x 10^6 cells/ml. While maintaining darkness, O_2 was added to 5% in the gas phase, and the mixtures were shaken vigorously for 4 min. Immediately following the O_2 treatment, the cultures were exposed for 6 min to light (320 $\mu E \cdot m^{-2} \cdot h^{-1}$ PAR) filtered through a solution of 1% $CuSO_4$ with mixing. At the end of the selection period, the cells were washed with BS medium and either resuspended in the same medium or plated for cell counting.

Chemochromic screening: Individual colonies surviving mutagenesis and selection were transferred to square petri dishes that can easily accommodate an 8 x 8 colony matrix and the square chemochromic sensor. Following a 7-14 day growth period, the agar plates were made anaerobic overnight to induce the algal hydrogenase and then preexposed to 21% O_2 for different periods of time in the dark to deactivate the WT phenotype. The plates were immediately transferred to an anaerobic glove box, the sensor applied, and the colonies were illuminated for 3 minutes to photoevolve H_2. At the end of the illumination period, the sensors were analyzed for the location of blue dots, corresponding to the algal colonies that still evolved H_2 following the O_2 pretreatment. The identified clones were transferred from the original plate to liquid BS + 10 mM acetate, and were cultivated for further characterization.

H_2-Evolution Assay: Mid-log phase algal cultures were harvested and resuspended in phosphate buffer (8) supplemented with 15 mM glucose and 0.5% v/v ethanol and were then made anaerobic with Ar bubbling. Concurrently, 2 ml of an enzymatic O_2-scrubbing system (13) that consisted of 1mg/ml glucose oxidase and 27720 units/ml catalase was dispensed into dialysis tubing (6-8 kD MW cutoff) and made anaerobic as above. The dialysis bags were added to the cell suspensions and the vials were sealed, covered with aluminum foil, and incubated at room temperature for 4 h. Following this induction treatment, the cell suspensions were kept at 4 °C overnight. The assay reaction consists of exposing the cells to various levels of O_2 for two minutes, reestablishing anaerobiosis, and adding reduced methyl viologen to serve as the electron donor to the hydrogenase. The reactions mixtures were incubated in the dark for 15 minutes at 30 °C in a shaking water bath, and the reaction was stopped by adding trichloroacetic acid. The presence of H_2 was detected by gas chromatography.

RESULTS

Figure 1 shows the dose response curve when WT cells were treated with the mutagen EMS (46 mM for various periods of time). The survivors from the 10, 15 and 20 minute cultures (corresponding to 66, 56, and 42% survival) were harvested (see methods) and used in future experiments.

Figure 2 shows the subsequent treatment histories of the various populations. Each of the three polygenic mutant populations were initially subjected to the PR selection, and individual surviving clones were subjected to the chemochromic screening. Screening and preliminary characterization of representative clones obtained from the populations PR8, PR9, PR10, failed to yield mutants with significantly improved O_2-tolerance. The insufficient enrichment of desirable mutants by this particular experiment will be discussed later. The populations surviving the PR selection were maintained in liquid BS plus acetate and were then subjected to the MZ procedure. Figure 3 shows the killing kinetics of the MZ selections, where less than 3% of the initial population density survived in each case. The apparent decreased killing rate of the MZ14 population was probably caused by incomplete mixing of the gas and liquid phase during the dark deactivation treatment. Following resuspension in liquid BS, the resulting cultures were diluted and spread onto agar to obtain individual colonies derived from single cell clones.

Two hundred and forty clones from each of the three populations that survived the MZ selection pressure were isolated for the chemochromic screening assay. The colonies on agar plates were exposed to 21% O_2 for various periods of time for a maximum of 10 minutes before screening.

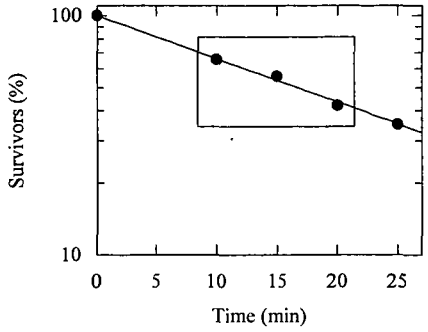

Figure 1: Ethylmethane sulfonate (EMS) mutagenesis of WT *C. reinhardtii* using 5µl/ml (46mM) EMS and a 10ml suspension of $7x10^6$ cells/ml. The harvested populations are indicated.

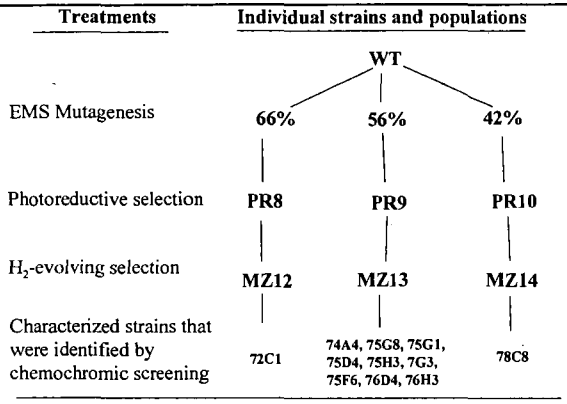

Figure 2: Treatment histories of the various strains

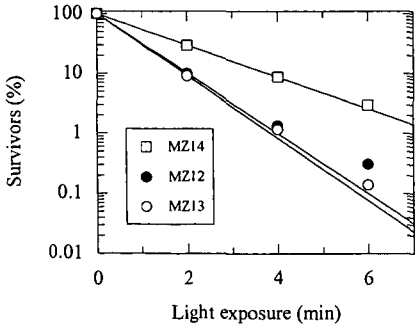

Figure 3: Metronidazole selection of the photoreductive selection survivors (PR8, PR9, and PR10), giving rise to MZ12, MZ13, and MZ14 respectively. The anaerobically induced cells were preexposed for 4 minutes to 5% O_2 before illumination.

The clones that produced the most H_2 under these conditions were further characterized using the methyl viologen assay. Table 1 summarizes the characteristics of the indicated selected clones. The parameters used to initially characterize the mutants included the maximum rate of H_2 evolution measured without any exposure to O_2 (V_0), and the amount of remaining H_2-evolution activity following an exposure to 2% O_2 for two minutes (% of V_0). The % of V_0 parameter was used to roughly compare the relative O_2-tolerance of the mutants compared to the WT strain. Four strains were more fully characterized by titrating the H_2-evolving activity following deactivation of the enzyme with increasing levels of O_2 for 2 minutes. The O_2 I_{50} was estimated by fitting the data to a single exponential decay function. Inspection of Table 1 reveals that all of the mutants identified by the screening assay are improved with respect to V_0 and O_2-tolerance compared to their parental WT strain. The V_0's were increased in all of the mutants, with a 2.3-fold increase in strain 75D4. The I_{50}'s, were increased by 3.7- and 4.4-fold in the strains 76D4 and 76H3. The least improved strain, 78C8, had only a 9% increase in O_2-tolerance compared to the WT strain, and may represent the minimum phenotype for surviving the conditions used in this H_2-evolving selection experiment.

The strain 76D4 was remutagenized with EMS (61% survival), selected using the MZ procedure with a selective pressure of 40% O_2 in the dark for 5 minutes, and finally screenedfollowing deactivation with 100% O_2 for 5 minutes. A resulting clone, 141F2, had over a 2-fold increase in I_{50} compared to its parent (76D4) and almost a 10-fold improvement compared to the grandparent WT strain.

MZ population [A]	Strain	V_0 [B] (μmoles H_2/(mg Chl x h)	% of V_0 [C]	O_2 I_{50}
-----	WT	39	0.26%	0.22
MZ12	72C1	81	14%	-----
MZ13	76D4	78	18%	0.82
	76H3	72	35%	0.96
	74A4	64	15%	-----
	75G8	50	26%	-----
	75G1	82	17%	-----
	75D4	88	18%	-----
	75H3	67	27%	-----
	75G3	73	29%	-----
MZ14	78C8	64	9%	-----
MZ24	141F2	86	49%	2.04

Table 1: Characteristics of selected strains. A: see Fig. 2. B: maximum rate of H_2 evolution without any exposure to O_2. C: rate of H_2 evolution following deactivation by pre-exposure of the cells to 2% O_2 for 2 minutes (expressed as % of V_0). D: The O_2 concentration (in %) that reduces V_0 by 1/2 (2 minute exposure).

DISCUSSION

Mutagenesis of *C. reinhardtii* cells was induced by exposure to EMS, an agent that alkylates the keto groups of guanines and thymine. This causes anomalous base-pairing upon the replication of DNA (14) and ultimately results in transition mutation (G≡C becomes A=T). The frequency of mutants among survivors increases with mutagen dose, but so does the damage to the genetic background (15). Therefore, killing rates of less than 60% were chosen to minimize damage to the remainder of the genome. The problem of decreased mutant frequencies among the survivors is normally solved by employing effective selection procedures.

However, upon finding little improvement in O_2-tolerance in the populations obtained from the first photoreductive selection, it appeared that either the hydrogenase was not mutated, or the conditions employed were not sufficiently specific for the enrichment of desirable O_2-tolerant mutants. Since improved mutants could be generated by MZ selection (Table 1), but were not recovered from the original PR populations, the PR procedure clearly needs improvement. We have reexamined the initial PR selection protocol (see Materials and Methods section) and have determined that the initial O_2 concentration in the anaerobic jar could have been significantly decreased by cellular respiration of the cultures during the application of the selective treatment. This could and apparently did reduce the effectiveness of the selective pressure. This problem was solved by replacing the gas mixture daily until the culture became chlorotic indicating that the

majority of the cells are dead. Preliminary results obtained from this modification appear promising and will be published elsewhere.

The results of this paper clearly demonstrate the utility of the chemochromic screening technique. It has not only allowed us to rapidly identified mutants with desired phenotypes but also permitted the rapid assessment of the effectiveness of the selection procedures themselves. It is also encouraging that all of the strains that were identified with the chemochromic sensor were improved compared to their parental strain upon further characterization.

The mutants identified with the chemochromic sensor were chosen for further characterization based on the intensity of the color change following an exposure to various pretreatment doses of O_2. The clones that demonstrated the best potential, based on the intensity of the color change, were obtained from the MZ13 population, and were most heavily sampled. Given the range of increased O_2-tolerance (% of V_0, Table 1) detected among the 10 sampled first round mutants, one could argue that there is more than one genotype that gives rise to the O_2-tolerant phenotype. Three obvious possibilities exist: (a) different amino acid substitutions at a single critical residue, (b) random substitutions distributed throughout the O_2-sensitive domain, or (c) mutations of genes other than the hydrogenase that cause a decrease in intracellular O_2 concentration, such as through increased rates of respiration.

The ultimate goal of our research is to create an organism that photo-oxidizes water to H_2 under aerobic conditions using solar energy. Our current results are encouraging, and validate the use of classical mutagenesis/selection to obtain the desirable organisms.

ACKNOWLEDGMENTS

This work was supported by the U.S. Department of Energy Hydrogen Program. We thank Dr. Se-Hee Lee for making the sensors.

REFERENCES

1. Weaver, P.F., Lien, S., and Seibert, M. (1980) in *Proceedings of the Fifth Joint US/USSR Conference of the Microbial Enzyme Reactions Project*, Jurmala, Latvia, USSR, pp. 461-479.
2. Adams, M.W.W., Mortenson, L.E., and Chen, J.-S. (1981) *Biochim. Biophys. Acta* **594**, 105-176.
3. Happe, T., Mosler, B., and Naber, D. (1994) *Eur. J. Biochem.* **222**, 769-774.4
4. Roessler, P.G., and Lien, S. (1984) *Plant Physiol.* **75**, 1086-1089.
5. Maione, T.E., and Gibbs, M. (1986) *Plant Physiol.* **80**, 364-368.
6. Schulz, R. (1994) *J. Mar. Biotechnol.* **4**, 16-22.
7. McBride, A.C., Lien, S., Togasaki, R.K., and San Pietro, A. (1977) in *Biological Solar Energy Conversion*, Mitsui, A., Miyachi, S., San Pietro, A., and Tamura, S. eds. Academic Press, New York, NY.
8. Ghirardi, M.L., Togasaki, R.K., and Seibert, M. (1997) *Appl. Biochem. Biotechnol.* **63-65**, 141-151.
9. Schmidt, G.W., Matlin, K.S., and Chua, N.-H. (1977) *Proc. Natl. Acad. Sci. USA* **74**, 610-614.
10. Seibert, M., Flynn, T., Benson, D., Tracy, E., and Ghirardi, M. (1998) In *Biohydrogen* (Zaborsky, O.R., et al. eds), Plenum Publishing Corporation, New York, NY.
11. Benson, D.K., Tracy, C.E., and Bechinger, C. (1996) In *Proceedings of the 1996 U.S. DOE Hydrogen Program Review*, vol. II, 605-624, NREL/CP-21908430.
12. Harris, E.H. (1989) *The Chlamydomonas Sourcebook*, Academic Press, New York.
13. Packer, L., and Cullingford, W. (1978) Z. Naturforsch. **33c**, 113-115.
14. Klug, W.S., and Cummings, M.R. (1983) *Concepts in Genetics*, Charles E. Merrill Publishing Company, Columbus, Ohio.
15. Bos, C.J. (1987) Curr. Genet. **12**: 471-474.

PHOTOSYNTHETIC HYDROGEN AND OXYGEN PRODUCTION BY GREEN ALGAE

E. Greenbaum and J. W. Lee

Oak Ridge National Laboratory
P. O. Box 2008
Oak Ridge, TN 37831

Summary

Photosynthesis research at Oak Ridge National Laboratory is focused on hydrogen and oxygen production by green algae in the context of its potential as a renewable fuel and chemical feed stock. Beginning with its discovery by Gaffron and Rubin in 1942, motivated by curiosity-driven laboratory research, studies were initiated in the early 1970s that focused on photosynthetic hydrogen production from an applied perspective. From a scientific and technical point of view, current research is focused on optimizing net thermodynamic conversion efficiencies represented by the Gibbs Free Energy of molecular hydrogen. The key research questions of maximizing hydrogen and oxygen production by light-activated water splitting in green algae are (1) removing the oxygen sensitivity of algal hydrogenases; (2) linearizing the light saturation curves of photosynthesis throughout the entire range of terrestrial solar irradiance — including the role of bicarbonate and carbon dioxide in optimization of photosynthetic electron transport and (3) constructing real-world bioreactors, including the generation of hydrogen and oxygen against workable back pressures of the photoproduced gases.

Introduction

Photosynthetic hydrogen production by green algae was discovered in the pioneering experiments of Gaffron and Rubin (1942). This work was followed up by Gaffron and his colleagues in a series of seminal papers (Gaffron, 1960; Kaltwasser *et al.*,1969; Stuart and Gaffron,1971 & 1972;) as well as many others. From the point of view of renewable fuels and chemical feedstock production, it is light-activated simultaneous photoproduction of hydrogen and oxygen that is of primary interest. The pioneering experiments in this field were performed by Spruit (1958) who developed a novel two-electrode polarographic technique for the simultaneous measurement of hydrogen and oxygen transients by the green alga *Chlorella*. The principle conclusion he came to was that hydrogen and oxygen metabolisms are closely related and they derived from water splitting. Later work by Bishop and Gaffron (1963) indicated that light-dependent evolution of hydrogen appeared to require both photosystems.

Research on photosynthetic hydrogen production as a renewable energy source began in the 1970s (Gibbs, *et al.*, 1973; Lien and San Pietro, 1975, Mitsui *et al.*, 1977). Using the two-electrode technique Bishop *et al.* (1977) measured and interpreted hydrogen and oxygen production from a large group of green algae. However, due to the buildup of hydrogen and oxygen, with subsequent inhibition (*vide infra*) these reactions could be followed for only several minutes. Using a flow system that removed inhibitory oxygen, it was shown (Greenbaum, 1980) that sustained simultaneous photoproduction of hydrogen and oxygen could be observed for hours. In prior experiments using a glucose-glucose oxidase trap, Benemann *et al.* (1973) demonstrated hydrogen production from water by a chloroplast-ferredoxin-hydrogenase system. Measurement of the hydrogen analog of the Emerson and Arnold photosynthetic unit size (Greenbaum, 1977a, b) indicated that photogenerated reductant expressed as molecular hydrogen was derived from the mainstream of the photosynthetic electron transport chain. Direct measurement of the turnover time of photosynthetic hydrogen production (Greenbaum, 1979 and 1982) demonstrated that this parameter was comparable to the turnover time of oxygen production. It was also shown (Greenbaum, 1988) that net conversion efficiencies of 5-10% could be achieved in the linear low-intensity region of the light saturation curve.

Research Problems

The hydrogenase enzyme is synthesized de novo under anaerobic conditions. In normal

photosynthesis carbon dioxide is the preferred electron acceptor for photogenerated reductant from Photosystem I. However, direct kinetic competition between hydrogen evolution and the Calvin cycle can easily be observed (Graves et al. 1989; Cinco et al. 1993). The three scientific research problems associated with photosynthetic hydrogen and oxygen production are (1) oxygen sensitivity of hydrogenase; (2) antenna size, bicarbonate and the light saturation problem; and (3) the minimum number of light reactions required to split water to molecular hydrogen and oxygen.

Oxygen Sensitivity of Hydrogenase

In the application of intact unicellular green algae for hydrogen production one is confronted with the problem of oxygen sensitivity of the hydrogenase enzyme. Hydrogenase is synthesized under anaerobic conditions and, at present, must be kept that way in order to preserve its functionality. In one approach, oxygen and hydrogen by green algae are coproduced in the same volume. Therefore, a way must be found to prevent inhibition of hydrogenase activity by the photosynthetically produced oxygen. This challenging problem is the focus of research at the National Renewable Energy Laboratory (Ghirardi *et al.*, 1997).

Antenna Size, Bicarbonate and the Light Saturation Problem

In full sunlight, ≈ 1000 W/m^2, there exists a kinetic imbalance between the rate of photon excitation of the reaction centers and the ability of the thermally-activated electron transport chains to process photogenerated electrons. Whereas the reaction centers can receive photoexcitations at the rate of ≈ 2000 sec^{-1}, movement through the electron transport chain is of the order of 200 sec^{-1} or less (Gibbs *et al.*, 1973). Therefore, normal photosynthesis saturates at much less that full sunlight, typically $\approx 10\%$.

Since there is little opportunity to increase the rate of thermally-activated electrons through the photosynthetic electron transport chain, an alternate strategy is to reduce the antenna size. Kinetic balance between the rate of photon excitation and rate of photosynthetic electrons can, in principle, be balanced, even at full sunlight, by reducing the absolute antenna size per reaction center. If such a response could be achieved in a real-world system, photosynthetic productivity on a per chlorophyll basis would increase and high solar irradiances would be converted to useful biomass energy. Linearization of the light saturation curve of photosynthesis was demonstrated by Herron and Mauzerall (1972). Melis *et al.* (1998) have demonstrated linearization of the light saturation curve for high-light grown cultures of *Dunaliella*. These results indicate that the concept is technically correct.

An additional complication of the light saturation problem involves the requirement of bicarbonate to optimize electron transport through Photosystem II. Since carbon dioxide/bicarbonate are the exclusive sink for photosynthetically generated reductant they need to be removed so that the flow of electrons produces hydrogen rather than carbon dioxide fixation compounds. Complete removal of carbon dioxide, however, impairs electron transport in Photosystem II and further reduces the saturating light intensity for sustained simultaneous photoproduction of hydrogen and oxygen by about factor of 10. Qualitatively speaking, light saturation occurs at about 10 W/m^2. One strategy to overcome this limitation is to take advantage of the differential affinity of CO_2/bicarbonate between the Photosystem II binding site and the Calvin cycle. Such an approach has been explored by Cinco *et al.* (1993) in which light-activated hydrogen and oxygen evolution as a function of CO_2 concentration in helium were measured for the unicellular green alga *Chlamydomonas reinhardtii*. The concentrations were 58, 30, 0.8 and 0 ppm CO_2. The objective of these experiments was to study the differential affinity of CO_2/HCO_3^- for their respective Photosystem II and Calvin cycle binding sites vis-à-vis photoevolution of molecular oxygen and the competitive pathways of hydrogen photoevolution and CO_2 photoassimilation. The maximum rate of hydrogen evolution occurred at 0.8 ppm CO_2. The key result of this work was that the rate of photosynthetic hydrogen evolution can be increased, at least partially, by satisfying the Photosystem II CO_2/HCO_3^- binding site requirement without fully activating the Calvin-Benson CO_2 reduction pathway. These preliminary experiments suggest that mutants of *Chlamydomonas reinhardtii* that have a genetically engineered low CO_2 affinity for the

Calvin cycle and relatively higher affinity for the PS II CO_2/HCO_3^- binding site may be good candidates to explore for relieving the CO_2 part of the light saturation constraint.

Thermodynamic Driving Pressure of Photosynthetic Hydrogen Production

We have shown that the thermodynamic driving pressure of hydrogen production in the green alga *Scenedesmus* D_3 is equal to or greater that one atmosphere. This was accomplished by measuring the rate of photosynthetic oxygen production by *Scenedesmus* in one-atmosphere of pure hydrogen. The practical significance of this work is that it helps to minimize the amount of pump work required to deliver hydrogen at a useable pressure. At a minimum, the amount of energy saved is $\Delta W = RT\ln(P_{final}/P_{initial})$. Since this is the reversible equilibrium thermodynamic value, the actual value for real gases, including irreversible processes, will be several times this. The amount of energy saved can be calculated to be in the range 68,500 - 114,200 J mol^{-1}. ΔG_P^o for the reaction, $H_2O \rightarrow H_2 + \frac{1}{2}O_2$, is 237,200 J mol^{-1}. Another significant aspect of this result is that it demonstrates for the first time that the oxygen evolution enzyme is insensitive to the presence of high concentrations (*i.e.*, pure) hydrogen. That is to say, unlike the well-known sensitivity of the hydrogenase enzyme to even low concentrations of oxygen, the oxygen evolving complex of photosynthesis is unaffected by the presence of hydrogen. The indirect method of measuring oxygen was necessary because it is experimentally impossible to measure photosynthetically produced hydrogen against a background carrier gas of pure hydrogen since the gas sensitive semiconducting detectors that are used for the hydrogen analysis are saturated in pure hydrogen. Isotopic labeling experiments are currently under way for direct measurement of hydrogen production.

[Note: Much of the text of this abstract has been previously published. Please see E. Greenbaum and J. W. Lee, "Photosynthetic Hydrogen and Oxygen Production by Green Algae: An Overview," in *BioHydrogen*, O. Zaborsky, Ed. pp.235-242 (1998). [Copyright Plenum Press, New York, 1998]

References

Bishop NI and Gaffron H (1963) On the interrelation of the mechanisms for oxygen and hydrogen evolution in adapted algae. In Photosynthetic Mechanisms in Green Plants, B. Kok and A. T. Jagendorf, Eds. (Natl. Acad. Sci.-Natl. Res. Council, Washington, DC), pp. 441-451

Bishop NI, Fricke M, and Jones LW (1977) Photohydrogen production in green algae: water serves as the primary substrate for hydrogen and oxygen production. In Biological Solar Energy Production , A. Mitsui, S. Miyachi, A. San Pietro, and S. Tamura, Eds. (Academic Press, New York) pp. 1-22

Cinco RM, MacInnis JM and Greenbaum E (1993) The Role of Carbon Dioxide in Light-Activated Hydrogen Production by *Chlamydomonas reinhardtii*. Photosyn. Res. 38: 27-33 (1993)

Gaffron H (1960) Energy storage: photosynthesis. In Plant Physiology **IB**: 4-277

Gaffron H and Rubin J (1942) Fermentative and photochemical production of hydrogen in algae. J. Gen. Physiol. 26: 219-240

Ghirardi ML, Togasaki RK and Seibert M (1997) Oxygen sensitivity of algal hydrogen production. Appl. Biochem. Biotech., in press

Gibbs M, Hollaender A, Kok B, Krampitz, LO and San Pietro A (1973) Proceedings of the Workshop on Bio-Solar Conversion, September 5-6, 1973, Betheseda, MD, NSF RANN Grant GI 40253 to Indiana University

Graves DA, Tevault CV and Greenbaum E (1989) Control of Photosynthetic Reductant: The Effect of Light and Temperature on Sustained Hydrogen Photoevolution in *Chlamydomonas* sp. in an Anoxic Carbon Dioxide Containing Atmosphere. Photochem. Photobiol. 50: 571-576

Greenbaum E (1982) Photosynthetic hydrogen and oxygen production: kinetic studies. Science 215: 291-293

Greenbaum E (1977a) The photosynthetic unit size of hydrogen evolution. Science 196: 878-879

Greenbaum E (1977b) The molecular mechanisms of photosynthetic hydrogen and oxygen production. In Biological Solar Energy Production , A. Mitsui, S. Miyachi, A. San Pietro, and S. Tamura, Eds. (Academic Press, New York) pp. 101-107

Greenbaum E (1979) The turnover times and pool sizes of photosynthetic hydrogen production by green algae. Solar Energy 23: 315-320

Greenbaum E (1988) Energetic efficiency of hydrogen photoevolution by algal water splitting. Biophys. J. 54: 365-368

Greenbaum E (1980) Simultaneous photoproduction of hydrogen and oxygen by photosynthesis. Biotechnol. Bioengin. Symp. 10, 1-13

Greenbaum E, Lee JW, Blankinship SL and Tevault CV (1997b) Hydrogen and oxygen production in mutant Fud26 of *Chlamydomonas reinhardtii* Proceedings of the 1997 U.S. DOE Hydrogen Program Review. May 21-23, 1997, Herndon, VA, in press.

Greenbaum E, Lee JW, Tevault CV, Blankinship SL, Mets LJ, and Owens TG (1997a) Photosystem I measurement in mutants B4 and F8 of *C. reinhardtii*. Science 277: 167-168, Nature, in press.

Greenbaum E, Lee JW, Tevault CV, Blankinship SL and Mets LJ (1995) CO_2 Fixation and photoevolution of H_2 and O_2 in a mutant of *Chlamydomonas* lacking Photosystem I. Nature 376: 438-441

Herron HA and Mauzerall D. (1972) The development of photosynthesis in a greening mutant of *Chlorella* and an analysis of the light saturation curve. Plant Physiol. 50: 141-148

Kaltwasser H, Stuart TS and Gaffron H (1969) Light-Dependent Hydrogen Evolution by *Scenedesmus*. Planta (Berlin) 89: 309-322.

Lee JW, Tevault CV, Owens TG and Greenbaum E (1996) Oxygenic photoautotrophic growth without Photosystem I. Science 273: 364-367

Lien S and San Pietro A (1975) An Inquiry into Biophotolysis of Water to Produce Hydrogen, NSF RANN report under grant GI 40253 to Indiana University

Melis A, Neidhardt J, Baroli I, and Benemann, JR (1998) Maximizing photosynthetic productivity and light utilization in microalgae by minimizing the light-harvesting chlorophyll antenna size of the photosystems. These proceedings, in press

Mitsui A, Miyachi S, San Pietro A and Tamura S, Eds. (1977) Biological Solar Energy Production (Academic Press, New York)

Spruit CJP (1958) Simultaneous photoproduction of hydrogen and oxygen by *Chlorella*. Mededel. Landbouwhogeschool (Wageningen/Nederland) 58:1-17

Stuart TS and Gaffron H (1972) The mechanism of hydrogen photoproduction by several algae. Planta (Berlin) 106: 91-100

Stuart TS and Gaffron H (1971) The kinetics of hydrogen photoproduction by adapted *Scenedesmus*. Planta (Berlin) 100: 228-243

PRODUCTION OF HYDROGEN FROM BIOMASS BY PYROLYSIS/STEAM REFORMING

S. CZERNIK, R. FRENCH, C. FEIK, AND E. CHORNET
National Renewable Energy Laboratory
1617 Cole Boulevard, Golden, CO 80401

Keywords: biomass pyrolysis, bio-oil, steam reforming

INTRODUCTION

Hydrogen is the most environmentally friendly fuel that can be efficiently used for power generation. While burning or oxidising it generates steam as the only emission. At present, however, hydrogen is produced almost entirely from fossil fuels such as natural gas, naphta, and inexpensive coal. In such a case, the same amount of CO_2 as that formed from combustion of those fuels is released during hydrogen production stage. Renewable biomass is an attractive alternative to fossil feedstocks because of essentially zero net CO_2 impact. Unfortunately, hydrogen content in biomass is only 6-6.5% compared to almost 25% in natural gas. For this reason, on a cost basis, producing hydrogen by the biomass gasification/water-gas shift process cannot compete with the well-developed technology for steam reforming of natural gas. However, an integrated process, in which biomass is partly used to produce more valuable materials or chemicals with only residual fractions utilised for generation of hydrogen, can be an economically viable option.

The proposed method, which was described earlier[1], combines two stages: fast pyrolysis of biomass to generate bio-oil and catalytic steam reforming of the bio-oil to hydrogen and carbon dioxide. This concept has several advantages over the traditional gasification/water-gas shift technology. First, bio-oil is much easier to transport than solid biomass and therefore, pyrolysis and reforming can be carried out at different locations to improve the economics. A second advantage is the potential production and recovery of higher value added co-products from bio-oil that could significantly impact the economics of the entire process. In this concept, the lignin-derived fraction would be separated from bio-oil and used as a phenol substitute in phenol-formaldehyde adhesives while the carbohydrate-derived fraction would be catalytically steam reformed to produce hydrogen. Assuming that the phenolic fraction could be sold for $0.44/kg (approximately half of the price of phenol), the estimated cost of hydrogen from this conceptual process would be $7.7/GJ[2], which is at the low end of the current selling prices.

In previous years we demonstrated, initially through micro-scale tests then in the bench-scale fixed-bed reactor experiments[3] that bio-oil model compounds as well as its carbohydrate-derived fraction can be efficiently converted to hydrogen. Using commercial nickel catalysts the hydrogen yields obtained approached or exceeded 90% of those possible for stoichiometric conversion. The carbohydrate-derived bio-oil fraction contains a substantial amount of non-volatile compounds (sugars, oligomers) which tend to decompose thermally and carbonize before contacting the steam reforming catalyst. Even with the large excess of steam used, the carbonaceous deposits on the catalyst and in the reactor freeboard limited the reforming time to 3-4 hours. For this reason we decided to employ fluidized bed reactor configuration that should overcome at least some limitations of the fixed-bed unit. Even if carbonization of the oil cannot be avoided, still the bulk of the fluidizing catalyst would be in contact with the oil droplets fed to the reactor. Catalyst regeneration can be done by steam or carbon dioxide gasification of carbonaceous residues in a second fluidized bed reactor providing additional amounts of hydrogen.

EXPERIMENTAL

The bio-oil was generated from poplar wood using the NREL fast pyrolysis vortex reactor system[4]. The oil was comprised of 46.8% carbon, 7.4% hydrogen, and 45.8% oxygen with water content of 19%. It was separated into aqueous (carbohydrate-derived) and organic (lignin-derived) fractions by adding water to the oil at a weight ratio of 2:1. The aqueous fraction (55%

of the whole oil) contained 22.9% organics ($CH_{1.34}O_{0.81}$) and 77.1% water.

U91, a commercial nickel-based catalyst used for steam reforming of natural gas, was obtained from United Catalysts and ground to the particle size of 300-500μ.

The aqueous solution was steam reformed using a bench-scale fluidized bed reactor shown in Figure 1. The two-inch-diameter inconel reactor supplied with a porous metal distribution plate was placed inside a three-zone electric furnace. The reactor contained 150-200g of commercial nickel-based catalyst from United Catalysts ground to the particle size of 300-500μ. The catalyst was fluidized using superheated steam, which is also a reactant in the reforming process. Steam was generated in a boiler and superheated to 750 C before entering the reactor at a flow rate of 2-4 g/min. Liquids were fed at a rate of 4-5 g/min using a diaphragm pump. Specially designed injection nozzle supplied with a cooling jacket was used to spray liquids into the catalyst bed. The temperature in the injector was controlled by a coolant flow and maintained below the feed boiling point to prevent evaporation of volatile and deposition of nonvolatile components. The product collection line included a cyclone that captured fine catalyst particles and, possibly, char generated in the reactor and two heat exchangers to condense excess steam. The condensate was collected in a vessel whose weight was continuously monitored. The outlet gas flow rate was measured by a mass flow meter and by a dry test meter. The gas composition was analyzed every 5 minutes by a MTI gas chromatograph. The analysis provided concentrations of hydrogen, carbon monoxide, carbon dioxide, methane, ethylene, and nitrogen in the outlet gas stream as a function of time of the test. The temperatures in the system as well as the flows were recorded and controlled by the G2/OPTO data acquisition and control system.

The measurements allowed to determine total and elemental balances as well as to calculate the yield of hydrogen generated from the biomass-derived liquid feed.

RESULTS AND DISCUSSION

The overall steam reforming reaction of any oxygenated organic compound can be presented as follows:

$$C_nH_mO_k + (2n-k)H_2O = nCO_2 + (2n+m/2-k)H_2$$

Thus the maximum (stoichiometric) yield of hydrogen is 2+m/2n-k/n moles per mole of carbon in feed. The steam reforming experiments in the fluidized bed reactor were carried out at the temperature of 800°C and 850°C. The steam to carbon ratio was held at 7-9 while methane-equivalent gas hourly space velocity $G_{C1}HSV$ was in the range of 1200-1500 h^{-1}. At 800°C a slow decrease in the concentration of hydrogen and carbon dioxide and an increase of carbon monoxide and methane in the gas generated by steam reforming of the carbohydrate-derived oil fraction was observed. These changes resulted from a gradual loss of the catalyst activity, probably due to coke deposits. As a consequence of that, the yield of hydrogen produced from the oil fraction decreased from the initial value of 95% of stoichiometric (3.24 g of hydrogen from 100 g of feed) to 77% after 12 hours on stream. If a water-gas shift reactor followed the reformer the hydrogen yields would increase to 99% and 84% respectively. During eight hours of reforming at 850°C, the product gas composition remained constant, as presented in Figure 2. This indicates that no catalyst deactivation was observed throughout the run time. The yield of hydrogen produced from the bio-oil fraction was approximately 90% of that possible for stoichiometric conversion. It would be greater than 95% if carbon monoxide underwent the complete shift reaction with steam. Only small amounts of feed were collected as char in the cyclone and condensers, and little or no coke was deposited on the catalyst.

CONCLUSIONS

We successfully demonstrated that hydrogen could be efficiently produced by catalytic steam reforming carbohydrate-derived bio-oil fraction using a commercial nickel-based catalyst in a fluidized bed reactor. Greater steam excess than that used for natural gas reforming was necessary to minimize the formation of char and coke (or to gasify these carbonaceous solids) resulting from thermal decomposition of complex carbohydrate-derived compounds.

At 850°C with a steam to carbon ratio of 9 the hydrogen yield was 90% of that possible for stoichiometric conversion during eight hours of the catalyst on-stream time. This yield could be 5-7% greater if a secondary water-gas shift reactor followed the reformer.

Coke deposits were efficiently removed from the catalyst by steam and carbon dioxide gasification, which restored the initial catalytic activity.

ACKNOWLEDGMENTS

The authors are thankful to the U.S. Department of Energy Hydrogen Program, managed by Mr. Neil Rossmeissl and Ms. Catherine Gregoire-Padró, for financial support of this work.

REFERENCES

1. D. Wang, S. Czernik, D. Montané, M. Mann, and E. Chornet, I&EC Research, 36 (1997) 1507.
2. M.K. Mann, P.L. Spath, K. Kadam, In Proceedings of the 1996 U.S. DOE Hydrogen Program Review, Miami, FL, May 1-2, 1996, NREL/CP-430-21968; pp. 249-272.
3. D. Wang, S. Czernik, and E. Chornet, Energy&Fuels, 12 (1998) 19.
4. J.W. Scahill, J. Diebold, C.J. Feik, In Developments in Thermochemical Biomass Conversion, A.V. Bridgwater and D.G.B. Boocock (eds.), Blackie Academic&Professional, London 1997, pp.253-266.

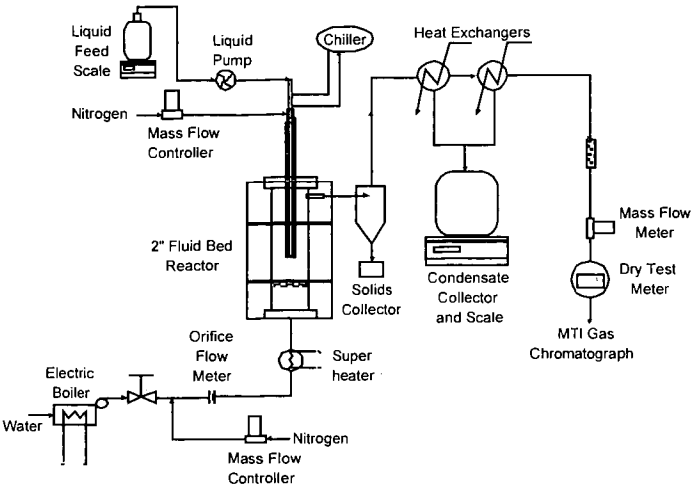

Figure 1. Schematic of the 2" fluidized bed reactor system

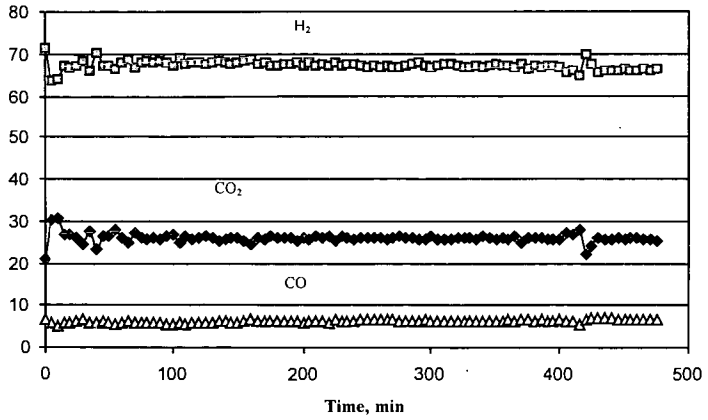

Figure 2. Reforming Gas Composition

DEVELOPMENT OF POROUS CERAMIC MEMBRANES FOR A SOLAR THERMAL WATER-SPLITTING REACTOR

Abraham Kogan

Solar Research Facilities Unit, The Weizmann Institute of Science, P.O. Box 26, Rehovot 76100, Israel

The efficiency of hydrogen production by solar thermal water splitting (HSTWS) depends strongly on reactor temperature. The process must be conducted at least at about 2100 °C, in order to be of practical significance. Stabilized zirconia, with a maximum useful temperature of 2300 °C, is a suitable HSTWS reactor construction material. A crucial element in the solar thermal water-splitting reactor is the porous ceramic membrane that enables separation of hydrogen from the hot water splitting reaction products. Zirconia porous membranes are manufactured by powder sintering at about 1800 °C. When such a membrane is exposed in the solar reactor to a higher temperature, it looses its gas permeability due to pore closure by continued sintering. Efforts were made to inhibit the membrane sintering process and to postpone its fast occurrence to higher temperatures, by the use of special stabilized zirconia powders consisting of particles with a rounded shape. The fast sintering of membrane samples made of a homogeneous powder of relatively large spherical particles, prepared by the Sol-Gel method, occurred at some 200 °C above the normal zirconia sintering temperature. The overall picture gathered from our experiments suggests, however, that it will be hardly possible to bridge the temperature gap between the normal sintering temperature of stabilized zirconia and the HSTWS reactor temperature, by the use of stabilized zirconia powders of a particular morphology.

Keywords: solar hydrogen production; zirconia membranes; microspherical powder ceramics.

Introduction

Water vapor can be dissociated by exposure to a high temperature at reduced pressure. In the hydrogen production process by solar thermal water splitting (HSTWS), water vapor is heated by highly concentrated solar radiation and is partially dissociated. Hydrogen is separated from the hot mixture of water dissociation products by gas diffusion. Part of the gas mixture is extracted from the reactor cavity by diffusion through a porous ceramic membrane. It is enriched with hydrogen. The oxygen-enriched gas mixture leaves the reactor cavity bypassing the porous membrane (1).

The thermodynamic efficiency of a HSTWS reactor increases with increasing reactor temperature. The results of an extensive computer simulation study indicate that a temperature of at least 2100 °C must be maintained in the reactor, for the process to be of practical value (2). The inner structural components of the reactor can be manufactured from stabilized zirconia, a material that exhibits chemical, mechanical and thermal stability and fair thermal shock resistance up to 2300 °C. The porous ceramic membrane utilized for hydrogen separation by gas diffusion presents, however, a special problem. Porous ceramic membranes are obtained by sintering powders at a high temperature. Zirconia powders are sintered at 1700–1800 °C. When a porous zirconia membrane is subject to a temperature exceeding its normal sintering temperature, the sintering process continues resulting in loss of gas permeability, due to membrane densification and pore closure (1).

In an effort to develop zirconia porous membranes useful for our application, we tried to inhibit the sintering process and to postpone its fast occurrence to temperatures beyond the working temperature of the HSTWS reactor, by the use of special zirconia powders consisting of particles with a rounded shape. The results of this study are reported below.

Experimental Procedure and Results

Composition of Powders for Membrane Sample Preparation. The fast clogging of a porous zirconia membrane exposed to an elevated temperature is illustrated by the two SEM × 500-magnification photographs of Figure 1. These photographs were taken after 2 h and 22 h of exposure to 1750 °C, respectively. The membrane sample shown in Figure 1 was made of a CaO-stabilized zirconia powder that was prepared by repeated pelletization, calcining at 1600 °C for 24 h, milling and collection of the relatively coarse particle powder.

Dr. R. Fischer, of the Israel Ceramics and Silicates Institute (ICSI), Haifa, Israel, suggested that the fast sintering of zirconia membranes, made of powders consisting of quasi-spherical or of spherical particles, would be hindered and delayed to higher temperatures. We solicited the collaboration of ICSI in the development of porous membranes characterized by improved stability with respect to pore closure at high temperature.

In order to determine the stabilized zirconia composition suitable for our purpose, ICSI prepared samples of zirconia powder doped with 5.6, 8 and 12% yttria. They were sintered at 1700 °C for 5 h. Subsequently, they were exposed in a solar furnace to 1900 °C for 1.5 h. The ZY-8 and ZY-12 ceramic samples preserved their original shape, whereas the ZY-5.6 sample disintegrated into powder. An XRD analysis of the heat-treated samples showed that the ZY-8 and ZY-12 ceramics were monophase tetragonal and cubic, respectively, while the ZY-5.6 ceramic underwent partial tetragonal-monoclinic phase transition. Obviously, phase transition is the cause of the sample destruction.

The ZY-8 composition was chosen as the basic material for the preparation of stabilized zirconia samples.

We obtained from ICSI two series of stabilized zirconia membranes for the experiment. One series consisted of samples made of spheroidal particle powders. The powders utilized in the preparation of the second series of samples consisted of homogeneous spherical particles obtained by the Sol-Gel method.

Membranes Made of Spheroidal Particle Powders. The particle-size range of powders used in the preparation of the first series of membrane samples is listed in Table 1. The samples were sintered at 1850 °C for 1 h. They were then fired at 1700 °C for 33.7 h in an electric furnace. All these samples were cracked after the firing.

The features of the membrane microstructure degradation, following the 1700 °C/33.7-h firing period, are depicted in Figures 2–4.

The SEM × 5000-magnification picture of a membrane particle (Figure 2a) was taken after a 1850 °C/1-h sintering. The particle consists of 1–5-μm granules. After the additional firing at 1700 °C/33.7-h (Figure 2b), the big granules grew bigger by diffusion of material from smaller neighboring granules. The granule mean linear size grew more than twofold. Small cracks developed between adjacent granules. At the SEM × 500-magnification level (Figure 3a,b), it is observed that as a result of the prolonged additional firing, clusters of particles are formed by interparticle bridges. The clustering process implies apparently stress generation between neighboring clusters, which leads to initiation of fissures (Figure 3b). The SEM × 50-magnification picture (Figure 4) exhibits mature cracks across the sample.

Membranes Made of Spherical Particle Powders. The Sol-Gel process of ceramic powder production eliminates milling and granulation operations. This method enables production of free flowing powders consisting of homogeneous microspheres of a predetermined size. Low sinterability of these powders was expected, in view of their morphology.

In the second series of membrane samples, prepared at ICSI from 8% yttria-stabilized zirconia powders by the Sol-Gel method, the main variable was the diameter of the powder particle. Membrane samples were prepared from microspherical particle powders, the particle diameter varying at the range 25 μm ≤ d ≤ 50 μm. The samples were sintered for 5 h at 1700–1750 °C. Then they were fired in the solar furnace at higher temperatures.

Table 1. Spheroidal Particle Powders

Powder designation	Particle morphology	Particle size (μm)
FZ1	Spheroidal	35–45 + submicron fines
FZ2	Spheroidal	95–110 (50%) + 15–30 (50%)
FZ3	Spheroidal	22–44 (no fines)
FZ4	Spheroidal	10–20 (no fines)
FZ1'	Spheroidal	As FZ1 – with a fraction at the 15–20 range
JZ1	Spheroidal – with improved sphericity	20–44
JZ3	Spheroidal – with improved sphericity	53–63
JZ2	Spheroidal – with improved sphericity	63–74
JZ2	Spheroidal – with improved sphericity	> 74
JZ4	Spheroidal – with improved sphericity	< 20
A3	Non-spherical	3

Figure 5a is a SEM × 500-magnification picture of a sample made of a powder of d ≤ 25-μm particles sintered at 1750 °C for 5 h. After an additional treatment at 1900 °C/1.5 h + 1980 °C/1.5 h, the porous structure of the sample was completely destroyed (Figure 5b). By contrast, another sample made from a d ≥ 50-μm powder emerged from the same heat treatment sequence with almost unchanged open porosity (OP ≈35%) (Figure 5c). A similar heat treatment "surviving" sample made of a d = 35-μm powder was exposed to an additional 1750 °C/33.7-h firing in an electric furnace. It still preserved its porous structure, but some of the microspherical particles were split (Figure 6).

Conclusions

Our attempts to develop porous membranes from stabilized zirconia that undergo fast sintering at temperatures much higher than the normal zirconia sintering temperature met only with partial success. With membrane samples made of a homogeneous powder of relatively large spherical particles, prepared by the Sol-Gel method, we were able to demonstrate considerable retardation (~ 200 °C) of membrane blocking up by sintering.

The overall picture gathered from our experience suggests, however, that it will be hardly possible to bridge the ca. 500 °C gap between the normal sintering temperature of stabilized zirconia and the reactor operating temperature by powder doping or by the use of powders of special particle morphology.

Besides metal oxides, there are other refractory materials that melt and sinter at extremely high temperatures, as seen in Table 2. We were reluctant to consider the utilization of membranes made from these materials, because we foresaw that they would undergo chemical attack in the presence of the water splitting reaction products. When this issue was brought up during a discussion with Dr. P. Bardham, Head of the Cellular Ceramics Division at Corning Corporation, he observed that some of the above-mentioned materials, when exposed to HSTWS working conditions, might develop a thin protective layer that would prevent their disintegration by chemical attack.

Efforts will be made to obtain samples of such materials and test them at HSTWS reactor working conditions.

Table 2. Some High Melting Point Ceramics

Carbides	Melting point (°C)	Borides	Melting point (°C)	Nitrides	Melting point (°)
TiC	3160	TiB	2980	TiN	2930
ZrC	3030	ZrB	3040	ZrN	2980
HfC	3890	HfB	3100	HfN	3310

Acknowledgment. This study was supported by the Heineman Foundation for Research, Education, Charitable and Scientific Purposes, Inc., Rochester, NY. The author gratefully acknowledges the generous support of the Foundation. Thanks are expressed to the staff of ICSI, who supplied the ceramic samples for the experiments.

References

(1) Kogan, A. Direct solar thermal splitting of water and on-site separation of the products. II. Experimental feasibility study. *Int. J. Hydrogen Energy* **1998**, *23*, 89–98.

(2) Kogan, A. Direct solar thermal splitting of water and on-site separation of the products. I. Theoretical evaluation of hydrogen yield. *Int. J. Hydrogen Energy* **1997**, *22*, 481–486.

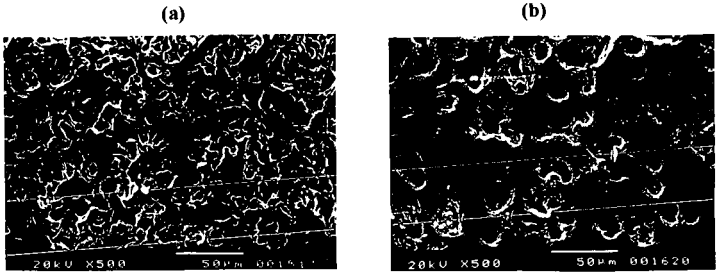

Figure 1. ZY-8-stabilized zirconia porous membrane from (-100/+325) powder. (a) After 1750 °C/2 h. (b) After 1750 °C/22 h.

Figure 2. FZ1 + A3 membrane – SEM × 5000. (a) After 1850 °C/1 h. (b) After 1850 °C/1 h + 1700 °C/33.7 h.

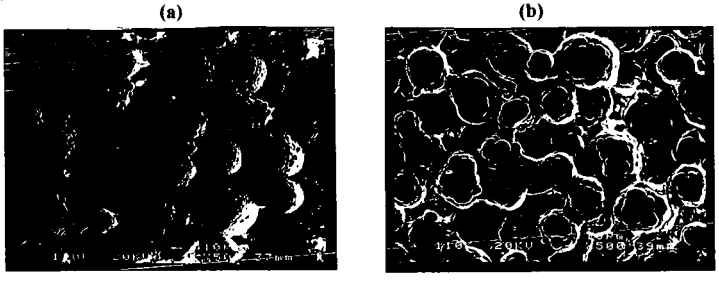

Figure 3. FZ1 + A3 membrane – SEM × 500. (a) After 1850 °C/1 h. (b) After 1850 °C/1 h + 1700 °C/33.7 h.

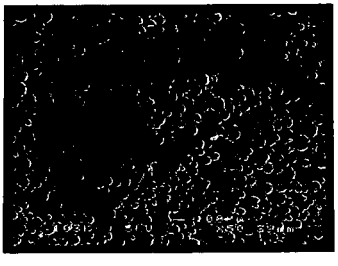

Figure 4. FZ2 + A3 membrane – SEM × 50. After 1850 °C/1 h + 1700 °C/33.7 h.

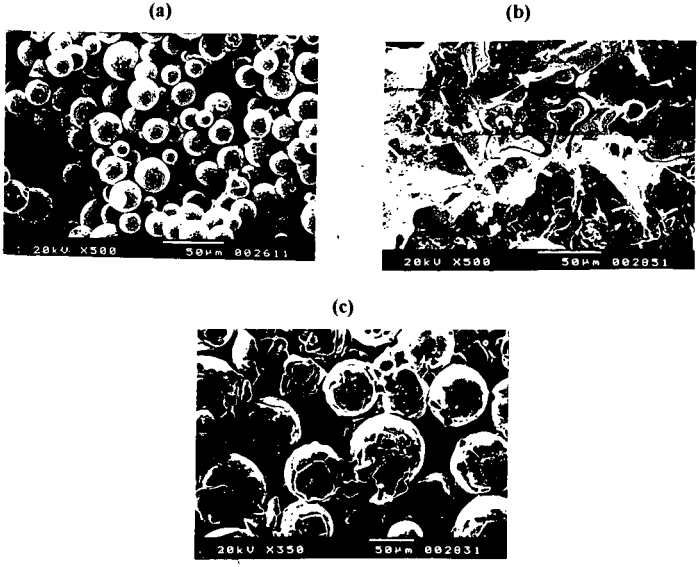

Figure 5. Membrane from Sol-Gel powder. (a) $d \leq 25$ µm particles, 1750 °C/5 h. (b) $d \leq 25$ µm, 1750 °C/5h + 1900 °C/1.5 h + 1980 °C/1.5 h. (c) $d \geq 50$ µm, 1750 °C/5h + 1900 °C/1.5 h + 1980 °C/1.5 h.

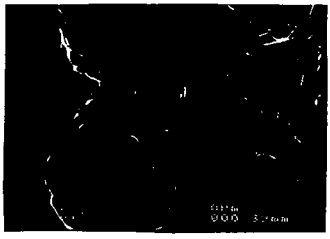

Figure 6. Membrane from Sol-Gel powder – d = 35 µm, 1750 °C/5 h + 1900 °C/1.5 h + 1980 °C/1.5 h + 1750 °C/33.7 h.

AN ULTRASAFE HYDROGEN GENERATOR: AQUEOUS, ALKALINE BOROHYDRIDE SOLUTIONS AND Ru CATALYST

Steven C. Amendola, Stefanie L. Sharp-Goldman, M. Saleem Janjua,
Michael T. Kelly, Phillip J. Petillo, and Michael Binder

MILLENNIUM CELL LLC
8 Cedar Brook Drive
Cranbury NJ 08512
(732) 249-3250 ext 230
e-m@il: steven @ amendola.com

ABSTRACT

A novel, simple, convenient, and safe, chemical process generates high purity hydrogen gas on demand from stable, aqueous solutions of sodium borohydride, $NaBH_4$, and ruthenium based (Ru), catalyst. When $NaBH_4$ solution contacts Ru catalyst, it spontaneously hydrolyzes to form H_2 gas and sodium borate, a water-soluble, inert salt. When H_2 is no longer required, Ru is removed from the solution and H_2 generation stops. Since this H_2 generator is safer, has quicker response to H_2 demand, and is more efficient, than commonly used H_2 generators, it is ideal for portable applications.

INTRODUCTION

PEM fuel cells are attractive power sources for providing clean energy for transportation and personal electronics applications where low system weight and portability are important. For powering these systems, H_2 gas is the environmentally desirable anodic fuel of choice since only water is formed as a discharge product. A major hurdle is how to generate/store controlled amounts of H_2 fuel directly without resorting to high temperature reformers with significant heat signatures or bulky, pressurized cylinders.

Background of the Borohydride H_2 Generator

Our safe, portable H_2 generator overcomes these problems by using aqueous, alkaline, sodium borohydride ($NaBH_4$, tetrahydroborate) solutions which are extremely stable. However, as found by Schlesinger et al. (1), in the presence of selected metal (or metal boride) catalysts, this solution hydrolyzes to yield H_2 gas and water-soluble, sodium metaborate, $NaBO_2$.

$$NaBH_4 + 2\,H_2O \xrightarrow[\text{catalyst}]{} 4\,H_2 + NaBO_2 \qquad [1]$$

This hydrolysis reaction occurs at different rates depending on the catalyst used and its preparation method. Levy et al. (2) and Kaufman and Sen (3) investigated cobalt and nickel borides as catalysts for practical, controlled generation of H_2 from $NaBH_4$ solutions. We studied ruthenium (Ru) based catalyst supported on ion exchange resin beads. Using Ru is based on the work of Brown and Brown (4), who investigated various metal salts and found that ruthenium and rhodium salts liberated H_2 most rapidly from borohydride solutions. We chose Ru because of its lower cost. Ru catalysts are not consumed during hydrolysis and are reusable. We have designed our system so that reaction [1] is either self- regulating or carefully controllable. To generate H_2, $NaBH_4$ solution is allowed to flow onto a Ru catalyst, or $NaBH_4$ solution is injected onto Ru catalyst. This ensures fast response to H_2 demand i.e. H_2 is generated only when $NaBH_4$ solution contacts Ru catalyst. When H_2 is no longer needed, $NaBH_4$ solution is removed from Ru catalyst and H_2 production ceases. With molecular weights of $NaBH_4$ (38) and 2 H_2O (36), forming $4H_2$ (8), reaction [1] has a H_2 storage efficiency of 8/74 = 10.8%.

In addition to H_2, the other discharge product, $NaBO_2$, commonly found in laundry detergents, is safe. Unlike phosphates, borates are not environmentally hazardous in water supplies. Table 1 compares operational and safety features of generating H_2 via base-stabilized $NaBH_4$ solutions and via reactive chemical hydrides. Our generator is considerably safer/more efficient than producing H_2 via other reactive chemicals. The heat generated by our system (75 kJ/mole H_2 formed), is less than what is produced by other hydrides (>125 kJ/mole H_2), and ensures a safe, controllable chemical reaction.

The total amount of H_2 produced by reaction [1] depends on $NaBH_4$ solution volume and concentration. H_2 generation rates are primarily a function of Ru catalyst active surface area. H_2 pressure/flow rates can be accurately controlled and made self-regulating by numerous feedback

mechanisms. An added attribute of our generator is that generated H_2 gas also contains water vapor. Since prehumidified H_2 is needed in PEM fuel cells, $NaBH_4$ based H_2 generators should increase PEM fuel cell performance.

Experimental

Ru catalyst supported/dispersed on anionic exchange resin beads was prepared by ion exchange. Appropriate amounts of $RuCl_3$-$3H_2O$ were dissolved in deionized water and acidified with HCl to convert $RuCl_3$ into $[RuCl_6]^{-3}$.This H_3RuCl_6 solution was added to a weighed amount of anionic and cationic exchange resin beads which had been previously washed and dried at 50°C. The resulting slurry was allowed to stand at ambient temperature for 24 hours while stirring at regular intervals to maintain uniformity. The slurry was then dried by evaporation at 50°C. After drying, H_3RuCl_6, now impregnated in the resin, was reduced by addition of 20% $NaBH_4$, 15% NaOH, 65% H_2O solution. As prepared, our catalyst may be either metallic Ru or Ru boride of the form Ru_2B. The black, Ru coated resin beads were washed, dried, and separated with a 40 mesh sieve. Ru loadings were ~5% by weight.

In typical H_2 generation experiments ~30 ml of 20%$NaBH_4$ solution containing 10% NaOH was thermostated in a sealed flask fitted with an outlet tube for collecting evolved H_2 gas. Ru coated resin beads, were placed in a stainless steel screen container and dropped into the solution to begin H_2 generation. $NaBH_4$ solution could contact Ru catalyst through the screen, H_2 could exit, while lightweight resin beads were prevented from floating to the top of the solution. Although solutions were thermostated, temperatures near the catalyst were certainly higher due to the exothermic reaction. The outlet tube exhaust was placed under an inverted, water filled, graduated cylinder situated in a water-filled tank. Generated H_2 was measured by monitoring water displaced from the graduated cylinder as the reaction proceeded.

Results and Discussions

We evaluated anionic and cationic exchange resin beads as catalyst supports for Ru catalyst. Table 2. lists normalized H_2 generation rates for various ion exchange resin beads. Catalyst supports were evaluated based on their H_2 generation rates in liters H_2 generated/sec.-gram catalyst. This convenient standard meaningfully compares catalyst supports in our system because Ru catalyst performances are normalized with respect to catalyst weight. Table 2 illustrates that for catalytically generating H_2 from $NaBH_4$ solutions with ~5% Ru supported on ion exchange resins, anionic resins are better than cationic resins. A-26 and IRA-400 (Rohm and Haas) anion exchange resins when used as supports for Ru gave the highest H_2 generation rates.

Figure 1 plots H_2 volumes generated as a function of time for ~0.25 grams combined weight of Ru supported on IRA 400 anion exchange resin beads immersed in 20% $NaBH_4$, 10% NaOH, and 70% H_2O (wt %) solution at various temperatures. Volumes of H_2 generated by Ru catalyzed $NaBH_4$ hydrolysis increased linearly with time:

$$-4d[NaBH_4]/dt = d[H_2]/dt = k \qquad [2]$$

Under our experimental conditions of relatively high $[BH_4^-]$ and low catalyst weights (and surface area), k is constant for a given temperature. This example of zero order kinetics implies that the first step in reaction [1] involves a surface reaction, most likely BH_4^- adsorption on Ru catalyst. We have observed zero order kinetics for $NaBH_4$ hydrolysis even at $[NaBH_4]$ as low as 0.1%. Catalyzed $NaBH_4$ hydrolysis ultimately depends on $NaBH_4$. It would therefore not be surprising if diffusion controlled, first order kinetics dominates at very low $[NaBH_4]$ and/or high catalyst weights where catalyst sites are not totally occupied. From the data in Fig. 1., an activation energy for Ru catalyzed hydrolysis of $NaBH_4$ (obtained by plotting log [H_2 generation rate] vs. reciprocal absolute temperature, 1/T), was computed to be 47 kJ $mole^{-1}$. This value compares with activation energies found (3) for $NaBH_4$ hydrolysis catalyzed with other metals: 75 kJ $mole^{-1}$ for Co, 71 kJ $mole^{-1}$ for Ni, and 63 kJ $mole^{-1}$ for Raney Ni.

As reaction [1] proceeds, $NaBO_2$ eventually exceeds its solubility limit and precipitates out of solution. We were concerned that this solid may block catalyst sites thereby affecting subsequent H_2 generation rates. To test this, 5 ml. of $NaBH_4$ solution was catalytically hydrolyzed to completion and the total generated H_2 measured. Although H_2 generation rates slowed as the reaction proceeded, nevertheless, >70% of the stoichiometric amount of H_2 was generated based on the amount of $NaBH_4$ in solution. This indicated that reaction [1] is quite efficient and that $NaBO_2$ precipitation at these concentrations/conditions does not seriously interfere with catalyst operation. If water generated by PEM fuel cells could be returned to $NaBH_4$ solutions, additional H_2 could be generated because $NaBO_2$ would remain in solution.

We can estimate achievable power levels from our H_2 generator. Assuming a standard PEM fuel cell operates at ~0.7V, generating 1 gram H_2/min is equivalent to 26.8 A-hr X 60 min/hr X 0.7V X 1/min = 1125 watts, i.e. 1liter H_2/minute can power a 100W fuel cell. Since ~5% of the 0.25 grams of our total catalyst weight was active Ru, Figure 1 illustrates that our H_2 generator produced the equivalent of ~ 0.3kW per gram Ru catalyst at 25°C and ~ 2kW/gram Ru catalyst at 55°C! Greater H_2 generation rates (and power levels) are expected for higher Ru loadings.

Prototypes of our H_2 generator have been used to power a commercial 35 watt H_2/air PEM fuel cell. For applications requiring long-term operation, H_2/air PEM fuel cells together with a $NaBH_4$ H_2 generator is considerably more advantageous than using rechargeable batteries. Our $NaBH_4$ generator can be quickly refueled by simply filling the reservoir with fresh $NaBH_4$ solution (the Ru catalyst is reusable).

Conclusions

Stabilized $NaBH_4$ solutions are an effective source for producing H_2. Due to system simplicity ($NaBH_4$ solution simply contacts Ru to produce H_2), it can be used for numerous applications where H_2 gas is used e.g. PEM fuel cells. High H_2 generation rates have been achieved from $NaBH_4$ solutions with tiny amounts of Ru supported on anion exchange resins. Optimizing catalyst loading, supports, and [$NaBH_4$], will lead to greater H_2 generation rates.

Acknowledgements

We thank Mike Strizki of the NJ Department of Transportation for constant encouragement and many enlightening technical suggestions. Kudos to Martin M. Pollak and Jerome I. Feldman of GP Strategies Inc. for their unfailing enthusiasm and constant support throughout this effort. We are grateful to Andersen-Weinroth for their interest and continued support. This research was partially funded by the State of New Jersey Commission on Science and Technology.

References

1. H.I.Schlesinger, H.C.Brown, A.E.Finholt, J.R.Gilbreath, H.R.Hockstra and E.K. Hyde, "New Developments in the Chemistry of Diborane and the Borohydrides", Journal of the American Chemical Society, 75, 215 (1953).

2. A. Levy, J.B. Brown, and C.J. Lyons, "Catalyzed Hydrolysis of Sodium Borohydride", Industrial and Engineering Chemistry 52,-211(1960).

3. C.M. Kaufman and B. Sen, "Hydrogen Generation by Hydrolysis of Sodium Tetrahydroborate: Effects of Acids and Transition Metals and Their Salts", Journal of the Chemical Society, Dalton Trans. 307 (1985).

4. H.C. Brown and C.A. Brown, "New, Highly Active Metal Catalysts for the Hydrolysis of Borohydride", Journal of the American Chemical Society, 84,1493(1962).

Table 1. Comparison between generating H_2 by chemical hydrides and by aqueous borohydride solutions.

PARAMETERS	CONVENTIONAL CHEMICAL HYDRIDE	BOROHYDRIDE
System	Water dripping on solid hydride	Borohydride solution contacting catalyst
Theoretical H_2 Storage	<10%	10.8%
H_2 contaminants	Possibly CO and CO_2 (from binders) Possibly SO_2 or NO (from acids)	None expected
Heat generated	Excessive	Moderate
Components carried	Water and dry hydride	Borohydride solution and catalyst
What limits H_2 generation rate?	Rate at which water drips on solid hydride	Surface area of catalyst
What determines total H_2 produced?	Amount of solid hydride	Amount of borohydride solution
H_2 source	Water +Solid	Solution + Catalyst
Is reactant moisture sensitive?	Yes	No
Technical roadblocks	Solids tend to cake. Binders are needed to hold solids together	?
If too much liquid enters cell	Violent reaction	Reaction rate is limited by catalyst surface area.

Table 2. Rate of H_2 generated catalytically per gram of catalyst (Ru + support resin) for various anionic and cationic support resins in 20% $NaBH_4$,10% NaOH, 70% H_2O solution at 25°C. All catalysts had ~5% Ru loading.

Ru Resin Support	Time to generate 1 liter H_2 gas (seconds)	Weight of Ru + support (grams)	Liters H_2/sec. per gram catalyst X 10^3
ANIONIC RESINS			
A-26	1161	0.2563	336
A-26	633	0.5039	313
IRA-400	1173	0.2565	332
IRA-400	773	0.4116	314
IRA-900	1983	0.2555	197
Dowex 550A	672	0.7692	193
Dowex MSA-1	791	0.7691	164
Dowex MSA-2	1028	0.7691	126
A-36	1415	0.2550	111
CATIONIC RESINS			
MSC-1B	2351	0.2592	164
Dowex HCR-W2	895	0.7631	146
MSC-1A	1382	0.5054	143
Amberlyst 15	2871	0.2563	136
Amberlyst 15	1324	0.5054	149
Dowex 22	1818	0.7678	72
Dowex 88	6163	0.2556	63

Figure 1. Volume of H_2 generated as a function of time by 5% Ru supported on IRA 400 anion exchange resin in 20% $NaBH_4$,10% NaOH, 70% H_2O solution at various temperatures.

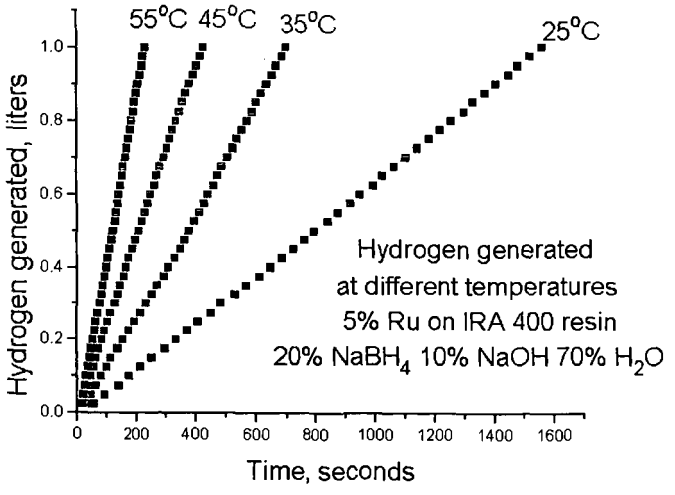

SUSTAINABLE HYDROGEN FOR THE HYDROGEN ECONOMY

Ronald W. Breault, Andrew W. McClaine, Jonathan Rolfe, and Christopher Larsen
Thermo Power Corporation
Waltham, MA 02454-9046

INTRODUCTION

Hydrogen has immense potential as an efficient and environmentally-friendly energy carrier of the future. It can be used directly by fuel cells to produce electricity very efficiently (> 50%) and with zero emissions. Ultra-low emissions are also achievable when hydrogen is combusted with air to power an engine or to provide process heat, since the only pollutant produced, NO_X, is then more easily controlled. To realize this potential, however, cost-effective methods for producing, transporting, and storing hydrogen must be developed.

Thermo Power Corporation has developed a new approach for the production, transmission, and storage of hydrogen. In this approach, a chemical hydride slurry is used as the hydrogen carrier and storage media. The slurry protects the hydride from unanticipated contact with moisture in the air and makes the hydride pumpable. At the point of storage and use, a chemical hydride/water reaction is used to produce high-purity hydrogen. An essential feature of this approach is the recovery and recycle of the spent hydride at centralized processing plants, resulting in an overall low cost for hydrogen. This approach has two clear benefits: it greatly improves energy transmission and storage characteristics of hydrogen as a fuel, and it produces the hydrogen carrier efficiently and economically from a low-cost carbon source.

Our preliminary economic analysis of the process indicates that hydrogen can be produced for $3.85 per million Btu, based on a carbon cost of $1.42 per million Btu and a plant sized to serve a million cars per day. This compares to current costs of approximately $9.00 per million Btu to produce hydrogen from $3.00 per million Btu natural gas, and $25 per million Btu to produce hydrogen by electrolysis from $0.05 per Kwh electricity. The present standard for production of hydrogen from renewable energy is photovoltaic-electrolysis at $100 to $150 per million Btu.

The overall objective of the current project is to investigate the technical feasibility and economic viability of the chemical hydride (CaH_2 or LiH) organic slurry approach for transmission and storage of hydrogen with analysis and laboratory-scale experiments, and to demonstrate the critical steps in the process with bench-scale equipment. Specific questions which have been addressed in work to date include:

- What is the formulation and physical properties of slurries that meet the energy density criteria?
- What are the organics that can be used to form the slurry?
- What are the conditions required for hydrogen generation?
- What are the properties of the slurry after hydrogen generation?
- What is the projected efficiency and cost of hydrogen production?

DISCUSSION

The way in which the metal hydride/water reaction would be used in a closed loop system for the storage and transmission of hydrogen is illustrated in Figure 1. The process consists of the following major steps: (1) slurrying the metal hydride with a liquid carrier and transporting it to the point(s) of use, (2) generating hydrogen on demand from the metal hydride/liquid carrier slurry at the point of use by adding water and then transporting the resulting metal hydroxide/liquid slurry back to the hydride recycle plant, and (3) drying, separating, and recycling the metal hydroxide to the metal hydride at the centralized recycle plant and returning the liquid carrier for reuse.

A variety of metal hydrides react with water at ambient temperature to produce high purity hydrogen. Examples of reactions are:

$$CAH_2 + 2H_2O \rightarrow Ca(OH)_2 + 2H_2 \uparrow$$
$$LiH + H_2O \rightarrow LiOH + H_2 \uparrow$$
$$LiBH_4 + 4H_2O \rightarrow LiOH + H_3BO_3 + 4H_2 \uparrow$$
$$NaBH_4 + 4H_2O \rightarrow NaOH + H_3BO_3 + 4H_2 \uparrow$$

The hydrogen generation capability of these hydrides when reacted with water is outstanding. For example, the volume of H_2 (STP) produced by complete hydrolysis of 1 kg (2.2 lb) of lithium hydride is 2800 liters (99 ft^3), and by 1 kg (2.2 lb) of lithium borohydride is 4100 liters (145 ft^3).

In Table 1, the energy density of these hydrides when reacted with water is presented and compared to gasoline, as well as the storage of H_2 as a liquid, gas, and a reversible hydride. The energy densities of the reactive hydrides are given on the basis of the initial hydride mass. The energy densities of the hydride/water reaction are respectable when compared to gasoline or methanol, with $LiBH_4$ having the highest energy densities on both a mass and volume basis. The heat of reaction must be removed during the H_2 generation.

The comparison is based on the energy densities of the initial hydride as a 50% slurry and the mass and volume of the storage container assuming a 20% void fraction in the container when the hydride is completely spent. The LiH, $LiBH_4$, and $NaBH_4$ hydrides exceed the volumetric energy density goal by moderate factors (1.09 to 1.64). LiH and $LiBH_4$ exceed the gravimetric energy density goal by moderate factors (1.03 to 1.41), with CaH_2 slightly lower than the goal. It should be noted that energy density is not the only criterion that needs to be compared. Other factors such as cost and ease of handling must also be considered. In summary, several hydride/water reactions exceed the performance goals for both the volumetric and gravimetric energy densities. An additional feature is the ability to generate H_2 on demand and to control the rate of reaction by regulating the rate of water addition to the hydride bed. If desired, H_2 can also be generated at a high pressure for direct use in pressurized fuel cells without compression.

PRELIMINARY DESIGN OF HYDROXIDE REGENERATION SYSTEM

A preliminary design of the hydroxide to hydride regeneration system was conducted to identify process stream conditions and to allow the major equipment components to be sized such that a capital equipment cost could be developed. The system is shown in Figure 2. The analysis was conducted for both lithium hydroxide and calcium hydroxide regeneration.

The material and energy balances for the two metals were conducted for a plant supplying hydrogen to 250,000 cars. Such a plant would produce enough slurry to produce 13 tons of H_2/hr. It would be small relative to typical chemical engineering projects, however. The first Fluid Catalytic Cracking (FCC) plant was three times larger and today's FCC plants are 25 times larger.

Lithium hydroxide is combined with carbon for the reduction and fuel, streams 1, 2a and 2b, to form stream 3, and is fed to the top of an indirect vertical heat exchanger, which preheats the incoming reactants while cooling the stream containing the lithium hydroxide, streams 5 and 6. The possibility for removing heat from the indirect fired process heater is also provided, streams 7 and 8. The hot preheated and partially reacted reactants, stream 4, enter the reduction reactor in which they are heated indirectly to the reaction temperature by combustion of the recycled carbon monoxide, stream 10, and additional fuel, stream 12, with preheated air, stream 11. The possibility of adding direct heat to the reactor is accomplished by adding oxygen to the reduction reactor by stream 9. The products of reduction leave the reduction reactor through stream 5. Within the reactant preheater, the lithium hydride is formed through the non-equilibrium kinetics as the mixture of lithium, hydrogen, and carbon monoxide is cooled. Additional heat is taken out of the product stream for the generation of electrical energy, which is added back into the reduction reactor to reduce the additional fuel.

The product, lithium hydride, is separated from the carbon monoxide in the hot cyclone, stream 16. This is further cooled to produce additional power, which is also added to the reduction reactor. The hot carbon monoxide, stream 15, is passed through a self recuperator to get a cold stream of CO, which could have a barrier filter installed to remove all the lithium hydride and a blower to circulate the CO, stream 18. This stream is reheated with the incoming CO and fed into the indirect process heater as discussed above. The hot combustion products leaving the solids preheater, stream 8, are used to preheat the combustion air and produce power, which is fed back into the reduction reactor. The energy efficiency of the hydrogen storage is obtained by dividing the heat of combustion of the hydrogen in the metal hydride by the heat of combustion of the carbon used for the reduction and the additional fuel. The results are: lithium (52.1%) and calcium (22.9%).

ECONOMICS OF THE APPROACH

The preliminary economics for the process are obtained by first developing a capital cost for the process equipment and then estimating the operating cost to define the needed sales price of the metal hydride for the required after tax return on the investment.

The capital equipment costs for the process are shown in Table 2 for the lithium process. These estimates, as well as the operating cost estimates, were obtained using standard chemical engineering practice. The operating cost assumptions are shown in Table 3.

The sensitivity of the cost of the hydride and the rate of return as a function of plant size and carbon cost is shown in Figures 3 and 4 for lithium. In Figure 3, the cost of hydrogen is plotted versus the plant size for four values of the cost of carbon. For a 250,000 car-per-day plant, the cost of hydrogen is on the order of $3.61 per million Btu at a carbon cost of one-cent per pound and a fixed return on the investment of 15 percent. In Figure 4, the effect of plant size and carbon cost for a fixed hydrogen cost on the rate of return is shown. In this case, if the hydrogen can be sold for a value of $4.57 per million Btu, the return to the investors can range from 15 to 65 percent, depending on plant size and carbon price. The same trends are seen for calcium.

SUMMARY AND FOLLOW ON ACTIVITIES

The results of the work to date are:

- Best Organic - Light Mineral Oil
- Best Hydrides -LiH & CaH_2
- +95% Hydrogen Release/Recovery
- Reaction rate controllable
- pH/Pressure Control
- Stable slurry
- Polymeric dispersants sterically stabilize the suspension
- Cost of Hydrogen $2.75 to $6.00 per 10^6 Btu

REFERENCES

1. Block, D. and Melody, I, "Plans For A U.S. Renewable Hydrogen Program," Florida Solar Energy Center, Proceedings of 10th World Hydrogen Energy Conference, Cocoa Beach, FL, June 20-24, 1994.

2. Ulrich, "A Guide To Chemical Engineering Process Design And Economics," John Wiley & Sons, 1984.

3. Breault, Ronald W., Rolfe, J., and McClaine, A., "Hydrogen For The Hydrogen Economy," 24th Coal Utilization and Fuel Systems Conference, Clearwater, FL, March 8-11, 1999.

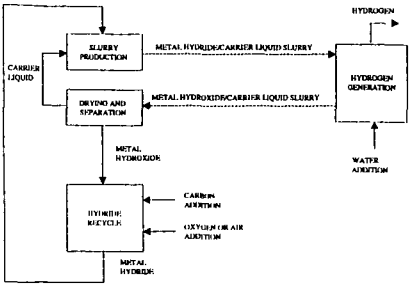

FIGURE 1. Simplified Process Diagram for Hydrogen Transmission/Storage With a Metal Hydride

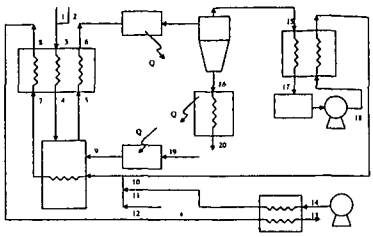

FIGURE 2. Hydroxide Regeneration System

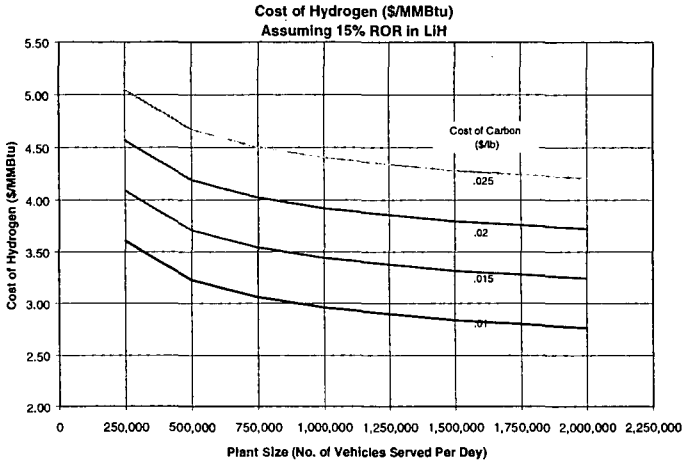

FIGURE 3. Sensitivity of Hydrogen Cost to Carbon Cost and Plant Size for Lithium Hydride

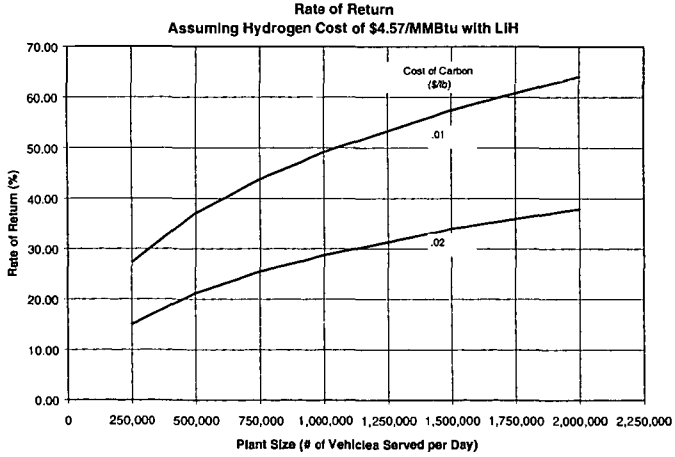

FIGURE 4. Sensitivity of Rate of Return to Carbon Cost and Plant Size for Lithium Hydride

TABLE 1. Comparison of Metal Hydrides to Other Hydrogen Storage Methods and Gasoline

Hydride	H_2 Volume Per Mass Hydride (STP ft^3/lb)	Energy Density		Water Reaction Enthalpy/HHV	Fraction Hydrolysis H_2 (lb H_2 per lb Hydride)	Hydride Density (gm/cm^3)
		HHV/Mass, Btu/lb	HHV/Bulk Volume (Btu/gallon)			
Ca H_2[1]	17.1	5,850	92,800	0.396	0.0958	1.90
Li H(1)	45.2	15,500	99,600	0.388	0.254	0.77
Li B H4(1)	65.9	22,600	124,500	0.212	0.370	0.66
Na B H4(1)	38.0	13,000	116,700	0.157	0.213	1.074
Fe Ti H(1.6)(2)	2.7	935	42,900	0.122(4)	0.0153	5.5
Liquid Hydrogen[3]	—	61,100	35,650	—	—	0.07
Gaseous Hydrogen (5000 psia, 300 K)	—	61,100	15,574	—	—	0.03058
Gasoline	—	20,600	130,000	—	—	—

(1) Reaction with Water
(2) Dissociation by Heating
(3) Liquid Fuel
(4) Based on Dissociation Energy

TABLE 2. Capital Cost - Lithium Hydride Regeneration

		Total cost
1	Furnace Cost, base 70m3	9,236,116
2	Solids preheater, 70 m3	9,236,116
3	Condensor, base 100MW	-
4	Hydride Reactor, Base 35m3	720,417
5	Blower, H2 from sep.base, 75m3/s	270,254
6	Steam Turbine Generator	25,693,663
7	Cent Slurry sep.	189,413
8	Hydride cooler, base 70 m3	9,236,116
9	Heat Exch/recuperator, base 20e9J/s	2,814,328
10	Hydrocarbon Decomp, base 100MW	-
	Sum, Total Cost	57,396,424

TABLE 3. Operating Cost Assumptions

Carbon	Variable, \$0.67 to 1.67/10^6 Btu
Fuel	\$2.5/10^6 Btu
Labor	
-Operators	25 at \$35,000/yr
-Supervision & Clerical	15% of Operators
Operators	
Supervision & Clerical	
Maintenance & Repairs	5% of Capital
Overhead	50% of Total Labor and Maintenance
Local Tax	2% of Capital
Insurance	1% of Capital
G&A	25% of Overhead
Federal and State Tax	38% of Net Profit

NOVEL TECHNIQUE FOR THE PRODUCTION OF HYDROGEN USING PLASMA REACTORS

Christopher L. Gordon, Philip J. Howard, Lance L. Lobban, and Richard G. Mallinson
School of Chemical Engineering and Materials Science,
University of Oklahoma, Norman, OK 73019

ABSTRACT

Natural gas is one of the major sources of hydrogen via steam reforming. Alternate routes for the conversion of methane to more valuable products, such as higher hydrocarbons and hydrogen, have also drawn a lot of interest from researchers. Plasma reactors have been found to be an effective technique for the activation of methane at low temperatures. Cold plasmas can be generated by pulse streamer discharges (corona discharges) or by micro-discharges on the dielectric surface (silent discharges). The electron discharges are capable of exciting and decomposing the feed gas molecules. The corona reactor consists of dc current, a point to plane geometry, and zeolite catalyst in the reaction zone. The feed gases consist of methane, hydrogen, and oxygen. Methane conversion and hydrogen selectivities of 55% and 75%, respectively, have been found over X zeolite, and 20% and 70%, respectively, at high throughputs over Y zeolite with residence times on the order of seconds. Power consumption as low as 20 eV/ converted CH_4 molecule has been achieved.

INTRODUCTION

With large increases in proven natural gas reserves worldwide, it can be expected that natural gas will play an increasingly important role in energy and chemicals supplies in the 21st century. The production of hydrogen from natural gas has also received more attention. Catalytic steam or CO_2 reforming of methane, the principal component of natural gas, is the principal process for the hydrogen production. About 50% of all hydrogen is produced from natural gas, and 40% of this is produced by steam reforming (1). A recent review by Armor (2) presents an excellent summary of the issues of hydrogen production by both conventional and potential technologies. While hydrogen production from fossil sources produce CO_2, methane has a significantly lower CO_2 impact than other fossil sources, see Table 1.

Table 1. CO_2 co-production with fossil hydrogen sources (3).

CO_2/H_2	Hydrogen Source Technology
0.25	Methane steam reforming
0.31	Pentane steam reforming
0.33	Partial oxidation of methane
0.59	Partial oxidation of heavy oil
1.0	Partial oxidation of coal

Hydrogen is an important feedstock for the synthesis of ammonia, methanol, hydrochloric acid and so on. Hydrogen should become the ultimate non-polluting fuel, although it appears that it will be produced initially from fossil sources, and methane is the best source. There are two reversible reactions involved in methane steam reforming:

$$CH_4 + H_2O \leftrightarrow CO + 3\,H_2 \qquad \Delta H_{298} = 206 \text{ kJ mol}^{-1} \qquad [1]$$

$$CO + H_2O \leftrightarrow CO_2 + H_2 \qquad \Delta H_{298} = -41 \text{ kJ mol}^{-1} \qquad [2]$$

The overall reaction is:

$$CH_4 + H_2O \leftrightarrow CO_2 + 4\,H_2 \qquad \Delta H_{298} = 165 \text{ kJ mol}^{-1} \qquad [3]$$

Methane steam reforming is thermodynamically favorable at high temperatures (the operating temperature is usually higher than 800°C) and low pressure. An intensive energy input is required due to the high temperature operation, and the endothermic nature of the reaction requires extremely large heat fluxes. While this is the primary commercial process, the

constraints make the process relatively expensive and economically attractive only on a very large scale (a characteristic of all processes which operate at extreme temperatures due in significant part to the over-riding need to maximize energy efficiency).

To drive these reactions at much lower gas temperatures, a cold or non-equilibrium plasma can be used (4). The cold plasma is characterized by high electron temperatures and low bulk gas temperatures (as low as room temperature). Therefore, gas heating is not a significant energy sink with cold plasmas. For an electrically driven system, the energy converted to heat should be minimized since this is a relatively inefficient heating method. Additionally, the advantage of small thermal masses and small temperature gradients directly impact the economy of scale of the process. While the low temperature system may not significantly increase efficiency with increases in scale size, it may potentially operate economically at much smaller scales than for high temperature systems. We have previously reported the methane conversion to higher hydrocarbons via corona discharge (5,6) and plasma catalytic conversion (7-9). We have found that the corona discharge is an efficient and effective technique for the low gas temperature (as low as 40°C) methane conversion.

These systems exhibit non-equilibrium behavior, allowing production of substantial yields of C_2 hydrocarbons at very low temperatures. Hydrogen is a substantial co-product formed from both methane coupling and product dehydrogenation. Water is formed in only small quantities. Oxidative conditions, in both the dc system and also in ac systems, also produce substantial hydrogen yields with significant CO formation. CO_2 formation can vary, but generally CO_2 is a minor product. C_2 products may still be formed, but in lower quantities. Work to this point in time has focused on the production of hydrocarbon or oxygenate products and not on maximization of hydrogen production.

EXPERIMENTAL

The experimental apparatus will be essentially the same as has been previously described (5-9). The reactor is a quartz tube or quartz lined stainless tube. The reactor is heated (when needed) by a cylindrical furnace placed around the reactor. An Omega K-type thermocouple is attached to the outside wall of the reactor to monitor and control the gas reaction temperature. The temperature measured in this way has been calibrated against the internal temperature, and has been discussed elsewhere (5,6). When a low gas temperature is employed for the gas discharge reactions, the reactor is cooled outside by flowing room air. For the low temperature reactions (less than 100°C), the gas discharge is usually initiated at room temperature. Then the gas will be self-heated by the plasma. The gas temperature can be controlled by adjusting the flow rate of the flowing room air outside the reactor. The flow rates of feed gases methane, hydrogen, oxygen and helium are regulated by mass flow controllers (Porter Instrument Co. model 201). The gas from the reactor flows through a condenser to remove condensable liquid and is then analyzed by the chromatograph. A CARLE series 400 AGC (EG&G) was used for the detection of products. In some cases, a MKS mass spectrometer is used for on line analysis and for temperature programmed oxidation of carbon deposited on catalytic materials. Recovered liquids are analyzed off-line using a Varian GC with appropriate columns.

In the present reactor design, the plasma is generated in a gap between two stainless steel electrodes as diagrammed in Figure 1. The upper electrode, which may be a wire (generally dc) or a circular plate (generally ac) is centered axially within the reactor tube, while the lower electrode is a circular plate with holes for gas to flow through and positioned perpendicular to the reactor axis and a fixed distance below the top electrode. Catalyst beds (when used) are generally placed on the lower electrode, but placement below the lower electrode, outside of the discharge zone, is possible. The dc corona discharge is created using a high voltage power supply (Model 210-50R, Bertan Associates Inc.). The lower plate electrode is always held at a potential of zero volts (i.e., grounded). The ac power source consists of a primary AC power supply, transformer, wave generator, and an energy analyzer. An Elgar Model 251B power source supplies the primary AC power. A Wavetek Model 182A wave generator sends a sinusoidal wave signal at the selected frequency to the primary power supply. A midpoint grounded Magnetec Jefferson high voltage transformer supplies the secondary power to the reactor system. The secondary voltage is generally varied from 3.75 to 8.75 kV. An Elcontrol Microvip MK 1.2 energy analyzer measures primary power usage. The catalysts which will be used in some experiments is a NaY or NaX zeolite in a powder form (<80 mesh). The preparation and characterization of these zeolites has been discussed elsewhere (4-6). Other materials may be tried as well.

RESULTS

The previous investigations on oxidative conversion of methane by gas discharges in the absence (5,10) and/or presence (6-9) of heterogeneous catalysts have confirmed that cold plasma methane conversion proceeds via a free radical mechanism, where the formation of methyl radicals is the rate-controlling step. The oxygen used under those conditions will induce significant oxidation of methane and hydrocarbon products to produce carbon oxides (mostly carbon monoxide). The selectivity of higher hydrocarbons is thereby reduced. Methyl radicals also may be generated from reaction of methane with hydrogen radicals (10):

$$CH_4 + H \leftrightarrow CH_3 + H_2 \quad [8]$$

Hydrogen radicals are produced relatively easily within cold plasmas (11). One may supply hydrogen instead of oxygen for initiating higher hydrocarbon formation. It can be expected that a 100% selectivity of higher hydrocarbons will be achieved from methane and hydrogen plasma reactions except for possible carbon formation. In general, methyl radical formation is thought to be responsible for the initiation of radical reactions leading to higher hydrocarbon production. The methyl radical also can be formed by reaction of methane with other radicals (e.g., CH_3, O, OH, and so on). In addition to the formation from radical reactions (e.g., reaction [8]), methyl radicals can be produced by electron-methane collisions (10). The hydrogen radical may also be an essential ingredient for the removal of undesired carbon deposition, which has a negative effect on gas discharges:

$$C + H \leftrightarrow CH \quad [9]$$

$$CH + H \leftrightarrow CH_2 \quad [10]$$

However, it has also been found that hydrogen appears to inhibit methane conversion in a discharge in the absence of a catalyst (12). The reason for this inhibition by hydrogen may be explained by the following reaction (5):

$$CH_3 + H_2 \leftrightarrow CH_4 + H \quad [11]$$

The inhibition was also observed during the plasma catalytic methane conversion over NaY zeolite.

The effects of hydrogen in the feed on methane conversion, Figure 2, and product selectivities, Figure 3, shows that the C_2 yield is higher than that achieved with plasma oxidative conversion of methane (7,8). The oxygen concentration is held constant at 2.5% while the ratio of methane and hydrogen is changed to achieve different partial pressures. It is also shown that the C_2 yield and methane conversion do not change significantly with the increasing hydrogen feed concentration. Most of the C_2 product is acetylene (more than 85%). Hydrogen yield is reduced and higher CO selectivity is observed with increasing hydrogen feed concentration in the presence of oxygen. This suggests that CO formation is not favored under conditions of higher hydrogen yield, and the higher hydrogen feed concentrations enhance CO formation

Small amounts of oxygen added to the feed improve C_2 hydrocarbon production. The oxygen enrichment, Figure 4, in the gas feed reduces the C_2 selectivity but causes significant increases in methane conversion that more than offsets the loss of selectivities up to a maximum at about 2 percent oxygen. However, with very small amounts of oxygen, carbon deposition can cause deactivation of the reactions, Figure 4. The reason for the increase in the methane conversion with increasing oxygen partial pressure is that other active species are generated in addition to hydrogen radicals when oxygen is present in CH_4/H_2 plasmas. These new active species include O, oxygen anion and OH radicals. All of these strongly abstract hydrogen from methane. Hydrogen yield under the influence of added oxygen generally increases with increased oxygen in the feed.

Recent results from one experiment with a methane and oxygen (4/1) mixture and no diluent has shown that hydrogen, acetylene and CO are the major products in the dc system with catalyst. These results are shown in Figure 5.

CONCLUSIONS

Substantial hydrogen production has been observed as a by-product to methane conversion in low temperature plasmas. Various configurations and operating conditions have been used, including ac and dc power, with and without catalysts, under oxidative and non-oxidative conditions and at elevated pressures. The ability of a low temperature, and elevated pressure, process to efficiently produce hydrogen from methane holds significant promise for providing substantial increases in hydrogen utilization on shorter time frames and, perhaps most significantly, on smaller scales than may be achievable with thermal systems.

REFERENCES

1. Barbieri, G., and Di Maio, F.P., *Ind. Eng. Chem. Res.* **36**, 2121(1997).
2. Armor, J. N., *Applied Catalysis A: General*, **176**, 159(1999).
3. Scholz, W. H., *Gas Sep. Purif.*, 7, 131 (1993).
4. Venugopalan, M., and Veprek, S., *in* "Topic in Current Chemistry: Plasma Chemistry IV." (Boschke, F.L. Ed.), p.1, Springer-Verlag, New York, 1983.
5. Liu, C-J., Marafee, A., Hill, B., Xu, G.-H., Mallinson, R., and Lobban, L., *Ind. Eng. Chem. Res.* **35**, 3295(1996).
6. Marafee, A., Liu, C-J., Hill, B., Xu, G-H., Mallinson, R., and Lobban, L., *Ind. Eng. Chem. Res.*, **36**, 632(1997).
7. Marafee, A., Liu, C., Xu, G., Mallinson, R. and Lobban, L., *Applied Catalysis A: General*, **164**, 21 (1997).
8. Liu, C-J, Mallinson, R. G. and L. L. Lobban, *Journal of Catalysis*, **179**, 326(1998).
9. Lobban, L., Liu, C.-J., and Mallinson, R., *Applied Catalysis A: General*, **178**, 17(1999).
10. Oumghar, A., Legrand, J.C., Diamy, A.M., and Turillon, N., *Plasma Chem. and Plasma Proc.* **15**, 87 (1995).
11. Hollahan, J.R., and Bell, A.T., "Techniques and Applications of Plasma Chemistry", John Wiley & Sons, New York, 1974.
12. Meshkova, G.I. and Eremin, E.N., *Russ. J. Phys. Chem.* **44**, 255(1970).

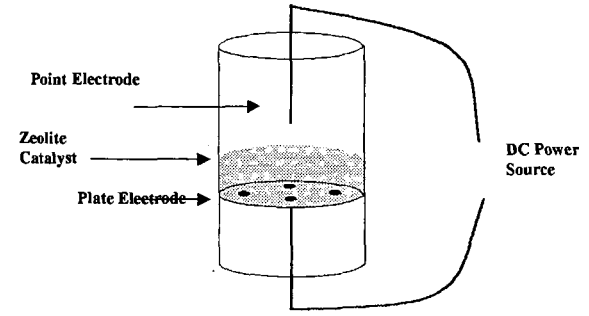

Figure 1. Point-plate dc Reactor Configuration with Catalyst Bed.

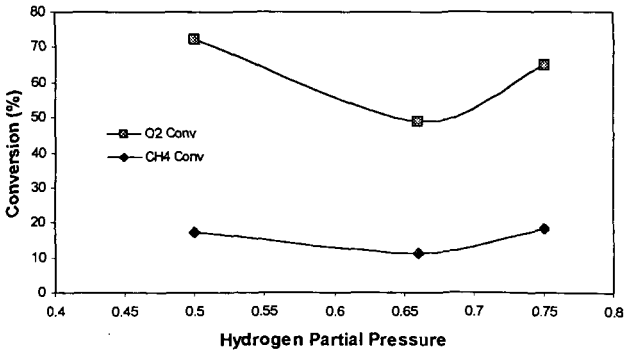

Figure 2. Methane Conversion at varying hydrogen partial pressures with constant oxygen concentration (2.5%) and balance methane, dc power over NaY Zeolite at 2 Bar.

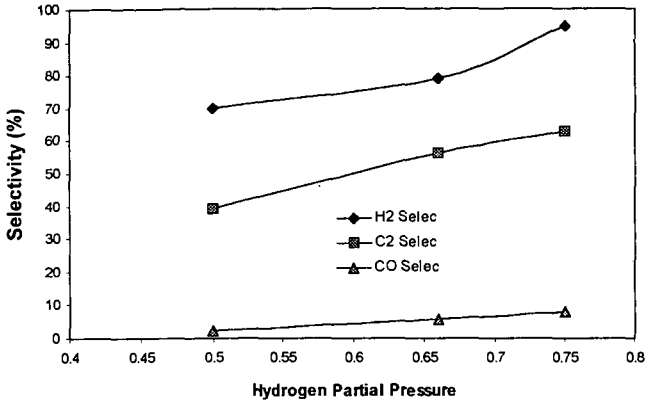

Figure 3. Product Selectivities at varying hydrogen partial pressures, dc Power over NaY Zeolite at 2 Bar.

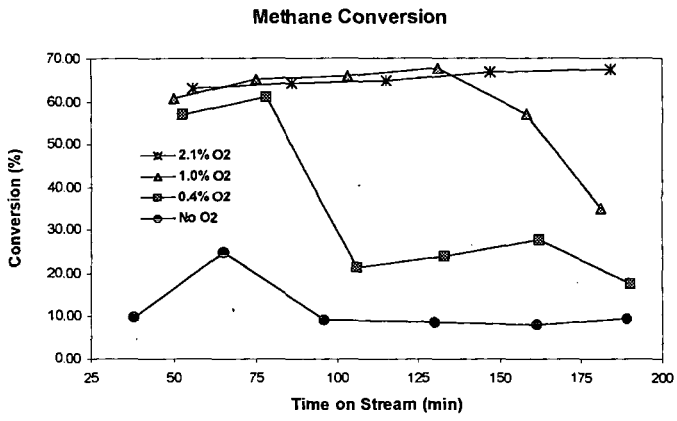

Figure 4. Methane Conversion vs. Reaction Time for Different O_2 Amounts.

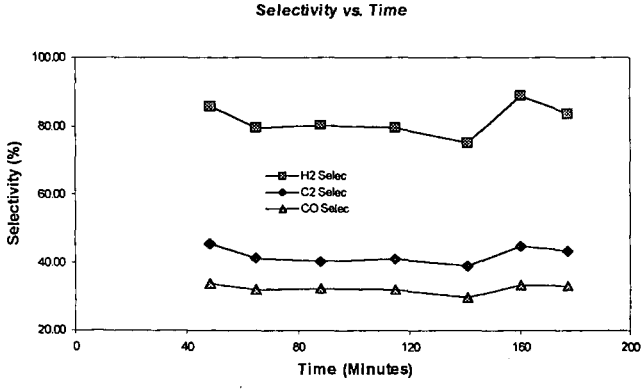

Figure 5. Product Selectivities for CH4/O2 = 4/1

TECHNOECONOMIC ANALYSIS OF HYDROGEN PRODUCTION FROM WESTERN COAL AUGMENTED WITH CO_2 SEQUESTRATION AND COALBED METHANE RECOVERY

Pamela Spath, Wade Amos
National Renewable Energy Laboratory
1617 Cole Blvd.
Golden, CO 80401
Harold Chambers, Diane Revay Madden, Denny Smith
Federal Energy Technology Center
P.O. Box 10940
Pittsburgh, PA 15236
Walter Shelton
EG&G Technical Services of West Virginia
3604 Collins Ferry Rd.
Morgantown, WV 26065

KEYWORDS: Hydrogen production, coal gasification, CO_2 sequestration

ABSTRACT

Hydrogen production via gasification of low sulfur western coal is being evaluated in a joint effort between the National Renewable Energy Laboratory (NREL) and the Federal Energy Technology Center (FETC). This work differs from past evaluations because it focuses on sequestering CO_2 and recovering coalbed methane. The off-gas stream, containing primarily CO_2, which is produced during hydrogen purification is used to displace methane from unmineable coalbeds. This methane is then utilized within the gasification-to-hydrogen system. Several processing schemes are being evaluated for maximizing hydrogen production or co-producing hydrogen and electricty. A combination of the following process steps are being used in these analyses: coal gasification, gas clean-up, shift conversion, hydrogen purification, hydrocarbon reforming, power generation, and hydrogen storage and transportation. The lowest cost storage and delivery method will be determined based on several factors including production rate, transport distance, and end use. A discussion of the cases being studied is presented.

INTRODUCTION

A collaborative effort to study the feasibility of producing hydrogen from low Btu western coal with an emphasis on CO_2 sequestration and coal bed methane recovery is being undertaken. The researchers at FETC are using their expertise in the field of coal gasification along with their existing models to examine coal gasification and gas clean-up. Because of extensive past technoeconomic analysis in the areas of hydrogen production, storage, and utilization NREL is examining the process steps associated with these operations using their previously developed models. Both parties are working to analyze CO_2 sequestration and coalbed methane recovery along with the possibility of power co-production. The models are being updated and integrated to incorporate the details of each system design as well as to account for the heat integration of the overall system.

COAL ANALYSIS

Wyodak coal was selected as a suitable coal that meets the needs of this study. This is a low rank Western coal that is inexpensive to produce and is available in an abundant supply. Additionally, the state regulations in Wyoming permit the extraction of coalbed methane making this site attractive for CO_2 sequestration and coalbed methane recovery. The elemental analysis and heating value of the Wyodak coal used in this work can be seen in the following table (EIA, 1995).

Table 1: Wyodak Coal Analysis

Ultimate Analysis	(Weight %, dry basis)
Carbon	67.6
Oxygen	17.7
Hydrogen	4.8
Nitrogen	1.2
Sulfur	0.8
Ash	7.9
Moisture, as-received (wt%)	26.6
Heat of combustion, HHV ,as-received	20,073 J/g (8,630 Btu/lb)

GASIFIER TECHNOLOGY

The Destec gasifier which is a two-stage entrained, upflow gasifier is being used for this analysis. The gasifier is currently being demonstrated under FETC's Clean Coal Technology Program at the Wabash River Coal Gasification Repowering Project in West Terre Haute, Indiana. The gasifier operates at a temperature of 1,038 °C (1,900 °F) and a pressure of 2,841 k Pa (412 psia). For hydrogen production the gasifier must be oxygen blown in order to minimize the amount of nitrogen in the syngas. Nitrogen is a strongly adsorbed component in the pressure swing adsorption (PSA) unit and will reduce the hydrogen recovery rate even at low levels. The feed is a coal/water slurry containing 53 wt% solids. The following is the syngas composition exiting the gasifier:

Table 2: Syngas Composition

Component	N_2	Ar	H_2	CO	CO_2	H_2O	CH_4	H_2S	NH_3	COS
mol %	0.6	0.7	27.7	27.4	16.5	26.6	0.0939	0.1399	0.2	0.0061
Heat of combustion, HHV, = 419 J/g (180 Btu/lb)										

From the composition listed in Table 2 it is apparent that reforming of the syngas for hydrogen production is not necessary because the gasifier produces only a trace amount of hydrocarbons. However, in order to maximize hydrogen production, one or more shift reactors will be needed to convert the carbon monoxide to hydrogen.

HYDROGEN PRODUCTION OPTIONS

Two options are currently being evaluated: Option 1 is maximum hydrogen production and Option 2 is co-production of hydrogen and power with the hydrogen being produced from the syngas and the power from recovered methane. See the simple block flow diagrams shown in Figures 1 and 2. The shaded blocks are the process steps that differ between the two options. Time permitting, other options for co-production of hydrogen and power will be tested in the future. In order to compare the economics as well as the overall CO_2 emissions from each option, the base case analysis will include only the process steps associated with coal gasification, shift, and hydrogen purification (i.e., none of the steps associated with CO_2 sequestration or coalbed methane recovery will be included in the base case). All of the options studied in this joint venture will be compared to this base case.

Figure 1: Option (1) - General block flow of maximum H_2 production

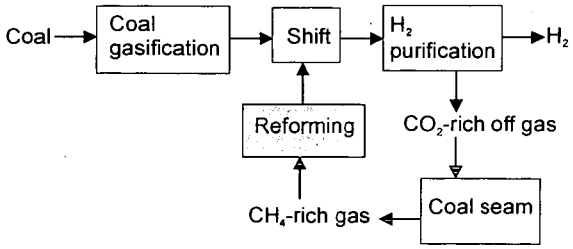

Figure 2: Option (2) - General block flow of H_2 Production from Syngas and Power Production from Recovered CH_4

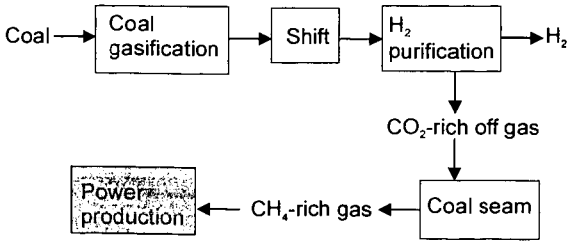

HANDLING SULFUR IN THE SYNGAS

Because the syngas from the gasifier contains approximately 1,400 ppm of H_2S several schemes for handling the large sulfur concentration are being examined to determine which will be the most economical. Four potential schemes have been configured and are depicted in the drawings below (Figures 3 - 6). The dashed boxes contain the process steps which are different between the four schemes. Overall heat integration is not shown in these figures.

For the ZnO bed, the inlet H_2S concentration needs to be in the10-20 ppm range. The high temperature shift (HTS) catalyst can tolerate concentrations up to 200 ppm but typically operates at lower levels whereas sulfur is a poison for the low temperature shift (LTS) catalyst and thus the H_2S needs to be reduced to a level below 0.1 ppm. Shift catalyst manufacturers produce a "dirty" shift catalyst which requires a sulfur concentration of at least 200 ppm in the inlet gas. Depending on the regulations for injecting sulfur into the ground, scheme 3 which does not remove the sulfur from the syngas, may not be a possibility. Also, note that there is not a scheme which incorporates the dirty shift catalyst with sulfur recovery via HGCU because HGCU would always be used prior to the shift reactors.

Figure 3: Sulfur scheme (1) - regular shift catalyst with hot gas clean up (HGCU)

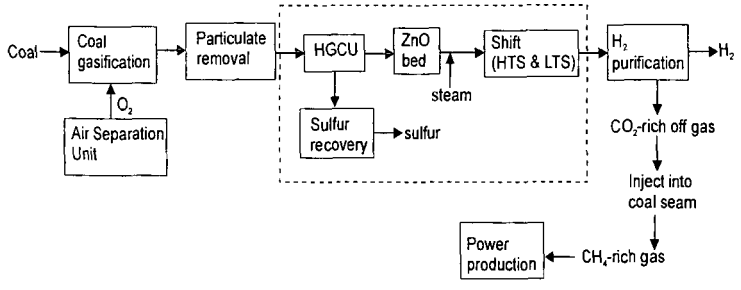

Figure 4: Sulfur scheme (2) - regular shift catalyst with cold gas clean up

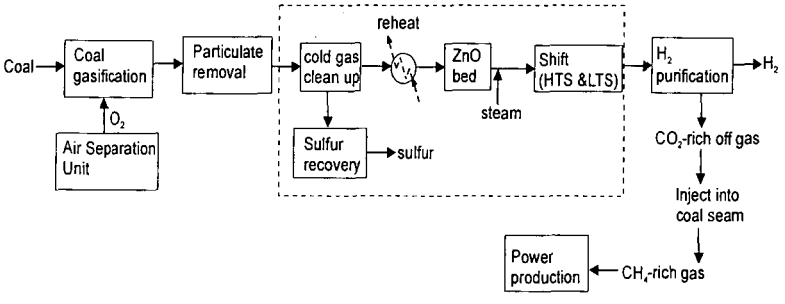

Figure 5: Sulfur scheme (3) - dirty shift catalyst with no sulfur recovery

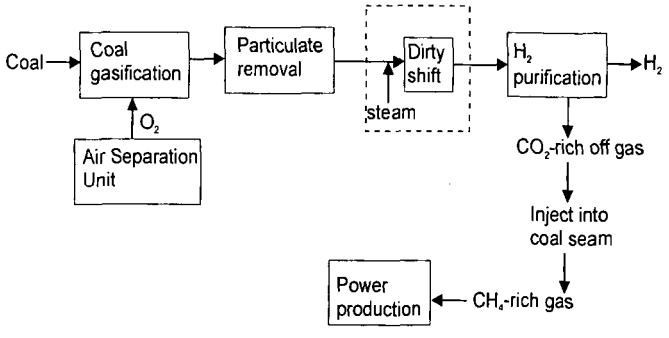

Figure 6: Sulfur scheme (4) - dirty shift catalyst with sulfur recovery via cold gas clean up

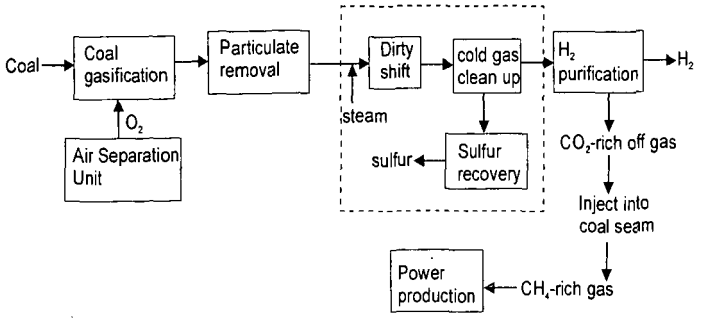

The coal gas leaving the gasifier contains entrained particles of char and ash. Particulate removal will be performed through cyclone separators and ceramic candle type hot-gas filters. Hydrogen purification will be done using a PSA unit. Because this unit operates at a pressure considerably lower than the coal seam, the off-gas must be compressed prior to injection.

CO_2 SEQUESTRATION AND CH_4 RECOVERY

Based on data from previous studies (Gunter *et al*, and Hendriks, 1994) this analysis assumes that two molecules of CO_2 are being injected for every one molecule of CH_4 released from the coalbed. This is based on worldwide data which shows that on average a little more than twice as much CO_2 can be stored in a methane field, on a volumetric basis, than the amount of CH_4 extracted. The off-gas from the hydrogen purification unit which contains primarily CO_2 (about 68 mol%) must be compressed from 2.7 MPa (392 psi) to a pressure of 3 - 14 MPa (500- 2,000 psi) which is the pressure range generally found in coalbed methane reservoirs (The American Association of Petroleum Geologists, 1994). Compressing the off-gas will require a significant amount of electricity. To adequately determine the overall reduction in CO_2 emissions for each option studied, the CO_2 emissions associated with electricity production must be added to the overall CO_2 balance of the system. Therefore, the net reduction in CO_2 will actually be less than the amount of CO_2 captured in the off-gas from the PSA unit. Additionally in the case of co-production of power, any CO_2 emitted during this process step must be included in the overall CO_2 balance to get a complete picture of the reduction in CO_2 emissions.

STORAGE AND TRANSPORTATION

In order to determine the effect of hydrogen storage and transport on the delivered cost of hydrogen, the following scenarios are being examined and incorporated into the analysis:

(1) bulk delivery:
- 16 km (10 mi) one-way
- 160 km (100 mi) one-way
- 1,610 km (1,000 mi) one-way

(2) on site consumption: 12 hours of storage; no transport.

(3) gas station supply: weekly hydrogen delivery; driving distance of 160 km (100 mi) round trip; supplying multiple stations along the way; hydrogen use of 263 kg/day (580 lb/day) per gas station.

(4) pipeline: 3 km (5 mi) to the nearest pipeline infrastructure; no storage; an additional 160 km (100 mi) pipeline for hydrogen delivery to end user for which the cost is shared by 5 companies.

The cost of storing and transporting hydrogen depends on the amount of hydrogen the customer needs and how far their site is from the production facility. The most economical mode of storage and delivery (i.e., liquid, compressed gas, metal hydride or pipeline delivery) will also vary depending on production rate and distance. For example, while liquid hydrogen delivery is one of the cheapest methods of transporting hydrogen long distances, it requires a large capital investment for a liquefaction facility and there can be significant transfer losses during loading and unloading. This large capital investment at the production site, along with product losses, can make another method of delivery more cost effective.

The above cases represent four likely scenarios for hydrogen use. In each case, the cheapest delivery and storage method will be identified, along with the associated incremental cost that must be added to the production cost to get the total delivered cost of hydrogen. The technoeconomic analysis for this work will be completed this fall.

REFERENCES

1. Gunter, W.D; Gentzis, T.; Rottenfusser, B.A.; Richardson, R.J.H. (September 1996) "Deep Coalbed Methane in Alberta, Canada: A Fuel Resource with the Potential of Zero Greenhouse Gas Emissions." Proceedings of the Third International Conference on Carbon Dioxide Removal. Cambridge, Massachusetts.

2. Hendriks, C. (1994). *Carbon Dioxide Removal from Coal-Fired Power Plants.* Kluwer Academic Publishers. Dordrecht, Netherlands.

3. The American Association of Petroleum Geologists. (1994). Hydrocarbons from Coal. AAPG Studies in Geology #38. Tulsa, Oklahoma. Edited by Ben Lae and Dudley D. Rice.

4. Energy Information Administration. (February 1995) "Coal Data: A Reference." DOE/EIA-0064 (93).

ON PERSPECTIVES OF CO_2-FREE PPRODUCTION OF HYDROGEN FROM HYDROCARBON FUELS FOR SMALL SCALE APPLICATIONS

Nazim Muradov
Florida Solar Energy Center,
1679 Clearlake Road, Cocoa, Fl 32922

KEYWORDS: Hydrogen, Hydrocarbon, Pyrolysis

ABSTRACT

All conventional options of hydrogen production from fossil fuels, primarily, natural gas (e.g. steam reforming, partial oxidation) are complex, multi-stage processes that produce large quantities of CO_2. In general, there are two ways to solve CO_2 emissions problem:
a) sequestration of CO_2 produced by the conventional methods of hydrogen production, and
b) decomposition (thermal, thermocatalytic, plasmochemical) of hydrocarbon fuels into hydrogen and carbon. The capture of CO_2 from the process streams and its sequestration (underground or ocean disposal) is costly, energy intensive, and poses uncertain ecological consequences. The main objective of this work is to develop a viable process for CO_2-free production of hydrogen via one-step thermocatalytic decomposition of hydrocarbon fuels into hydrogen and carbon. This process could be the basis for the development of compact units for on-site production of hydrogen from hydrocarbon fuels (e.g. natural gas and gasoline) at gas refueling stations. The concept can also be used for a CO_2-free production of hydrogen for fuel cell applications (mobile and stationary).

INTRODUCTION

In the near- to medium-term future hydrogen production will continue to rely on fossil fuels, primarily, natural gas (NG). For decades, steam reforming (SR) of NG has been the most efficient and widely used process for the production of hydrogen. Other conventional processes for hydrogen production from fossil fuels: partial oxidation (PO), autothermal reforming (AR), steam-oxygen gasification of residual oil and coal) are more expensive than SR. The SR of NG process basically represents a catalytic conversion of methane (a major component of the hydrocarbon feedstock) and water (steam) to hydrogen and carbon oxides, and consists of three main steps: a) a synthesis gas generation, b) water-gas shift reaction, and c) gas purification (CO_2 removal). Four moles of hydrogen are produced in the reaction with half of it coming from the methane and another half from water. The energy requirement per mole of hydrogen produced for the overall process is equal to 40.8 kJ/mole H_2. To ensure a maximum conversion of CH_4 into the products, the process generally employs a steam/carbon ratio of 3-5, the process temperature of 800-900°C and pressure of 35 atm. A steam reformer fuel usage is a significant part (up to 30-40%) of the total NG usage of a typical hydrogen plant. There is no by-product credit (except for steam) for the process and, in the final analysis, it does not look environmentally benign due to large CO_2 emissions. The total CO_2 emission from SR process reaches up to 0.4 m^3 per each m^3 of hydrogen produced. Heavy residual oil and coal based hydrogen production processes result in the emission of enormous volumes of CO_2 (up to 0.8 m^3 per m^3 of H_2). Therefore, the problem of large scale production of hydrogen from fossil fuels and its utilization as a major energy carrier in the near future will be tied up with the development of effective, economical and environmentally acceptable ways of managing CO_2 emissions. In general, there are two ways to solve the problem of CO_2 emissions:

- Sequestration of CO_2 produced by the conventional methods of hydrogen production from fossil fuels, and
- Decomposition (thermal, thermocatalytic, plasmochemical) of hydrocarbon fuels into hydrogen and carbon

CARBON SEQUESTRATION

The main purpose of carbon sequestration is to keep CO_2 emissions from reaching the atmosphere by capturing and diverting them to secure storage. The perspectives of CO_2 capture and sequestration (ocean or underground disposal) is actively discussed in the literature [1-3]. The commercially available processes for CO_2 separation and capture include: physical and chemical absorption, physical and chemical adsorption, low temperature distillation and gas-separation membranes. It should be noted, however, that the capture, transportation and sequestration of CO_2 are energy intensive and costly processes. Thus, according to [3], the capture and disposal of CO_2 add about 25-30% to the cost of hydrogen produced by the SR of NG. The total electric energy consumption to pressurize CO_2 to 80 bar, transport it 100-500 km and inject it to the underground disposal site is estimated at approximately 2000 kJ/kg CO_2. World average for CO_2

emission associated with the electricity production is 0.153 kg of CO_2 per each kWh produced [2]. Thus, the amount of CO_2 produced as a result of the capture of CO_2 from the concentrated streams (after pressure swing adsorption, PSA, unit) of SR process and its sequestration reaches up to 0.1 kg per kg of sequestrated CO_2. In principle, CO_2 can also be captured from the stack gases of the hydrogen plant (where it is presented in a highly diluted form) and sequestrated, however, the energy cost of this operation would be very high. For example, it was estimated that the cost of eliminating CO_2 emissions from stack gases of advanced power generation plants range from $35 to 264 per ton of CO_2 [4]. It was also estimated that the costs of CO_2 separation, capture, and compression to the required pressure would make up about three fourths of the total cost of ocean or geologic sequestration [5]. According to [6], the energy consumption associated with CO_2 recovery from the stack gases by hot K_2CO_3 solutions amounts to 3000 kJ/kg CO_2. In consequence, the total CO_2 emissions from CO_2 capture, transportation, and underground disposal could easily reach 0.25 kg CO_2 per kg of sequestrated CO_2. Thus, CO_2 sequestration is an energy intensive process and, in the final analysis, does not completely eliminate CO_2 emission. In addition to this problem, some uncertainties remain regarding the duration and extent of CO_2 retention (underground or under the ocean) and its possible environmental effect.

THERMOCATALYTIC PYROLYSIS OF HYDROCARBON FUELS

Thermal (thermocatalytic) decomposition (pyrolysis) is the most radical way for a CO_2-free production of hydrogen from hydrocarbons, particularly, NG:

$$C_nH_m \rightarrow nC + m/2H_2$$

$$CH_4 \rightarrow C + 2H_2 + 75.6\ kJ$$

The energy requirement per mole of hydrogen produced from methane (37.8 kJ/mole H_2) is somewhat less than that for the SR process. The process is slightly endothermic so that less than 10% of the heat of methane combustion is needed to drive the process. The process is environmentally compatible, as it produces relatively small amounts of CO_2 (approximately 0.05 m^3 per m^3 of H_2 produced, if CH_4 is used as a fuel). It should be noted, however, that the process could potentially be completely CO_2-free if a relatively small part of hydrogen produced (approximately 14%) is used as a process fuel. In addition to hydrogen as a major product, the process produces a very important by-product: clean carbon. Currently, the total world production of carbon black is close to 6 mln tons per year, with prices varying in the range of hundreds to thousands dollars per ton, depending on the carbon quality [7]. The carbon black has a great market potential both in traditional (rubber industry, plastics, inks, etc.) and new areas.

Low pressure and high temperatures (up to 1400°C) are favorable for the complete thermal decomposition of methane. Attempts have been made to use catalysts to reduce the maximum temperature of the decomposition of various hydrocarbon fuels. In [8], for example, the authors used alumina, silica-alumina, silica-magnesia and other contacts at 800-1000°C for decomposition of NG and light hydrocarbons. The data on the catalytic decomposition of methane using Co, Cr, Ni, Fe, Pt, Pd and Rh-based catalysts have also been reported in the literature [9, 10]. In all cases, carbon produced was burned off the catalyst surface to regenerate its initial activity. In this regard, these processes display no significant advantages over the conventional processes (for example, SR) because of large CO_2 emissions.

The main objective of our work is to develop a thermocatalytic process for the simultaneous production of hydrogen and carbon from different hydrocarbon fuels (NG, liquid hydrocarbons) [11-13]. The use of carbon-based catalysts offers significant advantages over metal catalysts since there is no need for the separation of carbon from the catalyst surface: carbon produced builds up on the surface of the original carbon catalyst and can be continuously removed from the reactor (for example, using a fluidized bed reactor). There is a lack of information in the literature on the catalytic properties of various forms and modifications of carbon in methane decomposition reaction. We determined the catalytic activity of various carbon materials (graphite, carbon black, different types of activated carbon) for methane decomposition reaction over the range of temperatures from 700 to 900°C. It was found that the activated carbon produced from coconut shells displayed the highest initial activity among other forms of carbon, producing gas with hydrogen concentration up to 70-75%v at 850°C. In all cases, there were no methane decomposition products other than hydrogen and carbon and traces of ethane and ethylene detected in the effluent gas. Poor performance of the graphite and carbon black catalysts can be explained by the structure and size of carbon crystallites.

From the thermodynamic point of view the pyrolysis of liquid hydrocarbons is more favorable than the decomposition of methane, as almost 1.5-2 times less energy is required to produce a unit volume of hydrogen. We studied catalytic pyrolysis of a wide range of liquid hydrocarbons (pentane, hexane, octane, gasoline and diesel fuel) using different carbon-based catalysts. In the presence of activated carbon (coconut) the steady state pyrolysis of liquid hydrocarbons was achieved over period of approximately one hour. For example, gasoline pyrolysis over activated carbon (coconut) at 750°C produced gas consisting mainly of hydrogen (45-50 v.%) and methane (40-45 v.%) with relatively small fraction of C_2+ hydrocarbons (<10 v.%). The gas production rate reached 650 mL/min per mL/min of gasoline. In the case of diesel fuel the concentrations of hydrogen and methane in the effluent gas were in the range of 25-30 and 35-40 v.%, respectively (balance: C_2^+ hydrocarbons).

COMPARATIVE ASSESSMENT OF DIFFERENT HYDROGEN PRODUCTION PROCESSES

Thermocatalytic pyrolysis (TP) of NG is a technologically simple one-step process without energy and material intensive gas separation stages, while SR is a multi-step and complex process. The techno-economic assessment showed that the cost of hydrogen produced by thermal decomposition of NG ($58/1000 m^3 H_2, with carbon credit), is somewhat lower than that for the SR process ($67/1000 m^3 H_2) [14].

The decomposition of methane can also be carried out plasmochemically. In a paper [7], the authors advocated a plasma-assisted decomposition of methane into hydrogen and carbon. It was estimated that up to 1.9 kWh of electrical energy is consumed per one normal cubic meter of hydrogen produced. Since almost 80% of the total world energy supply is based on fossil fuels [1], one can expect the electricity-driven hydrogen production processes to be among major CO_2 producers. A comparative assessment of the hydrogen production by SR, without and with CO_2 (after PSA unit) sequestration, electrolysis, plasmochemical decomposition (PD) and TP (with CH_4 and H_2 as a process fuel options) of NG is depicted on Figure. The comparison is based on two very important parameters, which reflect the energetic and ecological features of the processes. The first parameter (*En*) is equal to the total volume of NG consumed (both as a feedstock and a fuel) for the production of a unit volume of H_2 (*En* =NG/H_2, m^3/m^3). The second parameter (*Ec*) is equal to the total volume of CO_2 produced from both the feedstock and fuel usage of NG per a unit volume of H_2 produced (*Ec*= CO_2/H_2, m^3/m^3). Evidently, the lesser are both *En* and *Ec* parameters, the better is a hydrogen production process. For the sake of simplicity and comparability, it was assumed that NG was the primary fuel (at the power plant) for the water electrolysis and PD of NG. In fact, this assumption leads to rather conservative value for *Ec* parameter since NG share in total energy supply is only 19% and, what is more, NG produces 1.9 and 1.7 times less CO_2 (per kWh produced) than oil and coal, respectively [1]. The following conclusions can be extracted from Figure.

1. The processes with the large consumption of electric energy (water electrolysis, PD of NG) are characterized with the highest NG consumption and CO_2 emission per unit of hydrogen produced. It should be noted, however, that this conclusion is based on the world average energy production scenario, therefore, in countries with a large non-fossil fuel energy sector (hydroelectric, nuclear energy) both *En* and *Ec* parameters could be much lower.
2. SR with CO_2 capture (after PSA unit) and sequestration produces 30% less CO_2 emission than SR without CO_2 sequestration.
3. SR with CO_2 sequestration consumes 33% less NG than TP process, however, it produces 5 times more CO_2 emission.
4. TP of NG is the only fossil fuel based process which shows a real potential to be a completely CO_2-free hydrogen production process

SMALL SCALE HYDROGEN PRODUCTION UNITS

TP process does not include many material and energy intensive technological steps required by the conventional processes (SR, PO and AR), such as a two step water gas shift reaction, preferential oxidation, CO_2 removal, steam generation, etc. This is a significant advantage that TP holds over conventional processes, because it may potentially result in more simple, compact, and cost effective hydrogen production units. Based on our preliminary experimental data on gasoline pyrolysis, we project the volumetric power density of the TP-processor at approximately 0.8-1.0 kW_{th}/L. A comparative assessment of small scale hydrocarbon fuel processors based on SR, PO, PD and TP processes is presented in the Table.

There are several potential uses for the TP-based fuel processor (TPP):

1. The TPP can be used for on-site production of hydrogen at gas filling stations. TPP directly converts natural gas (or other hydrocarbon fuels) into methane-hydrogen blends, e.g HYTHANE™ (H_2:CH_4= 30:70 v.%/v.%) which can be used by ICE vehicles. Due to the flexibility of the TPP, it can produce different H_2-CH_4 mixtures in a single step, whereas, the conventional processes require 2 steps: initial production of hydrogen and then blending it with methane.

2. The TPP can be used in combination with fuel cells, for example, polymer electrolyte fuel cells (PEFC) for stationary applications (e.g. buildings, resort areas, etc.). It is known that PEFCs impose very stringent limitations on the level of CO impurity in the hydrogen feedstock ([CO]< 100 ppmv). TPP perfectly fits these requirements for it produces hydrogen that is completely free of carbon oxides.

3. The TPP can be combined with a PEFC for transportation applications. The TP process does not include bulky gas separation stages, and, therefore, leads to a compact fuel processor perfectly suited for on-board applications. On the other hand, mobile application of TPP is associated with the necessity for storing solid carbon on-board of a vehicle (approximately 3-8 kg per refueling, depending on feedstock).

4. Special CO_2-sensitive applications (space, mines, medicine, etc.).

One of the major issues associated with the proposed technology is related to a byproduct carbon. The amount of carbon produced at average gas filling station is estimated at approximately 250 kg per day (based on HYTHANE™ production from NG). A 10 kW TPP/PEFC power system is expected to produce approximately 0.7 kg/h of clean carbon. Carbon produced can be conveniently collected by special trucks, stored at the central collector and sold at reasonable prices.

ACKNOWLEDGEMENTS

This work was supported by the U.S. Department of Energy and the Florida Solar Energy Center (University of Central Florida).

REFERENCES

1. Nakicenovic, N. *Energy Gases: The Methane Age and Beyond;* IIASA, Working Paper-93-033; Laxenburg, Austria, 1993; pp 1-23
2. Blok, K; Williams, R.; Katofsky, R.; Hendriks, C. *Energy* **1997**, *22*, 161-168
3. Audus, H.; Kaarstad, O.; Kowal, M. *Proceedings of 11th World Hydrogen Energy Conference;* Stuttgart, Germany, 1996; pp 525-534
4. International Energy Agency, *Carbon Dioxide Capture from Power Stations*, IEA, 1998
5. Herzog, H.. *IV Intern. Conf. Greenhouse Gas Control Technologies,* Switzerland, 1998
6. Gritsenko , A. *Cleaning of Gases from Sulfurous Compounds;* Nedra: Moscow, 1985
7. Fulcheri, L.; Schwob, Y. *Int. J. Hydrogen Energy* **1995,** *20*, 197-202
8. Pohleny, J; Scott, N. *U. S. Patent No 3,284,161* (UOP), 1966.
9. Callahan, M. *Proc. 26th Power Sources Symposium;* Red Bank, N.J, 1974; 181
10. Pourier, M; Sapundzhiev, C. *Int. J. Hydrogen Energy* **1997**, 22, 429-433
11. Muradov, N. *Int. J. Hydrogen Energy* **1993**, *18*, 211-215
12. Muradov, N. *Proceedings of 11th World Hydrogen Energy Conference;* Stuttgart, Germany, 1996; pp 697-702
13. Muradov, N. *Energy & Fuel* **1998**, 12, 41-48
14. Steinberg, M.; Cheng, H. *Proceedings of the 7th World Hydrogen Energy Conference;* Moscow, USSR, 1988; p.699
15. Ogden, J.; Steinbugler, M.; Kreutz, T. *8th Annual U.S. Hydrogen Meeting*, Alexandria, VA, 1997, 469

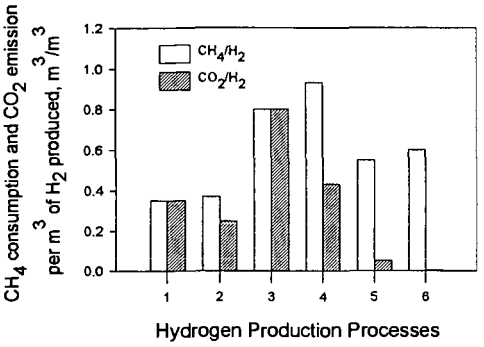

FIGURE. COMPARATIVE ASSESSMENT OF DIFFERENT HYDROGEN PRODUCTION PROCESSES:
1- SR, 2- SR with CO_2 sequestration, 3- electrolysis,
4- PD, 5- TP (CH_4- fuel), 6- TP (H_2- fuel)

TABLE. COMPARATIVE ASSESSMENT OF HYDROGEN PRODUCTION PROCESSES FOR SMALL SCALE APPLICATIONS

Process characteristics	Steam Reforming	Partial Oxidation	Plasmochem. Decompos.	Thermocatal. Pyrolysis
Capacity of small scale units, $10^3 m^3/h$	0.1-5.9	0.02-4.0	2.0	N/A
Commercial availability	Yes	Yes	Yes	No
Number of steps	3	3	1	1
Maximum temperature, °C	850-900	1400	Plasma	800-900
Need for WGSR and CO_2 removal units	Yes	Yes	No	No
Special process requirements	Steam	Oxygen/Air	Electricity 1- 2 kWh per $m^3 H_2$	None
Need for catalyst	Yes	No/Yes	No	Yes
Fuel flexibility	Low	High	Moderate	High
Tolerance to sulfur in a feedstock	Very low	High	Moderate	High
Useful byproduct	None	None	Carbon	Carbon
Efficiency, %	78.5	80	95	92.8[1)]
Process CO_2 emission[2)]	High	High	None	None[3)]
Power density, kW/L (kW/kg)	0.9 kW/kg[4)]	0.9 kW/kg[5)]	4 kW_e/L	0.8-1 kW/L[6)]

1) - total efficiency with carbon as a byproduct;
2) - does not include CO_2 generated at power plants
3) - part of H_2 is used as a fuel
4) - methanol steam reformer, [15]
5) - PO of gasoline, [15]
6) - based on our experimental data on TP of gasoline

FUEL PROCESSING OPTIONS FOR PROTON EXCHANGE MEMBRANE FUEL CELL SYSTEMS FOR MOBILE APPLICATIONS

R.A.J. Dams, P.R. Hayter, S.C. Moore
Wellman CJB Ltd.
Airport Service Road
Portsmouth
Hampshire PO 3 5 PG
United Kingdom

Keywords: Fuel Processing
Proton Exchange Membrane Fuel Cells
Mobile Transport Applications

INTRODUCTION

A fuel cell converts the chemical energy of a fuel directly to DC electricity and will do so continuously as long as a fuel (typically hydrogen or a hydrogen-rich gas) and oxidant (oxygen in air) are fed to it. Hydrogen can be provided in elemental form as a liquid or gas or can be derived by a chemical process from a suitable liquid feedstock such as an alcohol, liquid hydrocarbon or ether. Oxygen is normally available from ambient air or stored in elemental form in specialised applications.

Fuel cells are generally divided into two categories: low and high temperature. Low temperature fuel cells have as an electrolyte, either an acid (Phosphoric Acid - PAFC) or alkaline solution (Potassium Hydroxide - AFC) or a proton conducting membrane which is solid (PEMFC). In high temperature fuel cells, the electrolytes can be molten salts (Molten Carbonate - MCFC) or ion conducting ceramics (Solid Oxide - SOFC).

Of the fuel cell types, PEMFCs are most suitable for transport applications. Although PAFCs are closer to commercialisation, there is little room for major improvements in performance. Efforts are mainly concentrated on cost reduction through mass production. PEMFCs are still in the development phase and offer the possibility of improved performance and reduced costs in the near to middle future. High temperature fuel cells are still in the research and development phase and it will be some considerable time before they become a commercial proposition.

OPTIONS FOR SUPPLY OF HYDROGEN

Hydrogen can be supplied to a PEMFC stack in elemental form using a storage system or as a constituent of a gas stream resulting from the processing of a feedstock such as an alcohol, liquid hydrocarbon or ether. Whilst pure hydrogen produces a better performance from the fuel cell and eliminates the problems of poisoning, hydrogen storage techniques result in physically large systems and introduce logistic problems for refuelling. A number of techniques have been considered including compressed gas, liquid, hydride, glass microspheres, activated carbon and carbon nanofibres. All these techniques have drawbacks which prevent them from being an ideal solution, although the claims for carbon nanofibres, if substantiated could change this assessment.

As a consequence of this situation, much work has been done on fuel processing of alcohols, liquid hydrocarbons or ethers for transport applications. A fuel processor converts a suitable feedstock into a hydrogen-rich gas. The percentage of hydrogen is determined by the technique used. A number of fuel processing techniques have been evaluated for fuel cell applications. These include steam reforming, partial oxidation and authothermal reforming.

PROCESSING OF ALCOHOLS, HYDROCARBONS AND ETHERS

The fuel processor extracts hydrogen from a suitable feedstock. Much work has been done using alcohols such as methanol for transport applications. The

lack of a methanol infrastructure has caused a shift in the direction of liquid hydrocarbons such as gasoline, diesel RFG & LPG. Ethers, such as dimethylether have also been considered.

Carbon monoxide in the reformate feed to a PEMFC decreases the performance dramatically, but reversibly. The typical exit gas from a steam reforming fuel processor contains carbon monoxide at a concentration of 0.3% in approximately 75% hydrogen/25% carbon dioxide. A carbon monoxide concentration of less than 10 ppm is desirable and a concentration less than 2 ppm shows no effect on the performance of a PEMFC at all. Carbon dioxide acts mainly as an inert diluent. However, there is evidence that a certain amount of carbon dioxide is converted *in situ* to carbon monoxide with the consequent affect on performance. Much work has been done on combating the deleterious effect of carbon monoxide on the performance of PEMFC systems. A number of methods have emerged to achieve this:

1. the introduction of a bleed of air/oxygen into the reformate stream:
2. the introduction of a gas clean-up stage between the fuel processor and the anode side of the PEMFC stack;
3. the development of anode electrocatalysts containing ruthenium in addition to platinum to increase carbon monoxide tolerance.

These solutions, both singly and in combination, restore cell performance.

STEAM REFORMING

A hydrogen rich stream can be produced by the steam reforming of hydrocarbons, alcohols or ethers with or without the presence of a catalyst. The use of a catalyst results in lower temperatures and shorter reaction times. The objective of a catalytic steam reforming process is to liberate the maximum quantity of a hydrogen held in the water and feedstock fuel. Carbon in the feedstock is converted into carbon monoxide by oxidation with oxygen supplied in the steam. Hydrogen in the fuel, together with hydrogen in the steam, is released as free hydrogen. The reaction is endothermic. Practically, the reformed gas contains a large percentage of hydrogen, with carbon dioxide, carbon monoxide, methane and unreacted steam. In addition, prior to the reforming stage, it is necessary to remove traces of any components which will poison and deactivate the steam reforming catalyst or the fuel cell anode electrocatalyst. Therefore, as well as the reforming stage, the following steps may be required:

1. feed pre-treatment/desulphurisation;
2. pre-reforming (depending on the feedstock);
3. carbon monoxide conversion to carbon dioxide;
4. preferential oxidation or some other gas clean-up

In situations where low carbon monoxide levels are required, such as for fuel cells, carbon monoxide conversion is often achieved in two stages. The first step takes place as a high temperature shift stage (300-450°C) and the second as a low temperature shift stage (180 - 270°C). Because of the thermodynamics, gas leaving the low temperature shift will still contain a level of carbon monoxide greater than that acceptable for use in the fuel cell. A further stage of catalytic treatment is required to reduce the carbon monoxide level to less than 10 ppm

As an alternative to direct steam reforming, another process configuration which may be adopted is to include a stage of pre-reforming. This system consists of an adiabatic reactor containing a high activity catalyst. The outlet gas from this stage would have a high percentage of methane with other

negligible hydrocarbons present. Such a system operates at a lower temperature (400 - 500°C) than the direct reforming route and enables a lower overall steam to feed ratio to be used. Furthermore, as the gas leaving the pre-reformer is rich in methane, higher levels of preheat can be applied to the reformer feed without risk of cracking and carbon laydown.

PARTIAL OXIDATION REFORMING

Partial oxidation systems rely on the reaction of a hydrocarbon feedstock in a limited supply of oxygen or air to prevent complete oxidation. Traditionally it is carried out without the presence of a catalyst, although catalytic partial oxidation systems are being developed for fuel cell applications. The oxygen is supplied in air. Carbon in the fuel is converted into carbon monoxide whilst the hydrogen in the fuel is released as free hydrogen. The product gas now contains the residual nitrogen from air. Partial oxidation is an exothermic reaction and 17% of the (lower) heat of combustion of the gasoline is released. This raises the temperature of the product gases to approximately 870°C so no external heat source is required. Catalytic partial oxidation attempts to bring about the desired reaction with oxygen using a catalyst. This will enable a lower operating temperature to be used and hence reduce the oxygen consumption. The main difficulty in this area is the development of a durable catalyst which can promote the desired partial oxidation reaction whilst preventing other undesirable reactions from taking place.

AUTOTHERMAL REFORMING

Partial oxidation and steam reforming processes can be combined such that the exothermic partial oxidation reaction heat can be utilised by the endothermic steam reforming reaction. This system is known as autothermal reforming. The partial oxidation and steam reforming reactions can be carried out with or without a catalyst. The use of a catalyst is always accompanied by a potential catalyst poisoning problem by sulphur or lead components in the hydrocarbon or by carbon formation. There is little information in the literature about autothermal reforming of higher hydrocarbons. However, the Johnson-Matthey 'Hot-Spot™' technology has been developed to allow autothermal reforming of methanol. Unlike other autothermal reactors, which require complex heat exchange mechanisms between the exo and endothermic stages, the Hot-Spot™ reactor functions by catalysing steam reforming and partial oxidation on the same catalyst.

'CLEAN-UP' OF FUEL PROCESSING EXIT GAS

The more favoured methods of fuel processing, ie steam reforming, partial oxidation and autothermal reforming, require a further stage of gas processing or 'clean-up' due to the significant quantities of carbon monoxide produced during the processing reactions. The presence of carbon monoxide acts as a severe poison towards the platinum electrocatalyst in the PEMFC at its typical operating temperature of 80°C. Carbon monoxide preferentially adsorbs onto the catalyst surface and thus prevents the hydrogen adsorption necessary for the electrochemical reaction. Carbon monoxide concentrations above 10 ppm are known to cause substantial degradation in PEMFC performance. Ideally the concentration should be no more than 2 ppm. Therefore, it is necessary to include a further stage of gas clean-up prior to the fuel cell to reduce the carbon monoxide concentration to acceptable levels for introduction of the reformate into the cell. A number of processes are available for the removal of carbon monoxide from a gas stream:

1. chemical reduction;
2. membrane separation;
3. water gas shift;

4. chemical oxidation

Chemical reduction of carbon monoxide, ie methanation, is effected over a heterogeneous catalyst such as nickel on alumina at approximately 600°C. However, if large concentrations of carbon monoxide are present then due to the stoichiometry of the reaction there can be a substantial reduction in the hydrogen concentration of the fuel gas.

The use of silver palladium alloy membranes at the fuel processor exit can be used to produce ultra pure hydrogen for the fuel cell. The membrane allows the hydrogen to diffuse through its metallic crystal structure whilst remaining impermeable to the remaining gases produced by the reformation process. Although proven, the technology is at present expensive due to material costs. In addition, the thickness of the membranes (150 microns) necessitates the use of high pressure differentials for the production of acceptable hydrogen flow rates. High parasitic losses are, therefore, placed on the overall system. Research presently underway is focused on developing much thinner membranes (5-25 microns) supported on ceramics. Reductions in cost and operating pressures are, therefore expected without compromising the membrane strength.

The use of a heterogeneous catalyst such as copper/zinc oxide can be used to effect the water gas shift reaction. Since the catalysed reaction is carried out at approximately 200°C, thermal integration with the fuel processor may be possible. The utilisation of the reaction is advantageous since it can increase the hydrogen content of the processed fuel by 30-40%. However, reductions in carbon monoxide concentrations below 20 ppm are not practically possible and, as such, a further stage of gas clean-up is still required.

Finally, carbon monoxide may be selectively oxidised in the presence of hydrogen by air injection into the reformate over a suitable heterogeneous catalyst. Catalytic reactors to date have been used on either packed bed or monolithic designs. Noble metals such as platinum and rhodium (or mixtures of) are particularly active whilst copper based catalysts also show good activity for carbon monoxide oxidation. The reactor operating temperature for the selective oxidation is determined by the catalyst composition, with the reactors showing optimum activity and selectively within a relatively small temperature range. Close thermal control of the exothermic reaction is therefore necessary to maximise the reaction efficiency.

PRACTICAL FUEL PROCESSING ON BOARD A VEHICLE

Major technical challenges for an integrated fuel processor and fuel cell for a vehicle are as follows:

Start-up time
Response to transients
Methanol quality
Catalyst deactivation
Emissions
Conversion efficiency
Size
Cost

It is perceived that for a fuel cell vehicle to be successful in the market place, it will have to perform at least as well as an internal combustion engine vehicle. This means that start up time and response to transient power demands are critical features. At the present time, fuel processors fall short of these goals. The lowest start up times from cold reported are typically several minutes. The quality of the feedstock has an effect on the rate of deactivation of the copper/zinc catalysts traditionally used for steam reforming. The emissions from a fuel cell vehicle with an onboard reformer will not be zero. However, nitrogen oxides and carbon monoxide emissions should be close to zero.

Hydrocarbons and particulate matter should be substantially reduced. There will be no sulphur emission. The emission goal for a fuel cell vehicle with an on-board fuel processor is the Super Ultra Low Emission Vehicle Limit set by California. Conversion efficiency of the feedstock should be as close to 100% as possible. Carryover of unreacted feedstock into a carbon monoxide selective oxidation system affects the performance resulting in an increase in carbon monoxide content of the exit gas. The system efficiency of a PEMFC system incorporating a reformer is predicted to be around 33%. Such a figure should be obtainable over a wide operating range. A reformer for use on-board a vehicle should be as small and light as possible, easy to manufacture using a simple design and cheap materials. The eventual cost target suggested by the motor industry is between $30/45 per kW.

UNMIXED REFORMING: AN ADVANCED STEAM REFORMING PROCESS

Ravi V. Kumar, Jerald A. Cole and Richard K. Lyon
Energy and Environmental Research Corporation
18 Mason
Irvine, California 92618

ABSTRACT

Unmixed Reforming is a novel steam reforming process to convert fossil fuels to hydrogen. It has been developed mainly for small scale generation of hydrogen. The target application is electric power generation in buildings and automobiles using fuel cells. The Unmixed Reforming process has been demonstrated in a packed bed reactor using diesel fuel and natural gas as the feedstock. The average purity of hydrogen in the product stream was around 70%, with the balance being primarily methane, carbon monoxide and carbon dioxide. In Unmixed Reforming, the catalyst is not deactivated by coke or sulfur. The coke is burnt off during a regeneration step. A significant portion of the sulfur is rejected as sulfur dioxide. The process has been simulated by performing chemical equilibrium calculations in different zones of the catalyst bed.

INTRODUCTION

There has been considerable increase in interest in fuel cells due to their higher efficiencies and environmental friendliness. Low temperature fuel cells are being considered for electric power generation in commercial and residential buildings and automobile applications. The low temperature fuel cells require a continuous supply of high-purity hydrogen.

Steam reforming is the most economical means of converting fossil fuels to hydrogen at large scales. Natural gas is principally used as the fossil fuel.

Using methane as an example, the principal reactions in the steam reformer are as follows:

$$CH_4 + H_2O = CO + 3H_2 - \Delta \qquad (1)$$

$$CH_4 + 2H_2O = CO_2 + 4H_2 - \Delta \qquad (2)$$

The reforming reactions are highly endothermic and hence require that additional fuel be combusted to supply heat. Both the reforming reactions are equilibrium limited. The methane conversion is maximized by carrying out the reforming reactions at temperatures between 750 to 850°C. In the conventional steam reforming processor long tubes packed with catalyst are used to heat the reactants up to the required temperature. The tubes are contained in a gas-fired furnace.

The limitations of conventional steam reforming at small scales are two-fold—cost of reformer and efficiency (Adris et al., 1996). First consider the cost. The metal tubes are heated in a fired furnace. The metal wall of the tubes reaches temperatures of 900°C and the flue-gas reaches temperatures in excess of 1000°C. The tubes are made of high alloy nickel-chromium steel. The tubes are expensive and account for a large portion of the reformer cost. Second, the efficiency of reformer decreases at small scales due to heat transfer limitations and parasitic heat losses. The transfer of heat from the combustion products to the reactants is an inherently inefficient process, and in any practical system, especially for smaller scales, it is not possible to transfer all of the energy released by combustion into the process being heated.

If small scale hydrogen production is to be practical, the issues of cost and efficiency should be addressed. The Unmixed Reforming (UMR) process was developed to address these issues. UMR, like conventional reforming, can be used to generate hydrogen from a variety of liquid and gaseous fuels such as natural gas, landfill gas, propane, methanol, gasoline, diesel fuel, JP-8, etc.

PROCESS DESCRIPTION

UMR relies on an EER-patented process (Lyon, 1996) known as Unmixed Combustion (UMC) to heat the packed bed. In the UMC process the combustion is carried out by alternately cycling air and fuel over a metal, in this case nickel, placed in a packed bed reactor. The metal is dispersed on a high surface area catalyst support. When air is passing over the bed, the nickel oxidizes to form nickel oxide in an highly exothermic reaction. Most of the heat is deposited on the ceramic matrix since there are no gaseous products for this oxidation reaction. The subsequent and separate introduction of a fuel will release additional energy while reducing the nickel oxide back to metallic nickel. The heat thus generated in-situ is then available for the endothermic steam reforming reactions. Nickel was chosen as the metal for UMC, since it is the most common catalyst for the steam reforming reactions. The UMR process was improved by introducing a carbon dioxide acceptor (e.g. calcium oxide) into the catalyst bed.

The three steps of the UMR process are shown in Figure 1. The figure portrays the progress of the reaction starting at the left of the figure and moving toward the right. The three steps are referred to as the reforming step, the air regeneration step and the fuel regeneration step. During the reforming step, fuel and steam react over the catalyst to produce hydrogen through conventional steam reforming chemistry. The calcium oxide is converted to calcium carbonate as it captures some of the carbon dioxide formed during the reforming reactions. This shifts the reforming reactions to higher conversions, thus improving the purity of the hydrogen product stream. During the next process step, air is passed through the packed-bed reactor to oxidize the catalyst. The heat released by the oxidation reaction raises the temperature of the bed. This decomposes the calcium carbonate to produce calcium oxide, while releasing carbon dioxide into a vent gas stream. In the final process step, fuel is introduced to the packed bed, reducing the oxide form of the catalyst back to its elemental form and further increasing the temperature.

The primary reactions that are occurring in the reactor are as follows:

Reforming Step

$$CH_4 + H_2O = CO + 3H_2 - \Delta \quad (3)$$

$$CH_4 + 2H_2O = CO_2 + 4H_2 - \Delta \quad (4)$$

$$CaO + CO_2 = CaCO_3 + \Delta \quad (5)$$

Air Regeneration Step

$$2Ni + O_2 = 2NiO + \Delta \quad (6)$$

$$CaCO_3 + \Delta = CaO + CO_2 \quad (7)$$

Fuel Regeneration Step

$$CH_4 + 4NiO = CO_2 + 2H_2O + 4Ni + \Delta \quad (8)$$

The carbon dioxide acceptor material, calcium oxide, serves three functions in the process. First it provides additional "thermal mass" to transfer sensible heat from the regeneration step to the reforming step of the process. Second, the adsorption of carbon dioxide by the calcium oxide to produce calcium carbonate is an exothermic chemical reaction that also delivers energy to the reforming reactions in the form of chemical potential energy. During the air regeneration step, heat released by oxidation of nickel is largely absorbed by the process of decomposing the calcium carbonate to calcium oxide, and this substantially moderates the temperature rise of the packed bed. Much of the enthalpy of nickel oxidation is thereby stored as chemical potential energy in the calcium oxide. That chemical potential energy is subsequently released during the reforming process when calcium oxide is converted back to calcium carbonate. This method of using the interconversion between calcium oxide and calcium carbonate to supply heat to the reforming process, is a far more efficient means of transferring energy to the reforming process even than relying solely on the sensible heat stored in the ceramic catalyst support matrix. Furthermore, reducing the temperature rise during regeneration reduces parasitic heat losses from the reactor and promotes process efficiency. Finally, the presence of the solid-phase acceptor material improves the reaction equilibrium for reactions (1) and (2). By removing carbon dioxide from the products of the steam reforming process, equilibrium is shifted toward greater hydrogen production, reduced carbon monoxide and carbon dioxide concentrations, and increased fuel conversion.

Catalyst poisoning by carbon formation during reforming is not a problem, since any carbon formed is burnt off during the air regeneration step. UMR is also tolerant of fuel sulfur, which makes it a more robust process than conventional steam reforming. In conventional steam reforming sulfur must be removed from the feedstock fuel before it sees the catalyst, otherwise the catalyst is deactivated by the formation of nickel sulfide. In UMR, on the other hand, sulfur reacts with both nickel and calcium oxide during the reforming step, but is rejected as sulfur dioxide during the air regeneration step.

MATERIALS AND METHODS

The UMR process was studied in pilot scale and bench scale experimental systems. A simple schematic of the pilot scale system that was used to perform the experiments is shown in Figure 2. The pilot scale system consists of a dual packed bed reactor system. Switching valves are used to deliver steam and fuel, air and finally fuel to the packed bed for the three steps of the UMR process. The reactors are packed with a blended mixture of the catalyst and the carbon dioxide sorbent. The catalyst is Nickel supported on calcium aluminate and the carbon dioxide sorbent is dolomite. The particle sizes for the catalyst and dolomite are around 1 to 7 mm. A back pressure regulator is used to set the pressure in the reactor which in the reforming step is to 2–7 bar. The pressure during the regeneration step is around 1–2 bar. The reformate (reformer product) stream was analyzed using online infrared gas analyzers. The readings from the online analyzers were verified using gas chro-

matography with a thermal conductivity detector. The system was designed to produce 100 standard liters per minute of hydrogen, which is sufficient to generate 10kW of electricity using a Proton Exchange Membrane fuel cell. The bench scale system consisted of a single packed bed reactor.

The UMR process was simulated by modeling the packed bed reactor as a series of equilibrium reactors. The packed bed was divided into five zones. The reforming, air regeneration and fuel regeneration steps were subdivided in to twenty, fifteen and five sub-steps respectively. The feed gas stream during each sub-step enters the first zone and reaches thermodynamic chemical equilibrium with the solid phase in the first zone. The gas leaving the first zone enters the second zone and reaches equilibrium with the solid phase in the second zone, and so forth. The equilibrium calculation were performed using a NASA chemical equilibrium code (McBride and Gordon, 1996). The steam to fuel molar ratio during the reforming step was set to be three. The length of the time steps for the reforming, air regeneration and fuel regeneration steps were assumed to be 300, 225 and 75 seconds respectively. The model adjusts the fuel and steam flow rate during the reforming step to stabilize the maximum temperature during the UMR process to a preset value. A PID algorithm was used to adjust the fuel and steam flow rate. The flow rates for air and fuel during the regeneration steps were kept constant. The model was run for multiple cycles until steady state conditions were obtained.

RESULTS & DISCUSSION

Pilot plant experiments, using diesel fuel, have demonstrated product gas hydrogen concentrations typically averaging 70+ percent and as high as 85 percent under certain conditions, with the balance primarily CH_4, CO and CO_2. Figure 3 shows data collected over a one hour period of the pilot plant operation during which the average purity of hydrogen in the reformate stream was maintained at 70%. The reforming step was conducted for 300 seconds. The variation in the gas composition is a result of the cyclic UMR process. At the beginning of the reforming step the hydrogen concentration is low since the NiO in the bed is still being reduced to Ni by fuel. As the reforming step progresses the temperature of the packed bed decreases and as a result the methane concentration in the reformate stream increases and the carbon monoxide concentration decreases.

For low temperature fuel cells the concentration of CO needs to be reduced to 50 ppm, and hence a high H_2 to CO ratio is preferable in the reformate stream. The UMR process was able to generate a hydrogen product gas with an average H_2 to CO molar ratio in excess of 10. Competing technologies such as partial oxidation produce a reformate stream with H_2 to CO molar ratios ranging from less than 2 to about 3, while conventional steam reforming attains a ratio of about 5.

Bench scale experiments using diesel fuel have shown that for typical fuel sulfur concentrations there is no detectable sulfur in the product gases to at least the sub-ppm level. In the bench scale experiments, when sulfur was added to diesel fuel at a concentration of 2000 ppm by weight only 5 ppm H_2S was detected in the product gases. In pilot scale experiments using diesel fuel the sulfur concentration in the reformate stream was around 12 ppm.

Due to the manner in which fuel is oxidized in UMR, the byproduct exhaust gases contain no oxides of nitrogen, and the emissions of carbon monoxide are typically less than 10 ppm. Therefore, relative to conventional reforming, and when compared with most alternative hydrogen production processes, UMR is nearly pollution free.

The predicted UMR dry gas product composition using the theoretical model is shown in Figure 4, when methane is used as the fuel. The figure shows that the temperature of the gas leaving the bed decreases during the reforming step. The carbon monoxide concentration decreases as the temperature decreases. The model predicts that the methane concentration in the product gas is low (< 3%) and that the concentration of hydrogen in the product gas increases during the reforming step.

ACKNOWLEDGEMENTS

The authors would like to acknowledge the support of U.S. Defense Advanced Research Project Agency (contract #DAAH01-95-C-R162) and U.S. Department of Energy and Edison Technology Solutions (contract #DE-FC02-97EE50488).

REFERENCES

Adris, A.M., Pruden, B.B., Lim, C. J. and Grace, J.R., 1996, On the Reported Attempts to Radically Improve the Performance of the Steam Methane Reforming Reactor, Canadian J. Chem. Eng., 74, p177.

Lyon, R.K., 1996, Method and Apparatus for Unmixed Combustion as an Alternative to Fire. U.S. Patent No. 5,509,362.

McBride and Gordon, 1996, Computer Program for Calculation of Complex Chemical Equilibrium Compositions and Applications, NASA Reference Publication 1311.

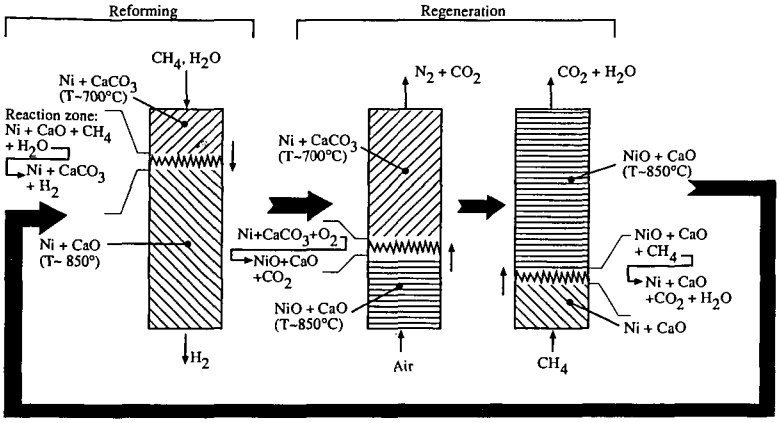

Figure 1. Illustration of the Unmixed Reforming process. The steam reforming of methane (left) produces hydrogen in an endothermic reaction which absorbs some of the sensible heat of the packed bed. Carbon dioxide, produced by the reforming reaction is absorbed by calcium oxide to form calcium carbonate. Once the calcium oxide is all consumed, the reactor must be both chemically and thermally regenerated using the unmixed combustion process as shown in the middle and right-side portions of the figure.

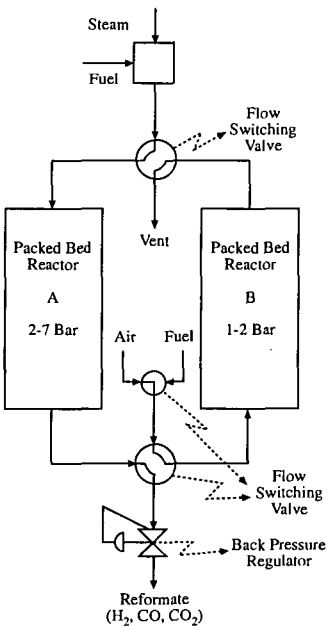

Figure 2. Schematic of experimental system.

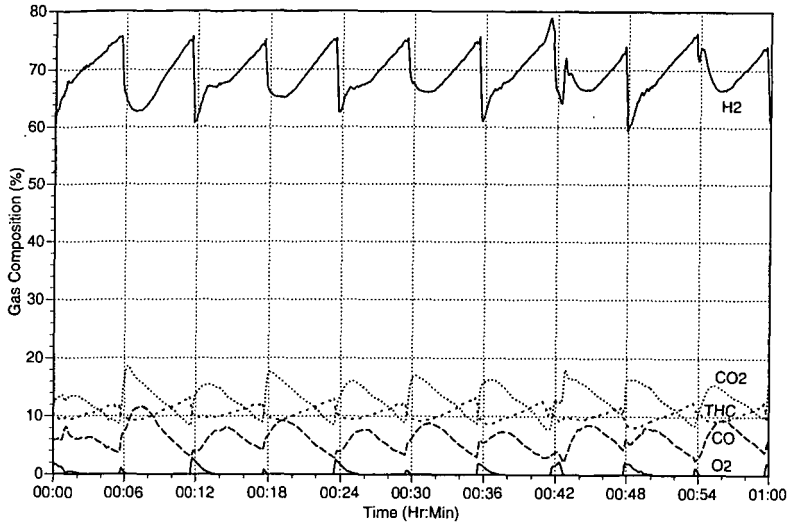

Figure 3. Experimental gas composition data from the Unmixed Reformer (THC - Total Hydo Carbon).

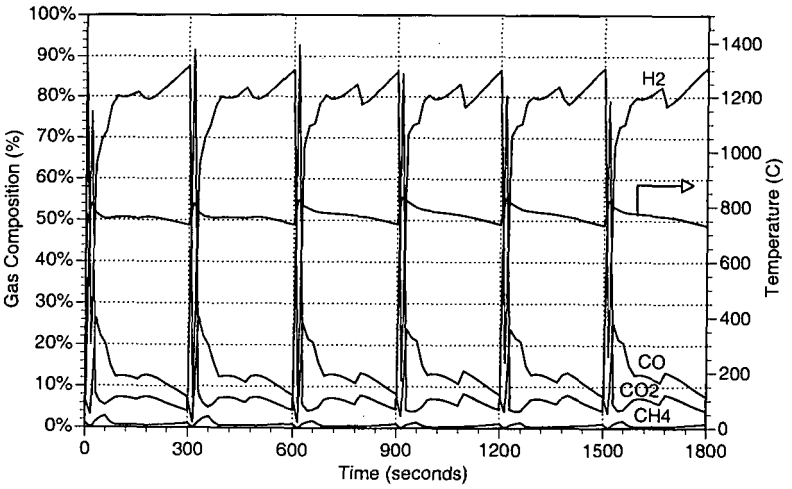

Figure 4. Predicted Unmixed Reformer gas composition using model.

FUEL-FLEXIBLE PARTIAL OXIDATION REFORMING OF HYDROCARBONS FOR AUTOMOTIVE APPLICATIONS

J. P. Kopasz, R. Wilkenhoener, S. Ahmed, J. D. Carter, and M. Krumpelt
Chemical Technology Division
Argonne National Laboratory
9700 South Cass Ave
Argonne, IL 60439

KEYWORDS partial oxidation, fuel-flexible reforming, hydrogen production

INTRODUCTION

Research is underway to develop fuel cells for ultra-low-emission vehicles. However, automotive and petroleum companies have pointed out that the successful commercialization of fuel-cell-powered electric vehicles in the near future will depend, to a large extent, on the availability of a refueling infrastructure.[1] This infrastructure is completely lacking for hydrogen. To tap into the existing fuel infrastructure, fuel processors capable of converting liquid hydrocarbon fuels into hydrogen are required. Fuels of interest include gasoline, diesel, methanol, ethanol, and natural gas.

There is some debate about which hydrocarbon fuel is optimal for fuel cell systems. Methanol and ethanol are widely available commodity chemicals and have numerous advantages as fuel (easy to reform, water soluble, renewable, etc.). Gasoline and diesel have the advantage over the alcohols of existing refueling infrastructures and higher energy density. However, they are blends of different kinds of hydrocarbons and are believed to be more difficult to reform. Kumar et al., at Argonne National Laboratory, have developed a partial oxidation catalyst that can convert a broad range of alcohols and hydrocarbon fuels into a hydrogen-rich product gas.[2, 3] Tests in micro-reactors have shown high conversion and hydrogen yields from methane, methanol, ethanol, 2-pentene, cyclohexane, i-octane, hexadecane, gasoline, and diesel.

The overall partial oxidation reaction can be written as:

(1) $C_nH_mO_p + xO_2 + (2n-2x-p)H_2O = n\,CO_2 + (2n-2x-p+m/2)H_2$

This can be thought of as an exothermic oxidation reaction combined with an endothermic steam-reforming reaction.

(2) Oxidation $C_nH_{2n+2} + 1/2(3n+1)O_2 = nCO_2 + (n+1)H_2O$
(3) Steam Reforming $C_nH_{2n+2} + 2nH_2O(g) = nCO_2 + (3n+1)H_2$

The overall partial oxidation or autothermal catalytic reforming can be exothermic or endothermic. The main factor determining the heat balance for the reaction is the oxygen-to-carbon ratio. The thermal neutral point (where enthalpy of the reaction is zero) varies from an x/n ratio of 0.23 for methanol to 0.37 for iso-octane. For autothermal reforming, it is advantageous to run in the exothermic region, but at a low x/n ratio to maximize the yield of H_2. The experiments reported here were performed with an x/n ratio of 0.5, except for methanol and ethanol experiments, which were performed at a lower x/n (0.32 and 0.25) to compensate for the oxygen already present in the alcohol.

EXPERIMENTAL APPROACH

The catalytic partial oxidation reforming of hydrocarbon fuels was demonstrated in a series of experimental activities, beginning with micro-reactor studies and progressing up to bench-reactor-scale investigations. Since gasoline and diesel fuels are blends of different types of hydrocarbons, the studies were initially carried out with representatives of the different types of hydrocarbons present in these fuels, e.g., iso-octane for paraffins and toluene for aromatics. A schematic of the micro-reactor apparatus is shown in Fig. 1. The liquid fuel and water are pumped through separate vaporizer coils. The vapors then combine with oxygen to form the reactant mix that flows into the micro-reactor. The reactor is a 10.6 mm-ID tube packed with ~2 g of catalyst. The temperature is controlled by a surrounding furnace. Samples are drawn from the product stream and analyzed with a gas chromatograph or gas chromatograph–mass spectrometer. Temperatures and pressures are measured above and below the catalyst bed. In order to facilitate comparisons between the

various fuels, micro-reactor tests were generally run with a fixed carbon-to-oxygen ratio and a slight excess of water with respect to equation 1 [$H_2O > (2n - 2x - p)$].

Fig. 1
Schematic of Experimental

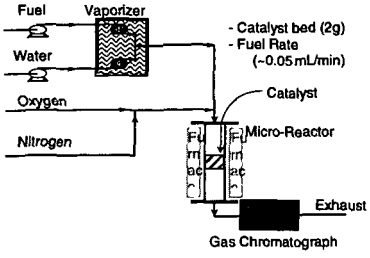

RESULTS AND DISCUSSION

Hydrogen production from the partial oxidation reforming of several of the fuels tested is shown in Table I. The table lists the hydrocarbon feed, the reactor temperature at which complete conversion of the hydrocarbon was achieved and the percentages of hydrogen, carbon monoxide, and carbon dioxide measured in the product gas. The last three columns list the calculated percentages of the gases that would exist at equilibrium at the different temperatures. Using the Argonne catalyst, we were able to convert these hydrocarbons at less than 700°C. Comparison between the experimental and equilibrium gas compositions indicates that the use of the catalyst allows for lower carbon monoxide and slightly higher hydrogen concentrations than what might be achieved at equilibrium at these temperatures.

Table 1. Experimental Product Gas Composition Compared with Equilibrium Compositions Calculated for the Given Feed Mixture and Experimental Temperature

Fuel	Temperature for complete conversion, °C	Experimental (%, dry N_2 free)			Equilibrium (%, dry N_2 free)		
		H_2	CO	CO_2	H_2	CO	CO_2
Iso-octane	630	60	16	20	57	20	19
Toluene	655	50	8	39	49	23	26
2-Pentene	670	60	18	22	56	21	21
Ethanol	580	62	15	18	62	18	16
Methanol	450	60	18	20	60	19	17

Table I also indicates that the two alcohols (methanol and ethanol) are reformed at substantially lower temperatures than the other species. Of the fuels considered for partial oxidation reforming, alcohols should be considerably easier to reform since they are already partially oxidized.

There is a substantial difference in the temperature at which complete conversion of the hydrocarbons was achieved, even between the two alcohols studied. Figure 2 illustrates the temperature dependence of hydrogen production from the partial oxidation reforming of methanol and ethanol using the Argonne partial oxidation. The two alcohols behave quite differently.

Fig. 2
Hydrogen Production from Partial Oxidation Reforming of Alcohol Fuels

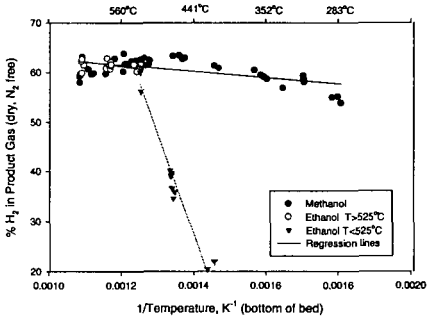

Methanol was easily reformed throughout the temperature range investigated. This fuel yielded a product gas that had hydrogen concentrations in the 55 to 65% range (on a dry N_2 free basis), with the product gas varying only slightly in composition with changes in temperature. The temperature dependence of ethanol reforming was quite different, with the product composition varying strongly with temperature in the range of 410 to 525°C. At 470°C, the product gas from ethanol reforming contained only about 35% hydrogen, compared to about 60% hydrogen for methanol reforming at the same temperature. For temperatures greater than 525°C, hydrogen production from ethanol was almost identical to that from methanol. However, the maximum hydrogen yield for the reactant mix with methanol was 70.2%, while that for ethanol was 71%. Defining hydrogen selectivity as the measured hydrogen yield divided by the maximum, we find slightly lower hydrogen selectivity for ethanol in the high temperature region (88%) than for methanol (91%). This was due to the formation of methane in the ethanol reforming. The ethanol reformate contained substantial amounts of methane over the entire temperature range investigated, with the reformate containing about 5% methane at 640°C, while the methanol reformate contained an order of magnitude less methane at this temperature.

Fig. 3
Hydrogen Production from Partial Oxidation Reforming of Alkanes and Alkenes

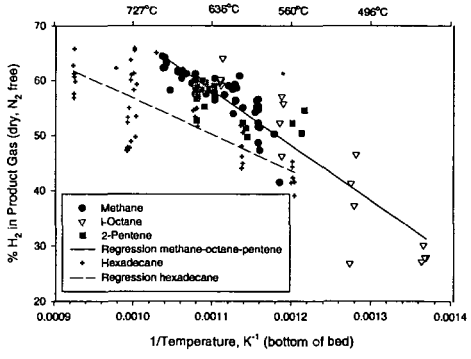

The effect of temperature on hydrogen production from reforming of methane, iso-octane, and 2-pentene is shown in Fig. 3. These hydrocarbons were more difficult to reform autothermally than the alcohols, as expected. Temperatures of nearly 650°C were needed to approach 60% hydrogen in the product gas. Hydrogen selectivities of 90% for methane and 88% for iso-octane and 2-pentene were obtained. The hydrogen concentration at a given temperature was similar regardless of the hydrocarbon. The data for methane, iso-octane, and 2-pentene all fall on the same regression line (see

Fig. 3). Hydrocarbon length over the range of C1 to C8 and the presence of unsaturation appear to have little affect on the product composition.

Increasing the hydrocarbon length to C16 (hexadecane) was observed to lead to lower hydrogen content in the product gas. Hexadecane reforming showed a temperature dependence similar to that observed for methane, iso-octane, and 2-pentene (i.e., similar slope in Fig.3). However, higher temperatures were needed to reach comparable hydrogen content in the product gas. This appears to be due to increased methane formation from hexadecane. At 650°C, the product gas from hexadecane reforming contained 6% methane (dry, nitrogen free), while that from iso-octane reforming contained only about 2% methane.

The iso-octane and hexadecane experiments also pointed out some potential difficulties in reforming longer hydrocarbons. The product gas from iso-octane and hexadecane reforming contained small amounts of benzene. This is illustrated in Table II, which compares the output from thermal reforming (no catalyst present) and catalytic reforming (catalyst present) of iso-octane. Benzene was present in the product gas at concentrations of about 0.1-0.2% for temperatures from 600 to 725°C when the catalyst was present; however, no benzene was detected in the product gas when the catalyst was absent. This suggests that benzene is formed as a side product during the reforming of C8 hydrocarbons. Studies on the formation of aromatics from C8 hydrocarbons have indicated that the most likely mechanism for benzene production involves formation of xylenes, which then form benzene by trans alkylation reactions.[4]

Table 2. Effect of Catalyst on Product Composition

	Product Composition at 725°C, % (dry, N_2 free)					
	H_2	O_2	CH_4	CO	CO_2	C_6H_6
No Catalyst	0.0	10.2	17.7	39.6	26.1	0.0
Catalyst	57.9	0.0	4.3	19.2	18.1	0.2

We have also investigated the reforming of cyclohexane, a possible benzene precursor, and toluene, a benzene derivative. The hydrogen production from partial oxidation reforming of cyclohexane and toluene did not exhibit the same temperature dependence as did that from reforming the alkanes and the alkene discussed previously. The product composition was much less sensitive to temperature for these cyclic compounds (see Fig. 4). Hydrogen selectivity was still high, but slightly lower for toluene (82%) than for cyclohexane (91%) and the non-cyclic alkanes (88%). The lower temperature dependence suggests that a different mechanism may be controlling the reforming of cyclohexane and toluene.

Fig. 4
Hydrogen Production from Partial Oxidation Reforming of Cyclohexane and Toluene

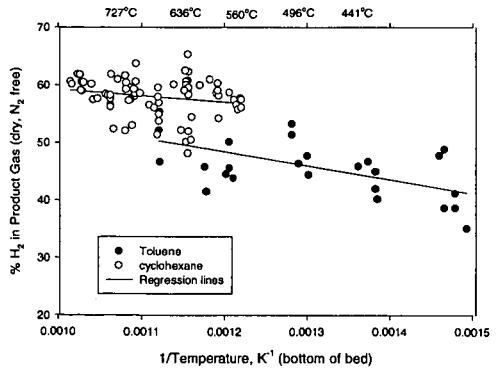

The results from reforming toluene suggest that if benzene, xylene, or other aromatics are formed at low levels as side products in the reforming of branched hydrocarbons they can be reformed. Increasing the temperature will increase the conversion of these aromatics to hydrogen, but not as effectively as it increases the rate of conversion of alkanes to hydrogen.

The ability of the Argonne catalyst to reform several types of hydrocarbons suggested that this catalyst would be able to reform commercial petroleum fuels. Therefore, we proceeded with tests of commercial gasoline and diesel fuel. The product composition from autothermal reforming of a commercial premium gasoline is shown in Fig. 5. Hydrogen concentrations in the product gas approaching 60% on a dry N_2 free basis were obtained at temperatures ≥700°C. The slope of the plot of inverse temperature versus hydrogen content in the product gas is similar to that found for the reforming of methane, iso-octane, and 2-pentene, suggesting a similar mechanism. However, methane concentrations in the product gas are higher than what we have seen from reforming the simple hydrocarbons. Commercial gasoline contains sulfur, a known catalyst poison, at levels of over 100 ppm. However, no change was observed in the product composition after 40 h of intermittent gasoline reforming, indicating it has some

Fig. 5
Product Distribution from Partial Oxidation Reforming of Premium Gasoline

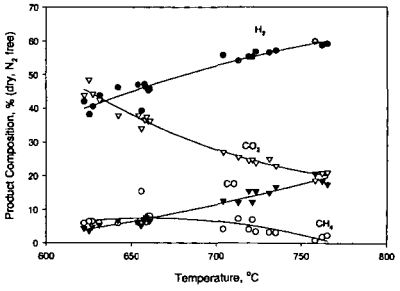

resistance to sulfur poisoning.

Reforming of diesel fuel proved slightly more difficult. Methane was observed in higher concentrations in the product gas from diesel reforming than in the product from gasoline reforming. Higher reforming temperatures were needed to decrease the methane and increase the hydrogen in the product gas. At 850°C we were able to obtain a product gas with hydrogen concentrations >50% on a dry N_2 free basis (see Fig. 6).

CONCLUSIONS

Micro-reactor tests indicate that our partial oxidation catalyst is fuel-flexible and can reform conventional (gasoline and diesel) and alternative (ethanol, methanol, natural gas) fuels to hydrogen rich product gases with high hydrogen selectivity. Alcohols are reformed at lower temperatures (< 600°C) while alkanes and unsaturated hydrocarbons require slightly higher temperatures. Cyclic hydrocarbons and aromatics have also been reformed at relatively low temperatures, however, a different mechanism appears to be responsible for their reforming. Complex fuels like gasoline and diesel, which are

Fig. 6
Product Distribution from Partial Oxidation Reforming of Diesel Type 2

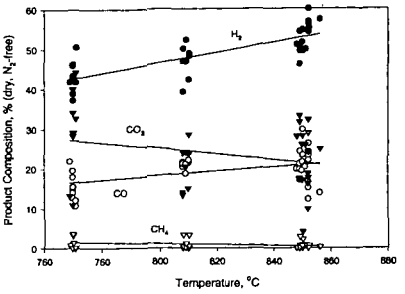

mixtures of a broad range of hydrocarbons, require temperatures of > 700°C for maximum hydrogen production.

ACKNOWLEDGMENTS

This work was supported by the U.S. Department of Energy, Office of Advanced Automotive Technologies, in the Office of Automotive Technologies, under contract No. W-31-109-ENG-38.

REFERENCES

1. R. L. Espino, "Fuels Processing for PEM Fuel Cells - Fuel Industry Perspective," Annual Automotive Technology Development Contractor's Coordination Meeting-PNGV Workshop on Fuel Processing for PEM Fuel Cells, Dearborn, MI, 23-27 October 1995.
2. R. Kumar, S. Ahmed and M. Krumpelt, Electric and Hybrid Vehicle Technology 96, 1996.
3. S. Ahmed, R. Doshi, R. Kumar, and M. Krumpelt, Electric and Hybrid Vehicle Technology '97, p. 77, 1997.
4. C. Marshall, Argonne National Laboratory, private communication, 1999.

Hydrogen Production via Methanol – Steam Reforming using Catalysts containing a Hydrotalcite Phase Structure

L.M. Kearns, J.C. Amphlett, E. Haliop, H.M. Jenkins, R.F. Mann and B.A. Peppley

Department of Chemistry and Chemical Engineering
Royal Military College of Canada
Kingston, Canada.

Abstract

Steam reformation of methanol is an actively studied process for supplying hydrogen rich fuel gas to proton-exchange membrane (PEM) fuel cells. The purpose of the present investigation is to improve activity and thermal stability of our optimized Cu/Zn/Al formulation. Cu/Zn/Cr, Cu/Zn/Cr/Al, Cu/Zn/Ce, Cu/Zn/Ce/Al, Cu/Zn/La and Cu/Zn/La/Al were prepared at different calcination temperatures. The catalysts were thoroughly characterized and activity studies were run at 250°C with 1:1 methanol/steam using a pulse reformer. Characterization results indicate that the hydrotalcite skeletal structure is still intact in catalysts calcined up to 300°C. The activity of the Cu/Zn/Cr catalyst calcined at 300°C of the calcination series was significantly higher than for any other catalyst series in the study with very little deactivation during the duration of the run. Activity studies using a high pressure reactor also showed superior activity for the Cu/Zn/Cr catalyst with analysis of the spent catalyst indicating very little structural damage.

1. Introduction

With growing support for environmental issues, there is incentive to develop an efficient, clean electric power system to operate stationary power plants and vehicles such as cars, buses and submarines. The increased interest is caused both by a search for an alternative energy source for the decreasing supply of fossil fuels and the increasingly stringent regulations for emission levels that are coming into effect in many parts of the world. A promising system actively being developed is the hydrogen fed Proton Exchange Membrane (PEM) fuel cell. The many benefits include a significant increase in energy efficiency and reduction of emissions by as much as 90%; specifically reducing CO_2 emissions by 40%[1]. A liquid fuel is the desirable form for transport and storage of hydrogen. Steam reformation of methanol is the most widely studied system for production of hydrogen rich gas to be utilized at the anode of a PEM fuel cell as compared to hydrocarbon reformation and steam reformation of ethanol[2,3]. Methanol, as a reactant in steam reformation, is a relatively inexpensive renewable fuel that produces less environmentally harmful products than the internal combustion of conventional petroleum fuel. We have developed an improved $CuO/ZnO/Al_2O_3$ catalyst for methanol steam reforming. Our latest formulation gives higher activities than commerial catalysts for the range of temperatures and time on line investigated [4,5].

Experience with our optimal catalyst showed that enhanced activity was correlated with the presence of hydrotalcite structure, therefore other elements that can be incorporated in a hydrotalcite structure may also show high activity and possibly higher thermal stability. Also, structures that resisted sintering would lower the rate of deactivation of a proposed catalyst. Cerium, Chromium and Lanthanum were incorporated in some catalyst formulations. These elements have potential to form hydrotalcite structures with Cu and Zn with or without Al present. Lanthanum has also been used to improve thermal stability of catalysts. The principle is that the small sized La atoms fit between the atoms in the phase structure and act as a physical block to inhibit sintering. Modified catalysts of Cu/Zn/Ce, Cu/Zn/Ce/Al, Cu/Zn/Cr, Cu/Zn/Cr/Al, Cu/Zn/La and Cu/Zn/La/Al were prepared at different calcination temperatures.

2. Experimental

2.1 Catalyst Preparation

The catalyst was prepared by a coprecipitation method using a dilute mixed Cu, Zn, X (X=Al,Ce,Cr,La) - nitrate solution and a solution of Na_2CO_3. The two solutions were simultaneously added to distilled water with vigorous stirring, using pumps whose flow rates were adjusted to keep the pH of the resulting mixture precisely at 7.0. The precipitate was filtered, washed, reslurried, then filtered again before drying at 110°C for 16 hrs. The precursor was crushed into smaller particles, then calcined in air at the specified temperature (300, 400, 550 or 650°C) for 6 hrs.

2.2 Catalyst Characterization

The catalyst series were characterized using thermal gravimetric analysis (TGA), x-ray powder diffraction (XRD) for phase structure analysis, N_2 adsorption for total surface area and CO chemisorption for copper surface area. Copper dispersion was calculated from the results of copper content and copper surface area. Surface studies were carried out using diffuse reflectance infrared fourier transform spectroscopy (DRIFTS).

TGA analyses were done using a TA Instruments Thermograph Model 2050 controlled by a Thermal Analyst 3000 computer. The He flow rate was 100 ml/min. The temperature was increased at 10°C/min. The first derivatives of the TGA curves (%Mass vs. Temperature) were calculated and used to determine the decomposition profile for the precursor phase structure.

XRD powder patterns were obtained using a Scintag diffractometer. Scans were taken at a 2θ step size of 0.03° between 10 and 60° using Cu-$K\alpha_1$ (nickel filtered) radiation. Cu and Zn crystallite sizes were calculated from the line broadening of the CuO(111) and ZnO(101) lines respectively using the Debye-Sherrer Method.

2.3 Study of Catalyst deactivation

The high pressure test reactor used for part of the activity studies was a fully automated tubular fixed-bed reactor. The catalyst was pelletized and screened to obtain a particle size distribution of 20-25 mesh. A

1.0 g sample of the catalyst material was diluted in α-Al_2O_3 of identical mesh size to ensure that uniform plug flow and isothermal operation were achieved.

The catalyst was activated at 240°C in 1:1 molar methanol-steam vapour. The liquid hourly space velocity (LHSV) was 47 h^{-1} assuming a catalyst bulk density of 1.2 kg L^{-1}. After two hours of conditioning at 240°C a steady-state conversion was achieved and the catalyst was considered to be fully activated. The temperature of the reactor was then increased to 280°C and operated continuously for the duration of the test.

The pulse reformer consisted of a reactor containing 15 mg of catalyst and 200mg of alpha alumina. Twenty five, 10 microlitre pulses of 1:1 methanol/water were passed through the catalyst bed in a stream of UHP helium at a flow rate of 35 ml/min. The reaction temperature was 250 C. The product gas was separated on a Porapak Q column in a Gow Mac Gas Chromatograph using a TCD detector.

3. Results and Discussion

3. 1 Aluminum Containing Series

Cu/Zn/Al precursor, prepared using the optimal preparation procedure, was calcined in air at specified temperatures (300, 400, 550 and 650°C) for 6 hrs. The calcined catalysts were thoroughly characterized and activity studies were carried out. TGA results indicated that residual hydrotalcite was present for catalysts calcined at temperatures of 400°C or below. The hydrotalcite phase partially reformed in catalysts that were placed in water except for the catalyst calcined at 650°C. Very little hydrotalcite

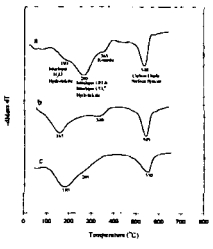

Figure 1. First derivative of TGA curve for Cu/Zn/Al a) precursor; b) catalyst calcined at 300°C; c) after reconstitution of b).

reformed for the catalyst calcined at 550°C. In an environment of 1:1 steam/methanol it is conceivable that the hydrotalcite structure would have the ability to be in dynamic equilibrium with its reaction environment. CuO and ZnO were observed as very weak peaks for the catalyst calcined at 400°C. These peaks grew larger as the calcination temperature of the catalyst increased with appearance of $ZnAl_2O_4$ for the catalyst calcined at 650°C. An XPS study of the catalyst series clearly showed the change from the full hydrotalcite structure to an oxycarbonate followed by formation of oxide. There was strong correlation between high catalyst activity and presence of the hydrotalcite phase, either as the fully developed phase structure, as seen in the precursor, or as a partially decomposed (dehydroxylated) phase as observed in the catalysts calcined at 300°C and 400°C. The activities, with respect to methanol-steam reforming of the precursor and catalysts calcined at 300°C and 400°C were similar and significantly higher than for the

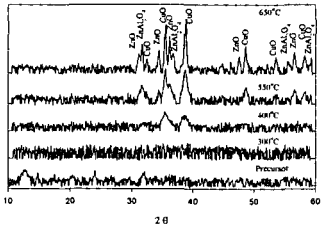

Figure 2. XRD profiles for Cu/Zn/Al catalyst series calcined at various temperatures.

catalysts calcined at higher temperatures which contained significantly less residual hydrotalcite structure. Presence of hydrotalcite in the catalyst structure appears to be imperative in obtaining a catalyst with optimum activity.

3.2 Lanthanum and Cerium Containing Series

The TGA curves for the Cu/Zn/La, Cu/Zn/La/Al, Cu/Zn/Ce and Cu/Zn/Ce/Al catalyst series were very similar. A large proportion of the precursor consisted of the hydrotalcite phase with some rosasite as observed by the presence of their respective characteristic decomposition temperatures. A very large peak was observed in the 1st derivative of the TGA curves at approximately 500°C which was due to decomposition of surface carbon oxides. TPD (temperature programmed desorption) experiments in which

samples of the desorbing gases were analysed by mass spectrometry for each range of temperature, confirmed the assignment of the peaks from the 1st derivative of the TGA curves.

For these catalyst series, the precursors were XRD amorphous. A broad peak was observed between 34° and 36° 2θ for the catalysts calcined at 300°C which became more intense for the catalysts calcined at 400°C. Peaks for CuO and ZnO were observed for catalysts calcined at 550°C and 650°C. The activities of the Cu/Zn/La and Cu/Zn/Ce series were similar to the Cu/Zn/Al series as were the rates of deactivation. The precursor and catalysts calcined at 300°C and 400°C had the highest activities.

3.3 Chromium-Containing Catalysts

From TGA and TPD results the presence of a hydrotalcite structure was confirmed in precursors for both the Cu/Zn/Cr and Cu/Zn/Cr/Al formulations. The broad overlapping decomposition temperature range for the intralayer OH and interlayer CO_3^{2-} was shifted to a lower temperature centred at 210°C for the Cu/Zn/Cr/Al precursor and 190°C for the Cu/Zn/Cr precursor. Upon placing samples calcined at 300°C in water, reconstitution of the hydrotalcite was observed as with the other formulations. Very little surface carbon oxide species were present on the Cr catalyst series compared to any other catalysts studied. Also, the decomposition temperature for the surface carbon oxide species was shifted to a lower temperature of 440°C for the Cu/Zn/Cr precursor compared to 540°C for the Cu/Zn/Cr/Al precursor. In the XRD profiles,

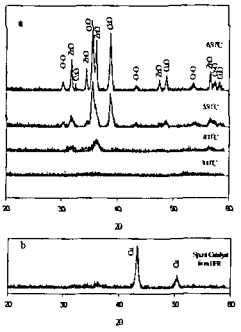

Figure 3. XRD profiles for the a) Cu/Zn/Cr series calcined at various temperatures; b) spent Cu/Zn/Cr catalyst calcined att 300°C. The catalyst war removed from the high pressure reactor after 7 days at 280°C.

shown in Figure 3, the catalyst calcined at 300°C was XRD amorphous, as well as the precusor whose XRD profile is not shown. Very broad peaks attributed to zincite (ZnO) were observed for the catalyst calcined at 400°C. The ZnO crystallites were much smaller in the Cu/Zn/Cr catalyst than in the Cu/Zn/Cr/Al catalyst. Tenorite (CuO) was not observed until 550°C. CuO appears to be highly disperse (XRD amorphous). Chromium oxide appeared only in the catalysts calcined at 550°C and 650°C.

The low quantity of surface carbon oxides observed by FTIR indicates that Cr containing catalyst formulations are less basic than the other catalysts studied. Bands due to OH groups and hydrogen bonding between the interlayer hydroxy groups and carbonates of hydrotalcite were present.

The activity of the Cu/Zn/Cr catalyst calcined at 300°C was higher than the Cu/Zn/Al catalyst with very little deactivation during the duration of the run. The activity study of the Cr series is shown in Figure 4. The activities of the Cu/Zn/Cr/Al series was similar to that of the Cu/Zn/Al series except that the catalyst calcined at 550°C also had as high an activity as the same series of catalysts calcined at lower temperatures.

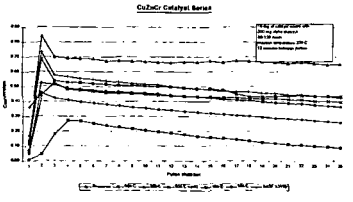

Figure 4. Deactivation study of the Cu/Zn/Cr series using a pulse reformer. Reaction was carried out at 250°C With 1:1 methanol/steam and pulses every 12 minutes.

4. Characterization of Spent Catalysts

4.1 Cu/Zn/Al

Characterization of the spent Cu/Zn/Al catalyst was carried out on the catalyst calcined at 300°C since it was the catalyst in the series with the highest activity. The XRD profile showed the presence of relatively large crystallites of zincite. No tenorite was observed, so if any CuO was present it was

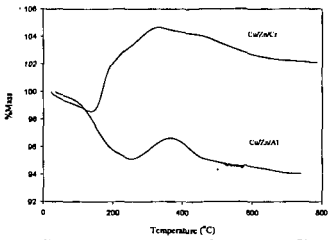

amorphous or XRD invisible. Metallic Cu was observed in the XRD profiles and was evidently stable to air at room temerature. The very low weight loss of the spent catalysts in comparison to the fresh catalysts, observed in the TGA, indicated that very little hydroxycarbonate phases had remained intact after

Figure 5. TGA curves for the spent Cu/Zn/Cr and Cu/Zn/Al catalysts calcined at 300°C. The Cu/Zn/Cr catalyst was run at 280°C for for 170 hours while the Cu/Zn/Al catalyst was run at 240°C in a high pressure reactor. The reactant feed was 1:1 methanol steam.

completion of the reaction run. A weight loss of 7% was observed compared to 18% for the fresh catalyst. The initial decrease in the TGA scan of the spent catalyst coincided with those found for the precursor hydrotalcite representing decomposition of interlayer H_2O and intralayer OH/interlayer CO_3^{2-}. The structure of the spent catalysts was considerably changed compared to the fresh catalyst. A gain in mass was observed beginning at 230°C (Figure 5) in the TGA curve. The mass increase was the result of formation of CuO from Cu metal during heating in air.

4.2. Cu/Zn/Cr

The Cu/Zn/Cr spent catalyst that was characterized was calcined at 300°C and run in the high pressure reactor for 170 hours at 280°C in a 1:1 ratio of methanol/steam reactant flow. The XRD profile of the spent Cu/Zn/Cr catalyst is shown in Figure 3b. Cu metal was the only phase observed. Crystallite size was determined using the Debye-Sherrer method and was found to be 19 nm. ZnO was not observed in the spent Cu/Zn/Cr. TGA analysis, shown in Figure 5, indicated that stable Cu metal began oxidizing at 190°C. A mass increase of more than 5% was observed.

5. Conclusions

The most active catalyst formulation was Cu/Zn/Cr. The catalyst calcined at 300°C gave the highest activity of any catalyst. In all cases, the catalyst calcined at 300°C gave higher activities than catalysts in the same calcination series. The Cu/Zn/Cr catalyst calcined at 300°C showed very little deactivation in the activity studies for reactions run in the pulse reformer and the high pressure reactor. Analyses of the spent catalysts gave very interesting results. For the Cu/Zn/Al catalyst, relatively large ZnO and Cu metal crystallites were observed by XRD. Whereas with the Cu/Zn/Cr spent catalyst, only crystallites of Cu metal were observed. The ZnO remained well dispersed during the test reaction using the high pressure reactor. Also, the Cu metal appeared to be more active in the Cu/Zn/Cr spent catalyst as observed in Figure 5 where oxidation of Cu metal during the TGA run occurred at a much lower temperature and in much greater abundance than for the Cu/Zn/Al spent catalyst. These findings help to identify the differences in the Cu/Zn/Cr catalyst, calcined at 300°C and may indicate why this catalyst has significantly higher activity and thermal stability.

References

1. P. Patil, P. Zegers, J. Power Sources 49 (1994) 169.

2. B.A. Peppley, J.C. Amphlett, L.M. Kearns, R.F. Mann, Methanol-Steam Reforming on $Cu/ZnO/Al_2O_3$, Part I: The Reaction Network, Appl. Catal., submitted for publication.

3. B.A. Peppley, J.C. Amphlett, L.M. Kearns, R.F. Mann, , Methanol-Steam Reforming on $Cu/ZnO/Al_2O_3$, Part 2: A Comprehensive Kinetic Model, Appl. Catal., submitted for publication.

4. B.A. Peppley, "A Comprehensive Kinetic Model of Methanol-Steam Reforming on $Cu/ZnO/Al_2O_3$ catalyst". Ph.D. Thesis, Royal Military College of Canada, Kingston, Ontario, Canada, (1997).

5. R.O. Idem and N.N. Bakhshi, Chem. Eng. Sci. 51 (1996) 3697.

SYSTEM OPTIMIZATION AND COST ANALYSIS OF PLASMA CATALYTIC REFORMING OF HYDROCARBONS

L. Bromberg, D.R. Cohn, A. Rabinovich, N. Alexeev, A. Samokhin
MIT Plasma Science and Fusion Center
Cambridge MA 02139

and

R. Ramprasal, S. Tamhankar
BOC Gases
New Brunswick NJ 84501

Abstract
Thermal plasma reforming offers advantages in hydrocarbon reforming specially in small to medium scale plants and in plants with fast transients. The combination of a thermal plasma reformer operating in the range between partial oxidation to steam reforming with a catalyst bed will be described. Reduced concentrations of CO (1-3% vol) can be achieved, with high hydrogen yields and minimal plasmatron electrical power requirements. A model for the cost of hydrogen production by this method, including hydrogen cleanup, has been developed. The model uses experimentally determined conversion yields and operational parameters. The conditions that result in system optimization and cost minimization have been determined.

1 Introduction

Manufacturing of hydrogen from natural gas, biofuels and other hydrocarbons, is needed for a variety of applications. Plasma technology could provide important improvements in reforming hydrocarbon fuels for the production of hydrogen-rich gas for fuel cells and other applications. The plasma conditions (high temperatures and a high degree of ionization) can be used to accelerate thermodynamically favorable chemical reactions or provide the energy required for endothermic reforming processes. Plasma reformers can provide a number of advantages:

- economically attractive operation in small scale hydrogen production applications
- operation with a broad range of fuels, including natural gas and biofuels
- decreased problems of catalyst sensitivity and deterioration
- compactness and low weight (due to high power density)
- fast response time (fraction of a second)
- minimal cost
- high conversion efficiencies

Hydrogen-rich gas could be efficiently produced in compact plasma reformers with a variety of hydrocarbon fuels including natural gas, biomass, and others. The technology could be used to manufacture hydrogen for a variety of stationary applications (e.g., distributed, low pollution electricity generation from fuel cells or hydrogen-refueling gas stations for fuel cell driven cars). It could also be used for mobile applications (e.g., on-board generation of hydrogen for fuel cell powered vehicles).

In this paper, the cost issues of a plant that incorporate a plasma reformer are investigated. It is assumed that the plant operates on natural gas, although the plasmatron is capable of operating in a wide range of fuels. The experimental results of plasma reforming of natural gas are quickly reviewed in section 2. A model of a process plant is developed, and a model for determining the hydrogen cost is described in section 3. The sensitivity of the cost to capital cost, cost of natural gas and to manpower requirements are then presented in section 4. The tradeoff between higher conversion and increased electrically energy consumption in the plasmatron is described in section 5. Finally, the conclusions and direction of additional work is described in section 6.

2 Plasma reforming

Plasma devices referred to as plasmatrons can generate very high temperatures (>2000 C) with a high degree of control, using electricity [1]. The heat generation is independent of reaction chemistry, and optimal operating conditions can be maintained over a wide range of feed rates and gas composition. Compactness of the plasma reformer is ensured by high energy density associated with the plasma itself and by the reduced reaction times, resulting in short residence time. Hydrogen-rich gas can be efficiently produced in plasma reformers with a variety of hydrocarbon fuels (gasoline, diesel, oil, biomass, natural gas, jet fuel, etc.) with conversion efficiencies into hydrogen-rich gas close to 100% [2,3].

The plasma conditions (high temperatures, high degree of dissociation and substantial degree of ionization) can be used to accelerate thermodynamically favorable chemical reactions without a catalyst or provide the energy required for endothermic reforming processes.

The technology could be used to manufacture hydrogen for a variety of stationary applications e.g., distributed, low pollution electricity generation from fuel cells [4]. It could also be used for mobile

applications (e.g., on-board generation of hydrogen for fuel cell powered vehicles) and for refueling applications (stationary sources of hydrogen for vehicles).

A previous paper [5] presented results of plasma catalytic conversion of methane, using partial oxidation. In this section, more recent results are very briefly described. Figure 1 shows the hydrogen yield as a function of the specific energy consumption (electrical power required for a given hydrogen throughput). The best results are 95% yield at a specific energy consumption of 13 MJ/kg H_2. These results were obtained without the use of a heat exchanger. It is estimated that with a heat exchanger and with improved thermal management, the specific energy consumption can be decreased to 7 MJ/kg H_2 (0.18 kWhr/m^3 H_2) at slightly higher yield (97%). These numbers will assumed in the calculations below.

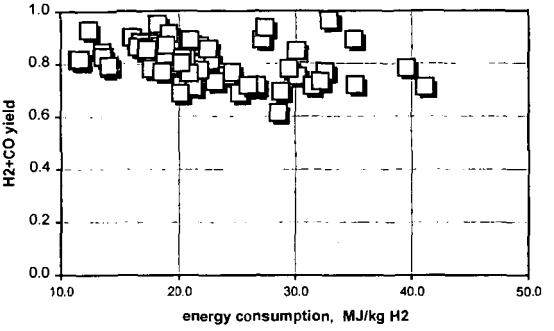

Figure 1. Hydrogen yield as a function of specific energy consumption for plasma catalytic reforming of methane.

3 Costing model

The cost of the hydrogen produced through a plasmatron process is investigated in this section. It is assumed that the hydrogen rich gas is produced at pressure so that it is not necessary to pressurize the hydrogen rich gas prior to the pressure swing absorption section. Air, not oxygen, is used as the oxidizer, which means that the synthesis gas contains a large amount of nitrogen. It is also assumed that methane is the hydrocarbon used, although other hydrocarbons can also he utilized. Further assumptions are that the system has good thermal management, and the power consumed by the plasmatron as well as the exothermic energy released by the partial oxidation process are used to produce the steam required for the system. Steam is required mainly in the water-shift reaction. There is an excess of steam for the steam shifter of 200%.

The capital costs of the system, for a 8570 m^3/hr (5000 scfm) are shown in Table 1. The syngas is at pressure, and there is no need for boiler to produce steam since it can be produced by the syngas itself prior to the water shift reaction, which occurs at relatively low temperatures. If the plant is amortized over 10 years, then the amortized capital cost is on the order of $500k per year.

Table 1. Capital costs for system with 8570 m^3/hr

NG compressor	$250,000
Air compressor	$250,000
Reforming Reactor	$50,000
plasmatron	$500,000
convertor (power supply)	$300,000
spares	$50,000
Shift Reactor	$500,000
Syngas compressor	$0
H2 PSA	$1,500,000
Waste-to-Steam Boiler	$0
Air Blower for Boiler	$0
Incinerator	$0
Cap cost total	$3,400,000
Installation	$680,000
Plant Cost (Installed)	$4,080,000

The operational costs depend on the number of personnel operating the plant. Since the high power plasmatron is a well-established technology, it is assumed that the system is automated and needs minimal supervision. Maintenance to the plasmatron, consisting in replacing the electrodes, needs to be performed every 1000 hours of operation, and lasts only a few minutes. During plasmatron maintenance, the system can continue to operate at reduced level. Several plasmatrons are used in the system, and electrode replacement is carried out one by one.

The power requirements are shown in Table 2. The syngas is at pressure when leaving the plasmatron reactor. Air compression requires more power than the corresponding oxygen compression. The power requirements are dominated by the plasmatron power requirements of 1500 kW.

Table 2. Power consumption in 8570 m^3/hr plant

NG Comp. power, kW	100
Air Comp. power, kW	200
Syngas Comp., kW	0
Plasmatron power, kW	1500
Total Power, kW	1800

The cost of the natural gas is assumed to be $2.5/MMBTU, and the electricity cost is $0.05/kWhr. Assuming that 8 full time people (all shifts) are required in the plant (at a cost of $70000/person-year), then the annual costs are given in Table 3, for 8570 m^3/hr.

Table 3. Annualized costs for a 8570 m^3/hr hydrogen plant

Labor	$560,000
Catalyst	$100,000
Power	$600,000
Other	$1,801,237
Total Op. + Util.	$3,061,237
Total cost Op+util+cap	$3,571,237

With an annual hydrogen production of 720K MMBTU, then the cost of the hydrogen is about $5/MMBTU. This is a very preliminary look at the cost, and more detailed calculations will be presented at a later time.

The model can be used to determine the cost of the hydrogen as a function of the plant capacity. Figure 2 shows the results from this calculations, assuming that the cost of the equipment (capital cost) scale linearly with plant capacity.

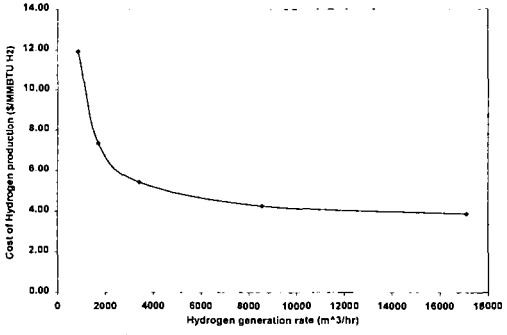

Figure 2 Cost of hydrogen as a function of the plant capacity.

4 Sensitivity of hydrogen cost

The dependence of the hydrogen costs on the capital cost, the methane cost and the required personnel is described in this section.

The sensitivity of the cost of hydrogen to the cost of natural gas in shown in Figure 3. The cost of the hydrogen is about $3.5/MMBTU more expensive than the cost of the natural gas. For free natural gas, the cost of the hydrogen is about $4/MMBTU.

From Table 3, it can be seen that the bulk of the cost is due to the natural gas, with the electrical power about 1/3 of the natural gas cost. Increasing the cost of the capital equipment by a factor of 2.5 increases the hydrogen cost from $6.1/MMBTU to $7.2/MMBTU, for 3430 m^3/hr plant capacity. Increasing the cost of electricity to $0.10 /kWhr increases the cost of hydrogen to $6.9/MMBTU.

The effect of the automation can be seen in Figure 4. 8 people per year corresponds to 2 persons attending the plant at all times, both at the control room and in maintenance operations. If plasma operation can decrease the required supervision, then the hydrogen cost can be decreased substantially. If only 2 personnel are required, for light supervision, transients and maintenance, then the hydrogen cost can be decreased to about $4/MMBTU, which is about just 75% higher than the cost of the natural gas feedstock.

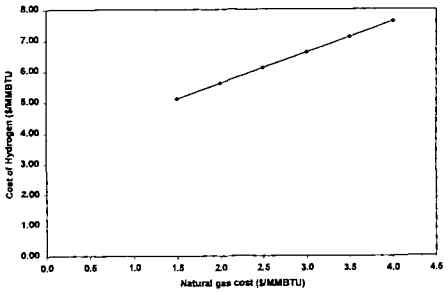

Figure 3. Hydrogen cost as a function of natural gas cost, for a 3430 m^3/hr plant capacity

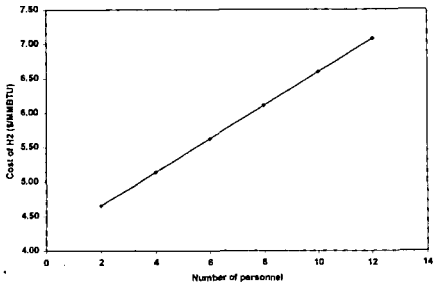

Figure 4. Hydrogen cost as a function of number of plant attendants, for a 3430 m^3/hr plant capacity

5 Tradeoff between methane conversion and specific energy requirement

As mentioned in the sections above, there is a tradeoff between the methane conversion and the hydrogen yield. A simplified curve illustrating this tradeoff is shown in Figure 4. For a specific energy consumption less than about 0.17 kWhr/m^3 there is a sharp drop in the methane conversion. At the higher specific energy consumption, the methane conversion does not increase much.

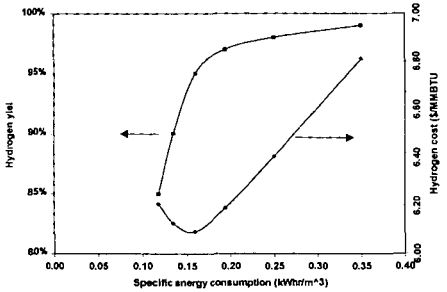

Figure 5. Methane yield and cost of hydrogen as a function of the specific energy, for 3430 m^3/hr plant capacity

Figure 5 also shows the hydrogen cost as a function of the specific energy consumption. All the other parameters are the same as in the previous sections. There is a well-defined minimum in the cost. To the left of the minimum, the hydrogen yield is decreasing because of not enough conversion of methane, and to the right of the minimum the electrical cost is increasing faster than the hydrogen yield. It is important to determine experimentally the minimum cost.

6 Discussion and conclusions

Plasma reforming of natural gas has been briefly described. A process involving plasma reforming of natural gas for the production of hydrogen is then modeled to determine the cost and the cost-sensitivity of hydrogen produced by the process. Although preliminary, the costs indicate that there may be methods of producing hydrogen at competitive costs, specially important for small capacity hydrogen generating units.

Several assumptions need to be demonstrated experimentally. It is necessary to demonstrate the lower specific energy consumption assumed in the paper, by the use of better thermal management and heat recovery. It is necessary to operate the plasmatron at high pressure, to minimize the required pumping power. This could have substantial effect in the case of liquid feedstock, since it requires little power to pressurize the liquid but substantial power to pressurize the reformate. If electrode life or other effects limit the plasma reformer operation at high pressure, then a reformate compressor needs to be included in the system. Heat recovery requires a heat exchanger that was not included in the cost calculations.

The lifetime of the catalyst is another unknown. Sulfur in the feedstock is readily transformed into H_2S which needs to be removed from the system but which does not affect the catalyst.

The costing model is continuously being improved.

Ackwoledgements

This work was supported by US Department of Energy, Grant No DE-FG04-95AL88002.

References

[1]. For recent reviews of plasma technology, see:MacRae, D.R., *Plasm. Chem and Plasm. Processing*, 9 85S (1989); also see: Fauchais, P. and Armelle Vardelle, *Thermal Plasmas, IEEE Transactions on Plasma Science* **25** 6 1258-1280 (1997).

[2] Kaske, G., L. Kerke, and R. Muller, *Hydrogen Production in the Huls Plasma-Reforming Process*, Hydrogen Energy Progress VI, 1 (1986).

[3] Muller, R., *The Use of Hydrogen Plasma Processes in the Petrochemical and Iron-Smelting Industries*, in: Hydrogen Energy Progress IV, 3 885 (1982).

[4] L. Bromberg, D.R. Cohn, A. Rabinovich and N. Alexeev, *Plasma Catalytic Reforming of Methane* accepted for publication in *Int. J. of Hydrogen Energy*.

[5] L. Bromberg, .R. Cohn, A. Rabinovich and N. Alexeev, presented at the 1999 Annual Peer Review of the Hydrogen Program, Denver CO 1999 (to be published)

PERFORMANCE TESTING OF HYDROGEN TRANSPORT MEMBRANES AT ELEVATED TEMPERATURES AND PRESSURES

K. S. Rothenberger, A. V. Cugini, R. V. Siriwardane, D. V. Martello, J. A. Poston, E. P. Fisher,
U.S. Department of Energy - Federal Energy Technology Center
Pittsburgh, PA 15236 and Morgantown, WV 26507.

W. J. Graham,
Parsons Infrastructure and Technology Group - Federal Energy Technology Center
Library, PA 15129.

U. Balachandran and S. E Dorris,
Argonne National Laboratory, Argonne, IL 60439.

Keywords: Membranes, Hydrogen, Gas separation

ABSTRACT

The development of hydrogen transport ceramic membranes offers increased opportunities for hydrogen gas separation and utilization. Commercial application of such membranes will most likely take place under conditions of elevated temperature and pressure, where industrial processes producing and or utilizing hydrogen occur, and where such membranes are theoretically expected to have the greatest permeability. Hydrogen separation membrane performance data at elevated temperature is quite limited, and data at elevated pressures is conspicuously lacking. This paper will describe the design, construction, and recent experimental results obtained from a membrane testing unit located at the U.S. Department of Energy's Federal Energy Technology Center (FETC). The membrane testing unit is capable of operating at temperatures up to 900°C and pressures up to 500 psi. Mixed-oxide ceramic ion-transport membranes, fabricated at Argonne National Laboratory (ANL), were evaluated for hydrogen permeability and characterized for surface changes and structural integrity using scanning electron microscopy/ X-ray microanalysis (SEM/EDS), X-ray photoelectron spectroscopy (XPS) and atomic force microscopy (AFM), as a function of temperature, pressure, and hydrogen exposure.

INTRODUCTION

The demand for hydrogen is expected to rise in coming years with increases in its use both directly as a fuel and indirectly in the synthesis or upgrading of fuels required to meet increasingly more demanding environmental standards. However, inexpensive and abundant sources of hydrogen, such as coal gasification, natural gas reforming, and off-gas streams from various process industries, usually contain hydrogen mixed with other gases. Recovery of hydrogen from these dilute streams would increase hydrogen supplies, improve overall process efficiencies, and provide a key component in the development of Integrated Gasification Combined Cycle (IGCC) power systems, fuel cells, advanced transportation fuel technology development, and "Vision 21" combination power and fuel production facilities. Advances in the area of membrane technology may provide the basis for improved methods of hydrogen recovery and thus reduce the cost associated with hydrogen production. Properly designed hydrogen membranes could be used to tailor syngas feed composition to optimize reactions producing fuel and/or chemical products.[1]

Currently, several research organizations are engaged in the development of hydrogen transport membranes or their precursor materials.[2] Membrane materials range from organic polymers to metals to ceramics. Non-porous ceramic membranes are particularly desirable because they can be made exclusively selective to hydrogen and are durable enough to withstand the harsh conditions of temperature, pressure, and chemical exposure that would probably be encountered in commercial application. Practical application of these membranes would likely employ a high total pressure on the retentate (inlet) side coupled with reduced pressures on the permeate (outlet) side to enhance the flux. Hydrogen flux through these membranes is expected to be optimal in the range of 700-900°C and increase with increasing hydrogen partial pressure gradient across the membrane. However, obtaining characterization information at these conditions is difficult, and data at elevated pressures (and pressure drops) is particularly scarce. The goal of the current work is to measure and characterize membrane performance at these elevated temperature and pressure conditions.

EXPERIMENTAL SECTION

Non-porous ceramic disk membranes were fabricated by a process developed at Argonne National Laboratory (ANL). Membranes used in this study were of composition $BaCe_{0.80}Y_{0.20}O_3$ (BCY), prepared by mixing appropriate amounts of $BaCO_3$, CeO_2, and Y_2O_3, then calcining the mixture at

1000°C for 12 h in air. This powder was then ball-milled and calcined again at 1200°C for 10 h in air. After obtaining phase-pure powder (by x-ray diffraction), the BCY powder was mixed with 40 vol.% metallic nickel powder to increase its electronic conductivity. The powder mixture was then uniaxially pressed and sintered for 5 h at 1400-1450°C in an atmosphere of 4% hydrogen/balance argon.

Membranes for pressure and flux testing were mounted using a brazing process developed at ANL, in 0.75" O.D. Inconel 600 tubing that had been drilled out to form a small seat to accommodate the membrane. Unmounted membranes of the same composition were also supplied for characterization studies. Because the pressure tested membranes had to be pre-mounted, the before-and-after characterization studies refer to membranes of the same composition and fabrication, but *not* the same physical membranes.

Membrane pressure and flux testing was performed on the Hydrogen Technology Research (HTR) facility, currently under construction at FETC. The facility makes use of high pressure hydrogen handling infrastructure previously put in place for the study of high pressure hydrogenation reactions.[3] For membrane testing, the unit has an operating range to 900°C temperature and 500 psig pressure (and pressure drop). The Inconel tubing containing the pre-mounted membrane from ANL was welded to an additional length of 0.75" O.D. Inconel 600 tubing. The membrane was hung in an inverted configuration and attached to a second piece of 0.75" OD Inconel tubing by means of a 0.75" I.D x 1.125" O.D. x 3.125" long Inconel 600 sleeve. A ceramic fiber heater was positioned around the sleeve. The entire assembly was suspended within a 2 gallon stainless steel autoclave under nitrogen gas. A simplified drawing of the test assembly is shown in Figure 1. Inert gas pressure tests were performed using static pressure by pressurizing the portion of the tubing and sleeve below the membrane, i.e., forcing the membrane *onto* the seat of the tubing. For inert gas testing only, the upper (permeate) side of the membrane was left exposed to air and monitored for leaks by means of a bubbler. Pressure was stepped in approximately 50 psi increments with hold times of approximately 0.5 h between increments. For hot tests, heat up and cool down was performed at the rate of 120°C per hour while at a slight inert gas over pressure. Pressure was increased only after the unit had obtained target temperature. When the unit is completed, hydrogen flux measurements will be performed in a similar configuration, except that air will be totally excluded from the system and the reactor casing will be actively purged with nitrogen gas. The permeate side of the membrane will be swept with argon gas, and the effluent will be monitored with a gas chromatograph for hydrogen concentration.

Atomic Force Microscopic (AFM) images of the membrane were obtained using a Quesant Instrument Corporation AFM (Model-Resolver). X-ray photoelectron spectroscopy (XPS) spectra were recorded with a Physical Electronics model 548 XPS system. The binding energies were referenced to the C(1s) level at 284.6 eV for adventitious carbon. XPS data were obtained at various temperatures ranging from room temperature to 650°C. X-ray microanalysis was performed at room temperature and 575°C using a JOEL 840-A scanning electron microscopy equipped with a Noran Instruments Micro-Z energy dispersive spectrometer, which was interfaced to a Noran Instruments Voyager-4. Detector resolution, as referenced to the Manganese Kα spectra line, was 148 eV.

RESULTS AND DISCUSSION

Cold membrane pressure tests were conducted using nitrogen and helium gases (separately) in the HTR unit. In each test, the ANL-1 disk membrane was pressurized in steps to 400 psig at ambient temperature. The membrane was held for approximately 0.5 h at each pressure and for 2 h at 400 psig. No leakage could be detected, either via a bubbler on the outlet side of the membrane, or via monitoring the pressure on the inlet side of the membrane. The pressure tests demonstrated that the membrane itself, as well as the ceramic-to-metal seal, was gas tight to 400 psig.

A hot membrane pressure test was conducted using nitrogen gas in the HTR unit. In this test, the ANL-1 disk membrane was heated to 800°C under a slight over pressure of nitrogen and held under these conditions for 17 h before pressure testing. During pressurization, no leakage could be detected up to and including 400 psig. At 450 psig, a small loss of pressure was observed together with bubble formation on the outlet side of the membrane. The leakage rate was measured at 1.6 mL/min at 450 psig. The leak persisted as the pressure was decreased in the same step wise fashion, although it slowly diminished in rate to 0.6 mL/min at 350 psig, and was undetectable at pressures below 200 psig. After decreasing to ambient pressure, the membrane was repressurized to 250 psig in the same step wise fashion and the leakage rate was confirmed. The membrane was again depressurized and cooled to ambient temperature. After cooling, the membrane was repressurized to 250 psig with cold nitrogen and the leakage rate was reconfirmed.

Following the hot membrane pressure test, visual inspection of the membrane revealed a powdery whitish coating on and around the membrane. Small areas of green discoloration were observed around the surface of the normally gray membrane. Some of the brazing material appeared to have migrated from around the edge of the membrane toward the center, moving a distance of approximately 0.5 mm. The braze migration had previously been observed during hot temperature-ambient pressure flux testing at ANL. Visual inspection under an optical microscope revealed cracks in the membrane surface along the perimeter of the disk, as well as cracks in the brazing material itself.

SEM/X-ray microanalysis was conducted to determine the changes in morphology, elemental distribution and compositional changes that occur to a fresh membrane upon heating. No major morphological changes were observed after heating the membrane from room temperature to 575°C. Elemental distribution was uniform and remained uniform following heating and hydrogen exposures at 575°C.

SEM examination of the membrane before testing showed an apparent two phase structure of mixed Ba-Ce-Y oxides (spinodal decomposition appearance in the back scattered electron images) decorated with 2 - 20 μm 'diameter' sized nickel-rich nodules (Figure 2, left image). A similar image from the membrane after pressure testing is shown in Figure 2 (right image). The nickel rich nodules seem to have grown in size during exposure to the test conditions. The membrane surface also appeared to be covered by a film of some material on the side exposed to 450 psi nitrogen.

AFM was also utilized to determine both the surface morphology and the surface roughness. AFM images of the fresh membrane and the membrane after the pressure test with nitrogen are shown in Figure 3. The fresh membrane had structure containing nodules with an average surface height of 1.34 μ. The surface morphology changed after the pressure test. The original structure with nodules was not present after the pressure test and the average surface height was 1.89 μ. This change in the surface roughness and morphology could be due to the deposition of carbon and other materials during mounting of the membrane, the nitrogen pressure test, or other associated handling.

XPS was utilized to determine the elemental composition and oxidation states of elements at approximately the top 50 Å of the surface of a fresh membrane upon heating. Ni 2p spectra of the fresh membrane at room temperature and 650°C are shown in Figure 4. At room temperature nickel was in the oxidized form and the intensity of the nickel peak was low. When the surface was heated up to 650°C, the intensity of the nickel peak increased substantially and the oxidation state of nickel changed to the metallic state. The ratios of Ni/Ba, Ni/Ce, and Ni/Y at the surface increased when the temperature was increased, but they decreased again when the surface was cooled back to room temperature. Thus, the nickel migrates to the surface and preferentially resides at the surface relative to the other elements at higher temperature. When the XPS analysis was performed at room temperature with the membrane after the pressure test, it was not possible to detect Ni, Ba, Ce, and Y on the surface. The intensity of the carbon peak was very high indicating that carbon may have been deposited on the surface during the pressure test. When the surface was heated to 300°C, the intensity of the carbon signal decreased by 33% and a small amount of yttrium was detected on the surface. When the surface was heated to 650°C, there was a 60% decrease in the amount of carbon, and it was possible detect all the elements on the surface. The amounts of Ni and Y were higher on the surface relative to the other elements at 650°C. This differs from the observations made with the fresh membrane at 650°C in which the concentrations of barium and nickel were higher than those of the other elements.

CONCLUSION

The membrane and sealing methodology are impermeable to the inert test gases nitrogen and helium. In addition, both membrane and seal are structurally capable of withstanding a pressure differential of 400 psig, at least for the limited hold times employed in these tests. However, at 800°C, the membrane and seal would not withstand a pressure of 450 psig nitrogen and developed a leak. At this time, it is not known whether the failure was strictly a pressure effect, or if the elevated temperature and possible migration of some of the brazing material was involved. It is likely that exposing the membrane to atmospheric oxygen on the permeate side contributed to its demise. At high temperature, the membrane will also transfer oxygen, and the presence of what is probably oxide contamination around the membrane after the hot pressure test indicates that some degradation of the membrane and/or sealing materials may have occurred during the test. Both SEM and AFM indicated that the pressure tested membrane surface was coated with an impurity material, although it cannot be determined whether this occurred as a direct result of the pressure test or from other handling or exposure. XPS analysis indicates that significant elemental and oxidative changes occurred on the membrane surface upon heating. In particular, pools of metalic nickel migrated to the membrane surface at elevated temperature. The nickel "islands" may very well contribute to the

ability of the membrane to transfer hydrogen by facilitating molecular dissociation. However, such changes may also affect membrane strength. High temperature-high pressure hydrogen flux measurements for these membranes are of great interest and should be obtainable shortly.

ACKNOWLEDGEMENTS

The work at ANL was supported by the U.S. Department of Energy, Federal Energy Technology Center, under Contract W-31-109-Eng-38.

REFERENCES

1. Enick, R.M.; Hill, J.; Cugini, A.V.; Rothenberger, K.S. *Prepr. Pap., Am. Chem. Soc. Div. Fuel Chem.*, **1999**, 45, Published elsewhere in this volume (page numbers unknown as of submission date).

2. (a) Balachandran, U.; Guan, J.; Dorris, S.E.; Liu, M. Extended abstract of presentation at the AIChE 1998 Spring Meeting, New Orleans, LA, March 8-12, 1998. (b) Fain, D.E.; Roettger, G.E. *Trans. of the ASME*, **1993**, 115, 628-633. (c) Peachey, N.M.; Snow, R.C.; Dye, R.C. *J. Membrane Sci.*, In press.

3. Cugini, A.V.; Krastman, D.; Lett, R.G.; Balsone, V. *Catal. Today* **1994**, 19, 395-408.

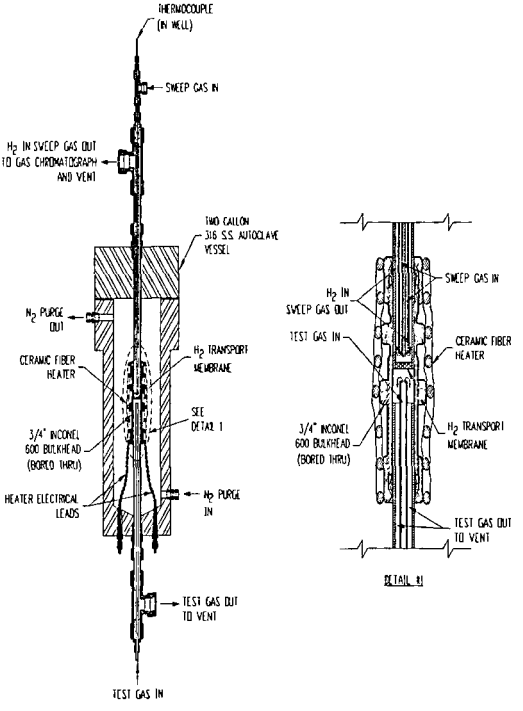

Figure 1: Membrane Testing Unit Experimental Configuration

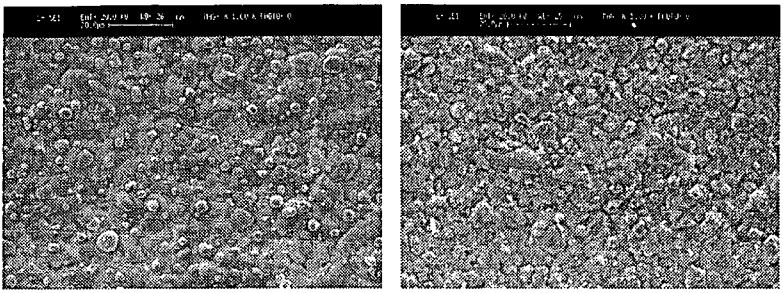

Figure 2: SEM images of the fresh membrane surface (left) and after exposure to 450 psig. nitrogen at 800 °C. (right)

AFM Images of Fresh Membrane and after Nitrogen Pressure Test

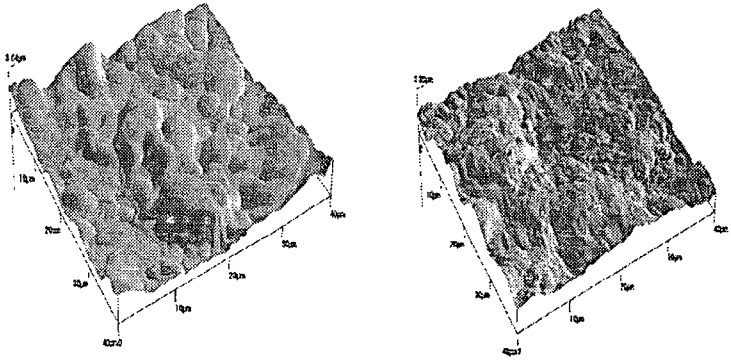

(a) Fresh Membrane (b) Membrane after Pressure Test

Figure 3: AFM Images of fresh membrane (left) and membrane after test (right)

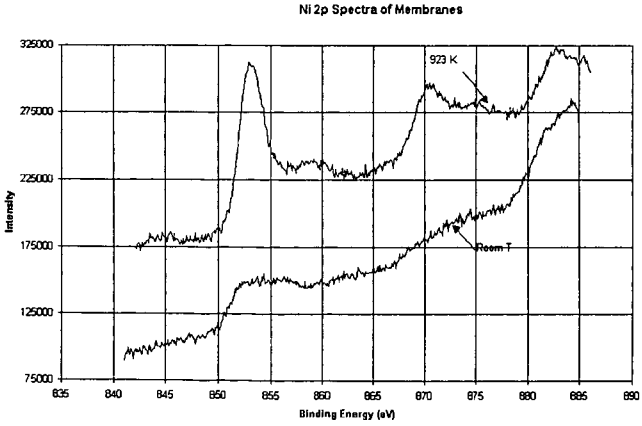

Figure 4: Ni 2p spectra of the fresh membrane at 650 C (top) and room temperature (bottom)

A MODEL OF A HIGH TEMPERATURE, HIGH PRESSURE WATER-GAS SHIFT TUBULAR MEMBRANE REACTOR

R.M. Enick and J. Hill
Department of Chemical and Petroleum Engineering, University of Pittsburgh
1249 Benedum Hall, Pittsburgh, PA, 15261

A. V. Cugini and K. S. Rothenberger (DOE); H.G. McIlvried (Burns and Roe Services)
Federal Energy Technology Center, U.S. Department of Energy
P.O. Box 10940, Pittsburgh, PA 15236-0940

Keywords: membrane, hydrogen, water-gas shift

ABSTRACT

The reversible water-gas shift reaction is characterized by a very low equilibrium constant at elevated temperatures (>800°C). CO conversion at these temperatures is typically less than 40%. Higher conversions of CO can be achieved under these conditions only if one of the products, H_2 or CO_2, is removed from the reactor mixture. Several novel membranes are being developed for rapid H_2 diffusion/permeation and high H_2 selectivity at these high-temperature conditions. Therefore a model of a non-catalyzed tubular membrane reactor has been developed to evaluate the feasibility of achieving high levels of CO conversion at elevated temperatures via removal of H_2 from the reaction-side gas mixture along the length of a plug flow reactor. The model can provide membrane permeability values that must be achieved to attain desired levels of conversion in specified reactor geometry.

INTRODUCTION

The water-gas-shift reaction has been studied extensively as a basis for the production of hydrogen. In many applications, including ammonia synthesis or fuel reforming for fuel cells, the maximum acceptable level of CO in hydrogen is in the parts per million range. The water-gas shift reaction can also take place in other processes where CO and H_2O are present, such as methanol synthesis and supercritical water oxidation of organic compounds.

$$CO + H_2O \Leftrightarrow CO_2 + H_2 \qquad 1$$

This reaction has no change in the number of moles (or the volume) as the reaction proceeds, therefore the equilibrium conversion is not affected by pressure. Side reactions associated with the water-gas-shift reaction are usually not significant. The equilibrium constant for this exothermic reaction (K, which can be expressed in terms of the concentrations of the reactants and products, Eq. 2) decreases with temperature. For example, the value of K decreases from 4523 at 366.5 K (93.3°C, 200°F) to 0.47 at 1366.5 K (1093.3°C, 2000°F).

$$K = ([CO_2][H_2])/([CO][H_2O]) \qquad 2$$

Therefore, conversion of CO to CO_2 (low concentrations of CO and H_2O, high concentrations of CO_2 and H_2, high values of K) is favored at low temperature[1]. Most heterogeneous catalysis studies of the water-gas shift reaction have been conducted at temperatures less than 450°C. Examples of commercial water-gas shift catalysts include Fe_3O_4-Cr_2O_3 and $CuZnO/Al_2O_3$[2]. The kinetics associated with these catalysts can be adequately described with pseudo-first order or power law kinetics[2]. Another study of the stationary and transient kinetics of this reaction[3] indicates that various mechanisms and kinetic expressions have been proposed for the water-gas shift, and that Langmuir-Hinshelwood and power-law kinetic models are adequate. The water-gas shift reaction also occurs in some processes that do not employ catalysts. For example, the supercritical water oxidation of organic wastes (typically conducted at 400-550°C, 200-300 bar) typically does not employ a catalyst because of the rapid destruction rates that are achieved. The very high rate of the water-gas shift reaction observed in this system[4,5,6] is attributed to the formation of "cages" of water about the reactants under supercritical conditions and very high water concentrations.

There is relatively little information on the kinetics of the water-gas shift reaction at elevated temperatures (>600°C). This can be primarily attributed to the diminished value of K, which would limit CO conversion to unacceptably low levels. Catalysts are typically not used at elevated temperatures because of the rapid rate of the non-catalyzed reaction and the difficulty of identifying a catalyst that would be stable at these extreme conditions. A study of the opposing reactions of the water-gas shift reaction was conducted at extremely high temperatures and low pressure[7] (800-1100°C, 1 bar). No catalyst was employed. Power-law kinetic expressions

developed for the forward and reverse reactions were substantially in agreement with a homogeneous chain mechanism. Despite the rapid attainment of equilibrium conversions without a catalyst, the ability to convert high temperature (800-1000° C) CO-rich combustion gases into hydrogen fuel via the water-gas shift reaction is limited by the low equilibrium conversions of CO.

It has long been recognized that high levels of conversion in equilibrium-limited reactions can be achieved only if one or more of the products can be simultaneously extracted during the reaction. (For a given value of K in Eq. 2, if the concentration of either CO_2 or H_2 is reduced, the concentrations of CO and H_2O must also decrease, thereby increasing conversion.) For example, a method for producing H_2 via the water-gas shift reaction with carbon dioxide removal was recently demonstrated[8]. In this study, a calcium-based sorbent was introduced to a non-catalyzed reactor operating in the 500-600°C temperature range. The CO_2 product reacted with the sorbent and formed calcium carbonate, diminishing the gas phase concentration of CO_2 and increasing CO conversion. Several research groups have recently developed hydrogen-permeable membranes that might also he used in a different approach to increasing CO conversion. The use of these membranes in a plug flow reactor would result in the removal of hydrogen from the reaction mixture, leading to an increase in CO conversion. Several types of membranes are now under development. Los Alamos National Laboratory has fabricated composite Pd/Ta membranes using vapor deposition techniques[9]. Measurements in the 300-400°C range indicate that the pressure-dependence of the gas flux is not proportional to $\Delta(P_{H2}^{0.5})$ as in the case with membranes that are rate-limited by bulk diffusion. This implies that surface effects are significant in the determination of hydrogen flux. Argonne National Laboratory is developing proton-conducting ceramic membranes. These dense ceramic membranes are fabricated from mixed protonic/electronic conductors and have been tested at 800°C. Their hydrogen selectivity is very high because they do not have interconnected pores, and the only species that pass through them are those that participate in proton conduction[10] (e.g. hydrogen). Inorganic membranes, composed of ceramics developed by Oak Ridge National Laboratory[12], have interstitial pores with diameters as small as 5 angstroms and act as molecular sieves, have been tested at temperatures less than 600°C. An assessment of a conceptual plant that produces hydrogen from coal using these inorganic membranes[11] was recently completed.

OBJECTIVE

The goal of this investigation is to develop a model of a tubular, plug-flow, non-catalyzed, membrane reactor for the high temperature, high pressure water-gas shift reactor. This model will be used to assess the viability of obtaining a high purity hydrogen product from synthesis gas. Specifically, it will be used to estimate the surface area of the membrane required to achieve a desired level of CO conversion or hydrogen recovery. Alternately, it can be used to provide estimates of the hydrogen permeability a membrane must exhibit to attain a specified CO conversion or H_2 recovery in a reactor with a specified membrane area. This information, in conjunction with cost data for the membranes, can then be used to evaluate the economic feasibility of the process. A model of a reactor with hydrogen-permeable membranes has been previously developed[13] for CO_2 control in IGCC systems using water-gas shift integrated with H_2/CO_2 separation. This system employed microporous ceramic membranes, Fe-Cr and Pt/ZrO_2 catalysts, maximum pressure of 70 bar, maximum pressure drop across the wall of the membrane of 25 bar, and temperatures up to 400°C. Another water-gas shift membrane reactor model was developed for a Fe-Cr catalyzed reactor operating at 400°C and low pressures with a Pd membrane[14]. The model developed in this work will focus on a higher temperature (>800°C), high pressure (25-50 bar), high pressure drop (up to 50 bar), non-catalyzed tubular membrane reactor with either Pd/Ta composite membranes, proton conducting dense ceramic membranes, or microporous ceramic diffusion membranes.

MODEL DESCRIPTION

The basis of the model is a tubular membrane located within a coaxial cylindrical shell. The feed gases are introduced on the shell-side (reaction-side, annular-side, retentate-side, raffinate-side) of the reactor. As the reaction proceeds, hydrogen will permeate the membrane if the concentration of the hydrogen on the reaction-side (shell-side) exceeds the concentration on the tube-side (permeate-side). As the reaction gases proceed down the length of the reactor, hydrogen will continue to permeate the membrane if the partial pressure of hydrogen on the reaction side exceeds the permeate hydrogen partial pressure, increasing the conversion of the CO. The CO_2-rich retentate exits the reactor on the shell-side. A low-pressure, high-purity hydrogen permeate stream is recovered from the tube-side. It is desirable not use a sweep gas to avoid the need to for a subsequent hydrogen-sweep gas separation unit. This will result in a substantial pressure drop across the wall of the membrane, however. The basic design equations for a tubular, plug flow reactor were incorporated into the model[15]. The model predicts the

performance of the reactor under steady-state isothermal or adiabatic conditions. The adiabatic model accounts for the heat of reaction being transferred to the reaction gases and the permeate. The reactants and products are assumed to behave as ideal gases. The pressure drop along the length of the reactor is assumed to be negligible for both the retentate-side and the permeate-side of the reactor. Published correlations for K[1,13] can be used for pseudo-first order or power-law kinetic expressions that may include the equilibrium constant. The low pressure, high temperature (800-1100°C) results of Graven and Long[7] are used to model the reaction kinetics. (During this investigation, more accurate rate expressions for the water-gas shift reaction at elevated temperature *and* pressure will be determined.) The appropriate expressions for the permeation of hydrogen in the dense, proton-conducting ceramic membrane or expressions for permeability of H_2, CO, and CO_2 (i.e. membrane selectivity) in the microporous metal or ceramic membranes[9,12] are incorporated to account for the flow of gases through the membrane. The flux of hydrogen through these membranes, R_{H2}, is proportional to the "permeability" of the membrane, k_{H2} and inversely proportional to the membrane thickness, t_m. The driving force for the hydrogen flux is related to the hydrogen partial pressure or molar concentration of hydrogen, C_{H2}, raised to the exponent n (the units of k are dependent upon the value of n).

$$R_{H2} = A_m\, k_{H2}\, (C_{H2,retentate}{}^{n} - C_{H2,permeate}{}^{n})/t_m \qquad 3$$

If transport through a membrane with surface reaction and ionic transport is limited by surface reactions, n = 1. If flux through the membrane is diffusion-limited, n = 0.5. Intermediate values of n ($0.5<n<1$) have also been reported[14]. During this investigation, values of n at elevated temperature and pressure will be determined for each membrane.

RESULTS

The following conditions are associated with a conceptual coal processing plant for producing hydrogen while recovering carbon dioxide[16]. Because membrane parameters have not yet been established at these conditions, a high value of permeability was selected to clearly illustrate the effect of hydrogen removal on conversion.

Catalyst	No catalyst used at this high temperature
Mode of Operation	Isothermal
Temperature	850°C
Reaction-Side	Annular-side, Shell-side
Pressure on reaction-side	27.572 bar
Pressure on tube-side	0.9869 bar
Reactor length	200 cm
Reactor (shell) diameter	4.0 cm
Tube-side sweep gas	None
Membrane	Proton Transport
Membrane diameter	2.0 cm
Permeable gases	Hydrogen Only
Membrane thickness	0.1 cm (1 mm)
Membrane driving force	$C_{H2,retentate}{}^{0.5} - C_{H2,permeate}{}^{0.5}$
Membrane permeability	10 $cm^2/min(mol/liter)^{0.5}$
CO inlet flow rate	10 gmol/min
Steam inlet flow rate	11 gmol/min
Hydrogen inlet flow rate	5.0 gmol/min
Reaction kinetics	Reference 7

Table 1. Model Conditions and Assumptions Used in the Example Problem

Conversion of CO *in the absence of a membrane* is 38.2% at 850° C, which is 99% of the equilibrium value. The *membrane reactor* profiles of molar flow rates of the components are illustrated in Figure 1. As the CO and H_2O react near the inlet, their molar flow rates decrease as the hydrogen flow rate on the reactor-side increases. The CO and H_2O continue to decrease as the CO_2 concentration increases along the length of the reactor. The hydrogen also begins to permeate the membrane because the concentration on the annular-side is greater than the hydrogen concentration on the tube side. Because the rate of hydrogen generation is initially greater than the rate of permeation, the hydrogen flow rate on the annular-side increases from 5 to 7 mol/min along the length of the reactor between 0 - 15 cm.

Figure 1. Flow Rate Profiles within the Membrane Reactor

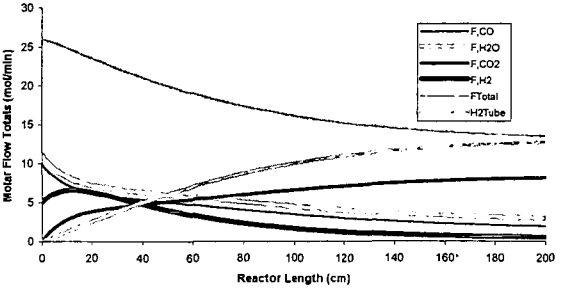

After 15 cm, the rate of permeation exceeds the generation due to reaction and the flow rate of hydrogen on the annular-side decreases. As the end of the reactor is approached, the permeate flow rate of hydrogen approaches a limiting value because the concentration of the hydrogen on the annular-side (raffinate), 0.013 mol H_2/liter is approximately equal to the concentration on the tube-side (permeate), 0.011 mol H_2/liter. CO conversion has increased to 81%. The permeability of the membrane has a significant effect on the performance of the reactor. Figure 2 illustrates the conversion of CO that can be achieved in this particular membrane reactor as a function of the membrane permeability. For a permeability of 0 (impermeable membrane), the conversion is 38.5%. As the permeability increases beyond 10 $(cm^2/min)(mol/liter)^{0.5}$, the limiting conversion of 84% is attained. To achieve comparable conversions with membranes of lower permeability, the length of the membrane tube must increase to provide more area for the hydrogen removal, increasing the membrane reactor size and cost.

Figure 2. Effect of Membrane Permeability on CO Conversion

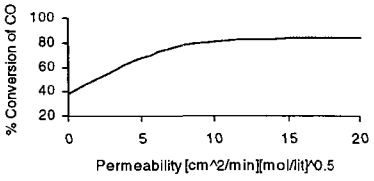

CONCLUSIONS

A model of a tubular, plug flow membrane reactor has been developed for evaluating the effect of hydrogen permeable membranes on the conversion of CO in the water-gas shift reaction. The model has been developed for very high temperature systems (>800°C) that do not employ a catalyst. The model can incorporate hydrogen permeation/diffusion models that are appropriate for novel membranes currently being developed at several national laboratories. This tool will be used to assess the levels of CO conversion, H_2 purity and recovery, and CO_2-rich retentate flow rate and recovery that can be realized in a reactor of specified geometry if these novel membranes are incorporated. The model can also be used to provide "targets" for hydrogen permeability that would be required to make this technology economically feasible.

REFERENCES

1. Benson, H. E.; Processing of Gasification Products; Ch. 25 in Chemistry of Coal Utilization, Elliot, M., ed.; John Wiley and Sons; New York, NY, 1981.
2. Keiski, R.I.; Desponds, O.; Chang, Y.; Somorjai, G.A.; Kinetics of the Water-Gas Shift Reaction Over Several Alkane Activation and Water-Gas Shift Catalysts; Applied Catalysis A: General, 101 (1993) 317-338.
3. Keiski, R.; Salmi, T.; Niemisto, P.; Ainassaari, J.; Pohjola, V.J.; Stationary and Transient Kinetics of the High Temperature Water-Gas Shift Reaction; Applied Catalysis A: General, 137 (1996) 349-370.
4. Helling, R.K.; Tester, J.W.; Oxidation Kinetics of Carbon Monoxide in Supercritical Water; Energy and Fuels, 1 (1987) 417-423.

5. Holgate, H.R.; Webley, P.A.; Tester, J.W.; CO in Supercritical Water: The Effects of Heat Transfer and the Water-Gas Shift Reaction on Observed Kinetics; Energy & Fuels, 6 (1992) 586-597.
6. Rice, S.F., Steeper, R. R.; Aiken, J. D.; Water Density Effects on Homogeneous Water-Gas Shift Reaction Kinetics; J. Phys. Chem. A, 102(16) (1998), 2673-2678.
7. Graven, W. M.; Long, F. J.; Kinetics and Mechanisms of the Two Opposing Reactions of the Equilibrium $CO + H_2O = CO_2 + H_2$; J. Amer. Chem. Soc. 76 (1954) 2602.
8. Han, C.; Harrison, D.P.; Simultaneous Shift Reaction and Carbon Dioxide Separation for the Direct production of Hydrogen; Chemical Eng. Sc. 49(24B) (1994) 5875-5883.
9. Peachey, N. M.; Snow, R. C.; Dye, R. C.; Composite Pd/Ta Metal membranes for Hydrogen Separation; Journal of Membrane Sciences (in print).
10. Balachandran, U.; Guan, J.; Dorris, S. E.; Liu, M.; Development of Proton-Conducting Membranes for Separating hydrogen from Gas Mixtures; extended abstract of presentation at the AIChE 1998 Spring Meeting, New Orleans, LA, March 8-12, 1998.
11. Parsons Infrastructure and Technology Group; Decarbonized Fuel Plants Utilizing Inorganic Membranes for Hydrogen Separation; presented at the 12th Annual Conference of Fossil Energy Materials, May 12-14, 1998, Knoxville, Tennessee.
12. Fain, D. E.; Roettger, G. E.; Coal Gas Cleaning and Purification with Inorganic Membranes; Trans. of the ASME Journal of Engineering for Gas Turbines and Power, 115 (July 1993) 628-633.
13. Netherlands Energy Research Foundation; Combined Cycle Project – IGCC with CO_2 Removal Project Area – An Attractive Option for CO_2 Control in IGCC Systems: Water Gas Shift with Integrated Hydrogen/Carbon Dioxide Separation (WIHYS) Process – Phase 1 Proof of Principle; Alderliesten, P. T. and Bracht, M., eds.; Contract JOU2-CT92-0158, Final Report (1995).
14. Uemiya, S.; Sato, N.; Ando, H.; Kikuchi, E.; The Water Gas Shift Reaction Assisted by a Paladium Membrane Reactor; Ind. Eng. Chem.Res. 30 (1991) 585-589.
15. Fogler, H. S.; Elements of Chemical Reaction Engineering, Second Edition; Prentice Hall, Englewood Cliffs, NJ (1992).
16. Parsons Infrastructure and Technology Group; Decarbonized Fuel Plants for Vision 21 Applications, WYODAK Coal Substitution; DOE/FETC Report, April 13, 1999.

A FIRST-PRINCIPLES STUDY OF HYDROGEN-METAL INTERACTION IN VARIOUS METALS

Yasuharu Yokoi, Tsutomu Seki and Isamu Yasuda
Fundamental Technology Research Laboratory, Tokyo Gas Co., Ltd.
Tokyo, 105-0023, Japan

KEYWORDS: Hydrogen Separation Membrane, Hydrogen Dissolution, First-Principles Calculations

INTRODUCTION

Hydrogen-metal systems have been the subject of numerous investigations because of their potential applications such as hydrogen separation membranes and hydrogen storage alloys. As for the hydrogen separation membranes, palladium membranes are principally 100% selective for hydrogen separation [1]. Steam reformers equipped with the Pd membranes were developed and have been tested in Japan to produce pure hydrogen from city gas [2]. The performance of this type of membrane reformer directly depends on hydrogen permeability of the membranes. This has led us to develop the membranes with higher hydrogen permeability.

One of the effective approaches to increase the hydrogen permeability of the membranes is alloying. The alloying of Pd with silver is effective to enhance the hydrogen dissolution and thereby to increase the hydrogen permeability of the membrane [1]. The Ag-alloying is also effective to depress the α-β miscibility gap to well below room temperature, although it lies below 300°C and pressures below 20 atmosphere in Pd-H system without Ag-alloying. The β phase has a considerably expanded lattice compared with the α phase; for example, a H/Pd ratio of 0.5 results in an expansion of about 10% by volume, which should cause mechanical damages to the membranes after dissolution/evolution cycles during the operation of the reformer.

In the present work, we have applied first-principles calculations to the study of hydrogen-metal interactions in various metals and alloys. Our goal is to develop the membranes with higher hydrogen permeability than the conventional Pd/Ag alloys and mechanical reliability under the practical operating conditions. Our computations have focused on the heat of hydrogen dissolution and the hydrogen-induced lattice expansion that should be correlated with the hydrogen permeability and the mechanical reliability.

MATERIALS AND METHODS

All calculations in this study were implemented with the code CASTEP [3]. In the calculations, the valence electron orbitals are expanded in plane waves, whereas the core electrons are described by ultrasoft pseudopotentials. In the present investigation we selected an energy cut-off of 380 *eV*. The energy functional consists of the gradient-corrected local density approximation. Figure 1 illustrates the periodic supercell models for hydrogen occupation at interstitial sites in bcc (V, Nb, Ta, Cr, Mo and W) and fcc (Ni, Pd, Pt, Cu, Ag and Au) metals. The models consist of four metal atoms and one hydrogen atom. The initial positions of metal atoms and the initial values of lattice constants were those from experimental values of pure metals. The initial position of the hydrogen atom was either the octahedral site (O-site) or the tetrahedral site (T-site). The final geometry was obtained when the calculated forces acting on the atoms and stress on the supercell became smaller than the threshold values. To evaluate the relative expansion of the lattice induced by the interstitial hydrogen, geometry optimizations of the pure metals were also employed. The heat of hydrogen dissolution was calculated according to the following expression: $E_{diss} = E_{(host+H)} - E_{host} - 1/2\, E_{H2}$, where $E_{(host+H)}$ is the total energy of the optimized model for the hydrogen-metal system, E_{host} is of the pure metal, and E_{H2} is of the hydrogen molecule. The optimized bond length of H-H bond of the hydrogen molecule was confirmed to be nearly equal to the experimental value.

RESULTS

From the geometry optimization for the pure metals, all optimized fcc and bcc cells were nearly cubic. The lattice constants of the optimized cells are plotted versus the experimental values in Figure 2.

The O-site occupation for the bcc metals was confirmed not to be a stationary point on the potential energy surface (PES) except for V and Mo, whereas the T-site occupation was found to be the stationary point. As for the fcc metals, both interstitial sites were confirmed as the stationary point.

All optimized supercells for the hydrogen-metal systems were found to expand in comparison with for pure metals. The optimized fcc cells for both the O- and T-site occupation maintained cubic. The average percentage of the lattice expansion for the O- and T-site occupation was 1.5% and 2.5%, respectively. The optimized bcc cells, on the other hand, were distorted. The average percentage for the O- and T-site occupation was 1.5% and 1.7%, respectively. Figure 3 shows the changes in the lattice constants for Pd and V as the representative of the fcc and bcc metals. The hydrogen occupation at the O-site in V was found to induce the lattice expansion of about 4.7% in the direction of the c-axis, in spite of small contraction of the lattice in the directions of the a- and b-axis. In the case of Pd, the relationship between the lattice expansion and the hydrogen concentration was also examined. The models used in this examination were constructed by adding hydrogen atoms 'one by one' to the original supercell model. The volume of the optimized fcc cells (in $Å^3$) was 59.82, 62.17, 64.29, 66.04 and 67.82 for H/Pd ratio of 0, 0.25, 0.5, 0.75 and 1, respectively.

Figure 4 shows E_{diss} for the fcc metals. As for Ni and Pd, the O-site occupation was found to be more stable than the T-site occupation, whereas the T-site occupation was found to be more stable for Pt, Cu, Ag and Au. Figure 5 shows E_{diss} for the bcc metals. The T-site was suggested to be the stable interstitial hydrogen site for all bcc metals evaluated in this study.

To study the effects of alloying of Pd with Ag on the hydrogen solubility, E_{diss} for Pd/Ag alloy was evaluated in the same manner. Figure 6(a) illustrates the supercells for the Pd/Ag alloy. These models consist of three Pd atoms, one Ag atom and one hydrogen atom. There are two distinguishable O-sites in these models; one is the center of the octahedron consisting of four Pd atoms and two Ag atoms (O_α-site), and the other is the center of the octahedron consisting of six Pd atoms (O_β-site). The calculated E_{diss} is shown in Figure 6(b) in comparison with that of the O-site occupation for the pure Pd. The value of $|-E_{diss}|$ of the O_β-site occupation was larger, whereas that of the O_α-site occupation was smaller, than that of the O-site occupation for the pure Pd.

DISCUSSION

As for the optimized lattice constants for the pure metals and the optimized bond length of H-H bond of hydrogen molecule, the agreement between the calculations and the experiments is quite satisfactory. This suggests that the calculated value of the lattice constants of the hydrogen-metal systems and the calculated relative expansion induced by the interstitial hydrogen are reliable. In this study we have estimated the lattice expansion of pure Pd induced by the hydrogen occupation at the interstitial sites; for example, a H/Pd ratio of 0.5 results in an expansion of 7.5% by volume. An experimental value corresponding to this estimation has been reported to be about 10% in the literature [1]. We have also evaluated the lattice expansion of V. From the result shown in Figure 3, the O-site occupation in V was found to induce the lattice expansion of 4.7% in the direction of the c-axis. This is qualitatively in line with the experimental fact that the lattice is expanded in the direction of the c-axis about 10% [4].

Figure 4 shows that the hydrogen occupation at both interstitial sites was found to be stable for the fcc metals. The O-site occupation is more stable than the T-site occupation for Ni and Pd. This suggests that the O-site occupation should be observed experimentally. As has been expected from the results, the O-site occupation for Ni and Pd has been experimentally observed [4,5]. As for the other fcc metals: Pt, Cu, Ag and Au, the T-site occupation is more stable than the O-site occupation. This suggests that the T-site occupation in these fcc metals should be experimentally observed, although this has not been reported yet to the best of our knowledge. On the other hand, the T-site occupation is stable for the bcc metals shown in Figure 5. As has been expected from the results, the preference of T-site occupation has already been reported for these bcc metals [4,5]. As for V, the O-site occupation, which occurred with the expansion of about 10% in the direction of the c-axis, has been also reported [6]. This also agrees with the present calculation result that the O-site occupation in V is stable as well as the T-site occupation shown in Figure 5 and the O-site occupation induces the lattice expansion with the distortion shown in Figure 3.

As the experimental heat of hydrogen dissolution (ΔH_s) plotted on Figure 4 and Figure 5 were estimated by applying Sieverts's law, the values may have large errors in high hydrogen concentration (far from H/M = 0) ranges [7]. Nevertheless the calculated E_{dis} qualitatively correlated with the experimental ΔH_s. Before turning to a closer examination of the alloying of Pd with Ag, it is desirable to discuss the deviation of the calculated E_{dis} from the experimental ΔH_s for Pd. The deviation for Pd shown in Figure 4 is somewhat larger than that of V, Nb and Ta, which are exothermic for the hydrogen dissolution as well as Pd. The dependence of ΔH_s for Pd on hydrogen concentration has been experimentally studied in the previous literature [4]. In this literature, the experimental heat of hydrogen dissolution for Pd at H/Pd = 0.25, which is equal to the H/M ratio of the calculated model shown in Figure 1, have been reported as blow –20 kJ/mol. The deviation of E_{dis} from the experimental value reduced by the correction for the hydrogen concentration. The calculated E_{dis} is believed to be reliable enough to discuss the qualitative difference in the heat of hydrogen dissolution.

The hydrogen permeability of metals is proportional to their solubility and diffusion coefficient of hydrogen. Since the hydrogen solubility increases with $-\Delta H_s$, increasing of $-\Delta H_s$ is effective to improve the hydrogen permeability. It has been reported that the high hydrogen solubility in Pd/Ag alloys leads to high permeability in the 20 to 25% Ag range [1]. According to this literature [1], about 150 mg of hydrogen can dissolve in 100g of the Pd/Ag alloys at 1 atmosphere and 183°C. This H/M ratio is below 0.25. As the hydrogen dissolution in Pd/Ag alloys is exothermic, the H/M ratio decreases with the increase in temperature. The steam reformers are usually operated above 500°C [2], then the hydrogen diffusion membranes made of the Pd/Ag alloys have hydrogen of the H/M ratio below 0.25. The simple calculation models for 25% Ag - Pd shown in Figure 6(a) have three O_α-sites and one O_β-site. Since the O_β-site occupation has been found to be more stable than the O_α-site occupation in the present study, hydrogen is suggested to occupy only the O_β-sites below 0.25 of the H/M ratio. As shown in Figure 6(b), the $-\Delta H_s$ for the O_β-site occupation is larger than that for the O-site occupation for in pure Pd. In this way, it suggests that the $-\Delta H_s$ of the Pd/Ag alloys is greater than that of the pure Pd in the low hydrogen concentration ranges. This is the reason for the high hydrogen solubility in the Pd/Ag alloys in the higher temperatures and contributes to high permeability. Hydrogen begins to occupy the O_α-sites with the increase in the H/M ratio. As shown in Figure 6(b), the $-\Delta H_s$ for the O_α-site occupation is smaller than that for the O_β-site occupation as well as for the O-site occupation for in pure Pd. This is the mechanism for the depression of the hydrogen dissolution at lower temperatures.

CONCLUSIONS

Interactions between various metals and hydrogen have been studied by using a periodic density functional theory at a generalized gradient approximation. Geometry optimizations were carried out for lattice constants of various metal-hydrogen systems as well as for stable sites of interstitial hydrogen. Both tetrahedral site (4-coordinated sites) hydrogen and octahedral site 6-coorinated sites) hydrogen was found to be stable and to induce lattice expansion. Reported experimental heat of hydrogen dissolution has been well reproduced from the calculated total energies. Similar estimations were carried out for Pd/Ag alloys that are used as hydrogen permeable membranes in hydrogen production. The theoretical calculations suggested that Ag-alloying enhance hydrogen dissolution in Pd. These can explain fairly well the increased hydrogen permeability by alloying Ag into Pd.

REFERENCES

1. A. G. Knapton, Platinum Metals Review, 21 (1977) 44.
2. Y. Ohta, M. Gondaira, K. Kobayashi, Y. Fujimoto and K. Kuroda, in Extended Abstracts of AIChE Annual Meeting, 1994, San Francisco.
3. The CASTEP code, originally written by M. C. Payne, is marketed by Molecular Simulations, Inc.
4. Y. Fukai, *"The Metal Hydrogen System"*, Springer, Series in Materials Science Vol. 21 (1993) Chap. 4.
5. D. Richter, R. Hempelmann and R.C. Bowman *"Hydrogen in Intermetallic Compounds II : Surface and Dynamic Properties,Applications"*, Springer, Topics in Applied Physics, Vol. 67 (1992) Chap. 3.
6. I. Okuda, H. Asano and M. Hirabayashi, Trans. JIM, 21 (1980) 89.
7. H.M. Lee, Metall. Trans., 7A (1976) 431.

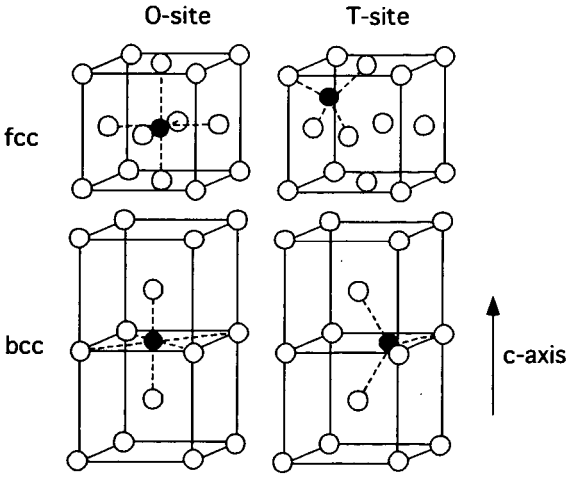

Figure 1. Periodic supercell models for hydrogen occupation at interstitial sites in bcc and fcc metals. Closed circles: Hydrogen; Open circles: Metal.

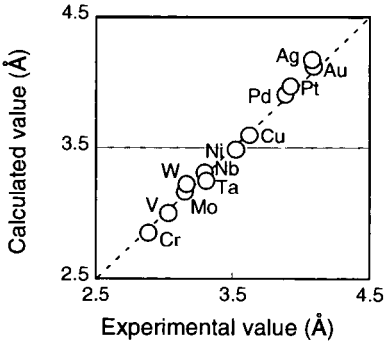

Figure 2. Correlation between calculations and experiments for lattice constants of various metals.

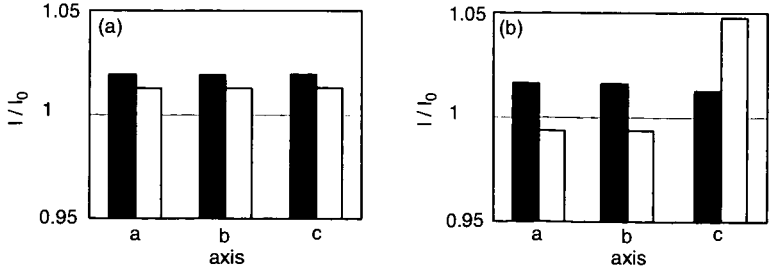

Figure 3. Relative expansion of the lattice constants by the interstitial hydrogen. (a) Pd, (b) V, Closed bars: T-site occupation; Open bars: O-site occupation.

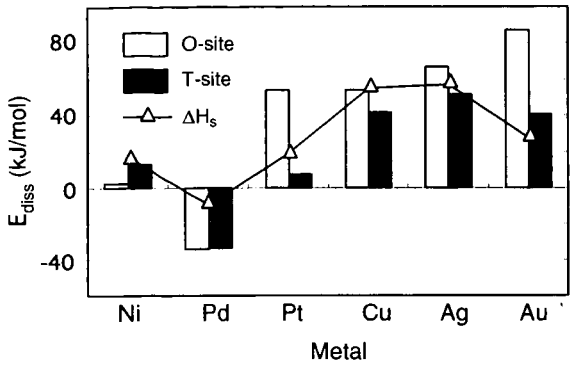

Figure 4. Calculated E_{diss} for vaious fcc metals in comparison with experimental ΔH_s.

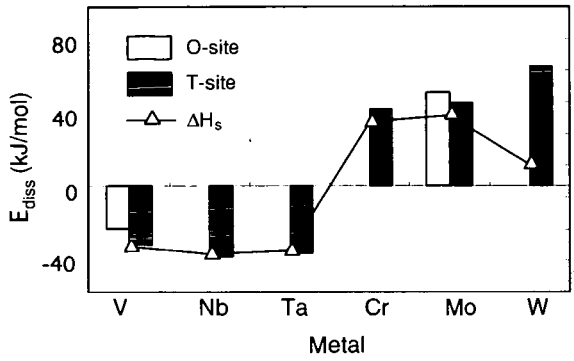

Figure 5. Calculated E_{diss} for vaious bcc metals in comparison with experimental ΔH_s. The O-site occupation is not stable for Nb, Ta, Cr and W.

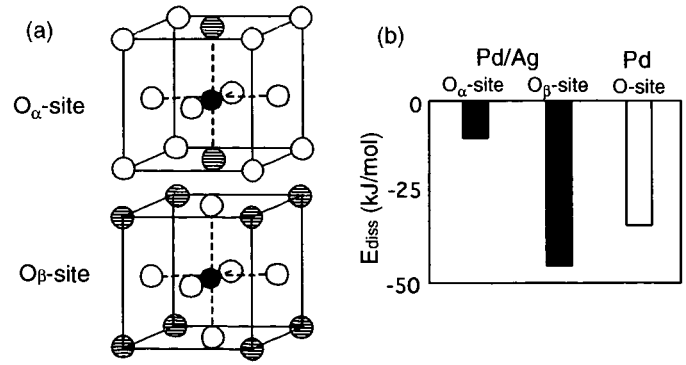

Figure 6. Relative expansion of the lattice constants by the interstitial hydrogen.
(a) Interstitial O-sites in the Pd/Ag alloy model, shaded circles: Ag, (b) calculated E_{diss}.

Hydrogen Separation using Ternary Polymer Blend Compared with the Inorganic High Surface Area Zeolite Materials

Kal R. Sharma Ph.D. PE
Center for Computational Statistics, MS 4A7, Department of Applied and Engineering Statistics, George Mason University, Fairfax, VA 22030-4444

The gas separation of hydrogen by semi-permeable membrane technology can be achieved by the use of ternary, miscible polymer blend of tetramethylhexaflurobisphenol-A-polycarbonate, polyamide and aromatic polyether ketone. Simultaneous increases in permeability and permselectivity can be achieved. Mesoscopic simulations were performed to understand the permselectivity in porous inorganic high surface area materials such as zeolite. This was compared with the polymeric membrane technology. The inorganic materials has well controlled and tailored porosity. In situ separation of hydrogen can be used in fuel cells, underwater gill applications, chemical and biological sensing, neutralization devices, encapsulant applications, encryption of acoustic signature of structures. The permselectivity issues in zeolite material is discussed. Permeability as a function of pore size distribution and tortuosity is presented for the inorganic high surface area material.

A robust design for membrane using polymeric system that acts as semipermeable membrane for purification of Hydrogen, Methane, Nitrogen and Carbon dioxide from process stream subsequent to cooling the gases was developed. The performance of the process for the purification using the membrane technology was appraised. A mathematical model is proposed for the permeability and permselectivity in polymeric membrane.

Systematic variations of the chemical structure can be used to achieve simultaneous increases in permeability and permselectivity. Systematic variations in the chemical structure and its effect on gas permeability and chain packing in substituted polycarbonates, for example, are proposed in the design of the membrane technology for separating hydrogen from a process stream. This process stream subsequent to cooling, may contain Hydrogen, Carbon Monoxide, Carbon Dioxide and Hydrocarbons. The membrane is proposed to be formulated from a ternary blend of miscible polymers or polymeric alloy. The permeability of Hydrogen can be written as a simple product of an average diffusivity, D, and an effective solubility, S, of the penetrant in the polymer matrix:

$$P = D * S \qquad (1)$$

For conditions of negligible downstream pressure, the solubility coefficient, S, is equivalent to the secant slope of the gas sorption isotherm evaluated at upstream conditions. The average diffusivity, D, provides a measure of the effective mobility of the penetrant in the polymer matrix between the conditions at the upstream and downstream side of the film. The second key index of the performance of the membrane material is the separation factor, or permselectivity,

$$\alpha_{A/B...D} = P_A/\Sigma P_{A...D} \qquad (2)$$

The ideal separation factor, by combining the two equations is,

$$\alpha_{A/B...D} = \{D_A S_A /\Sigma D_{A..D} S_{A..D}\} \qquad (3)$$

where $D_A/\Sigma D_{A..D}$ is the diffusivity selectivity, and $S_A/S_{A..D}$ is the solubility selectivity. The solubility selectivity is determined by the differences in condensibility of the 5 penetrants and by their interactions with the membrane material. The diffusivity selectivity is based on the inherent ability of polymer matrices to function as size and shape selective media through segmental mobility and intersegmental packing factors. The glassy state of the polymeric system can have an influence on the porosity of the macrostructure. Typically there is a tradeoff between permeability and permselectivity. Exceptions are the polyimides, sulfonated aromatic polyether ketones, polyamides etc. Certain structural variations can substantially increase the permeability and permselectivity. Some of the design factors in material selection for the membrane technology include substitutions which inhibit chain packing, rotational mobility, miscibility, compatibility and compatibilizability.

Ternary miscible blends can increase the permeability and the glassy state can improve permselectivity. Chain packing inhibition can increase the permeability and decrease in permselectivity. Incompatibility can decrease the permselectivity and increase the permeability. An optimal can be found by simultaneously inhibiting chain packing and rotational mobility about flexible linkages which can lead to increases in both permeability and permselectivity. Decrease of mobile linkages can increase the permselectivity without decrease in permeability. Compatibilzed alloy can improve the chemical stability of the membrane. Hydrophobicity can be increased to prevent the damage from condensibles by configurational manipulation of the polymer backbone. For example, Tetramethylhexaflurobisphenol-A polycarbonate blended with polyamide or with aromatic polyether ketone is an interesting system for the membrane material. When selecting a blend vs copolymer the commercial availability and molecular weight ranges of the products are to be considered carefully. Reversible sorption of the gas can be effected by alloying a salt into the system.

The morphologies of the miscible, immiscible and partially miscible polymer blends are another consideration in the membrane material selection. In a immiscible blend, two phases are present: 1) discrete phase (domain) which is lower in concentration and 2) continuous phase, which is higher in concentration. The miscible polymer blends exhibit single phase morphology. Partially miscible polymer blends may form completely miscible blend at a different concentration. The two phases in partially miscible blends may not have well-defined boundary. Each component of the blend penetrates the other phase at a molecular level. The molecular mixing that occurs at the interface of a partially miscible two-phase blend can stabilize the domains and improve interfacial adhesion.

A multicolumn membrane separator system is proposed for the separation and recovery of all of Hydrogen, Methane, Nitrogen and Carbon dioxide gases from process stream. A cooling stage is proposed to get the gases to temperatures where the polymeric membrane can withstand prior to the separation steps. Multiple sets of membrane separators are selected. For example six of them can be in parallel and may contain a membrane with a high permselectivity for Hydrogen and designated as A beds, B beds three in parallel that in a similar manner can remove the Methane, C beds, three in parallel to remove the Nitrogen and D beds, 2 in parallel to remove the Carbon di-oxide. Each bed of each set goes through a cyclic sequence of diffusion and concentration, adsorption/desorption and other complementary steps. Pressure and Temperature of these reactor systems are interesting variables and as a first approximation not considered as variables in the study.

The process performance was evaluated using design packages such as ECLIPSE and ASPEN. Different process scenarios were evaluated in this manner. The purity level, recovery (%), secondary product in each cycle are the parameters of interest. The waste gases generated has to be accounted for. Purge requirements is another process consideration. The optimization variable is cost. Flexibility of operation is also another salient consideration in this analysis. The number of beds in A, B, C and D were varied in the different scenarios.

The membrane can be formed by dissolution in dipolar aprotic solvents such N-Methyl-2-Pyrrolidone, Dimethyl Sulfoxide, Tetramethyl urea, Hexamethylphospharimide at elevated temperature. These solutions prepared at dilute concentrations of the polymers (about 5%) can be centrifuged and degassed and then the membranes cast onto glass plates. The membranes can be vacuum devolatilized and to remove the residual stress and defects. Thin membranes can be achieved by careful preparation. The permeability and permselectivity of the gases needs to be determined experimentally.

A model for the dependence of polymer structure on the permeability and permselectivity of the membrane is proposed. The different mechanisms such as substitution, miscibility, compatibility, morphology are modeled and the effects delineated. The models for miscibility in ternary blends are improved. The compositions of miscibility and conditions of phase separation can be calculated using the binary interaction model, and Equation of State such as the lattice fluid theory mentioned above. The interrelationships between permeability, permselectivity and polymer phase behavior is proposed to be captured in the model. The role of the morphology of the membrane in general and the glassy state, crystallinity and composition is proposed to be quantified.

The permeability in the inorganic high surface area material such as zeolite can be estimated from the diffusivity calculations. The diffusion through the solids with the macroporous microporous mesoporous distribution is given by;

$$D_{A,tot,eff} = D_{A,tot}\,\varepsilon''/\tau \qquad (4)$$

where the tortuosity factor is given by;

$$\tau = s'/\cos 2\phi \qquad (5)$$

For example the tortuosity is 2 when $\phi = 450$, $s' = 1$. The experimental range for tortuosity is 1.5-7. The ϕ is the angle of the pores whereby the cylindrical molecules travel a secϕ greater distance. The shape factor s' is used to correct for the non-cylindrical pores. The average pore radius can be determined from the pores sized distribution. The Kelvin equation relates the capillary radius to vapor pressure at which condensation occurs:

$$P(r)/P_{sat} = \exp(-2\sigma\cos\theta V_m/r\,RT) \qquad (6)$$

where θ is the wetting angle

$$r = t + 2\sigma\cos\theta/(RT \ln(P_{sat}/P)) \qquad (7)$$

The average pore radius can be determined from the PSD (Pore Size Distribution).

$$r_{psd} = \int r\,V(r)\,dr / \int V(r)\,dr \qquad (8)$$

The number of saddle points in the pores size distribution is a measure of the presence of the macro pore, meso pore and micro pores. For pores of uniform size;

$$D_{A,tot,eff} = D_{a,tot}\,\varepsilon''/\tau \qquad (9)$$

The total diffusion coefficient (bulk & Knudsen) in fluid phase and the porosity and tortuosity are the key parameters that affect the effective diffusivity. The porosity takes into account the fact that all of the material between the two faces of the solid is not entirely fluid phase. The zeolite material with tailored porosity can be used as a molecular sieve and thus be used in the process to separate the Hydrogen from the process stream. The tortuosity accounts for the case when the distance traveled by the fluid molecule in pore is much greater than distance between the two solid faces. For the trimodal distribution of macropores, mesopores and micropores;

$$D_{A,tot,eff} = (\theta^2_{macro}/1/D_{AB} + 1/D_{A,K,macro}) \qquad (10)$$

Flow through macropores

$$+ (\theta^2_{macro}/(1/D_{AB} + 1/D_{A,Kmeso}))$$

Flow through mesopores

$$+ (\theta^2_{macro}\,(1 + 3\theta_{macro})/(1-\theta_{macro})(/\,(1-(1+N_B/N_A)y_A/D_{AB} + 1/D_{A,Kmicro})$$

Flow through micropores + macro/micro series

The micro-meso cutoff is 15 A and macro meso cutoff is 12.5 nm.

The multicomponent diffusivity was assumed to be the same as the binary diffusivites in the vapor phase with the predominant process being bulk and viscous diffusion. The Knudsen diffusion is accounted for by the collisions with the container walls. The collision integral for diffusion is a function of the Lennard Jones interaction potential parameter and is a simple arithmetic average of the pure component values. The temperature is a strong parameter for the bulk binary diffusion values and the molecular weight is key contributor.

Acknowledgments

Kal R. Sharma Ph.D. PE acknowledges Victoria F. Haynes Ph.D., Group Vice President and Chief Technical Officer, BF Goodrich, Brecksville, OH his mentor in industrial research, Richard Turton, Professor, Chemical Engineering, West Virginia University, Morgantown, WV his mentor in academic research, Prof. Nithiam T. Sivaneri, Professor and Associate Chair, Mechanical and Aerospace Engineering, West Virginia University, Morgantown, WV, Prof. Edward J. Wegman, Chair and Director, Center for Computational Statistics, George Mason University, Fairfax, VA, Prof. Eva Marand, Chemical Engineering at the Virginia Polytechnic and State University, Blacksburg, VA, Susan Meek, at the Virginia's Center for Innovative Technology, Herndon, VA, Dr. Richard Shuford, Branch Chief, Polymers Research Branch at the Army Research Laboratory, Aberdeen Proving Ground, MD and his associates at Independent Institute of Technology.

THE APPLICATION OF A HYDROGEN RISK ASSESSMENT METHOD

Dr. Michael R. Swain
Eric S. Grilliot
University of Miami

Dr. Matthew N. Swain
Analytical Technologies, Inc.

ABSTRACT

A comparison of the predicted results from a calibrated CFD model with experimentally measured hydrogen data was made to verify the calibrated CFD model. The experimental data showed the method predicted the spatial and temporal hydrogen distribution in the garage very well. A comparison is then made of the risks incurred from a leaking hydrogen-fueled vehicle and a leaking LPG-fueled vehicle.

INTRODUCTION

The following is brief description of using a Hydrogen Risk Assessment Method (HRAM) to analyze the risk associated with hydrogen leakage in a residential garage. The four-step method is as follows:

1. Simulation of an accident scenario with leaking helium.
2. Calibration of a CFD model, of the accident scenario, using helium data.
3. Prediction of the spatial and temporal distribution of leaking hydrogen using the calibrated CFD model.
4. Determination of the risk incurred by hydrogen compared to a currently used fuel.

EXPERIMENTAL

Steps 1 and 2 were performed for a home refueling station, installed in a residential garage, to test the ability of the CFD model to predict hydrogen concentrations in a single car residential garage. The work was conducted utilizing a half scale model of the garage. The garage employed a vented garage door. The door was designed to provide adequate ventilation for a vehicle parked in the garage leaking hydrogen at a rate of 7200 liters/hr (at full scale). The garage geometry is depicted in Figure 1.

Figure 2 shows the general flow pattern created by the leaking low density gas (either helium or hydrogen). The gases rise over the leak, travel diagonally across the ceiling toward the garage door, exiting through the upper garage door vent. The loss of gases out of the upper vent draws fresh air into the lower vent. These gases flow across the floor toward the rear of the garage.

Experiments were conducted at three gas leakage rates; 900 l/hr, 1800 l/hr, and 2700 l/hr, using both helium and hydrogen. The predictions of the model and the experimental data were in good agreement. Figure 3 shows an example of the comparison of experimental data and computer model results. The data shown is for a hydrogen leakage rate of 2700 l/hr. Sensor location 7 was chosen because that location recorded the highest concentration of hydrogen during the test. The other sensor locations showed similar correlation between experimental and calculated data.

RESULTS

The model was used to compare gas leakage from vehicles stored in residential garages. Leakage from a LPG fueled vehicle was compared to leakage from a hydrogen-fueled vehicle. The comparison was based on a Ford Taurus sized vehicle stored in a single car garage of slightly different dimension, than the home refueling station test, but with the same vented garage door.

The computer model representation of the ventilated garage was run to predict the behavior of a LPG fueled vehicle. The leakage rates chosen for the LPG fueled vehicle were 848.2 liters/hr and 4334 liters/hr. These represent upper and lower bounds on the leakage rate of propane from a fuel line fracture that produced a 7200 liter/hr hydrogen leakage rate. The 848.2 liter/hr flow rate would occur if laminar flow was assumed in the hydrogen and propane leaks being compared. The 4334 liter/hr flow rate would occur if turbulent flow was assumed in the hydrogen and

propane leaks being compared. Due to differences in density and viscosity the volumetric leakage rate of propane was lower than that of hydrogen which was 7200 l/hr.

Figures 4-6 show the results after 2 hours of leakage. The figures show surfaces of constant gas concentration that represents the lean limit of combustion. Figure 4 is a plot of the surface of constant 4.1% hydrogen concentration at by volume. 4.1% hydrogen in air is the upward propagating lean limit of combustion for hydrogen-air mixtures (Coward 1961, Hansel 1993, Lewis 1961, and Ordin 1997). This is the lowest concentration of hydrogen considered combustible. The cloud under the front of the vehicle in Figure 4 represents the volume of burnable gas after 2 hours of leakage at 7200 liters/hr. Figure 5 is a plot of the surface of constant 2.1% propane concentration at by volume. 2.1% propane in air is the upward propagating lean limit of combustion for propane-air mixtures (Coward 1961, Hansel 1993, Lewis 1961, and Ordin 1997). This is the lowest concentration of propane considered combustible. The cloud covering almost the entire floor of the garage represents the volume of burnable gas after 30 minutes of leakage at 848 liters/hr. Figure 6 is a plot of the surface of constant 2.1% propane concentration at by volume. The cloud covering the entire floor of the garage represents the volume of burnable gas after 30 minutes of leakage at 4334 liters/hr.

CONCLUSIONS

It can be seen that the volume of combustible gas created by the hydrogen-fueled vehicle is much smaller than the volume created by the LPG fueled vehicle. This was true regardless of which of the two propane flow rates was assumed. It should be noted that the combustible cloud produced by the LPG fueled vehicle was continuing to grow. The volume of combustible gases produced by the hydrogen fueled vehicle had reached steady state after 1 hour as seen in Figure 7. Figure 7 shows the surface of constant 4.1% hydrogen concentration, which is the lean limit of combustion for hydrogen.

ACKNOWLEDGEMENTS

The authors would like to thank the Department of Energy and Sandia National Labs, without whose support this work would not have been possible.

REFERENCES

Coward, H.F., and G.W. Jones. 1952. Limits of Flammability of Gases and Vapors, Bureau of Mines Bulletin 503

Hansel, J.G., G.W. Mattern, and R.N. Miller. 1993. "Safety Considerations in the design of Hydrogen Powered Vehicles", Int. J. Hydrogen Energy, Vol. 18, No. 9, pp 790

Lewis, B. and G. VonElbe. 1961. Conbustion, Flames and Explosions of Gases, 2nd Edition New York: Academic Press

Ordin, P.M. 1997. Safety Standards for Hydrogen and Hydrogen Systems, National Aeronautics and Space Administration, NSS 1740.16, Office of Safety and Mission Assurance, Washington D.C.

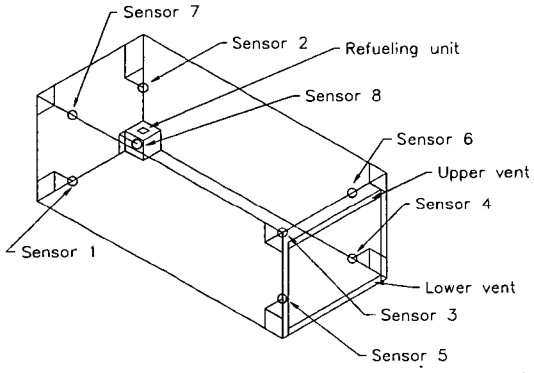

Figure 1 - Half-scale garage geometry

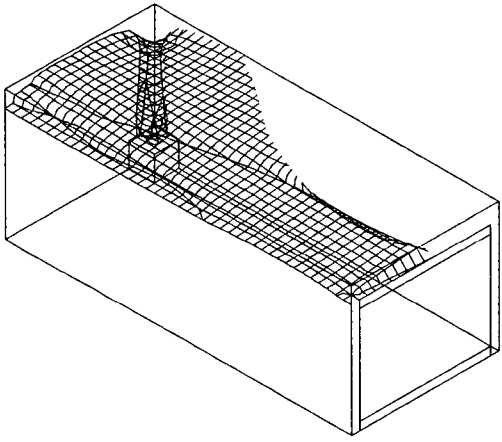

Figure 2 - General flow pattern

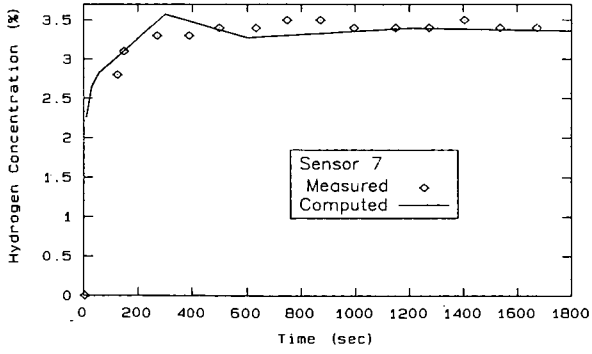

Figure 3 - Hydrogen results comparison (Sensor 7)

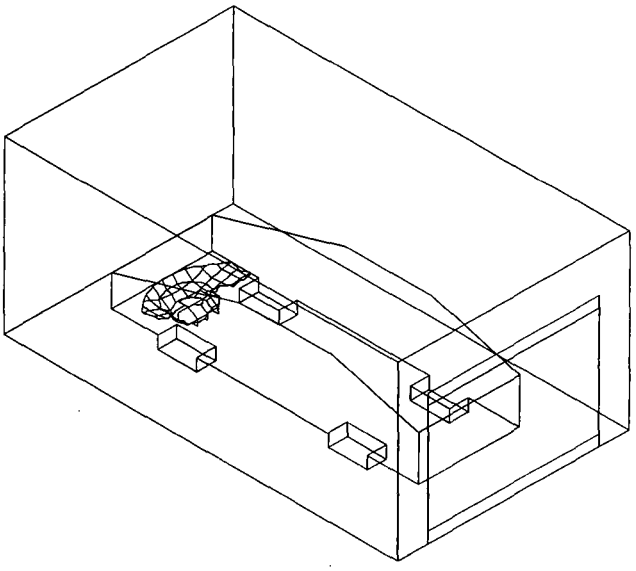

Figure 4 - Surface of constant 4.1% hydrogen concentration after 2 hours of leakage at 7200 liters/hr

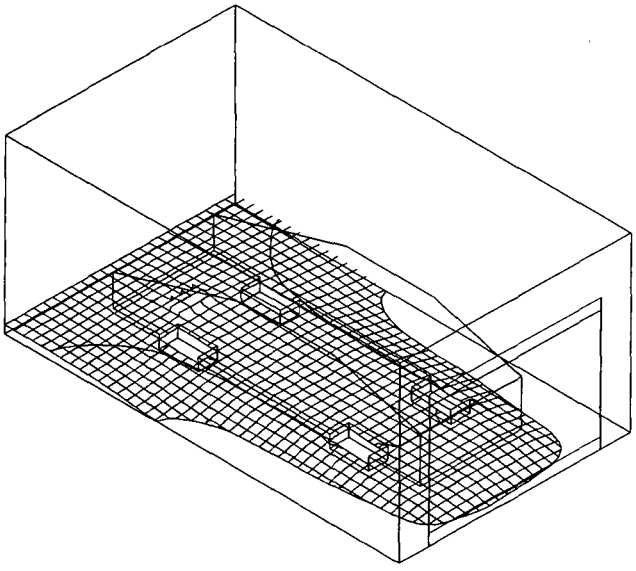

Figure 5 - Surface of constant 2.1% propane concentration after 2 hours of leakage at 848.2 liters/hr

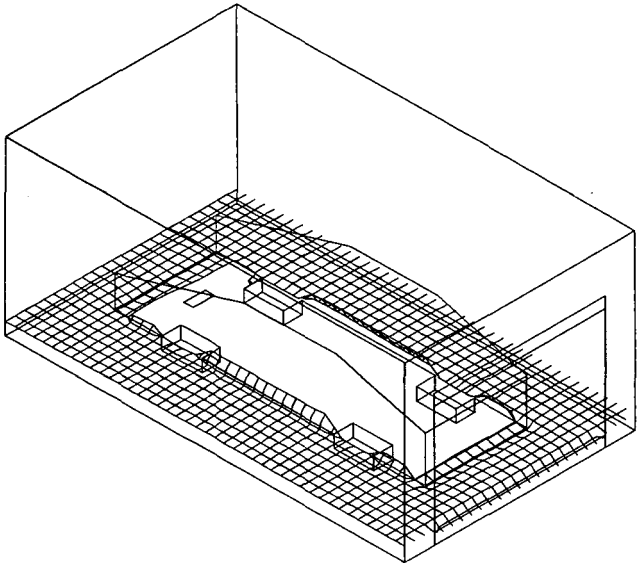

Figure 6 - Surface of constant 2.1% propane concentration after 2 hours of leakage at 4334 liters/hr

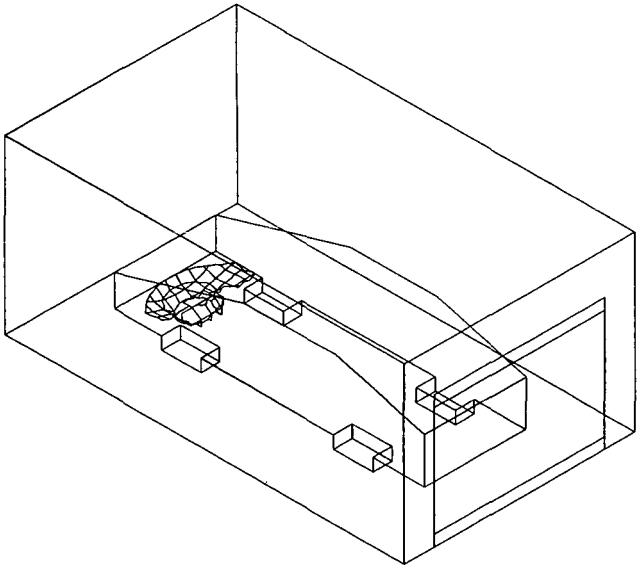

Figure 7 - Surface of constant 4.1% hydrogen concentration at 1 hour

LOW COST HYDROGEN SENSORS FOR HYDROGEN FUEL SAFETY

Mark Daughtery, Dave Haberman, Carlton Salter
DCH Technology, Inc.
Valencia, California

David Benson
National Renewable Energy Laboratory
Golden, Colorado

Barbara Hoffheins
Oak Ridge National Laboratory
Oak Ridge, Tennessee

Use of hydrogen as an energy carrier is increasing. Production and handling of hydrogen in industry is not new, but there are many new applications as a commercial fuel that bring its use into the public domain. Adequate safety monitoring equipment must parallel the advent of this technology. DCH Technology, in conjunction with the National Renewable Energy Laboratory (NREL) and Oak Ridge National Laboratory (ORNL), is developing and commercializing solid-state hydrogen sensors. They are designed to be inexpensive, small, and chemically inert. The NREL Fiber Optics sensor requires no electrical power at the sensing point and is ideal for high electromagnetic environments. The ORNL thick film sensor is versatile and can operate from a small battery. Data from combinations of multiple sensors can be fed into a central processing unit via fiber optics or telemetry to provide hydrogen situational awareness for small and large areas. These sensor technologies, functional attributes, and applications are presented below.

THICK FILM HYDROGEN SENSOR (TFHS)

The sensing mechanism of the ORNL sensor relies on the reversible absorption of atomic Hydrogen into and out of palladium metal in proportion to the ambient partial pressure of hydrogen gas. Changes in hydrogen concentration in the palladium matrix lead to corresponding changes in the electrical resistance of the palladium that are easily measured. The sensor consists of four palladium resistors (or legs) that are arranged in a Wheatstone bridge configuration. Figure 1 depicts the sensor and its schematic representation. The current prototype sensor chip is 2.5 cm x 2.5 cm x 0.06 cm. Two of the legs serve as reference resistors and are passivated with a thick-film resistor encapsulant to prevent entrance of hydrogen into the underlying palladium layer; thus, changes in the resistance of the palladium caused by temperature variation are compensated.

The sensor concept was successfully demonstrated using prototypes fabricated with thin film techniques. Then the sensor was designed for thick film fabrication for a variety of reasons. Effective passivations, difficult to achieve with thin films, can be made more impermeable using glass-based, thick-film compositions. Glass frit, an important component of most thick-film compositions, is formulated to provide maximum adhesion, chemical resistance, and stability over a wide range of operating conditions. A thick-film sensor is also inherently simpler, more rugged, and much less expensive to manufacture in quantity. These ideas were incorporated in the hydrogen sensor designs patented in 1994 (Lauf 1994) and 1995 (Hoffheins 1995). The palladium resistor material used in fabricating sensor samples was developed and patented by DuPont Electronics (Felten 1994).

Theoretically, the diffusion of hydrogen into a thin layer of palladium occurs on the order of milliseconds. In laboratory tests, however, the time constant of the test setup can prevent direct observation of the actual response time of the sensor. Figure 2 shows the response of a sensor to increasing concentrations of hydrogen from 0 to 2% in air. The sensor was placed in a small test chamber (50 cm^3). Hydrogen was added to air in 0.1% increments, while flow was maintained at a constant rate. Each step was 60 seconds. The sensor began to respond at the level of 0.2% H_2 in air. For each successive increment of hydrogen, sensor output increased and leveled off in 9 seconds. This time includes the time constant of the test chamber of about 2 seconds. The response in the range between 0 and 2% hydrogen is linear, so calibration is easily accomplished.

Currently the sensor is being tested to a list of specifications of interest for several commercial applications. Materials are being optimized for conditions that will typically never go above 2% H_2 in air. The temperature range is -40°C to +60°C. The sensor has been successfully tested between 20°C and 200°C [Hoffheins 1998]. In general, the response is faster at the higher temperatures, but the magnitude of the response is lower because of reduced hydrogen solubility

in the palladium. An acceptable response time for the intended commercial applications is 3 seconds. The raw output from current prototypes does not meet that requirement; however, methods to use the rate of response and the dc output with external circuitry to predict the hydrogen concentration are being examined. Another very important performance objective is that the sensor is insensitive to the following compounds: CO, CO_2, CH_4, NH_3, propane, butane, and acetylene. In preliminary tests, sensors were exposed to carbon monoxide, propane, and methane. The response indicated little or no effect on the sensor. The sensor appears to be insensitive to these compounds. More tests will be conducted with the above and other compounds to verify this performance.

APPLICATIONS FOR THE TFHS

DCH Technology is commercializing the TFHS. This device is most applicable as a low cost alarm sensor. The principal applications currently being addressed are for hydrogen powered automobiles, personal safety badges, and remote area monitoring.

The safety badge application has been chosen for initial market penetration because the environmental requirements match current knowledge of the performance of the sensor. DCH has built a prototype badge that is approximately the size of a standard business card and roughly one-quarter of an inch thick. DCH is undertaking a more detailed market analysis to determine customers and distribution partners, additional functional benefits (such as activating a vibrator to signal hydrogen), specific sensor technical requirements, and cost targets. A product specification will be developed from this data and an initial product will be built and distributed for alpha testing. In parallel with the product definition effort, DCH and ORNL will complete the technical bounding of the sensor operational characteristics, including response time, cross-sensitivity, and applicable firmware.

Sensors for automotive applications are being developed now. There are three general areas of interest: Low level alarms to sense leaks from hydrogen storage and delivery lines; sensors for high concentrations of hydrogen that exist in the output of reformers or inputs to fuel cells; and medium level sensors that are needed in the exhaust stream of an internal combustion engine running on hydrogen. The sensors considered in this paper are for the low level alarm application.

The automotive requirements for the device are low cost (one to four dollars per sensing point), rapid response, rugged and repeatable operation in the automotive environment, and a unit life of ten years. In addition, there cannot be any false positives, and the size of the sensor must be small enough to fit into critical areas.

The automotive requirements are considerably more stringent that those for the safety badge. The operating temperature range is very broad, from –40°C to over 60°C. While the TFHS is thermally self compensating by design, the sensor response speed decreases with decreasing temperature and the sensitivity decreases with increasing temperature. ORNL and DCH are currently investigating the sensor response under these conditions. Software methodologies are being investigated to provide interpretive decision making based on sensor output to both speed up response speed and to activate hierarchical responses to decreasing, continuing or increasing hydrogen concentrations.

The automotive operating environment can expose a sensor to a multitude of gases and vapors. The sensor must have no cross sensitivity and not be poisoned by such chemicals. To address these requirements, DCH and ORNL are testing the sensor against other gasses, such as CO_2, CH_4, NH_3, O_2 variations, water vapor, acetylene, and chemical vapors to which the sensor could be exposed. Additional considerations under evaluation are susceptibility of the sensor and associated wiring and electronics to electromagnetic interference. Also, sensor ruggedness and durability are being characterized. Finally, after all these technical considerations are put to rest, the sensor must meet the cost goals of the automotive industry.

All of these parameters are being addressed in cooperation with major automotive manufacturers. Publicly sold fuel cell powered cars are on the horizon and the need for low cost hydrogen sensors that meet the needs of the automotive environment is now.

The final application area being addressed for the TFHS is for monitoring of large industrial areas, both indoor and outdoor, which have risks of hydrogen leakage. DCH is aware of industrial disasters that were prevented because the company involved discovered the leak using a portable sensor. DCH intends to make hydrogen sensing simple and cost effective so

companies can easily install the protection they need. In particular, DCH is developing a wireless transmission capability to attach to the TFHS for remote and/or large area monitoring. A receiver unit will collect transmitted signals from multiple sensors. This unit can then be hard wired into control electronics or its output signal transmitted to remote control stations. The receiver could be one of many a large area network. DCH is presently evaluating transmitter suppliers as well as looking at making the transmitter in-house. In parallel, DCH is developing the market analysis to determine operating and cost specifications. In a few months, DCH will finalize the specifications and make the make/buy decision. This action will be followed by development of a prototype, obtaining FCC approval, and alpha testing.

FIBER OPTICS HYDROGEN SENSOR (FOHS)

The use of a fiber-optic, hydrogen-gas-leak detector has advantages of inherent safety (no electrical power in the vicinity of the sensor), reduced electromagnetic interference, lightness of weight, and low cost. Most if not all of the needed electro-optic components could be integrated into a single application-specific integrated circuit (ASIC) for economical mass production. An analysis of the probable manufacturing costs has shown that it should be possible to mass-produce similar detectors for about $5 each (not including the cost of the optical fiber).

In this design, a thin-film coating at the end of a polymer optical fiber senses the presence of hydrogen in air (Benson, et al 1998). When the coating reacts reversibly with the hydrogen, its optical properties are changed. Light from a central electro-optic control unit is projected down the optical fiber where it is reflected from the sensor coating back to central optical detectors. A change in the reflected intensity indicates the presence of hydrogen. The fiber-optic detector offers inherent safety by removing all electrical power from the sensor sites and reduces signal-processing problems by minimizing electromagnetic interference. Critical detector performance requirements include high selectivity, response speed, and durability as well as potential for low-cost production.

Preliminary experiments were conducted with simple sensors. The end of a polymer optical fiber was coated with 500-nm WO_3 and a superficial layer of 10-nm palladium. Figure 3 shows a calibration curve obtained from such a sensor in air with various concentrations of hydrogen. The reflected signal at 850 nm is attenuated by the optical absorption in the WO_3 in proportion to the reaction with hydrogen, which in turn is proportional to the hydrogen concentration. The sensitivity is adequate for detection of the hydrogen well below the lower explosion limit of 4% in air.

A self-contained, hand-held portable fiber-optic hydrogen sensor was designed and built. The light source is a high- brightness, broad-spectrum "white" (phosphor-enhanced) LED. The light from the LED is projected into the proximal end of a 1-mm-diameter polymer optical fiber and transmitted through a 1 x 2 coupler to an exit port on the instrument. The optical-fiber sensor is plugged into that port with a standard fiber-optic ST connector. Light reflected from the sensor coating on the distal end of the fiber is retumed to the instrument, and half of its power is directed through one of the coupler legs to a dichroic mirror. The dichroic mirror splits the return light beam into long- and short-wavelength portions that fall separately on two different photo-diode amplifiers. The voltage signals from the two photo-diodes are divided one by the other in an analog divide circuit. Figure 4 shows a schematic illustration of the detector's design features.

APPLICATIONS FOR THE FIBER OPTIC HYDROGEN SENSOR

Initially the FOHS was developed for automotive use because it will not inject any electrical circuitry into the sensed area and the signal transmission is over the fiber, which is insensitive to electromagnetic interference. However, this sensor needs further development work to accelerate the response time, especially at the low temperatures required by the automotive specifications. In the mean time, there are two applications for which the sensor, in its current state of development, can be used. The first is as a weld quality sensor. A sensor can be attached to the weld within hours after the weld is completed and used to measure the rate of hydrogen out gassing, which indicates the concentration of dissolved hydrogen in the welded steel. Using this process, the weld condition can be read in minutes. The current methods for measuring the concentration of dissolved hydrogen in welded steel require approximately a day to read and must use witness samples. The fiber optic sensor could be used, as a secondary standard, in conjunction with the existing method. As the faster method becomes proven, standards for its use as a primary weld quality sensor could be established.

The second application is in monitoring battery rooms. Again, multiple fibers would be easily distributed throughout the room and monitored at a central location. In this application, the fiber optic approach displays its inherent advantages of multi-point sensing and installation versatility.

INTEGRATED APPLICATIONS

DCH plans to mix and match these two technologies, along with the DCH Robust Hydrogen Sensor monitor, to provide optimal situation awareness in complex hydrogen use environments. To do this cost effectively, DCH is planning to develop common electronic packages which include easily modifiable software inputs to not only tailor the sensors to the customers unique application, but moreover, to give the user the tools to modify and expand their hydrogen sensing capabilities.

SUMMARY

DCH Technology is commercializing state of the art hydrogen sensors developed by Oak Ridge National Laboratory and the National Renewable Energy Laboratory. This blend takes the scientific knowledge resident in these laboratories and creates applicable, timely, and meaningful commercial products that assist the development of the hydrogen fuel economy. These sensors are necessary to help carry this development into the public domain.

Key Words: Hydrogen, Sensors, Safety

References

Benson, D. K., C. E. Tracy, and D. S. Bechinger, 1998. "Fiber Optic Device for Sensing the Presence of a Gas. U. S. Patent No. 5,708,735.

Felten, J.J. 1994. "Palladium Thick Film Conductor." U.S. Patent No. 5,338,708.

Hoffheins, B.S. and R.J. Lauf. 1995. "Thick Film Hydrogen Sensor." U.S. Patent No. 5, 451,920.

Hoffheins, B.S., R.J. Lauf, T.E. McKnight, and R.R. Smith, 1998. "Design and Testing of Hydrogen Sensors for Industrial Applications," *Polymers in Sensors, Theory and Practice,* ACS Symposium Series 690, N. Akmal and A.M. Usmani, pp. 90-101.

Lauf, R.J., B.S. Hoffheins, and P.H. Fleming. 1994. "Thin-Film Hydrogen Sensor." U.S. Patent No. 5,367,283.

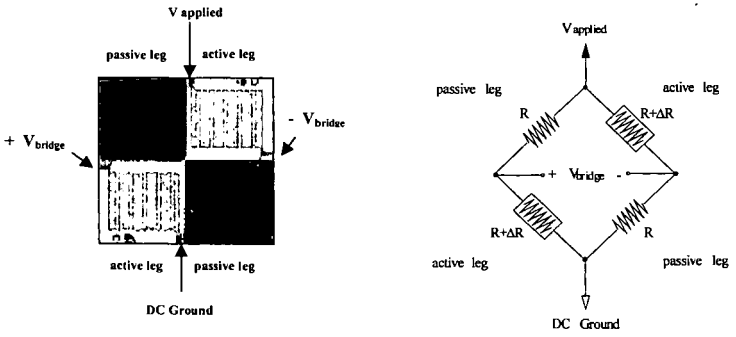

Figure 1. Thick Film Hydrogen Sensor Chip and Schematic Representation

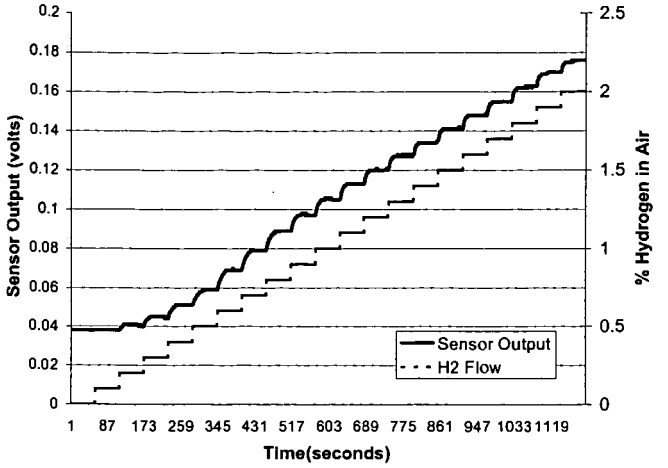

Figure 2. Sensor response to increasing concentrations of hydrogen in air

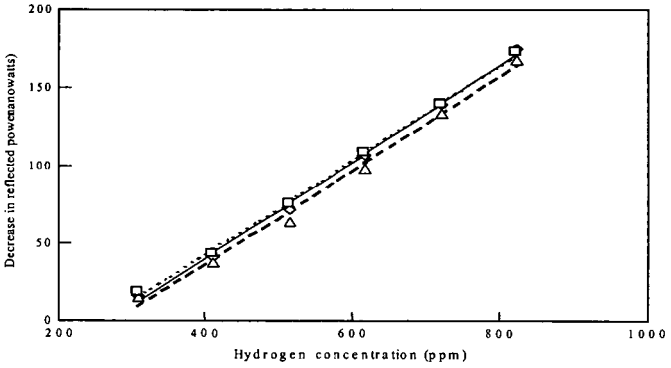

Figure 3. Calibration curves for a simple reflective WO_3/Pd-coated F-O sensor.

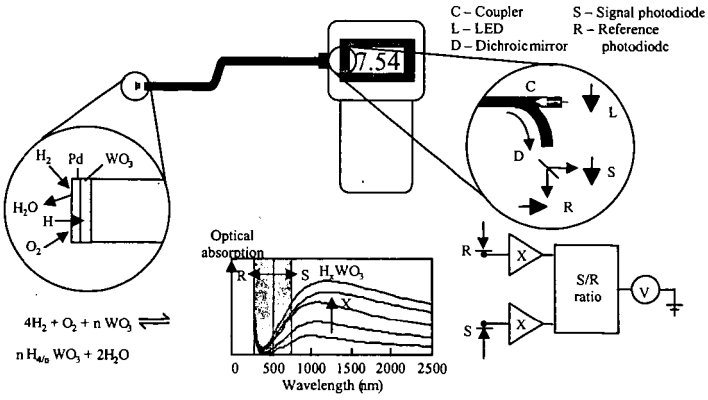

Figure 4. Schematic diagram of the prototype portable fiber-optic, hydrogen-gas-leak detector showing selected design features.

THE INTERNATIONAL ENERGY AGENCY'S HYDROGEN RESEARCH AND DEVELOPMENT ACTIVITIES

Carolyn C. Elam and Catherine E. Gregoire Padró,
National Renewable Energy Laboratory, Golden, CO, USA
Gary Sandrock, SunaTech, Inc., Ringwood, NJ, USA
Bjorn Gaudernack, Institute for Energy Technology, Kjeller, Norway
Neil P. Rossmeissl, U.S. Department of Energy, Washington, D.C., USA

Keywords: Hydrogen, International Energy Agency, Integrated Systems

INTRODUCTION

Today, hydrogen is primarily used as a chemical feedstock in the petrochemical, food, electronics, and metallurgical processing industries, but is rapidly emerging as a major component of clean sustainable energy systems. It is relevant to all of the energy sectors - transportation, buildings, utilities, and industry. Hydrogen can provide storage options for baseload (geothermal), seasonal (hydroelectric) and intermittent (PV and wind) renewable resources, and, when combined with emerging decarbonization technologies, can reduce the climate impacts of continued fossil fuel utilization. Hydrogen is truly the flexible energy carrier for our sustainable energy future.

International Energy Agency

The International Energy Agency (IEA) was established in 1974, following the first oil crisis and is managed within the framework of the Organization for Economic Cooperation and Development (OECD). The mission of the IEA is to facilitate collaborations for the economic development, energy security, environmental protection and well-being of its members and of the world as a whole. As part of this effort, the IEA launched the Production and Utilization of Hydrogen Program, known as the Hydrogen Agreement, in 1977 to advance hydrogen production, storage and end-use technologies and to accelerate hydrogen's acceptance and widespread utilization.

The use of hydrogen as an energy carrier is considered a mid- to long-term goal. This is due to infrastructure barriers, particularly in the storage area. Likewise, safety issues, both real and perceived, are concerns for acceptance of hydrogen by the general population. Finally, hydrogen production from renewables will likely not be cost-competitive with fossil-based production, at least in the near-term. Thus, the Hydrogen Agreement is focused on pursuing technologies that will help overcome some of the infrastructure barriers and/or result in the reduced cost of hydrogen systems.

- On-board storage in vehicles is one of the major barriers to the acceptance of hydrogen powered vehicles. Metal hydrides and similar storage medium, like carbon, are thought to have the greatest potential for the safe, on-board storage of hydrogen. However, work-to-date has not proven cost effective due to the inability of current hydride technology to meet the hydrogen storage percentages required for maintaining vehicle weights within a reasonable range.

- To achieve the advantages of a "hydrogen future," namely a reduction in carbon emissions, hydrogen must be able to be cost-effectively produced from renewables. Thus, the Hydrogen Agreement has been pursuing R&D in the solar production area, both biological and electrochemical. The electrochemical approach is, of course, hindered by the fact that photovoltaic technology is not yet cost-effective. Thus, it cannot compete with existing technology, except possibly in small niche markets. Much must still be learned about photobiological processes before we are able to understand the economic potential of this production technology.

- Achieving the vast potential benefits of a hydrogen system requires careful integration of production, storage and end-use components with minimized cost and maximized efficiency, and a strong understanding of environmental impacts and opportunities. System models combined with detailed life cycle assessments provide the platform for standardized comparisons of energy systems for specific applications. Individual component models form the framework by which these system designs can be formulated and evaluated.

- The use of hydrogen in the metals, chemicals, glass, food, electronics, fertilizer, petroleum and space industries is well established. The range of uses has been increasing as has the consumption by specific application. Historically, hydrogen has had an excellent safety record. The many studies, R&D efforts, and experience base have contributed to the publication of regulations, standards, industrial data sheets and technical reports. Hydrogen safety is an issue of every aspect from production to utilization and continues to be of the utmost importance; not only to those researching, designing and working with it; but to the general public, local authorities, insurance agents, etc., as well.

TECHNOLOGY ACTIVITIES

Integrated Systems

Through the IEA Integrated Systems activities, twenty-four component models were developed to model hydrogen production, storage, distribution and utilization (see Table 1). Guidelines for a standardized modeling platform were defined to ensure that the component models could be linked to simulate fully integrated systems. Using the component models, two integrated systems were evaluated for grid-independent remote village applications: PV-electrolysis-metal hydride-PEM fuel cell system and wind-electrolysis-compressed gas-internal combustion engine generator set. Using resource data for the region and a demand profile for a similar-sized village, the system components were designed to provide constant power to the villagers. For the location used in this study, the PV system required about 1/6th of the storage of the wind system, even though the PV resource exhibited significant seasonal variation compared to the wind resource. Similarly, a comparative study of hydrogen storage technologies for a remote renewable energy system examined relative costs of compressed hydrogen gas, low-temperature metal hydride and high temperature metal hydride storage systems for a grid-independent system supporting a village of 100 homes in Central America. The analysis showed that, while the compressed gas storage system had the lowest capital cost, the low-temperature metal hydride system was the easiest to operate and maintain, and was therefore the overall lowest cost system. [1-8]

In support of the Integrated Systems activities, fourteen international hydrogen demonstration projects were critically evaluated and compared, with system performance measurement as the central focus. Safety and regulatory issues were also considered. Representatives of these demonstration projects provided technical data and participated in the review workshops. Additionally, the international participants were able to visit a number of the demonstration sites to see the facilities and meet with the project engineers. The list of the projects that were reviewed is shown in Table 2.

Photoproduction of Hydrogen

As part of the IEA activities, the concept of using solar energy to drive the conversion of water into hydrogen and oxygen has been examined from the standpoints of potential and ideal efficiencies, measurement of solar hydrogen production efficiencies, surveys of the state-of-the-art, and technological assessments of various solar hydrogen options. The analysis demonstrated that the ideal limit of the conversion efficiency for 1 sun irradiance is ~31% for a single photosystem scheme and ~42% for a dual photosystem scheme. However, practical considerations indicate that real efficiencies will not likely exceed ~10% and ~16% for single and dual photosystem schemes, respectively. Four types of solar photochemical hydrogen systems were identified: photochemical systems, semiconductor systems, photobiological systems and hybrid and other systems. A survey of the state-of-the-art of these four types was performed and each system (and their respective subsystems) was examined as to efficiency, potential for improvement and long-term functionality. The following four solar hydrogen systems were identified as showing sufficient promise for further research and development: [10]

- Photovoltaic cells plus an electrolyzer
- Photoelectrochemical cells with one or more semiconductor electrodes
- Photobiological systems
- Photodegradation systems

Most photobiological systems use bacteria and green algae to produce hydrogen. These systems hold great promise for long term sustainable hydrogen production, but face two major barriers for meeting the cost limitations. These barriers are the fairly low solar conversion efficiencies of these systems of around 5-6%, and the fact that nearly

all enzymes that evolve hydrogen from water are inhibited in their hydrogen production by the presence of oxygen. Research efforts are focusing on overcoming this oxygen intolerance by developing strains of the green algae, Chlamydomonas, which contain oxygen-evolving enzymes, and thus can produce oxygen and hydrogen simultaneously. Genetic alterations of Chlamydomonas are being investigated in attempts to improve the solar conversion efficiencies. These new genetic forms are predicted to reach efficiencies on the order of 10%.

Photoelectrochemical production uses semiconductor technology in a one-step process of splitting water directly upon sunlight illumination by combining a photovoltaic cell and electrolysis into a single device. Research efforts are being focused on identifying structures and materials that will meet the high voltage requirements to dissociate water, not be susceptible to the corrosiveness of the aqueous electrolytes used in the electrolytic process, and are cost-effective. Amorphous silicon devices are one of the types most favored, due to their lower cost. These photovoltaic devices have achieved efficiencies of 7-8%. Photovoltaic devices using more expensive materials, have demonstrated efficiencies of 12.4%. [9] Researchers are now working to combine the low cost materials and high conversion efficiency materials to achieve a practical application of this promising technology.

Metal Hydrides and Carbon for Hydrogen Storage

The use of hydrogen as a vehicle fuel requires a storage means that has inherent safety and both volumetric and gravimetric efficiency. Metal hydrides offer alternatives to the storage of hydrogen in gaseous and liquid form. They store hydrogen in an essentially solid form and offer the potential for volume efficiency, high safety, low pressure containment and ambient temperature operation. Unfortunately, most known hydrides are either heavy in comparison to the hydrogen they carry or require high temperature for hydrogen release. In the past few years, carbon adsorbent materials have also gained attention as a possible, cost-effective storage medium for hydrogen. Whereas carbon was once considered only as a cryoadsorbent for hydrogen, there is growing belief it can be used at ambient temperature. However, much must still be learned about consistent and high-purity production of these materials and the nature and potential for hydrogen storage. [11]

Work has been progressing to develop a variety of hydride and carbon materials for on-board storage, working towards both improved gravimetric capacity (5 weight %) and lower temperature (100-150°C) release of hydrogen. Building on the advances reported by the Max Planck Institute, Germany, [12] several international collaborations have been established to further develop the catalyzed sodium aluminum hydrides for hydrogen storage. The joint efforts of the experts has led to the identification of a material capable of 5 weight percent reversible hydrogen storage at 150°C, the necessary target for economic on-board hydrogen storage for vehicles. [11] The experts are now working to meet the new target of 5 weight percent at 100°C.

RESEARCH AND DEVELOPMENT NEEDS/FUTURE ACTIVITIES

Many advances were made in the longer-term photoproduction area. This includes identification of a semi-conductor-based hydrogen production system capable of 12.4% solar efficiencies and the construction of a process development scale bioreactor. However, this work is still at the early development stage. A variety of materials and organisms remain under investigation. System design is also an area that still requires a great deal of effort.

Hydrogen use in non-energy processes, such as the chemical, metallurgical, and ceramics industries was also identified as an area where a concentrated research effort could facilitate the increased utilization of hydrogen. Annually, these industries account for nearly 50 percent of the world's 500 billion Nm^3 hydrogen consumption. Process improvements and novel synthesis approaches could lead to overall efficiency improvements and reduced environmental impacts. Likewise, increased market share for hydrogen in these arenas should lead to expedited infrastructure development, a necessity for facilitating the advancement of the energy-related and renewable-based applications.

Approximately 95% of the hydrogen produced today comes from carbon containing raw material, primarily fossil in origin. The conventional processes convert the carbon to

carbon dioxide, the majority of which is discharged to the atmosphere. The growing awareness of the impact of greenhouse gas emissions on global climate change has necessitated a reassessment of the conventional approach. Integrating carbon dioxide sequestration with conventional steam reforming will go a long way towards achieving "clean" hydrogen production. Likewise, improving the robustness of pyrolytic cracking technologies for the conversion of hydrocarbons to hydrogen and pure carbon should not only improve the process economics, but also its applicability to a variety of feeds. Finally, the thermal processing of biomass can yield an economic and carbon neutral source of hydrogen.

SUMMARY

As we enter the new millennium, concerns about global climate change and energy security create the forum for mainstream market penetration of hydrogen. Ultimately, hydrogen and electricity, our two major energy carriers, will come from sustainable energy sources, although, fossil fuel will likely remain a significant and transitional resource for many decades. Our vision for a hydrogen future is one of clean sustainable energy supply of global proportions that plays a key role in all sectors of the economy. We will implement our vision with advanced technologies including direct solar production systems and low-temperature metal hydrides and room-temperature carbon nanostructures for storage. Hydrogen in the new millennium is synonymous with energy supply and security, climate stewardship, and sustainability.

REFERENCES

1. Bracht, M., A. De Groot, C.E. Gregoire Padró, T.H. Schucan, and E. Skolnik, 1998, "Evaluation Tool for Selection and Optimization of Hydrogen Demonstration Projects. Application to a Decentralized Renewable Hydrogen System," Hydrogen Energy Progress XII, J.C. Bolcich and T.N. Veziroglu, eds., 1243-1254.
2. de Groot, A., M. Bracht, C.E. Gregoire Padró, T.H. Schucan, and E. Skolnik, 1998, "Development of Guidelines for the Design of Integrated Hydrogen Systems," Hydrogen Energy Progress XII, J.C. Bolcich and T.N. Veziroglu, eds., 75-86.
3. Schucan, T.H., E. Skolnik, M. Bracht, and C.E. Gregoire Padró, 1998, "Development of Hydrogen Technology Component Models for Systems Integration," Hydrogen Energy Progress XII, J.C. Bolcich and T.N. Veziroglu, eds., 111-120.
4. Gregoire Padró, C.E., V. Putsche, and M. Fairlie, 1998, "Modeling of Hydrogen Energy Systems for Remote Applications," Hydrogen Energy Progress XII, J.C. Bolcich and T.N. Veziroglu, eds., 2247-2262.
5. Gregoire Padró, C.E., 1998, "International Cooperative Development of Design Methodology for Hydrogen Demonstrations," Proceedings of the 9th Annual U.S. Hydrogen Meeting, Vienna, VA, 187-194.
6. Putsche, V, and C.E. Gregoire Padró, 1998, "Systems Modeling of Renewable Hydrogen Production, Storage, and Electricity Generation using ASPEN Plus," Proceedings of the Electrical Energy Storage Systems Applications and Technologies Meeting, Chester, U.K., 95-102.
7. Gregoire Padró, C.E., 1998, "Renewable Hydrogen Energy Systems for Grid-Independent Energy Systems," Proceedings of the 1998 Colorado Renewable Energy Conference.
8. Gregoire Padró, C.E. and M.J. Fairlie, 1998, "Renewable Hydrogen for Rural Electrification," Poster at the Village Power '98 Conference.
9. Khaselev, Oscar and John A. Turner, 1998, "A Monolithic Photovoltaic-Photoelectrochemical Device for Hydrogen Production Via Water Splitting," *Science*, Vol. 280, 425.
10. Bolton, James R., 1996, "Solar Photoproduction of Hydrogen," IEA Technical Report, IEA/H2/TR-96.
11. Elam, Carolyn C. (ed.), 1998, "IEA Agreement on the Production and Utilization of Hydrogen: 1997 Annual Report."
12. B. Bogdanovic' and M. Schwickardi, 1977, "Ti- Doped Alkali Metal Aluminum Hydrides as Potential Novel Reversible Hydrogen Storage Materials," J. Alloys and Compounds, 253-254, 1-9.

Table 1. Component Models Developed for Production, Storage, Distribution and Utilization

Technology	Team Lead
Production	
PV-Electrolysis	Spain
Wind-Electrolysis	USA
Grid-Electrolysis	USA
Steam Methane Reforming	USA
Biomass Gasification	USA
Biomass Pyrolysis	USA
Coal Gasification	Netherlands
Storage	
Low/High Pressure Gas	Canada
Metal Hydrides	USA
Liquefaction	Japan
Chemical Storage	Netherlands
Chemical Hydrides	Switzerland

Technology	Team Lead
Distribution	
Transport Tanker	Japan
High Pressure Pipeline	USA
Low Pressure Pipeline	USA
Tank Truck	Japan
Methanol Transport	Netherlands
Utilization	
PEM Fuel Cell	Canada
Phosphoric Acid Fuel Cell	Spain
Solid Oxide Fuel Cell	USA
Molten Carbonate Fuel Cell	USA
Gas Turbine	USA
Internal Combustion Engine	USA
Refueling Station	USA

Table 2. Hydrogen Demonstration Projects

Project	Lead
Solar H_2 Production Facility	Electrolyser
Demonstration Plant for H_2 Production and Use in Fuel Cell	ATEL
Solar H_2 Pilot Plant with 3 Storage Systems	INTA
Stand Alone PV-H_2 Small Scale Power System (SAPHYS)	ENEA
Alkaline Bipolar Electrolyser	ENEA
Off Peak Storage System	Kogakuin University
CO_2 Fixation and Utilization in Catalytic Hydrogenation Reactor	RITE
H_2 Vehicle	Mazda
H_2 Rotary Engine Cogeneration System	Mazda
H_2 Production Utilizing Solar Energy	Kansai Electric Power Co., Mitzubishi
Development of Solar H_2 Processes	Helsinki University of Technology
Solar H_2 Fueled Truck Fleet and Refueling Station	Clean Air Now, Xerox
Genesis Ten Passenger PEMFC Vehicle	Energy Partners
Schatz Solar H_2 Project	Humboldt State University
City of Palm Desert Renewable H_2 Transportation	Humboldt State University

MODELING OF SUSTAINABLE HYDROGEN PRODUCTION / STORAGE ENERGY SYSTEMS FOR REMOTE APPLICATIONS

Eric Martin and Nazim Muradov
Florida Solar Energy Center,
1679 Clearlake Road, Cocoa, FL 32922

KEYWORDS: Modeling, Sustainable Hydrogen Production, Fuel Cell

ABSTRACT

The results from computer simulation of an integrated renewable hydrogen energy system with daily and seasonal energy storage are reported in this paper. The main components of the energy system are a photovoltaic array, PEM electrolyzer, PEM fuel cell, battery, pressurized hydrogen storage unit, controller, and electric load. The modeling was performed using modified TRNSYS simulation software. System size, performance, and cost trade-offs were analyzed by simulating two short-term energy storage scenarios: one with a large battery storage capacity (approximately one day) and one with a much smaller capacity (two hours). Results show that a system with a small battery storage capacity is more desirable in the interest of system renewability, however it is more capital cost intensive.

INTRODUCTION

The concept of stand-alone renewable energy systems that use hydrogen as an energy storage medium has attracted much attention recently. The main objective of this work is to develop an efficient tool to assist in the design and evaluation of integrated solar hydrogen production/storage energy systems (ISHES). We have conducted an extensive literature search on different ISHES demonstration projects and the existing computer simulation software packages (CSP) (for example, references [1-5]).

In the simulation of the ISHES, batteries are included for short-term storage of electricity generated by the photovoltaic (PV) array and the fuel cell. In the interest of keeping the ISHES system as renewable as possible, it is desirable to utilize as few batteries as possible in the system design. Batteries tend to have a much shorter lifetime (5-10 years) compared to the renewable sources of electricity found in the system (20 years). However, as the amount of battery storage capacity decreases, the sizes of other system components, such as hydrogen storage capacity and size of the PV array, increase in order to compensate. In order to investigate this system trade-off, two simulation studies have been conducted on the proposed ISHES. Case 1 has a large battery storage capacity (approximately one day) and Case 2 has a much smaller capacity (two hours).

METHODS

We chose the TRNSYS simulation package, created by the Solar Energy Laboratory (SEL) at the University of Wisconsin-Madison, to be the main platform for the system integration and simulation [6]. TRNSYS is transient simulation software with source code written in FORTRAN. No models for the core components of the ISHES (fuel cell, electrolyzer, and hydrogen storage) are currently included with the standard version of the TRNSYS software. However, the SEL has collected many applicable component models, written by various users, and currently uses them to demonstrate the capabilities of the software.

The following paragraphs outline individual component specifications used in the simulation. These specifications have been optimized such that the renewable energy system can meet the load requirements with zero percent system downtime. The length of each simulation was one year, beginning in January and ending in December.

Location/Weather Conditions. Typical meteorological year (TMY) data which includes average values for solar insolation, ambient temperature, and humidity for Orlando, FL (28° N) has been used as a starting point for the simulation.

Load Profile. The peak load each day is 10 kW, which occurs in the early evening, and the daily average load is 2.5 kW. The daily, peak, and average loads that the ISHES system must supply also take into account losses encountered in AC/DC power inversion, DC/DC voltage conversion, and power requirements of various system components (i.e. controller).

Batteries. Case 1 includes a total of four deep cycle solar batteries. The batteries are connected in series, which maintains a battery bus voltage of 48 V. The battery string has a capacity of 125

Ah, which permits the batteries to store 2 hours of required system amperage based on a daily consumption of 58 kWh. Case 1 represents a situation where the batteries are only able to supply the system load when electricity production switches between the PV array and the fuel cell. No means of safety back-up power is provided in the event that the PV array and fuel cell become inoperable.

Case 2 include a total of 12 batteries arranged in an array of three parallel strings of four batteries each. In this case, each parallel string has a capacity of 635 Ah. With 1905 Ah total storage capacity, the battery array has the ability to solely power the load for 1.25 days, based on 58 kWh daily consumption. This scenario provides some back up power in the event that system interruptions are encountered with the PV array or fuel cell. Also, in this case, the size of the battery array prevents the need for the fuel cell to be solely responsible for powering the load every evening, when the PV array is inactive. Instead, the fuel cell is only required to supply power when the battery state-of-charge drops below a certain "safe" limit, caused by consecutive days of low solar insolation.

Photovoltaic Array. For case 1, a total of 588 individual modules are used in the simulation, and the array is configured with 147 parallel strings of 4 modules each. Each module is assumed to be rated at 100 W at standard test conditions (irradiance = 1000 W/m^2, cell temperature = 25 °C), therefore the peak power output of the array is expected to be 58.8 kW. The panels are tilted at an angle of 45° (28° + 17°), which optimizes electricity production during the winter months, due to the sun's wintertime position in the sky.

For case 2, a total of 256 of the same modules are used, and the array is configured with 64 parallel strings of 4 modules each. The panels are also tilted at an angle of 45°, and the peak output of the array at standard test conditions is expected to be 25.6 kW.

Electrolyzer. For these simulations, data for a high pressure (1000 psi) PEM type electrolyzer has been used in place of the alkaline data that was provided along with the TRNSYS subroutine. The PEM electrolyzer has a total of 25 cells and each cell is assumed to have an area of 279 cm^2. The electrolyzer operates at an efficiency of approximately 75%, producing approximately 0.48 kg/h (90 slpm) of hydrogen at 500 A.

Hydrogen Storage. A pressurized tank is included in these simulations that stores hydrogen as it is produced by the electrolyzer. The maximum pressure of the tank is 1000 psi. For case 1, an optimized storage volume of 20 m^3 is used in the simulation, allowing a maximum of 90 kg of hydrogen to be stored at ambient (25 °C) temperatures. For case 2, an optimized storage volume of 10 m^3 is used, allowing a maximum of 45 kg of hydrogen to be stored at 25 °C.

Fuel Cell. The PEM fuel cell used in these simulations operates on hydrogen and air and contains a total of 50 cells. Each cell has an area of 300 cm^2. The stack produces a total of 11.6 kW of DC power at 32 V and 363 A. The stack operates at an efficiency of 44% consuming 0.683 kg/h (127 slpm) of hydrogen.

Power Conditioning. In the ISHES simulation, four power conditioning devices are included. A maximum power point tracker (MPPT) maintains optimum performance of the PV panels by ensuring that the array operates at the maximum power point on its I-V curve. A DC to DC converter upgrades the fuel cell output voltage to the battery bus voltage. A diode prevents the back flow of current from the battery array and fuel cell to the electrolyzer. This ensures that the only source of power for the electrolyzer is the PV array. Finally, a DC to AC inverter is included to invert the DC power supplied by the battery array to AC power required by the electric consumer. The efficiency of all power conditioning devices is assumed to be approximately 90%.

Controller. A single controller device oversees total system operation in the ISHES simulation. By assessing the requirements and/or output available of every system component, including the electric load, the controller makes appropriate decisions to optimize system performance. These decisions include whether to connect or disconnect individual components to/from the system and whether power generated by the PV array is sent to the electrolyzer, for hydrogen generation, or to the battery array, for use by the electric consumer. The controller also decides whether the battery array contains sufficient charge to power the load under dark conditions, or whether the fuel cell should be activated to power the load and recharge the battery.

RESULTS AND DISCUSSION

Figures 1 and 2 show simulation results for case 1 and 2 respectively. In these graphs, the dark solid line shows seasonal variations (shown on the top axis) of the amount of hydrogen stored in

the pressurized tank. This amount is expressed as a fraction of the total storage capacity of the tank (shown on the left axis). All remaining plots on these graphs were created using the bottom axis to show daily variations.

The power required by the load and the power produced by the PV array are shown as dashed lines on these graphs. This data has been plotted for a simulated first week of February, occurring during the simulation year. The month of February represents a "worst case" scenario, for it is expected to be the month with the lowest average solar insolation. The values are read off of the right hand axis in units of watts (please note that the power produced by the PV array in case 1 has been divided by a factor of 2 such that it can be plotted on the same graph as the load).

Finally, the battery state of charge (SOC) is shown on these graphs as a dotted line. Similar to fractional hydrogen storage, battery SOC is expressed as a fraction of the total battery storage capacity. This plot has also been created for the first week of February, and its value is read off of the left axis.

Along with the design of each individual ISHES component, total system operation plays a major role in system performance, size, and cost. Each of the individual components are intimately linked together in some way, therefore changing the size or operational parameters of one component has the potential to disturb the balance of the entire system. Simulations of the proposed ISHES have been conducted with the intent of optimizing system performance, rather than cost, however it is expected that an optimized system will also be the most cost effective. The primary parameter that is intended to be the basis for optimization is the value for hydrogen storage. Other mandatory system criteria included use of a PEM type fuel cell and electrolyzer, maximizing battery lifetime, and maintaining zero percent system downtime.

As seen in Figure 1 and 2, fluctuations in battery SOC occur according to the relative size of the battery array. With a small battery array, as in case 1, SOC decreases rapidly under dark conditions. Upon reaching a lower limit, chosen to prevent excessive battery discharge, the fuel cell is activated to recharge the battery as well as power the load. With a larger battery array, as in case 2, the fuel cell is activated less often under dark conditions, due to the slower rate of battery array discharge.

Optimizing the PV array for wintertime performance maximizes the use of the fuel cell, which represents mainly a capital expense. By also requiring fuel cell activation during the summer months, when solar insolation is the greatest and the fuel cell ordinarily may not be needed depending on the battery array capacity, this expensive piece of equipment is used to its fullest extent rather than allowing it to lye dormant for several months.

The same fuel cell has been simulated in both case 1 and 2, and the frequency of its activation affects overall system cost. As seen by the results of simulations for case 1 and case 2, a system trade-off exists among battery array storage capacity, hydrogen tank storage capacity, and the size of the PV array. As previously discussed, the fuel cell is activated more often in case 1 due to the smaller battery array storage capacity. This case utilizes more hydrogen over the course of the year and subsequently requires a hydrogen storage tank that is twice the size of the tank in case 2 (see METHODS section). This is due to the fact that with a smaller battery array, less energy can be stored in that short-term medium. Since the same amount of energy is required in each case, more energy must be stored in the form of hydrogen. Since the values of solar insolation are identical in both cases, case 1 also requires a larger PV array (see METHODS section) to support the increased hydrogen production requirement. It is expected that case 1 will be more capital cost intensive than case 2, due to the fact that a larger hydrogen storage tank and larger PV array would cost more to implement than the added battery storage capacity.

Depending on what time of year the start-up of the ISHES system occurs, the hydrogen tank should be initially charged with the amount of hydrogen found in Figures 1 or 2 that corresponds to that particular time of year. The optimized storage tank values of maximum pressure and storage volume ensure that the tank is never completely empty, and rarely completely full to account for expected variation in weather conditions. Starting up the ISHES with a different value than what is found in Figure 1 or 2 will perturb this balance. Starting with more hydrogen than necessary will not cause system downtime, however the system will be overdesigned and will not utilize the full potential of each system component. Starting with less hydrogen than depicted will eventually cause system downtime during the winter season.

In principle, other methods of hydrogen storage (i.e. in the form of metal hydrides) could be used in ISHES and potentially lower the cost of the storage component. It is evident that the relative amount of hydrogen stored will essentially remain the same, therefore, for the purpose of system

performance optimization, the method of hydrogen storage is not essential. This issue will become important during cost optimization of the ISHES. The same holds true for an addition of an oxygen storage sub-system to the ISHES. Storing oxygen produced by the electrolyzer for use in the fuel cell (rather than ambient air) could potentially increase the overall cost of the system. However, since the use of oxygen affects the efficiency, and consequently size and cost of the fuel cell, the added cost of oxygen storage will have to be weighed against the reduced cost of the fuel cell.

CONCLUSIONS

TRNSYS was chosen as a viable platform for performing simulations on the proposed ISHES. The main components of the energy system are a photovoltaic array, PEM electrolyzer, PEM fuel cell, battery, pressurized hydrogen storage unit, controller, and electric load. The simulation code was customized in order to model the specific characteristics of proposed system components. A realistic load profile was chosen as an example application for the renewable energy produced by the ISHES system, and system components have been designed and optimized to meet this load with zero percent system downtime. Results from simulations of two cases, one with four batteries and one with twelve batteries, show that a system with fewer batteries and, therefore one that is more renewable, requires a larger PV array to supply necessary power, and may be more costly. The details of this cost analysis, along with the potential to store oxygen produced by the electrolyzer and the use of metal hydrides to store hydrogen, have been left until a system cost optimization is conducted.

ACKNOWLEDGEMENTS

Authors would like to acknowledge the financial support provided by U.S. Department of Energy, Energy Partners, Inc., Caribbean Marine Research Center, and the Florida Solar Energy Center, and the technical support provided by Solar Energy Laboratory/ University of Wisconsin-Madison.

REFERENCES

1. C. Gregoire Padro, V. Putche, M. Fairlie, *Proc. XII World Hydrogen Energy Conference,* Buenos Aires, Argentina, 1998, 2247.

2 J. Vanhanen, P. Lund, *Int. J. Hydrogen Energy,* v.20, 575, 1995.

3. H. Barthels, W. Brocke, K. Bonhoff, et al. *Int. J. Hydrogen Energy,* v.23, 295, 1998.

4. P. Lehman, C. Chamberlin, *Int. J. Hydrogen Energy*, v.16, 349, 199.

5. S. Galli, G. De Paoli, A. Ciancia, *Proc. X World Hydrogen Energy Conference,* Cocoa Beach, Florida, USA, 1994, 439.

6. S. Klein, W. Beckman, et al. TRNSYS A transient system simulation program. Solar Energy Laboratory, University of Wisconsin-Madison, WI 53706, 1992.

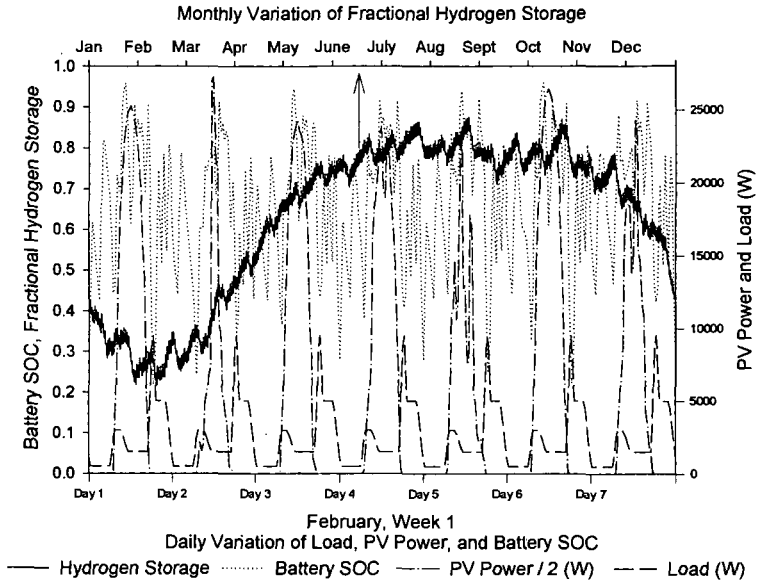

Figure 1: Case 1 Simulation Results

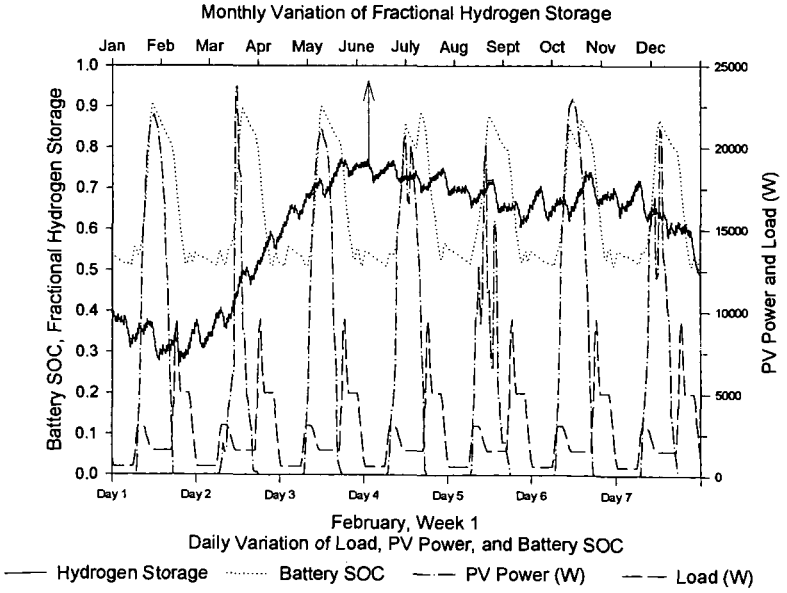

Figure 2: Case 2 Simulation Results

Hydrogen For A PEM Fuel Cell Vehicle Using A Chemical-Hydride Slurry

Ronald W. Breault, Christopher Larson, Jonathan Rolfe
Thermo Power Corporation

INTRODUCTION

Because of the inherent advantages of high efficiency, environmental acceptability, and high modularity, fuel cells are potentially attractive power suppliers. Worldwide concerns over clean environments have revitalized research efforts on developing fuel cell vehicles (FCVs). As a result of intensive research efforts, most of the subsystem technologies for FCVs are currently well established. These include: high power density PEM fuel cells, control systems, thermal management technology, and secondary power sources for hybrid operation. For mobile applications, however, supply of hydrogen or fuel for fuel cell operation poses a significant logistic problem.

A great many technologies have been investigated as candidates for the onboard storage of pure hydrogen for FCVs. These technologies include: 1) compressed hydrogen, 2) liquefied hydrogen, 3) rechargeable metal hydride, 4) carbon adsorption and hybrid systems, and 5) liquid hydrides and other chemical hydrides. However, the volume and/or weight energy densities of these onboard hydrogen storage technologies are significantly lower than those of internal combustion engines or the DOE hydrogen plan. Therefore, development of a high energy density subsystem to supply hydrogen for fuel cell operation is an urgently needed technology for the successful development of FCVs.

To supply high-purity hydrogen for FCV operation, Thermo Power Corporation (THP) has developed an advanced hydrogen storage technology. In this approach, a chemical (light metal) hydride/organic slurry is used as the hydrogen carrier and storage media. At the point of use, high purity hydrogen will be produced by reacting the hydride/organic slurry with water. The fluid-like nature of the hydride/organic slurry will provide us a unique opportunity for pumping, transporting, and storing these materials. In addition, the spent hydride can relatively easily be collected at the pumping station and regenerated utilizing renewable sources, such as biomass, natural gas, or coal at the central processing plants. Therefore, the entire process will be economically favorable and environmentally friendly. The final product of the program is a user-friendly and relatively high energy storage density hydrogen supply system for fuel cell operation.

BACKGROUND AND TECHNICAL APPROACH

Pros and cons of the currently available and advanced hydrogen storage technologies, along with expected performance of the proposed technology, are summarized in Table 1. A plot showing how chemically-reacting hydrides compare with other fuels is shown in Figure 1.

An essential feature of the THP approach is to develop a relatively high energy storage density hydrogen supply system based on exothermic chemical reactions between metal hydrides and water. Hydrogen production via metal hydride and water reactions is a well-established industrial process. In fact, several groups of researchers have investigated the metal hydride/water reaction process to supply hydrogen for fuel cells for mobile power generations. In this research, it has been identified that reaction rate control, frequent on/off operation, and safety of the operation could be significant problems for high energy density operations.

One of the key technical challenges in the program is, therefore, to precisely control the metal hydride and water reaction. In our approach, the continuous organic slurry media will act as a path for dissipating heat that is generated from the hydride/water reaction. Furthermore, by controlling surface chemistry of the organic media, the water/metal hydride reaction rate can easily be controlled. This concept is shown in Figure 2. In Figure 2a, a sketch is shown of two hydride particles, one surrounded by oil and one not. The oil layer inhibits the water access to the hydride and thereby controls the rate of reaction, which would otherwise be explosive. In Figure 2b, the hydride suspension is shown to exemplify how the dispersant acts to hold the particle in suspension within the oil and further inhibit the reaction with water.

Because of the reaction rate control afforded by the organic media, the hydrogen reactor can be a simple device. Water and hydride slurry are metered into the reactor, where they are thoroughly mixed to ensure complete reaction. This reaction goes to completion quickly, leaving a powdery waste. Hydrogen production rate is controlled by the injection rate of water and hydride. Heat

released by the reaction can be absorbed by the evaporation of water. No complicated control systems are needed to ensure proper and safe operation of the hydrogen reactor.

The water required for thermal control and hydrogen reaction is provided by condensed vapor from the hydrogen fuel cell. Only a small reservoir of water is required for startup, makeup, and surge demand. Thus, the required water does not significantly affect the volumetric and gravimetric energy storage densities.

The slurry form of hydride has other benefits beyond reaction control. The hydride fuel can be handled as a liquid, simplifying transportation, storage, and delivery. Use of a slurry permits refueling similar to current gasoline filling stations, allowing the tank to be easily topped-off at any time. The hydroxide waste products produced by the hydrogen system can be washed from the onboard storage tank during the slurry filling operation. Both the hydride fuel and hydroxide waste product can be easily transported between the distribution centers and a central recycling plant.

The used reactant slurry containing LiOH is returned to a central processing plant where the LiOH is recycled to LiH in a large-scale chemical process. The LiH is remixed with the slurry fluid and transported back to refueling stations scattered over a large area as needed. The basic energy input to the system is provided at the central plant and can be from a variety of energy sources, including fuels like coal, biomass, natural gas, and petroleum oil. All environmental emissions occur at the central processing plant. The vehicle is zero emission, with no hydrocarbon, CO, or CO_2 emissions. The central plant can include more sophisticated emission cleanup processes than would be possible for an onboard processing system.

An important concept feature that needs to be pointed out is the recovery and recycle of the spent hydride at centralized processing plants using a low cost fuel, such as coal or biomass. Regeneration process analysis has indicated that recycling can be performed utilizing a carbothermal process with minimum energy input and at a low cost. Compared to current hydrogen costs of about $9.00 to $25.00 per million Btu, this concept should enable hydrogen costs as low as $3.00 per million Btu to be realized for a LiH system[1&2]. Also, because the hydride reaction will liberate only pure hydrogen, fuel cell catalyst life should be maximized, resulting in high system performance and reliability.

PROTOTYPE DEVELOPMENT

The major objectives of this hydrogen generation development effort are twofold. The first is to use a laboratory-scale system to determine optimum materials and hydrogen generation process conditions to achieve high specific energy for hydrogen supply. The second objective is the design and fabrication of a prototype hydrogen generation system capable of supplying 3.0 kg/hr of high purity hydrogen for fuel cells.

Although there are numerous metal hydrides and organic carrier candidate materials, only a limited number of metal hydrides and organic carrier materials can be used to satisfy DOE's goals of specific weight and volume. One of the essential considerations for the metal hydride is its hydrogen generation efficiency, which includes reaction chemistry between metal hydride and water to complete hydrolysis reactions in a safe and controlled manner. The organic carriers should be chemically inert toward metal hydrides and spent hydrides for storing and transporting, and during hydrolysis reaction. These materials also should be easily separated from spent hydrides, either thermally or mechanically, and be recycled for reuse. Although regeneration of the spent hydrides is not part of the technical effort of this program, it is an important issue for economical and commercial development of the technology.

In the initial effort, we thoroughly analyzed, both theoretically and experimentally, the reaction chemistry of a variety of metal hydrides and water, and the chemical stability of the organic carriers in contact with metal hydrides and spent hydrides. Since detailed hydrolysis reaction kinetics of the metal hydride/organic carrier slurry were not known, we conducted experiments using a high-pressure (2000 psi) and high-temperature (232°C) vessel with temperature, pressure, and magnetic stirrer control capabilities (500 cm^3 internal volume). For this investigation, we selected the candidate materials based on the guidelines listed in Table 2.

In the development of a hydride/water activation system, several ideas were considered. These are:

- Single Tank Reactor
- Slurry Atomization Reactor
- Water Bathed Reactor
- Auger-aided Water Vaporizing Reactor

The single tank reactor, shown in Figure 4, is the simplest system. However, several problems exist for this system. The heat exchanger allows hot spots, increasing hydrocarbon contamination. It will also have a slow response to H_2 demand. Furthermore, it is likely that not all hydride will react, leaving a hazardous waste product, and a large volume containing pressurized hydrogen.

The atomized slurry reactor, shown in Figure 5, was conceptualized to remove heat from 15μm droplets by direct hydrogen heat transfer. This system is complicated and has a wear-prone slurry atomization system. The ½ m^3/sec H_2 flow rates needed for cooling are quite high. In addition, the heat exchanger may be fouled by dust. There is also the likelihood of poor hydride/water mixing reducing generation efficiency, and a large pressurized hydrogen volume is required.

In the water-bathed reactor configuration, shown in Figure 6, heat is removed by the recirculated flow of water. Excess water assures low reaction temperature and complete reaction in a relatively small water to air heat exchanger. Problems, such as the water soaked LiOH waste product and the weight of wasted water, push this concept outside the system goals. The water could be separated by a filter or a filter press, but neither a filter or filter press system allows the concept to reach the weight goals. Also, unfiltered particles will wear the recirculation pump.

In the auger-aided reactor, shown in Figure 7, reactants are pumped to a mixing auger. At 300 rpm, the auger mixes, crushes particles, and eliminates foaming within the hydrogen generation reactor. The waste product contains 10% by mass of water and is a dry, free-flowing powder. About three times the stoichiometric water is added and vaporized by the heat of reaction to control the temperature.

The hydrogen water vapor content in the auger-aided reactor depends on the heat exchanger outlet temperature. Vapor condensation is slowed by the presence of hydrogen, increasing the size of the heat exchanger. The water vapor content could also be reduced by using hydride as a desiccant. This hydrogen production system device achieves the weight and volume goals.

Based on the preliminary analysis and testing of the various concepts discussed above, a prototype system to produce up to 3 kg/hr of hydrogen was designed. This system is shown in Figure 8. To produce the hydrogen, 0.5 l/min 60% LiH slurry flows into the auger reactor, along with 1.4 l/min water for reaction and vapor cooling. The system produces up to .75 kg hydrogen per run. A 1.6 gallon reservoir of 60% LiH slurry, a 5.5 gallon water reservoir, and a 12 gallon hydroxide container make up the reactant and product volumes. A computer controls the hydride and water pumps. Data acquisition of pertinent pressures, temperatures, hydrogen flow, hydrocarbon, and water vapor content are recorded. The system is self-contained on a rolling cart.

A valveless ceramic piston pump is used for the LiH slurry and a gear pump is used for water flow. Three heat exchanger cores with 8-10" fans are used to condense the water from the hydrogen. Table 3 summarizes the energy, mass, and volumetric densities for the system, assuming storage of 15 kg H_2. To meet the design goals of 3355 Whr/kg and 929 Whr/l, our system must weigh less than 179.9 kg and must have a volume of less than 649.6 l. Table 3 shows that the system designed will meet the weight goal and exceed the volume goal.

SUMMARY

In summary, the following can be stated:

- A hydride/water activation process (the hydrogen generation reactor) has been developed.
- Thermal management design for prototype system has been established.
- A chemical hydride slurry can be used to generate hydrogen for transportation vehicle applications.
- The system has the potential to be safe and easy to use.
- Chemical hydride-based systems can achieve DOE's energy density goals.

REFERENCES

1. Breault, Ronald, "Advanced Chemical Hydride Hydrogen Generation/Storage System for PEM uel Cell Vehicles," to be published in the DOE Office of Advanced Automotive Technology FY 1999 Annual Progress Report.

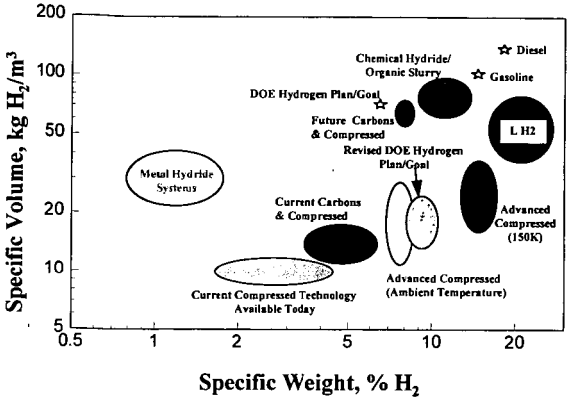

FIGURE 1. Summary of Current and Future Hydrogen Storage Systems

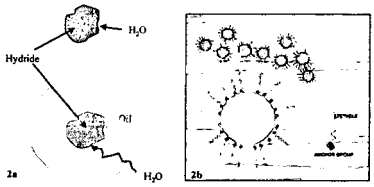

FIGURE 2. Hydride-Water Reaction Concept

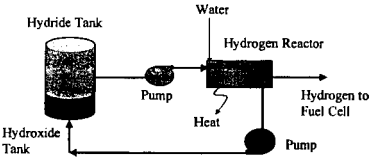

FIGURE 3. Hydrogen – Hydride Concept

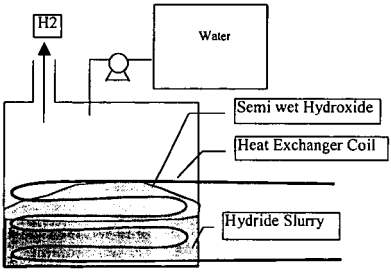

FIGURE 4. Simple One Tank Concept

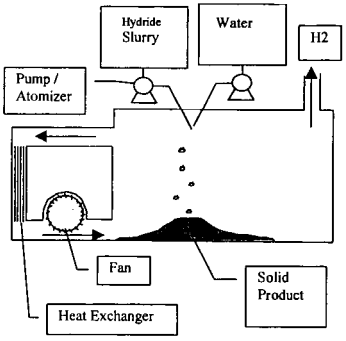

FIGURE 5. Atomized Slurry Reactor Concept

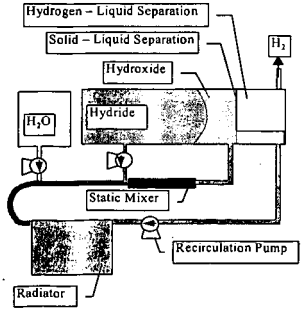

FIGURE 6. Water Bathed Reactor Concept

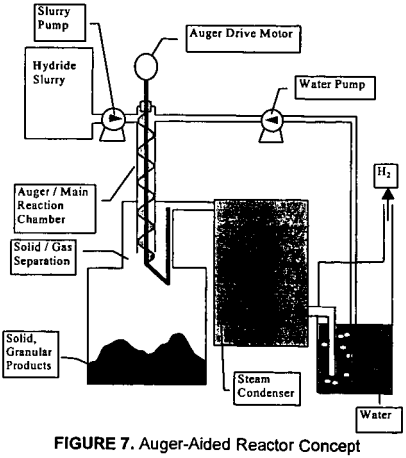

FIGURE 7. Auger-Aided Reactor Concept

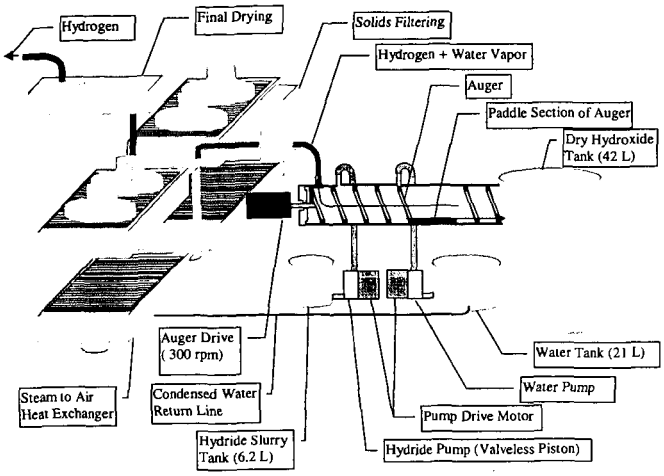

FIGURE 8. Auger-Aided Reactor System Being Built

TABLE 1. Hydrogen Storage Technology Status

Storage Technology	Specific Weight (HHV)		Specific Volume (HHV)		Remarks
	Wh/kg	$\%H_2$	Wh/L	kg H_2/m^3	
DOE Goal • Liquid/Gas	3963/5323	9.9/13.4	1100/828	28/21	-DE-RA02-97EE50443
Liquid H_2 • Cryogenic	6350	16.1	1250	32	-Not including boil-off loss
Gaseous H_2 • 5000 psia	2630	6.7	780	20	-Could be better with new high-pressure tanks
Carbon Adsorption • 794 psi at 78°K	2858	7.2	1535	39	-New materials with better capacities
Liquid Hydride • Methylcyclohexane	2070	5.9	1618	46	-Need more fundamental research
Proposed Chemical Hydride Slurry • CaH_2	2670	6.8	2430	62	-Includes weight and volume of the container, and ancillary components
• LiH	5050	12.8	2430	62	-Does not include reactant water, which is assumed to be provided partially from exhaust gas
• $NaBH_4$	4760	12.1	2570	65	
• $LiBH_4$	6350	16.1	2640	67	

TABLE 2. Considerations for Selecting Metal Hydrides and Organic Carriers

Metal Hydrides	*Organic Carriers*
• High specific energy density • High hydrogen generation efficiency • Relatively inert during storage before and after reaction with water • Ease of regeneration • Low costs	• Non-reactive with metal hydrides and spent hydrides • Low molecular weight • Easy to recycle (easy to separate from spent hydride and water, and to collect for reuse)

TABLE 3. System Mass and Volumetric Design Summary

		Wt (kg)	Vol (L)
65% Lithium Hydride Slurry		95.5	
Hydroxide			
Heat Exchanger	Direct Gas to Air HX Copper Tube, Aluminum Fin	31.38	82.5
Hydride Tank	Stainless	20	120
Hydroxide Tank	Plastic	12	310
Hydride Metering Pump	Valveless Piston	6.8	4
Water Metering Pump	Gear Pump + DC Control	3	2.5
Auger Drive Motor	1/8 Hp, 5.5:1 Bodine DC Gear Motor	4	2.3
Auger Construction	SS Materials	5	10
Total		177.7	531.3
System Goals (kg, l)		179.9	649.6
System Values (watt-hr/kg, watt-hr/liter)		3397	1136
Goals (watt-hr/kg, watt-hr/liter)		3355	929

ELECTROCHEMICAL INVESTIGATION OF $Y_xZr_{1-x}Mn_mFe_nCo_pV_oCr_q(m+n+o+p+q=2)$ ELECTRODE FOR Ni-MH BATTERY APPLICATION

N.Rajalakshmi, K.S.Dhathathreyan
Centre for Electrochemical and Energy Research
SPIC Science Foundation
111, Mount Road
Guindy, Chennai 600 032, INDIA
&
Sundara Ramaprabhu
Magnetism and Magnetic Materials Laboratory
Department of Physics
Indian Institute of Technology
Chennai 600 036, INDIA

ABSTRACT:

The AB_2 type Laves phase hydrogen absorbing alloys are being investigated as suitable electrode materials for Ni-MH batteries, because of their higher electrochemical capacity. The electrochemical properties like electrode potential, reversible electrochemical capacity and diffusion coefficient as a function of state of charge in the $Y_xZr_{1-x}Mn_mFe_nCo_pV_oCr_q(m+n+o+p+q=2)$ electrodes were investigated in an alkaline solution. The reversible electrochemical capacity of the electrode was found to be in excess of 450 mAh/g and hydrogen concentration was estimated as 3.5 hydrogens/formula unit. The process that occur in the electrode during charge and discharge, has been studied by Cyclic Voltammogram(CV) experiments, carried out at different sweep rates. It was found that at low sweep rates, the hydrogen concentration on the surface increases due to longer polarisation and the hydrogen concentration approaches a value which favours a metal hydride formation. The diffusion coefficients were also evaluated with respect to state of charge. The results will be presented in the paper.

INTRODUCTION:

AB_2 hydrogen storage alloys are promising for negative electrodes in Ni-MH batteries for their higher discharge capacities and better resistance to oxidation than those of AB_5 alloys[1,2]. As AB_2 type multiphase hydrogen storage alloys are mainly composed of C14, C15 Laves phase, and some solid solutions with bcc structure, there exist abundant boundaries, with enriched electrochemically catalytic elements as active reaction sites and diffusion pipes for transporting reactants and products. However, the activation and electro-catalytic activity of the alloy electrode is still inferior to that of the $MmNi_5$ based alloy [3]. The main reasons for the slow activation and low electro-catalytic activity are: an oxide layer is formed on the surface of the alloy grains, and this oxide layer is a bad electrical conductor, hence impedes the diffusion of hydrogen and absence of Ni content layer on these AB_2 alloy surface results in a lower surface activity for hydrogen absorption/desorption [4].

The hydrogen storage properties of the alloys, whether as an electrode or as a storage medium, are initially related to their composition and vary widely with small changes in the type and the amount of substituent elements[5]. Thus, depending on the battery use, it is possible to design the electrode characteristics by changing the alloy compositions. The choice of the material is based on the desirable metal-hydrogen bond strength for use as electrodes in aqueous media and an appreciable hydrogen storage capacity/partial substitution for both the A and B sites, dramatically improves the cycle lifetime and the electrochemical discharge capacity has been optimized by substituting various metals as partial constituents, and by moving the composition ratio from stoichiometry. This has resulted in the preparation of four or five component Laves phase hydrogen storage alloys with discharge capacities over 400 mAh/g[6]. Knosp et al [7] have studied the Laves phase alloys of composition $(Zr,Ti)(Ni,Mn,M)_x$ where M= Cr,V,Co,Al and x= 1.9 to 2.1 with hexagonal C14 or cubic C15 structure in order to select the most suitable AB_2 alloys as an active material for Ni-MH batteries . Kim et al [8] studied the hydrogen storage performance and electrochemical properties of $ZrMn_{1-x}V_xNi_{1.4+y}$ (x= 0.5,0.7; y =

0.0 to 0.6) and found that the major factor controlling the electrode properties was the specific reaction surface area and the exchange current density depending upon the composition. The maximum electrochemical capacity experimentally observed was found to be 338 mAh/g for $ZrMn_{0.5}V_{0.5}Ni_{1.4}$, and the discharge efficiency was found to be 85%. Hence fundamental studies on the charge/discharge characteristics are required for improving the performance of a Ni-MH battery [9,10]. The present work focuses on elucidating the electrochemical properties like charge/discharge characteristics, diffusion coefficient etc., or an AB_2 compound with the composition Y_xZr_{1-x} $Mn_mFe_nCo_pV_oCr_q(m+n+o+p+q=2)$ and the processes that occur during charge and discharge were also evaluated.

EXPERIMENTAL:

Hydrogen storage alloys of composition Y_xZr_{1-x} $Mn_mFe_nCo_pV_oCr_q(m+n+o+p+q=2)$ were prepared by arc melting in an argon atmosphere. The buttons were turned upside down and remelted 5 to 6 times in order to get good homogeneity and the alloy buttons were annealed at 900 K for about 3 days. The intermetallics were pulverized mechanically into powders in an agate mortar. Structure and phase density of the sample was characterized by X-ray diffraction (XRD). The samples prepared had an overall AB_2 phase.

For the electrochemical measurements, the electrodes were prepared by grinding the alloy into 75 μ size and mixing it with copper powder in the ratio of 1:3 with a PTFE binder. The putty form of the mixture was mechanically pressed onto a current collector (Ni mesh) at RT. Then the electrode was sintered at 300°C for about 3 hrs under vacuum. The geometric area of the electrode was about 2 cm^2. The counter electrode was Pt, has a much larger geometric area than the WE. The electrolyte 31% KOH, which is the same as that used in the alkaline batteries, were prepared from reagent grade KOH and deionised water. The electrodes were tested for their charge-discharge characteristics, initial capacity, cycle life and diffusion coefficient. The electrochemical measurements were carried out in a flooded electrolyte condition in open cells. Potentials were monitored using a saturated calomel as reference electrode. The electrochemical measurements include the diffusion coefficient as a function of state of charge and also the electrochemical processes that occur during charge/discharge. These measurements were carried out using a EG & G galvanostat/potentiostat Model 273, with the available techniques like chronopotentiometry, cyclic voltammetry and constant potential coulometry.

RESULTS AND DISCUSSION:

The electrochemical capacity of a hydride electrode depends on the amount of reversibly absorbed hydrogen in the hydriding material. Fig. 1 shows the charge/discharge curves of the electrode after 30 cycles. The electrode showed the highest electrochemical charging capacity of 470 mAh/g, which corresponds to a hydrogen concentration of 3.5 hydrogens/formula unit. Hydrogen evolution was found to occur around –1.35V.This shows that the metal-hydrogen bond is not weak, and hence hydrogen can react with the alloy for hydride formation. However, if the bond is very strong, the metal hydride electrode is extensively oxidised, and cannot store hydrogen reversibly. The coulombic efficiency was found to be 85%, the charging potential and the discharging potential was around –0.9 and –0.5V respectively. The electrochemical charging capacity was found to be slightly lower when the electrode is charged at the 2C rate (80 mA) compared to the 1C rate (40 mA) as shown in Fig 2. As already mentioned, the highest electrochemical capacity was observed only after 30 cycles and then the capacity remained constant for almost 100 cycles, as shown in Fig.3, which clearly reveals that degradation of the electrode material is very slow.

To estimate the diffusion coefficient parameter D/a^2, the following procedure was carried out. The alloy was fully activated by charging and discharging the electrode for about 30 cycles. Then the electrodes with different states of charge were equilibrated until an equilibrium potential was reached. Initially, the activated electrode was discharged at constant potential at three different states of charge. In order to secure a zero concentration of hydrogen at the surface of each individual particle, the electrode was

discharged at a constant anodic potential of –0.56V(SCE). Discharge curves obtained for seven different charged states are given in Fig. 4. For large times in Fig.4, an approximately a linear relationship exists between log (i) and t, which is consistent with the equation

$$\text{Log(i)} = \log\{(6FD(C_0-C_s)/da^2\} - (\Pi^2/2.303(D/a^2)t \qquad (1)$$

Where C_0 is the concentration in the bulk of the alloy and a constant surface concentration Cs, ± sign indicates the charge (-) and discharge (+) process [11]. From the slope of the linear portion of the corresponding curves in Fig.4, the ratios of D/a^2 were estimated.

The diffusion coefficient may also be determined from the amount of charge transferred [12]. Assuming that the hydride alloy particles are in spherical form, the diffusion equation is,

$$\partial(rc)/\partial t = D\,\partial^2(rc)/\partial r^2 \qquad (2)$$

where c is the concentration of hydrogen in the alloy, t is the time, D is an average(or integral) diffusion coefficient of hydrogen over a defined concentration range, and r is a distance from the centre of the sphere. Since the discharge process was carried out under a constant current condition, it is reasonable to assume that a constant flux of the species at the surface and uniform initial concentration of hydrogen in the bulk of the alloy. Thus, the value of D/a^2 may be evaluated for large transition times,τ,

$$D/a^2 = 1/[15\{Q0/I - \tau\}] \qquad (3)$$

Where Qo is the initial specific capacity (c/g), I is the current density (A/g) and τ is the transient time (s), ie the time required for the hydrogen surface concentration to become zero. The ratio Qo/I corresponds to the discharge time necessary to discharge completely the electrode under hypothetical conditions, when the process proceeds without the interference of diffusion. Thus D/a^2 were calculated using the above equation for different states of charge and are given in Fig.5. As shown in Fig.5, the ratio of D/a^2 is almost independent of the state of charge with an average value of 0.37 *10-5 s-1. Assuming that the average particle radius is 15 μm, the effective diffusion coefficient of hydrogen through the Y_xZr_{1-x} $Mn_mFe_nCo_pV_oCr_q$(m+n+o+p+q=2) electrode was estimated to be $8.32 * 10^{-12}$ cm^2/s. This value is in consistent with the diffusion coefficient of hydrogen in Nickel alloys , which are in the range $20*10^{-12}$ to $56 * 10^{-12}$ cm^2/s estimated using a permeation technique[13-15]. Fig 6 shows the cyclic voltammogram(CV) of an activated sample of the alloy after 5 cycles ranging from –0.6 t0 –1.4 v vs SCE at various scanning rates. The definite peaks at potentials ranging from –0.9 to –1.2 v were observed and these adsorption peaks indicate that there are H atoms adsorbed on the surface due to the formation of the hydride. The counterparts responsible for the desorption of hydrogen from the alloys were also observed and are shown in Fig 7 in the range –0.1 to –0.6. At low sweep rates, the hydrogen concentration on the surface increases due to longer polarisation and the hydrogen concentration approaches a value for the hydride formation.

ACKNOWLEDGEMENTS:

The authors are thankful to the Management, SPIC Science Foundation, for the financial assistance and for the facilities provided to carry out this work.

REFERENCES:

1. S.R.Ovshinsky, M.A.Fetcenko, J.Ross, Science, 260(91)(1990), 176
2. X.L.Wang, S.Suda,S.Wakao, Z.Phys.Chem 183(1994), 297
3. H.Sawa,S.Wakao, Mater.Trans JIM, 31 (1990)487
4. A.Zuttel, F.Meli and L.Schlapbach, J Alloys and Compounds 231(1995) 645
5. T.Sakai,K.Oguro,H.Miyamura,N.Kuriyama,A.Kato,H.Ishikawa and K.Iwakura, J Less Common Metals 231(1995) 645
6. H.Nakano, I.Wada and S. Wakao, Denki Kagaku, 672 (1994) 953
7. B.Knosp, C.Jordy,Ph.Blanchard and T.Berlureau, J Electrochem soc 145, (1998) 1478
8. Dong-Myung Kim, Sang-Min Lee, Jae-Han Jung, Kuk-Jin Jang and Jai-Young Lee, J Electrochem Soc 145(1998) 93
9. H.Inoue, K.Yamataka,Y.Fukumoto and C.Iwakura, J Electrochem Soc 143(1996) 2527
10. M.P.Sridhar Kumar, W.Zhang,K.Petrov, A.A. Rostami and S.Srinivasan, J Electrochem soc 142 (1995) 3424
11. G.Zheng, B.N.Popov and R.E White, J.Electrochem Soc 142(1995) 2695
12. G.Zheng, B.N.Popov and R.E White, J.Electrochem Soc 143(1996) 834
13. W.M.Robertson, Metall Trans., 8A, (1977) 1709
14. R.M.Latanision and M.Kurkela, Corrosion, 39,(1983),174
15. W.M.Robertson, Metall Trans., 10A, (1979) 489

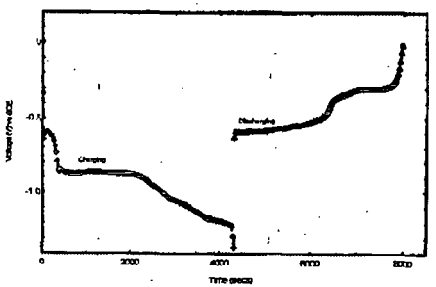

Fig. 1. Charge-Discharge characteristics of the electrode at 1C rate

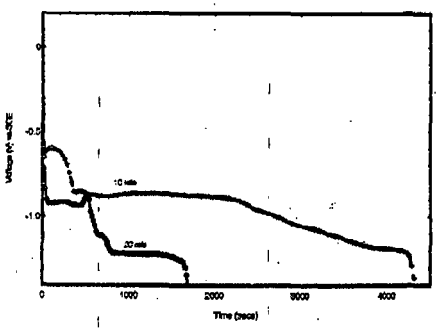

Fig. 2 Capacity dependence with different charging rates

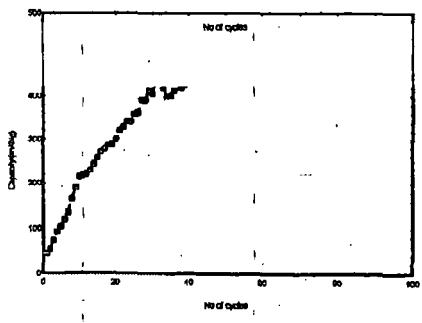

Fig. 3 Capacity variation with Cycle Number

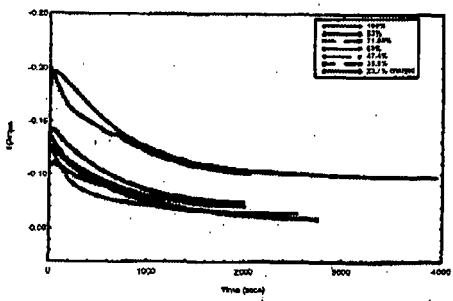

Fig. 4 Constant potential discharge curves at different states of charge

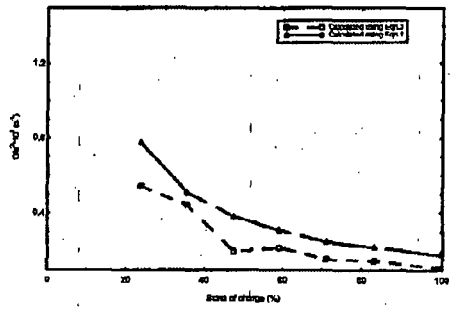

Fig. 5 Dependence of Diffusion coefficient with state of charge

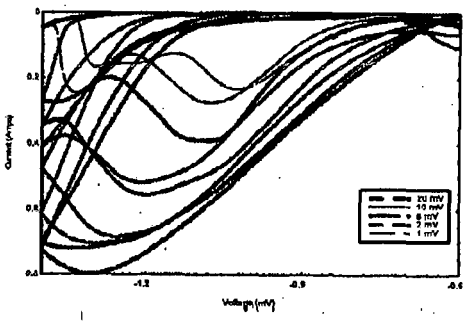

Fig. 6 Cyclic Voltammogram(CV) of the electrode for absorption at various sweep rates

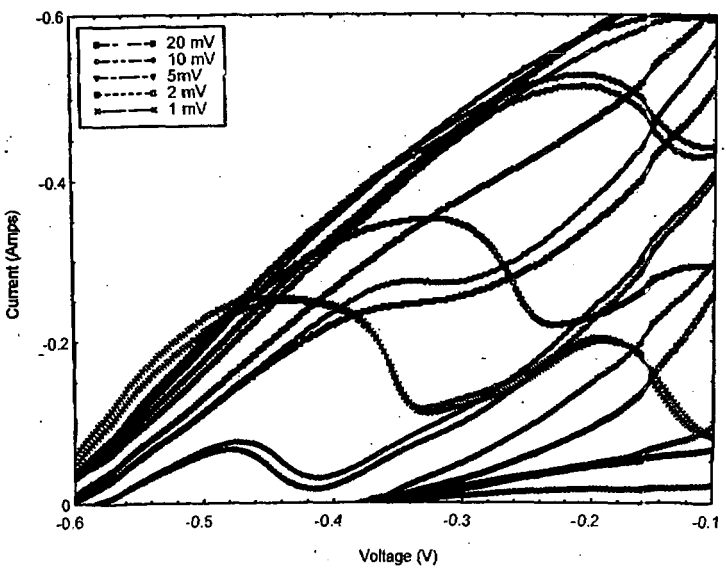

Fig. 7 Cyclic Voltammogram(CV) of the electrode for desorption at various sweep rates

INTERACTION OF HYDROGEN WITH NANOPOROUS CARBON MATERIALS

T. D. Jarvi, J. Sun, L. F. Conopask, and S. Satyapal

United Technologies Research Center
Energy Systems, MS 129-90
411 Silver Lane
East Hartford CT 06108

KEYWORDS: Carbon nanotubes, carbon nanofibers, hydrogen adsorption

INTRODUCTION

High-density hydrogen storage represents a key enabling technology to the widespread implementation of portable, hydrogen-based, fuel cell systems. In the long term, portable fuel cells will use stored hydrogen fuel due to power density and systems simplification issues. Although automotive applications remain the primary industry focus at the present moment, we may expect that small portable systems will eventually become extremely important as well. Moreover, effective hydrogen storage may enable fuel cell power for a wide array of applications not presently considered viable. Clearly, fuel cell systems of any size can benefit from improved hydrogen storage technologies, therefore success in this area will have lasting societal impact.

Hydrogen's low molecular weight makes storage as a compressed gas less effective than for other fuel gases, such as methane. This fact drives compressed hydrogen storage pressures to very high values, thus requiring expensive storage systems to reach reasonable gravimetric capacities. Volumetric capacities for compressed hydrogen storage are well below the target values at pressures as high as 60 MPa. Other hydrogen storage systems have been developed including storage as a cryogenic liquid, in metal hydrides, physisorption on carbon or other sorbents, and chemical hydrides (such as dehydrogenation of organic molecules). While progress has been made, no hydrogen storage technology meets the stringent requirements that are imposed by an automotive fuel cell system [1,2].

Recently several reports have suggested that hydrogen storage in carbon nanomaterials, such as carbon nanotubes and nanofibers may exhibit storage capacity that meets (or perhaps exceeds) DOE goals for automotive fuel cell applications [1,3,4]. At first glance these suggestions appeared counter-intuitive since surface science studies of hydrogen adsorption on graphite, for example, were necessarily conducted at very low temperature in order to stabilize the adsorbate [5]. It seems clear that if the reports of high capacity are correct that these new materials must exhibit interactions with carbon that exceed those of more typical carbon materials, like activated carbon. In this study, we set out to determine if the interactions between carbon nanomaterials and hydrogen were greater than between prototypical activated carbon and hydrogen to understand these storage results.

Hydrogen storage technologies can be compared on the basis of gravimetric and volumetric storage capacities. Both of these capacities must meet certain targets in order for a hydrogen storage system to reach viability [1,2]. The storage capacity requirements for a hydrogen-fueled fuel cell vehicle derive from requiring fuel cell vehicles to exhibit comparable range and gas storage system weight and volume to conventional automobiles. To achieve a 500 km range, the hydrogen storage system must exhibit a volumetric capacity of 60 kg H_2/m^3 and a gravimetric capacity of 6.2 wt. % H_2 for an installed system [1,2]. It is important to consider both gravimetric and volumetric storage capacities as weight and volume are both important in the automotive application. Another factor of prime importance is the energy penalty associated with the storage method. For example, liquifaction of hydrogen consumes about 1/3 of the lower heating value of the hydrogen. Ideal hydrogen storage systems would store hydrogen at high-density using relatively low pressure and ambient temperature.

Figure 1 compares various hydrogen storage technologies with the DOE goal [1]. Compressed gas storage is clearly the most developed technology and it shows good gravimetric capacity but low volumetric capacity at suitably high pressure. In contrast, metal hydrides show moderately good volumetric capacity, and poor gravimetric capacity. Some metal hydrides exhibit better capacities than the range indicated on Fig. 1, e.g. magnesium hydride. Generally, however, these materials suffer other problems; in the case of magnesium hydride, the dissociation temperature is very high and the material undergoes decrepitation following cycling. Newer (or perhaps resurgent) technologies for the storage of hydrogen include chemical hydrides and cryogenic adsorption on activated carbon.

Carbon nanofibers have been reported to store from 30-300% hydrogen by weight at about 112 atm [3,4]. By comparison, methane, the most compact organic arrangement of carbon and hydrogen, is 25% hydrogen by weight [6]. Despite the counter-intuitive nature of these results, because of the potential societal impact of high-density hydrogen storage, attempts were made to reproduce these results. To the best of our knowledge, other such attempts have failed [7,8].

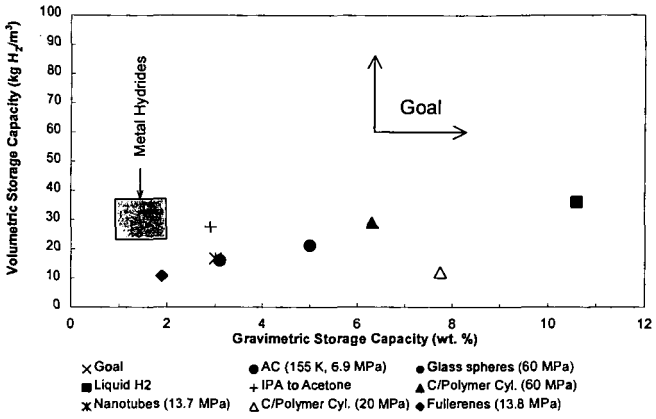

Figure 1: Comparison of gravimetric and volumetric storage capacity of various hydrogen storage technologies [1].

Recent careful studies reported that carbon nanotubes stored hydrogen at 5-10 wt% [1,9]. These later reports suggested to us that increased interactions with hydrogen arise in carbon nanotubes. Enhanced interactions were clearly required to explain the data, because typical carbon materials (activated carbon) show very low capacity at near-ambient temperature [10]. While less dramatic than the nanofiber claims, these results were very significant, in the context of Fig. 1. Especially important in these later experiments was the fact that high pressure was not required in order to store hydrogen at high density.

In general, the experimental procedures followed in the study of hydrogen storage within carbon nanomaterials have been inconsistent. This makes a systematic comparison of the various experiments impossible to perform. Nevertheless, it is useful to tabulate the results of some of these experiments. Table 1 summarizes some of the data reported in the literature for hydrogen storage in new carbon structures. Notice that the data cover a range of storage conditions and show highly variable capacity. The variety of conditions encountered in the data in Table 1 precludes a separation of the effects of storage condition from material structure (e.g. nanotube *vs.* nanofiber). Therefore the purpose of this study was to perform well-controlled adsorption of hydrogen on various carbon nanostructures to determine the relative interaction of hydrogen with these materials.

Table 1: Hydrogen Storage in Carbon Nanostructures

Sample	T / K	P / atm	x_{wt} / %	Ref.
Nanofibers	298	112	35	3,4
Nanotubes	~133	~1	5-10	1,9
Nanotubes	340	136	4	11
Fullerenes	673	101	2.4	12

EXPERIMENTAL

We used the following carbon materials in this study: single walled carbon nanotubes from Rice University [13] and the University of Kentucky [14], activated carbon (BPL from Calgon Carbon Corporation), and carbon nanofibers synthesized in our laboratory. Single-walled carbon nanotubes from Rice University were estimated to be 90% pure with a diameter of 1.2 nm [13,15]. Nanotubes from the University of Kentucky were estimated as 50-70% pure SWNT by volume [14]. Carbon nanotubes were formed into "nanopipes" by processing the Rice University nanotubes [16]. A sample was placed in a mixture of concentrated sulfuric and nitric acids (3:1 by volume) and the solution was sonicated for about 24 hours at 30-40 °C. This procedure had a yield of about 50%. We synthesized carbon nanofibers by catalytic decomposition of ethylene over various catalysts in the temperature range of 500-700 °C [17]. Scanning electron microscopy and transmission electron microscopy were used to characterize the synthetic nanofibers. Calorimetry experiments made use of an isothermal flow

microcalorimeter (CSC, model 4400) at atmospheric pressure and 25 °C. Hydrogen was delivered as a pure gas at a flow rate of 10 cc/min. Degassing samples above 100 °C under vacuum overnight minimized surface contamination by residual water.

RESULTS AND DISCUSSION

Among structural questions, the nature of the synthetic nanofibers was of the greatest interest. Other researchers have characterized carbon nanotubes extensively by SEM, TEM, XRD, and Raman spectroscopy, so we did not further characterize those samples. The synthetic nanofiber sample that we were most interested in was synthesized on ceramic pellets. Insulating ceramic pellets were placed in the entrance region of the reactor in an attempt to improve the uniformity of the reactant temperature distribution. These insulating pellets were estimated to reach a temperature of ca. 500 °C during reactor operation and over several syntheses produced a large quantity of nanofiber (ca. ¼ kg) material. All of our nanofibers were synthesized using smooth surfaces.

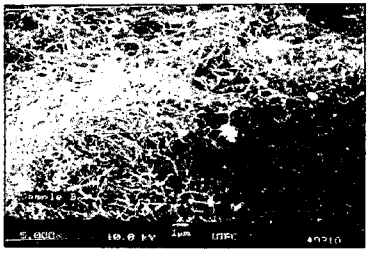

Figure 2: SEM image of carbon nanofibers synthesized by ethylene decomposition over a mixed oxide surface at ca. 500 °C.

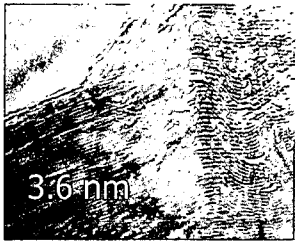

Figure 3: High resolution TEM image of carbon nanofibers synthesized by ethylene decomposition over a mixed oxide surface at ca. 500 °C.

Figure 2 shows a SEM micrograph of nanofibers synthesized on the oxide surface. In general, the structure is fibrous and few large clumps of amorphous carbon were observed in this sample. The question of the microstructure of the material could only be answered by high-resolution TEM imaging. One question was whether the structure of this material was similar to the material that Rodriguez et. al. have claimed store large quantities of hydrogen [3,4]. Figure 3 shows a high resolution TEM image of a carbon fiber synthesized on the oxide pellets. Graphite-like plane spacing is observed in this sample (ca. 0.36 nm). This measurement cannot be made to a high degree of precision without a standard specimen installed in the TEM during imaging. Therefore, this value is indistinguishable from that of graphite (0.34 nm). The plane spacing runs parallel to the fiber axis along most of its length, Fig. 3. There are some regions where the fiber axis bends and in these areas the plane spacing appears at an angle to the fiber axis. This result shows that the material we have synthesized is different than the GNF materials used in other studies [17].

Isothermal flow microcalorimetry reveals the degree of interaction of the adsorbate (hydrogen) with the sorbent. This method is sensitive to both the total heat of adsorption ΔH_{ads}^{total}, and the mass storage capacity, x_{wt}, as shown in eq. 1.

$$Q/m = \frac{1}{M_{H_2}} \Delta H_{ads}^{total} x_{wt} \qquad (1)$$

Rather than measuring isosteric heats of adsorption as a function of coverage, here ΔH_{ads}^{total} refers to the total heat released in going from the clean surface to the equilibrium coverage, per mole of hydrogen adsorbed. In essence, eq. 1 translates the heat of adsorption from an adsorbate basis to a sorbent basis. The point of this relationship is to show that the measured quantity (Q/m) will track changes in both the mass capacity and the heat of adsorption. Therefore, this technique should reveal differences among various carbon sorbents if such differences are significant.

Figures 4-7 show the calorimetry data for hydrogen adsorption on various carbon materials. All of the heat data are normalized to the initial mass of the sorbent. In these experiments mass change following adsorption is difficult to detect. Figure 4 shows the calorimetry data for BPL, a typical activated carbon used for natural gas storage [18]. The significance of the structure observed in the calorimetric curves is presently under investigation. Peak heights and areas in Figs. 4-7 are much smaller than those observed in typical chemisorption experiments [19].

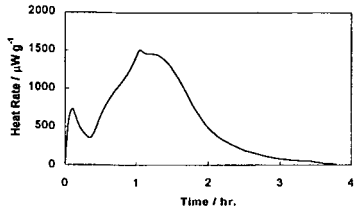

Figure 4: Hydrogen adsorption calorimetry data for BPL; hydrogen flow rate, 10 cc/min, 25 °C.

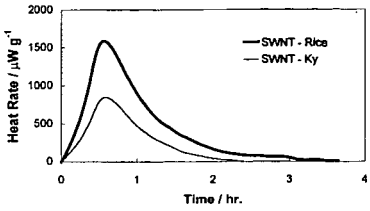

Figure 5: Hydrogen adsorption calorimetry data for carbon nanotubes; hydrogen flow rate, 10 cc/min, 25 °C.

Figure 5 shows the calorimetry data for hydrogen adsorption on the carbon nanotube samples. The Rice University sample displays a higher peak height and area than the University of Kentucky sample. This result can be rationalized either by a higher fraction of nanotubes or more active residual soot in the Rice sample. While the differences between these samples may be significant, as we will see later the total heat released is comparable to that when activated carbon is exposed to hydrogen (Fig. 4, Table 2).

One concern with the nanotube samples was whether hydrogen could access the interior of the tubes. If the tube interiors were not accessible, we might expect a lower measured heat due to a lower heat of adsorption on the tube exterior, as well as a lower mass capacity [6]. Figure 6 compares the hydrogen adsorption calorimetry for the Rice sample in both nanotube and "nanopipe" form. Processing the nanotubes to make pipes increases the degree of interaction of the hydrogen with the nanotube sample. While the effect of cutting the tubes is not extremely large, it is the most significant change observed in this study. Several possible explanations for this behavior exist. The processing step could: 1) increase surface area through opening the tube ends, 2) increase the heat of adsorption due to allowing access to more energetic surface sites, 3) increase adsorption capacity. We cannot rule out any of these possibilities at the present time. The initial rate of heat release is also significantly higher for the cut sample, which may indicate a different mechanism of adsorption or increased availability to sites with a higher adsorption potential.

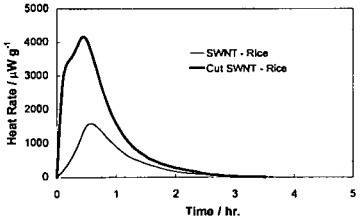

Figure 6: Hydrogen adsorption calorimetry data on carbon nanotubes; hydrogen flow rate, 10 cc/min, 25 °C.

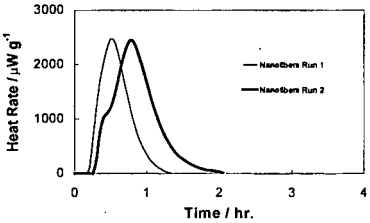

Figure 7: Hydrogen adsorption calorimetry data on synthetic carbon nanofibers; hydrogen flow rate, 10 cc/min, 25 °C.

Figure 7 shows the hydrogen adsorption calorimetry data for our nanofibers. This plot shows two different runs on the same sample. Following the first run the sample was placed in a vacuum oven at ~100 °C overnight and the experiment was repeated under identical conditions. The apparent shift in the peak maximum toward longer times is not significant because the zero on the time axis is arbitrary. Qualitatively the peak shape and height appear consistent from these two runs. The reasonable agreement between runs demonstrates the reproducibility of the technique.

The total heat released in the adsorption process (eq. 1) can be obtained simply by integrating the calorimetric signal over the period of the experiment. Table 2 shows the *semi-quantitative* results of these measurements. Since the statistical certainty on these measurements is not clear, we prefer to discuss these data qualitatively. The BPL sample shows one of the largest heat

releases obtained, consistent with the fact that this sample has a high micropore volume of 0.5 cm^3/g making it a good sorbent for adsorbed natural gas storage [18]. The nanotube samples show somewhat decreased interaction with hydrogen relative to BPL. However, the "cut" nanotubes show the largest heat released of all samples, demonstrating either an increased heat of adsorption or an improved adsorption capacity. The nanofiber sample shows a total heat release that is somewhat less than that of BPL. The run-to-run variability can be judged qualitatively by comparing the two nanofiber runs. The results can be reproduced within about 27%. For the low-level signals observed in these experiments, we consider this degree of reproducibility very good.

Table 2: Semi-quantitative calorimetry results

Sample	Q/m (J/g)
BPL	7.8
U Ky Nanotubes	2.6
Rice University Nanotubes	5.5
"Cut" Rice University Nanotubes	13.9
Nanofibers, Run 1	4.3
Nanofibers, Run 2	5.9

The primary purpose of the calorimetry measurements was to look for extremely strong interactions between carbon nanotubes or nanofibers and hydrogen. The basis of comparison was a high quality activated carbon, BPL. From the measurements obtained we can say that the interactions of these materials are comparable to the interactions of activated carbon and hydrogen. Of course, the possibility exists for offsetting changes in the heat of adsorption and capacity (eq. 1), e.g. an increase in ΔH_{ads}^{total} and a decrease in x_{wt}. However, we interpret the data as suggesting a relative constancy of both quantities. Therefore, our initial question of some fundamentally different interactions between carbon nanotubes or nanofibers and hydrogen has been answered for conditions of atmospheric pressure and ambient temperature.

During the course of this experimental study, the computational chemistry community has been very active [6,20-25]. Several papers have sought to answer the same questions addressed here. These studies have made use of well-known interaction potentials for both C-H_2 and H_2-H_2 interactions. In one instance the carbon-hydrogen interaction potential (well depth) has been used as an adjustable parameter in an attempt to fit the experimental data of Rodriguez et. al. [3,4]. The conclusion from these studies is that the interaction potentials must be adjusted beyond physically reasonable limits in order to fit the data [21]. As a feasibility study, these computational studies are extremely valuable since years of materials optimization can be conducted in short order using adjustable computer models [6].

CONCLUSIONS

Hydrogen storage in new carbon nanostructures like carbon nanotubes and nanofibers appeared in the literature rather recently. Early experiments were conducted using different materials under different conditions leaving little conclusive evidence for good storage capacity. In this study we have characterized the interaction of hydrogen using isothermal flow microcalorimetry under constant conditions with high purity materials. Our data shows that the interaction of hydrogen with carbon nanotubes and nanofibers is comparable to the interaction of hydrogen with activated carbon. In view of our results, the results of attempts by other groups to reproduce the reported high storage capacities, and recent computational work, we conclude that carbon nanotubes and carbon nanofibers are not suitable as high-capacity hydrogen storage materials.

ACKNOWLEDGEMENTS

We acknowledge funding and permission to publish from Michael Winter and Jim Irish at UTRC. We enjoyed discussions of this work with Harvey Michels and Margaret Steinbugler of UTRC, Bryan Murach, Les Van Dine, and Tim Bekkedahl of International Fuel Cells, Sanjeev Mukerjee of Northeastern University, and Bob Bowman of the Jet Propulsion Laboratory.

REFERENCES

1. A.C. Dillon, K.M. Jones, T.A. Bekkedahl, C.H. Kiang, D.S. Bethune, and M. J. Heben, *Nature*, 386 (1997) 377.
2. M.A. DeLuchi, *Int. J. Hydrogen Energy*, 14 (1989) 81.
3. A. Chambers, C. Park, R.T.K. Baker, and N.M. Rodriguez, *J. Phys. Chem. B*, 102 (1998) 4253.

4. S. Hill, "Green Cars go Further with Graphite," New Scientist, December 28, 1996.
5. W. Liu and S.C. Fain, Jr., *Phys. Rev. B*, 47 (1993) 15965.
6. Q. Wang and J.K. Johnson, J. Phys. Chem. B, In press (1999).
7. C.C. Ahn, Y. Ye, B.V. Ratnakumar, C. Witham, R. C. Bowman, and B. Fultz, *Appl. Phys. Lett.*, 73 (1998) 3378.
8. Y. Ye et al., *Appl. Phys. Lett.* 74 (1999) 2307.
9. A.C. Dillon, T.A. Bekkedahl, A.F. Cahill, K.M. Jones, and M.J. Heben, In: *Proceedings of the 1995 DOE Hydrogen Program Review*, Vol. II, p. 521, NREL/CP-430-20036.
10. D. P. Valenzuela, and A. L. Myers, In: *Adsorption Equilibrium Data Handbook*, Prentice Hall, 1989.
11. T. Yildirim, Presented at the MRS Symposium, Boston MA, Paper S1.4, December 1998.
12. E. Brosha, Presented at the MRS Symposium, Boston MA, Paper S2.9, December 1998.
13. cnst.rice.edu/tubes/index.shtml
14. www.carbolex.com
15. A. Thess et. al., *Science*, 273 (1996) 483.
16. J. Liu et. al., *Science*, 280 (1998) 1253.
17. N.M. Rodriguez, *J. Mater. Res.*, 8 (1993) 3233.
18. J. Sun, S. Chen, M.J. Rood, and M. Rostam-Abadi, *Energy and Fuel* 12 (1998) 1071.
19. S. Satyapal, T. Filburn, J. Trela, J. Strange, "Novel Amine Sorbents for Separation of Carbon Dioxide", Submitted to: *Industrial and Engineering Chemistry Research*, 1998.
20. Q. Wang and J.K. Johnson, *J. Chem. Phys.*, 110 (1999) 577.
21. Q. Wang and J.K. Johnson, *J. Phys. Chem. B*, 103 (1999) 277.
22. Q.Y. Wang and J.K. Johnson, *Molecular Physics*, 95 (1998) 299.
23. Q.Y. Wang and J.K. Johnson, *Int. J. Thermophysics*, 19 (1998) 835-844.
24. F. Darkrim and D. Levesque, *J. Chem. Phys.*, 109 (1998) 4981.
25. M. Rzepka, P. Lamp, M.A. de la Casa-Lillo, *J. Phys. Chem. B*, 102 (1998) 10894.

Catalytically Enhanced Sodium Aluminum Hydride as a Hydrogen Storage Material. Craig M. Jensen, Kevin Magnuson, Ragaiy A. Zidan, Satoshi Takara, Allan G. Hee, Nathan Mariels, and Chrystel Hagen, Department of Chemistry, University of Hawaii, Honolulu, HI 96822.

For decades, hydrogen has been targeted as the utopian fuel of the future due to its abundance and environmental friendliness. A major difficulty in the utilization of hydrogen as a fuel is the problem of onboard hydrogen storage. High pressure and cryogenic hydrogen storage systems are impractical for vehicular applications due to safety concerns and volumetric constraints. This has prompted an extensive effort to develop solid hydrogen storage systems for vehicular application. Metallic hydrides [1,2] activated charcoal [3,4] and carbon nanotubules [5] have been investigated as hydrogen carriers. Unfortunately, despite decades of extensive effort, especially in the area of metal hydrides, no material has been found which has the combination of a high gravimetric hydrogen density, adequate hydrogen dissociation energetics, and low cost required for commercial vehicular application [6].

The dissociation of hydrogen from sodium aluminum hydride, $NaAlH_4$, is not a single concerted process. It has been found to occur by the series of discrete reactions seen in equations 1, 2, and 3 [7-9]. Their independence is verified by the observation of a series

$$3\ NaAlH_4 \text{ ----------> } Na_3AlH_6 + 2\ Al + 3\ H_2 \qquad (1)$$

$$Na_3AlH_6 \text{ ----------> } 3\ NaH + Al + 3/2\ H_2 \qquad (2)$$

$$3\ NaH \text{ ----------> } Na + 3/2\ H_2 \qquad (3)$$

of equilibrium plateau pressures. The first two of these reactions are thermodynamically favorable at moderate temperatures and liberate 1.8 and 3.6 weight percent, wt %, hydrogen. However, $NaAlH_4$ has generally been discounted from consideration as a potential hydrogen storage material due to slow dehydriding kinetics [9] and the severe conditions required for its rehydriding [10]. Thus this material has not been developed as a rechargeable hydrogen carrier despite its high gravimetric hydrogen density and favorable dehydriding thermodynamics at moderate temperatures.

In 1996, Bogdanovic reported [11,12] that doping of $NaAlH_4$ with a few mole percent of titanium significantly enhanced the kinetics of the dehydriding and rehydriding processes. The temperature required for rapid dehydriding of $NaAlH_4$ was found to be

lowered from 200 C to 150 C. The conditions required for rehydriding were also dramatically reduced to 170 C and 150 atm. It was also noted that these materials showed the application-relevant properties of no hysteresis on cycling and negligible plateau slopes. Unfortunately, the hydrogen capacities of the materials produced by Bogdanovic quickly diminish upon cycling. Following the initial dehydriding of the titanium doped material, only 4.2 of the lost 5.6 wt % could be restored under the moderate conditions employed in these studied. The hydrogen capacity is further diminished to 3.8 wt % after the second dehydriding cycle and reduced to only 3.1 weight percent after 31 cycles. This lack of stability along with the still unacceptably high (150 C) temperature required for their rapid dehydriding, precludes them from consideration as viable onboard hydrogen carriers. This work, however, suggested that sodium aluminum hydride might be adapted for application as a practical hydrogen storage material.

The Bogdanovic materials were prepared by evaporation of suspensions of $NaAlH_4$ in solutions of titanium precursors. We recently found that titanium doping of $NaAlH_4$ also occurs upon mechanically mixing the liquid catalyst precursor, titanium tetra-*n*-butoxide, $Ti(OBu^n)_4$ with the aluminum hydride host [13]. The resulting purple materials are visually very distinct from the brown powders obtained through Bogdanovic's procedure. While our homogenization technique is equivalent to ball milling of the material, there is compelling evidence that a chemical reaction also transpires in the process.

The materials resulting from our homogenization process have kinetic and cycling properties that are much closer to those required for a practical hydrogen storage medium [13]. The material undergoes rapid dehydriding at 120 C and proceeds at an appreciable rate even at 80 C. The temperature required for rapid kinetics in the first dehydriding is further lowered to 100 C after the preliminary dehydriding-rehydriding cycle. The cyclable hydrogen capacity is also improved in the advanced titanium doped material. Over 4.0 wt % hydrogen can be evolved through 10 dehydriding-rehydriding cycles.

We have found that the dehydriding of $NaAlH_4$ is also kinetically enhanced upon doping with zirconium through our procedure [14]. The zirconium doped material has a further improved, 4.5 wt % cyclable hydrogen capacity. In contrast to the titanium doped material, the catalytic effect is most pronounced for the second rather than the first dehydriding process and inferior kinetics are observed for the first dehydriding reaction.

We have found that titanium and zirconium can act in concert to optimize dehydriding/rehydriding kinetics while achieving a 4.5 wt % cyclable hydrogen capacity.

The chain of advancement in the development of metal catalyzed $NaAlH_4$ is illustrated by comparison of the thermal programmed desorption spectra of the third dehydriding cycle of the various doped materials. As seen in Fig 1, hydride that was doped with titanium through the method of Bogdanovic has a cyclable hydrogen capacity of 3.2 wt % and dehydriding behavior that is markedly improved over undoped $NaAlH_4$. Titanium doping through our homogenization technique further enhances the kinetics of the first dehydriding reaction and improves the cyclable hydrogen capacity to over 4.0 wt %. The zirconium doped material shows improved kinetics for the second dehydriding process and a cyclable

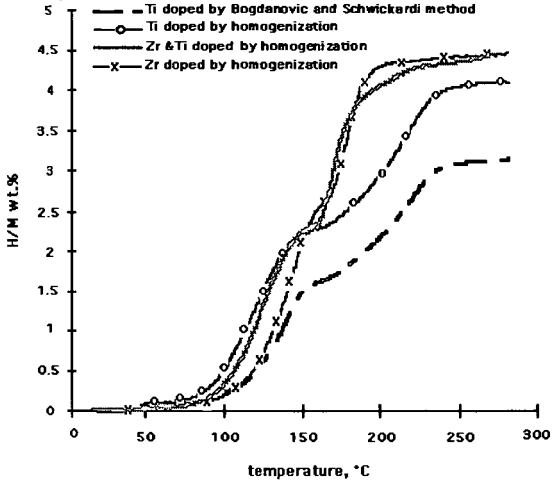

Fig. 1. Thermal programmed desorption (2 C min^{-1}) of hydrogen from various doped samples $NaAlH_4$ after 3 cycles of dehydriding/rehydriding.

hydrogen capacity of 4.5 wt %. Finally the titanium/zirconium doped material exhibits dehydriding behavior that is a virtual superpositioning of the behavior of homogenized titanium doped material for the first dehydriding process and the zirconium doped material for the second dehydriding process while maintaining a cyclable hydrogen capacity of 4.5 wt %. The finding of rapid dehydriding at 100 C in conjunction with a stable, hydrogen cycling capacity of 4.5 wt % suggests the application of these materials as hydrogen carriers for onboard fuel cells.

References

1. G. Sandrock, S. Suda, and L. Schlapbach, in L. Schlapbach (ed.), *Hydrogen in Intermetallic Compounds II, Topics in Applied Physics,* Vol. 67, Springer-Verlag, 1992, Chap. 5, p. 197.
2. G. Sandrock, in Y. Yurum (ed.), *Hydrogen Energy Systems: Production and Utilization of Hydrogen and Future Aspects*, NATO ASI Series, Kluwer Academic Publishers, 1994 p 253.
3. C. Carpetis, and W. Peshka, *Int. J. Hydrogen Energy*, *5* (1980) 539.
4. R.K.Agarwal, J.S. Noh, J. Schwarz, and R. Davini, *Carbon*, *25* (1987) 219.
5. A.C.Dillion, K.M. Jones, T.A. Bekkedahl, C.H. Kiang, D.S. Bethune, M. Heben, *Nature*, *386* (1997) 377.
6. S. Suda, and G. Sandrock, *Z. Phys. Chem.*, *183* (1994) 149.
7. W.E. Garner and E.W. Haycock, *Proc. Roy. Soc.* (London), *A211* (1952) 335.
8. E.C. Ashby and P. Kobetz, *Inorg. Chem*, *5* (1966) 1615.
9. T.N. Dymova, Y.M. Dergachev, V.A. Sokolov, and N.A. Grechanaya, *Dokl. Akad. Nauk SSSR* , *224* (1975) 591, Engl. ed (1976) 556.
10. T.N. Dymova, N.G. Eliseeva, S.I. Bakum, and Y.M. Dergachev, *Dokl. Akad.Nauk USSR* , *215* (1974) 1369.
11. B. Bogdanovic and M. Schwickardi, International Symposium on Metal-Hydrogen Systems, August 25-30, 1996, Les Diablerets, Switzerland.
12. B. Bogdanovic and M. Schwickardi, *J. Alloys and Compounds*, *1-9* (1997)253
13. C.M. Jensen, R. Zidan, N. Mariels, A. Hee, and C.Hagen, *Int. J. Hydrogen Energy*, *23* (1999) in press.
14. R.A. Zidan, S. Takara, A.G. Hee, and C.M. Jensen, *J. Alloys and Compounds* (1999) in press.
15. R. Ehrlich, A.R. Young, D.D. Perry, *Inorg. Chem*, *4* (1965) 758.

PERFORMANCE OF AN AMBIENT PRESSURE CELL STACK OPERATING UNDER SYNTHETIC GASOLINE REFORMATE

S. Kocha, A. Gaskins, P. Plasse, and D. Wheeler
International Fuel Cells, LLC
South Windsor, CT 06074

KEYWORDS: Fuel Cell, Reformate, PEM

INTRODUCTION

Recently, proton exchange membrane fuel cells (PEMFC) have gained worldwide attention as a possible practical replacement to the internal combustion (IC) engine for automotive applications. International Fuel Cells is actively engaged in PEMFC technology using hydrogen as well as reformed gasoline as a fuel source for automotive and stationary applications. Gasoline reformate from a fuel processor arriving at a PEM cell anode is expected to contain small quantities (10-50 ppm) of carbon monoxide. It is well known that CO is a poison to the platinum anode catalyst when present even in small concentrations of ppm in the fuel feed stream. Carbon monoxide adsorbs on active sites on the surface of the catalyst that would otherwise be available to H_2 for dissociation into monoatomic H_{ads} (Tafel step) for subsequent oxidation. In other words, the Tafel reaction which is the slower of the two step Tafel-Volmer reaction mechanism reaches rate limiting conditions earlier due to unavailability of participating reaction sites. The extensive coverage (~80%) at low (65°C) temperatures causes a precipitous drop in anode limiting current and degradation in cell performance referred to as CO poisoning. There are several ways to deal with the residual CO that enters the fuel cell stack. One is to develop new catalysts that are more tolerant to CO either by the mechanism of CO oxidation using OH^- ions at lower potentials. Another is the use of alloys that have components with a lower heat of adsorption to CO. Still a third pathway is to inject small amounts of air into the fuel feed [1,2] so that the CO is oxidized by oxygen at the catalyst surface, thereby recovering surface area for the hydrogen oxidation reaction and raising the cell performance. In the latter case, some hydrogen will also be oxidized, depleting the fuel and, hence, will result in an efficiency loss. A certain amount of heat will also be generated due to the oxidation of both hydrogen and CO.

The reverse shift reaction may also take place, since fuel feed consists of CO_2 , which in addition to causing a dilution effect may participate in the production CO or some other reduced form of CO_2 [3]. Thus a poisoning effect due to CO_2 may be observed.

In this paper, we present results on the effect of dilution of fuel, CO, CO_2 poisoning and, its mitigation by air injection, as well as selectivity of air injection.

EXPERIMENTAL

A low loaded (0.10 mg/cm^2 Pt anode; 0.37 mg/cm^2 Pt cathode; Gore 15 micron membrane) as well as a higher loaded "CO tolerant" catalyst (0.40Pt-0.20Ru mg/cm^2 anode; 0.30 mg/cm^2 , 0.40 mg/cm^2 cathode on Gore 15 micron membrane) were tested with H_2/CO or synthetic reformate gases at the anode while using air on the cathode. The electrochemically active area of the cell was 327 cm^2. The dry synthetic reformate composition used was CO_2 = 21%, N_2 = 30%, H_2 = 49%. An existing in-house software was used to acquire cell performance data. Special precautions were taken in the experimental test rig to ensure safety in the introduction of air into the fuel stream. Care was taken to ensure that the lower flammable limit (~5% oxygen in hydrogen or ~25% air in hydrogen) was not approached.

Gas chromatographic (GC) mass balance analyses of dry gasses entering and leaving the anode were carried out to determine the CO converted to CO_2 and to better understand the mechanism of CO oxidation particular to this system. GC measurements of dried gases were carried out at the fuel inlet and exit. In these studies CO in pure hydrogen was used rather than synthetic reformate in order to determine both the CO converted as well as CO_2 formed. (The CO_2 formed would not be measurable if synthetic reformate containing 21% CO_2 were used.) Impurities of CO_2 at the inlet, as well as unused oxygen and unoxidized CO (at low air bleeds) at the fuel outlet, were measured. All measurements were repeated 3-4 times for reproducibility.

RESULTS AND DISCUSSION

We report below the data on an MEA in a single cell having 0.1mg/cm^2 anode platinum loading and 0.37 mg/cm^2 cathode loading. Results are reported at 65°C and ambient pressure. Hydrogen utilization was 90% and air utilization 30% at 647 mA/cm^2. Figure 1 shows a "calibration" performance curve using pure H_2, performance curve with 20 ppm CO in H_2, and 0.5% air

injection. The anode polarization loss at 400 mA/cm^2 was >300 mV. A complete performance curve was obtained at 0.25% air bleed. The air injection reduced the polarization to ~250 mV. At 647 mA/cm^2, the air injection was increased in discrete steps up to 2.5% at which point the performance loss reached a minimum ~20 mV. Figure 2 shows the discrete steps in which the air bleed was increased at 647 mA/cm^2. In the last two steps, the CO is shut off after which the air bleed of 2.5% is shut off. A ~5-10 mV increase in performance is observed when the CO is turned off.

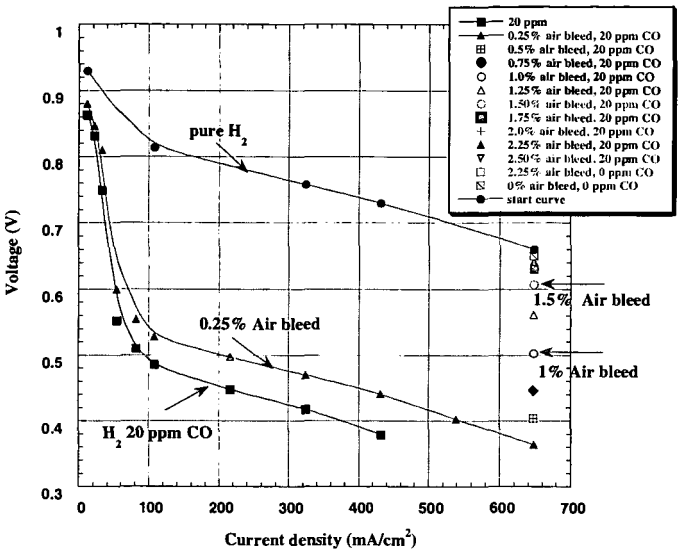

Figure 1 Performance curves depicting the loss in performance with the introduction of 20 ppm CO and the mitigation of CO poisoning with the use of an air bleed in the fuel feed stream. A complete curve with 0.25% air bleed is plotted as well as gain in performance with increasing air bleed at 647 mA/cm^2 at 65°C and 100 kPa.

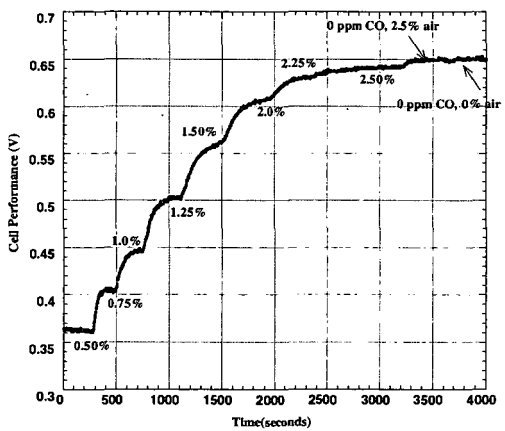

Figure 2 Details of the enhancement in performance during the step wise increase in air bleed at 647 mA/cm^2 of figure 2 at 65°C and 100 kPa.

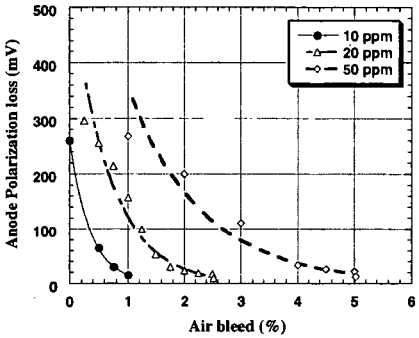

Figure 3 Variation of anode polarization with air bleed as a percentage of total anode fuel flow at 65°C and 100 kPa. (anode platinum loading 0.1 mg/cm^2)

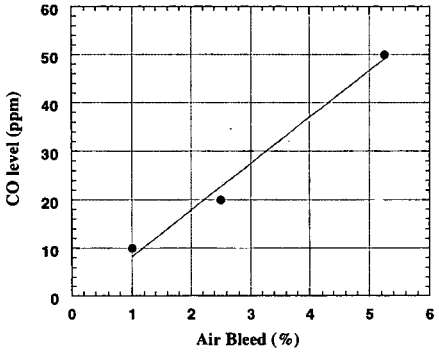

Figure 4 Dependence of the % air bleed required to raise the performance of a CO poisoned MEA (anode platinum loading 0.1 mg/cm^2) to within 10-15 mV of its hydrogen–air performance at 65°C and 100 kPa.

The rate at which the performance was enhanced (or anode polarization/cell loss decreased) with increasing % air bleed at 647 mA/cm^2 is shown in figure 3. The performance loss decreases at an exponential rate with % air bleed. Figure 4 summarizes the approximate amount of %air needed to be injected for different CO amounts in the fuel stream for performance recovery to within ~20 mV. The ratio of air bleed (21% oxygen) to CO level is a constant at about 200 and is a measure of the selectivity of the CO oxidation.

Mass Balance on low loaded (0.10 mg/cm^2 Pt anode) Pt anode

As described in the experimental section gas chromatographic studies were conducted to determine the mass balance of CO, air, and impurities (CO_2 ~8 ppm) entering and exiting the anode. The air bled in also contains 0.04% CO_2. The gases measured at the inlet and exit are dry gases. At 20 ppm CO inlet conditions with 2% air injection, the mass balance is shown in table 1. We observed that oxygen in the air bleed is not fully utilized and exits the anode along with CO_2 and even unoxidized CO at low air bleeds. The selectivity of CO oxidation based on the mass balance is of the order of 100:1.

TABLE 1 20ppm CO in hydrogen, 65°C, V_{OC}, 2% air bleed

	Inlet Flow	Exit Flow	|Inlet-Exit|
CO ppm	20.4	0.0	20.4
CO_2 ppm	15.0	43.1	28.1
N_2%	1.51	1.60	0.10
O_2%	0.43	0.11	0.30
CO oxidized	=20.4ppm		
O_2 used	=0.30% = 3000ppm		
O_2 unused	=0.11% = 1100ppm		

Figure 5 shows three performance curves, namely the hydrogen-air curve, 50% hydrogen and 50% nitrogen, 49% hydrogen, 30% N_2, and 21% CO_2. (simulated reformate with no CO). The losses due to dilution by N_2 at 647 mA/cm^2 is ~25 mV and the additional loss due to CO_2 poisoning is ~ 70 mV. At 647 mA/cm^2 air was bled into the anode in small increments until the cell performance was recovered. At 0.6% air bleed the performance reaches to within 10-15 mV of the maximum possible diluted performance. Further air bleed did not result in any performance gain. Figure 6 shows the effect of air bleed when the anode is subject to simulated reformate + 10 ppm CO. Combining the results in figures 6 and 7, it appears that the air bleed required for recovering the performance is approximately the sum of that required for CO_2 and CO individually and is ~1.75%.

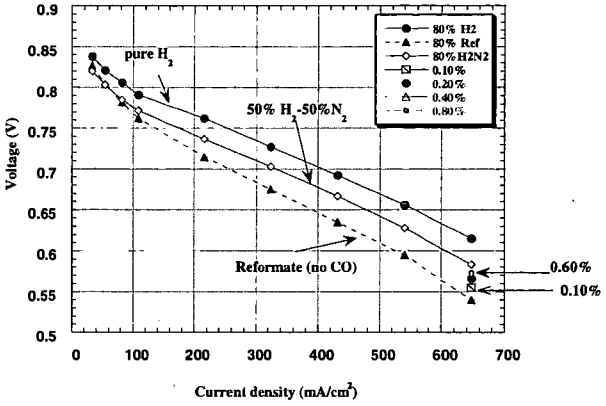

Figure 5 Single Cell Stack Performance with anode gas compositions of pure H_2, H_2-N_2 and simulated reformate containing 49%H_2:21%CO2:30%N_2
+ Air Bleed (% of total anode flow)

High loaded Pt-Ru anodes (0.40Pt-0.20Ru mg/cm^2)

Figure 7 compares the effect of reformate with 10 ppm CO with and without air bleed at 538 mA/cm^2 with time. The air bleed required for this Pt-Ru catalyst with 10 ppm CO in reformate is of the order of 0.6% and less than that for a lower loaded Pt anode (1%) for the same CO ppm in reformate.

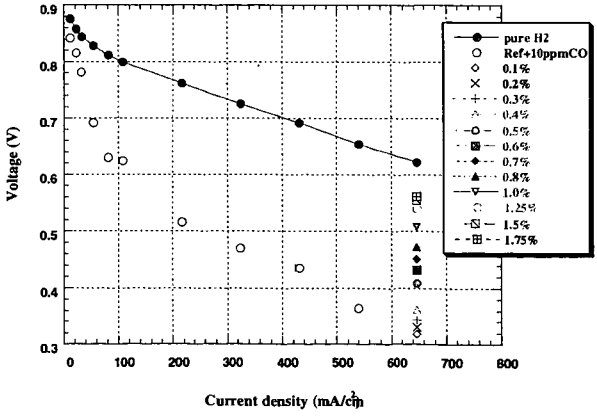

Figure 6 Performance curves showing the effect of reformate containing 10 ppm CO and step increases in air bleed at 647 mA/cm^2 that recovers the poisoning losses.

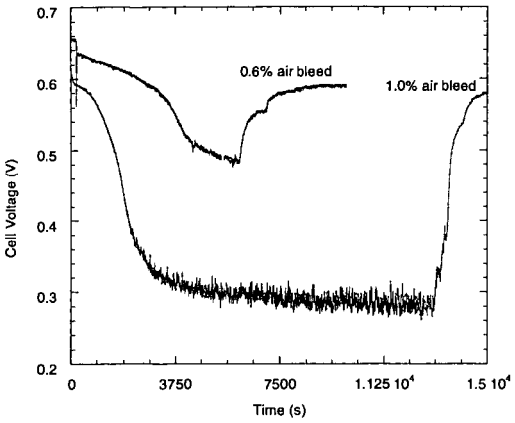

Figure 7 Comparison of cell voltage at constant current density of 647mA/cm^2 versus time. The upper curve corresponds to a Pt-Ru anode of 0.4-0.2 mg/cm^2 loading and the lower curve corresponds to anode with a Pt loading of 0.3 mg/cm^2. Both cathodes had 0.3 mg/cm^2 of Pt. The PtRu anode shows lower anode polarization losses and a lower air bleed of 0.60% is required to mitigate the poisoning.The cell temperature and pressure are 65°C and 100 kPa.

Voltage Oscillations

In the process of assessing the CO tolerant properties of different anode catalysts by testing for MEA performance, we observe an oscillatory phenomena. At high current densities and/or high CO ppms, the performance of the fuel cell fluctuates systematically with a relatively fixed amplitude and period. Air bled into such an oscillating system causes the oscillations to decline in frequency and eventually dampens out the amplitude. The period of oscillation is quite definite; if air is bled in, the period increases until finally oscillations cease in time when the air bleed is sufficient. With very low anode loadings of 0.1mg/cm^2 oscillations were not observed. Although the total number of available sites is reduced with a lower loading, the fraction of available sites for hydrogen oxidation stays the same following an adsorption isotherm. When the number of available sites are very low, the instrumentation is not sensitive enough to measure low amplitude oscillations.

CONCLUSIONS

The air bleed required to regain the performance and alleviate carbon monoxide poisoning was determined for different CO concentrations in hydrogen. Air injection was also found to recover losses caused by the much milder CO_2 poisoning. The air bleed to recover performance loss due to the combined effect of CO and CO_2 was found to be additive. In the presence of reformate with 10 ppm CO only ~ 0.5% air bleed was required for a higher (0.4Pt-0.2Ru mg/cm^2) loaded Pt-Ru anode. Mass balance of the CO and converted CO_2 as well as excess oxygen were measured using gas chromatography. The amount of air bleed will affect the fuel efficiency of the stack and power plant.

REFERENCES

1. S. Gottesfeld and J. Pafford, *J. Electrochem Soc.*, **1988**, 135, 2651
2. D. Sutton, Report at the **1992** *Fuel Cell Seminar*, Tucson , AZ.
3. J. Giner, *Electrochim. Acta*, **1963**, 8, 857

OPTIMAL OPERATING TEMPERATURE AND PRESSURE OF PEM FUEL CELL SYSTEMS IN AUTOMOTIVE APPLICATIONS

Bhaskar Balasubramanian, Frano Barbir and Jay Neutzler
Energy Partners, L.C.
1501 Northpoint Parkway
Suite 102, Technology Center
West Palm Beach, FL 33407

INTRODUCTION

The automotive industry is currently faced with the challenge to develop cleaner and energy efficient vehicles in order to meet the reduced toxic emissions standards. The proton exchange membrane (PEM) fuel cell system offers the most promising solution that would enable both efficiency improvement and emissions reduction in automobiles. Since fuel cells use hydrogen as the fuel, in order to facilitate an early market entry, the stacks are being integrated with reformers (fuel processors) that produce hydrogen from conventional fuels such as gasoline, methanol, natural gas, or propane. It is also a viable technology for decentralized power generation. Gasoline being the established vehicle fuel in terms of supply and distribution is best suited for automotive PEM fuel cell system while natural gas is the popular choice for small residential or stationary power applications.

The PEM fuel cell may be operated at pressures ranging from near ambient to about 6 atm and at temperatures between 50 and 90°C. High power density is obtainable at higher operating pressures but the net system efficiency may be lower on account of the power needed for air compression. High power density is also obtained at the higher operating temperatures, however it may pose a significant challenge for water and heat management especially at lower operating pressure. A lower operating temperature, on the other hand, makes waste heat rejection into the environment difficult particularly in hotter surroundings. Therefore selection of operating temperature and pressure of the automotive PEM fuel cell system must be based on (a) high net system efficiency, (b) small component size, and (c) neutral or positive water balance so that the vehicle does not have to carry on-board water reservoir.

In order to select the optimal operating temperature and pressure of the automotive fuel cell system Energy Partners developed a steady-state mathematical model of the entire fuel cell system that estimates the system and component parameters (such as mass flows, reaction rates, heat fluxes and loads, heat exchanger size, component and net system efficiencies etc.) at various operating temperatures and pressures and at various power levels.

SYSTEM DESCRIPTION

As shown in Figure 1, the automotive fuel cell system consists of the following major components or subsystems:

- Fuel Processor (which includes exhaust heat recovery in burner)
- Compressed Air Delivery
- Fuel Cell Stack
- Heat and Water Management
- Exhaust (Expander)

Figure 2 is a 3-D representation of the complete automotive fuel cell system. The fuel to be reformed in this case is gasoline. Epyx Corp.[1] successfully demonstrated a partial oxidation based fuel processor. Gasoline is reformed to produce a reformate stream consisting of approximately 40% hydrogen, 20% carbon dioxide, and balance nitrogen (dry basis) after CO clean-up. A typical reformate stream leaves the fuel processor at near 160-170°C saturated with water vapor. The wet gas is then conditioned to the stack temperature, the condensed water removed in a separator, and sent to the fuel cell anode fully humidified at that temperature. Compressed ambient air is humidified before it is supplied to the cathode. The unutilized/excess hydrogen from the fuel cell anode exhaust is burnt with the excess air (from the cathode exhaust) in the tail gas catalytic combustor (TGC). Exhaust gases from the TGC are then expanded to recover part of the energy needed for compression. In most applications the fuel cell temperature is controlled using water. However, for an automotive system like the one described here, an anti-freeze liquid such as propylene glycol is preferable. Heat from the coolant loop is rejected in an air-cooled heat exchanger or radiator. Water is consumed in the fuel processor in the steam-reforming and shift reactions, and in the humidification of air. In addition water is needed as the cooling medium in the fuel processor Water is produced in the stack as a result of the reaction between H_2 and O_2, and also in the TGC by combusting hydrogen. For an automotive system it is important to have a neutral water balance to avoid on-board de-ionized water supply. Therefore, liquid water is separated from all gas streams (fuel cell exhaust gases and the TGC exhaust) and conditions maintained so as to achieve neutral water balance. The electrical power generated by the fuel cell is used to power the auxiliary

loads (compressor/expander, pumps, radiator fan, and control equipment) in addition to that required by the automotive propulsion unit.

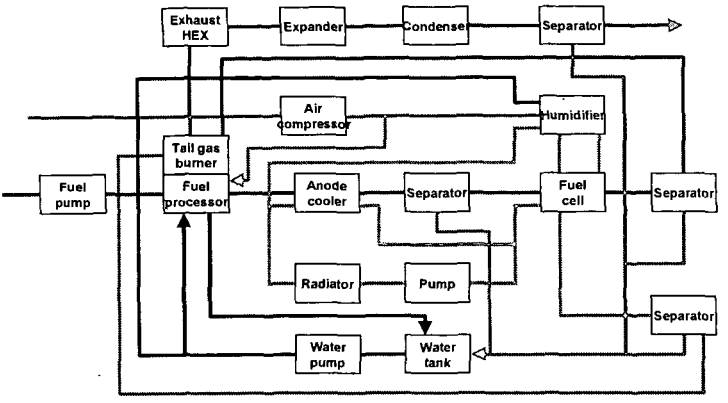

Figure 1. Automotive PEM Fuel Cell System Block Diagram

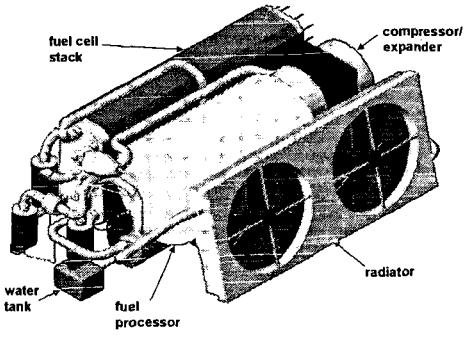

Figure 2. A 3-D Representation of the Automotive PEM Fuel Cell System

MODEL DESCRIPTION

Based on the laws of conservation of mass and energy a complete set of equations was developed to compute mass and energy balance of each species in the system. The model takes into account all the chemical reactions involved in the fuel processor, fuel cell, TGC, etc., and the energy changes associated with the phase change of some of the species due to changes in temperature, pressure, etc.

Fuel Processor:

The fuel processor combines partial oxidation, steam reforming and water gas shift reactions to produce hydrogen, which for gasoline reforming can be represented as:

$C_8H_{18} + (12.5)/\phi\ O_2 + (16 - 25/\phi)\sigma\ H_2O \rightarrow aCO_2 + bCO + cCH_4 + dH_2 + eH_2O$

where:

ϕ = equivalence ratio, (stoichiometric air/fuel ratio to actual air to fuel ratio)

σ = ratio of actual to theoretical H_2O in the fuel processor

The coefficients (of the products and unconverted reactants) are calculated based on the mass balance of each of the species involved in fuel processing. The efficiency of fuel processing is then computed as the ratio of the heating value of product hydrogen to that of gasoline reformed. In order to reduce the CO content to less than 100 ppm (to prevent poisoning of the Pt anode catalyst), CO is further preferentially oxidized (PROX) using air over a special catalyst. Approximately, for 1% of the CO in the reformate and twice the excess oxygen needed, 2.5% of the hydrogen in the reformate is also oxidized resulting in an efficiency of 97.5% for preferential

oxidation. Thus based on the amount of hydrogen required, the model calculates the mass flows of the reacting species.

Fuel Cell:

The stoichiometric amounts of H_2 and O_2 consumed in the electrochemical reaction in the fuel cell are computed by Faraday's law. However, since neither H_2 nor O_2 is present as pure gas excess amounts are supplied to the fuel cell and the unused H_2 is burnt with the unused O_2 in the TGC later for heat integration with the reformer. The H_2 stoichiometric ratio depends on the actual fuel cell flow field design. The power generated by the fuel cell stack is a product of the individual cell voltage, current density and the number of cells. The current and voltage are related according to the polarization curve and an experimentally determined curve is used in the model. The fuel cell efficiency is defined as the ratio of the electrical power output to the heating value of H_2 fed.

$$\eta_{FC} = (I \cdot V_{cell}) / (\Delta H_{H_2} \cdot \text{Mass } H_2 \text{ fed})$$

It can thus be seen that high efficiency is obtainable at higher fuel cell potential and lower H_2 stoichiometry. However for any given power output a high fuel cell operating voltage leads to larger stack.

Air Supply and Exhaust Heat Recovery:

Unused H_2 from the fuel cell is combusted in the TGC and the heat generated is utilized in the fuel processor for preheat and/or steam generation. Combustion being exothermic, temperature of the exhaust gases is relatively very high and the heat is utilized in an expander to generate part of the power needed for air compression. It will be explained later that an expander is necessary for a pressurized system. Power recovered in the expander is computed using isentropic equations. Similarly, based on O_2 flow needed for the fuel cell, air flow is computed and compressor is sized accordingly.

Water and Heat Management:

The coolant flow is computed depending upon the heat generated in the fuel cell and the operating temperature. Accordingly, the model calculates the cooling duty needed in the coolant loop and estimates size and other parameters for the radiator.

System Efficiency:

The overall system efficiency is a product of the efficiencies of the fuel processor, the PROX unit, the fuel cell and balance of plant (η_{BOP}). η_{BOP} is the ratio of the net power to the gross power produced by the fuel cell. The difference between gross power and net power includes power needed to run compressor/expander, fans, pumps, solenoid valves, relays, controller, etc.

RESULTS AND DISCUSSION

The model briefly described above was used to perform steady state simulations to calculate the following system parameters (based on the input parameters and assumptions outlined in Table 1): (a). fuel consumption, air and water requirements; (b) fuel cell parameters (size and number of cells); (c) parasitic load requirements or BOP analysis.

Table 1. Input parameters

Net power output:	50 kW
Fuel cell polarization curve:	EP laboratory results
Cell nominal voltage:	Variable
Operating pressure:	Variable from 101.3 to 308 kPa
Operating temperature:	Variable from 50 to 80 °C
Reactants humidification:	both gases 100% RH at operating temp.
Stack ΔT:	10°C
Stack pressure drop:	15 and 30 kPa
Stoichiometry:	2.0 cathode; 1.17 anode
Compressor efficiency:	0.8
Expander efficiency:	0.8
Expander inlet temperature (max):	150°C
Reformer efficiency:	0.8 (LHV)
Reformer fuel equivalence ratio:	3.13
Water/fuel ratio in reformer (mol):	22.84
Fuel:	Octane (C_8H_{18})
PROX stoichiometry:	2 (efficiency 0.97)
Reformer pressure drop:	15 and 30 kPa
Ambient conditions:	101.3 kPa, 30°C, 60%RH

Figure 3 shows the dependence of the system efficiency on fuel cell operating temperature and pressure. For the pressurized system a higher operating temperature results in a somewhat higher system efficiency and vice-versa for a low temperature system, which is mainly due to: (a) at low operating pressure, the expander recovers very less or no power, and (b) high operating temperature when coupled with low pressure necessitates large amounts of water recovery in the condenser which results in a very high parasitic load for the condenser fan. It should be noted that in these comparisons, the fuel cell voltage at nominal power was kept constant at 0.7 V/cell. A higher cell voltage results in higher efficiency but results in less power density (W/cm^2) or in other words a larger stack. Figure 4 shows relative stack sizes as a function of temperature and pressure at constant nominal system efficiency. High temperature and high pressure lead to the smallest stack size.

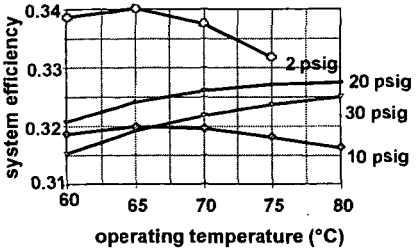

Figure 3. Effect of Operating Temperature and Pressure on System Efficiency

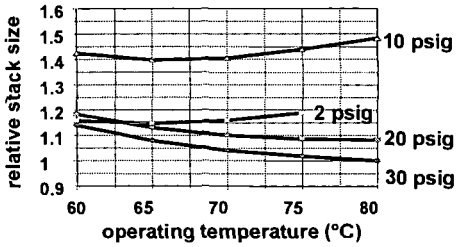

Figure 4. Effect of Operating Temperature and Pressure on Stack Size

However stack size is not the only criteria in selecting operating temperature and pressure. Size and performance of other components such as the fuel processor and radiator are also affected by pressure and temperature. Figure 5 shows the variation in heat load on the condenser and radiator with operating temperature and pressure. High temperature when coupled with low pressure shifts the heat load from the condenser to the radiator. On the other hand, high pressure and low temperature results in maximum heat rejection in the radiator. The major difference between these two components is that the radiator is liquid-to-gas heat exchanger while the condenser is a gas-to-gas heat exchanger. Heat transfer coefficients are significantly lower for the condenser, which means that for a given heat load the condenser requires much larger heat transfer area than the radiator. Figure 6 compares the heat transfer areas for the condenser and radiator as a function of temperature and pressure. The calculations assume a liquid/gas heat transfer coefficient of 60 W/m^2/°C and gas /gas coefficient of 15 W/m^2/°C and a fin-to-tube area of 10. The system that operates at high pressure (30 psig) and low temperature (60°C) requires the smallest heat exchanger. For automotive fuel cell systems heat exchanger size may very well be a limiting factor. At 30 psig and 60°C, there is no need for a condenser since all heat is rejected in the radiator.

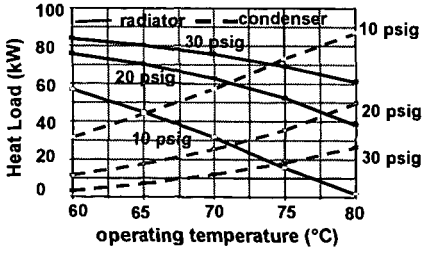

Figure 5. Radiator and Condenser Heat Load (50 kW net, constant efficiency)

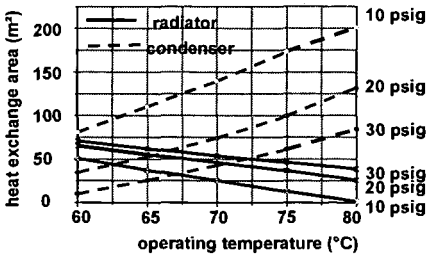

Figure 6. Required Heat Exchanger Area for a 50 kW (net) System

In all cases neutral water balance was accomplished such that enough water was condensed in the system to make up for the reformer process water and for air humidification. Water management poses a concern in systems that operate at low pressures and high temperatures since large amounts of water are needed for humidification.

With certain assumptions and limitations, the model also simulates the performance at off-design conditions such as partial loads and ambient conditions. Figure 7 shows projected system efficiency at various power levels. At 25% net peak power, the net system efficiency is around 39%. However for a realistic case, since the efficiencies of the compressor and expander are lower at lower pressures and lower power levels, the system efficiency is around 37%. Again, higher efficiencies (>40%) are obtainable at higher cell voltages at peak power. Ahluwalia et. al [2] have shown that 44.8% system efficiency is obtainable at 0.8 V/cell and 90% hydrogen utilization.

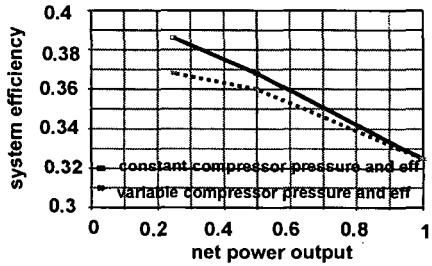

Figure 7. System Efficiency as Function of Net Power Output (30 psig, 80°C, 50 kW - peak power)

CONCLUSIONS

The numerical steady state model developed for performance simulation of the PEM fuel cell automotive system has proven to be a valuable tool for component sizing, trade-off analysis by varying system configurations, and optimizing system pressure and temperature. Results suggest that an automotive system should operate at high pressure (30 psig), but an expander must be used to recover power used for compression. Surprisingly, results indicate that a low temperature (60°C) results in smallest size of heat exchanger if neutral water balance is mandated. The model also predicts system efficiency at different loads. Higher efficiencies may be achieved at higher cell voltages, but that would result in large fuel cell stack, which may be a limiting factor for automotive applications with the state-of-the-art fuel cells.

ACKNOWLEDGEMENT

This work was supported by the U.S. Department of Energy, Office of Advanced Automotive Technologies, under contract no. DE-FC02-97EE50476.

REFERENCES

1. W.L. Mitchell, "Integrated Power System for Transportation - Advanced Fuel Processor Development", Fuel Cells for Transportation 98, Contractors Annual Progress Report, Vol. 1, pp23-27, U.S. Department of Energy, OAAT, Washington D.C., November 1998.
2. R.K. Ahluwalia, E.D. Doss, H.K. Geyer and R. Kumar, "Pressurized POX-Reformed Gasoline PEFC System", presented at the Pressure Effects Workshop, Argonne National Laboratory, Argonne, IL, December 1998.

PREPARATION OF PT-RU OR PT-MO SUPPORTED CATALYSTS FOR PEM OR DIRECT METHANOL FUEL CELLS FROM SINGLE-SOURCE MOLECULAR PRECURSORS

C. M. Lukehart[1], D. L. Boxall[1], J. D. Corn[1], M. Hariharasarma[1], W. D. King[1], K. C. Kwiatkowski[1], E. S. Steigerwalt[1], and E. A. Kenik[2]
(1) Department of Chemistry, Vanderbilt University, Nashville, TN 37235
(2) Metals and Ceramic Division, Oak Ridge National Laboratory, Oak Ridge, TN 37831

KEYWORDS: Binary alloy catalysts; PEM fuel cell catalysts; Direct methanol fuel cell catalysts

ABSTRACT

An overview of the synthesis and characterization of several Pt-Ru or Pt-Mo/Vulcan carbon nanocomposites and one Pt-Ru/graphitic carbon nanofiber nanocomposite is provided. Each binary metal alloy nanocluster composition is accessed through the thermal decomposition of a single-source molecular precursor containing the desired metal stoichiometry. Microwave heating techniques are used to form a Pt-Ru/Vulcan carbon nanocomposite within one minute of thermal treatment. The metal stoichiometry of individual alloy nanoparticles has been determined from on-particle EDS measurements obtained using HR-TEM(FEG) instrumentation. Preliminary DMFC testing results are also summarized.

INTRODUCTION

There is currently much interest in developing metal alloy catalysts having improved reactivity as anode catalysts in fuel cells.[1] Specifically, Pt-Ru alloys are commonly used as anode catalysts in direct methanol fuel cells (DMFCs) for the electrocatalytic oxidation of methanol.[2] Pt-Mo catalysts are of interest as anode catalysts in PEM fuel cells operating on reformate fuels due to their higher CO-tolerance relative to platinum metal catalysts.[3] Even though fuel cell anode catalysts might undergo significant chemical changes during conditioning or aging within a working fuel cell environment, there is a need to determine the dependence of fuel cell catalytic activity on the precise metal alloy stoichiometry of the initial catalyst as prepared. For practical considerations, there is interest in preparing fuel cell anode catalysts on conducting carbon supports to minimize the amount of noble metal required in a working fuel cell.

We are investigating the use of single-source molecular precursors as a means to better control the elemental stoichiometry of individual metal alloy nanoparticles formed on conducting carbon supports. While others have used heteronuclear clusters to prepare ruthenium-rich Pt-Ru/carbon nanocomposites of low total metal weight percent,[4] we have used heteronuclear noncluster or cluster compounds to prepare several Pt-Ru or Pt-Mo/carbon nanocomposites having high total metal loading and a platinum atomic percent of 50% or greater. In this report, we provide (1) an overview of the synthesis and characterization of several Pt-Ru or Pt-Mo/Vulcan carbon nanocomposites, (2) the rapid synthesis of a Pt_1Ru_1/Vulcan carbon nanocomposite using microwave heating, (3) the synthesis of a Pt_1Ru_1/graphitic carbon nanofiber (GNF) nanocomposite, (4) the determination of the metal alloy stoichiometry of individual alloy nanoclusters, and, (5) preliminary results from testing selected Pt-Ru/Vulcan carbon nanocomposites as DMFC anode catalysts.

EXPERIMENTAL

The single-source molecular precursors $[(\eta^3{:}\eta^3\text{-}2,7\text{-dimethyloctadienediyl})RuCl(\mu\text{-}Cl)_2PtClL]$, **1** (L= PPh_3, PEt_3, or ethylene),[5] $[Cl_2Pt(\mu\text{-bipyrimidine})Ru(2,2'\text{-bipyridine})_2][X]_2$, **2** (X= BF_4 or PF_6),[6] $[Pt_3(PPh_2CH_2PPh_2)_3\{HgRu(\eta\text{-}C_5H_5)(CO)_2\}_2][PF_6]_2$, **3**,[7] $[Ru\{\mu\text{-}2,3\text{-bis}(2\text{-pyridyl})\text{-quinoxaline}(PtCl_2)\}_3][BF_4]_2$, **4**,[8] $[Pt(pyridine)_2[Mo(\eta\text{-}C_5H_5)(CO)_3]_2$, **5**,[9] $[Pt(1,5\text{-cyclo-octadiene})(Me)[Mo(\eta\text{-}C_5H_5)(CO)_3]$, **6**,[10] $[Pt_3(PPh_2CH_2PPh_2)_3Mo(\eta\text{-}C_5H_5)(CO)][BPh_4]$, **7**,[11] where prepared by literature procedures, modifications of literature procedures, or by novel methods. Carbon supports included Vulcan™ Carbon XC-72R (Cabot Corporation) or GNFs prepared using published procedures.[12]

Metal alloy/carbon nanocomposites were prepared by depositing single-source molecular precursors from a solution onto the appropriate carbon support through evaporation of the solvent. Multiple depositions were sometimes employed. Thermal degradation of the deposited molecular precursors typically occurred in reactive [air (up to 350°C) and/or getter gas (350-650°C)] or inert [nitrogen (650-700°C)] gaseous environments. Thermal treatments were conducted either in a tube furnace using gas flow rates typically of 150 mL/min and heating rates typically of 15°C/min or in a microwave oven (Sharp Corporation, Model R-2M52B) operating at 2.45 GHz with a fixed power level of 600 Watts. Samples prepared by microwave heating were contained in a vial surrounded by a thermal bath of Vulcan carbon. Chemical microanalysis was performed by Galbraith Laboratories, Knoxville, TN.

Low-resolution TEM micrographs were obtained using a Philips CM20T transmission electron microscope operating at 200 kV and equipped with an EDAX detector, while HR-TEM micrographs and on-particle EDS spectra were obtained at ORNL using a Philips CM200FEG

TEM operating at 200 kV and equipped with an Oxford light element EDS detector and an EMiSPECT Vision data acquisition system. Powder XRD scans were obtained on a Scintag X1 diffraction system.

RESULTS

As shown in Table I, complexes **1** (L=C_2H_4), **2** (X=BF_4), **3**, and **4** which have Pt/Ru metal stoichiometries of 1:1, 1:1, 3:2, and 3:1, respectively, serve as single-source molecular precursors for Pt-Ru/Vulcan carbon nanocomposites having metal alloy fcc lattice constants consistent with those observed for bulk Pt-Ru alloys containing the same respective Pt/Ru metal ratios. These nanocomposites have metal loadings of 25-39 weight percent and metal alloy nanoparticle average diameters of 2.7-7.5 nm (as volume-weighted average diameters determined from XRD peak widths) or 2.6-5.7 nm (as number-averaged diameters determined from TEM micrographs). Only monomodal histograms of metal alloy particle sizes are observed.

Table I. Analysis of Selected Pt-Ru/Vulcan Carbon Nanocomposites

Metal Alloy Composition	*Molecular Precursor*	*Total M wt. %*	*Ave. Dia. (nm) (XRD/TEM)*	*fcc* a_{obs} *(Å)*	*fcc* $a_{expected}$ *(Å)*
Pt_1Ru_1	**1** (L=C_2H_4)	39	2.7/2.6	3.858(6)	3.864
Pt_1Ru_1	**2** (X=BF_4)	33	4.2/4.3	3.86(1)	3.864
Pt_3Ru_2	**3**	25	7.5/3.9	3.875(2)	3.876
Pt_3Ru_1	**4**	37	6.7/5.7	3.911(1)	3.895

As shown in Table II, complexes **5**, **6**, and **7** which have Pt/Mo metal stoichiometries of 1:2, 1:1, and 3:1, respectively, serve as single-source molecular precursors for Pt-Mo/Vulcan carbon nanocomposites having bulk metal analyses consistent with the Pt-Mo content of the respective molecular precursor. The value of the fcc lattice constants observed for these alloy nanocomposites is not a reliable indicator of Pt/Mo composition due to the very similar atomic radii of Pt and Mo. Full-profile Rietveld refinement of the powder XRD scans of these pure nanocomposites reveals best convergence at Pt/Mo ratios near to the metal content of the molecular precursors. These nanocomposites have metal loadings of 43-58 weight percent and metal alloy nanoparticle average diameters of 3.9-12.2 nm (as determined from XRD peak widths) or ca. 3.5 nm (as determined from TEM micrographs). Only monomodal histograms of metal alloy particle sizes are observed.

Table II. Analysis of Selected Pt-Mo/Vulcan Carbon Nanocomposites

Metal Alloy Composition	*Molecular Precursor*	*Total M wt. %*	*Ave. Dia, (nm) (XRD/TEM)*	*fcc* a_{obs} *(Å)*	*Pt:Mo Ratio by ICP-OES*
Pt_1Mo_2	**5**	58	12.2/3.5	3.9144(1)	0.5
Pt_1Mo_1	**6**	52	3.9/...	3.9183(1)	0.9
Pt_3Mo_1	**7**	43	4.6/3.4	3.9124(1)	2.9

Deposition of molecular precursor **1** (L=C_2H_4) having a Pt:Ru stoichiometry of 1:1 onto Vulcan carbon followed by microwave irradiation under appropriate gaseous atmospheres over a total heating period of less than 60 seconds gives the expected Pt_1Ru_1/carbon nanocomposite. A TEM micrograph of one such nanocomposite is shown in Figure 1. HR TEM micrographs reveal lattice fringes on the Pt_1Ru_1 particles consistent with a 1:1 alloy composition. A histogram of PtRu nanoparticle diameters reveals an average nanocluster diameter of 3.2 nm with a standard deviation of 0.66 nm and a size distribution of only ca. 1.4 nm at full-width-at-half-height. The Pt_1Ru_1 nanoclusters give a diffraction pattern consistent with a fcc cell exhibiting broad peaks as expected from the small average particle size of the Pt_1Ru_1 nanoclusters. Peak positions give a fcc lattice parameter of 3.867 Å, as expected for a 1:1 Pt:Ru alloy (see Table I).

Pt_1Ru_1 nanoclusters can also be formed on GNF carbon supports using complex **1** (L= C_2H_4) as a single-source molecular precursor. Deposition of this precursor onto a GNF support followed by the appropriate thermal treatment gives a Pt_1Ru_1/GNF nanocomposite, as shown in Figure 2. The metal alloy nanocrystals are highly dispersed on the GNF support.

The on-particle Pt:Ru metal stoichiometry of several Pt-Ru/Vulcan carbon nanocomposites prepared from single-source molecular precursors has been determined by EDS measurements using HR-TEM(FEG) microscopy. Pt:Ru atomic ratios obtained as raw data were corrected for an apparent loss of Ru from the outermost layer of the individual particles. A plot of these corrected Pt:Ru atomic ratios for a number of individual alloy particles of one such sample is shown in Figure 3. The major contribution to the experimental uncertainties shown is the error associated with the counting statistics of the detector.

Figure 1. TEM micrograph of a Pt_1Ru_1/Vulcan carbon nanocomposite prepared by microwave heating.

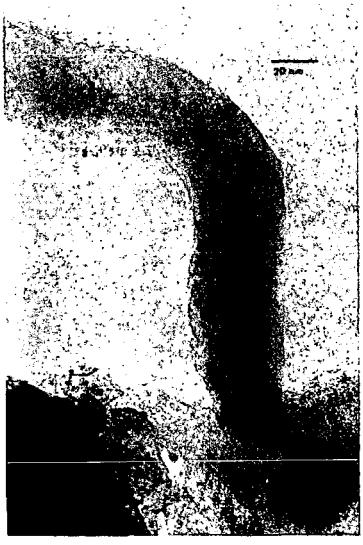

Figure 2. TEM image of a Pt_1Ru_1/GNF nanocomposite prepared using **1** ($L=C_2H_4$) as a single-source precursor for the alloy nanoclusters.

Such on-particle EDS measurements typically indicate that the Pt:Ru atomic ratio of individual metal alloy particles fall within one or two standard deviations of the bulk Pt:Ru elemental stoichiometry. As shown in Table III, the calculated weighted average of Pt:Ru atomic ratios determined from individual alloy nanoclusters within four different alloy/Vulcan carbon nanocomposites fall close in value to the bulk alloy stoichiometry as determined by chemical microanalysis. The experimental uncertainty of alloy compositions determined by chemical microanalysis has not been determined.

Selected Pt-Ru/Vulcan carbon nanocomposites prepared using complexes of type **1** or **2** as single-source molecular precursors have been tested as anode catalysts in DMFCs. Details of these testing procedures will be presented elsewhere. One such Pt_1Ru_1/Vulcan carbon nanocomposite exhibited a higher activity for methanol oxidation at open circuit and at low current densities than did a comparable commercial catalyst, while another Pt_1Ru_1/Vulcan carbon nanocomposite out-performed a comparable commercial catalyst at all higher current densities.

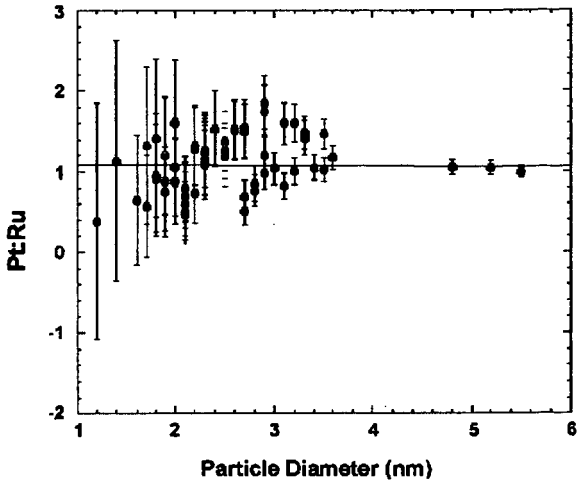

Figure 3. Corrected Pt:Ru atomic ratios for individual metal alloy nanoparticles as a function of nanoparticle size.

Table III. Comparison of Pt:Ru Atomic Ratios Determined by Chemical Analysis and by On-Particle EDS Analysis

Alloy/Vulcan C Nanocomposite	D_{TEM} *(nm)*	D_{EDS} *(nm)*	*Chemical Analysis (Pt_xRu_y)*	*Average EDS (Pt_xRu_y)*
Pt_1Ru_1	3.4 (0.9)	2.6 (0.8)	1.08	1.11 (0.03)
Pt_1Ru_1	-----	2.4 (0.4)	----	1.00 (0.06)
Pt_1Ru_1	2.6 (0.9)	3.0 (0.8)	0.90	0.88 (0.04)
Pt_3Ru_1	5.7 (3.1)	3.2 (0.7)	3.20	2.83 (0.11)

DISCUSSION

Seven heteronuclear noncluster or cluster complexes have been successfully used as single-source molecular precursors for the preparation of Pt-Ru or Pt-Mo/Vulcan carbon nanocomposites in which the metal stoichiometry of the molecular precursor provides significant control over the metal content of the resulting binary metal alloy nanoclusters. Thermogravimetric analysis of the thermal decomposition of the heptanuclear precursor **3** reveals a single mass-loss event corresponding to loss of the mercury content of the precursor. This result indicates that volatile main group metals can serve as bridging atoms in cluster precursors without being incorporated stoichiometrically into the resulting alloy nanocluster. In addition, this synthetic strategy can be used to prepare metal alloy/Vulcan carbon nanocomposites having high metal loading while maintaining relatively small average particle sizes for the alloy phase. Independent determination of the metal stoichiometry of metal alloy nanoclusters using full-profile Rietveld analysis of XRD patterns is possible and is typically reliable to within a 5 weight % variation of the content for each metal.

Pt_xRu_y/Vulcan carbon nanocomposites can be prepared very rapidly (<1 min) from deposited single-source molecular precursors using microwave heating of the conductive, particulate support. Normal thermal processing of deposited precursors to give binary metal alloy/Vulcan carbon nanocomposites using tube furnace heating requires typically 2-4 hours of thermal treatment. In addition to the rapid formation of the nanocomposite, microwave heating apparently minimizes metal diffusion on the carbon support to afford metal alloy nanoclusters having more narrow particle size distributions. The general scope of this synthetic method is being investigated.

The successful formation of Pt_xRu_y/GNF nanocomposites using a single-source molecular precursor is a unique method for obtaining metal alloy nanoclusters on a support having defined structural variety. GNFs can be prepared in which the graphite planes are oriented parallel, perpendicular, or in a herringbone pattern relative to the long axis of the carbon nanofiber. Growth of metal alloy nanoclusters on such ordered carbon supports provides an opportunity to study metal nanocluster-carbon matrix effects and DMFC activity as a function of the atomic and electronic structure of the carbon support. Such studies are under active investigation.

A critical factor in evaluating the practicality of preparing metal alloy nanoclusters by any synthetic method is the direct determination of the metal stoichiometry of individual alloy nanoparticles. By using HR-TEM(FEG) techniques, the metal stoichiometry of individual Pt-Ru alloy nanoclusters has been determined. Preliminary data indicate that metal alloy nanocluster composition is controlled to a high degree by the metal stoichiometry of the single-source precursor used in the synthesis. Further study of truly on-particle metal analysis will explore the general validity of this synthetic method. The observation of a partial loss of Ru during these on-particle analyses was unexpected. Interestingly, the extent of this Ru loss is dependent on alloy particle size and can usually be corrected for by assuming Ru loss from only the outermost unit cell thickness of the metal nanocluster. Due to the known volatility of ruthenium oxides, these results are consistent with the known presence of oxidized Ru species on the surfaces of Pt-Ru nanoparticles.[13] More detailed confirmation of this observation is anticipated. On-particle analysis of the metal alloy stoichiometry of the Pt-Mo/Vulcan carbon nanocomposites mentioned above (as well as others) is also under investigation.

CONCLUSIONS

Metal alloy/carbon nanocomposites can be formed using single-source molecular precursors to provide considerable control of the metal stoichiometry of the resulting binary metal nanocluster phase. Rapid thermal treatment using microwave heating affords metal alloy/carbon nanocomposites in which the metal nanoclusters have relatively narrow particle size distributions. True on-particle metal stoichiometries can be measured using HR-TEM(FEG) techniques; however, a correction for metal loss possibly due to the presence of surface oxidized species might be necessary for very small alloy particles. Study of the general scope of using this synthetic strategy to prepare binary, ternary, or higher order metal alloys is underway.

ACKNOWLEDGMENTS

Research support provided by the U.S. Army Research Office under grant numbers DAAH04-95-1-0146, DAAH04-96-1-0179, DAAH04-96-1-0302 and DAAG55-98-1-0362 is gratefully acknowledged by C.M.L. On-particle EDS and HR-TEM measurements performed at Oak Ridge National Laboratory were supported by the Shared Research Equipment (SHaRE) User Facilities at ORNL under contract DE-AC05-76OR00033 and by the U.S. Department of Energy under contract DEAC0596OR22464 with the Lockheed Martin Energy Research Corporation.

REFERENCES

(1) Hamnett, A. *Catal. Today* **1997**, *38*, 445.
(2) Reddington, E.; Sapienza, A.; Gurau, B.; Viswanathan, R.; Sarangapani, S.; Smotkin, E. S.; Mallouk, T. E. *Science* **1998**, *280*, (5370), 1735.
(3) Grgur, B.; Zhuang, G.; Markovic, N.; Ross, P. N. *J. Phys. Chem. B* **1997**, *101*, 3910.
(4) (a) Nashner, M. S.; Frenkel, A. I.; Somerville, D.; Hills, C. W.; Shapley, J. R.; Nuzzo, R. G. *J. Am. Chem. Soc.* **1998**, *120*, 8093. (b) Hills, C. W.; Nashner, M. S.; Frenkel, A. I.; Shapley, J. R.; Nuzzo, R. G. *Langmuir* **1999**, *15*, 690.
(5) Severin, K.; Polburn, K.; Beck, W. *Inorg. Chim. Acta* **1995**, *240*, 339.
(6) Sahai, R.; Rillema, D. P. *Inorg. Chim. Acta* **1986**, *118*, L35.
(7) King, W. D.; Lukehart, C. M. *J. Cluster Sci.* **1998**, *9*, 107.
(8) Rillema, D. P.; Sahai, R. *J. Chem. Soc., Chem. Commun.* **1986**, 1133.
(9) Braunstein, P.; Dehand, J. *J. Organometal. Chem.* **1970**, *24*, 497.
(10) Fukuoka, A.; Sadashima, T.; Endo, I.; Ohashi, N.; Kambara, Y.; Sugiura, T.; Miki, K.; Kasai, N.; Komiya, S. *Organometallics* **1994**, *13*, 4033.
(11) Ferguson, G.; Lloyd, B.; Puddephatt, R. J. *Organometallics* **1986**, *5*, 344.
(12) Nemes, T.; Chambers, A.; Baker, R. T. K. *J. Phys. Chem. B* **1998**, *102*, 6323.
(13) Rolison, D. R.; Hagans, P. L.; Swider, K. E.; Long, J. W. *Langmuir* **1999**, *15*, 774.

SELECTIVE CATALYTIC OXIDATION OF CO IN H_2 FOR FUEL CELL APPLICATIONS

Olga Korotkikh and Robert Farrauto
Engelhard Corporation
101 Wood Avenue
Iselin, New Jersey 08830-0770

KEYWORDS: selective oxidation of CO; PEM fuel cells; monoliths

ABSTRACT

A critical issue for the PEM fuel cell is the ability to delivery clean H_2 to the anode electrode the kinetics of which are greatly hindered by traces of CO present from the hydrocarbon steam reforming and water gas shift processes. A technology receiving much attention is the selective oxidation of CO to CO_2. Ideally the catalyst must selectivity oxidize about 1% (10,000 ppm) CO to less than 5 ppm without oxidizing any of the 30-70% H_2 present.

This paper will describe performance results of a newly developed catalyst for selective oxidation of CO for PEM fuel cell applications. The effect of space velocity, concentrations of CO, O_2/CO ratios and temperature on activity and selectivity will be presented.

INTRODUCTION

Development of the proton exchange membrane (PEM) fuel cell has been considerable during the last 10 years advancing the commercial possibilities for generating clean and efficient power for stationary and mobile source applications (1, 2). The system operates at about 70-80°C using H_2 as the anode fuel. Given the extensive infrastructure existing for natural gas (stationary source applications) and gasoline (mobile source) these are the preferred sources of H_2. The production of clean H_2 for the chemical industry from hydrocarbon feeds (3) is accomplished by a series of catalytic steps including desulfurization, steam reforming, water gas shift and CO removal by either selective oxidation, methanation or pressure swing absorption. All of these technologies are now being reviewed for possible use in the fuel cell.

In the early 1960's Engelhard developed and commercialized the Selectoxo™ catalyst and process for H_2 plants (4-6). The heart of this technology is a highly selective catalyst, which oxidizes up to 10,000 ppm CO without significantly oxidizing the 70% H_2 (dry) present. CO levels were reduced to less than 5 ppm under steady state conditions (50°C, 10,000 h^{-1} and 200-400 psig). The Selectoxo™ system was located downstream from the CO_2 and H_2O scrubber. For fuel cell applications the catalyst must operate at much higher space velocities at temperatures above about 90°C at ambient pressure in the presence of large amounts of CO_2 and H_2O. Furthermore, it must be designed for transient operation since power demands will vary considerably depending on the application. A large consumption of H_2 is undesirable since it decreases power generation and complicates heat management. Therefore, having a catalyst with high selectivity is critical.

EXPERIMENTAL

The Selectoxo™ catalyst contains 0.5% Pt supported on γ-alumina 1/8 inch tablets promoted with a base metal oxide. The alumina is impregnated with salts of Pt and base metal oxide, dried and calcined. The composition of the new catalyst has been modified and prepared as a powder suitable for deposition onto a monolith structure. We call this material monosel. The cordierite monolith is 400 cells per square inch and is dipped into a water slurry of the catalyst, dried and calcined. Typically washcoat loading of about 1.5 g/in^3 were obtained. For direct testing of powdered catalysts they were pressed and crushed into particles 40-60 microns in size.

The test gas contained between 1000 and 5000 ppm CO, 20 % H_2, 10% H_2O and varying O_2 to CO ratios with the balance N_2. When powders were tested they were diluted in a 1:2 ratio of catalyst to quartz. Monoliths were wrapped with insulation and fitted into the 1 inch ID quartz reactor. A control thermocouple was positioned in the inlet section of the catalyst bed.

The consumption of CO and generation of CO_2 was measured with a California Analytical Instruments infrared gas analyzer. O_2 consumed was measured with a Rosemount electrochemical analyzer. The generation of hydrocarbons was monitored with a Rosemount Analytical flame ionization analyzer, but under the conditions of these experiments here none was ever detected.

RESULTS

The comparison of powdered Pt/Al_2O_3 with monosel, at equal concentrations of Pt, at 90 and 150°C and O_2/CO ratios of 0.5 and 0.75 are shown in Table 1. The powder volumetric space velocity (VHSV) is 120,000 h^{-1}. The presence of the promoter metal oxide in monosel significantly increases the CO activity and conversion (X_{CO}) while maintaining excellent selectivity of O_2 for CO ($X_{O2\ for\ CO}$). Under all conditions the Pt/Al_2O_3 never obtains high CO conversions relative to monosel under realistic operating temperatures up to 150°C.

Figures 1 and 2 demonstrate the influence of oxygen excess above stoichiometric at different temperatures and space velocities for monosel deposited on a monolith. At 90°C and a VHSV of 20,000 hr^{-1} increasing oxygen improves the activity of the catalyst, but the selectivity decreases. At O_2/CO = 1 conversion of CO reaches 100% with the O_2 selectivity for CO about 50% (Figure 1).

Raising the temperature to 150°C (Figure 2) at a monolith VHSV of 80,000 hr^{-1} gives almost 100% CO and O_2 conversions at O_2/CO = 1.5. The O_2 selectivity for CO is 33%.

The results for 2000 and 5000 ppm CO are presented in the Table 2. At 90°C increasing the CO concentration from 2000 to 5000 ppm, under stoichiometric conditions (O_2/CO = 0.5), shows a constant CO conversion of 69%. The selectivity of O_2 for CO improves from 66 to 77.6%. Increasing the O_2/CO ratio to 0.75 increases CO conversion to almost 97% with similar selectivities of 64 vs. 68%. At O_2/CO = 1.0 the CO conversion reaches 100% while the selectivity decreases to about 50%. At 150°C 100 % conversion of CO is achieved at both 2000 and 5000 ppm at an O_2/CO = 1 with selectivities of about 50%. As the O_2/CO conversion is decreased from 0.75 to 0.5 the CO conversion decreases, but the total O_2 conversion remains almost 100% with an O_2 selectivity for CO of about 58% for 2000 ppm and 65% at 5000 ppm.

CONCLUSIONS

1. At 90°C, VHSV = 20,000 hr^{-1} and O_2/CO = 1 conversion of CO is about 100% with the O_2 selectivity for CO about 50%.
2. At 150°C, VHSV = 80,000 hr^{-1} and O_2/CO = 1.5 conversion of CO is about 100% with the O_2 selectivity for CO about 33%.
3. CO conversions of 100 % are achievable at O_2/CO = 0.75 (at 5000 ppm) and 1 (at 2000 ppm).
4. At 150°C, 100% CO conversion is obtained at an O_2/CO = 1. Selectivity of O_2 for CO is about 50%.

REFERENCES

(1) G. Acres, J. Frost, G. Hards, R. Potter, T. Ralph, D. Thompson, G. Burstein and G. Hutchins, Catalysis Today 38 (1997) 393
(2) R. Singh, Chemical Engineering Progress, 95(3),59 (1999)
(3) M. Twigg, Catalyst Handbook, Wolfe Publishers, London, England, 1989; Chapters 4-7
(4) M. Brown and A. Green, US 3,088,919 (May 7, 1963)
(5) J. G. Cohn, US 3,216,782 (November 9, 1965)
(6) M. Brown, AS. Green, J.G. Cohn and H. Anderson, Ind. Eng. Chem. 52(10)841(1960)

Table 1
Comparison of Powdered Pt/Al_2O_3 and Monosel Catalysts
(fraction 40-60 μ, VHSV~120,000 hr^{-1})

#	TEST CONDITIONS	Monosel		Pt/Al_2O_3	
		Xco, %	Xo_2 for CO, %	Xco, %	Xo_2 for CO, %
1.	At 90°C, O_2/CO=0.5	51	78	13.2	82
2.	At 90°C, O_2/CO=0.75	90	65	12.7	66.2
3.	At 150°C, O_2/CO=0.5	52.7*	61.6*	26.8	56.7

*) data were obtained with monosel on a monolith at a VHSV = 80,000 h^{-1}

Table 2
Effect of CO Concentration on Monosel Performance

#	TEST CONDITIONS	2000 ppm CO			5000 ppm CO		
		Xco, %	Xo_2, %	$Xo_{2\ for\ CO}$ %	Xco, %	Xo_2, %	$Xo_{2\ for\ CO}$ %
1	At 90°C, O2/CO = 0.5	68.9	98.1	66.1	69.0	87.0	77.6
2	At 90°C, O2/CO = 0.75	96.8	97.5	64.4	100	99.7	68.1
3	At 90°C, O2/CO = 1.0	100	99.6	50.7	-	-	-
4	At 150°C, O2/CO = 1.0	100	99.7	50.6	100	100	50.9
5	At 150°C, O2/CO = 0.75	90.6	99.5	57.8	97.5	100	64.6
6	At 150°C, O2/CO = 0.5	61.2	99.2	57.7	65.6	99.4	64.6

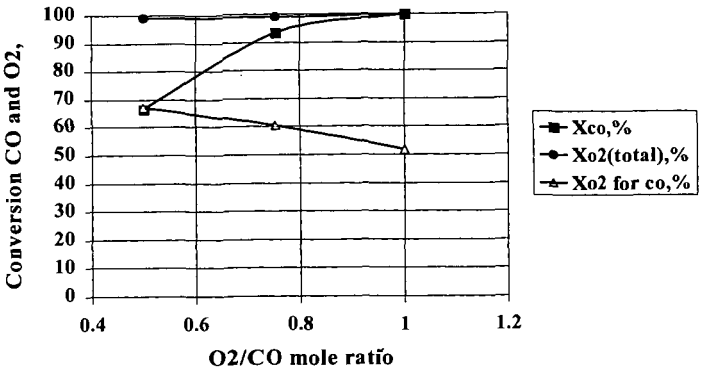

Fig. 1. Monosel on monolith activity and selectivity depends on O_2/CO (90°C, 1,000 ppm CO, 20% H_2, 10% H_2O, VHSV=20,000 hr^{-1})

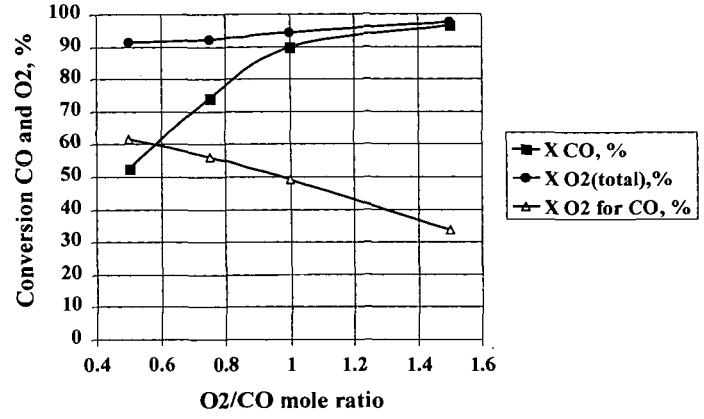

Fig. 2. Monosel on monolith activity and selectivity depends on O_2/CO mole ratio (150°C, 1,000 ppm CO, 20% H_2, 10% H_2O, VHSV=80,000 hr^{-1})

CATALYTIC REACTOR FOR IMPROVED CARBON MONOXIDE CONTROL WITHIN THE HYDROGEN FEED STREAM OF A PEM FUEL CELL

J. K. Hong, M. A. Inbody, J. C. Hedstrom, J. I. Tafoya and N. E. Vanderborgh

Fuel Cell Engineering
ESA-EPE, Los Alamos National Laboratory
Los Alamos, NM 87545 USA

KEYWORDS: PEM Fuel Cell, Carbon Monoxide Removal, Preferential Oxidation

INTRODUCTION

The proton exchange membrane (PEM) fuel cell is considered a promising energy conversion device, based on environmental and energy efficiency advantages.[1] Even though hydrogen-air PEM fuel cell systems have been considerably improved over the past two decades, direct hydrogen systems present challenges for wide-spread automotive applications.[2] The advantage of contemporary fuel cells becomes compromised if their deployment requires a new complicated hydrogen infrastructure. On-board reforming of contemporary clean fuels is an alternative approach for supplying hydrogen for these PEM fuel cell vehicles. Fuels for such clean vehicles include natural gas, reformulated gasoline, alcohols, ethers and other hydrocarbons.[3] Chemical conversion of these fuels using either partial oxidation or steam reforming generates a hydrogen stream diluted with carbon dioxide, nitrogen, steam and various contaminants including carbon monoxide. In the presence of CO stack efficiency is compromised, so fuel processing hardware must include features to manage impurities. The Fuel Cell Engineering Team at Los Alamos has pioneered successful approaches for gas cleanup. The effort combines catalyst development with novel reactor designs, perhaps suitable for future automotive applications. These large-scale experiments are supported by micro-scale investigations of catalyst performance. One important focus is to develop new approaches useful for achieving transient behavior of contemporary passenger vehicles. Such a gas clean-up device is termed a PROX (preferential oxidation) converter, even though oxidation is but one of the several reactions necessary for successful fuel cell system hardware.[4]

EXPERIMENTAL

Both micro-scale and larger (50-kW) device experiments are described. The micro-scale test stand permits catalyst evaluation using test gas mixtures selected to replicate operation with a variety of fuels, such as might result using a "multifuel reformer". For instance a simulated gasoline reformate might consist of 36% H_2, 17% CO_2, 28% N_2 and 17% H_2O. Small quantities of contaminants are added to such mixtures and then the mixtures are blended with controlled quantity of air. The resulting mixture is transferred to a volume of catalyst. Analytical tools including gas chromatography and gas chromatography mass spectrometry evaluate catalyst effectiveness. Considerable attention is paid to the fluid dynamics of the experiments to assure uniform gas composition, inlet temperature and laminar flow. These reactors can be either adiabatic ("hot spot") or isothermal, depending upon test conditions. The micro-scale reactor is used to determine performance data on a variety of catalyst types and to investigate techniques for effective control of other contaminants such as NH_3 or H_2S.

The large scale experiments replicate conditions used for microscale testing. One PROX reactor with three series, adiabatic sections is shown in Figure 1. Each section incorporates features to homogenize the gas mixture, to control entrance temperature and to assure laminar flow into the catalyst volume. Heat flow is primarily through convective processes. The overall large-scale design includes features designed to meet safety standards for hydrogen operation and to permit convenient exchange of catalyst samples and alteration of other internal features. The large experiment also permits dynamic measurement of gas composition and temperature within the catalyst volume to measure either "down the channel" or spatial (radial) data. Such information has proven very useful to confirm modeling predictions.

Experiments are computer controlled. The electronic systems sets appropriate reactant flows and controls temperatures and pressure. Importantly the data system also continuously evaluates for experimental faults such as hydrogen leaks and acts to terminate tests when certain release rates are reached.

RESULTS

Preferential oxidation depends upon rapid CO oxidation even in the presence of far larger mole fractions of hydrogen. The intent is to remove the CO with only small concurrent hydrogen oxidation. Although there have been significant improvements in anode fuel cell catalysts to increase CO tolerance, most contemporary systems dictate that inlet CO concentration should be set at below 30 ppm.

The removal rate of CO through oxidation on a platinum catalyst in the microscale reactor depends on the reaction temperature, as shown in Figure 2. The highest conversion of CO, or the lowest outlet CO concentration, is attained at 220°C and by further increase in reaction temperature leads to high outlet CO concentration. Additional experimental results support that increased CO found at temperatures exceeding 220°C is attributed to the rapid hydrogen oxidation at these temperatures which depletes oxygen and concurrent production of CO by the reverse shift reaction.

The inlet oxygen concentration was varied as shown in Figure 3 and the effect on CO control was measured. The outlet CO concentration was determined at 220°C and 260°C, respectively. At both reactions temperatures, oxygen is rapdly depleted by reaction with CO and H_2 at oxygen stoichiometry as high as to 3.0 based on the CO concentration. In this case a stoichiometry value of 1.0 is defined, for example, when the number of moles of oxygen is 0.5 that of the moles of CO—for example 250 ppm of oxygen, as a constituent of air, is added to a stream containing 500 ppm of CO. From Figure 3, an increase in oxygen stoichiometry at 220°C is found to be effective in reducing outlet CO concentration, while concurrent hydrogen loss is significant with the increase in oxygen stoichiometry at 260°C.

Figure 4 shows PROX device performance as a function of overall oxygen stoichiometry, summed for each of the stages based on the inlet CO content. Figure 4 shows results for an inlet concentration of 20,000, using three stages. The device output ranges from a CO concentration of 45 ppm to well below 20 ppm, depending upon conditions. In general these hydrogen-mixture cleanup devices perform as designed over a wide range of flow rates and inlet carbon monoxide concentrations.

Transient performance, CO control during a rapid change in either CO concentration or flow rate, can be achieved by either precise control of reactant flows or through intelligent catalyst design, or by a combination of these approaches. Transient performance at the 50-kW flow level during an event when a normal 8,000 ppm CO flow stream is changed to a 12,000 ppm CO gas stream. With appropriate alteration of the air injection rate, the device shows no performance degradation.

Other contaminants than carbon monoxide are troublesome. Some compounds will not influence PROX performance but can degrade stack performance. Others tend to poison the catalyst surfaces contained in the PROX device. The hydrogen generators also, at times, generate colloidal carbon ("soot"), a contaminant that can adversely influence PROX performance.

CONCLUSIONS

Gas cleanup-technology is an essential operation in on-board fuel processing systems. Today transportation fuel specifications are being adjusted to meet increasingly demanding environmental emission regulations. Cleaner fuels, especially low sulfur fuels, are more easily processed as hydrogen sources. New fuels, such as dimethyl ether, dimethoxy methane and gas-to-liquid ("Fischer Tropsch") compounds are additional steps along the pathway towards very clean vehicles. All of these clean fuels are also attractive candidates for fuel cell vehicles.

Although there has been considerable progress in gas clean-up technology, challenges remain. Such devices must address automotive applications with special requirements for low initial cost, ruggedness and reliability. Transients are also challenging, especially the transient during start-up of the vehicle. In these experiments the gases are

added to the catalyst at a temperature exceeding the "light-off" temperature. Special designs will be necessary to initiate operation within the 20 seconds, or so requirement, following a cold-soak period. Even so, much of the necessary technical design challenges for these devices have been successfully demonstrated.

REFERENCES

1. Nicholas E. Vanderborgh and Michael A. Inbody, "The Future of Fuel Cell Vehicles", presented at the 3rd Annual Symposium, Society of Electric Vehicle, Kawasaki, JP, December 2, 1998; LA-UR# 98-5858.
2. Firtz R. Kalhammer, Paul R. Prokopius, Vernon Roan and Gerald E. Voecks, "Status and Prospects of Fuel Cells as Automotive Engines, A Report of the Fuel Cell Technical Advisory Panel", prepared for the States of California Air Resources Board, Sacramento, CA, July 1998.
3. S. Ahmed, M. Krumpelt, R. Kumar, S. H. D. Lee, J. D. Carter, R. Wilkenhoener and C. Marshall, "Catalytic Partial Oxidation Reforming of Hydrocarbon Fuels", presented at Fuel Cell Seminar, Palm Springs, CA, November 1998.
4. Nicholas E. Vanderborgh, James C. Hedstrom, Jose Tafoya and Michael A. Inbody, "Preferential Oxidation for Improved Performance of PEM Fuel Cell Anode Feeds", presented at the Electrochemial Society Meeting, Seattle, Washington, May 4,1999.

ACKNOWLEDGEMENT

This work is supported by the United States Department of Energy, through its Office of Advanced Automotive Technologies.

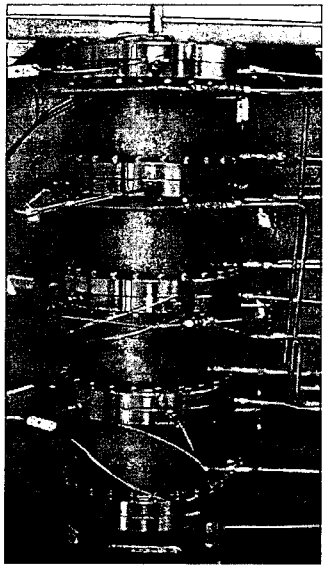

Fig. 1 The 50kWe modular PROX assembled at the PROX test facility.

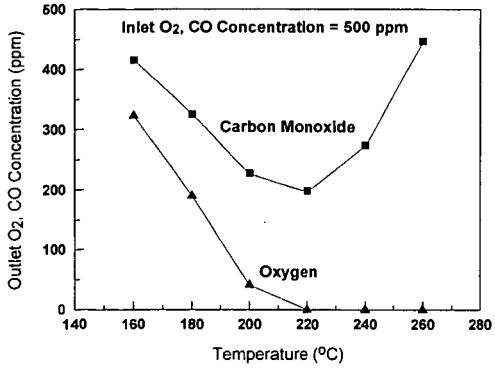

Fig. 2 The measured outlet oxygen and carbon monoxide concentrations with reaction temperature.

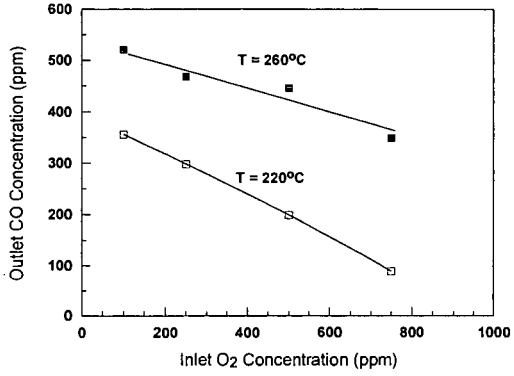

Fig. 3 The measured outlet carbon monoxide concentration as a function of inlet oxygen concentration.

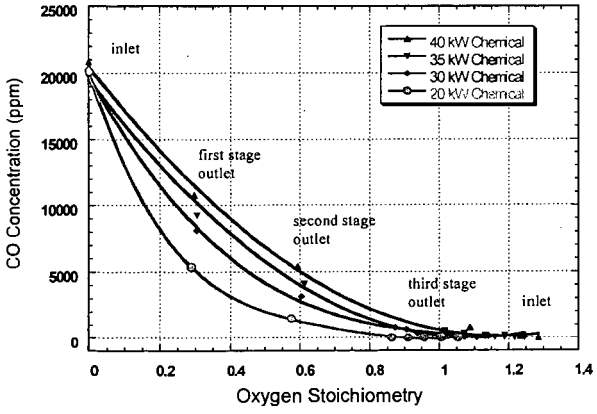

Fig. 4 PROX device performance as a function of overall oxygen stoichiometry.

COMPACT FUEL PROCESSORS FOR FUEL CELL ELECTRIC VEHICLES (FCEVs)

W. L. Mitchell, Prashant S. Chintawar, Mark Hagan, Bo-Xiong He, and S. K. Prabhu
Epyx Corporation, 15 Acorn Park, Cambridge, MA 02140

Keywords: fuel processing, fuel cell electric vehicles, reformer

Introduction

Faced with tough emission standards, auto manufacturers have started looking into technologies that offer feasible alternatives to internal combustion engines. Fuel cells offer many advantages including almost-zero emissions. Epyx Corporation, a subsidiary of Arthur D. Little, Inc., has developed a fuel-processor design that reforms hydrocarbon such as gasoline and generates hydrogen – needed to run fuel cell. In fact, Epyx is the first company ever to demonstrate a gasoline-based reformer. In addition to its lightweight and compact configuration, Epyx fuel processor operates on multiple fuels such as gasoline, ethanol, propane, and natural gas.

Background

Proprietary hybrid partial oxidation (POX) fuel processor is shown in Figure 1. The fuel processor consists of a series of catalytic beds, viz., steam reforming, high temperature shift (HTS), low temperature shift (LTS) and exhaust clean-up, operating over a wide temperature range to maximize hydrogen output. The exit CO concentration from the fuel processor is 0.2-0.5 % depending on the steam/carbon (S/C) ratio and temperature. However, for a proton exchanged membrane (PEM) fuel cell applications, the CO concentration must be below 50 ppm. Therefore, an additional CO clean-up stage called preferential oxidation (PROX) is also included. For the processing of sulfur containing fuels, the fuel processor also contains a compact desulfurization bed integrated inside the reactor vessel.

A fraction of the feedstock is combusted in the POX zone at about 700-1500 °C. The process effluent from POX zone consists of a mixture of CO, CO_2, H_2, H_2O, N_2 and residual methane. A highly active steam reforming bed holds the key to full fuel conversion and high efficiency. The POX residual methane is reformed into hydrogen in the steam reforming bed and CO is converted in the two shift reactors, viz., HTS and LTS.

Experimental

Based on the results from previous work at Epyx/A. D. Little, Inc., a fuel processing power system was designed using assumptions consistent with a light duty vehicle. The fuel processor system consists of three subsystems, viz., fuel processor, CO clean-up, and tailgas combustor. The assumptions involved in the design of the fuel processor include a use of PEM fuel cell operating at 3 atm and at a design power level of 10 kW (electric). The design power rating power corresponded to a fuel processor system that could operate on a thermal input of 45 kW.

Experimental studies were carried out to permit characterization of the entire system with regard to thermal balances, pressure balances, hydrogen purity effects, tailpipe emissions, and required control interaction. The system was operated on several conventional and alternative automotive fuels such as California Phase II reformulated gasoline (RFG), ethanol, natural gas, etc. The performance of fuel processor was quantified by measuring the conversion efficiency at a particular S/C ratio and equivalence ratio (ϕ).

To quantify the emissions from the fuel processor assembly, the exhaust product sample was connected to various analytical instruments listed below:

- Gas chromatograph equipped with a thermal conductivity detector (GC/TCD) for detection and quantification of H_2, N_2, CH_4, C_2H_2, C_2H_4, CO_2, and CO;
- Non-dispersive infra-red (NDIR) analyzer for CO and CO_2;
- Chemiluminescent NOx analyzer;
- Flame ionization detector (FID) hydrocarbon analyzer;

- Paramagnetic oxygen analyzer.

Results and Discussion

Recent efforts have focussed on incorporating advanced catalyst and heat exchanger concepts into the fuel processor design. This new generation of the design is sized to accommodate a 22 kW (electric) fuel cell power system. Experiments were conducted on this design with a variety of fuels and the fuel processor was characterized in terms of temperature and composition of each zone, operating conditions for the POX zone, and conversion efficiency.

The performance of the fuel processor measured as hydrogen efficiency with all the fuels is shown in Table 1. Hydrogen efficiency is defined on the basis of lower heating value of H_2 exiting the fuel processor to the lower heating value of the fuel fed to the unit. The extended testing of this new design indicate that advanced concepts employed have led to significant improvements in the efficiency, which exceed the 2004 Department of Energy PNGV (Partnership for New Generation of Vehicles) efficiency targets for fuel processors – currently set at 80%. It is also evident from Table 1 that such high efficiency of the fuel processor results in high fuel conversion or low slip of unconverted hydrocarbons, which assist in obtaining very low exhaust emissions. No degradation in the performance of the catalyst beds was evident after 600 h on-stream – a ramification of high fuel conversion.

Table 1. Epyx transportation fuel processor performance with various fuels

Fuel	Dry H_2 concentration* (%)	Fuel conversion (%)	Efficiency** (%)
RFG	43	98	83
Methanol	46	99	88
Ethanol	42	99	84
Natural gas	45	95	83

*: at the exit of the fuel processor
**: defined as ratio of lower heating value of H_2 at the exit to the lower heating value of the fuel fed to the fuel processor

As a first step in verifying the low emissions produced from a gasoline fed fuel processor, steady state emissions analysis was performed at the exhaust of tailgas combustor. Emission data gathered at 25 kW (thermal) input to the fuel processor show CO < 5 ppm, hydrocarbons < 4 ppm, and undetectable levels of NOx. Assuming FUD cycle with 12.5 kW (electric) average power requirement yields emissions in g/mile as shown in Table 2.

Table 2. Comparison of Epyx fuel processor emissions with California SULEV standards

Contaminant	California SULEV standard (g/mile)	Epyx fuel processor (g/mile)
CO	1.0	0.013
Hydrocarbon	0.01	0.017
NOx	0.02	0.003

These emissions are expected to reduce with modifications and tighter integration of the system.

Conclusions

Compact automotive fuel processor was designed, fabricated and tested with gasoline, natural gas, methanol, and ethanol. This design demonstrated efficiency numbers greater than PNGV 2004 targets and emissions comparable with California SULEV standards. Pathways have been identified to further improve the overall performance of the fuel processor. Detailed reaction models are being generated and validated; these models will be used in the future designs.

Acknowledgements

This work was funded by US Department of Energy, Office of the Transportation Technologies and co-funded by Illinois DCAA. Parts of this work were performed in conjunction with Plug Power LLC.

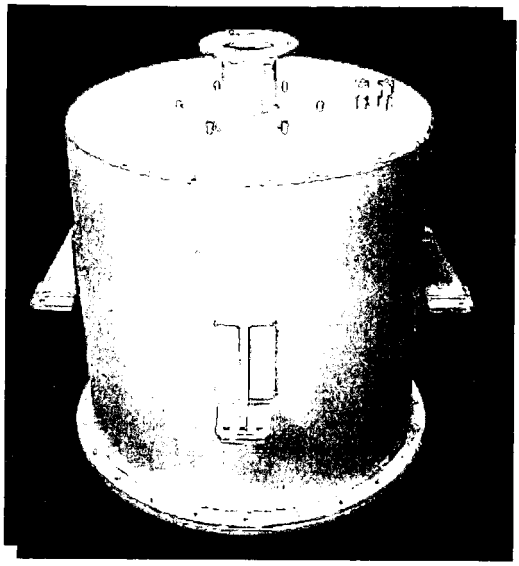

Figure 1. Epyx 22 kW (electric) multi-fuel processor

VALUE-ADDED PRODUCTS FROM THE ENLARGED WOMBAT REACTOR.

David L. Wertz, Stephen B. DuBose, Sheila Kosbab, Ashley D. Trahan, Johanna Wolf, Callie Bounds, and E. Ryan Smith, Department of Chemistry & Biochemistry and the Honors College, University of Southern Mississippi, Hattiesburg, MS 39406.

Key words: degrading tires, value-added products.

The WOMBAT process has been utilized to degrade scrap tires into several materials -- a black powder, a mat which has a shape similar to that of the original tire, fibers, steel, and highly discolored nitric acid.[1] Each of these materials is produced in large quantities, and the utilization of each is necessary to produce and environmentally acceptable and an economically useful bottom line for this method. The WOMBAT process has the potential for high through put of tires, and the tires do not require any pre-treatment. After the steel belts have been cleaved from the styrene-butadiene (SBR) matrix of the tire, the belts may be recovered from the reactor with minimal surface corrosion. Both the black powder and the SBR mats may be separated from the fibers and from each other. A schematic of the new and enlarged WOMBAT reactor is presented in Figure 1.

The chemistry of the WOMBAT process may be traced, to some extent, using x-ray fluorescence (XRF) spectrometry. The XRF experiment measures the secondary Xrays emitted by a sample using a separation technique based either on the differences in energies of the emitted Xrays or their differences in wavelengths.[2] For these experiments, a rhodium x-ray tube (operating at 35 kV and 30 ma) and a graphite monochromator were used. Shown in Figure 2 is the WDXRF spectrum of a 1" x 1" x ¼" piece of a tire. This spectrum contains several orders of the K_β and K_α wavelengths emitted by zinc (normally present in the 2-3% range in tires) which occur at λ = 1.30 Å and λ = 1.44 Å, respectively. Also noted is the K_α wavelength for sulfur (normally present in the 1.0-2.0% range in tires) at 5.37 Å.
Shown in Figure 3 is the WDXRF spectrum of the black powder recovered from the WOMBAT process. There is no K_β and K_α peaks indicative of zinc in this spectrum, indicating that the abundance of zinc in the black powder < the lower limit of detection for zinc in this sample. However, the sulfur K_α peak, at λ = 5.37 Å, is clearly discernible in this WDXRF spectrum, indicating that sulfur is retained in this powder.

In previous experiments, it has been shown that the black powder has an energy content ca. 30% higher than the typical bituminous coal and produces <1% high temperature ash. It may be co-combusted with lower energy fuels such as lignite and/or sawdust. However, because the powder retains sulfur, it may be used in processes that require vulcanized materials. Furthermore, because of its high surface area/mass ratio, the black powder also has potential for sequestering metal ions. Shown in Figure 4 is the WDXRF spectra of (a) the black powder and (b) the black powder after it had been dispersed into a solution containing copper(II) nitrate and then recovered. The latter spectrum contains large K_β and K_α x-ray peaks (at λ = 1.39 Å and λ = 1.54 Å, respectively) due to copper. Subsequent experiments have shown that most of the copper(II) sequestered onto the black powder may be removed from the powder by washing with water.

Having shown that the black WOMBAT powder will sequester copper(II) from an aqueous solution, we are investigating the sequestration properties of the powder towards other metal ions present in water, soil, and air and are also investigating its capabilities for sequestering organic moieties.

The SBR matrix, the other high carbon material recovered from the degradation of the tire, may be cleanly separated from the tire's steel belts and fibers. This SBR matrix, whose WDXRF spectrum is presented in Figure 5, contains considerable amounts of zinc, iron, and sulfur -- as evidenced by the characteristic peaks for these elements in the resulting WDXRF spectrum. This matrix has a high fuel value and produces only 3-4% HTA. In addition, as shown in the x-ray diffractogram presented in Figure 6, the HTA is principally ZnO.

The discolored WOMBAT liquid, which has a considerably reduced oxidizing powder, may be converted to inorganic nitrate salts such as potassium nitrate or ammonium nitrate. The x-ray diffractogram of the chemical product produced when the used WOMBAT liquid is reacted with potassium hydroxide is presented in Figure 7.

REFERENCES.

1. Wertz, D. L. et al., ***Am. Chem. Soc., Div. Fuel Chem.,*** 1998, 43, 796; 1998, 43, 349; 1997, 42, 741; 1995, 40, 879; 1994, 39, 815.

2. Jenkins, R., "X-Ray Fluorescence Spectrometry"; John Wiley & Sons, NY, 1988.

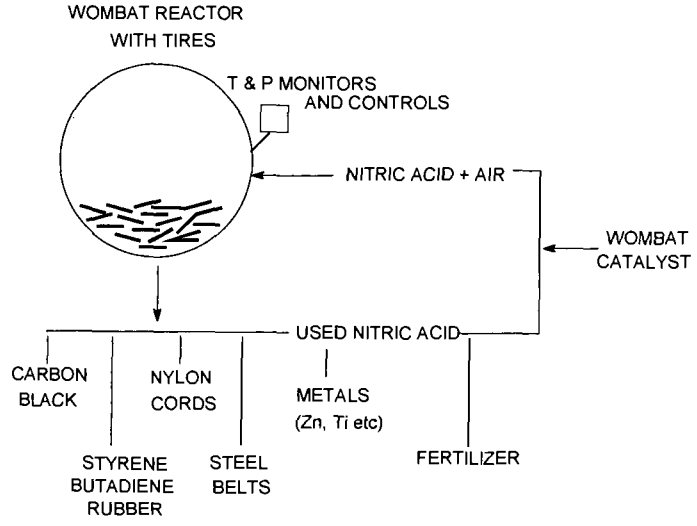

Figure 1. Schematic of new and enlarged WOMBAT reactor.

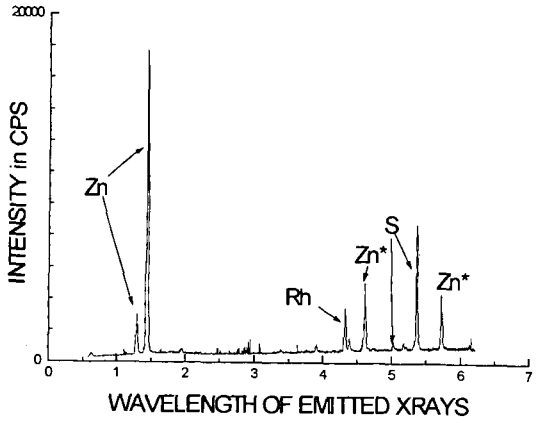

Figure 2. WDXRF spectrum of a 1" x 1" x ¼" piece of scrap tire.

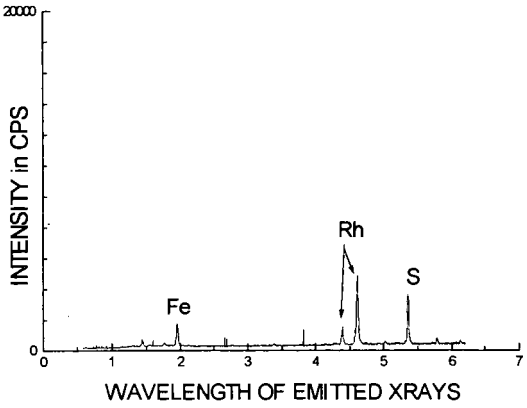

Figure 3. WDXRF spectrum of the black powder recovered from the WOMBAT reactor.

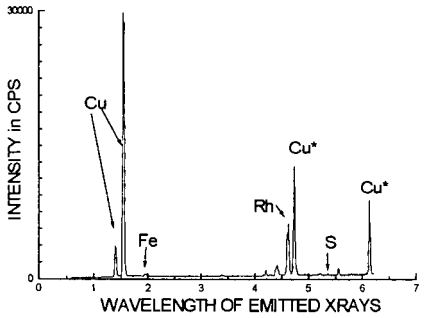

Figure 4. WDXRF spectra of the black powder prior to (circles) and after (squares) treatment with an aqueous solution containing copper(II).

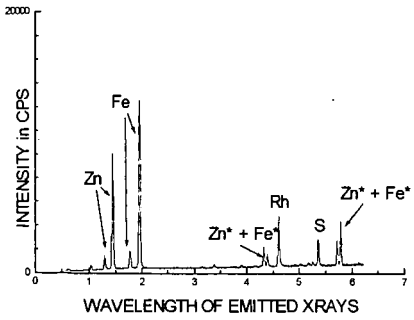

Figure 5. WDXRF spectrum of the SBR matrix recovered from the WOMBAT reactor.

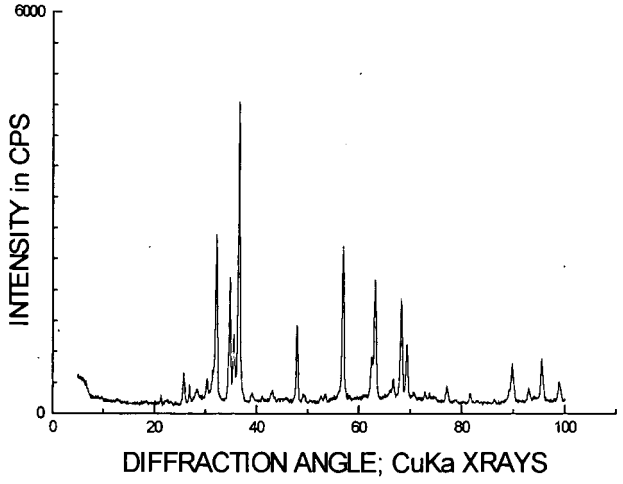

Figure 6. X-ray diffractogram of the HTA ash produced by combusting the SBR matrix.

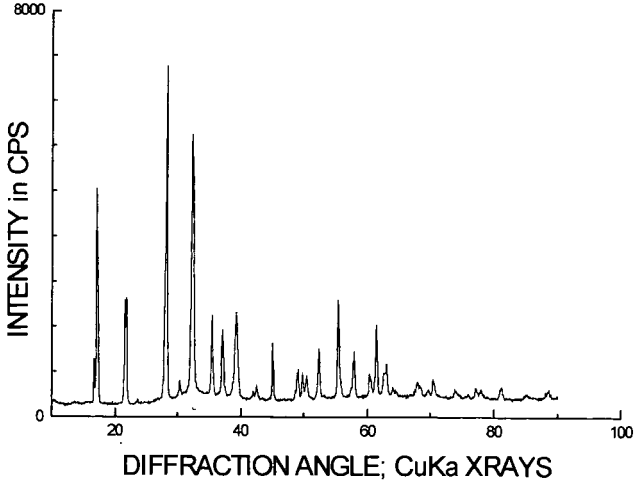

Figure 7. X-ray diffractogram of the solid produced from evaporating the mixture of "used" WOMBAT fluid and potassium hydroxide. XRD matches JCPDF 8-452, form IV ammonium nitrate.

PREOXIDATION EFFECTS ON THE ENERGETICS OF RAPID COAL PYROLYSIS

Hyok. B. Kwon
Department of Environmental Engineering
Kyungnam University, 449 Wolyoungdong Masan, 631-701 KOREA
and
Francis J. Vastola
Department of Materials Science and Engineering
Pennsylvania State University, University Park, PA 16802, U.S.A.

Keywords: rapid coal pyrolysis, preoxidation, energetics

INTRODUCTION

Thermophysical properties such as the pyroheat, specific pyroheat, and heat of pyrolysis of coal are important energetic data in design computations relating to various coal utilization processes. Moreover, these properties of coal continuously change during pyrolysis. Therefore, knowledge of the thermophysical properties of coal under conditions of rapid heating over a wide dynamic temperature range has important implications with respect to practical usage and fundamental research of coal. The endothermic heat effects during rapid coal pyrolysis have been identified qualitatively (1, 2) and quantitatively (3-5). Of particular interest in this work is the examination of the preoxidation effects on the energetics of rapid coal pyrolysis. This interest arises from the fact that mild preoxidation inevitably occurs during handling and storage prior to practical usage. This phenomenon is known as weathering and can alter the coal's calorific value, thermoplastic properties, beneficiation, coking, liquefaction, and gasification characteristics. This mild preoxidation also influence standard tests and other experimental results, and thus has important implications with respect to fundamental research on the structure and properties of coal. The objectives of this study were to determine the preoxidation effects upon subsequent pyrolysis energetics of a subbituminous coal.

EXPERIMENTAL

Apparatus. The main components of the calorimeter are the grid reactor, electrical system, and microcomputer. The microcomputer is coupled with the reactor through a voltage regulator and a multiplexed analog/digital converter for process control and data acquisition. Details of the apparatus and procedure are given elsewhere (3). The reactor is a SS (Type 315) grid which is electrically heated by a constant voltage power supply. Heating rates were controlled by an adjustable voltage regulator powered by an acid-lead battery. The low internal resistance batteries and regulator insure constant voltage at high currents (Figure 1). The SS mesh grid and a brass bar, used as a reference resistance, make up the heating circuit. The low resistance (5.17mΩ) and large mass (50g) of the reference resistor minimize the changes in resistance from the variation in temperature due to resistive heating. Therefore, the reference resistance can be assumed to be constant during the experiment. The pyrolysis temperature, defined as the temperature at the middle of the grid, is determined from a thin (50μm) chromel-alumel thermocouple. For a given constant voltage the grid temperature reaches a steady state at which the resistive heat input balances losses by heat transfer. After being held at the final steady state temperature for the desired time, the sample is cooled by turning the power off.

Calibration. A number of substances (Sn, Zn, Al; Aldrich Chemical Co., 5N) undergoing phase transitions at temperatures up to 933 K were tested (Table 1). Temperature calibration was carried out with melting temperatures of standard substances. At the same time, calorimetric calibration was carried out by using the enthalpies of fusion of substances at their temperatures.

Sample Selection. Coal samples were obtained from the Penn State coal sample bank. Proximate and ultimate analyses of the coals are provided by the Penn State coal database and are presented in Table 2.

Experimental Conditions. Experimental conditions are listed below:

1. sample size	; 6.5 ± 1.0 mg
2. particle size	; 100 microns (140 x 170 mesh)
3. drying	; vacuum dry overnight at 383 K and in situ for 10 min. at 393 K
4. duration of reaction	; 20 sec
5. final temperature	; 920 ± 20 K
6. heating rate	; 415 ± 30 K/s at 0.2 sec
7. soaking time	; 15 sec
8. data acquisition interval	; 20 ms
9. preoxidation level	; 1, 5, 10 and 24 hrs at 400 K with air in horizontal furnace

Procedure. After a thermocouple was welded to a new mesh, which was folded into a "sandwich" heating element, forming a 2.5 x 12 mm strip and connected across the electrodes, the cell was evacuated, charged with nitrogen gas, and prefired to prevent further physical and chemical change of the mesh. During the prefiring, the mesh expanded and annealed until it reached a steady state condition. Then, 5-10 mg of coal sample was loaded into the mesh. The particles had a uniform diameter of approximately 100 μm (140 x 170 US mesh). After the coal was loaded, the cell was charged with nitrogen gas. The coal was dried inside the reactor for 10 minutes at 393 K. Next, the coal-grid system was heated with a constant voltage pulse, then cooled via simple heat dissipation. The remaining grid-char runs were made.

Data Reduction. In order to derive the thermal properties from the raw data, it is necessary to follow the reduction procedure which is described below and graphed in Figure 2. The interpretation of each symbol is given in Table 3. Figure 1 shows the equivalent electrical circuit of the reactor. By measuring at 20 ms intervals, the two voltages e_s, e_r, and e_{sc}, the temperature of the system can be measured and the power input to the system, Wi, can be calculated versus time.

$$Wi = \frac{e_s e_r}{R_r}$$

The power loss from the system at a given temperature can be calculated by determining the convective and radiative heat loss versus temperature according to the expression

$$W_l = A(T_g - T_{rm}) + B(T^4_g - T^4_{rm})$$

The terms A and B can be obtained experimentally at the end of a char run by heating the system to a series of temperature and fitting the data to above equation using an iterative technique. A check can be made to ascertain whether the radiation coefficient, B, is physically valid or not hy comparing emissivity. By being able to measure the power input to the system versus time and temperature and by being able to calculate the power loss from the system versus temperature, net power absorbed by the system versus time can be calculated. From these values the integral of heat absorbed by the system versus time can be obtained. Each run would consist of three heatings, the grid alone, the coal sample in the grid, and finally the char remaining in the grid. By being able to normalize the runs to power absorbed versus temperature, the net heat absorbed by the grid, coal, and char is obtained (Figure 2d). The subtraction of the heat absorbed by the grid from that of the coal and the char runs enables the net heat requirements for heating the coal and the char to the final temperature to be obtained. The heat of pyrolysis is arrived at by subtracting the net heat absorbed by the char from that of the coal (Figure 2e). The differential of these values is shown in Figure 2f.

Preoxidation of Coal Sample. Preoxidized coal samples were prepared corresponding with 1, 5, 10, and 24 hrs of air exposure at 400 K with a horizontal furnace. Coal samples were dried 1 hr at 400 K, with nitrogen purging before oxidation. Oxygen uptake on coal samples was monitored as the gain in weight by a Fisher TGA system. Approximately 10 mg of coal were placed in the platinum sample bucket and the system was flushed with nitrogen (flow rate of 100 cc/min) for 20 min to displace air. The sample was then heated to 400 K and held at that temperature for 1 hr for drying. The nitrogen flow was then switched to dry air and changes in sample weight were monitored in time. The results are presented in Figure 3. As illustrated, the coal samples used in this study show a very mild oxygen chemisorption of 0.7% oxygen uptake after 10 hrs of air exposure. Since there is the strong possibility that gasification takes place even at the preoxidation temperature used in this study, values obtained from this thermogravimetric method provide a lower limit for the amount of oxygen added rather than an absolute one.

Estimation of Volatile Yields. Due to the reactor design, the weighing of the resulting char was difficult; therefore, the mass of remaining char could not be measured directly. Rather, the mass was estimated using heat capacity as an indicator. The basic assumption applied is that the heat capacity of char produced from the slow heating is equal to the heat capacity of char produced from rapid heating. That is, it is assumed that the heating rate will not affect the heat capacity of the remaining char. Then the mass of the char resulting from the coal pyrolysis was calculated from the experimental heat capacity data and the volatile yield was estimated. To assess the errors associated with assumption, the heat capacity of the char produced from rapid heating was also determined on a known mass basis.

RESULTS AND DISCUSSION

The thermophysical properties measured were 1) pyroheat, ΔHph, which is the energy required to heat coal to a given temperature and is the sum of the heat of pyrolysis and heat capacity over the heating temperature interval; 2) pyroheat capacity, Cph, which is the pyroheat normalized over a differential temperature interval; 3) heat of pyrolysis, ΔHpy, which is the thermal difference between heating coal and char to the same final temperature; and 4) pyrolysis heat capacity, Cpy, which is the heat of pyrolysis normalized over a differential temperature interval. The experimental results are presented in Tables 4 through 6.

Pyroheat. As can be seen from Table 4, pyroheat increases as temperature increases in the temperature range from room temperature to 900 K. And the unoxidized coal was the most endothermic and that the coal with the highest degree of preoxidation was the least endothermic during the pyrolysis. The pyroheats of unoxidized PSOC 64B, subbituminous B coal and the coal exposed at 400 K for 24 hrs are 993 J/g and 756 J/g at 900 K, respectively.

Pyroheat Capacity. The pyroheat capacity of coal increases up to 650 K as the energy demanded for the pyrolyzing coal increases. Above 650 K, the endothermic effect decreases and the pyroheat capacity falls to the same value as the char(Table 5). The pyroheat capacity of the char at 900 K decreases from 1.29 J/gK to 0.98 J/gK as the level of preoxidation increases. The maximum pyroheat capacities of unoxidized coal and the coal exposed at 400 K for 24 hrs are 2.16 J/gK at 610 K and 1.62 J/gK at 640 K, respectively.

Heat of Pyrolysis. The effects of preoxidation on the apparent heat of pyrolysis are presented in Figure 4. It shows that a 20% reduction in apparent heat of pyrolysis occurs within the first 10 hrs for the preoxidized coal sample. After this time interval, the apparent heat of pyrolysis approaches asymptotic values of 25% reduction. However, the effects of preoxidation could be appreciated more realistically if one examines the effective heat of pyrolysis, which is based on the actual participating fraction. Table 8 shows that the drastic 17% reduction for the coal preoxidized for 1 hrs continuously decreased to a 58% reduction for the coal preoxidized for 24 hrs. At the mild levels of preoxidation employed in this study, the effects on energetics were drastic. For example, the thermogravimetric results show that mild preoxidation of PSOC 64B resulted in only a slight oxygen uptake. However, under the rapid heating conditions, effective heat of pyrolysis for mildly preoxidized samples are reduced 58% when compared with the corresponding effective heat of pyrolysis for the unoxidized coals. The apparent heat of pyrolysis of unoxidized coal and the coal preoxidized for 24 hrs are 316 J/g and 242 J/g, respectively. The effective heat of pyrolysis of unoxidized coal and the coal preoxidized for 24 hrs are 1086 J/g and 456 J/g, respectively (Figure 5). For the preoxidized coals, the temperature at which maximum pyrolysis occurs shifts to higher temperature. However, after the initial oxidation, the temperature at which maximum pyrolysis occurs is not changed with further oxidation.

Effects of Preoxidation. The preoxidation effects on subsequent pyrolysis behavior are summarized in Table 8. The heats of pyrolysis decrease with the level of preoxidation. However, volatile yields increase with the level of preoxidation. The estimated mass of the char decreases from 70.9% to 46.9% of its original sample mass with the level of preoxidation. In other words, volatile yields increase from 29.1% to 53.1 % with the level of preoxidation. Volatile yields increase from 22.5% to 29.1% as the heating rate increase from 2 K/s to 400 K/s. The heating rate effect is enhanced with preoxidation. For example, volatile yields increase with preoxidation from 22.5% to 35.4% for a 2 K/s heating rate, while volatile yields increase from 29.1% to 53.1% for a 400 K/s heating rate (Table 9). Rapid heating generates higher pressure inside of coal very quickly due to increased rate of pyrolysis. The increased pressure differential enables the pyrolysis products to more rapidly leave the coal mass with much less chance of cracking and secondary reaction. Consequently, rapid heating increases the carbon removal efficiency of hydrogen, which results in the increased volatile yields of pyrolysis. Furthermore, preoxidation results in an activating effect on the bond breaking reaction. Therefore, the heating rate effect is enhanced by the preoxidation. The preoxidation effects on the volatile yields of pyrolysis are presented in Figure 6. The effect of preoxidation on both energetics and volatile yields of pyrolysis could be attributed to the oxygen functional groups, especially the phenolic-OH group. The phenolic-OH groups could reduce the endothermicity of the fragmentation reaction by their activating effect on bond breaking. The volatile yields increase with the heating rate. This heating rate effect is enhanced by the preoxidation due to its reducing effect on endothermicity, which results in the efficient use of a given energy. In summary, rapid heating causes more extensive fragmentation of preoxidized coal when compared with unoxidized coal. This demonstrates that the preoxidation causes a change in molecular structure and leads to the extensive fragmentation of preoxidized coal.

CONCLUSIONS

The effect of preoxidation on the subsequent rapid pyrolysis behavior is significant. Mild preoxidation reduces the endothermicity of pyrolysis drastically. The unoxidized coal is the most endothermic and the coal with the highest degree of preoxidation is the least endothermic during the pyrolysis. As a result, pyroheat, pyroheat capacity, and heat of pyrolysis decrease as the degree of preoxidation increases. The volatile yields increase with the level of preoxidation. The apparent heat of pyrolysis of unoxidized coal and coal preoxidized at 400 K with air for 24 hrs are 316 J/g and 242 J/g at 900 K, respectively. Their maximum pyroheat capacities are 0.96 J/gK at 590 K and 0.7 J/gK at 630K, respectively. The effective heat of pyrolysis of unoxidized coal and the coal preoxidized for 24 hrs are 1086 J/g and 456 J/g, respectively. The yields of volatiles for unoxidized

and preoxidized coal are 29.1% and 53.1%, respectively. However, the yields of volatiles with complementary slow heating (2 K/s) for unoxidized coal and preoxidized coal are 22.5% and 35.4%, respectively.

ACKNOWLEDGEMENTS

This study was made possible by financial support from the Coal Cooperative Program at The Pennsylvania State University. The authors thank the Penn State Coal Sample Bank and Data Base for supplying the sample and the analysis of the coal used in this study.

REFERENCES

1. Freihaut, J.D.; Zabielski, M.F.; Serry, D.J. *Prepr. Am. Chem. Soc., Div. Fuel Chem.* **1982**, 27, 89-98.
2. Morel, O.; Vastola, F.J. *Prepr. Am. Chem. Soc., Div. Fuel Chem.* **1984**, 29, 77-82.
3. Kwon, H.B., Ph.D. Thesis, Pennsylvania State University, **1987**.
4. Kwon, H.B.; Vastola, F.J. *Prepr. Am. Chem. Soc., Div. Fuel Chem.* **1993**, 38(4), 1168-1177.
5. Kwon, H.B.; Vastola, F.J. *Fuel Process. Technol.* **1995**, 44, 13-24.

Table 1. Calibration

Standard substance	Literature		Measured	
	m.p.(K)	ΔH fusion(J/g)	m.p.(K)	ΔH fusion(J/g)
Sn	505.1	60.7	496	71
			496	67
			495	70
Zn	692.7	113.0	688	120
			690	127
			691	125
Al	933.5	396.0	928	414
			920	423
			932	450

Table 2. Characteristics of coal used

PSU/DOE Ident . Number: PSOC-64B
Apparent Rank : Sub-bituminous B
Seam: Monarch , Wyoming
Mine: Big Horn

Proximate Analysis, wt. %:	As Rec'd	dry	daf
Moisture	22.1	-	-
Ash	4.6	5.9	-
Volatile Matter	33.7	43.3	46.0
Fixed Carbon	39.6	50.8	54.0
Ultimate Analysis, Wt. %:	**As Rec'd***	**dry**	**daf**
C	53.0	68.1	72.3
H	4.0	5.1	5.5
N	0.8	1.0	1.1
S(total)	0.3	0.4	0.5
O(by difference)	15.2	19.5	20.7

*Excludes Moisture

Calorific value, kJ/g:	
dmmc	28.1
dmmf	28.9

Table 3. Data reduction symbols

English symbols

A	Coefficient for conduction and convection
B	Coefficient for radiation
e	Voltage drop
H	Enthalpy
I	Current
R	Resistance
T	Temperature
W	Power

Subscripts

g	Grid
i	Input
l	Loss
r	Reference
s	System
rm	Room
tc	Thermocouple

Table 4. Pyroheat and Specific Pyroheat of Coal

Preoxidation Time(hr)	0		1		5		10		24	
Temperature (K)	⊿Hph (J/g)	Cph (J/gK)	⊿Hph (J/g)	Cph (J/gK)	⊿Hph (J/g)	Cph (J/gK)	⊿Hph (J/g)	Cph (J/gK)	⊿Hph (J/g)	Cph (J/gK)
350	47	0.73	50	0.65	40	0.65	36	0.56	37	0.55
375	71	0.93	73	0.85	62	0.81	56	0.72	57	0.71
400	99	1.14	102	1.04	89	0.97	80	0.87	78	0.86
425	132	1.33	131	1.23	118	1.11	106	1.02	104	0.99
450	171	1.52	167	1.42	148	1.25	135	1.17	133	1.11
475	213	1.70	207	1.60	182	1.39	167	1.30	166	1.23
500	260	1.85	252	1.77	219	1.51	201	1.42	199	1.33
525	311	1.98	302	1.91	261	1.62	243	1.52	232	1.42
550	365	2.07	357	2.01	306	1.71	286	1.59	273	1.50
575	428	2.13	414	2.09	352	1.78	330	1.64	317	1.55
600	483	2.16	467	2.14	401	1.81	372	1.67	355	1.60
625	533	2.16	53	2.16	450	1.81	415	1.69	396	1.62
650	594	2.13	580	2.17	499	1.79	459	1.68	439	1.62
675	648	2.06	631	2.13	543	1.73	502	1.64	480	1.58
700	699	1.95	690	2.03	585	1.63	546	1.57	522	1.50
725	749	1.81	743	1.87	629	1.50	585	1.47	564	1.39
750	797	1.68	791	1.67	669	1.36	623	1.36	598	1.27
775	835	1.55	830	1.49	698	1.21	652	1.26	623	1.15
800	862	1.44	859	1.38	724	1.11	679	1.17	646	1.07
825	894	1.36	876	1.31	744	1.05	701	1.12	667	1.02
850	926	1.32	901	1.27	765	1.02	729	1.09	689	0.99
875	959	1.30	934	1.25	796	1.01	761	1.08	723	0.98
900	993	1.29	967	1.25	827	1.01	793	1.07	756	0.97

Table 5. Pyroheat and Specific Pyroheat of Char

Preoxidation Time(hr)	0		1		5		10		24	
Temperature (K)	⊿Hph (J/g)	Cph (J/gK)	⊿Hph (J/g)	Cph (J/gK)	⊿Hph (J/g)	Cph (J/gK)	⊿Hph (J/g)	Cph (J/gK)	⊿Hph (J/g)	Cph (J/gK)
350	35	0.49	38	0.48	30	0.41	28	0.38	30	0.37
375	53	0.60	56	0.60	44	0.51	42	0.47	43	0.46
400	71	0.70	76	0.70	60	0.61	58	0.55	58	0.54
425	92	0.79	95	0.79	79	0.68	74	0.63	74	0.61
450	113	0.88	119	0.86	100	0.75	91	0.70	92	0.67
475	136	0.95	143	0.93	120	0.79	110	0.77	109	0.72
500	164	1.02	167	0.98	142	0.82	130	0.82	129	0.76
525	192	1.07	194	1.03	165	0.84	155	0.86	150	0.80
550	217	1.12	222	1.07	188	0.86	178	0.90	171	0.84
575	250	1.16	250	1.11	209	0.87	201	0.93	192	0.87
600	280	1.20	277	1.15	229	0.89	224	0.95	215	0.90
625	312	1.25	306	1.19	252	0.90	250	0.97	239	0.91
650	340	1.30	339	1.22	274	0.92	275	0.99	264	0.93
675	375	1.33	371	1.23	298	0.94	300	1.00	287	0.94
700	409	1.34	404	1.25	323	0.95	325	1.01	309	0.96
725	445	1.34	435	1.26	348	0.96	350	1.03	333	0.98
750	484	1.34	465	1.28	370	0.98	378	1.05	359	1.00
775	513	1.33	497	1.29	395	0.98	404	1.06	358	1.01
800	548	1.32	531	1.27	419	0.99	429	1.06	409	1.01
825	577	1.31	564	1.25	446	0.98	457	1.05	436	1.00
850	614	1.30	600	1.23	472	0.98	487	1.04	464	0.99
875	645	1.29	629	1.21	498	0.97	516	1.03	491	0.98
900	677	1.29	661	1.21	524	0.97	541	1.03	514	0.98

Table 6. Pyroheat and Specific Pyroheat of Pyrolysis

Preoxidation Time(hr)	0		1		5		10		24	
Temperature (K)	ΔHph (J/g)	Cph (J/gK)	ΔHph (J/g)	Cph (J/gK)	ΔHph (J/g)	Cph (J/gK)	ΔHph (J/g)	Cph (J/gK)	ΔHph (J/g)	Cph (J/gK)
350	11	0.21	11	0.13	9	0.21	8	0.15	7	0.15
375	17	0.30	16	0.20	17	0.27	13	0.21	14	0.21
400	27	0.40	25	0.28	28	0.33	21	0.28	19	0.27
425	40	0.50	34	0.37	38	0.40	32	0.35	28	0.34
450	57	0.61	46	0.48	47	0.48	43	0.42	40	0.41
475	76	0.71	63	0.59	61	0.56	56	0.49	55	0.47
500	95	0.80	84	0.71	76	0.65	70	0.56	68	0.54
525	118	0.88	107	0.81	95	0.75	87	0.62	81	0.59
550	147	0.93	133	0.89	118	0.82	107	0.66	102	0.63
575	177	0.96	163	0.94	142	0.88	128	0.69	124	0.66
600	202	0.96	189	0.97	170	0.91	147	0.71	139	0.69
625	220	0.92	216	0.97	197	0.91	164	0.71	155	0.70
650	253	0.86	240	0.96	224	0.88	182	0.70	175	0.70
675	273	0.77	258	0.93	245	0.82	201	0.66	192	0.66
700	290	0.65	286	0.85	262	0.72	220	0.59	212	0.58
725	303	0.52	307	0.72	281	0.59	234	0.50	230	0.48
750	312	0.39	325	0.53	298	0.44	245	0.38	239	0.35
775	322	0.27	333	0.35	302	0.29	248	0.27	237	0.22
800	313	0.16	327	0.20	304	0.17	248	0.17	236	0.12
825	316	0.08	311	0.12	297	0.09	243	0.11	230	0.05
850	312	0.03	300	0.07	291	0.05	241	0.07	224	0.02
875	313	0.01	304	0.05	298	0.04	244	0.05	231	0.00
900	316	0.00	306	0.00	303	0.00	252	0.00	242	0.00

Table 7. Estimation of Volatile Yields

	Heating Rate of Coal Run	Volatile Yields(%) Preoxidation Time (hrs) *				
	(k/s)	0	1	5	10	24
Cp, char (J/gk), orig. mass of coal	400	1.29	1.21	0.97	1.03	0.98
Cp, char (J/gk), known mass of char	0.2	1.82	1.83	1.9	1.94	2.09
	400	1.84				
Mass of Char (%) at 900 K, estimated	400	70.9	66.1	51.1	53.1	46.9
Volatile Yields (%), estimated	400	29.1	33.9	48.9	46.9	53.1

* At 400 K with air

Table 8. Effects of Preoxidation on Subsequent Pyrolysis Behavior (At 900 K with a 400 k/s Heating Rate)

	Preoxidation Time (hrs) *				
	0	1	5	10	24
Variation in Ap. Heat of Pyrolysis	1	0.97	0.96	0.8	0.77
Variation in Ef. Heat of Pyrolysis	1	0.83	0.57	0.49	0.42
Variation in Volatile Yields	1	1.16	1.68	1.61	1.82
Volatile Yields (%)	29.1	33.9	48.9	46.9	53.1
Apparent Heat of Pyrolysis (J/g)	316	306	303	252	242
pyroheat of Char (J/g)	677	661	524	541	514
Pyroheat of Coal (J/g)	993	967	827	793	756
Effective Heat of Pyrolysis (J/g)	1086	903	620	537	456

* At 400 K with air

Table 9. Effects of Heatng Rate on Volatile Yields

Heating Rate of Coal Run (k/s)	Volatile Yields (%) preoxidation Time (hrs) *				
	0	1	5	10	24
0.2	36.5	36.8	36.1	35.9	35.9
2	22.5			26.8	35.4
400	29.1	33.9	48.9	46.9	53.1

* At 400 K with air

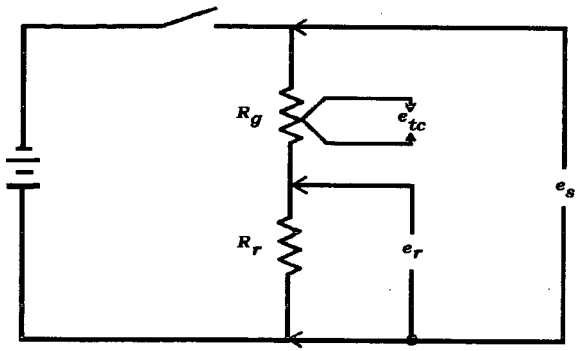

Fig. 1. Equivalent circuit of the heating system

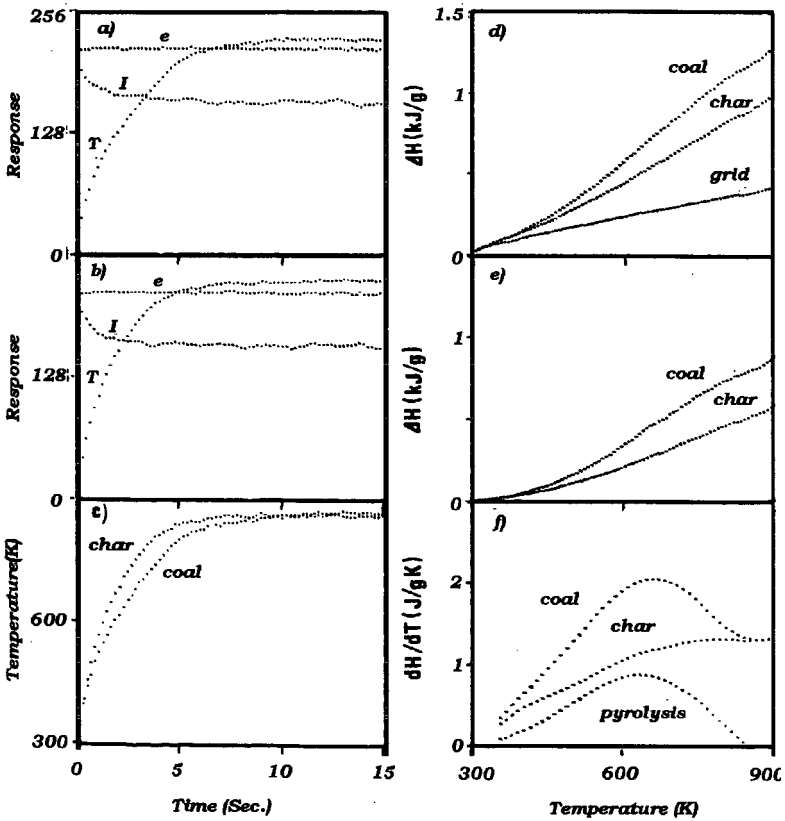

Fig 2. Data reduction: Coal run (a), char run (b), temperature profile (c), enthalpy change (d), normalized enthalpy change (e), and rate of enthalpy change (f).

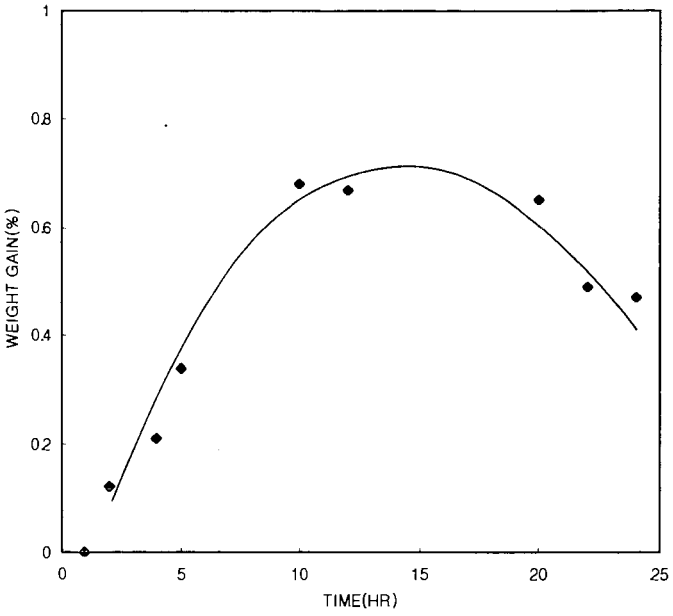

Fig 3. Weight Gain vs. Preoxidation Time

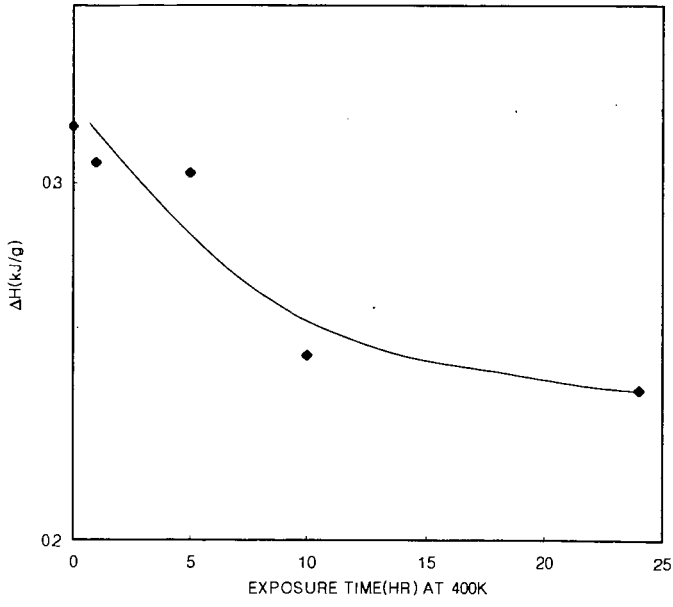

Figure 4. Apparent Heat of Pyrolysis (at 900 K) vs. Preoxidation Time

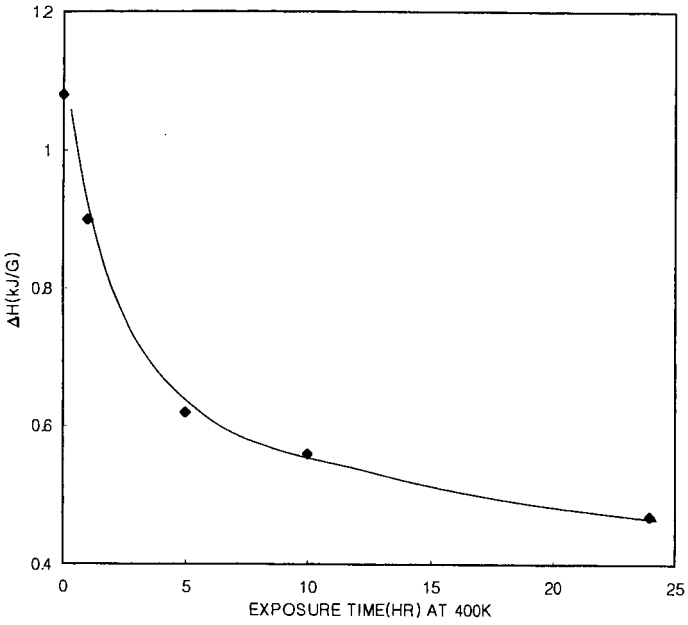

Figure 5. Effective Heat of Pyrolysis (at 900 K) vs. Preoxidation Time

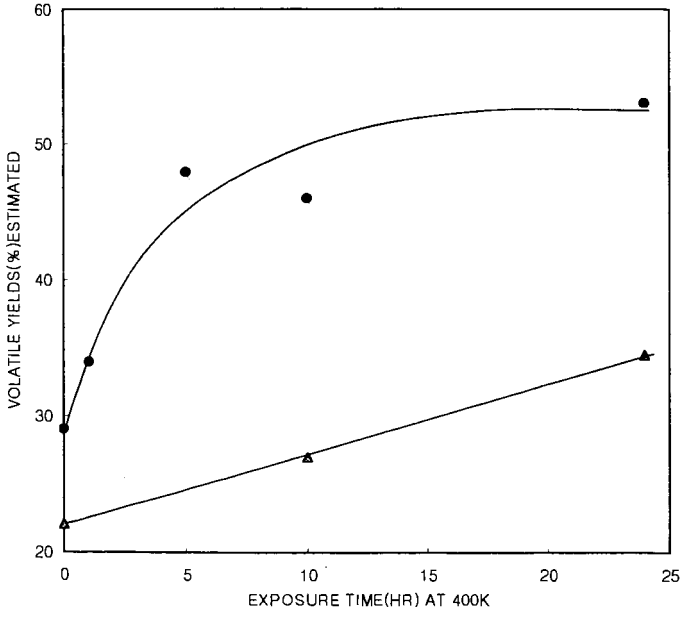

Figure 6. Volatile yields of pyrolysis (at 900 K) vs. Preoxidation Time for Different Heating Rates Heating Rate (K/s); 2(▲) and 400(●)

PREDICTING EFFECTIVENESS FACTOR FOR M-TH ORDER AND LANGMUIR RATE EQUATIONS IN SPHERICAL COORDINATES

Jianhui Hong, William C. Hecker, and Thomas H. Fletcher
Chemical Engineering Department, Brigham Young University, Provo, UT 84602

Keywords: effectiveness factor, Langmuir rate equation, correction function

INTRODUCTION

The effectiveness factor is widely used to account for the interaction between pore diffusion and reactions on pore walls in porous catalytic pellets and solid fuel particles. The effectiveness factor is defined as the ratio of the reaction rate actually observed to the reaction rate calculated if the surface reactant concentration persisted throughout the interior of the particle, i.e., no reactant concentration gradient within the particle. The reaction rate in a particle can therefore be conveniently expressed by its rate under surface conditions multiplied by the effectiveness factor.

The generalized steady-state equation in a spherical particle (a catalytic pellet or a solid fuel particle) may be expressed as:

$$\frac{d^2C}{dr^2}+\frac{2}{r}\frac{dC}{dr}-\frac{r'''}{D_e}=0 \tag{1}$$

where r''' is the intrinsic reaction rate per unit particle volume in mol/cm^3/sec (as a function of C), D_e is the effective diffusivity, C is the local oxygen concentration (as a function of r), and r is the radial distance from the origin. The boundary conditions are

$$C = C_s, \text{ at } r = r_s \tag{2}$$

and

$$\frac{dC}{dr}=0, \text{ at } r = 0 \tag{3}$$

The intrinsic reaction rate r''' can be in different forms. One way to represent the intrinsic reaction rate is to use an m-th order rate equation:

$$r''' = k_m C^m \tag{4}$$

where k_m is the kinetic coefficient in (mol/cm^3)$^{1-m}$ sec^{-1}, and m is the intrinsic reaction order. Another way is to use a Langmuir rate equation

$$r''' = \frac{k_1 C}{1+KC} = \frac{k_0 KC}{1+KC} \tag{5}$$

where k_1 and K are two kinetic parameters (the physical meanings of these two parameters depend on the mechanism leading to this rate equation), and k_0 is the ratio of k_1 to K. Note that the product of K and C is dimensionless.

The exact analytical solutions for the radial oxygen concentration profile and the effectiveness factor have been well established when the intrinsic reaction rate is first order.[1-3] Assuming that D_e is constant throughout the particle, the exact analytical solution for the effectiveness factor for a first order reaction is

$$\eta = \frac{1}{M_T}\left(\frac{1}{\tanh(3M_T)}-\frac{1}{3M_T}\right) \tag{6}$$

$$M_T = \frac{r_s}{3}\sqrt{\frac{k}{D_e}} \tag{7}$$

where r_s is the radius of the particle, k is the kinetic coefficient in 1/sec, and M_T is the Thiele modulus. Eq. 6 is referred to in this paper as the first order curve.

Bischoff[4] developed (in Cartesian coordinates) a general modulus for an arbitrary reaction rate form:

$$M_T = \frac{Lr'''(C)}{\sqrt{2}}\left[\int_0^{C_s} D(t)r'''(t)dt\right]^{-\frac{1}{2}} \tag{8}$$

where L is the characteristic length of the particle (defined as the volume of the particle/external surface of the particle), t is a dummy integration variable, r''' is the intrinsic reaction rate per particle volume in any form, and D is the effective diffusivity, which can be a function of oxygen concentration, but is assumed to be constant in this study for simplicity. The use of this general modulus in Cartesian coordinates brought all of the curves for various m-th order rate equations and the Langmuir rate equation with different values of K into a relatively narrow band (see Figure 1). In particular, the general modulus for m-th order rate equations was derived from Eq. 8:

$$M_T = L\sqrt{\frac{(m+1)}{2}\frac{k_m C_s^{m-1}}{D_e}} \tag{9}$$

For the Langmuir rate equation in Eq. 5, a general modulus can be derived from Eq. 8:

$$M_T = L\sqrt{\frac{k_1}{2D_e}\frac{KC_s}{1+KC_s}}[KC_s - \ln(1+KC_s)]^{-\frac{1}{2}} \tag{10}$$

If accuracy is not a major concern, all of the η vs. M_T curves in the narrow band can be approximated by the first order curve, as shown in Figure 1. The method of approximating the η vs. M_T curve of a non-first order reaction by the first order curve is referred to in this paper as the first order approximation. The first order approximation method becomes more and more accurate as M_T approaches zero and infinity. However, in the intermediate range of M_T ($0.2 < M_T < 5$), the first order approximation method leads to up to -34% error in Cartesian coordinates, as shown in Figure 1. Note that in Cartesian coordiantes the first order curve is

$$\eta = \frac{\tanh(M_T)}{M_T} \tag{11}$$

while in spherical coordinates the first order curve is Eq. 6.

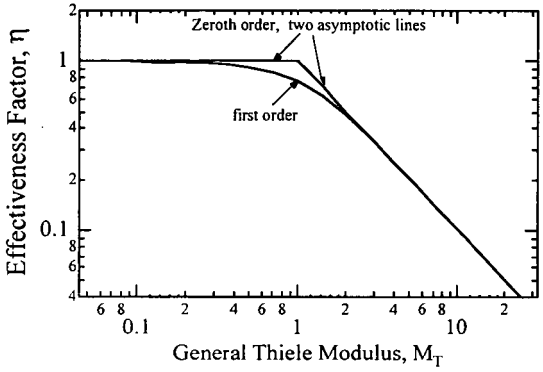

Figure 1. The effectiveness factor curves for first order and zeroth order reactions in Cartesian Coordinates. For reactions between zeroth order and first order extremes ($0 < m < 1$ or $0 < KC_s < \infty$), the curves lie in the narrow band bounded by the first order and the zeroth order curves.

RESULTS AND DISCUSSION

The Effective Reaction Order for An Arbitrary Reaction Rate Form

From the intrinsic m-th order rate equation (Eq. 4), it is easy to get

$$\ln(r''') = \ln(k_m C^m) = \ln(k_m) + m\ln(C) \tag{12}$$

From the above equation, it can be seen that if we plot ln(r''') vs. ln(C), we get a straight line, and the slope of this line is the reaction order m. Eq. 11 can be re-written as:

$$m = \frac{d\ln[r_{in}'''(C)]}{d\ln(C)} \tag{13}$$

For a reaction described by a Langmuir-Hinshelwood rate equation, there is no reaction order in an explicit sense. However, the right-hand side of Eq. 12 can be used as the definition of an **effective reaction order m_{eff}** for an arbitrary reaction rate form.

$$m_{eff} = \frac{d\ln[r_{in}'''(C)]}{d\ln(C)} \tag{14}$$

We now apply this definition to the Langmuir rate equation. Substitution of the Langmuir rate equation into Eq. 14 gives

$$m_{eff} = \frac{d\ln(\frac{k_1 C}{1+KC})}{d\ln(C)} = \frac{1}{1+KC}. \tag{15}$$

Note that for a Langmuir type reaction the ln(r''') vs. ln(C) curve is not a straight line. The slope of the curve (which is m_{eff}) is dependent on the local oxygen concentration. At the surface oxygen concentration C_s, the effective reaction order is

$$m_{eff,s} = \frac{1}{1 + KC_s} \qquad \text{for the Langmuir rate equation} \qquad (16.L)$$

Note that for an m-th order rate euqation, the effective reaction order is always equal to m. Therefore,

$$m_{eff,s} = m \qquad \text{for an m-th order rate equation} \qquad (16.m)$$

Evaluation of the First Order Approximation in Spherical Coordinates

Since catalytic pellets and porous solid fuel particles can be approximated more or less by spheres, rather than by semi-infinite flat-slabs, it is of more interest to study the performance of the first order approximation method in spherical coordinates. The values of the effectiveness factor predicted by the first order curve (Eq. 6) using the general moduli in Eqs. 9 and 10 were compared to the numerical solutions. It was found that in spherical coordinates, the first order approximation method predicted the effectiveness factor more accurately than in Cartesian coordinates, with errors ranging from -17% to 0% (see Table 1). In other words, all of the curves for various values of $m_{eff,s}$ were brought into a narrower band in spherical coordinates than the band in Cartesian coordinates (see Figures 1 and 2). From Table 1, it can be seen that: 1) as the value of M_T gets away from 0.707 in both directions, the error diminishes rapidly to zero; 2) as $m_{eff,s}$ decreases from unity to zero, the error increases from zero to -17%.

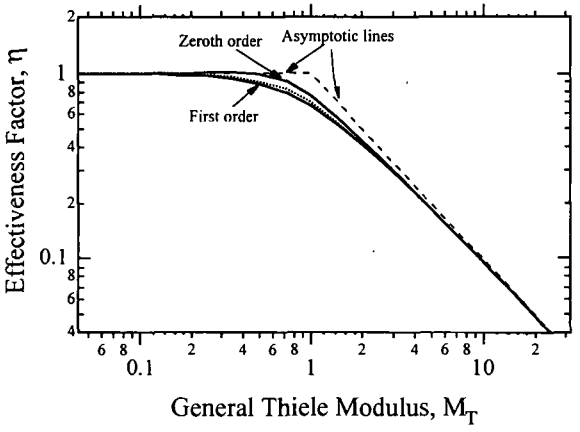

Figure 2. Effectiveness factor curves for first order and zeroth order reactions in spherical coordinates. For reactions described by the Langmuir and m-th order rate equations, the curves lie in the narrow band bounded by the first order and zeroth order curves. The dotted line in the band corresponds to m = 0.5 and corresponds approximately to $KC_s = 1$ ($m_{eff,s}$= 0.5 for both m-th order and Langmuir rate equations).

Table 1. The Errors (%) of the First Order Approximation Method Using the Modulus in Eq. 10

$m_{eff,a}$ / M_T	1.00	0.75	0.50	0.25	0.00
0.125	-0.019	-0.162	-0.342	-0.583	-0.925
0.25	-0.016	-0.588	-1.282	-2.188	-3.560
0.5	-0.013	-1.639	-3.672	-6.557	-12.375
0.707	-0.076	-2.162	-4.802	-8.618	-16.081
1	-0.215	-2.274	-4.756	-8.000	-12.392
2	-0.491	-1.584	-2.813	-4.277	-6.018
4	-0.679	-1.191	-1.774	-2.472	-3.156
8	-0.933	-1.186	-1.473	-1.821	-2.274

Note: The errors of the first order approximation method using the general Thiele modulus in Eq. 9 are almost identical to the values in this table.

Correction Function

It has been shown that in the intermediate range of M_T ($0.2 < M_T < 5$), the first order approximation method leads to up to -17% error. It is desirable to reduce the error using a multiplier with the first order curve (Eq. 6). Two correction functions were constructed to counter the errors associated with the first order approximation methods for m-th order rate equations and the Langmuir rate equation, respectively. By using the effective reaction order evaluated at the external surface oxygen concentration, these two correction functions can be unified into

$$f(M_T, m_{eff,s}) = (1 + \frac{\sqrt{1/2}}{\frac{1}{2M^2} + 2M^2})^{\frac{1}{2}(1-m_{eff,s})^2} \tag{17}$$

where $m_{eff,s} = m$ for m-th order rate equations, and
$m_{eff,s} = 1/(1+KC_s)$ for Langmuir rate equations.
The correction function is used as a multiplier before the right-hand-side of Eq. 6:

$$\eta = f\frac{1}{M_T}(\frac{1}{\tanh(3M_T)} - \frac{1}{3M_T}) \tag{18}$$

Note that this correction function is designed only for correcting the first order approximation in spherical coordinates, but not in Cartesian coordiantes.

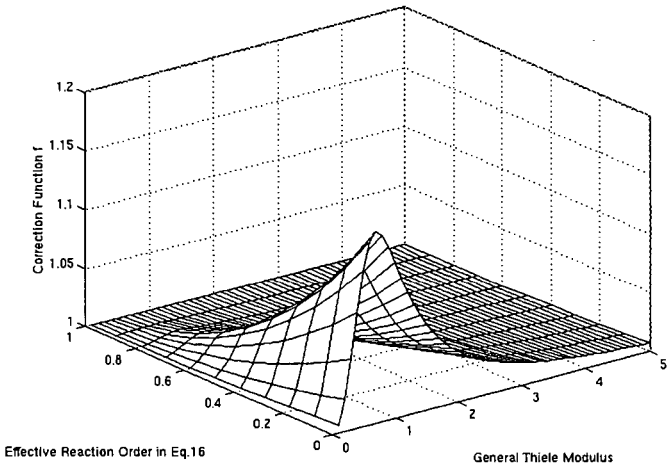

Figure 3. The correction function f vs. Thiele modulus M_T and the effective reaction order at external surface $m_{eff,s}$.

Accuracy of the corrected first order approximation

Compared to numerical solutions, the corrected first order approximation predicts the effectiveness factor within 3.0% errors (see Table 2). After the effectiveness factor is obtained, the overall reaction rate in a spherical particle can be easily calculated using

$$r'''_{obs} = \eta k_m C_s^m \tag{19}$$

for a m-th order type reaction, and

$$r'''_{obs} = \eta \frac{k_1 C_s}{1 + KC_s} \tag{20}$$

for a reaction described by the Langmuir rate equation.

CONCLUSIONS

Two correction functions were constructed to improve the accuracy of predicting the effectiveness factor for the Langmuir and m-th order rate equations, respectively. By using the

intrinsic effective reaction order evaluated at surface concentration, these two correction functions were unified (see Eq. 17).

The first order curve combined with the correction function developed in this study was able to predict the effectiveness factor for m-th order rate equations and the Langmuir rate equation within 3% in the whole range of M_T (including Zone I, Zone II and especially the transition zone). This "corrected first order approximation method" uses explicit analytical expressions to predict the effectiveness factor, and therefore is particularly suitable for repeated use in comprehensive computer codes.

Table 2. The Errors of the Corrected First Order Approximation Method Using the Proposed Modulus in Eq. 10

M_T \ $m_{eff,s}$	1.00	0.75	0.50	0.25	0.00
0.125	-0.019	-0.030	0.163	0.485	1.133
0.25	-0.016	-0.158	0.375	1.354	0.001
0.5	-0.013	-0.729	-0.113	1.208	1.394
0.707	-0.076	-1.161	-0.849	0.128	-1.246
1	-0.215	-1.387	-1.197	0.076	1.374
2	-0.491	-1.178	-1.136	-0.324	0.545
4	-0.679	-1.068	-1.256	-1.243	-1.144
8	-0.933	-1.153	-1.337	-1.494	-1.743

Note: The errors of the corrected first order approximation method using the general Thiele modulus in Eq. 9 are almost identical to the values in this table.

ACKNOWLEDGEMENTS

This study is supported by the Advanced Combustion and Energy Research Center (ACERC) at Brigham Young University, Provo, Utah 84602.

REFERENCES

1. Aris, R., *Chem. Eng. Sci.*, **6**, 262 (1957).
2. Thiele, E. W., "Relation between Catalytic Activity and Size of Particle", *Ind. Eng. Chem.*, **31**, 916 (1939).
3. Smith, J. M., *Chemical Engineering Kinetics*, McGraw Hill, New York (1981).
4. Bischoff, K. B., "Effectiveness Factor for General Reaction Rate Forms", *A.I.Ch.E J.*, **11**, 351 (1965).

KINETICS OF HIGH PRESSURE CHAR OXIDATION

Rebekah J. Sawaya, Jared W. Allen, William C. Hecker, Thomas H. Fletcher, and L. Douglas Smoot

Department of Chemical Engineering, Brigham Young University, Provo, Utah 84604

Keywords: char oxidation, intrinsic kinetics, high pressure, thermogravimetric analysis, intrinsic rate expression

INTRODUCTION

The intrinsic kinetics of char oxidation at atmospheric pressure have been extensively studied (1) and are fairly well agreed upon; however, kinetic data for char oxidation at elevated pressures are very limited. In addition standard kinetic models which work at low pressures apparently fail at high pressures.

Two types of kinetic models have been proposed as the rate law for high pressure char oxidation. The first, an nth order rate expression in the form of $r = A \exp(-E_a/RT) C_{Os}^n$ where C_{Os} is the oxygen concentration at the external surface of the burning particle, was the assumed model for the work of Monson et al.(2). They obtained data in a high pressure drop tube reactor using conditions from 1400 to 2100 K, 5% to 21% O_2 and 1 to 15 atmospheres. Their data showed a significant pressure dependence on the apparent rate coefficients (A and E_a) using an assumed oxygen reaction order of n = 0.5. Their conclusion was that the nth order rate expression was not adequate at high pressure conditions (2). The second type of kinetic model that has been used is a Langmuir expression of the form $r_{in} = kC_{O2}/ (1+ KC_{O2})$. Essenhigh and Mescher (3) attempted to apply this model to the data of Monson et al. by using a so-called "second effectiveness factor" and were able to predict Monson's data within a factor of two. Croiset et al. (4) performed experiments in a fixed-bed reactor from 2-10 atmospheres and 850-1200K with a bituminous coal char, and showed a decrease in pre-exponential factor with increasing pressure and a very weak total pressure effect above 6 atm. Ranish and Walker (5) studied graphite combustion and used the Langmuir model to explain changes in apparent activation energy and reaction order with changing temperature (733 to 842 K) and pressure (1 to 64 atm). Their data showed a slight decrease in oxygen order with increasing temperature.

In light of the limited high pressure kinetic data available and the conflicting conclusions resulting from the data that are available, it is clear that there is a need for extensive studies of the kinetics of char oxidation at high pressure.

The objective of this study is to determine the intrinsic (low temperature) high pressure kinetic rate expression for char oxidation over a range of char types and char prepara- tions. Specifically, since this is still a work in progress, the objective of this paper is to report the effect of pressure on the char oxidation kinetics of Pittsburgh #8 char.

EXPERIMENTAL

Two different samples of Pittsburgh #8 char – designated P1 and P2 - were used in this study. Both were produced in a methane flat-flame burner (FFB) by devolatilizing Pittsburgh #8 coal at high heating rate (10^4 to 10^5 K/s), in 3-4% O_2, and at peak gas temperatures of 1700-1800K. Sample P1 was produced at a FFB residence time of 65 ms and had a coal-to-char mass loss of 67% (6), while P2 was produced at a FFB residence time of 50 ms and had a coal-to-char mass loss of 58% (7).

All rate data for this study were obtained using a DMT high pressure thermogravimetric analyzer (HPTGA). The HPTGA allows for control of the total pressure, the flow rates and concentrations of the gases, and the gas temperature. Typically, for each run a 3-5mg sample was loaded into the mesh sample basket, the reaction chamber was brought to the desired temperature, pressure, and composition, and then, to start the run, the sample was lowered into the reaction chamber. A computer system recorded mass, pressure, and temperature continuously as a function of time. The slope of the mass loss curve was then determined and divided by the instantaneous mass (maf) mass to give the rate values on a "rate per gram available" basis.

Rate data were obtained for total pressures from one to 16 atm, oxygen mole fractions from 0.03 to 0.40, and temperatures from 748 K to 843 K. Activation energies were determined from standard Arrhenius plots (e.g. Figure 2), and oxygen reaction orders were determined from the slope of ln $[P_{O2}]$ vs. ln [rate] plots (e.g. Figure 3).

RESULTS AND DISCUSSION

Experimental runs performed at 15 different conditions using sample P1 were performed. Three runs were made at each condition; the average rates, along with the specified conditions for each run, are shown in Table 1. For each of the runs, plots of rate vs. char burnout such as those shown in Figure 1 were obtained. As can be seen, the char oxidation rate on a "per-gram-available basis" was found to be relatively constant, or independent of burnout, across a range of char burnouts from approximately 20 to 80%. A rate value representative of each run was calculated by averaging the rates at 10, 25, 50, and 75% burnout. Then, the values for each experimental condition (shown in the table) were obtained by averaging those values for the 3 runs at that condition.

The data obtained at 10% oxygen for both 1 atm and 4 atm were plotted in Arrhenius form to determine activation energy values, as shown in Figure 2. (Rate instead of rate constant was plotted on the ordinate since all data were obtained at the same P_{O2}). As can be seen, the data at both pressures are quite linear and appear to have essentially the same slope. The calculated activation energy values of 32.7 and 33.2 kcal/mol for 1 and 4 atm, respectively, are very consistent with the literature value of 32.9 +/- 1.4 kcal/mol determined by Reade (6) for Pittsburgh # 8 char at 1 atm.

The effects of oxygen partial pressure on char oxidation rates at 1 atm, 823K and at 4 atm, 773K are shown in Figure 3. At 1 atm the data are quite linear on the log-log plot indicating that an nth order model with n = 0.64 is consistent with the data. At 4 atmospheres the data points exhibit a slight nonlinear behavior and it appears the reaction order may be decreasing as the partial pressure of O_2 increases. This would indicate that the nth order assumption is insufficient as the pressure increases, and that the Langmuir changing order model may be more appropriate at higher pressures. More data are needed to verify this hypothesis. Work is in progress to obtain similar data at pressures up to 64 atm.

The effect of total pressure (between one and 16 atm) on oxidation rate was determined, and the resulting data are shown in Table 2 and in Figure 4. All values were obtained for char sample P2, at a temperature of 773 K, and at an O_2 partial pressure of nominally 0.4 atm. (The data obtained at 16 atm were at an O_2 partial pressure of 0.48 atm, but were corrected to 0.40 atm assuming an O_2 order of 0.7). It can been seen from the graph that there is a definite effect of pressure on oxidation rate, independent of the partial pressure of O_2. It appears as though rate increases as pressure increases, which would indicate further that the traditional nth order model is insufficient since it does not take into consideration the effect of total pressure.

CONCLUSIONS

The nth order model predominately used to characterize the kinetics of low pressure char oxidation is insufficient at higher pressures, and other models, such as the Langmuir model, need to be explored as possibilities for high pressure kinetic modeling. There appears to be a very definite effect of total pressure on char oxidation rate (independent of the oxygen partial pressure), as manifest by the fact that the reaction rate increased by a factor of three as the total pressure increased from one to 16 atm. The data also indicate that reaction order may be changing as oxygen partial pressure increases for higher total pressures.

REFERENCES

1. Suuberg, E.M., "Reaction Order for Low Temperature Oxidation of Carbons", 22nd Symposium (International) on Combustion; The Combustion Institute, Pittsburgh, PA, 79-87 (1988).

2. Monson, C.R., G.J. Germane, A.U. Blackham and D.L. Smoot, "Char oxidation and Elevated Pressure", Combustion and Flame, 100, 669 (1995).

3. Essenhigh, R.H. and A.M. Mescher, "Influence of pressure on the Combustion Rate of Carbon", 26th Symposium (International) on Combustion; The Combustion Institute, Pittsburgh, PA, 3085 (1996).

4. Croiset, E., C. Mallet, J.P. Rouan and J.R. Richard, "The Influence of Pressure on Char Combustion Kinetics", 26th Symposium (International) on Combustion; The Combustion Institute, Pittsburgh, PA, 3095 (1996).

5. Ranish, J.M. and P.L. Walker, "High Pressure Studies of the Carbon-Oxygen Reaction", Carbon, 31, 1, 135 (1993).

6. Reade, Walter, "An Improved Method for Predicting High-Temperature Char Oxidation Rates", M.S. Thesis, Chemical Engineering Department, Brigham Young University, Provo, UT, 1996.

7. Guo, Feng, "Kinetics and Mechanism of the Reaction of NO with Char: Effects of Coal Rank, Burnout, CaO, and Flue Gases", Ph.D. Dissertation, Chemical Engineering Department, Brigham Young University, Provo, UT, 1997.

Table 1. Test Conditions and Results* of Sample P1

P atm	T K	% O_2	PO_2 bar	Rate x 10^4 (g/g(a)*s)	P atm	T K	% O_2	PO_2 bar	Rate x 10^4 (g/g(a)*s)
1	823	3%	0.030	6.28	4	773	3%	0.122	5.03
1	823	5%	0.051	9.35	4	773	5%	0.203	6.82
1	823	10%	0.101	14.10	4	773	10%	0.405	15.29
1	823	20%	0.203	24.53	4	773	20%	0.811	20.55
1	823	40%	0.405	31.58	4	773	40%	1.621	27.81
1	798	10%	0.101	8.57	4	798	10%	0.405	32.14
1	773	10%	0.101	3.90	4	748	10%	0.405	6.62
					4	823	10%	0.405	56.51

*Each condition was replicated 3 times and average rates of 10%, 25%, 50%, and 75% burnout are given

Table 2. Test Conditions and Results of Sample P2

P atm	T K	% O_2	PO_2 bar	Rate x 10^4 (g/g(a)*s)	P atm	T K	% O_2	PO_2 bar	Rate x 10^4 (g/g(a)*s)
1	773	40%	.405	10.31	8	773	5%	0.405	24.70
1	773	40%	.405	10.53	8	773	5%	0.405	27.06
4	773	10%	.405	20.33	12	773	3.33%	0.405	24.28
4	773	10%	.405	15.93	12	773	3.33%	0.405	29.10
4	773	10%	.405	21.68	16	773	3%	0.486	31.49*
					16	773	3%	0.486	29.53*

* Rates are corrected to $P_{O2} = 0.4$ atm assuming reaction order of n = 0.7

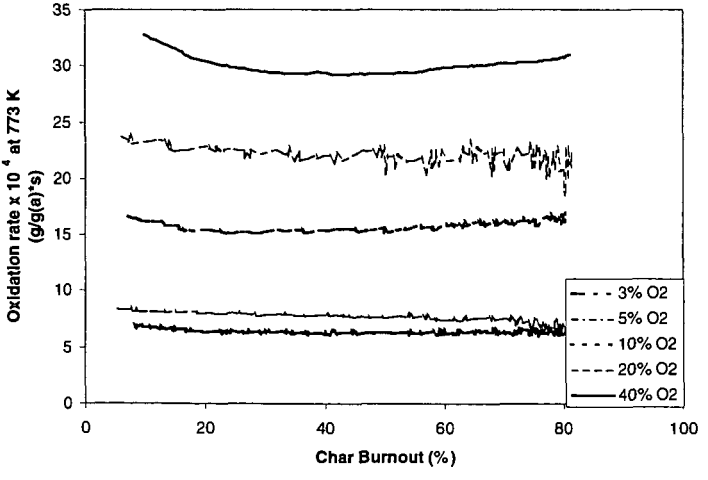

Figure 1. Effect of burnout on oxidation rate of Sample P1 at 4 atm, 773 K, and varying oxygen mole fraction.

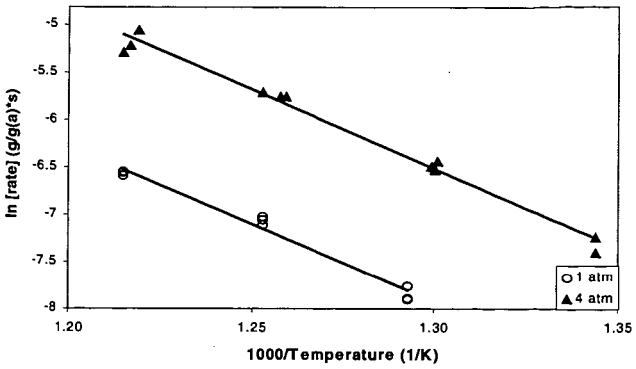

Figure 2. Arrhenius plots for oxidation rate of Sample P1 at 1 and 4 atm. All data taken at $y_{O2} = 0.10$. Activation energies are 32.7 kcal/mol and 33.2 kcal/mol at 1 atm and 4 atm, respectively.

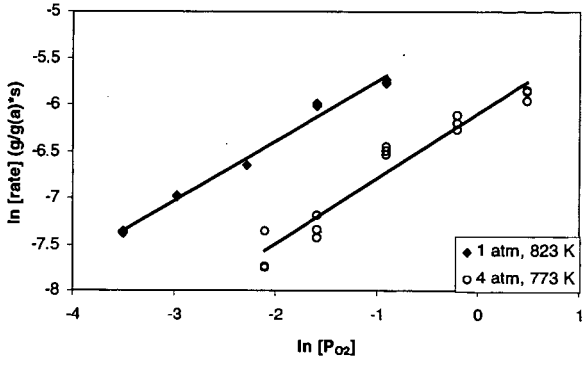

Figure 3. Effect of oxygen partial pressure on oxidation rate of Sample P1 at 1 atm (823 K) and 4 atm (773 K). Linear regression is applied to calculate reaction order using the nth-order kinetic model. Reaction orders are 0.64 and 0.70 for 1 atm and 4 atm, respectively.

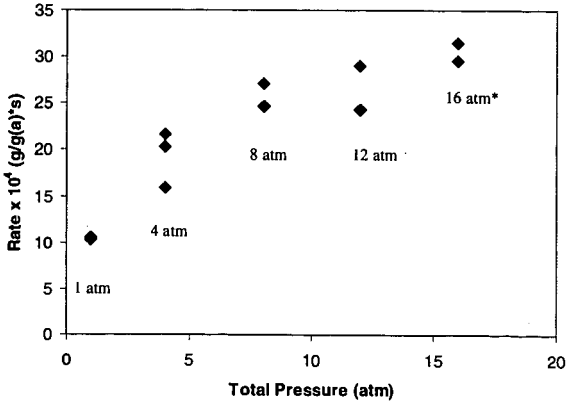

Figure 4. Effect of total pressure on oxidation rate of Sample P2 at $P_{O2} = 0.4$ atm and 773 K. *Rates at 16 atm are corrected to $P_{O2} = 0.4$ atm assuming reaction order of n=0.7

In situ CIR-FTIR Characterization of Catalytic Cracking of Supercritical Endothermic Fuels Over Different Zeolites

Zissis A. Dardas[1], William R. Moser[2], Louis J. Spadaccini[1] and David R. Sobel[1]
[1] United Technologies Research Center
East Hartford, CT, 06108
Tel: (860) 610-7371
Fax: (860) 610-7879
E-mail: dardasz@utrc.utc.com

[2]Worcester Polytechnic Institute
Department of Chemical Engineering
Worcester, MA, 01609

INTRODUCTION

Endothermic hydrocarbon fuels offer the potential to be utilized as heat sinks for increased cooling for high aircraft flight speeds by undergoing cracking reactions on a zeolite catalytic substrate prior to injection into the combustion system (1, 2). For maintaining high catalytic activities over the required fuel processing times, it is necessary to minimize the amount of coke that is rapidly formed on the catalyst as a by-product in these reactions. Early studies on different hydrocarbon catalytic processes under supercritical conditions including paraffin and olefin isomerization (3-7), xylene isomerization on Ga-containing molecular sieves (8), benzene and ethyl benzene disproportionation over USHY (9), isoparaffin-olefin alkylation over MCM materials (10) and Fisher-Tropsh synthesis on silica supported metal based catalysts (11) demonstrated the beneficial effect of supercritical reaction conditions on the catalyst activity. Product selectivity differences were also observed by comparing gas phase with supercritical processes. However, all these processes were performed at temperatures only slightly above the critical temperature of the system ($1 < T/Tc < 1.1$) where significant changes in the fluid density occur with changes of the pressure near the critical pressure (12). Therefore, the observed differences were attributed to gas-like diffusivities and liquid-like densities of the supercritical fluid. The liquid-like density of the supercritical fluid should result to the in situ extraction of the coke precursors from the catalyst pores.

Sobel et al. (2) demonstrated that high temperature cracking of endothermic jet fuels at supercritical pressures ($1 < P/Pc < 4$) over zeolites resulted in an increase of the catalyst life time relative to gas phase process conditions. This was surprising since at the high temperatures required for catalytic cracking of hydrocarbon fuels (well above 450 °C), very high pressures (above 2500 psi, i.e. $P/Pc > 8$) are demanded for the supercritical fuel to reach liquid-like densities. However, the development of high temperature, high pressure packed bed autogeneous infrared monitoring microreactors for heterogeneous catalysis based on Cylindrical Internal Reflectance (CIR) revealed for the first time that hydrocarbons exposed to micropores under supercritical catalytic cracking conditions led to super dense liquid like phase within the fine pore structure (13, 14). The super dense phase observed had the effect of maintaining the activity of zeolites under high conversion cracking conditions by solubilizing in situ coke precursor molecules, resulting in lower amounts of coke deposited within the zeolitic micropores.

EXPERIMENTAL

In situ infrared spectra were acquired using a Cylindrical Internal Reflectance (CIR) annular packed-bed micro-reactor described elsewhere (13, 14). The principle of this technique is the following: When an IR beam is directed through a polished cylindrical crystal at an incident angle exceeding the critical angle, it undergoes a number of internal reflections at the interface with the catalyst sample and penetrates into it. The penetration depth at each point of internal reflection (usually around 1-1.5 μm) depends on the incidence angle, the radiation wavelength and the ratio of the refractive indices of the sample and the crystal while the number of total internal reflections for a specified incident angle is a function of the length and diameter of the crystal. The high-pressure CIR-micro-reactor was mounted in the sample compartment of the FTIR spectrometer. The cell was encapsulated within a heated copper-alloy block. A high-pressure metering pump and a downstream back-pressure regulator were used to control fuel circulation. Approximately 20 seconds were required for the reactor to reach steady-state conditions. The nominal residence times (contact times) were kept con-

steady-state conditions. The nominal residence times (contact times) were kept constant and equal to 1.3 sec for tests performed at different pressures by adjusting the fuel flow rates. A Sigma 2000 gas chromatograph was used for reaction-product identification and analysis. The products were analyzed by a flame ionization detector and separated by a Chrompack 10-ft x 0.125-in. column of n-octane on 80/100 mesh Poracil C.

RESULTS AND DISCUSSION

Two different aluminosilicate zeolites were evaluated in this study:

(1) Promoted Octacat, a commercial mixture of 27 wt. percent ultra-stable H-Y zeolite (Si/Al = 9), 3 wt. percent HZSM-5 (Si/Al = 25) and 70 wt. percent dilution matrix (mainly kaolinite clays).

(2) Two commercial HZSM-5's with different Si/Al ratios (Si/Al = 30 and 126).

The Y-type zeolite has large-pores (7.4 °A) and three-dimensional structure formed by rings of 12 linked tetrahedra with circular-pore openings, while the ZSM-5 is a medium-pore, three-dimensional, 10-membered-ring system of circular (5.5 °A) and elliptical (5.1 x 5.7 °A) interconnecting channels. Norpar 12 (a mixture of C_{10} to C_{13} normal paraffins) was selected as a surrogate jet fuel. Tests were conducted at pressures up to 1000 psia and temperatures up to 1300 F.

Promoted Octacat

The FTIR spectra of the C-H bonds during catalytic cracking of Norpar 12 at 950 F are shown in Figure 1 for subcritical (180 psia), critical (300 psia) and supercritical (600 and 950 psia) pressures. The substantial increase in the spectrum intensity with pressure suggests an increased concentration of the hydrocarbon molecules within the zeolitic micro-pores. This is illustrated more clearly in Figure 2, which compares the density measured within the zeolite pores (proportional to the IR signal) with the density determined from thermophysical properties data for hydrocarbon mixtures provided in the NIST computer program SUPERTRAPP[3]. (Both fuel densities are normalized to the density at the critical point.) The results suggest a super-dense or liquid-like reaction mixture within the pores of the zeolite at supercritical pressures. This behavior should be beneficial for the in situ solubilization/extraction of the coke precursors from the zeolitic micro-pores, resulting in a stabilization of the catalyst. However, very dense fuel could limit the diffusion within the zeolitic micro-pores and, therefore, lower the reaction rate. Thus, there may be an optimum supercritical pressure (i.e., reaction mixture density) at which the catalyst performance is maximized, for a specified operating temperature and flow rate. Outside the micro-pores and on the external surface of the catalyst, the fuel behaves as a gas, with no coke-precursor extraction potential. Buildup of coke on the external surface could eventually block the pore openings, restricting access into the active sites, and result in a partial deactivation of the catalyst.

The catalytic cracking of Norpar 12 on P-Octacat at 950 F for subcritical and supercritical pressures is presented in Figure 3. For each operating pressure, the catalyst activity decreased with time-on-stream for the first 100 minutes, and then reached a steady state with no further deactivation over the 4-hour test. As shown in the figure, conversion to gaseous products is low at this moderate operating temperature, which was specified as the maximum allowable for preserving the optical properties of the ZnSe crystal. The results demonstrate that, for a constant residence time, the catalyst activity increases with increasing pressure.

The CIR-FTIR technique is capable of monitoring in situ the amount of coke formed during the course of the reaction because the area under the coke infrared spectral bands is roughly proportional to the amount of coke deposited on the catalyst. In Figure 4, the area of the infrared coke bands is plotted as a function of the time-on-stream. This figure illustrates that coke builds up rapidly, until a steady state is reached at which time the rate of coke formation apparently equals the rate of solubility of the coke precursors by the supercritical fluid. After 4 hours of reaction at 950 psia, the pressure was gradually decreased and a significant increase in the intensity of the coke spectral bands was observed that was accompanied by a corresponding decrease in the concentration of active zeolitic acid sites.

HZSM-5

In general, HZSM-5 would be expected to have a lower tendency for coke formation than P-Octacat due to the structural geometry and position of the acid sites, which make it difficult to form large polynuclear hydrocarbons. As previously mentioned,

the channels are narrower than the Y-type zeolite, and there are no large internal cavities. Therefore, there is little space available within the zeolitic micro-pores for coke precursor molecules to grow. Thus, coke formation occurs predominately on the external surface. The catalytic activity of HZSM-5 depends strongly on the Si/Al ratio, which determines the concentration of acid sites within the zeolite lattice. The lower the Si/Al ratio, the higher the conversion, but also the higher the tendency for coke formation within the micro-pores. Therefore, there is an optimum Si/Al ratio.

The effect of pressure on coke formation during the catalytic cracking of Norpar 12 over P-Octacat and HZSM-5 (Si/Al = 126) at 950 F is illustrated in Figure 5. These experiments were conducted by initiating the reaction at the highest pressure and maintaining it for 4 hours, whereupon the pressures were reduced sequentially. Infrared spectra were collected after 1 hour of steady operation at each of the lower pressures. As this figure indicates, the integrated area under the coke infrared bands is always significantly lower for HZSM-5 than for P-Octacat, most likely due to the smaller pore openings which restrict the size (molecular weight) of the coke precursors that can form and engender a higher fluid density (solubility) within.

The conversion to gaseous products by HZSM-5 is compared to that by P-Octacat in Figure 6. In these tests, HZSM-5 was tested at 700 psia while P-Octacat was tested at 950 psia. Since the HZSM-5 contains the smaller pores, its performance is expected to optimize at a lower supercritical pressure than P-Octacat, because of the trade-off between coke precursor solubility and species diffusion. As shown in the figure, HZSM-5 with Si/Al = 126 can operate at 60-percent conversion to gaseous products for long reaction times, while a lower Si/Al ratio of 30 resulted in high initial conversion but rapid deactivation. In comparison, P-Octacat (which contains 3 percent HZSM-5 with Si/Al=25) can maintain only 10-percent conversion to gaseous products at this temperature.

Reaction Endotherms

The chemical heat sink (endotherm) is a function of not only conversion but also product distribution. Furthermore, many applications of interest involve operation at fuel temperatures that are considerably higher than the 950 F limit of the CIR apparatus. To determine the heat sink attainable with the two catalysts at higher temperatures, tests were conducted in a Bench-Scale Reactor Rig. The results of these tests are presented in Figure 7, and show that P-Octacat has approximately twice the cooling capacity as HZSM-5. These results imply that P-Octacat has the higher selectivity for unsaturated olefinic species, and suggest that a choice between catalysts should be made based on the requirements of the application, i.e., lifetime vs. heat sink capacity. Furthermore, the data suggest that the P-Octacat could be improved by replacing HZSM-5, Si/Al=25 with Si/Al=126, and increasing its concentration.

CONCLUSIONS

Supercritical catalytic cracking of Norpar 12 over different zeolites resulted in higher catalyst activity and lower coke deposition within the zeolitic micropores relative to the low pressure gas phase reaction conditions. In situ CIR-FTIR analysis demonstrated that this beneficial effect was due to the condensation effect of the supercritical hydrocarbon fuel within the zeolitic micropores. The liquid-like density of the fuel resulted in an in situ extraction of coke precursors, suppressing the coke deposition in the catalyst. Supercritical catalytic cracking of Norpar 12 over various HZSM-5's resulted in higher fuel conversion and lower coke deposition relative to P-Octacat (a commercial faujasite-type zeolite) but also in lower fuel endotherm (i.e. lower fuel cooling capacity). However, a ZSM-5 with a Si/Al ratio of 126 was found to be the optimum catalyst, since it maintained its activity for long operating times.

LITERATURE CITED

(1) Spadaccini, L. J., Colket, M. B., and Manteney, P. J., Endothermic Fuels for High Speed Aircraft, Proceedings of the 1990 JANNAF Propulsion Meeting, October 1990.
(2) Sobel, D. R., and Spadaccini, L. J., International Gas Turbine and Aeroengine Congress & Exposition, Houston, TX, June 5-8, 1995.
(3) Tiltscher, H. W., and Schelchhorn, J., Angew. Chemie. Int. Ed., 20, 892 (1981).
(4) Tiltscher, H. W., and Schelchhorn, J., Phys. Chem., 88, 897 (1984).
(5) Tiltscher, H. W., and Hoffman, H., Chem. Eng. Sci., 45, 5 (1987).
(6) Ginosar, D. M., and Subramanian, B., J. Catal., 152, 31 (1995).

(7) Bhinde, M. V., and Hsu, C. Y., CA Patent, 2,693,373 (1992).
(8) Amelse, J. A., and Kutz, N. A., US Patent, 5,030,788 (1991).
(9) Manos, G., and Hoffman, H., Chem. Eng. Technol., 14, 73 (1991).
(10) Altaf, H., WO Patent, 9,403,415 (1994).
(11) Yokota, K., and Fujimoto, K., Ind. Eng. Chem. Res., 30, 95 (1991).
(12) Reid, R. C., Prausnitz, J. M., and Poling, B. E., The Properties of Gases and Liquids, MCGraw Hill, Inc., Fourth Edition, 36 (1987).
(13) Dardas, Z., Suer, M. G., Ma, Y. H., and Moser, W. R., J. Catal., 159, 204 (1996).
(14) Dardas, Z., Suer, M. G., Ma, Y. H., and Moser, W. R., J. Catal., 162, 327 (1996).

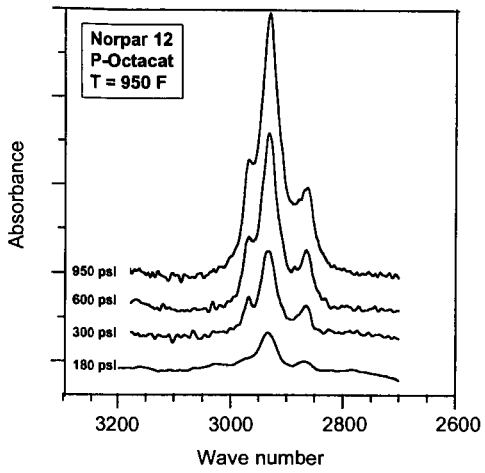

Figure 1. Infrared spectra of Norpar 12 hydrocarbon fuel C-H bonds within zeolite pores.

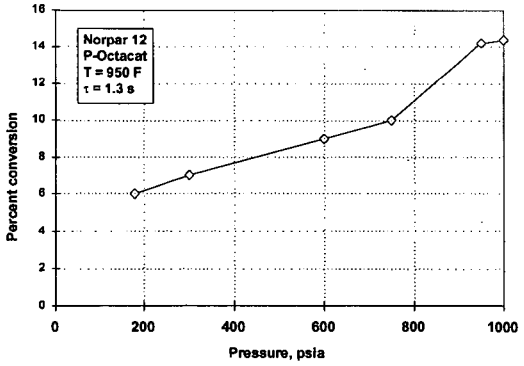

Figure 2. Reduced fuel density within zeolite pores.

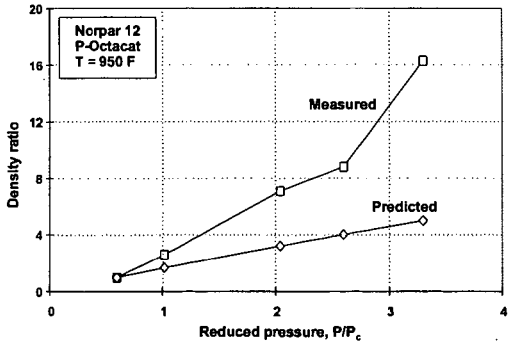

Figure 3. Conversion of Norpar 12 during catalytic cracking over P-Octacat.

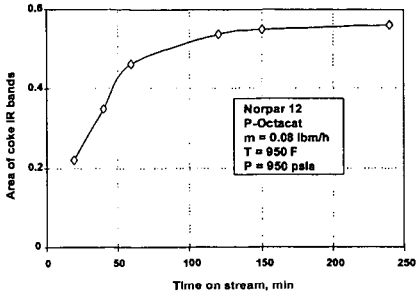

Figure 4. Area of coke infrared spectral bands.

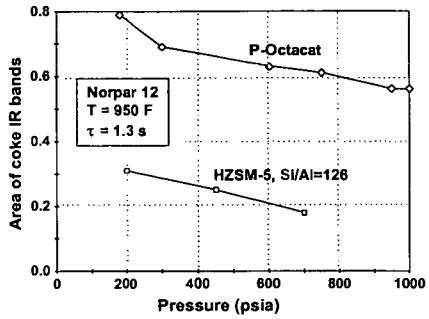

Figure 5. Effect of catalyst on coke deposition.

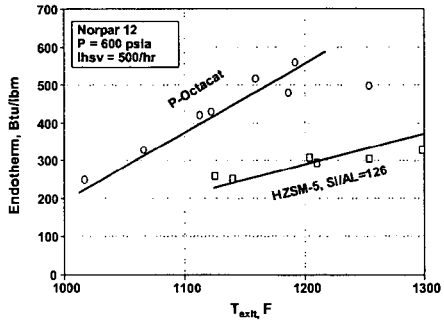

Figure 6. Degradation of catalytic activity

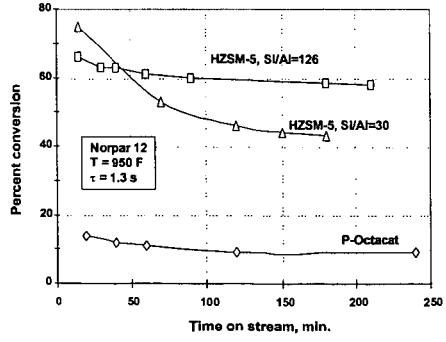

Figure 7. Endotherms for P-Octacat and ZSM-5, Si/Al=126.

FLOW PROPERTIES OF ASPHALT CEMENTS BY COMPOUNDING WITH SYNTHETIC POLYMERS

Pei-Hung Yeh, Ioan I. Negulescu and William H. Daly
Macromolecular Studies Group, Department of Chemistry,
Louisiana State University, Baton Rouge, LA 70803-1804
Louay N. Mohammad
Department of Civil Engineering and Environmental Engineering,
Louisiana State University, Baton Rouge, LA 70803

INTRODUCTION

Modification of asphalt cements with polymeric materials is widely used to improve pavement performances. Since the addition of polymers increases the cost of the corresponding polymer modified asphalt cement, industrial by-products and recycled polymers have been utilized as the modifiers within the past few years. However, understanding an asphalt-polymer system plays an important role in developing modified asphalts. This includes an understanding of the chemistry and mechanics of compatibility, reinforcement, and stability, and developing of new techniques to characterize modified asphalt binders.

Standard procedures for studying the physical and engineering properties of asphalt have been developed under auspices of the Strategic Highway Research Program (SHRP).[1] Testing and grading systems are based on measuring engineering properties that are related in a more rational way to the pavement performance. The new test methods offer the capability of measuring some properties such as rigidity, elasticity, brittleness, and durability in conditions that simulate loading and climatic conditions encountered in the field.

Our research has been devoted to characterizing asphalts and polymer modified asphalts. Polyethylene (HDPE), a recyclable waste polymer, was slightly chlorinated to improve its compatibility with asphalt.[2] Both HDPE and chlorinated polyethylene (CPE) modified asphalts were studied according to the Strategic Highway Research Program (SHRP) test methods to quantify the interaction of polymer with the asphalt matrix. The results of a testing protocol based upon thorough rheological evaluation of asphalts both before and after simulated aging, as well as three-point bending data at low temperature to ascertain brittleness will be reported. Preliminary characterization results on aspahlt cements prepared with a CPE modified binder will be presented.

MATERIALS AND METHODS

Asphalts and Polymeric Additives

Modified asphalts were prepared using AC-10 grade materials. Polymers investigated as asphalt additives were high density polyethylene (HDPE) and chlorinated polyethylene (CPE). The properties of HDPE and CPE's (5.8 and 24.5 wt% Cl) prepared for this study were determinated as previously described.[3]

The asphalt was heated to 150°C and stirred vigorously while either HDPE or CPE was added. Then the polymer asphalt blend was stirred at 150°C for 40 minutes.

Representative asphalts and modified asphalts were selected for thin film oven test (TFOT) and pressure aging vessel (PAV). All samples (50±0.5g) were aged in the TFOT oven @ 163°C for 5 hours under a continuous air flow. The TFOT samples were submitted to next aging step in the PAV at 100°C and 300 psi for 20 hours.

Differential Scanning Calorimetry (DSC)

Differential scanning calorimetry (DSC) data were obtained using a SEIKO DSC 220C instrument with a rate of 10°C/min. Each specimen was cooled from room temperature to -140°C, then heated from -140 to 160°C, and then was cooled from 160 to -100°C at the same rate. The glass transition temperatures (Tg), melting points (Tm), and enthalpy (ΔH) of the blend components were determined as previously described.[4]

Rheology Measurements

A dynamic shear rheometer (Bohlin CVO) was used for dynamic mechanical analysis of asphalt binders with the stress of 150 Pa @.1.5 Hz. The samples were "sandwiched" between two parallel plates with a diameter of 25 mm at a gap of 1 mm and cooled down to 5°C through one cycle before recording measurements. The reference temperature was taken as T= 64°C to comply with the performance graded asphalt binder specification particularized for the hot climate typical of Louisiana.

Bending Beam Rheometer measurements

The bending beam rheometer (Applied Test System) was used to characterize the low temperature stiffness response of PAV aged tank asphalts and asphalt/polymer blends. The data, which were recorded at six loading times (8, 15, 30, 60, 120, and 240 sec) for a load on the beam of 100 ± 5 g, allowed the calculation of the creep stiffness, S(t), and the creep rate of the sample under load, m, as the absolute value of the slope of the log creep stiffness versus log loading time curve.

Creep and Recovery Tests

A constant stress creep/creep recovery test was run at 50°C with a Haake rheometer (RheoStress RS150) using a 25 mm parallel plate system with a gap of 0.25 mm. During a first test stage, the specimen was subjected to a creep stress of 100 Pa. The resulting deformation were measured and recorded. The resiliency of the asphalt binders was evaluated after the first test phase, then the stress was released and the specimen was allowed to relax to an equilibrium deformation. The elastic recovery can be calculated by the retained deformation caused by the irreversible viscous flow process.

RESULTS AND DISCUSSION

The thermal behavior of asphalt/polymer blend is complex, and depends on asphalt sources and polymer types. Figure 1 is DSC curves of AC-10 blended with HDPE or CPE, which shows that the thermogram of AC10/HDPE blend has the melting peak (Tm) at 120°C. However, in the thermogram of AC10/CPE blend it moved down to 113°C. This phenomenon indicates that introduction of chlorine atoms onto the polymer chain can change the polymer polarity as well as the morphology by reducing the crystallinity. The resultant modification adjusts the interaction parameters to enhance dispersion of both the crystalline and amorphous regions into the asphalt phase. The Tm of CPE compounded with AC-10 decreases dramatically as the chlorine content increases. For instance, it has been observed that Tm of CPE (24.5 %wt Cl) went down to 46°C when blended with AC-10 (Figure 1).

Dynamic shear tests are advantageous because the data can be acquired in a loading mode that is similar to that of traffic loading. All isochronal sinδ curves of blends with HDPE as illustrated in Figure 2 approached unity at higher temperatures as the viscoelastic fluids begun to flow. A sinδ of unity confirms that the flow is Newtonian and that the polymer particles do not interfere with the measurement. However, as Figure 3 depicts, the sinδ of blends with CPE curves are substantially less than one. Clearly, the asphalt binders containing CPE are not Newtonian even at high temperatures. The chlorinated HDPE exhibits good interaction with the polar fractions of asphalt cement which could result in increased visco-elastic properties in AC10/CPE binders and improve the pavement performance.

In Strategic Highway Research Program asphalt specifications, the stiffness parameter, G*/sin δ, was selected to express the contribution of the asphalt binders to permanent deformations. G*/sinδ value should be larger than 1000 Pa @ 10 rad/s for the original binder. Higher values of the parameter ratio are expected to result in a higher resistance to permanent deformation. Isochronal plots of G*/sinδ (Figure 4) reveal distinct differences due to the modifiers ability to mix with asphalt. Both of the modified asphalts are qualified according to SHRP specification of the stiffness parameter at 64°C. However, only the blends containing chlorinated HDPE meet the SHRP specification at 70°C. Introduction of chlorine atoms enhances compatibility between the polymer additives and asphalt, thus the volume of the polymer rich phase is increased due to an improved 'solubility' in the asphalt. The increases are significant and are expected to result in improving pavement resistance to rutting when the pavement is open for service.

In order to evaluate the permanent deformation (rutting) and the fatigure cracking of aged asphalt binders, the SHRP specifications require determination of G* and its components for TFOT and PAV aged materials. The permanent deformation is related to the ratio G*/sinδ, which must be at least 2.2 KPa after TFOT aging at the specified high temperature. The product of G*sinδ (or G") is represented as fatigue cracking factor in asphalt pavements, i.e. a maximum limit of 5000 KPa at a low temperature in

the SHRP asphalt specifications. The ability to dissipate or relax the stress is a desirable binder character in resisting fatigue cracking. An inspection of Figure 5 shows that there is no significant difference between tank AC10 and AC10/HDPE in the TFOT stage. Gross phase separation occurs during thin film aging of the AC10/HDPE blend, which reduces the blend properties to those of unmodified asphalt. The $G^*/\sin\delta$ of AC10/CPE blend is somewhat higher than that of the aged tank asphalt; partial phase separation occurred in this blend at high temperature but the polymer is still contributing to the blend properties. All of these binders meet the qualification of SHRP specifications at 64°C. On the other hand, tests on the fatigue cracking for PAV asphalt binders (Figure 6) show that both the loss modulus (G") of the PAV aged AC/HDPE and of the AC/CPE blends are less than that of the PAV aged tank asphalt at all temperatures. Extrapolation of the data to the temperature at which $G^*\sin\delta$ reaches 5000 kPa illustrates this point. An estimate of the temperature for AC/HDPE or AC/CPE can be obtained from the intercept of the extrapolation which is much lower than that of the aged tank sample. It appears that a drastic reduction in the loss modulus can be attributed to the polymer additive (HDPE or CPE). This improvement should be effective in reducing age hardening and long term temperature cracking.

Preliminary low temperature creep properties of asphalt blends using a bending beam rheometer can be obtained by knowing the creep load applied to the beam and its deflection at several loading times during the test. According to SHRP program, the stiffness S(t) and the creep rate of the binder under load $m = |d \log S(t) / d \log(t)|$ are reported at the specified temperature after a 60 seconds loading, which simulates the stiffness after two hours at a 10°C lower temperature. A SHRP grade temperature should meet the specifcations S (t=60) ≤ 300 MPa and m-value (slope) ≥ 0.3. The data in Figure 7 indicate that all asphalt binders met the S(t) and m-value performance criteria for the chosen temperature (-12°C).

The creep and recovery measurements provide rheological data which are characteristic to a particular binder under conditions employed. The constant stress creep/creep recovery test in Figure 8 illustrates a significant difference between the deformation of CPE and HDPE blends. This observation might be an indication of their rutting resistance, i.e., the lower the deformation, the better the binder response to rutting, which is related to the composition of the asphalt binder. The AC10/CPE material showed a much more pronounced resistance to creep than AC/HDPE or pure asphalt at 50°C. Elastic creep recovery of asphalt samples can be observed after the stress is removed. As expected, the AC10/CPE blend exhibited higher creep recovery than HDPE blend due to the presence of the more elastic filler. On the other hand, the pure asphalt sample did not display any recovery and the presence of HDPE in asphalt did not improve any recovery percentage under these conditions. Therefore, it would be expected to have an asphalt binder with a rutting resistance higher than the maximum resistance imparted by the tank asphalt.

ACKNOWLEDGMENTS

This work was supported by a contract from the Louisiana Transportation Research Center. Special appreciation is extended to Harold Paul who served as the contract technical representative and provided helpful and incisive comments and suggestions.

REFERENCES

1. Anderson, D., Kennedy, T.W., Proceedings of the Association of Asphalt Paving Technologists, 1994, Vol 62, 481.
2. Canterino, P.J., Kahle, G.R., J. Appl. Polym. Sci., 1962, 6, 20.
3. Daly, W. H., Negulescu, I. I., Yeh, P.-H., Prep. Symp. Am. Chem. Soc., Div. Fuel Chem., 1998, 43, 1075.
4. (a). Daly, W. H., Qiu, Z-Y., Negulescu, I. I., Transportation Research Record, 1996, 1535, 54.
   (b). Daly, W. H., Qiu (Chiu), Z-Y., Negulescu, I. I., Transportation Research Record, 1993, 1391, 56.

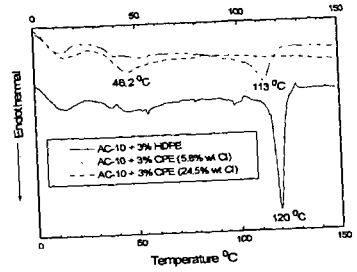

Figure1. DSC thermograms of asphalt AC-10 blended with HDPE or CPE

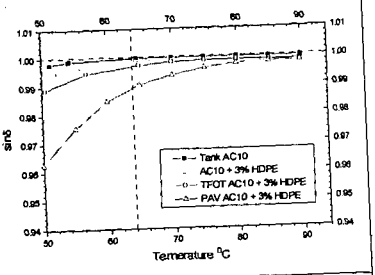

Figure2. Variation of sinδ with temperature for a blend of AC-10 with 3% HDPE

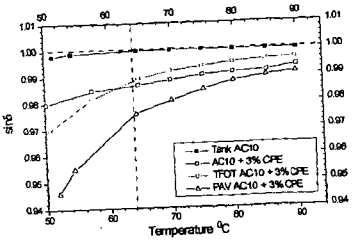

Figure3. Variation of sinδ with temperature for a blend of AC-10 with 3% chlorinated HDPE (5.8 wt% Cl)

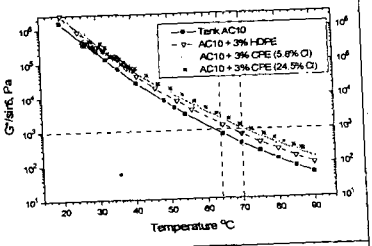

Figure4. Comparison between rutting factors of tank asphalt and blends with HDPE or chlorinated HDPE

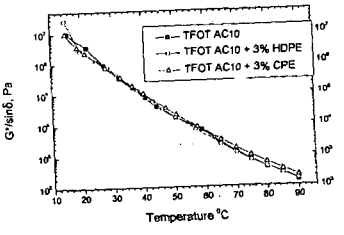

Figure5. Variation of G*/sinδ with temperature for tank asphalt and of blends with HDPE or chlorinated HDPE (5.8 wt% Cl)

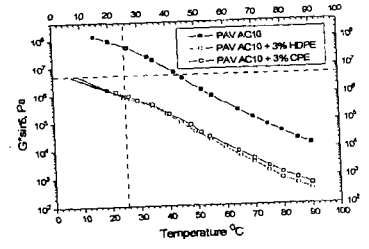

Figure6. Variation of G*sinδ with temperature for tank asphalt and of blends with HDPE or chlorinated HDPE (5.8 wt% Cl)

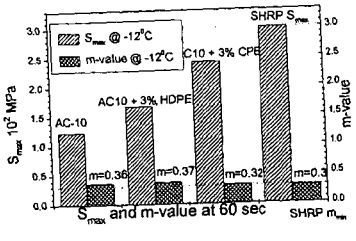

Figure7. Creep stiffness of PAV aged AC10 blends containing HDPE and chlorinated HDPE (5.8 wt% Cl)

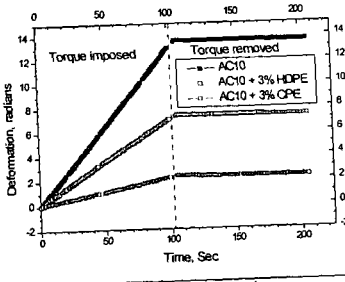

Figure8. Constant stress creep/creep recovery curves at 50°C of AC10 blends with HDPE or CPE (5.8 wt% Cl)

Hydrogenation Reactivity of Mono-Aromatic Compound in Polar Solvents over Ru/Al_2O_3 Catalyst

Hideyuki TAKAGI, Takaaki ISODA, Katsuki KUSAKABE
and Shigeharu MOROOKA

Department of Materials Physics and Chemistry,
Graduate School of Engineering, Kyushu University,
Fukuoka 812-8581, Japan

KEY WORDS: hydrogenation, mono-aromatic compound, polarity of solvent

INTRODUCTION

Hydrogenation of aromatic compounds is a key reaction in processes such as hydrorefining of heavy oil and production of petrochemicals. Platimun group metals have the advantage of high activity for the hydrogenation of aromatic compounds under mild reaction conditions. However, the hydrogenation activity of this metal catalyst is sometimes decreased by the presence of solvents. Thus, the solvent effects can be significant, especially for the case of noble metal catalysts, which are used for the hydrogenation of asphalthene, coal extracts and polymers under mild conditions. In a previous studies [1], we reported that oxidized Yallourn coal, which had been treated with aqueous H_2O_2 in the presence of 1-propanol at 70°C, was solubilized in ethanol at a yield of 80 wt%, based on the dry raw coal mass. The ethanol-solubilized coal was further hydrogenated over a Ru catalyst at 120°C under a hydrogen pressure of 10 MPa for 72 h [2]. As a result of this catalytic hydrogenation, the aromaticity of the coal structure was altered, and the pyrolysis reactivity was increased. However, hydrogenation reactivity of aromatic compounds in solvents other than ethanol has not yet been investigated.

In the present study, therefore, benzyl alcohol was subjected to hydrogenated using Ru/Al_2O_3 catalyst at 120°C under a hydrogenation pressure of 6 MPa. Lower alcohols, non-polar solvents and solvents containing oxygen, sulfur and nitrogen were used in these reactions, and their effect on the efficiency of the reaction was examined. Carboxylic acids were also added to the reaction system, and the effect of these compounds on the hydrogenation reactivity of aromatic compounds was also determined.

EXPERIMENTAL

Chemicals and Catalysts: Benzyl alcohol was used as substrate. Methanol (MeOH), ethanol (EtOH) and 2-propanol (2-PrOH) were used for alcoholic solvents; hexane, heptane and benzene were used for non-polar solvents; acetone, 1,4-dioxane, tetrahydrofuran (THF) and diethyl ether (DEE) were used for polar solvent containing oxygen; and dimethyl sulfoxide (DMSO), N,N-dimethyl formamide (DMF) and N-methyl-2-pyrrolidone (NMP) were used for polar solvents containing sulfur and nitrogen. Formic acid (HCOOH), acetic acid (CH_3COOH), butyric acid (C_3H_7COOH) and lauric acid ($C_{11}H_{23}COOH$) were selected for use as added carboxylic acids in the hydrogenation reaction of benzyl alcohol. An alumina supported ruthenium catalyst (Ru/Al_2O_3, Wako chemical Co., metal content=5wt%) was used as the hydrogenation catalyst.

Reaction: The hydrogenation reactions were performed in a 50 mL batch autoclave at 120°C for 0.5 h under a hydrogen pressure of 6 MPa, equipped with a magnetic stirrer, rotating at 1000 rpm. 3 g of substrate, 6 g of solvent, and 0.5 g of catalyst were mixed, and carboxylic acid, of which usage was 3g, was further added to the reaction system. After hydrogenation, the catalyst was separated by centrifugation. Products were qualitatively and quantitatively analyzed by GC-FID (Shimadzu, GC-14A) and GC-MS (Shimadzu, QP-5000), equipped with a capillary column. The hydrogenation conversion of substrate was calculated as the following equation.

$$\text{Hydrogenation conversion [\%]} = (1 - N/100) \times 100 \quad (1)$$

where N [%] was the yield of unreacted substrate. The δ value of a solvent was defined by

$$\delta = DN - AN \quad (2)$$

where DN is the donor number, and AN is the acceptor number, of the solvent [3-4]. The relative permittivity for a mixture of solvents i and j, P_{mix}, was calculated from the following equation.

$$P_{mix} = (P_i X_i + P_j X_j) / (X_i + X_j) \quad (3)$$

where P_i and P_j are the relative permittivites of solvent i and solvent j, respectively [5]. X_i and

X_j are the mass fractions of solvent i and solvent j, respectively, (X_i+ X_j = 1).

RESULTS

Figure 1 shows the product distributions for the hydrogenation of benzyl alcohol in the presence of the solvents. The conversion of benzyl alcohol was 76% in methanol, 82% in ethanol and 81% in acetic acid. This indicates that methanol, ethanol and acetic acid had little or no effect on the hydrogenation activity over the Ru/Al_2O_3 catalyst. When 2-propanol was used as the solvent, the total conversion of benzyl alcohol was decreased to 35%. When hexane and heptane, which are non-polar solvents, were used as the solvent, the hydrogenation conversion of benzyl alcohol was 75% and 61%, respectively. However, the conversion of benzyl alcohol was decreased to 35% by the addition of benzene. When acetone, THF, dioxane and diethyl ether were used as the solvent, the conversion of benzyl alcohol was 31, 36, 51 and 28%, respectively. These solvents strongly retarded the hydrogenation activity over the Ru/Al_2O_3. The hydrogenation of benzyl alcohol was completely inhibited when DMSO, DMF and NMP were used as the solvent.

Figure 2 shows the product distributions for the hydrogenation of benzyl alcohol dissolved in polar solvents in the presence of carboxylic acids over the Ru/Al_2O_3. When ethanol was used as the solvent, the hydrogenation of benzyl alcohol was increased in the presence of acetic acid, butyric acid and lauric acid. The added carboxylic acids remained unchanged during the hydrogenation reaction under the above reaction conditions. However, formic acid strongly inhibited the hydrogenation of benzyl alcohol. When THF and acetone were used as the solvent, the addition of acetic acid increased the hydrogenation reactivity, as observed in ethanol.

Figure 3 shows the pathways for the hydrogenation of benzyl alcohol over the Ru/Al_2O_3 catalyst at 120°C. The hydrogenation of aromatic ring (route 1) and the hydrogenolysis of hydroxy group (route 2) proceed competitively. The 1-cyclohexanylmethanol is converted to cyclohexanecarbaldehyde [6]. Toluene is produced via route 2 and methylcyclohexane is produced via hydrogenation of toluene.

DISCUSSION

Figure 4 shows the relationship between the hydrogenation conversion of benzyl alcohol and the δ values of the solvents. The donor number represents the parameter which is associated with the solvent basicity, while the acceptor number is the parameter which is associated with the solvent acidity. Thus, the effect of solvents on the hydrogenation reactivity of benzyl

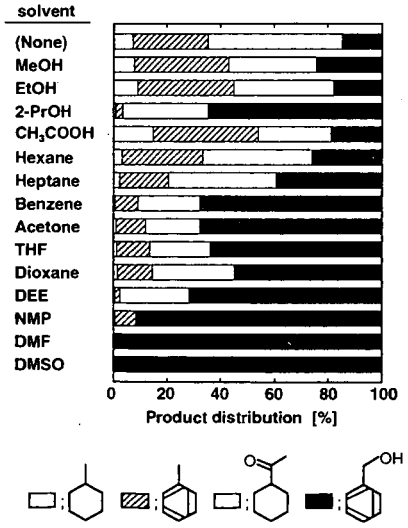

Figure1. Product distributions for the hydrogenation of benzyl alcohol over Ru/Al_2O_3 catalyst.

alcohol using the Ru catalyst is classified into four categories as follows: (1) Solvents with negative δ values are capable of accepting electrons, and methanol, ethanol, acetic acid and hexane are classified into this group. The conversion with respect to the hydrogenation of benzyl alcohol is approximately 80 % for all these solvents. Thus, the negative δ values of the solvents have no effect on the hydrogenation reactivity of benzyl alcohol over the Ru catalyst. (2) Benzene and 2-PrOH possess negative δ values and accept electrons. Since benzene was hydrogenated more preferentially than benzyl alcohol, the hydrogenation of benzyl alcohol was decreased in the presence of benzene. In the case of 2-PrOH, as shown in Figure 2, the yield of toluene is decreased in the presence of 2-PrOH to a greater extent than by methanol and ethanol. Meanwhile, the yield of cyclohexanecarbaldehyde in 2-PrOH is the same as that in methanol and ethanol. Thus, the hydrogenolysis of benzyl alcohol is suppressed by the addition of 2-PrOH. (3) Solvents with positive δ values are capable of transferring electrons, and acetone, THF, dioxane and diethyl ether can be classified into this group. In the presence of these solvents, the hydrogenation conversion decreases with increasing the δ values of the solvents. Ruthenium adsorbs oxygen-containing solvents via an interaction between the surface of the ruthenium and the pair of unshared electrons of the oxygen atom of the solvents. The active sites of the catalyst are occupied by electron donor solvents to a greater extent than electron acceptor solvents, and, as the result, the hydrogenation conversion of the substrate is decreased in the presence of members of this solvent group. (4) The activity of the Ru catalyst is inactivated in the presence of DMSO, DMF and NMP, which contain either sulfur or nitrogen.

Figure 5 shows the relationship between the hydrogenation conversion of benzyl alcohol and the relative permittivity of the solutions. The relative permittivity is related to solvent polarity. The relative permittivity is 13.1 for benzyl alcohol, 24.3 for ethanol, 20.7 for acetone and 7.4 for THF. The relative permittivity of acetic acid is 6.2, which is much smaller than that of formic acid, 58.0. Thus, the polarity of mixed solvents is decreased by the addition of acetic

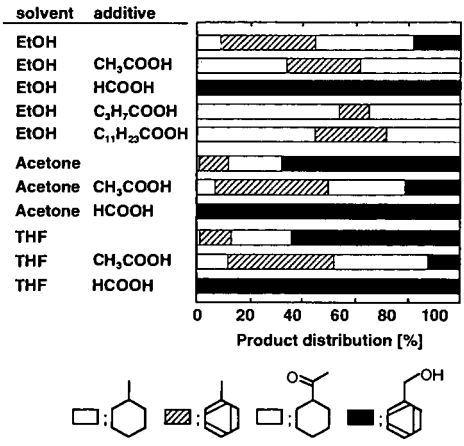

Figure 2. Product distributions for the hydrogenation of benzyl alcohol in polar solvents in the presence of carboxylic acids.

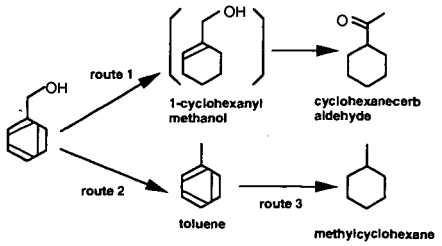

Figure 3. Pathway for the hydrogenation of benzyl alcohol over Ru/Al_2O_3 catalyst.

acid, and increased by that of formic acid. By the addition of acetic acid, the hydrogenation conversion of benzyl alcohol in ethanol, acetone and THF is increased, however, the hydrogenation reactivity is diminished by the addition of formic acid. Since formic acid is a solvent as protogenic as acetic acid, it is an electron acceptor. In addition, the relative permittivity of formic acid is much larger than that of acetic acid. Thus, the hydrogenation reactivity is affected by relative permittivity rather than the δ value for the case of formic acid.

CONCLUSIONS

1. A relationship between the hydrogenation reactivity of benzyl alcohol in polar solvent and the δ value of the solvent was found. Solvents with negative δ values did not affect the hydrogenation of benzyl alcohol over the Ru catalyst. However, solvents with positive δ values suppressed the hydrogenation of benzyl alcohol.
2. DMSO, DMF and NMP, which contained sulfur or nitrogen, deactivated the Ru catalyst.
3. The hydrogenation reactivity of benzyl alcohol in polar solvent was increased by the addition of acetic acid, butyric acid and lauric acid. The hydrogenation reactivity was related to the relative permittivity of solution. However, the hydrogenation reactivity was completely lost by the addition of formic acid with a high permittivity.

ACKNOWLEDGEMENTS

This research was supported by Japan Society for the Promotion of Science (JSPS), Organization of New Energy and Industrial Technology Development Organization (NEDO), and Center for Clean Coal Utilization, Japan (CCUJ). Support by Research for the Future Projects (Coordinator; Prof. M. Iino, Tohoku Univ.) and International Joint Research Program (Coordinator; Prof. M. Nomura, Osaka Univ.) is especially acknowledged.

REFERENCES

[1] Isoda, T.; Tomita, H.; Kusakabe, K.; Morooka, S.; Hayashi, J.-i. *Proc. of Intern. Conference on Coal Science* **1997**, *2*, 581.
[2] Isoda, T.; Takagi, H.; Kusakabe, K.; Morooka, S. *Energy Fuels* **1998**, *12*, 503.
[3] Gutmann, V. *Angew. Chem. Intenat. Ed.* **1970**, *9*, 843.
[4] Marzec, A.; Juzwa, M.; Betlej, K.; Sobkowiak, M. *Fuel Proc. Tech.* **1979**, *2*, 35.
[5] Fowler, F.W.; Katritzky, A.R.; Rutherford, R.J.D. *J. Chem. Soc. (B)* **1971**, 460.
[6] Nishimura, S.; Hama, M.; *Bull. Chem. Soc. Jpn.* **1966**, *39*, 2467.

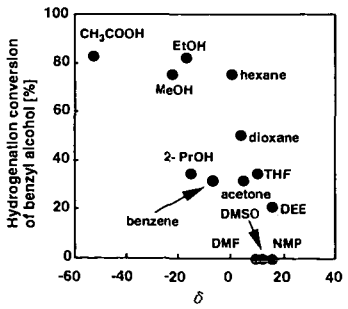

Figure 4. Relationship between hydrogenation conversion of benzyl alcohol and δ values of solvents.

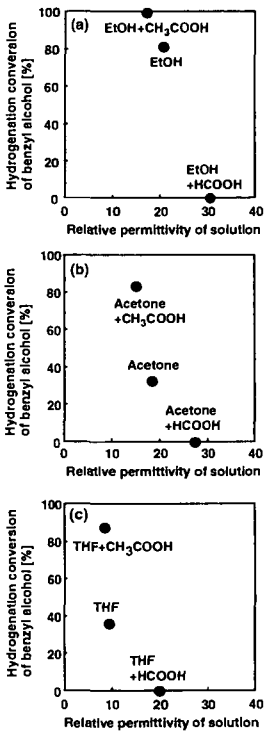

Figure 5. Relationship between hydrogenation conversion of benzyl alcohol and relative permittivity of solutions. Solvent; (a) EtOH, (b) acetone, (c) THF.

METHANE ACTIVATION AND AROMATIZATION WITHOUT USING OXIDANTS OVER Mo/H-ZSM-11 CATALYSTS

Shuang Li [a], Chunlei Zhang [b], Dongyang Wang[a], Qiubin Kan[a], Tonghao Wu [a], Liwu Lin[b]

(a. Department of Chemistry, Jilin University, Changchun, 130023;
b. State Key Laboratory for Catalysis, Dalian Institute of Chemical Physics , Chinese Academy of Sciences, PO Box 110, Dalian 116023, P. R. China)

Introduction

With the development of natural gas exploration, the catalytic conversion of methane has become one of the focal subjects of extensive research in heterogeneous catalysis. Methane aromatization without using oxidants, which produces high value and easily separated liquid aromatic hydrocarbons as well as effectively controls deep oxidation of methane, has intrigued many researchers recent years[1-6]. As regards the supports of catalysts for this reaction, only H-ZSM-5, SiO_2, Al_2O_3 and SAPO-34 *et al* have been used up to now, and the last two have relatively low activity and selectivity[4,5,6]. In our previous work[7], the catalytic performance of various zeolites supported Mo-based catalysts, such as H-ZSM-11, H-ZSM-8, and H-¦Âetc. were studied for methane non-oxidative aromatization, and possible structural rules of fine supports for this reaction were proposed. A new zeolite supported catalyst — Mo/H-ZSM-11 — was found for this reaction, which exhibits even better catalytic behavior than Mo/H-ZSM-5. In the present paper, some detailed information about Mo/H-ZSM-11 catalysts, such as the dependence of reaction temperature, space velocity of methane and MoO_3 loading on the catalytic performance of Mo/H-ZSM-11 catalysts have been studied and the optimization of the Mo/H-ZSM-11 catalyst was carried out.

Experimental

Synthesis of H-ZSM-11 zeolite and preparation of Mo/H-ZSM-11 catalysts. H-ZSM-11 (SiO_2/Al_2O_3 = 25, 50, 100, 200) was synthesized following the method in ref [8] using TBA^+ as template by hydrothermal method.

A mixture of MoO_3 and zeolite was made by grinding. A prescribed amount of MoO_3 with the above-prepared H-ZSM-11 zeolites was thoroughly ground, then calcined at 773K for 4h in air. So the Mo/H-ZSM-11 catalyst was obtained.

Catalytic Test. Methane non-oxidative aromatization reactions were carried out in a fixed-bed continuous-flow 8-mm i.d. quartz microreactor. The catalyst charge was 1.0 g (40 ~ 60 mesh). The reaction temperature is 973K. After pretreatment, pure methane was introduced into the reactor at a space velocity of $800h^{-1}$. The reaction mixture was analyzed by a on-line shimadzu GC-8A gas chromatograph in temperature programmed mode using a 3.5m Porapak P column and detected with TC detector. The methane conversion and product selectivity were calculated on a carbon number base without accounting for coking.

Results and Discussion

The effect of MoO_3 loading on the activity of Mo/H-ZSM-11 catalysts. Variations of the activity of Mo/H-ZSM-11 catalysts with different MoO_3 loadings are shown in Table 1. It can be seen that a maximum of methane conversion and benzene selectivity is observed at MoO_3 loading of 5wt%. Further increasing MoO_3 loading causes the decrease in methane conversion and aromatics selectivity notably. Therefore, the MoO_3 loading on H-ZSM-11 of about 3~5wt% is optimal, which is about the same as that on H-ZSM-5. The XRD patterns of Mo/H-ZSM-11 with different MoO_3 loadings show that the MoO_3 crystallite pattern could not be detected if the MoO_3 loading is less than 10%. It indicates that the Mo species are highly dispersed on the H-ZSM-11 zeolite in the as-prepared Mo/H-ZSM-11 catalyst.

The effect of reaction temperature on the activity of Mo/H-ZSM-11 catalysts. As shown in Fig. 1, the activity of Mo/H-ZSM-11 catalyst increases with rising temperature. It is similar to the phenomenon observed over Mo/H-ZSM-5 catalyst. This result is in correspondence with the thermodynamic calculation, that is, methane aromatization under non-oxidative condition is an endothermic reaction, therefore high temperature is more favorable to methane conversion. At different temperatures methane conversion all decrease with increasing time on stream, and the speeds of the decrease of methane conversion are in order of: 923K < 973K < 1023K < 1073K(Fig.1), that is, the higher the reaction temperature is, the faster the methane conversion decreases. This is probably due to the increase of the carbon depositing rate over Mo/H-ZSM-11 catalysts with increasing reaction temperature. By comparison, the Mo/H-ZSM-11 catalyst shows relatively higher activity and stability at 973K, and the selectivity to aromatics is also somewhat higher. So the optimal reaction temperature on Mo/H-ZSM-11 is ~ 973K. XRD patterns of reacted catalysts at various temperatures illustrate that the structure of H-ZSM-11 zeolite is not destroyed.

The effect of methane space velocity on the catalytic performance of Mo/H-ZSM-11. The effect of space velocity of methane on the catalytic performance of Mo/H-ZSM-11 is shown in Fig.2. Evidently, the activity of catalysts increase in order of 1500, 800, $250h^{-1}$ space velocity

of methane, that is, the lower the space velocity of methane, the higher the conversion of methane, and the higher the selectivity to aromatics. Clearly, lower space velocity of methane is favorable to the conversion of methane and aromatics production. This phenomenon is similar to that obtained over the Mo/H-ZSM-5 catalyst, which indicates that on the Mo/H-ZSM-11 catalyst ethylene could also be supposed to be the intermediate of methane non-oxidative aromatization. That is, the lower the space velocity, the longer the contact time between methane and the surface of the catalyst, and the larger amount of intermediate ethylene converted to aromatics.vorable to the conversion of methane and aromatics production. This phenomenon is similar to that obtained over the Mo/H-ZSM-5 catalyst, which indicates that on the Mo/H-ZSM-11 catalyst ethylene could also be supposed to be the intermediate of methane non-oxidative aromatization. That is, the lower the space velocity, the longer the contact time between methane and the surface of the catalyst, and the larger amount of intermediate ethylene converted to aromatics.

The effect of SiO_2/Al_2O_3 ratio on the activity of Mo/H-ZSM-11 catalysts. The effect of SiO_2/Al_2O_3 ratio on the activity of Mo/H-ZSM-11 is shown in Table 2. It can be seen that with decreasing SiO_2/Al_2O_3 ratio, the activity of Mo/H-ZSM-11 increases. That is, the higher the SiO_2/Al_2O_3 ratio is, the lower the methane conversion and selectivity to aromatics are. As is well known, the lower the SiO_2/Al_2O_3 ratio is, the more AlO_4 tetrahedral in zeolite framework there is, as a result, the stronger the acidity of H-ZSM-11. the more AlO_4 tetrahedral in zeolite framework there is, as a result, the stronger the acidity of H-ZSM-11.Therefore, the changes of catalyst activity with different SiO_2/Al_2O_3 ratios reflect the effect of zeolite acidity on the reaction.

Table 1 The effect of MoO_3 loading on activity of MoO_3/H-ZSM-11 catalysts[a]

MoO_3 loading	Methane conversion	Selectivity (%)		
(%)	(%)	Aromatics (C_6+C_7)	C_2	CO
1	4.79	86.0	8.90	5.10
3	8.18	91.5	5.10	3.40
5	8.59	93.1	4.94	1.99
6	7.77	87.7	7.10	5.20
10	5.65	86.2	9.88	3.90

a. SiO_2/Al_2O_3=25, reaction temperature 973K.

Table 2 The effect of SiO_2/Al_2O_3 ratio on activity of 3%wt MoO_3/H-ZSM-11 catalysts at 973K

SiO_2/Al_2O_3 ratio	Methane Conversion (%)	Selectivity (%)		
		Aromatics (C_6+C_7)	C_2	CO
25	8.18	91.5	5.10	3. 40
50	7. 87	92.2	4.89	2.89
100	7.11	91.3	5.15	3. 55
200	5.06	84.1	6.72	9.18

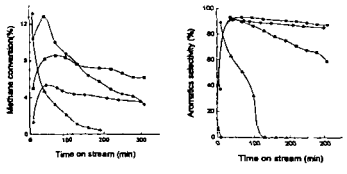

Fig.1 Methane conversion and aromatics selectivity over 5%MoO_3/H-ZSM-11catalysts with time on stream at different temperatures: 923K, ♦; 973K,■; ,1023K, •; 1073K,▲.

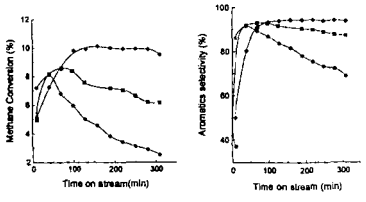

Fig.2 Methane conversion and aromatics selectivity over 5%MoO_3/H-ZSM-11 at different space velocity(◆, 250h^{-1}; ■, 800h^{-1}; •,1500h^{-1}).

References

[1] L. Wang, L. Tai, M. Xie, G. Xu, J. Huang and Y. Xu, Catal. Lett. 21(1993)35
[2] Y. Xu, S. Liu, L. Wang, M. Xie and X. Guo, Catal. Lett. 30(1995)135
[3] L. Chen, L. Lin, Z. Xu, T. Zhang, and X. Li, Catal. Lett. 39(1996)169
[4] S. Wong, Y. Xu, L. Wang, S. Liu, G. Li, M. Xie and X. Guo, Catal. Lett. 38(1996)39
[5]F. Solymosi, A. Erdohelyi and A. Szoke, Catal. Lett. 32(1995)43
[6]D. Wang, J. H. Lunsford and M.Rosynek, Paper presented at the 14th Meeting of the North American Catalysis Society, Snowbird, 1995;
[7] C. Zhang, S. Li, Y. Yuan et al. Catal. Lett. 56(1998)207
[8] G. A. Jablonski, L. B. Sand and J. A. Gard, Zeolites 6(1986)396